DOE/ET/20255-T2(Vol.5)
(DE84002711)

THE CROSBYTON SOLAR POWER PROJECT (PHASE I)

Technical Report of Work Accomplished from September 1, 1976–
February 15, 1978

February 1978

Work Performed Under Contract No. AC04-76ET20255

Texas Tech University
Lubbock, Texas

TECHNICAL INFORMATION CENTER
U. S. DEPARTMENT OF ENERGY

DISCLAIMER

This report has been reproduced directly from the best available copy.

Available from the National Technical Information Service, U. S. Department of Commerce, Springfield, Virginia 22161.

Price: Printed Copy A23
Microfiche A01

Codes are used for pricing all publications. The code is determined by the number of pages in the publication. Information pertaining to the pricing codes can be found in the current issues of the following publications, which are generally available in most libraries: *Energy Research Abstracts (ERA); Government Reports Announcements* and Index (*GRA* and I); *Scientific and Technical Abstract Reports (STAR);* and publication NTIS-PR-360 available from NTIS at the above address.

DOE/ET/20255-T2(Vol.5)
(DE84002711)
Distribution Category UC-62b

THE CROSBYTON SOLAR POWER PROJECT

(PHASE 1)

TECHNICAL REPORT OF WORK ACCOMPLISHED

FROM

SEPTEMBER 1, 1976 TO FEBRUARY 15, 1978

BY

TEXAS TECH UNIVERSITY,

E-SYSTEMS, INC.,

AND

FOSTER WHEELER ENERGY CORPORATION

SUBMITTED TO

THE

DEPARTMENT OF ENERGY

DIVISION OF SOLAR ENERGY

BY

TEXAS TECH UNIVERSITY

UNDER

CONTRACT NO. EY-76-C-04-3737

DR. JOHN D. REICHERT
PROJECT DIRECTOR

DR. HERBERT J. CARPER, JR.
PROJECT MANAGER

VOLUME V: APPENDICES A-L

The work reported here was performed by:

TEXAS TECH UNIVERSITY: Project Director - J. D. Reichert

Project Manager - H. J. Carper, Jr.

R. M. Anderson

C. A. Bell

R. M. Bethea

L. D. Clements

J. R. Dunn

W. T. Ford

A. L. Goldman

D. L. Gustafson

N. Guven

D. R. Haragan

D. P. Jordon

C. H. Keho

A. P. Kwatra

J. R. McDonald

W. M. March

C. M. Parrish

R. J. Pederson

T. L. Simpson

M. L. Smith

C. V. Vallabhan

F. P. Wagner

F. Williams

E-SYSTEMS, INC.

Program Director: W. E. Erikson

Program Manager: R. R. Walters

M. J. O'Neill

S. L. Hudson

D. E. Yakel

D. Muzzy

A. J. O'Donnel

J. L. Perry

L. Wilson

J. Smith

B. Sheard

A. Anderson

M. Quan

D. Halsey

D. Schools

V. Goldberg

D. Muzzy

The Project Director and Manger gratefully acknowledge our indefatigable secretarial and support staff:

Carolyn Barrier

Toni Smith

Tina Watts

Judy Clare

Fran Dupre

Lana Reed

Donna Cates

Nancy Birney

Sue Willis

Flo Meyers

Julio Garcia

Fran Schuessler

H. S. Leung

D. M. Barrett

S. Majumbar

D. A. Courtney

R. Callicutt

BRIEF TABLE OF CONTENTS

DETAILED TABLE OF CONTENTS

APPENDIX B RECEIVER SUBSYSTEM

APPENDIX A. OPTICAL-THERMAL-FLUID ANALYSES AND EXPERIMENTS

This appendix is a synthesis of analytical and experimental results centered on the optical properties of the concentrated solar energy, receiver absorption and heat loss characteristics, and internal-external heat transfer characteristics. Within this synthesis are contributions from E-Systems, Foster Wheeler, and a number of investigators at Texas Tech.

The appendix is arranged so that the problem of solar energy absorption by a working fluid is followed from the inside out. Analytical results provided by Foster Wheeler for modelling the internal heat transfer characteristics of the RPS steam-generating receiver confirm earlier analyses by E-Systems and Texas Tech. The problem of predicting flow stability in the steam receiver is addressed with the resulting recommendation by Foster Wheeler that most stability problems may be handled by insertion of a plenum between the subcooled and nucleate boiling regions of the receiver.

Results of static thermal stability tests with Caloria HT-43 confirm temperature limitations for hot oil operation. Experimental data from the E-Systems solar simulator show a close correspondence between predicted and measured receiver temperature profiles for water/steam and no apparent flow instability problems. Joule heated helical coil experiments at Texas Tech indicate that for that geometry there is an increase in internal heat transfer coefficient along the outer wall, compared with the inner wall. Experiments evaluating the effects of surface roughness on free convective heat transfer from a cylinder show an augmentation effect of 10 to 20%. The final experimental test covered is measurement of absorptivity as a function of incidence angle.

The optical analyses center on improved techniques developed at Texas Tech for handling mirror errors and on techniques for including multiple bounce reflections. The E-Systems efforts have included the effect of slope errors on reflected ray deviation, statistical distribution of circumferential slope errors, receiver energy interception as a function of receiver geometry and error level, and a revised flux distribution for an improved receiver geometry.

A-1 INTERNAL HEAT TRANSFER ANALYSES

This section continues the focus on the modelling and simulation of internal heat transfer performance for the FMDF receiver given in the Phase I, Segment I,report(1). Featured here are heat transfer simulation results for an RPS steam receiver and a preliminary evaluation of fluid flow stability provided under subcontract by Foster Wheeler Energy Corporation, Nuclear Department. The Foster Wheeler results are compared briefly with TTU and E-Systems results presented in Segment I. The applicability of these results to the ATS expected performance is discussed. Finally, there is a description of heat transfer expectations and restrictions for use of heat transfer oils directly in either an ATS or an RPS receiver.

A-1.1 Thermal/Hydraulic Analysès

Thermal and hydraulic analyses were performed by Foster Wheeler Energy Corporation for the RPS solar receiver design proposed by Texas Tech University and E-Systems for the Crosbyton Fixed Mirror Distributed Focus Solar Power Project. The objectives of these analyses were to evaluate the thermal performance and pressure drop calculations of the receiver and to establish the static and dynamic stability characteristics of the tubeside boiling flow.

The basic solar receiver-boiler is a once-through unit consisting of twenty (20) 0.375 in. outside diameter tubes which are spirally wrapped around the outside of a conical support structure. The bottom of the 57 ft. long cone (designated as X/R = 1.0) has a diameter of 2 ft., which tapers to a diameter of 1 ft. at the top of the receiver (X/R = 0.5). The uncoiled straight length of each of the 20 tubes is 431 ft.

In the basic design, subcooled (100°F) water at a pressure of 1000 psia enters the tubes from a plenum at the bottom of the receiver. This water is then heated by the absorbed solar insolation as it spirals upward along the length of the receiver, and is subsequently boiled and superheated.

Only the special case of 0° dish incidence, where the sun and receiver are in perfect alignment normal to the plane of the fixed mirror's open face, was considered. This condition results in a uniform concentration of solar radiation around the circumference of the receiver. Axial variations along the receiver were based on the tabulated values of solar concentration factor (C) versus axial receiver location (X/R) provided by the Texas Tech University. The thermal properties of the Inconel 617 material used for the tubing is given in Table A-1.

For the 0° incidence case, each individual tube will receive essentially the same heat input. Therefore, an averaged tube model was used for performance calculations. The average tube was divided into a number of elements for which individual heat balance and pressure drop computations were performed.

Thermal Model

The energy balance at the outer tube wall yields (see Fig. A-1):

$$Q_{absorb} = Io\alpha\beta - \sigma\varepsilon(T_1^4 - T_\infty^4) - h_{conv}(T_1 - T_\infty) \qquad (A\text{-}1)$$

where Io = normal incident of solar energy

α = absorptivity of receiver tube surface

β = reflectivity of collector mirror

TABLE A-1 THERMAL PROPERTIES OF INCONEL 617

Temperature ^{o}F	Thermal Conductivity Btu $in^2/ft\ hr\ ^{o}F$	Specific Heat Btu/lb/^{o}F
78	94	0.100
200	101	0.104
400	113	0.111
600	125	0.117
800	137	0.124
1000	149	0.131
1200	161	0.137
1400	173	0.144
1600	185	0.150
1800	197	0.157
2000	209	0.163

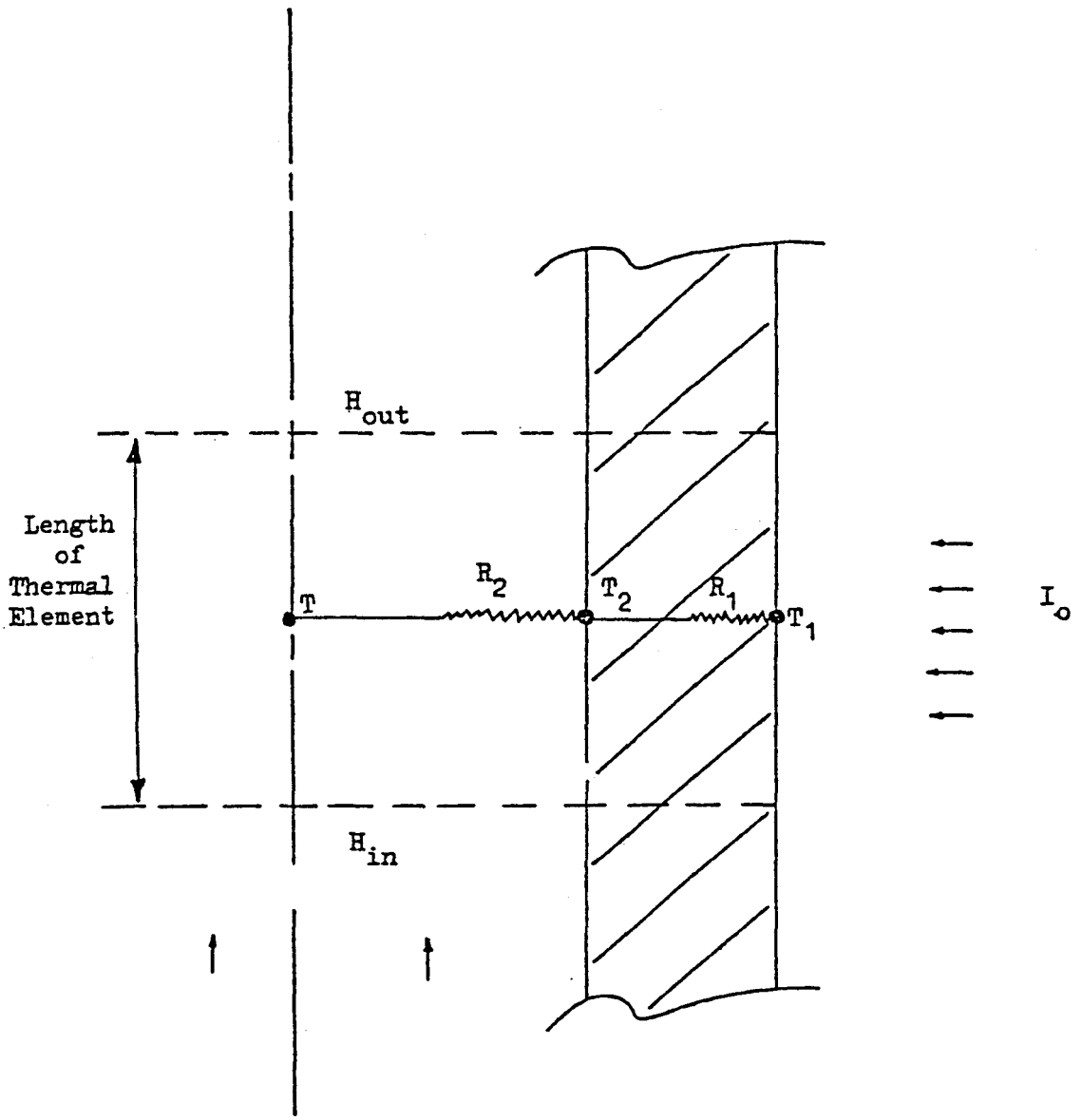

Figure A-1. Thermal Model

σ = Stefan-Boltzmann constant

ε = emissivity of receiver tube surface

h_{conv} = convection heat transfer coefficient outside receiver

T_1 = outside tube wall temperature, absolute

T_∞ = ambient temperature, absolute

Q_{absorb} = heat flux absorbed by receiver (O.D.)

The energy balance for a fluid element gives:

$$H_{out} = H_{in} + A\, Q_{absorb} \qquad \text{(A-2)}$$

where:

H_{out} = outlet enthalpy of the fluid element

H_{in} = inlet enthalpy of the fluid element

A = effective heat transfer area

In terms of fluid and wall temperatures, Q_{absorb} can be expressed as:

$$Q_{absorb} = \frac{T_1-T_2}{R_1} = \frac{T_2-T}{R_2} = \frac{T_1-T}{R_1+R_2} \qquad \text{(A-3)}$$

where:

R_1 = thermal resistance per unit area across the tubewall

R_2 = thermal resistance per unit area due to convection inside the tube

T = average temperature of the fluid element corresponding to the enthalpy of $(H_{in}+H_{out})/2$

T_2 = inside tube wall temperature

Substitution of Eq. (A-3) into Eqs. (A-1) and (A-2) yields:

$$\frac{T_1 - T}{R_1+R_2} = I\alpha\beta - \sigma\varepsilon(T_1^4 - T_\infty^4) - h_{conv}(T_1 - T_\infty) \qquad (A-4)$$

and:
$$H_{out} = H_{in} + \frac{A(T_1 - T)}{R_1 + R_2} \qquad (A-5)$$

Eqs. (A-4) and (A-5) together with the equation of state for water/steam properties

$$T = f(h, p) \qquad (A-6)$$

can be solved for T_1 and T (or H_{out}) by an iterative procedure, with given solar incidence intensity and tube side inlet fluid conditions. Q_{absorb} can of course be calculated from Eq. (A-1) once T_1 is known as a function of X/R.

Heat Transfer Correlations

The following heat transfer coefficients were used:

a) Subcooled Region

The Dittus-Boelter correlation is used (2)

$$Nu = 0.023\ Re_b^{0.8}\ Pr_b^{0.4} \qquad (A-7)$$

where: Nu = Nusselt No.

Re_b = bulk Reynolds number

Pr_b = bulk Prandtl number

b) Nucleate Boiling Region

Chen's Macro-micro heat transfer correlation (3) is used.

$$h = h_{mic} + h_{mac} \qquad (A-8)$$

or

$$h = S(0.00122)\ \frac{k_l^{0.79} c_l^{0.45} \rho_l^{0.49} g_e^{0.25} \Delta T^{0.24} \Delta p^{0.25}}{\delta^{0.5} \mu_l^{0.29} H_{fg}^{0.24} \rho_v^{0.24}}$$

$$+ F(0.023)(Re)_l^{0.8}(Pr)_l^{0.4}\ \frac{k_l}{D_e} \qquad \text{(A-9)}$$

Chen empirically obtained the values of two dimensionless functions, S and F, that allow for the variations in the boiling and forced convection components, respectively. Forster and Zuber's microconvective heat transfer relation for boiling and the Dittus-Boelter macroconvective heat transfer relation for forced convection are used.

c) Critical Heat Flux Correlation:

The possible existence of film boiling was checked by the critical quality given by the following equation (4):

$$X_{cr} = 1.0 + (0.139 - 0.071\ Pw^{0.186})\ q \times 10^{-5} \qquad \text{(A-10)}$$

where:

X_{cr} = Critical steam quality

Pw = pressure (atm)

q = heat flux ($kcal/m^2hr$)

This correlation is obtained in the following experimental range:

Pressure 51 ~ 171 atm (750 ~ 250 PSIA)

Mass Velocity 1.3×10^6 ~ 5.1×10^6 kg/m^2hr ($2.6 \sim 10 \times 10^6$ $lb/hrft^2$)

Heat Flux 0.5×10^5 ~ 5.5×10^5 $kcal/m^2hr$ ($0.18 \sim 2 \times 10^5$ $\frac{Btu}{hr\ ft^2}$)

d) Film Boiling Region:

If the local steam quality is greater than X_{cr}, the following film boiling coefficient, due to Bishop, Sandberg & Tong (5) is used:

$$\frac{hDe}{k} = 0.0193\ (Re_f)^{0.8} Pr_f^{1.23} \left(\frac{\rho_v}{\rho_{bulk}}\right)^{0.68} \left(\frac{\rho_v}{\rho_{sat}}\right)^{0.068} \quad \text{(A-11)}$$

f refers to film temperature given by $(T_2 + T)/2$,

T_2 = tube inner wall temperature

T = bulk fluid temperature

e) Superheated Region:

The Heineman's correlation is used (6)

$$Nu = 0.0133\ Re_b^{0.84}\ Pr^{0.33} \quad \text{(A-12)}$$

f) The thermal conductivity used for the Inconel 617 tubewall is given in Table A-1, and is correlated by the following formula:

$$k = 7.4244 + 0.00499T \quad \text{Btu/hr-ft-}^{o}\text{F} \quad \text{(A-13)}$$

condition is applicable for the temperature range:

$$78 \leq T \leq 2000^{o}\text{F} \quad \text{(A-14)}$$

Pressure Drop Correlations

a) Frictional Pressure Drop:

The frictional pressure drop in the subcooled liquid region as suggested by Mendler, et al (7) is used. For pressure from 800 to 1600 psia:

$$f/f_{iso} = 1 - 0.001\Delta T_f \qquad \text{(A-15)}$$

Here the isothermal friction factor f_{iso} is given by the Colebrook equation:

$$1/f_{iso} = -2 \log(\varepsilon/3.7D_e + 2.51/Re \sqrt{f_{iso}}) \qquad \text{(A-16)}$$

where: ε = pipe roughness

De = pipe hydraulic diameter

Re = Reynolds number

ΔT_f is calculated from:

$$\Delta T_f = q/h$$

where h is given by the Dittus Boelter equation and q is the local heat flux.

The minimum value of f/f_{iso} is 0.85

In the bulb boiling region, the Martinelli-Nelson two phase multiplier will be used (8) together with Colebrook's isothermal friction factor.

In the superheated region, the Colebrook's equation (A-16) is used directly.

The effect of coil spiraling on the friction factor is considered as an additional multiplier to the friction factor. The following formula due to Ito is used (9):

$$\frac{f_c}{f} = \left[Re\left(\frac{ro}{R}\right)^2 \right]^{0.05} \qquad \text{(A-17)}$$

where Re = Reynolds number inside the tube

ro/R = Tube radius/radius of curvature of coil

fc = friction factor of curved pipe

This formula correlates very well with experimental data as long as $Re\ (ro/R)^2$ is greater than 6.

b) Elevation Pressure Drop:

The elevation pressure drop is given by:

$$\Delta Pg = g/g_c \int_{Z_1}^{Z_2} dz/va \qquad \text{(A-18)}$$

where:

g = gravitational constant in the direction of flow

g_c = conversion factor

v_a = specific volume of fluid

Z_1, Z_2 = inlet and outlet evaluation of pipe.

For non-boiling heated regions va is equal to the bulk specific volume of the fluid. In the bulk boiling region, the specific volume is given by (10):

$$1/v_a = [(1 + X((\gamma/\alpha) - 1))/(1 + X(\gamma - 1))](1/vf) \qquad \text{(A-19)}$$

where: γ = slip factor

$\alpha = vg/v_f$

vg = specific volume of saturated vapor

vf = specific volume of saturated liquid

Both γ and α, are functions of the absolute pressure. γ and γ/α were curve-fitted using the experimental data given by Thom for the pressure range of 14.7 psia to 3206 psia (10). Further, if one assumes that the quality (X) change is linear, in the length of a nodal element i.e.

$$dX/dZ = (X^{out} - X^{in})\ L \qquad \text{(A-20)}$$

and the pressure change with the nodal element length, L, is small compared to the absolute pressure (i.e., γ and γ/α assumed to be constant), then the gravitational pressure drop will be given by:

$$\Delta Pg = (g/gc)\ (L/V_f)\ (B/D + D\text{-}B/D^2\ (1/(X^{out} - X^{in}))\ln\frac{(1+DX^{out})}{(1+DX^{in})} \qquad \text{(A-21)}$$

where $B = (\gamma/\alpha) - 1$

$D = \gamma - 1$

X^{out} = steam quality at element outlet

X^{in} = steam quality at element inlet

c) Acceleration Pressure Drop:

The acceleration pressure drop for the non-boiling heated region is given by:

$$\Delta P_a = G^2/gc(v_B^{out} - v_B^{in}) \qquad \text{(A-22)}$$

where v_B^{out} and V_B^{in} are the bulk specific volumes at outlet and inlet of an element respectively; and G is the mass velocity.

For the bulk boiling region, we have:

$$\Delta P_a = G^2/g_c(v_{eff}^{out} - v_{eff}^{in}) \qquad (A-23)$$

where v_{eff}^{out} and v_{eff}^{in} are the effective specific volumes at the outlet and inlet, respectively, given by (10):

$$V_{eff} = [1 + X(\gamma - 1)]\ \{1 + X[(\gamma/\alpha) - 1]\} \qquad (A-24)$$

Thermal/Hydraulic Performance Results

In each element under consideration, the conditions at the inlet are known. The energy balance equations (Eqs. A-4 and A-5) are first solved using an iterative procedure to obtain the outside tube-wall temperature and the fluid enthalpy at the exit of the element. The thermal resistance due to the tube and convection inside the tube are calculated based on the local conditions of the element. The pressure at the element exit is then computed using the correlations given above.

The incident radiation is equal to the product of the solar constant (300 Btu/ft^2-hr) and the concentration factor, C, which is a function of the location along the length of the receiver X/R. The following values are used in the analysis.

Inconel 617 tube material thermal properties per Table A-1

$\alpha = 0.9$

$\beta = 0.88$

$\varepsilon = 0.9$

$h_{conv} = 4.0$ Btu/hr ft^2 °F

The analysis used 431 elements (each element is 1 foot long). Waterside fouling was neglected. The calculated temperature distribution and heat flux of the receiver is shown in Fig. A-2. The calculated pressure profile is shown in Fig. A-3.

The results indicate that the superheated steam will exit at 738 psia. This gives a pressure drop of 262 psi, which is rather high for a steam generator with an inlet pressure at 1000 PSIA.

The superheated steam enthalpy at the steam generator exit is 1432 Btu/lb. If all incident radiation is absorbed by the receiver, the exiting steam will have an enthalpy of 1978 Btu/lb. Therefore an overall thermal efficiency for the receiver is calculated to be:

$$\eta = \frac{1432-70.36}{1978-70.36} \times 100 = 71.4\%$$

i.e., 71.4% of the incidence radiation is absorbed by the receiver.

The effect of water/steam pressure on the receiver performance was investigated and the results are summarized in Table A-2. As can be seen from this table, the increase in the system pressure increases the steam outlet temperature. However, the overall enthalpy pickup is decreased, resulting in the decrease in the overall thermal efficiency. This is mainly due to the increased heat loss associated with generally increased structural temperature as a result of pressure increase. Also note that the overall pressure drop decreases with increasing system pressure.

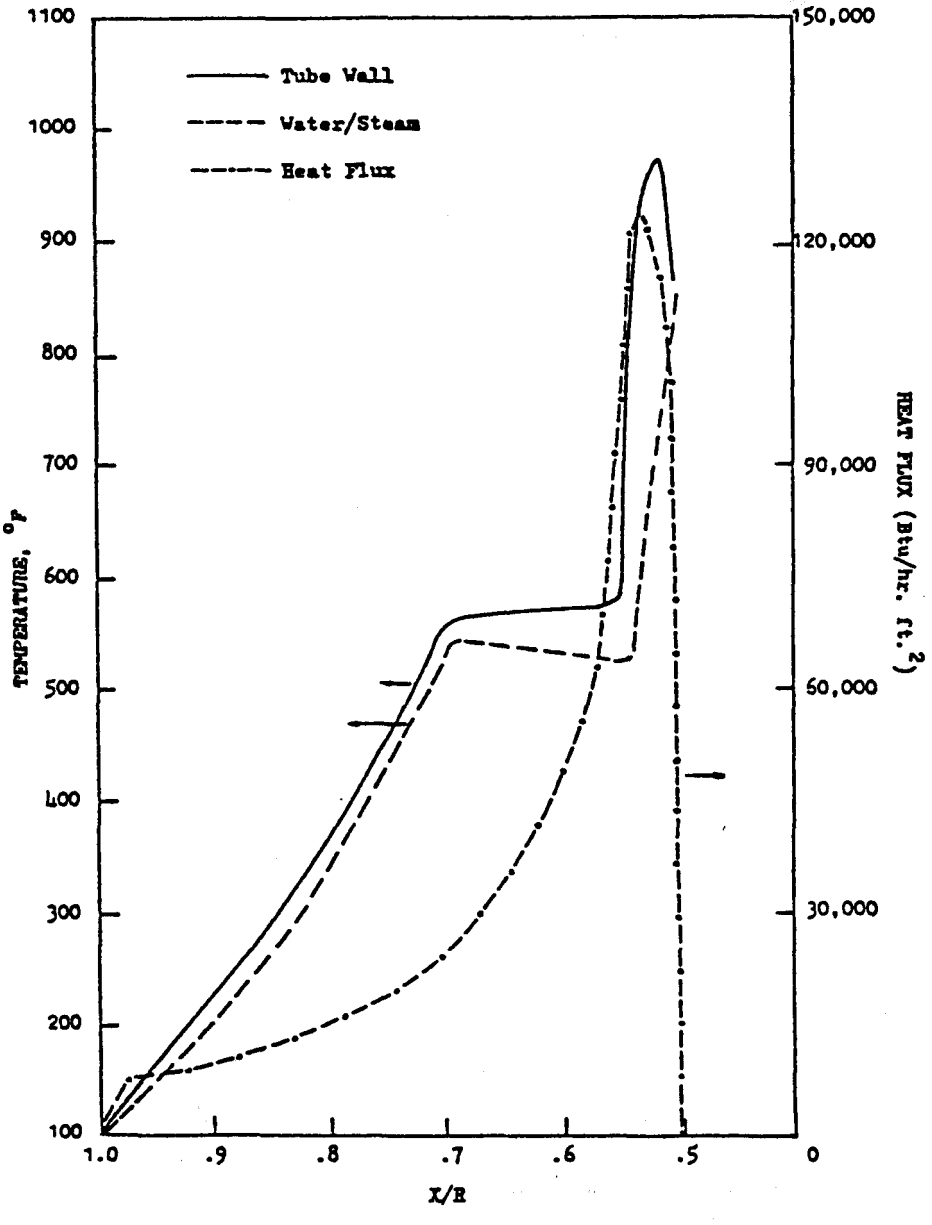

Figure A-2. Heat Flux and Temperature Profile at 0° Incidence

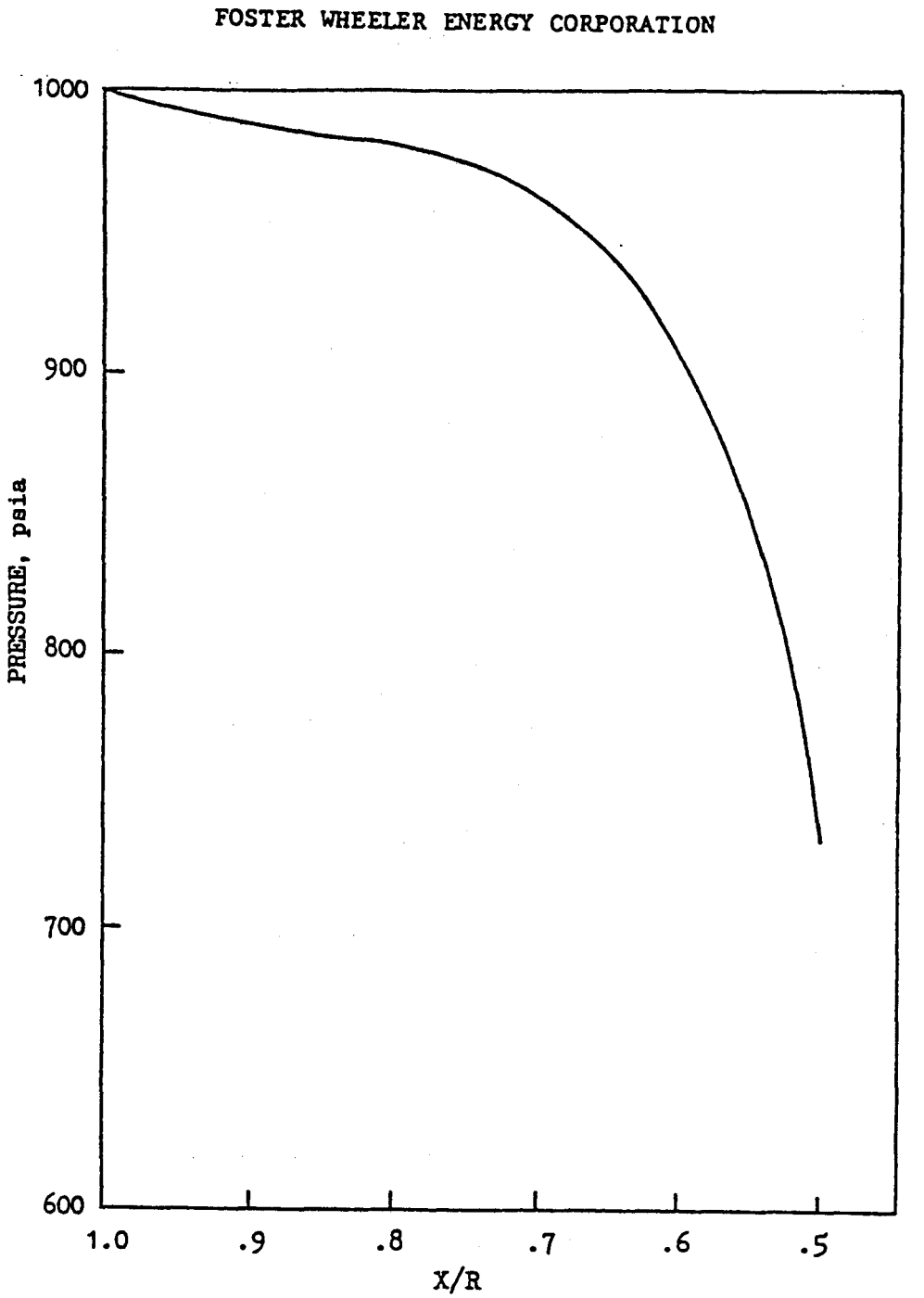

Figure A-3. Pressure Profile

TABLE A-2 EFFECT OF SYSTEM PRESSURE

ON RECEIVER PERFORMANCES

	Case 1	Case 2	Case 3
Inlet Pressure, psia	1000	1120	1160
Inlet Temperature, °F	100	100	100
Enthalpy Increase, Btu/lb	1362	1358	1358
Outlet Temperature, °F	854.2	858.3	860.6
Outlet Pressure, Psia	738	889.3	941.2
Pressure Drop, psi	262	231	219
Thermal Efficiency, %	71.4	71.2	71.2

Comparison Between Foster Wheeler, E-Systems and TTU Results

If we compare the temperature profiles shown in Fig. A-2 with those shown in A-4, we see that they are very nearly identical. The only significant difference is that since the Foster-Wheeler Model takes into account the effect of pressure drop on the saturation temperature during boiling, the Foster Wheeler curve shows a downward slope of temperature with X/R. The E-Systems and TTU simulations do not account for this effect.

A-1.2 Boiling Flow Stability Consideration

Two types of boiling instability were considered, namely static instability and dynamic instability.

Static Instability

The static instability of primary design importance in steam generators is the excursive instability of the Ledinegg type. A flow is subject to a static instability when the flow condition, if changed by a small perturabation, may not return to its original steady-state condition.

The static instability aspect of the subject once-through steam generator was analyzed for the condition specified in Section A.1. The results are presented in terms of the water/steam pressure drop versus the relative steam/water flow rate in Fig. A-5. Variation in the curve from positive to negative slope as the flow is increased indicates possible static instability. A small negative pertubation may drive the flow into a completely different state from the initial point.

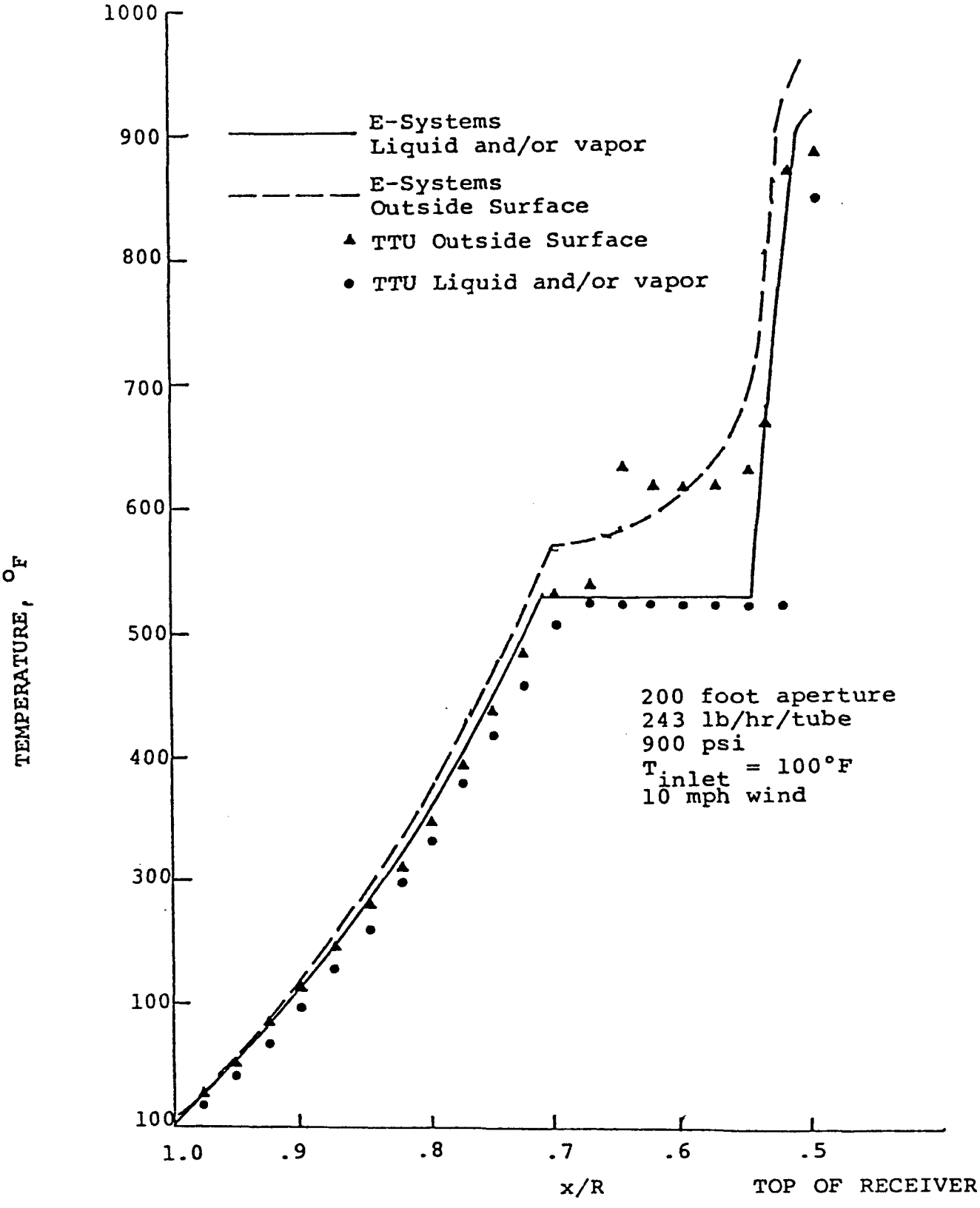

Figure A-4. Comparison of E-Systems and Texas Tech Receiver Analysis for the Nominal System

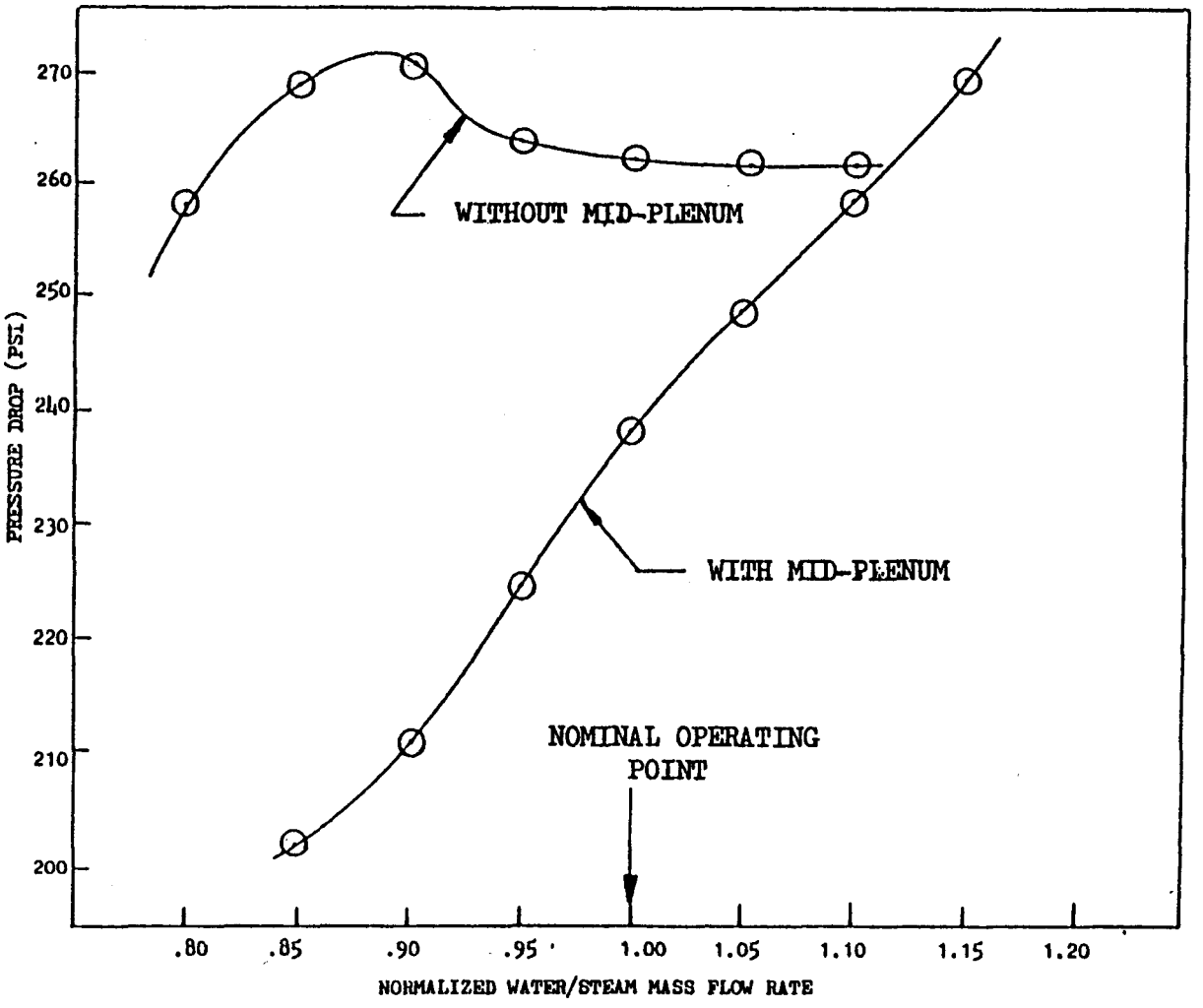

Figure A-5. Static Stability Diagram

Note that as the flow rate is increased, the pressure drop curve becomes negative. The reason for this behaviour can be explained by examining the pressure drop characteristics along the tube of the present design. From Figure A-3 it can be seen that this once-through unit has a very short superheated section. However, the pressure drop in this section contributes to almost one third of the total loss through the whole unit. As the flow rate is increased, the amount of superheat will decrease. When the pressure loss due to the superheated section is decreasing faster than the increase in the square of the mass flow rate, a negative slope in the pressure drop versus flow rate curve will result.

The presence of static boiling instability can be remedied by introducing a plenum between the subcooled and the boiling section of the steam generator. In doing so, the subcooled section pressure drop/flow characteristic will always have a positive slope. The pressure drop characteristic for the boiling and superheated section when such a plenum is introduced is shown by the lower curve of Figure A-5. Here a definite positive slope exists throughout the flow range which is indicative of statically stable water/steam flow.

Dynamic Instability

Dynamic flow instability is defined as sustained (or growing) oscillation of flow variables such as pressure drop, flowrate, fluid density, etc., within a tube.

Here a density-wave type of dynamic instability was investigated. This instability is due to the feedback and interaction between the various pressure drop components and is caused specifically by the lag introduced through the density head term due to the finite speed of propagation of density waves.

Consider an oscillatory subcooled flow entering a heated channel. The inlet flow fluctuations create propagating enthalpy pertubations in the single-phase region. The boiling boundary, $\lambda(t)$, defined as the instantaneous location of the point where the bulk fluid temperature reaches saturation, oscillates due to these enthalpy perturbations. Changes in flow and the length of the single-phase region combine to create an oscillatory single-phase pressure drop. At the boiling boundary, the enthalpy perturbations are transformed into quality (or void fraction) perturbations that travel up the heated channel with the flow. The combined effects of flow and void fraction perturbations and variations of the two-phase length create a two-phase pressure drop perturbation. However, the total pressure drop across the boiling channel is imposed externally by the channel feed system. Thus, the two-phase pressure drop perturbation produces a feedback perturbation of the opposite sign in the single-phase region which can either enforce or attenuate the imposed oscillation.

Since we are interested only in the possible on-set of dynamic instability a linear system analysis technique can be used. The computer code DYNAM (11) was used to check the dynamic instability. In this code the equation governing the conservation of mass, momentum and energy of the steam generator tube is first linearized about the operating condition. The dynamic analysis solves the linearized partial differential conservation equations using Laplace transformation of the temporal terms and integration of the spatial variations. The resulting equations represent the transfer functions for each spatial node. The computer code is then written in complex variable notation and employs frequency response techniques to develop the system transfer

function. The Nyquist stability criteria, used in control system theory, may then be applied to determine if the boiling channel is unstable, i.e., if flow oscillations will be magnified.

The complex locus of the open-loop transfer function for the present once-through steam generator unit is shown in Fig. A-6. Nyquist's theorem can be phrased as follows: "A necessary condition for a linear system to be unstable is that the complex locus of the open-loop transfer function passes through or encircles in a clockwise manner the unity point on the negative real axis." As indicated in Fig. A-6, the complex locus of the Nyquist plot for the present steam generator will encircle the -1 point, which indicates dynamic instability.

According to the density-wave type of dynamic instability theory, the location of the boiling boundary between the subcooled liquid and the two-phase boiling fluid inside a boiling channel is of primary importance in the determination of dynamic instability. Both theoretical and experimental considerations (see References 12 to 18) indicates that a critical boiling length or point of minimum stability exists for a boiling channel. Below this critical boiling length, dynamic stability will increase with a decrease in inlet subcooling. Above this critical boiling length, an increase in subcooling tends to stabilize the system. Since dynamic instability is caused by the existence of the boiling boundary between the single phase subcooled liquid and the two-phase boiling region, this boiling boundary can be eliminated if saturated liquid (i.e. no inlet subcooling) is introduced into the boiling channel. This can be done by introducing a plenum to seperate the heated subcooled section from the two-phase boiling section. Using zero subcooling to stabilize the present

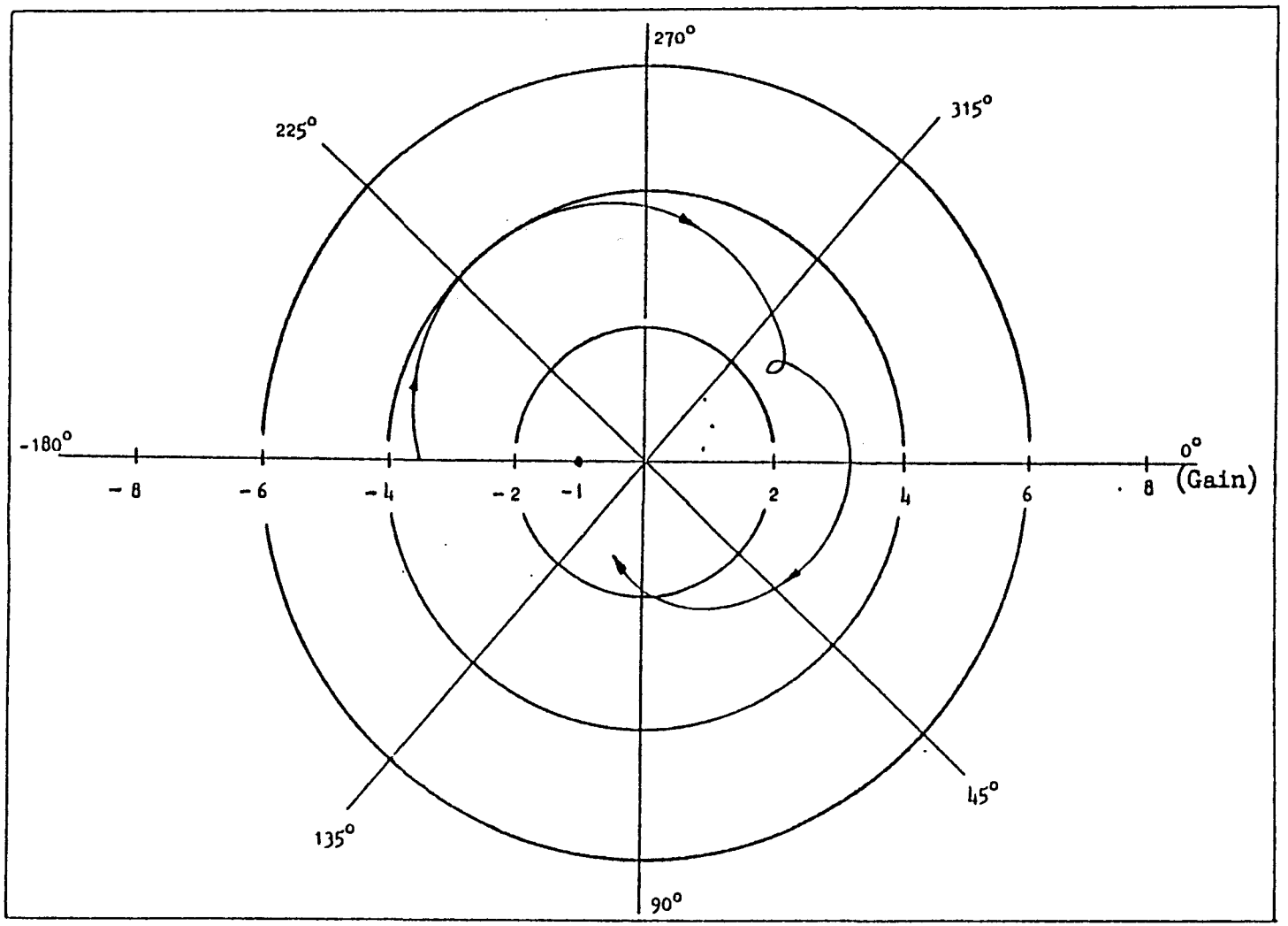

Figure A-6 Nyquist Diagram for Dynamic Stability of Steam Generator

design cannot be confirmed by the DYNAM Compute Code at this point because DYNAM is written in such a way that inlet subcooling is needed in order to run the program. Analysis and experimental data from References 12-19 tends to indicate that a boiling channel will always be dynamically stable if there is no inlet subcooling.

A-1.3 Application of The RPS Internal Heat Transfer Analyses to the ATS

All of the internal heat transfer analyses done to date have actually been for a single tube. Distinction between an analysis for the RPS and an analysis for the ATS is primarily the difference between considering twenty tubes as a parallel path or two tubes. There is, however, an effect due to increased angular acceleration in the ATS system which has not been accounted for. The increased angular acceleration is due to wrapping the tubes around a smaller diameter at a smaller pitch in the ATS than in the RPS. The differences in predicted heat transfer are expected to be rather small (underprediction of heat transfer coefficients in the ATS) but we would expect the pressure drop to be somewhat higher in the ATS because of the acceleration effects.

A-1.4 Use of Heat Transfer Oils in The ATS and RPS Receiver

The central concern when evaluating the possibility of using an organic heat transfer oil in the receiver of any solar thermal system must be the chemical stability of the oil. Fried (20) gives a great deal of information on the recommended configurations for conventional heat transfer oil systems and a ranking of heat transfer

effectiveness for a number of oils. In particular, he notes that hot oil vaporizers are designed to operate at heat fluxes not exceeding 12,500 Btu/ft^{2}hr. This rather modest heat flux corresponds to a solar collector concentration ratio of about 40.

In a most interesting study Seifert, et.al.(21) conducted a number of static heating-degredation experiments which resulted in a plot of percent weight loss per week as a function of temperature for a number of popular heat transfer oils. Data from these long term, static experiments showed only two fluids to be stable above 650°F (weight loss/week less than one percent) and none stable above 725°F.

There has been a similar test of thermal stability done as a part of the Central Receiver Solar Thermal Power Systems Program (22,23,24). The static tests in the Central Receiver Program differ from those reported by Seifert, et.al. in that the heat transfer oils were kept in contact with rocks and steel shavings during the high temperature endurance tests. Interestingly, the results showed that in some cases the thermal stability apparently is improved by the contact with rocks and steel shavings.

In none of the thermal stability studies reported to date has an organic heat transfer medium been exposed to conditions similar to a high concentration type solar power system. The solar irrigation demonstration being conducted at Willard, New Mexico, uses Caloria HT-43^R as the working fluid in the receiver, but the parabolic through collectors only give a 40X energy concentration. At the Willard site, fluid temperatures are limited to 425°F (25). An experiment which apparently is just getting under way as a part of the Central Receiver Solar Thermal Power Study uses organic heat transfer oils as part of

a dual fluid energy storage system (24). The dual fluid test loop uses steam heating of the oils, a thermocline storage unit, and a heat sink for the oil. This dual fluid loop will be used in a series of dynamic thermal fluid stability tests.

In none of the thermal fluid degredation studies noted has an organic heat transfer oil been exposed to conditions present in a high concentration solar receiver. There is sufficient thermodynamic penalty involved in using steam as the heat source for charging a thermocline, that it is attractive to be able to use the hot oils directly. Also, application of solar power as a supplement to conventional hot oil process heating systems would be much more feasible if there can be direct heat transport from the solar receiver to the process. However, before use of a heat transfer oil directly in a highly concentrating receiver can seriously be contemplated, experiments which define the degredation modes, degredation products, and expected heat transfer performance at high heat flux levels must be performed.

During this reporting period efforts at TTU have been directed towards design of a suitable dynamic test facility and some static stability testing of Caloria HT-43^{R}. Figure A-7 shows schematically what a dynamic test facility for direct heating of organic heat transfer oils might look like.

Static Heat Transfer Oil Stability Tests

A static stability test was designed and run using samples of Caloria HT-43 as a means of evaluating the oil's short term degredation properties. Samples of fresh heat transfer oil were encapsulated in a container made of stainless steel tubing about 3 1/2 in. long, closed at both ends with Swagelock fittings.

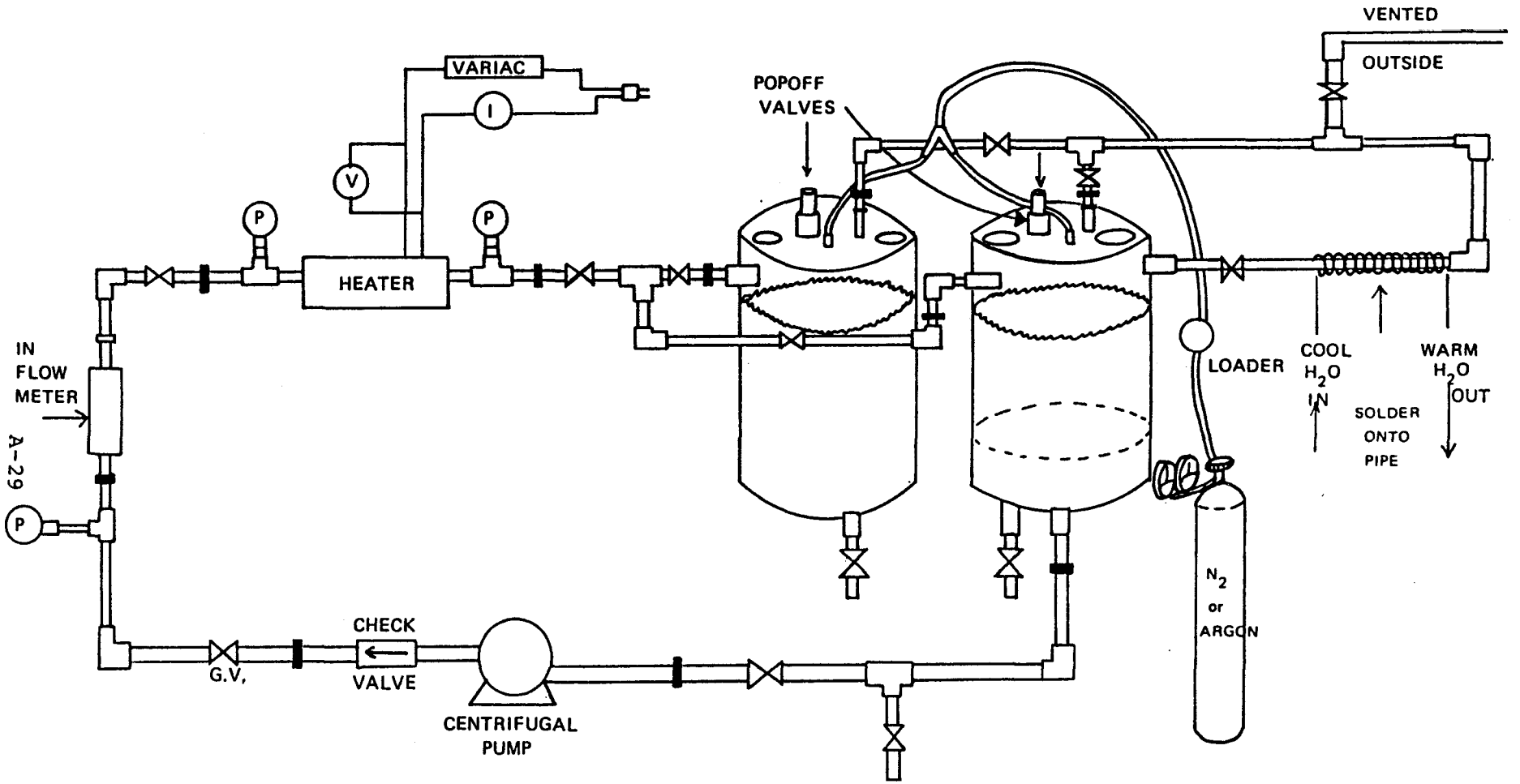

Figure A-7. Schematic Diagram of the Hot Oil Thermal Stability Test Equipment Design

Four samples were placed in a muffle furnace for a period of 24 hrs. at a temperature of 500°F. Two of these samples were then removed for analysis and the remaining two samples, plus an additional three samples were exposed for a period of 22 hrs. at approximately 750°F. Tests at conditions more extreme than the 750°F were aborted after three of the samples being exposed at 750°F exploded. The two remaining samples were removed from the muffle furnace and cooled to room temperature. One sample was opened and the contents analyzed, the other sample has been kept intact. It is interesting to note that the metal container of the remaining 750°F sample has expanded to the point that the Swagelok fittings holding the ends of the sample bomb on are impossible to remove. The three sample containers which did explode inside the furnace are shown in the photograph in Fig. A-8.

As a means of evaluating changes in chemical composition upon exposure to extreme temperatures for a long period of time, ultraviolet spectrographs were run on the original heat transfer oil. In Fig. A-9, the UV spectrographic analysis for the virgin oil and one of the samples exposed at 500°F are reproduced. We can see from this figure that there is relatively little degredation in the heat transfer oil. However, if we look at Fig. A-10 where we compare the ultraviolet spectrographic analysis for the virgin oil and oil exposed to 750°F we see that there definitely has been a shift in the ultraviolet absorption pattern, indicative of changes in physical composition. In addition, the virgin oil is a clear, yellowish liquid while the oil after exposure at 750°F is a very dark brown, having the consistency and the appearance of a well-used motor oil. The simple

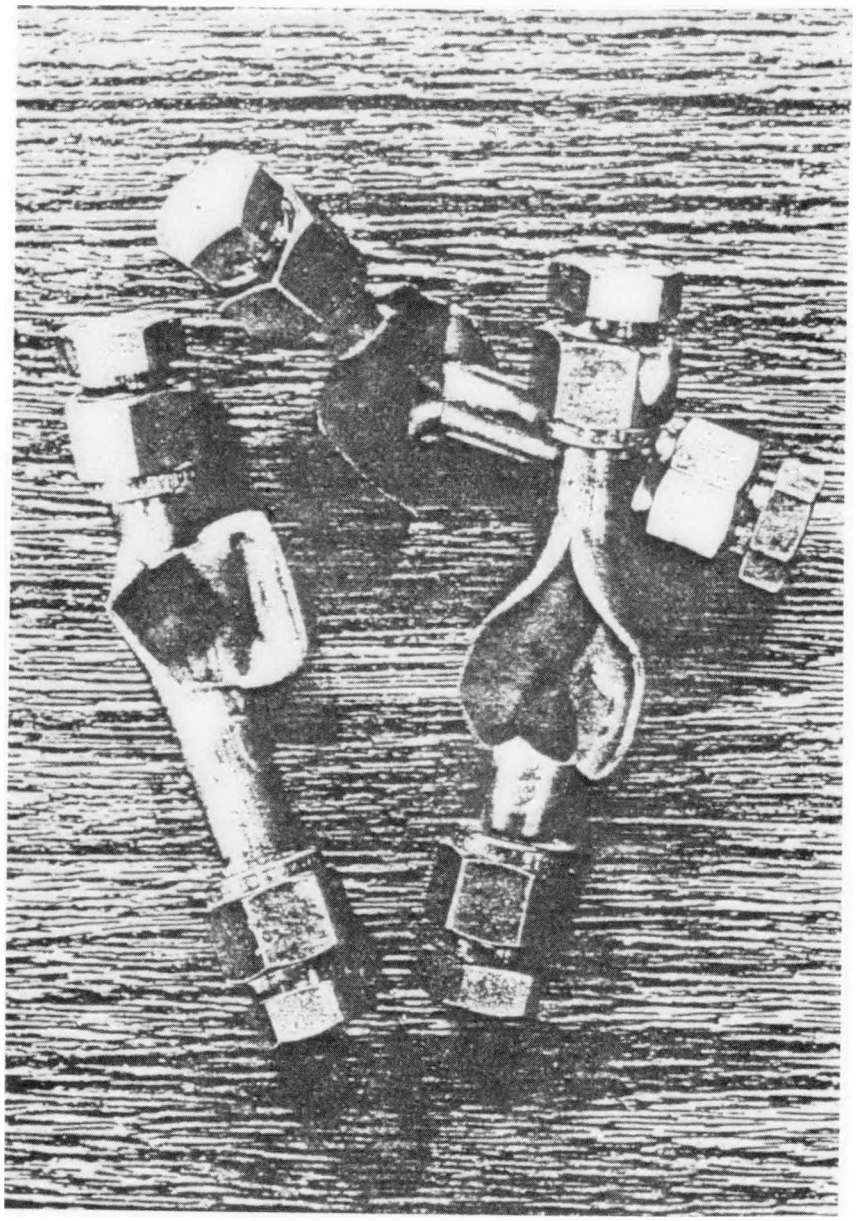

Figure A-8. Caloria HT-43 Sample Containers After Exposure for 22 Hours at 750°F

Figure A-9. Ultraviolet Absorption Spectrum for Caloria HT-43 After 24 Hours at 500°F

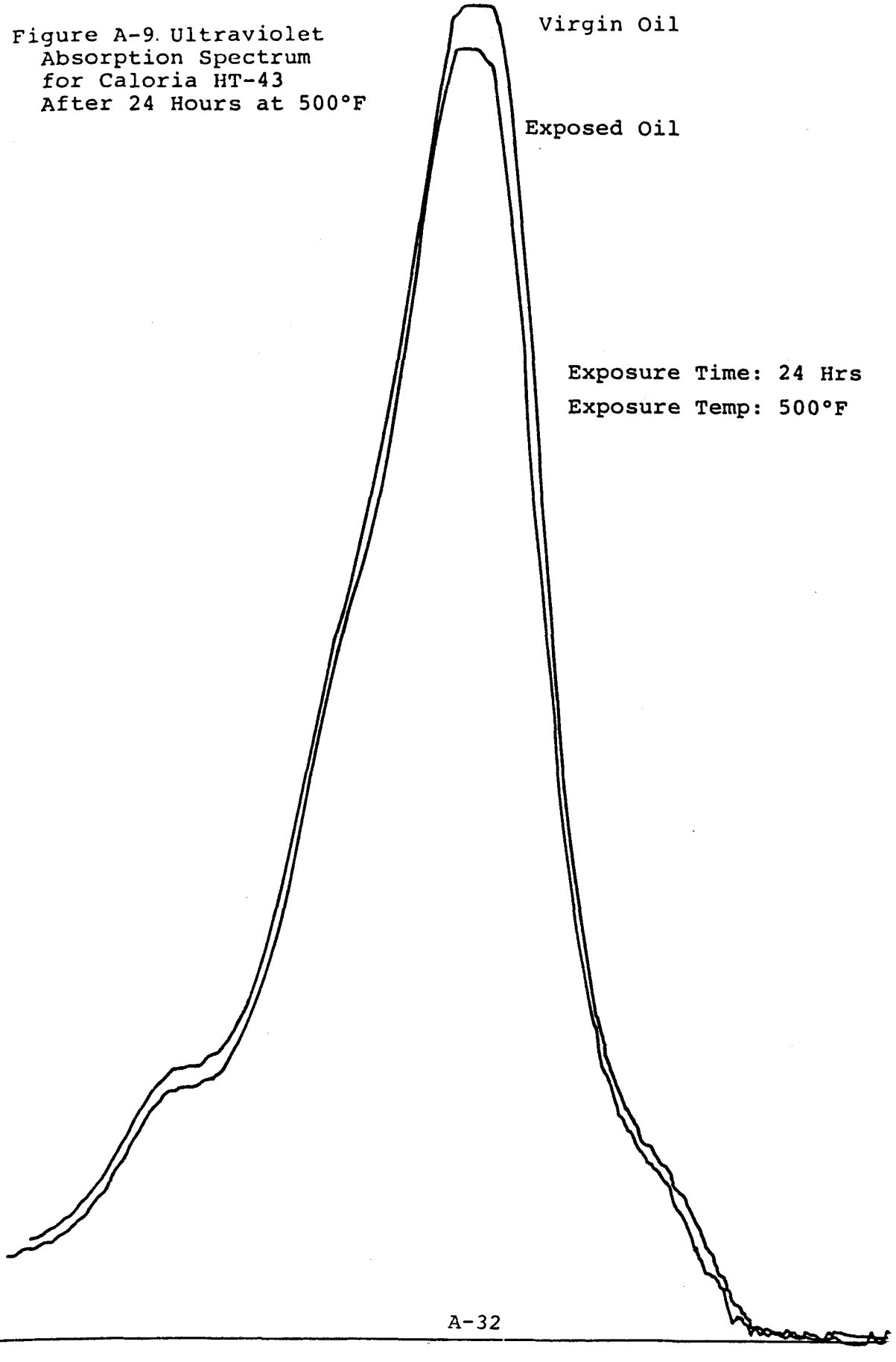

Figure A-10 Ultraviolet Absorption Spectrum of Caloria HT-43 After 22 Hours at 750°F

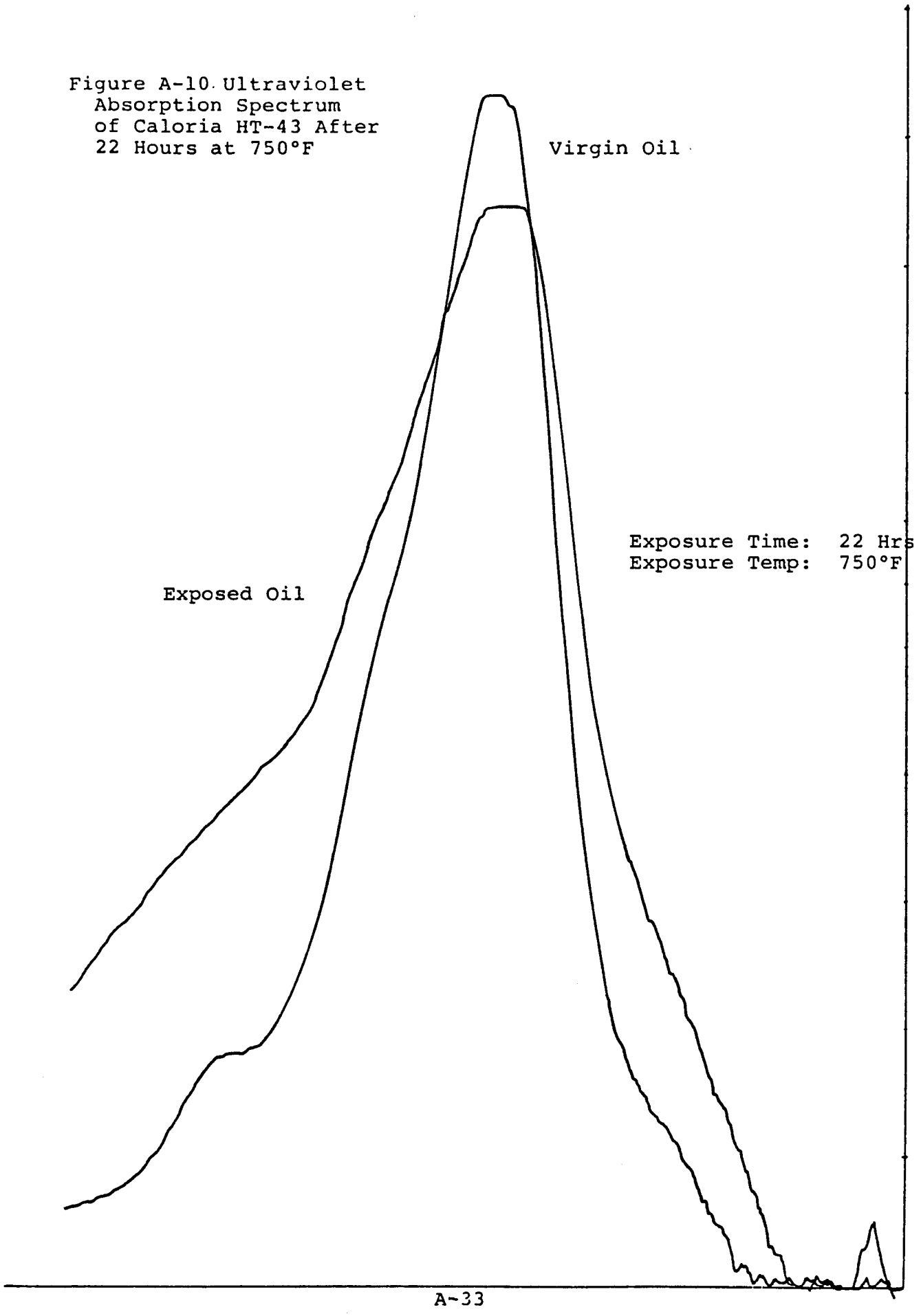

static experiments rather dramatically indicate that exposure for even relatively short times at conditions well in excess of the stability limit to the oil is courting, if not disaster inside a receiver, at least a great deal of trouble because of thermal decomposition.

A-2 HIGH HEAT FLUX RADIANT TEST FACILITY

The high heat flux radiant test facility at Texas Tech, like the joule heat test facility, is designed to provide an experimental evaluation of the thermal-fluid performance of individual sections of the solar receiver with the added capability of providing a radiant test environment. Figure A-11 shows a schematic diagram of the equipment and instrumentation of the test loop. The significant operating conditions/capabilities of the various system components are summarized as follows:

Pump:	Discharge pressure	1000 psi
	Flow rate	4 gpm
Flow meter:	Flow range	.2 to 4 gpm
	Operating pressure	1000 psi
Oil Heater:	Delivery Temperature	-- 600°F
	Flow rate	125 gpm
	Delivery pressure	50 psi
	Heating capacity	519 Btu/hr
Radiant Section:	Lamp power	132 kw
	Max test section size	1 ft X 3 ft

Pressure, temperature and flow measurements are obtained for the test section as well as appropriate other points in the test loop. The differential pressure transducer is used to provide an accurate measure of the receiver pressure drop for a given test condition. The radiant heat flux transducer, HY CAL Model C-1300, is used to map the distribution of incident radiant heat flux in the plane of the receiver surface. Calibration of the transducer was performed at radiant heat fluxes up to 600 suns intensity with a quartz filter to match the test facility radiation spectrum. The transducer is mounted in a water-cooled probe of the same diameter as the test coil

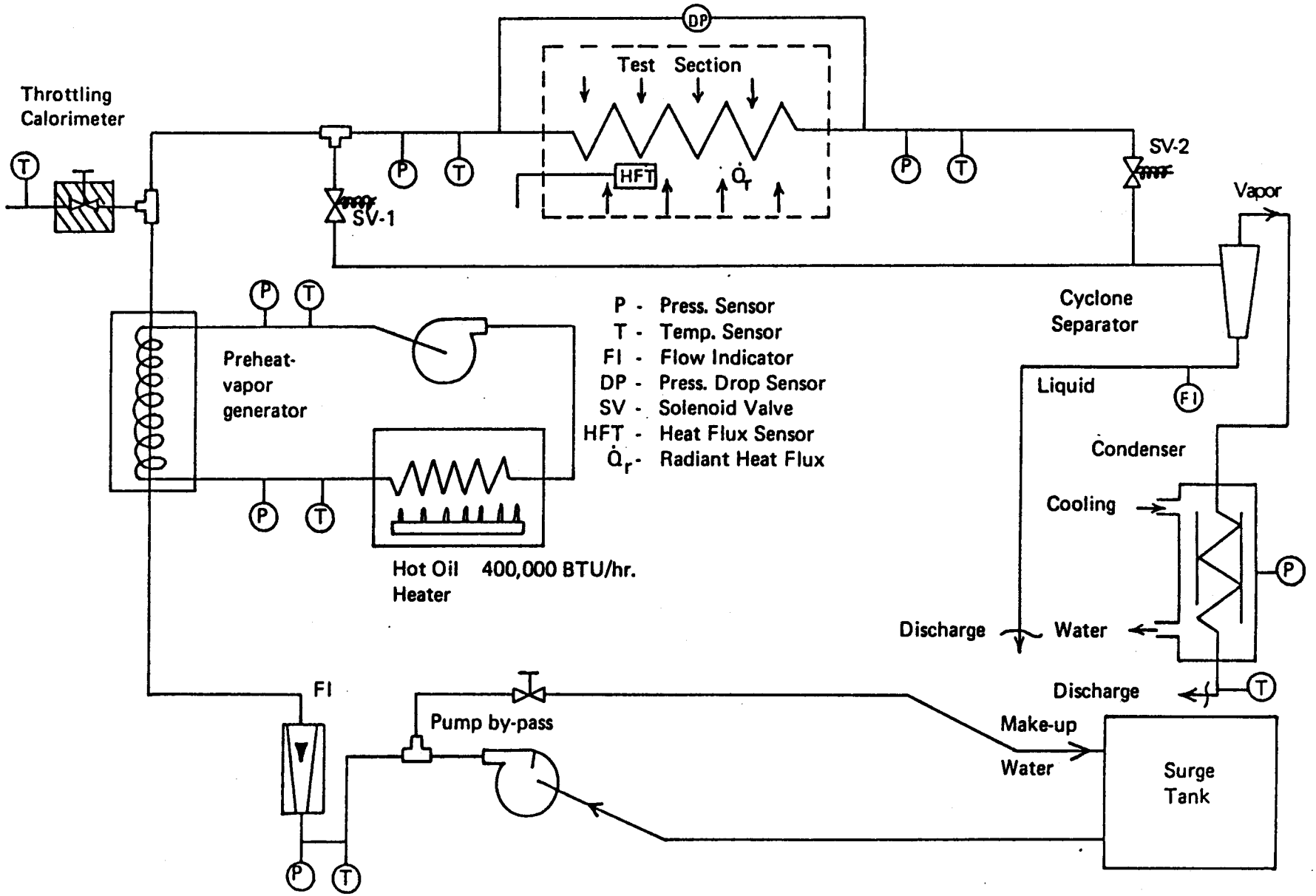

Figure A-11. High Flux Radiant Test Facility

to simulate the radiative environment under test conditions.

Since the purpose of the facility is to provide the ability to test individual sections of the receiver, inlet thermodynamic conditions to the test section must range from subcooled feedwater to superheated vapor, depending upon the region of interest. A gas-fired, hot-oil heater with an oil-to-water heat enchanger provides the energy source to deliver these conditions. The loop is deisgned to deliver superheated vapor to the test section inlet at 245 lbm/hr (the RPS-ATS single tube flow rate) for an oil temperature of 600°F. The oil flow loop will also be useful for future tests on oil degradation and thermal performance in a hight flux, radiant heating environment.

The heat flux in the radiant test section is provided from banks of Sylvania T-3 quartz lamps mounted in water-cooled aluminum panels. Each lamp is rated at 1600 watts at 240 V and each panel can hold a maximum of 34 lamps. The panels are typically arranged to form a triangular enclosure as shown in Fig. A-12 with the number, distribution, and coil-to-panel distance for the lamps being varied to obtain the desired test section heat flux. Average test section concentrations from 30 to 450 suns are possible. A test section length of 18" can be obtained by mounting two triangular sections end-to-end.

The initial tests, currently under way, are being directed toward an evaluation of the effect of coil radius of curvature on test section pressure drop. Initial measurements will be conducted in the single-phase regimes to correlate the experimental procedure against results from the literature with subsequent tests directed toward an evaluation of two-phase, helical flow pressure drop.

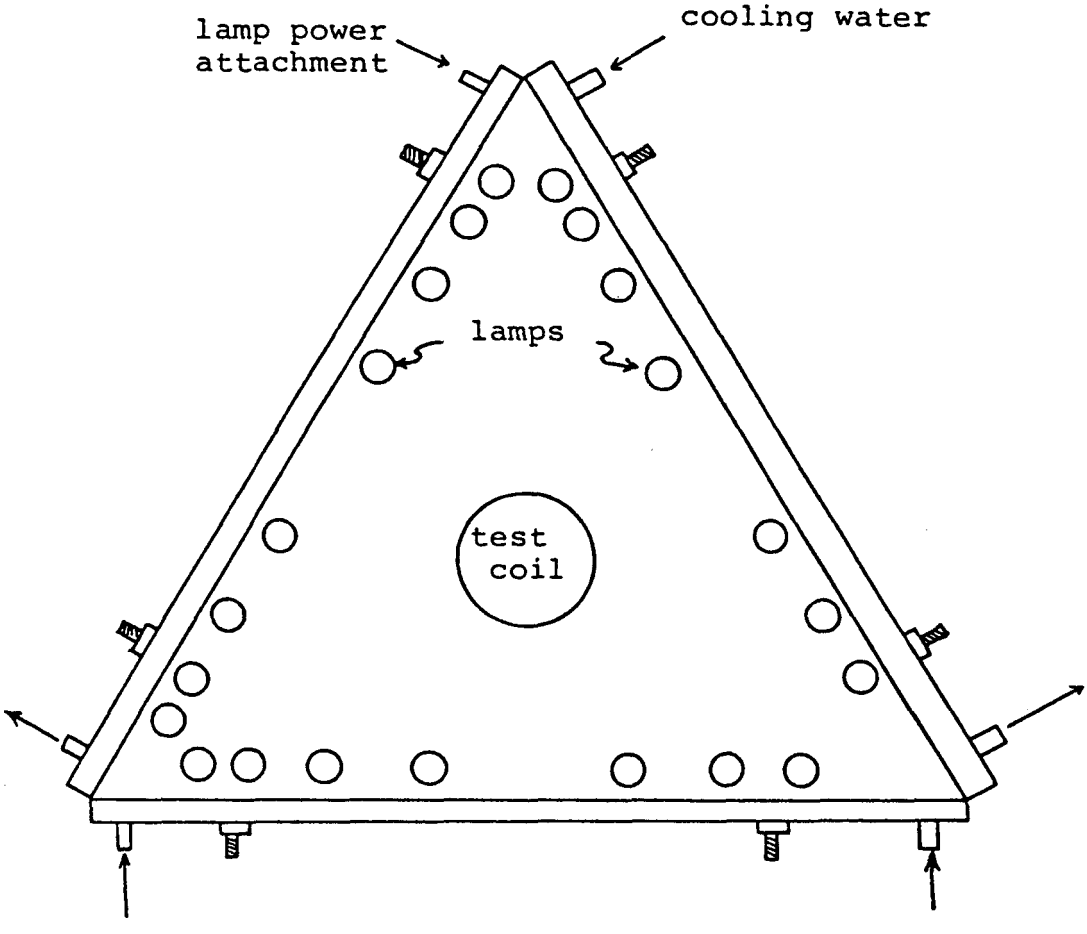

Figure A-12. Schematic of Typical Lamp Panel Configuration

A-3 SOLAR SIMULATOR TESTS ON AN FMDF RECEIVER

The objective of the receiver testing was to show that the boiler concept developed for the ATS and RPS systems is viable. There is concern for establishing all the internal working and heat transfer coefficients along the receiver in other test programs, but the main concern of this test program is to show that the receiver design concept does work. Analysis and testing of small segments of the receiver can investigate individual regions of the receiver, for example, the liquid heating region, boiling region and superheating region, but only testing of a complete receiver would clearly demonstrate overall operational characteristics.

As a means of testing the helically coiled receiver concept, E-Systems built a solar simulator test facility which uses quartz infrared lamps to simulate the solar fluxes associated with a FMDF concentrator of 45 to 50 feet in aperture diameter. This is about the smallest receiver that could be built to simulate the flow rates and tube sizes currently being considered for the 65 ft. ATS and 200 ft. RPS collectors. A 45 ft. aperture diameter FMDF collector would use a single tube, once through boiler design, whereas, a 200 ft. collector would have 20 tubes in parallel. The length of any single tube for the two collectors, 45 ft. and 200 ft. would be about the same, 400 to 500 ft. The actual receiver fabricated and tested was approximately 13.8 ft. long and with end outside diameters of 3 in. and 6 in. to establish a receiver size associated with a 1^0 optical flux cone for a collector of the 45 to 50 ft. aperture diameter.

A-3.1 Radiant Heating Profiles In The Solar Simulator

The solar fluxes that the solar simulator has to reproduce are fairly well defined for an FMDF system. The flux profile on the receiver is about 30 suns on the large end and reaches a peak of about 650 suns near the small end. The solar simulator can only do this in segments with lamp panels since each panel is 18.0 in. long and with a heated lamp length of 16.0 in. The best that can be done then, is to average the flux requirement over each panel length.

As discussed earlier in this appendix, at solar noon the solar concentration varies with receiver position as shown in Fig. A-13. This figure also shows how the nine 18.0 in. long quartz lamp panels can simulate the solar flux. Table A-3 shows the flux required for each panel to simulate the noontime condition. The nonaxisymmetric cases, all times other than solar noon, result in the receiver being heated on one side while the other side is in the shadow. The early morning and late afternoon situation is interesting since approximately 1/3 of the receiver is in the sun and the back 2/3 of the receiver is in a shadow. The receiver test facility was fabricated with quartz lamp panels in a triangular arrangement, discussed below, to simulate this nonaxisymmetric situation as well as the axisymmetric case.

A-3.2 Receiver Design and Fabrication

E-Systems went to Glitsch, Inc., a division of Foster-Wheeler Energy Corporation, to build a once-through boiler. Foster-Wheeler has experience with boilers for electrical generating systems

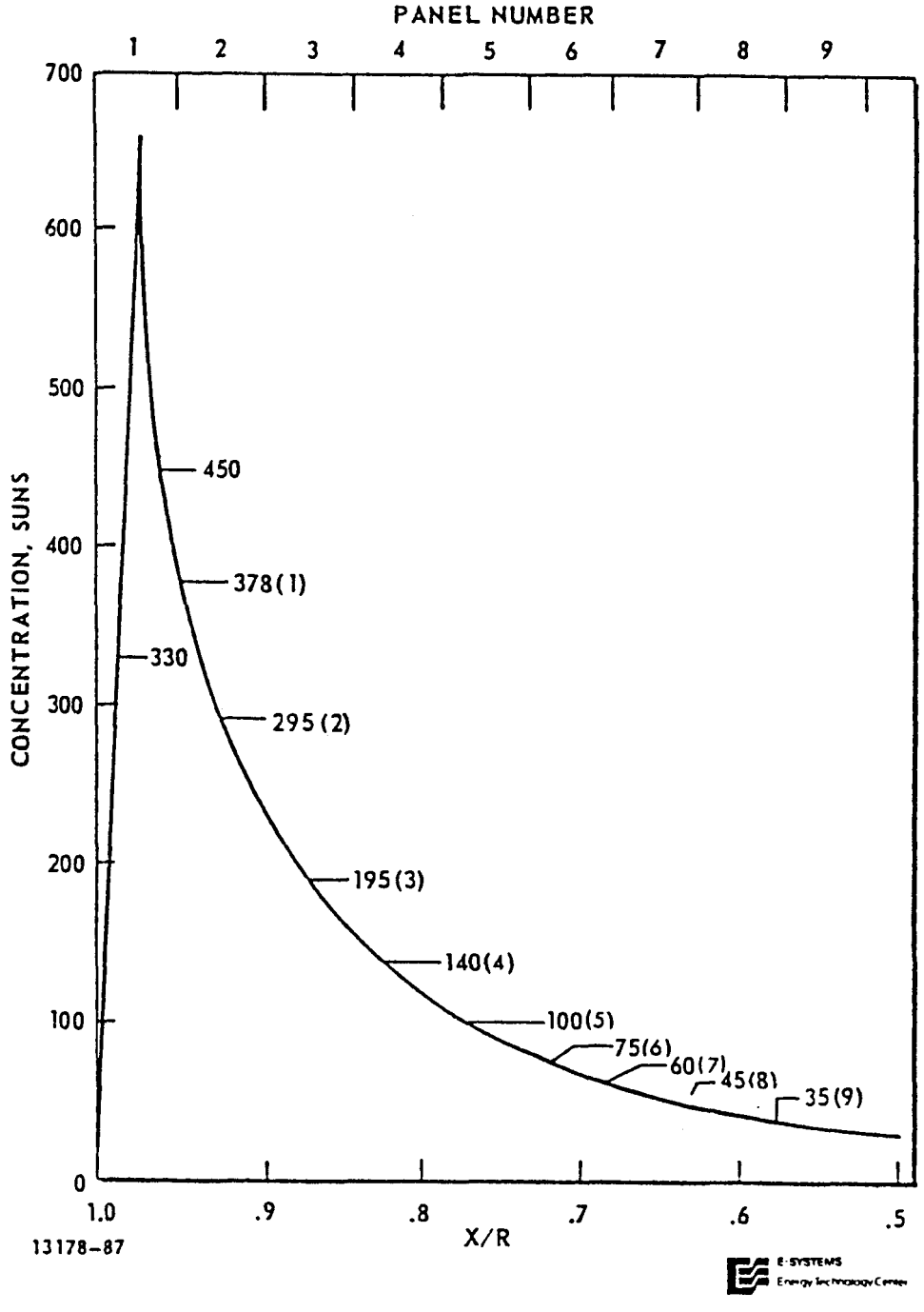

Figure A-13. Average Concentration Versus Position in the Solar Simulator and on the Test Receiver (Axisymmetrical Heating-Noontime)

TABLE A-3 REQUIRED HEAT FLUXES FOR THE SOLAR SIMULATOR

Panel Section Number	Solar Concentration Suns	Heat Flux BTU/Hr ft^2
1	378	99,792
2	295	77,880
3	195	51,480
4	140	36,960
5	100	26,400
6	75	19,800
7	60	15,840
8	45	11,880
9	35	9,240

Note: Heat Flux Calculated as Follows:

$$\text{Flux} = 300 \frac{\text{Btu}}{\text{hr ft}^2} \text{ (Suns) (Reflectance = .88)}$$

and Glitsch fabricates large shell tube heat exchangers for the petrochemical industry. The receiver built was a single tube once-through boiler shown in Fig. A-14. The overall length of the coil is 13.8 ft. The coil is a 1.0^0 cone with an outside diameter of 6.0 in. on the large end and 3.0 inches on the small end. The coiled portion of the boiler is one continuous tube of approximately 461.0 feet long. The tube has a 0.375 in. O.D. and 0.245 in. I.D. (0.065 in. wall) and the material is Inconel 600 since it was available in 20 ft. straight pieces.

Inconel 617 and 625 are more desirable materials, from a structural strength point of view, than Inconel 600. Inconel 600 does not have high strength above 1600^0F or high fatigue and creep strengths as compared to the 617 and 625 Inconel tubes. However, Inconel 600 was considered an acceptable material for a test receiver which should not see the high temperatures or field use for long periods of time. The figure also shows the support cone that Glitsch built to support the coiled tube. This support cone was fabricated of 12 gauge 304 stainless steel and to dimensions to fit snugly inside the coil. The tube coil was clamped to the support cone on both ends of the coil so that the coil would not shift or uncoil on the support cone. Fig. A-15 shows a close-up view of the receiver coils.

Glitsch coiled the tubing on a large lathe using a mandrel with the proper geometry so that the finished product, after springback, resulted in a coil permanently set at the desired dimensions. The support cone was formed by hammering flat sheets into prefabricated molds to attain the proper geometry. Since only 20 ft sections of tubing were used, a large number of tungsten inert gas (TIG) butt

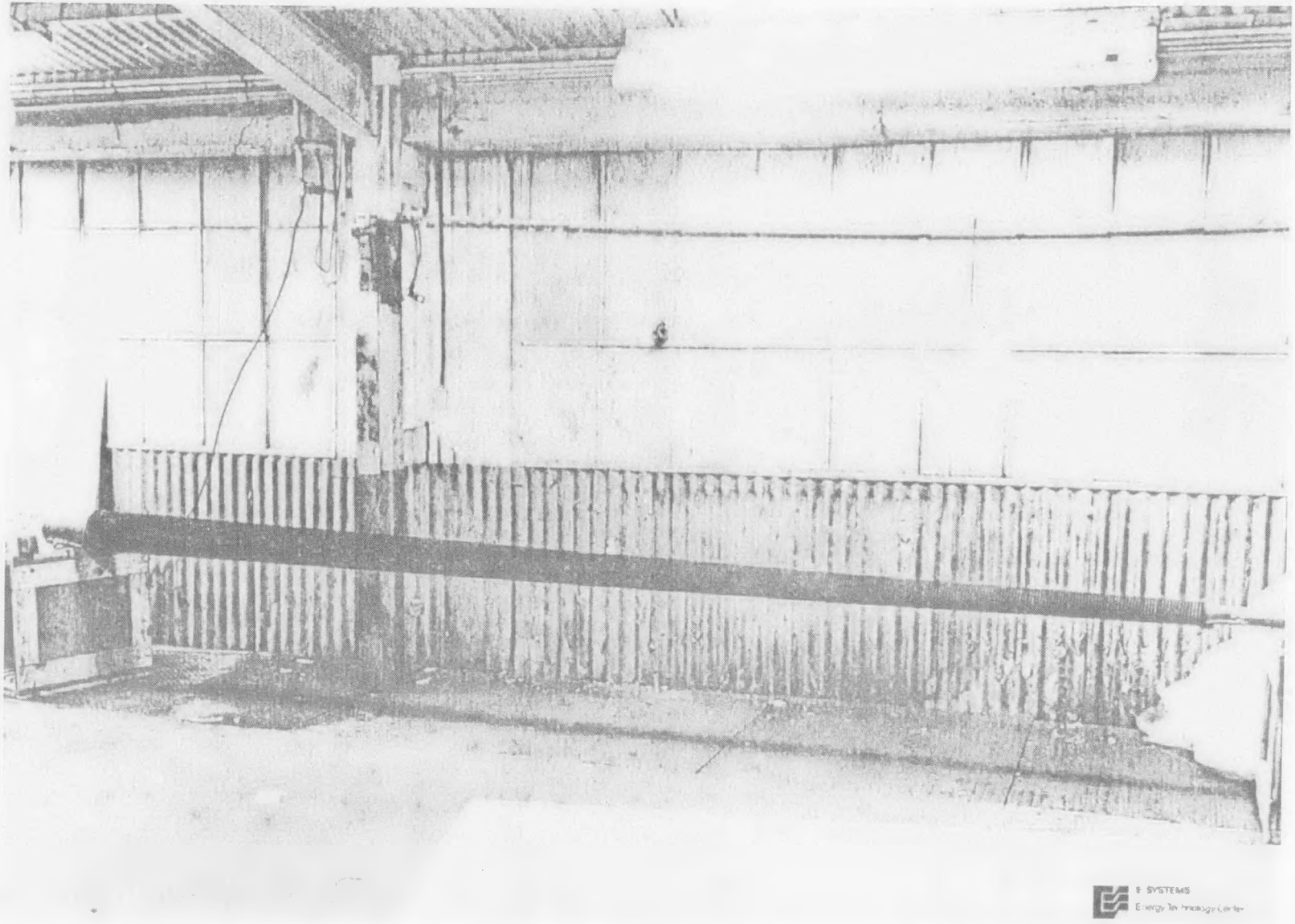

Figure A-14. Once Through Boiler on the Support Cone

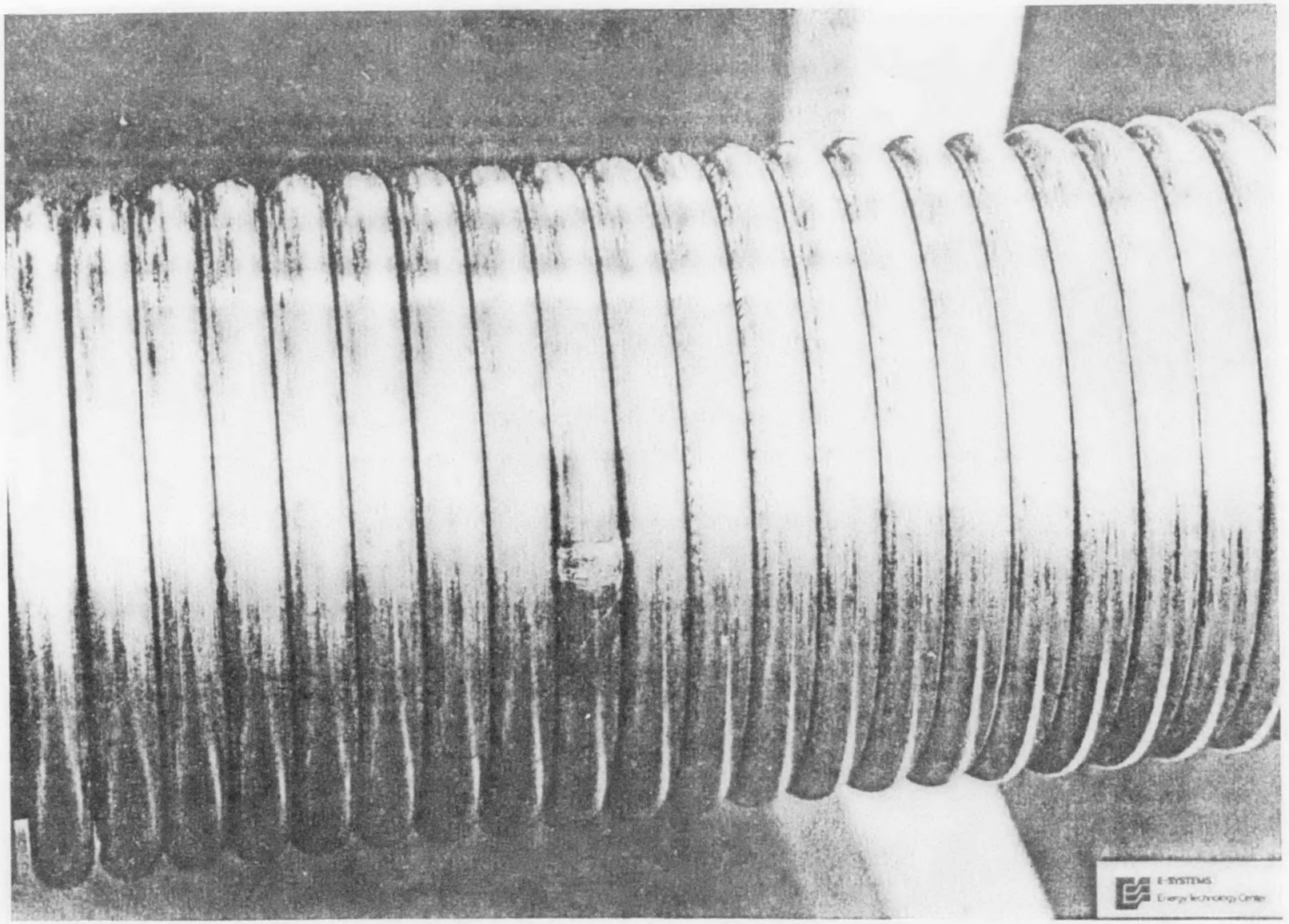

Figure A-15. Closeup View of the Receiver

welds were performed. These welds were done on straight sections before being turned on the lathe and all the welds were checked by 2000 psi pressure and die penetrant. Fig. A-15 shows how the butt welds look after being coiled. Pull tests were performed on sample welds and these welds failed near the ultimate strength of the tubing.

The receiver coil was coated with Tempil Corporation Pyromark 2500 flat black paint. This paint is reported to adhere to Inconel materials, to have high solar absorptance (α= 0.90) and to have a useful temperature to 2500^{0}F when properly applied, cured and vitrified. Glitsch and E-Systems working together were able to get a good coating on the receiver by wire brushing the tube surface, followed by two very thin coats of paint (total dry thickness of the two coats approximately 0.001 inches), followed by curing the paint at 480^{0}F for an hour and last vitrifying the coating at 1000^{0}F for an hour. The temperatures and times followed instructions from the paint manufacturer. Experience taught us that to get the desired Pyromark 2500 coating on Inconel 600 the total dry paint thickness had to be approximately 0.001 inches or less. To date, the coated receiver has been used in the solar simulator very successfully. The coating has been to temperatures in excess of 1200^{0}F, appears to have a high radiant absorptance and has not deteriorated during the preliminary tests. How this coating will hold up in the field in an actual FMDF collector still remains to be seen.

A-3.3 E-Systems Solar Simulator Test Facility

A solar simulator test facility was built up to test the once-through boiler. The facility consists of quartz infrared lamps

and panels, frames to mount the panels and receiver, water cooling for the panels, high pressure water pump system for the receiver feed water, electrical equipment to supply power to the lamps, instrumentation and recording equipment, and modifications to an existing building.

Sandia Laboratories in Albuquerque had fabricated the infrared lamp panels for another solar simulator test. Since these panels were available, E-Systems designed the solar simulator around these panels. The panels have a highly polished aluminum reflector and are sized for using the T3 size quartz infrared lamps. Fig. A-16 shows a closeup view of these panels. The panel is approximately 18.0 in. square with water cooling in the reflector panel and the two electrical busbars. The figure shows the busbars without lamps in the panels.

Fig. A-17 shows an end view of the panels forming a triangle around the receiver. The approach was to maintain the panels in an equilateral triangle and to have the closet lamp on each panel at a distance of 1.0 in. from the receiver.

A rigid "A" frame was fabricated to mount the receiver and lamp panels. This frame was made large and strong enough so that Unistrut type materials could be used to hold the panels in the proper relation to the receiver. The "A" frame was sized to hold nine lamp panels along its length to accommodate the heating of the 13.8 ft. long reciever. Fig. A-18 shows nine panels along the length (total number of panels used is 27) and how the frame is hinged on one side to allow the installation of the receiver and lamps into the panels.

The panels require cooling water to keep the panels temperatures below approximately 160^{o}F. A cooling water system was

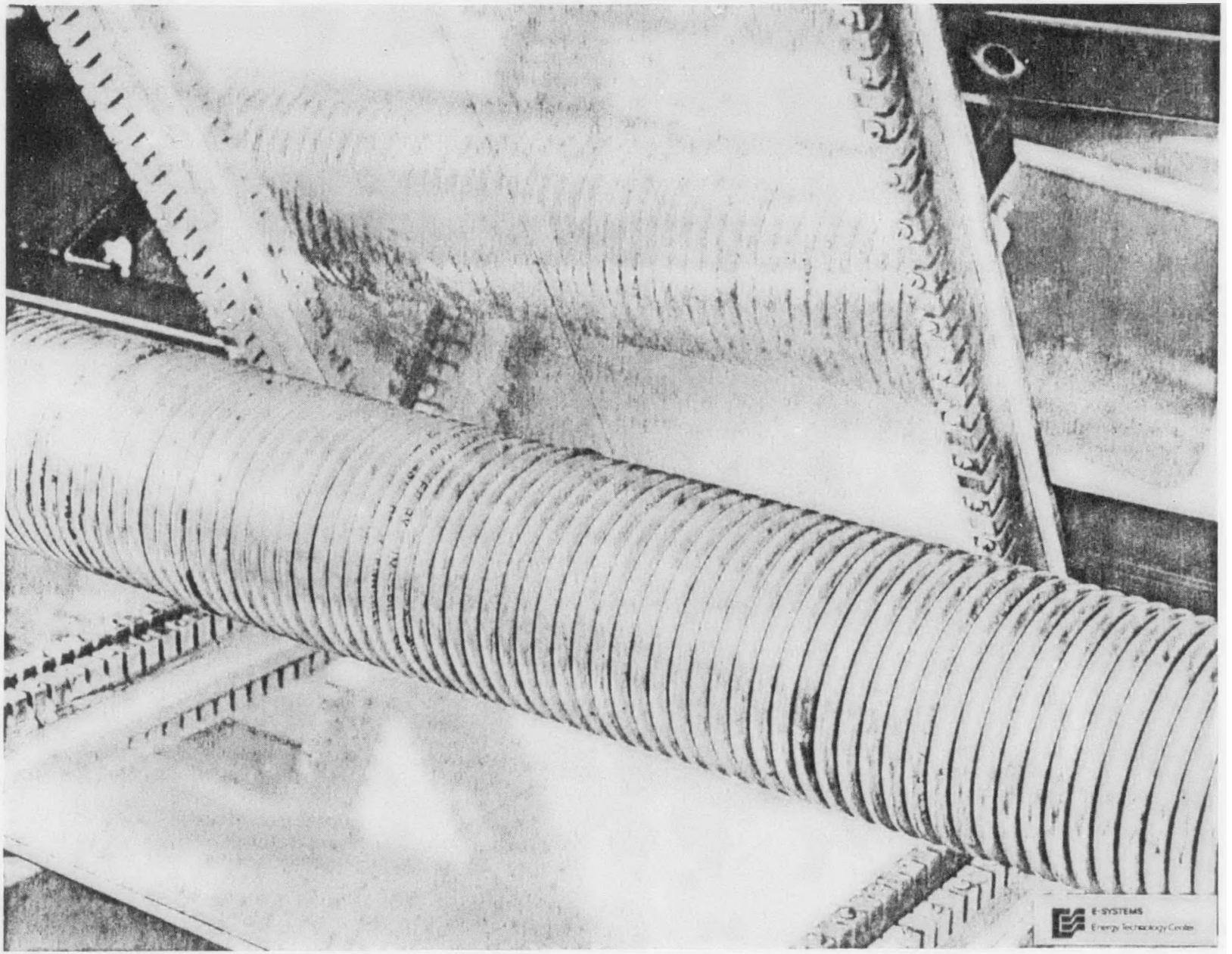

Figure A-16. Closeup of the Receiver and Lamp Panels

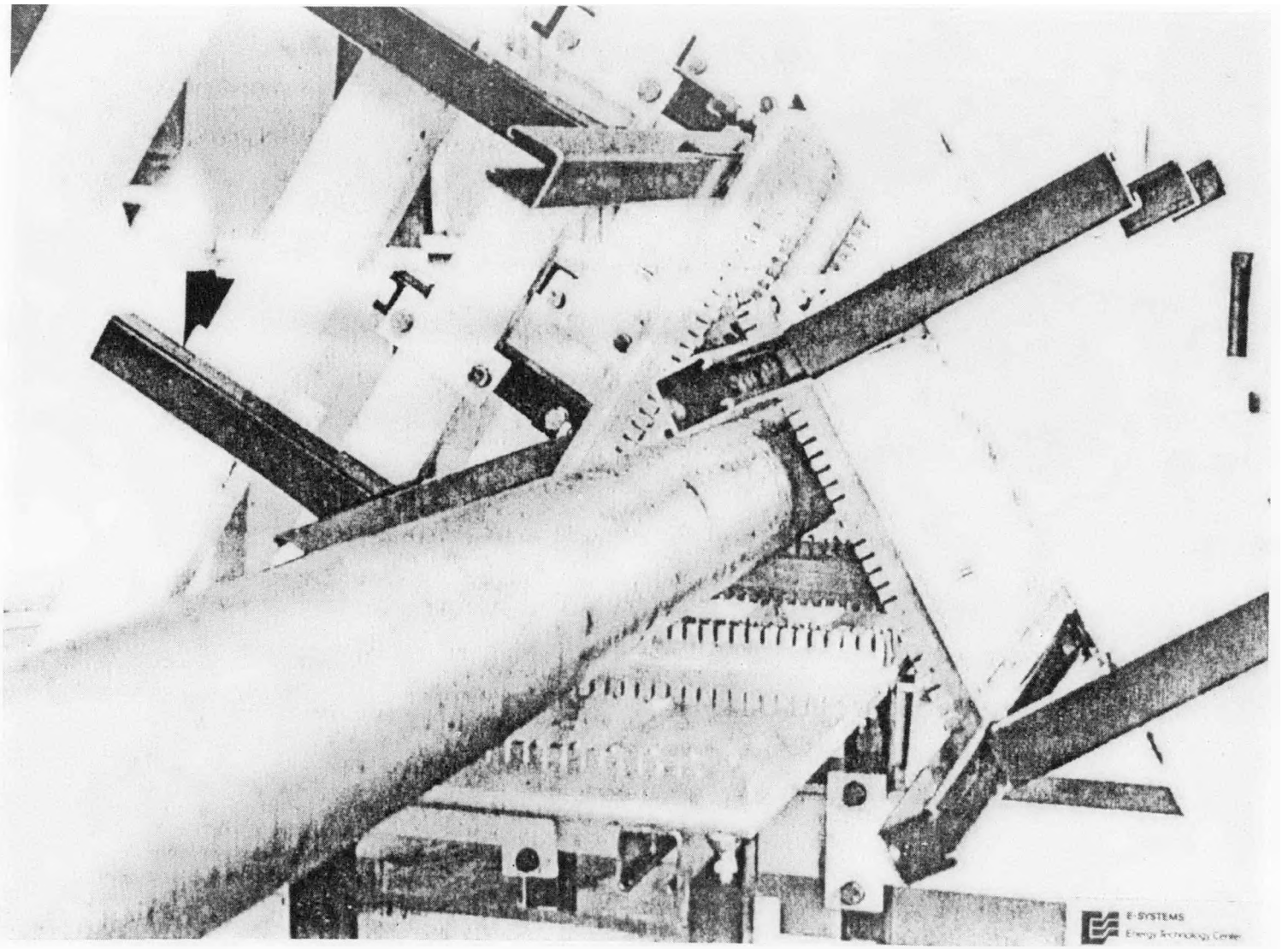

Figure A-17. Lamp Panels in Place Around the Receiver

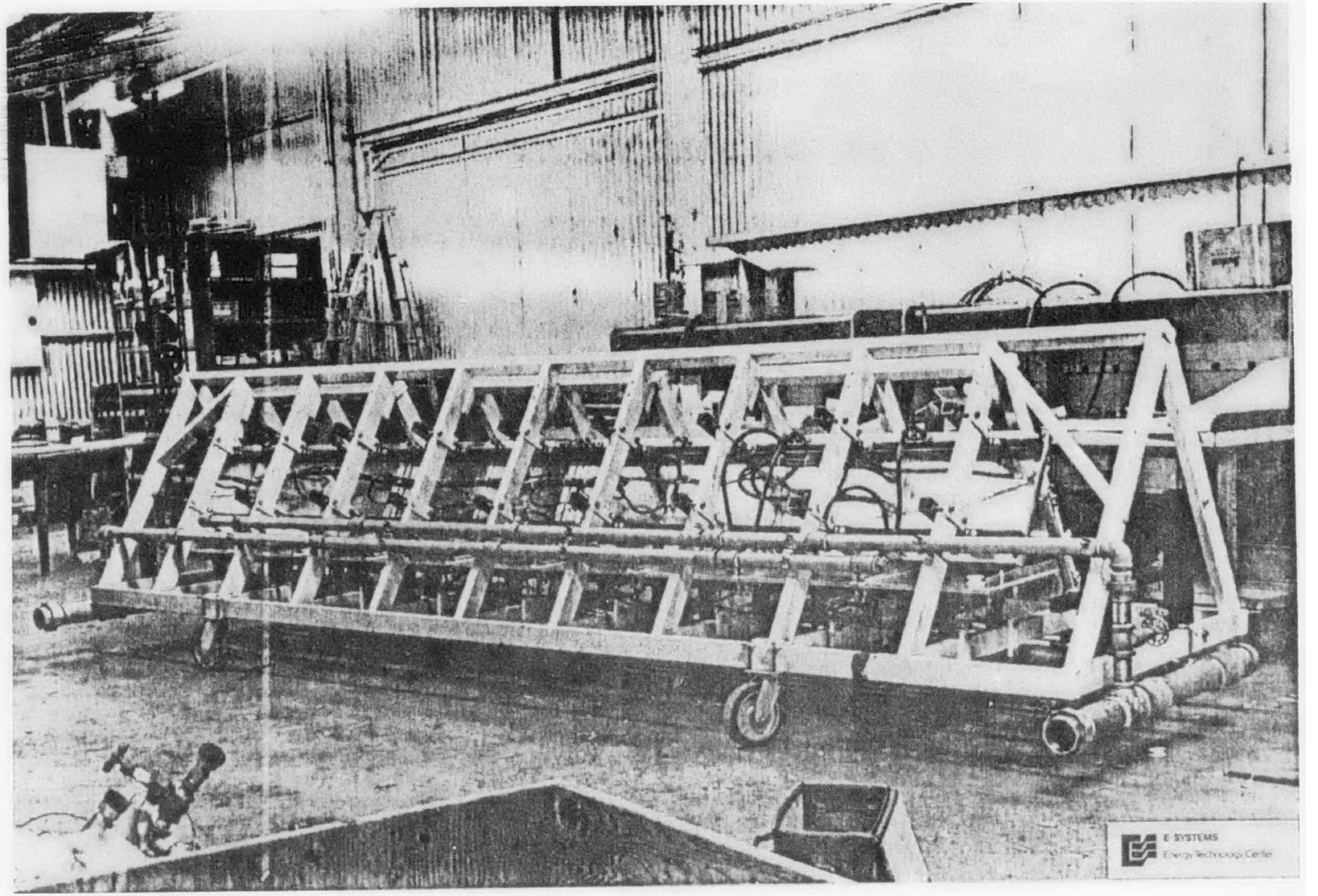

Figure A-18. Side View of the Solar Simulator

designed to cool each panel. The panels in these tests which had the highest fluxes (small end of the receiver) required approximately 3.0 gpm tap water in the panel serpentine and approximately 0.5 gpm for each of the two busbars. To accomplish these flow rates large water manifolds and plenums were assembled. Figure A-18 shows these manifolds and the large number of small hoses required. A tap water supply of 100 gpm at approximately 30 psig was made available.

A high pressure water pump system was developed to supply up to 1500 psig water at the maximum flow rate of 1.0 gpm to the test receiver. Tap water is run through a deionizer before entering the pump. Valves and regulators on the system maintain for a steady flow at any of the desired flow conditions for these tests. A schematic of the pump system and receiver water loop is shown in Figure A-19.

A-3.4 Solar Simulator Electrical System

The electrical system is centered around the electrical power requirements for the quartz infrared lamps. The results of the preliminary optical analysis presented above showed the heat flux required for the nine panels along the length of the receiver. Another optical analysis was performed on the lamp arrangement for each panel to match up with the required flux. This analysis showed that nine panels on the small end of the receiver (high heat flux end) would use 93 high power quartz lamps (200 watt per linear inch of lamp length at the rated 384 volts). The rest of the 18 panels would use 200 low power lamps (100 watt per inch lamp length at the rated 240 volts).

The panel electrical schematic evolved from this lamp

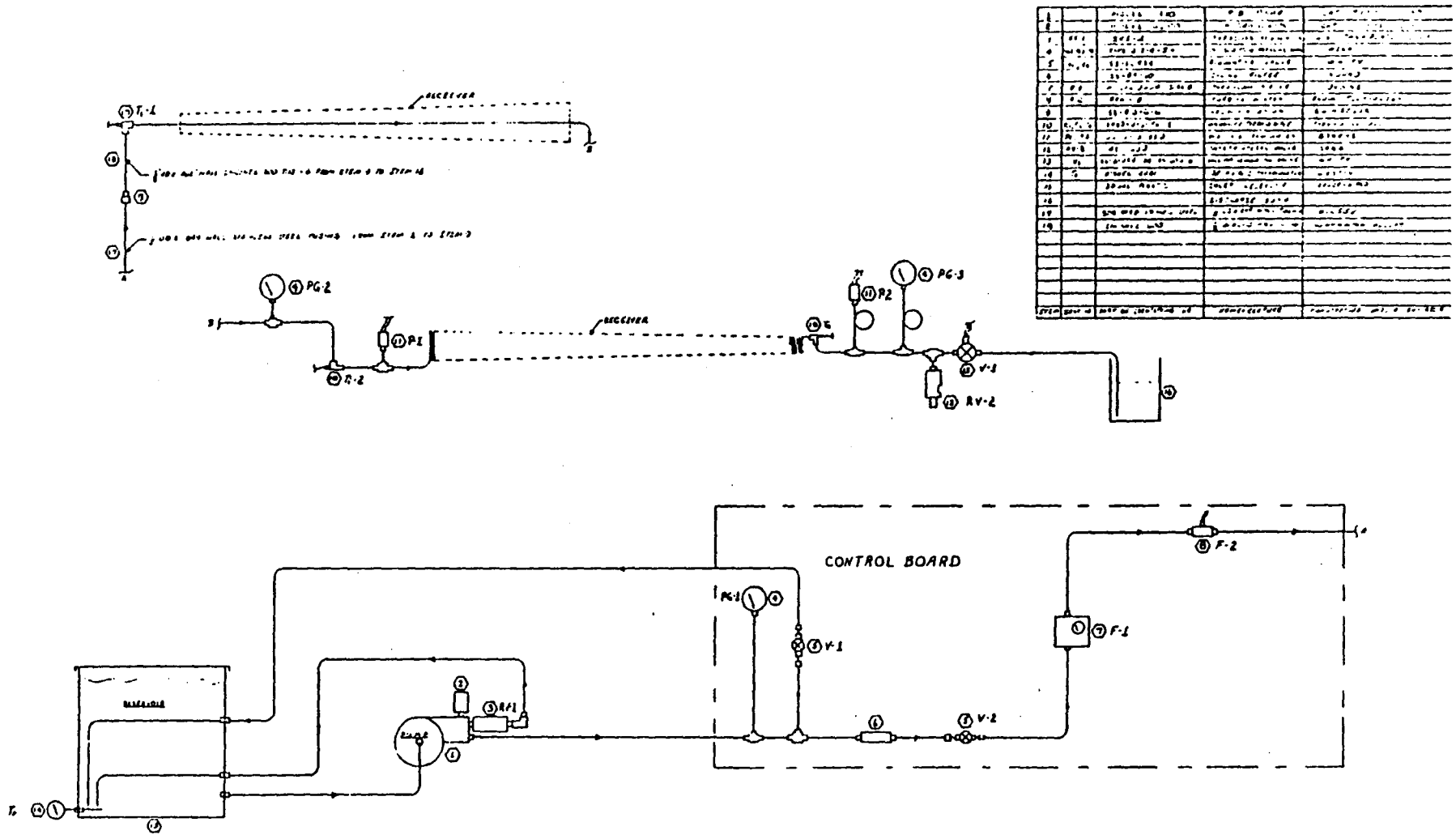

Figure A-19. Piping Schematic - Solar Receiver Test

requirement and this schematic is shown in Figure A-20. This schematic shows the series-parallel panel circuitry for the three phases, electrical power controller, 1000 amp circuit breaker and 1500 KVA transformer with 13,200 to 480 volt stepdown. The 13,200 voltage is available at the E-Systems facility but the electrical controller requires 480 volts input. The local electrical utility company, Garland Power and Light, loaned E-Systems the transformer and Sandia Laboratories in Albuquerque loaned E-Systems the electrical controller.

In between the transformer and controller a 1000 amp circuit breaker is used for circuit protection. The 3 ϕ power available to the controller then is about 831 KW at 480 volts. The electrical controller is a Research, Inc., Model 650 liquid cooled solid state unit with voltage output capability from 0 volts up to about 460 volts, with all three phases at the same voltage. Preliminary data on the electrical system indicates that the lamp arrangement analyzed has approximately the desired fluxes and requires 166 KW at 240 volts with 400 amps per phase.

The electrical power controller is a very valuable part of this test facility. The voltage or power can be varied or maintained at a steady state power setting. This controller could be used for transient tests since the lamps can be turned on or off in a matter of a few seconds. Also, the controller could be programmed to perform cyclic power conditions simulating cyclic cloud coverage.

The electrical schematic shown in Figure A-20 is for axisymmetric, noon time, heating of the receiver, or uniform flux in the triangular panel arrangement. For nonaxisymmetric cases, early morning or late afternoon, only the panels in one leg of the

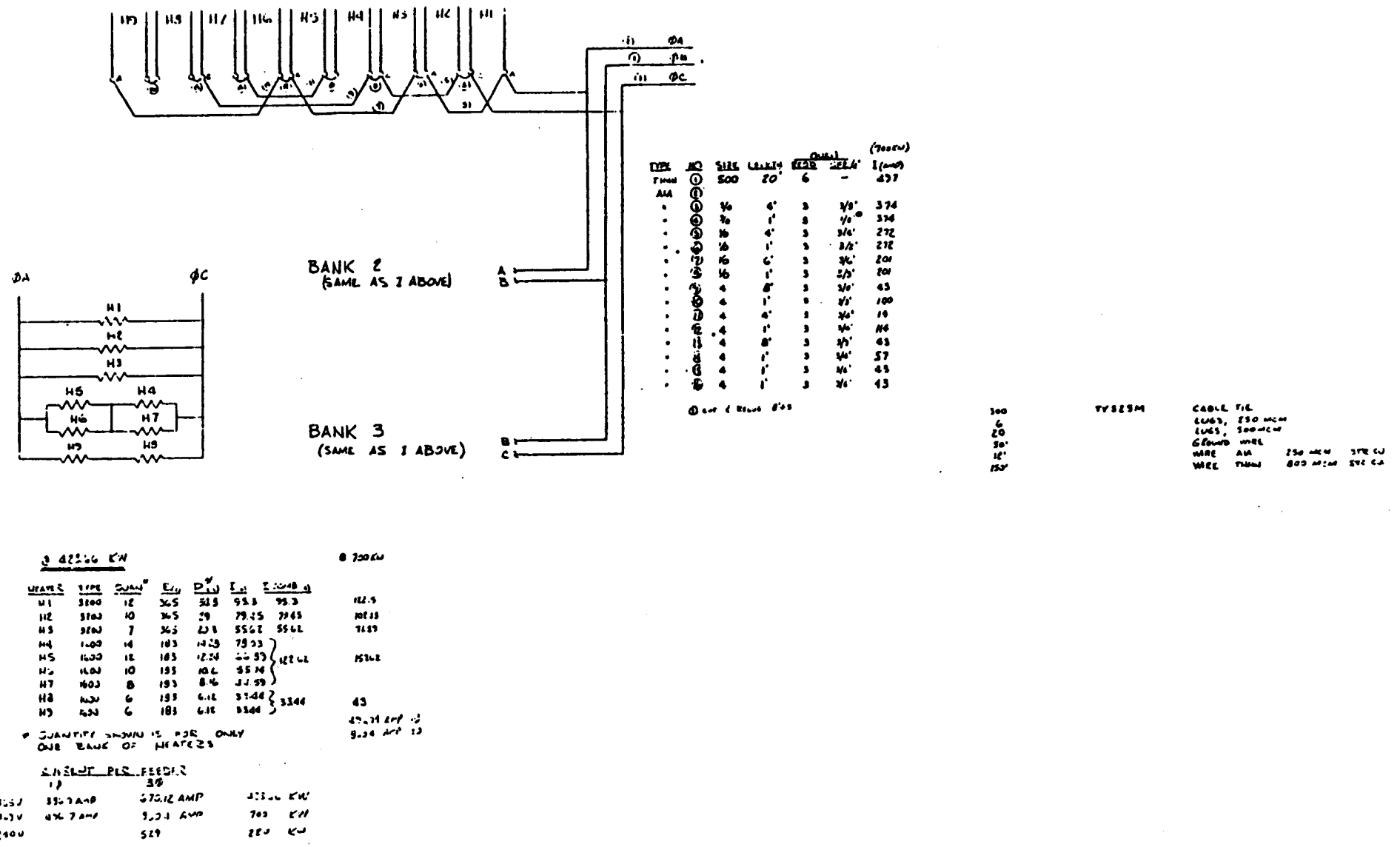

Figure A-20. Electrical Installation - Solar Receiver Test

triangle would be used for heating the receiver. This would result in 1/3 of the receiver circumference being heating and 2/3 being in a shadow. To achieve this nonaxisymmetrical case, the lamp panels would have to be rewired with the 3 ϕ power only going to nine panels along the length of the receiver. Rewiring to perform these tests is relatively easy.

E-Systems made available Building 511 for the test facility. As previously mentioned a transformer, circuit breaker and cooling water were modifications to this building. Inside the building a protective wall was built around the receiver to protect the test personnel and equipment from exposure to possible high voltage electrical shorts and to high pressure superheated steam in case of receiver leaks. Viewing ports were built into the wall for viewing the solar simulator during the actual tests. The cooling water and steam are dumped into a drain behind the building.

The current receiver tests are only being done with the receiver in a horizontal position. In the future, attempts might be made to run tests with the receiver elevated to a maximum of 45°. The quartz lamp elements sag and will not operate properly for very long time periods in excess of 45° from horizontal. The test facility could be modified to accomplish tests on an elevated receiver.

A solar simulator test facility has been established to perform tests on the 13.8 ft. long receiver associated with a 45 to 50 ft. dish. With relatively simple modifications, larger diameter and longer receivers could be tested in this solar simulator. The "A" frame is large enough for receivers in excess of 1.0 ft. in

diameter and with extensions on the frame more panels could extend its useful length. The existing electrical power available to the controller is in excess of 800 KW but this could be extended to approximately 2000 KW by changing out the circuit breaker and transformer. Additional modifications could be made to the building and more tap water could be attained for cooling purposes. This test facility should be a very valuable tool in the future for pretesting receivers before they are installed in the field.

A-3.5 Solar Simulator Test Instrumentation

The test instrumentation is an important part of the solar simulator facility. The instrumentation must produce and reproduce the test data to assure validity. In general, backup instrumentation was used throughout the facility. Pressure gauges backed up pressure transducers, visual flow meters backed up flow turbine transducers, thermometers backed up thermocouples and backup thermocouples were used in critical monitoring locations.

The flow, pressure and temperature monitoring locations in the receiver fluid loop are shown in Fig. A-19. Fluid pressures at the inlet and outlet of the receiver, water flow rate to the receiver, and the entering and exiting fluid temperatures are the most critical items monitored in the receiver loop. The inlet water and outlet steam pressures, water flow rate and exit steam temperatures are recorded on a Gould Brush Model 260 six channel high speed

recorder to establish any oscillations among these parameters.

The receiver water pump system can deliver a constant temperature steady flow rate at a pressure without any noticeable oscillations. Any oscillations recorded at the outlet conditions are a result of internally developed perturbations or possibly outlet high pressure drop valve.

The receiver is thoroughly instrumentated with thermocouples as shown in Fig. A-21. This figure shows all the locations of the thermocouples on the outside surface of the tube crown (maximum tube surface temperature), inside surface of the tube near the support cone (tube temperature is extremely close to the fluid temperature inside the tube), and the support cone itself.

The outside tube crown surface is monitored by 30 type K (Chromel-Alumel) insulated Inconel sheathed 0.040 in. O.D. thermocouples silver brazed to the tube crown. Six bead type thermocouples were also installed on the outside tube surface as a check on the sheathed type thermocouples. Fig. A-22 shows a typical sheathed type and Fig. A-23 shows a typical bead type thermocouple installation on the outside tube surface.

A thermal analysis has been performed on the sheathed thermocouples silver brazed to the outside tube surface. These thermocouples are exposed to the heat flux from the quartz infrared lamps. Results from this analysis is that the maximum temperature differential between the thermocouple reading and the tube surface temperature should not be more than approximately 20^0F for the highest flux region (1000,000 Btu/hrft^2) in the solar simulator. This 20^0F error is negligible compared to the 1200^0F expected

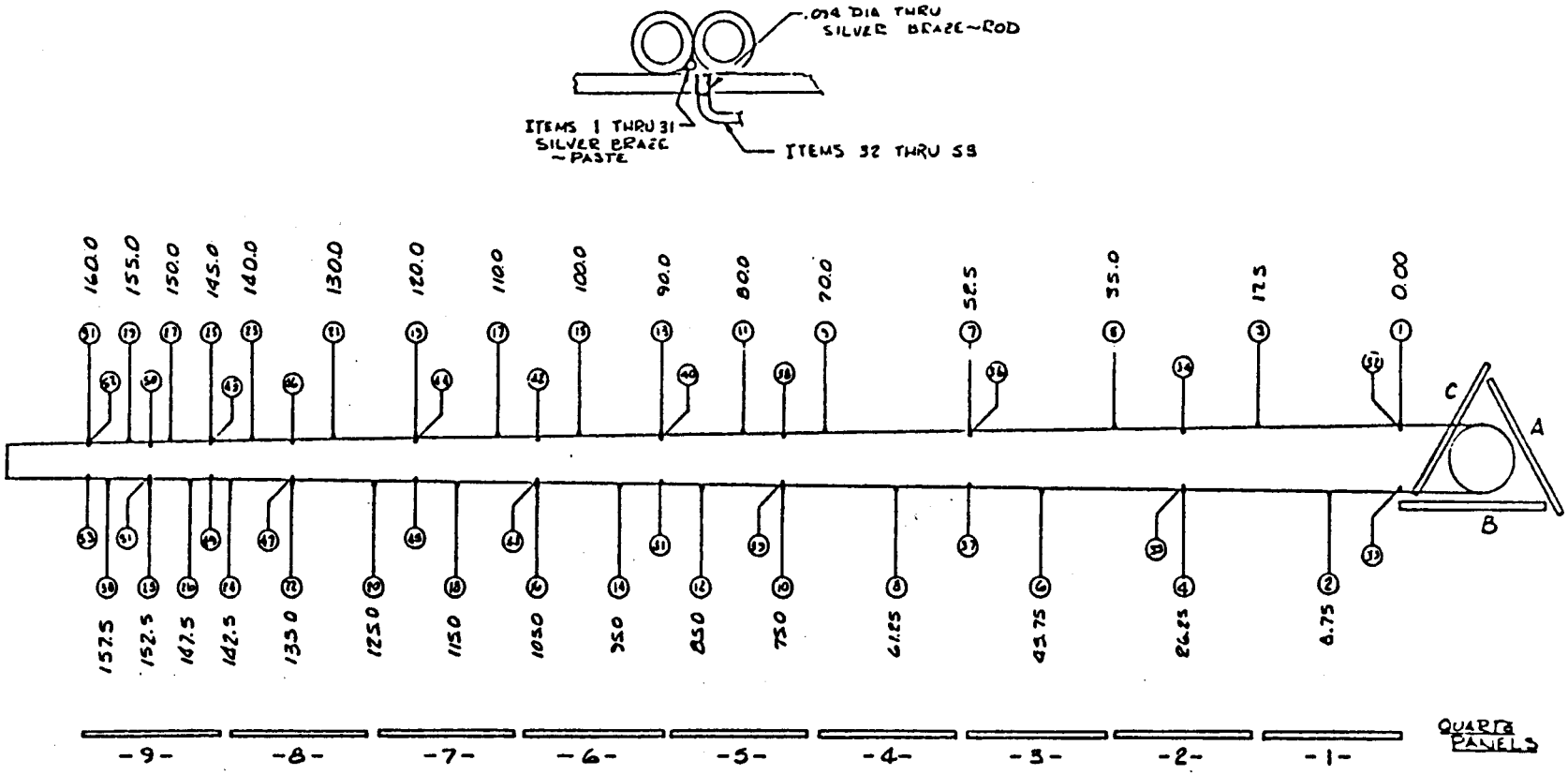

NOTE: OUTSIDE TUBE SURFACE TEMPERATURES WILL BE TAKEN IN SIMILAR LOCATIONS TO THE INSIDE TUBE SURFACE

Figure A-21. Thermocouple Installation - Solar Receiver Test

Figure A-22. To be added

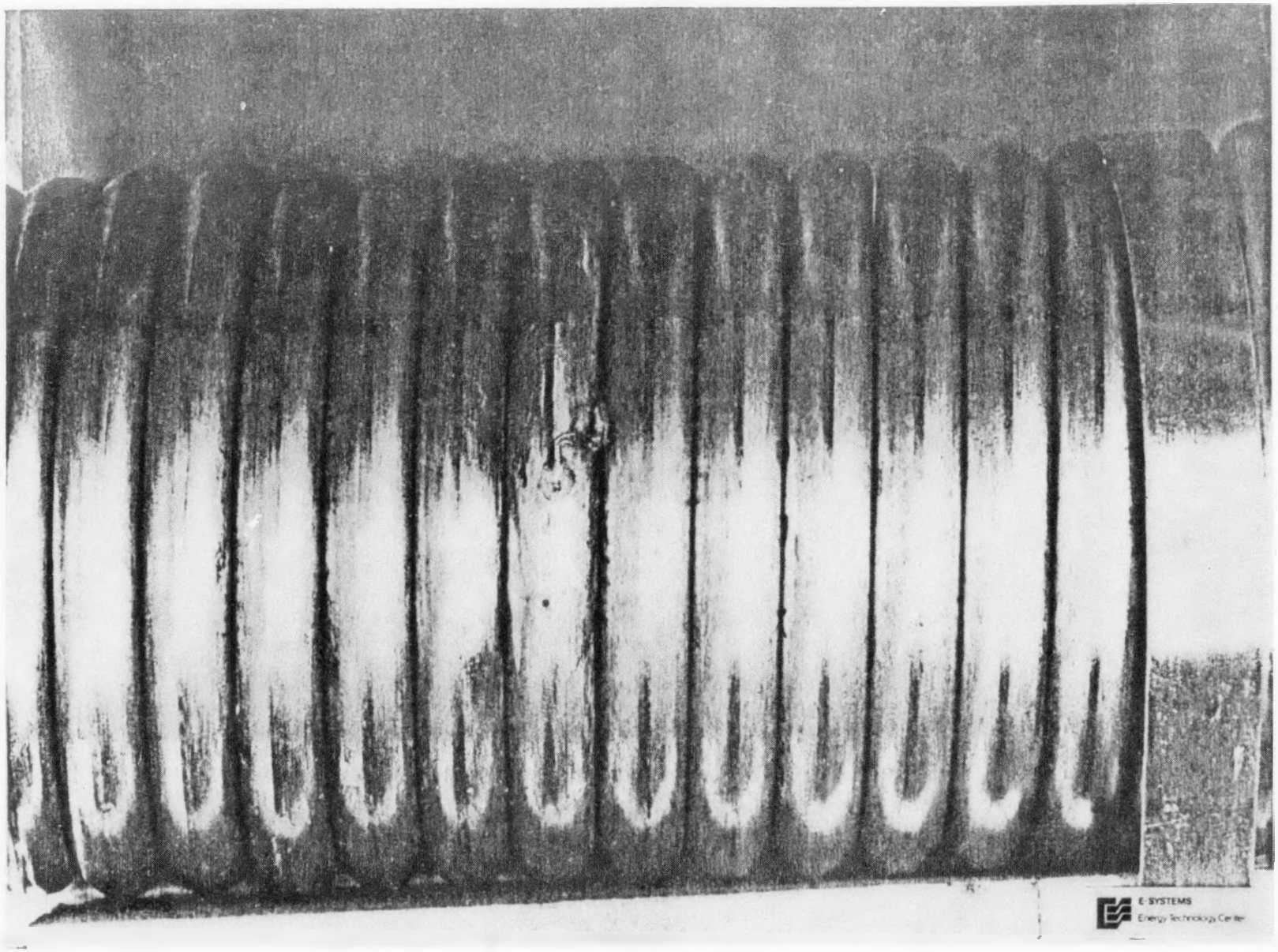

Figure A-23. Closeup View of the Thermocouples on the Outside of the Receiver

surface temperature.

The outside tube surface temperature is also monitored by an infrared thermometer. A Williamson Model 4510S thermometer with a 0.10 inch view window at a distance of 15.0 inches is mounted on the "A" frame and "looks" at the receiver surface through the gaps between the panels. This unit has the proper filters for quartz infrared lamps and gives another check on the outside surface thermocouples.

The inside tube surface temperature, approximately the fluid temperature, is monitored by another 30 thermocouples mounted in the same location on the receiver as the outside tube surface thermocouples. These inside thermocouples are similar to the outside ones except they are 0.0625 in. O.D. These too are silver brazed to the receiver tube. These thermocouples were installed to one tube and are not touching the adjacent tube wrap or the support cone. The installation technique of these thermocouples is shown in Fig. A-24.

The support cone has 22 bead type K thermocouples imbedded in it along its length.

All the thermocouple lead wires for the receiver are run inside the support cone and exit out the large end. The support cone acts as a shield for the lead wires from spurious electrical signals.

The total number of thermocouples on the receiver and support cone is 88. Two multipoint type K (0° to 1500°F temperature range) thermocouple recorders with a total capacity of 54 channels is being used to monitor approximately 50 of the most important receiver and support cone thermocouples. The other four channels

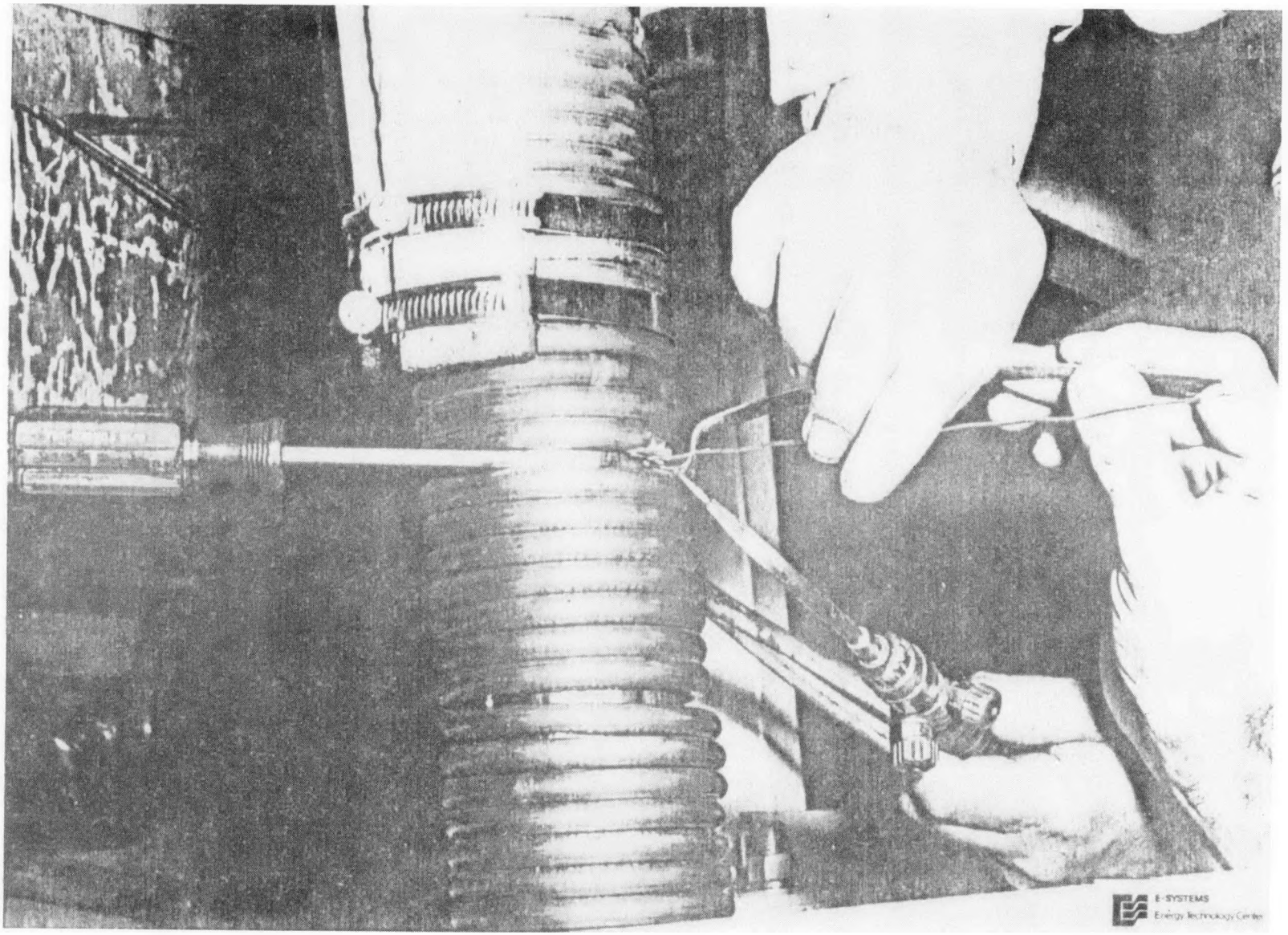

Figure A-24. Installation of the Inside Thermocouples to the Receiver

are retained for inlet water and outlet steam temperatures.

The heat fluxes were measured in the solar simulator with a Hy-Cal Model C-1821-F-60 hot wall calorimeter mounted in a "replacement" receiver. The "replacement" receiver must absorb the heat fluxes and optically "look" like the actual receiver in the solar simulator. The "replacement" receiver is an approximately 3.0 in. O.D. pipe with cooling water flowing through it to remove the absorbed heat and to keep the heat flux sensor at desired operating temperatures. Fig. A-25 shows the "replacement" receiver in the solar simulator for an actual heat flux test.

Establishing the heat fluxes circumferentially around the triangular panel arrangement and axially along the length of the lamp panels is important data for a solar simulator. The axial heat flux requirements for the nine panels simulating an axisymmetric case were presented earlier.

The approach is to set up the lamp arrangements for each panel from a preliminary optical analysis and then use the heat flux sensor to check the actual flux axially and circumferentially. Then the lamps can be rearranged in the panels to establish a more uniform circumferential flux and/or to match up closer with the desired axial fluxes. With a triangular panel arrangement, a perfectly uniform circumferential flux is difficult to attain but a fairly uniform flux has been attained in the solar simulator. This same heat flux sensor, "replacement" receiver and test approach will be used to set up non-axisymmetric heating cases in the solar simulator.

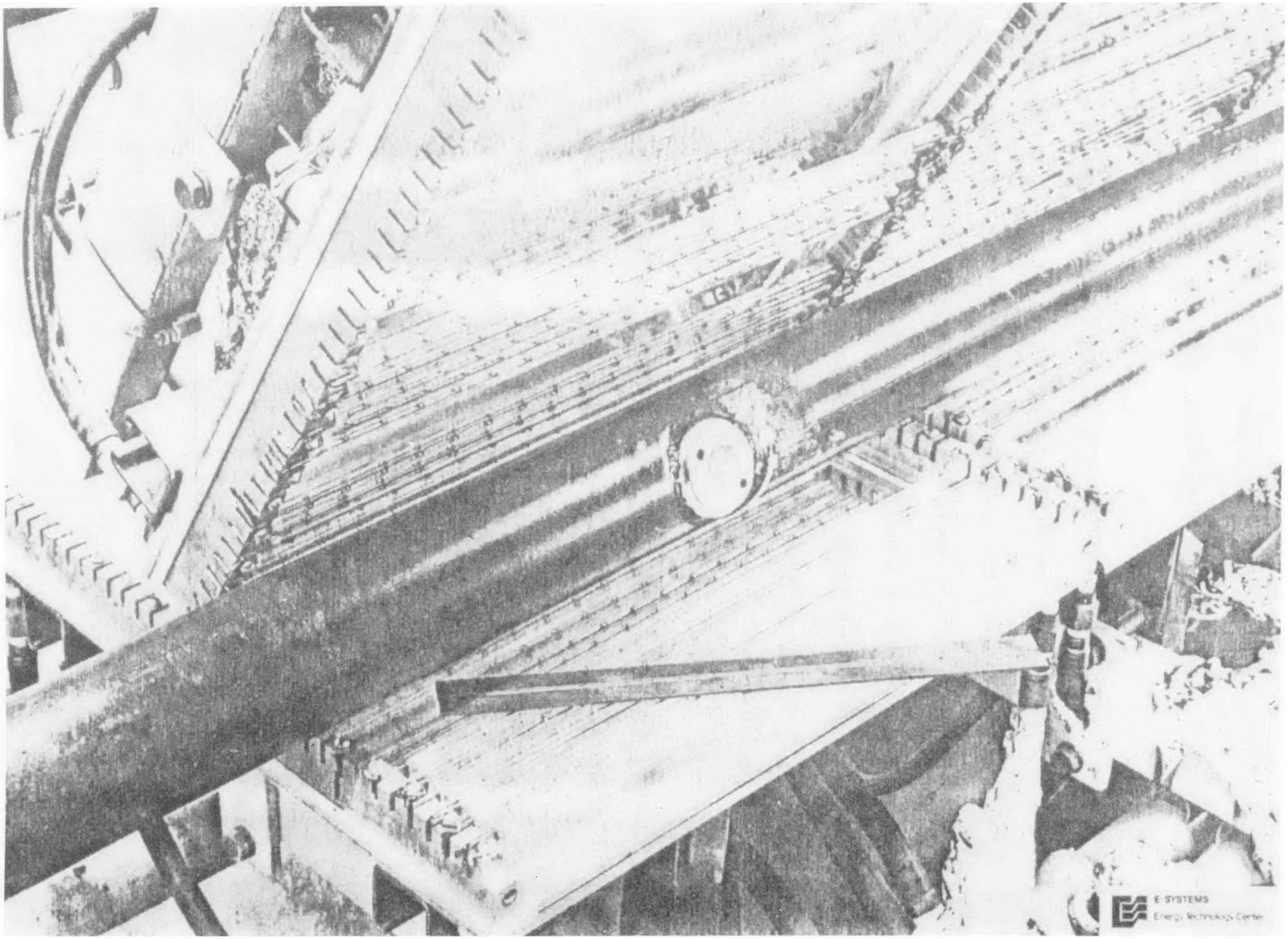

Figure A-25. Heat Flux Sensor Mounted in the "Replacement" Receiver

The geometry of the "replacement" receiver should be a 1^{o} cone with end diameters matching the actual receiver, 3.0 in. O.D. and 6.0 in. O.D. However, due to the high heat fluxes on the 3.0 in O.D. end of the receiver and the desire for good test data at this end a straight 3.0 in. O.D. pipe was used as a "replacement" receiver. This straight pipe is thought to produce very good test results at the high flux end and adequate data at the low flux end where a 3.0 in. O.D. pipe is simulating a 6.0 in. receiver. The heat flux sensor can be adjusted in and out of the pipe. For example, when testing the 3.0 in. O.D. high flux end the sensor is flush with the pipe, but when testing the low flux end the sensor is extended out to the 6.0 in. O.D. position even though the pipe is only 3.0 in. O.D.

The "replacement" receiver was coated with Pyromark 2500 flat black paint to make it optically "look" like the real receiver in the solar simulator. A thermocouple was mounted on the pipe surface near the heat flux sensor so that the pipe surface temperature could be monitored.

The panel water cooling system was instrumentated for measuring flow rate, pressure and temperatures. With the overall flow rate and temperature rise through the solar simulator, the heat removed by the cooling water can be estimated. The plenums supplying water to the panels have been calibrated and set at the desired flow distribution to the panel serpentines and busbars. This cooling system typically operates at a flow of 100 gpm at 30 psig. Under these operating conditions, the panels with the highest heat fluxes (highest cooling water flow requirements) were getting

about 3.5 gpm to the panel serpentine and about 0.5 gpm to each busbar, while the panels with the lowest heat fluxes were getting about 2.0 gpm to the serpentine and about 0.3 gpm to each busbar. Temperature indicators placed on the panels estimate that the maximum panel temperatures attained were 140°F which is under the desired limit of 160°F.

The panel cooling water system has a flow switch which shuts down the electrical controller when loss of flow trips the switch. The water cooled electrical controller has a similar switch in its water cooling loop. These flow switches are instrumented to protect the solar simulator from unexpected loss of cooling water.

The instrumentation to establish the electrical power to the quartz infrared lamps consisted of a digital voltmeter and a clamp-on ammeter. By checking the volts and amps for each leg of the 3ϕ controller the electrical power to the solar simulator can be calculated.

Spurious electrical signals were a problem early in the receiver tests. Primary source of the signals is the 60 Hertz noise generated by the high voltage and current in the test facility. The problem was eliminated by experimenting with shielding and grounding the instrumentation lead wires.

A-3.6 Preliminary Test Results

Preliminary test data has been taken on the once through boiler. To date, three different types of preliminary data on the receiver have been produced, 1) receiver temperatures versus length along the receiver for approximately steady state conditions, 2)

receiver fluid pressure drops versus flow rates and 3) heat fluxes in the solar simulator.

The receiver fluid temperatures in Figs. A-26 and A-27 show the proof of the boiler concept. Temperatures shown in these figures are extremely close to the predicted temperatures given earlier. The data in both figures are for approximately steady state axisymmetric cases with receiver inlet and outlet conditions in the range expected for this boiler. The break points between 1) the liquid heating region and the boiling region (x/R = .7 to .72) and 2) the boiling region and the superheating region (x/R = .53 to .57) match the analyses. The analyses showed about 104.8 KW of heat required to the receiver fluid flowing at 0.5 gpm whereas the two cases presented here had 92.7 and 94.9 KW which is close to the desired heat to the steam for flow rates of 0.43 and 0.5 gpm, respectively.

The heat flux from the panels was not known when this data was taken since the heat flux sensor tests were performed after these preliminary receiver tests. The lamp arrangement used was one established from the preliminary panel optical analysis. The lamp arrangement and power to the panels are producing heat fluxes which are close to the desired levels presented earlier, because of how close the test results are to the analyses results. The electrical power to the solar simulator was approximately 166 KW for both test cases presented. The electrical power is lower than expected and resulted in 57% of the electrical energy being converted to steam. The triangular panel solar simulator arrangement is more efficient than expected.

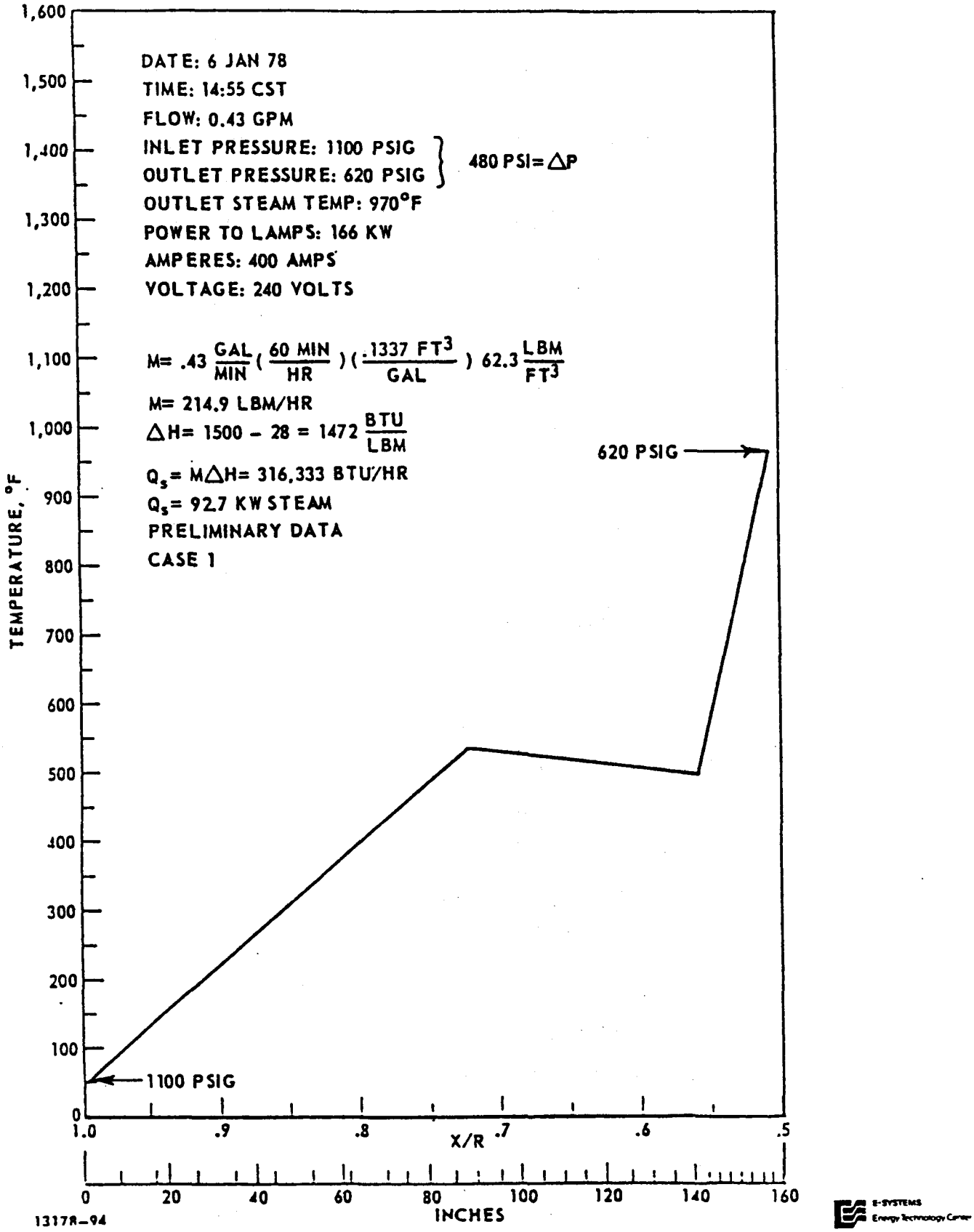

Figure A-26. Receiver Fluid Temperature Versus Length Along the Test Receiver (970°F Steam)

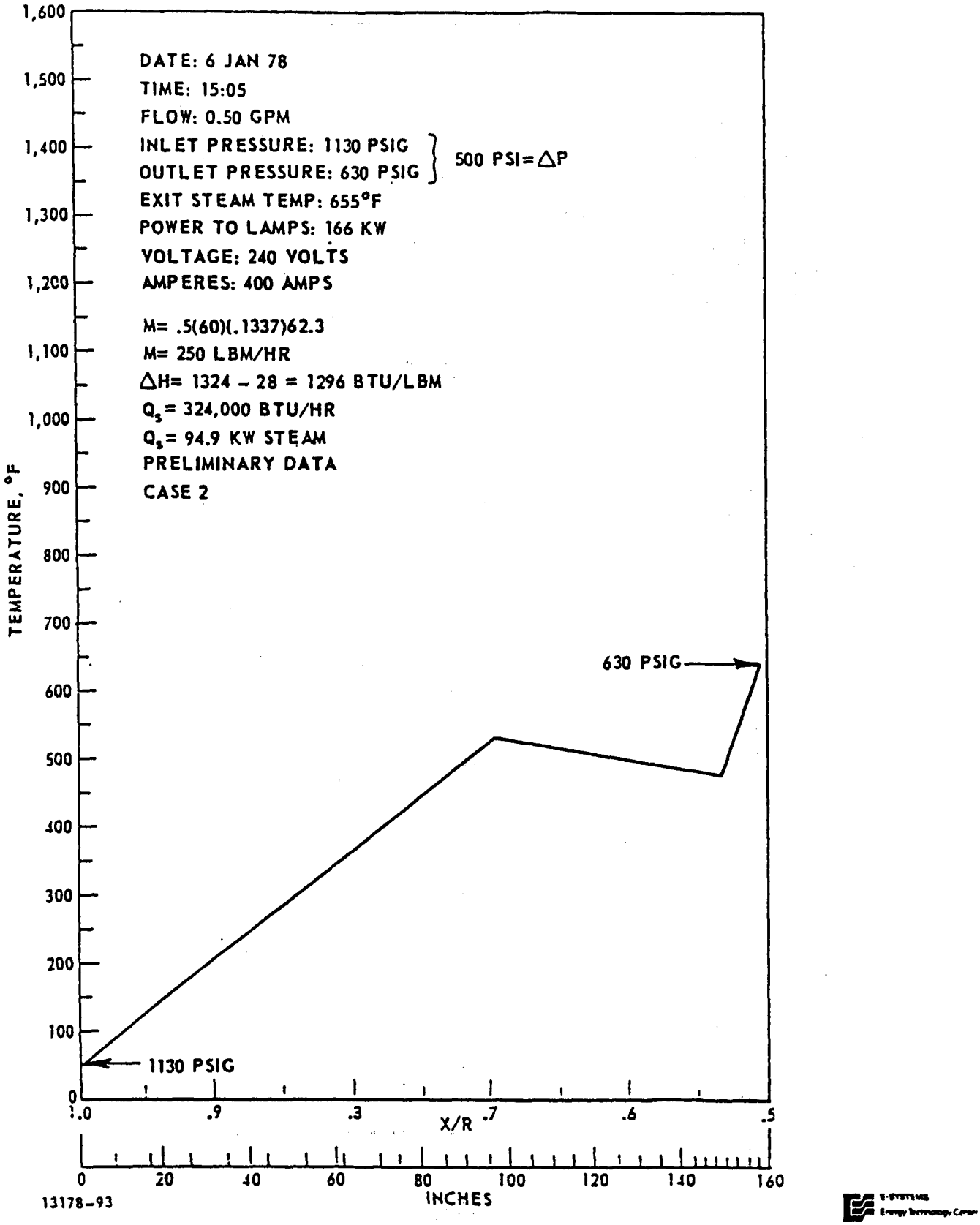

Figure A-27. Receiver Fluid Temperature Versus Length Along the Test Receiver (655°F Steam)

The fluid pressure drop for these two cases was higher than the analytical results. The ΔPs measured were 480 and 500 psi for fluid flow rates of 0.43 and 0.5 gpm, respectively.

The flow and pressures in the receiver were very steady with no visible oscillations or instabilities. For these preliminary tests, not all the instrumentation was operational. For example, the flow and pressure transducers were not in use and only a visual flow meter and gauges were used. Also, the outside tube surface thermocouples were not on the receiver for these tests.

The fluid temperatures presented are actually inside tube surface temperatures. As previously discussed, the inside tube surface and fluid temperatures should be approximately the same. The fluid temperatures do show the proper or desired trends since the three heating regions along the receiver are very distinct.

The time for the receiver to reach approximately steady state in the solar simulator is shown in Fig. A -28. It is obvious that more time will be required to reach conditions closer to steady state than the 26 minutes shown in this figure. The figure also shows how the support cone, receiver fluid, exit steam and tube outside surface temperatures heat up.

The preliminary pressure drop data for the receiver is interesting. First, the receiver ΔP versus flow rate for 65°F water with no heat input was tested. The inlet pressure on the water was varied from 250 to 1000 psig and did not appreciably affect the ΔPs measured. Fig. A-29 shows the ΔP versus flow rate for water only through the receiver. Table A-4 compares this data to the results of the preliminary analysis.

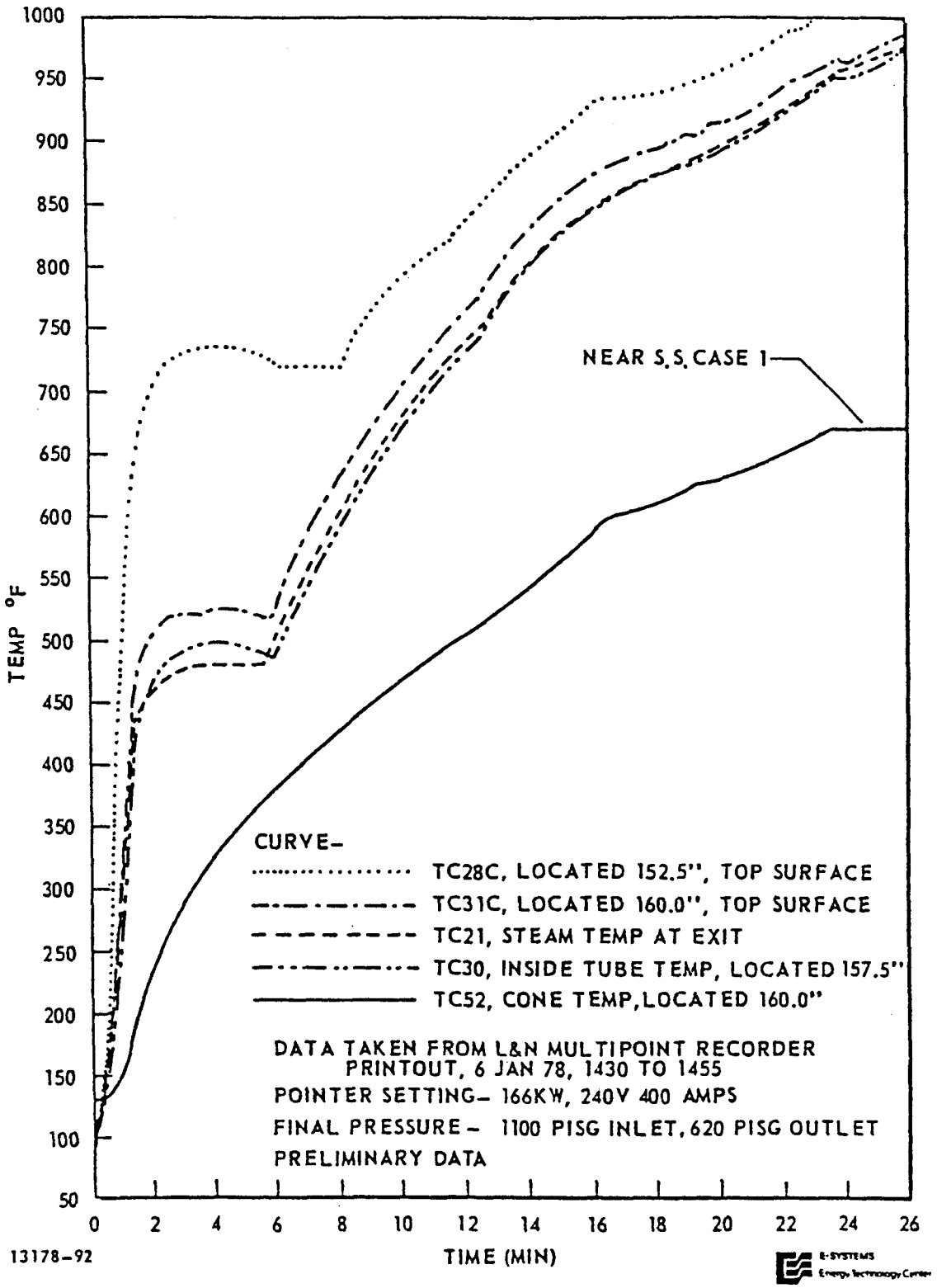

Figure A-28. Test Receiver Temperatures Versus Time (Case 1)

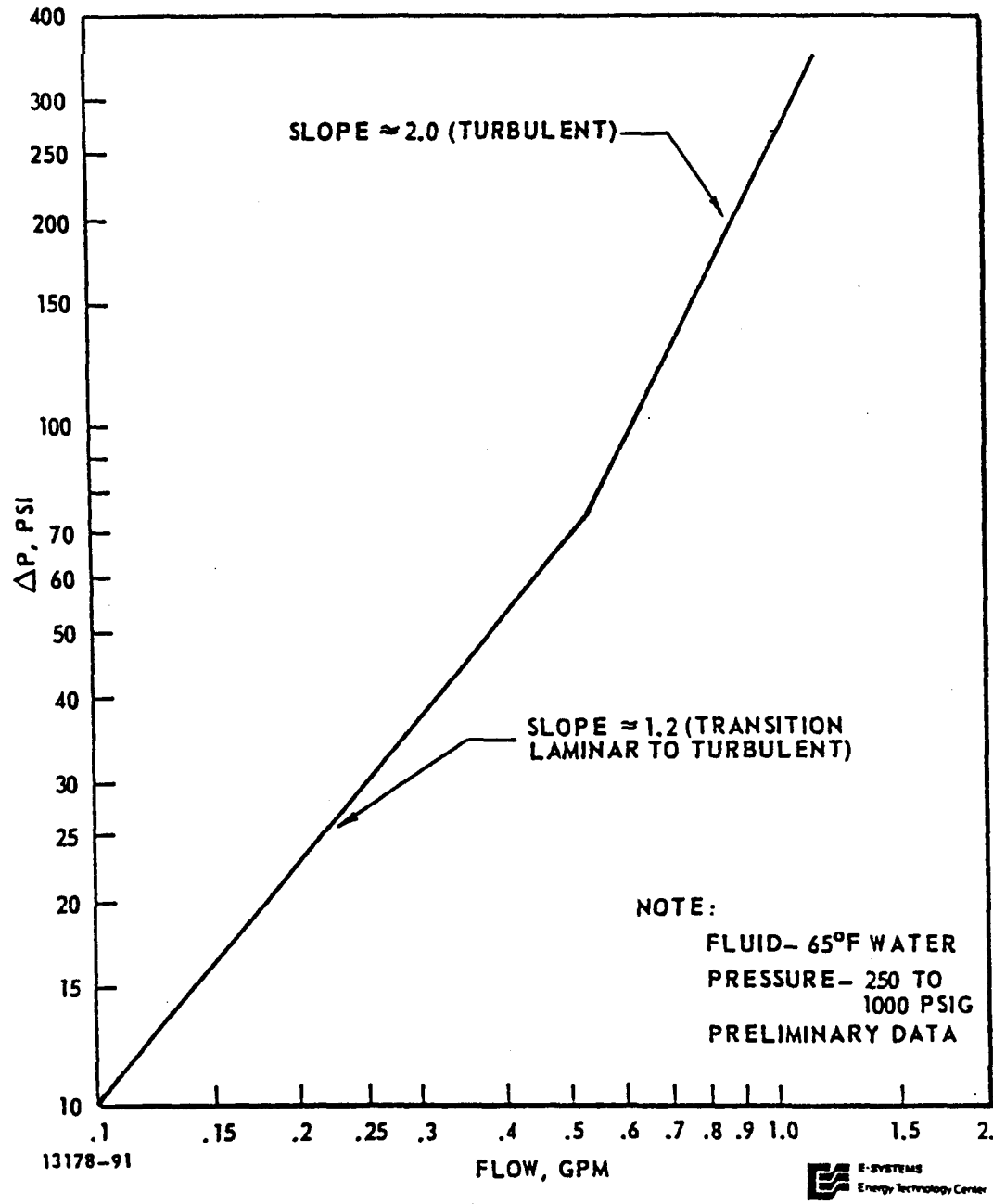

Figure A-29. Pressure Drop Versus Flow for Test Receiver (No Boiling)

TABLE A-4 PRESSURE DROP COMPARISONS (LIQUID FLOW ONLY - NO BOILING)
PRELIMINARY DATA

Flow, gpm	Velocity fps	Re	f_s	Calc. ΔP straight psi	Calc. ΔP curved psi	Meas. ΔP curved psi	$\frac{f_c}{f_s}$ factor
0.1	.68	1,235	.052	3.6	4.7	10.	1.3
0.25	1.7	3,087	.0207	8.9	10.0	30.	1.13
0.5	3.4	6,173	.036	63.	73.5	70.	1.17
0.75	5.1	9,260	.032	126.	150.	145.	1.19
1.0	6.8	12,350	.030	210.	254.	260.	1.21

The preliminary pressure drops measured for steam generation conditions indicate that a lot more data need to be taken. Table A-5 and Fig. A-30 show the ΔP versus flow rate data. This data indicates that as the inlet pressure increases the pressure drop in the receiver decreases. Of interest is that on two different test days with the same inlet conditions, the ΔP measured were different by approximately 20%. This is the reason why more test data will be taken to assure that the data are reproducible day after day.

Preliminary data with the heat flux sensor have been taken and a plot of heat flux circumferentially around inside the triangular panel arrangement is shown in Fig. A-31. This figure shows the heat flux variation inside the second triangle panel section from the small end (the highest heat flux section in the solar simulator). The desired flux for this panel section is 77,800 Btu/hr ft^2. The test data shows cyclic values from 72,500 to 83,000 Btu/hr ft^2 with an average of about 78,000 Btu/hr ft^2. This type of data is being taken for each of the nine panel sections along the length of the simulator. Emphasis will be put on matching the high heat flux panels and establishing uniform circumferential fluxes as possible. Axial heat flux plots of the high heat flux panels will also be made. The desired end result is an average panel heat flux circumferentially and axially matching the desired panel fluxes.

Figs. A-32 and A-33 show the heat fluxes in the second triangular section when the electrical power is shut off and when the electrical power is turned on in two steps, respectively. Both of these figures show how fast the quartz lamps can respond to step changes in electrical power. The heat flux has decayed 80% in

TABLE A-5 ΔP VERSUS FLOW (STEAM GENERATION)
PRELIMINARY DATA

Flow, gpm	P, in psig	P, out psig	ΔP, psi	
0.5	1100	640	460	
0.5	1200	780	420	
0.5	1240	900	340	
0.5	1260	920	340	
0.43	1100	720	380	
0.43	1100	620	480	Case 1
0.50	1130	630	500	Case 2

E-SYSTEMS
Energy Technology Center

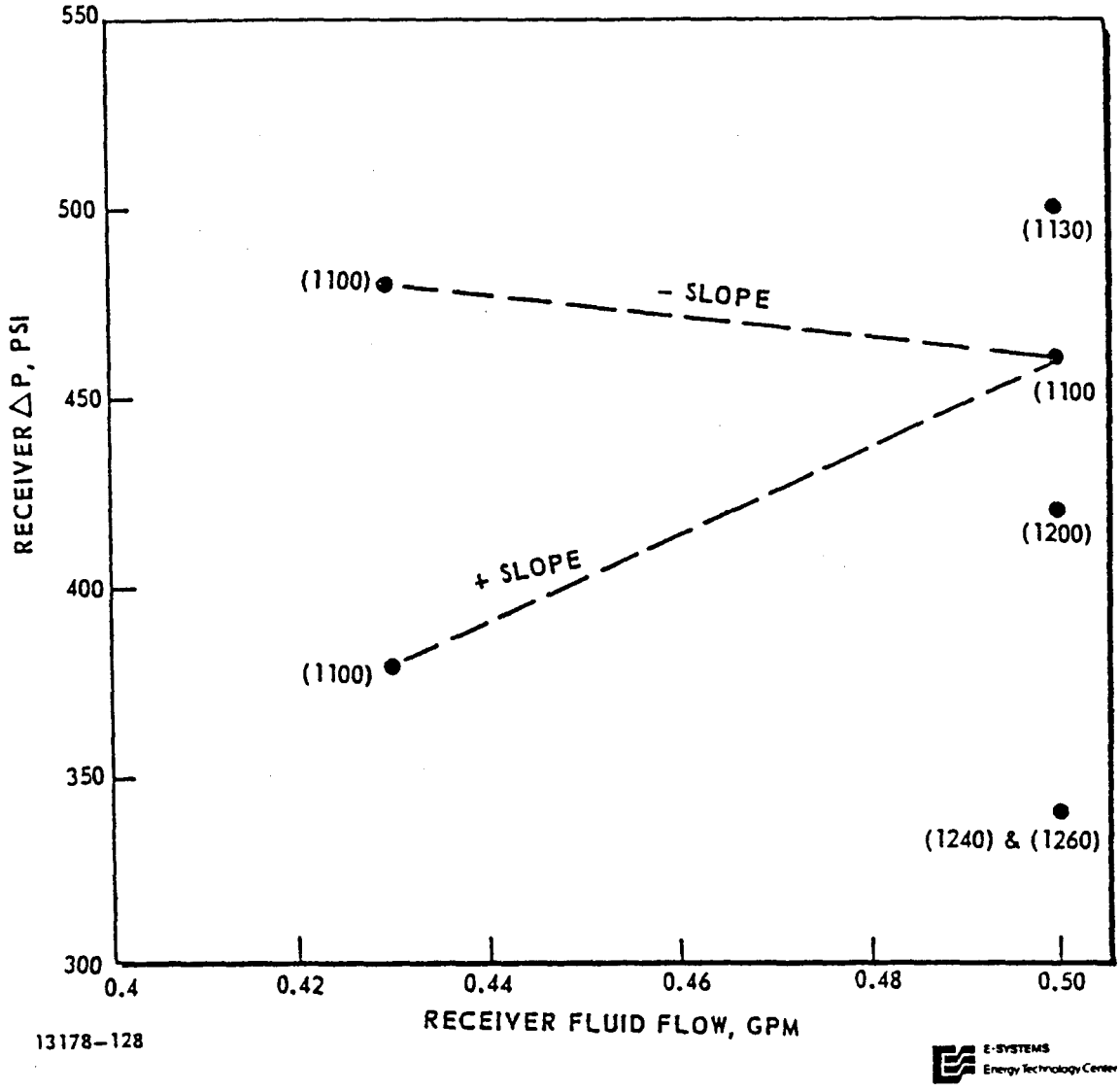

Figure A-30. Pressure Drop Versus Flow for Test Receiver (Steam Generation)

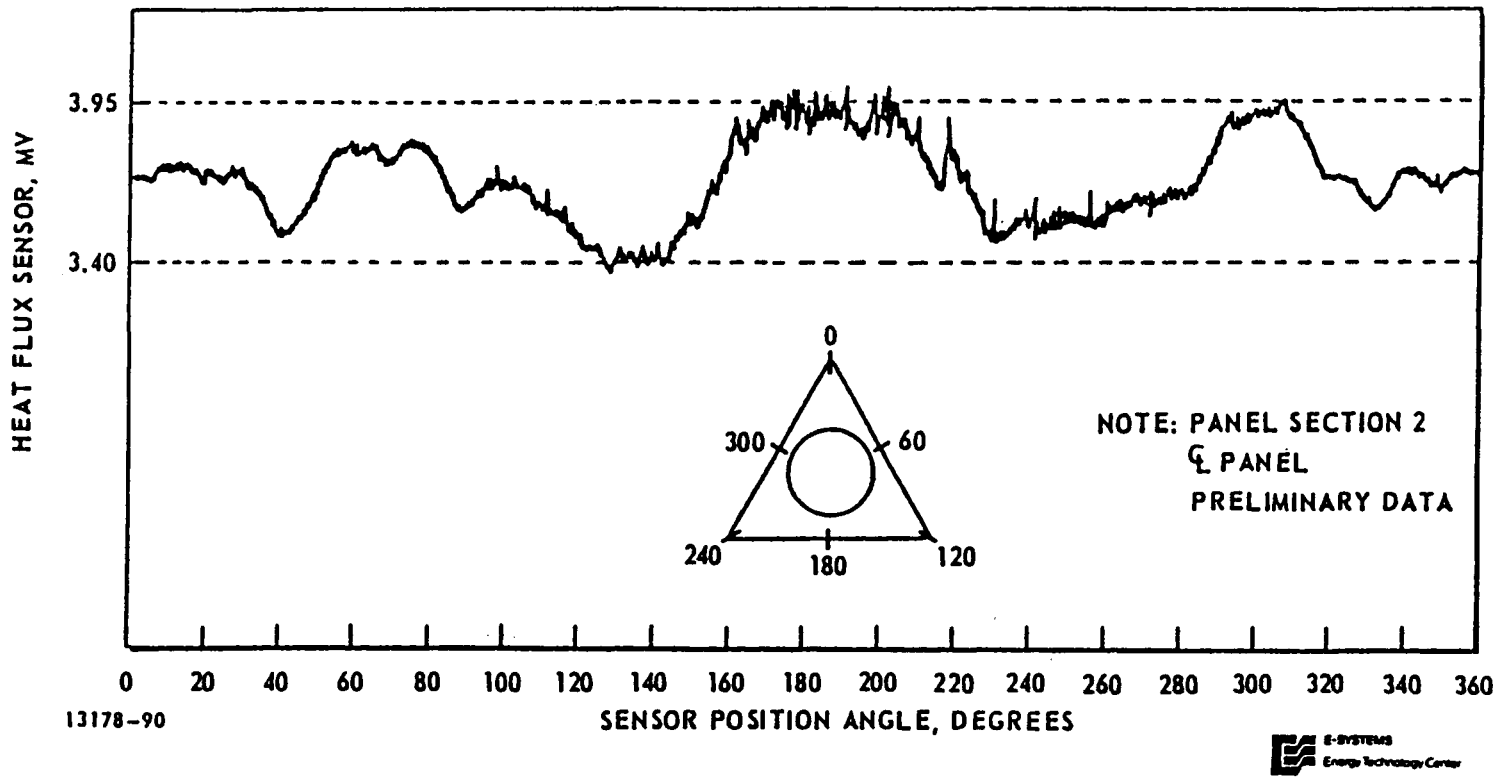

Figure A-31. Heat Flux Sensor Output Versus Position Angle in the Triangular Panel Section Number 2

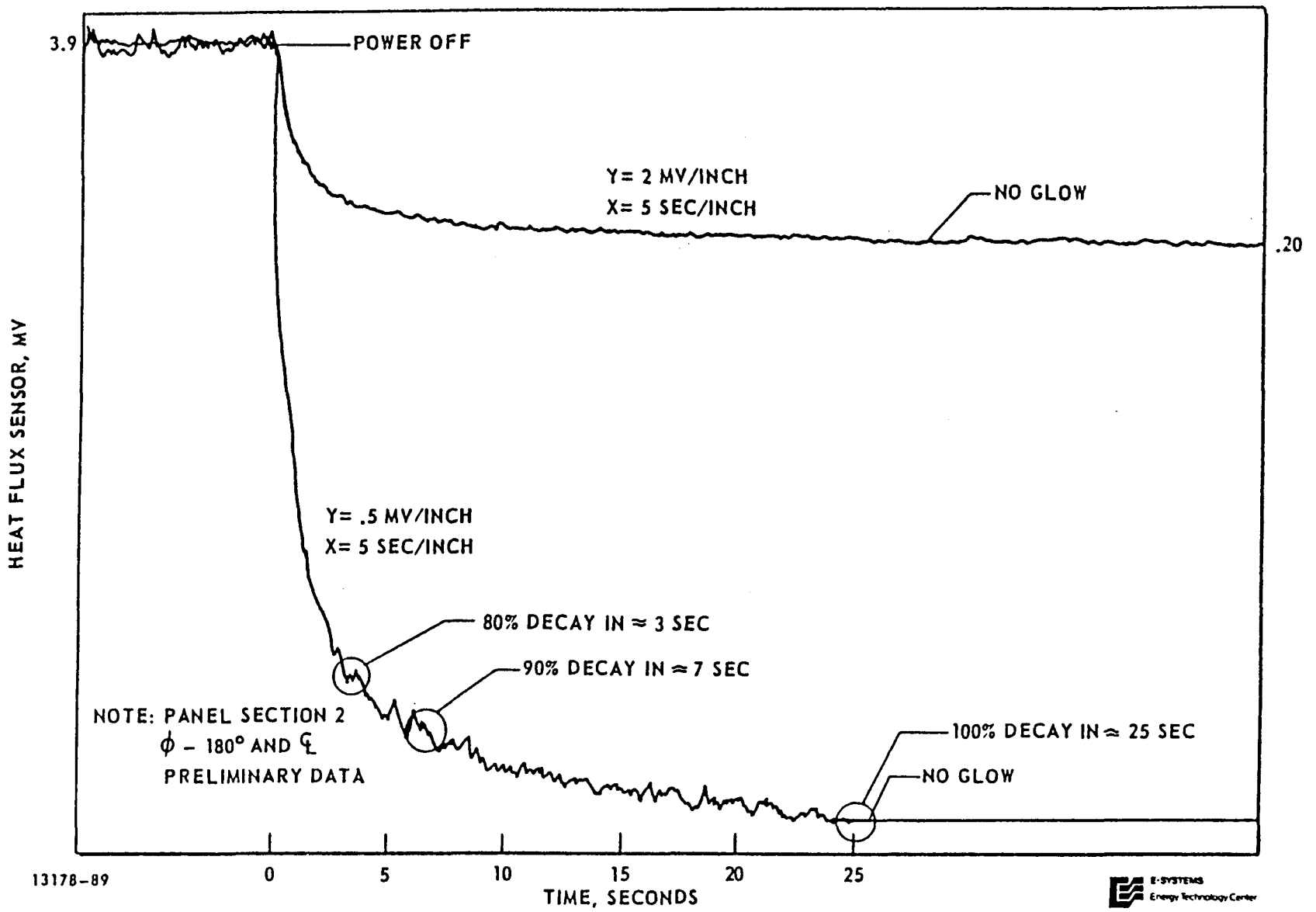

Figure A-32. Shutdown Transient - Heat Flux Versus Time

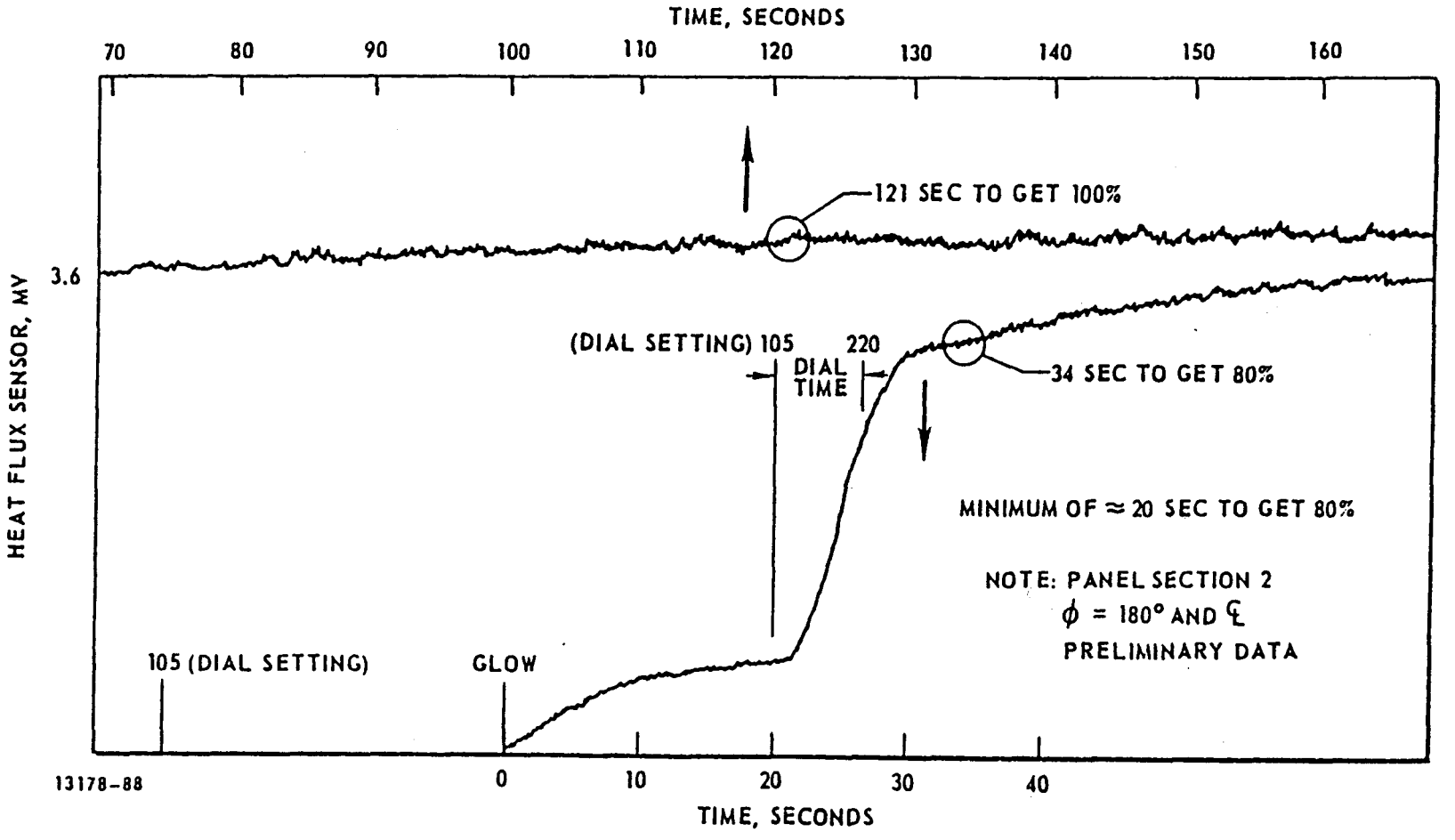

Figure A-33. Startup Transient - Heat Flux Versus Time

a matter of approximately 3 seconds after shutdown. It took about 34 seconds for the heat flux to build up to 80% with the two step heat input. A one step heat input could probably shorten the 80% heat flux case to about 15 seconds. This preliminary transient heat flux data will be used to plan future transient receiver tests.

A-3.7 Conclusions

Conclusions drawn to date with the preliminary data are that the concept of a single tube helically wound once through boiler does work, only stable flow conditions have been observed, and that the higher than expected pressure drops are probably reproducible and inheritant in the boiler. The test data show the boiler operating in the three distinct heating regions (1) liquid heating, (2) boiling and (3) superheating. The desired operating axisymmetrical case has 104.8 KW of heat going to the 0.5 gpm fluid flow along the length of the boiler. Tests to date, under similar axisymmetric heating and flow conditions, have heated the fluid up to 94.0 KW. The desired outlet superheated steam conditions have been attained, (1) pressures ranging from 500 to 1000 psig and (2) temperatures ranging from 500° to 1000°F.

The boiler tested has the geometry associated with a 45 to 50 ft. aperture diameter dish. The boiler tubing has the geometry being considered for future receivers. The test data from this test facility should be used to design the proposed larger multitube receivers.

A-4 TWO-PHASE FLOW HEAT TRANSFER IN HELICAL COILS

The two-phase flow heat transfer experiments being conducted at Texas Tech are the first part of an attempt to sort out effects of flow channel geometry and heat flux asymmetries on the heat transfer in the FMDF receiver. While there is a body of prior work dealing with helical flows, most has either dealt with single phase liquids or with low Reynolds number flows. If we consider developing two-phase flows in the turbulent regime, with very large length-to-diameter ratios, little information is available in the open literature.

The approach we are using is to use joule heating, with the tube itself being the heater, as a means of providing an easily controlled, easily measured heat source. Also, the individual effects of flow path geometry and heating asymmetry may easily be separated. Important variables for the helical flow tests are the radial acceleration component (affected by coil radius and pitch), the tube L/D radio, the degree of liquid subcooling, and the imposed heat flux. The prime factors in the study of axial asymmetry of heat flux are the period of the asymmetry (affected by heater geometry and fluid flow rate) and the amplitude of the heat flux swings. At this writing all of the effort has been devoted to getting the two-phase flow loop operable and preliminary helical flow tests. The original design for the axial asymmetry test section proved to be prohibitively costly, so those tests have been delayed. A new axial asymmetry test section is under design and should be fabricated soon.

A-4.1 Joule Heating Two-Phase Flow Loop

The two-phase flow loop which is shown in Fig. A-34 consists

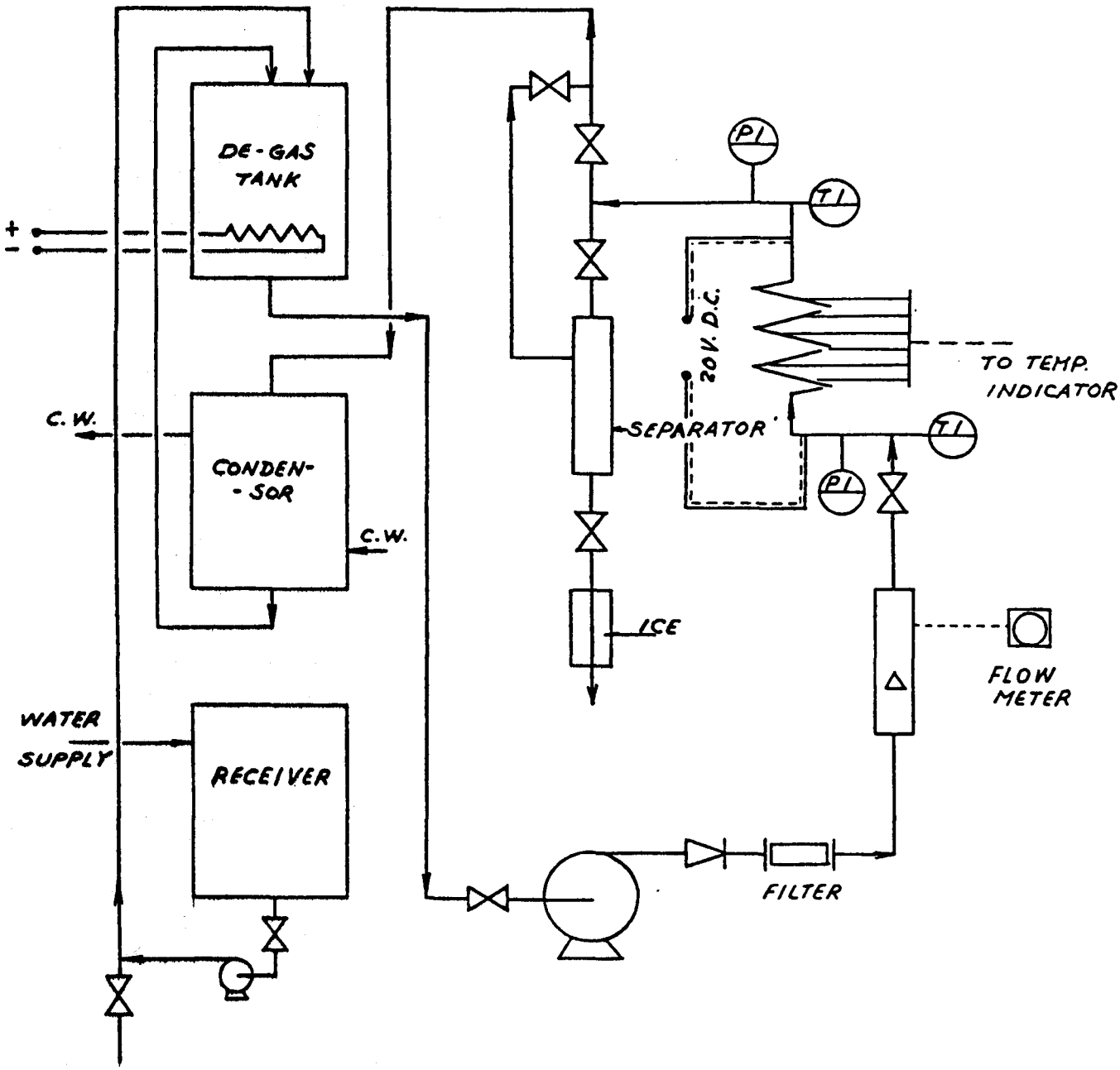

Figure A-34. Schematic Diagram of the Joule Heating Two-Phase Flow Loop

of several major parts:

1. Degas tank
2. Feed pump
3. Flow meter
4. Joule - heated test section
5. Impingement separator
6. Condensor

The purpose of the degas tank is two-fold, first, it acts as a holding tank for feed liquid, and since the tank is elevated approximately 16 ft. above the pump it provides net positive suction head for the pump. In addition, the degas tank has heat tracing around the outside in order to maintain the feed liquid as near saturation condition as possible. The purpose for this is that dissolved gases can play a fairly important role in supplying extra vapor to a developing two-phase flow and the excess vapor will likely cause a premature departure from nucleate boiling.

Two feed pumps are available for use with the test section. One is a for moderately low pressures ($\leq$ 150 psig), a Teel, bronze, rotary-gear pump, close coupled to a 3/4 hp motor. The second pump, which is used for pressures up to 550 psig, is a Moyno Model RA603 progressing cavity pump, powered by a 1 hp electric motor. Both of the pumps were chosen because they are positive displacement pumps and because both pumps introduce only negligible pressure variations in the flowing fluid. Both of the feed pumps are rated for a maximum delivery of approximately 3/4 of a gallon per minute at maximum pressure. The flow measuring device used in this system is a Ramapo Model Mark X flow meter with direct readout capability. This flow meter is an inductance

type rotameter with the float forming one leg of a variable reluctance Whetstone bridge. Two floats are available, one with a range of .075 to 1 gallon per minute and the other with a flow range of .005 to .15 gallon per minute. This allows operation at the extremely low flow rates to look at effects of turn-down on heat transfer.

The test sections used in the helical experiments were made up of 304 stainless steel, 1/4-inch outside diameter, .028-inch wall tubing. The test sections, at least for the initial tests that were done, were deliberately set up to match the pitch and the coil diameter the for RPS (200 ft. aperture diameter and 20 tubes wrapped around the receiver. In subsequent tests both pitch and the coil diameter will be varied to gain understanding of the effects of radial acceleration upon turbulent developing two-phase flows.

The two-phase flow loop has provision for measurement of steam quality down to extremely low qualities. The device is an Andersor Hi-eF, Model Model LCR50 impingement separator. The principle of this separator is that a mixture of gas and liquid enters trough the top and it hits an impingement plate. The vapor phase passes out midway down the separator and the liquid comes out the bottom. These devices have been successfully used as a means of quality measurement in the low to moderate quality regions.

The condenser is a very simple copper coil suspended in a water bath. Cooling water flows through the bath, condensing the steam. Then the condensate is returned to the degas tank, making a complete closed loop system.

Two test fluids will be used in this apparatus. To date doubly distilled water has been the test fluid since this would be the

same thing that will be used in the ATS and in the RPS systems. Later experiments will involve the use of Freon-113 as an analog fluid for water at very high pressures. Some experiments may be done using heat transfer oils at a later date.

The helical test section is instrumented with thermocouples placed at 3-inch intervals. Every other 3-inch interval involves a pair of thermocouples; one on the outside of the helix and one on the inside of the helix in order to compare heat transfer coefficients at a single location. The thermocouples were attached in the following manner: first, a pad of sodium silicate cement was laid on the surface of the tube itself. The cement was allowed to cure and then sanded down to a thickness of approximately 0.002 inch. This provides electrical insulation from the DC current in the tube, but still allows a reasonable contact between the thermocouple bead and the tube wall itself. The thermocouples were then press-fastened to the cement pad with Scotch Brand No. 365 fiberglass thermosetting tape. This technique has been found to be very satisfactory in holding the thermocouple bead tightly against the sodium silicate pad thus minimizing contact thermal resistance. Both Type K and Type J thermocouples are used in these experiments. Figure A-35 shows a thermocouple resting on the silicate pad and the fiberglass tape used to secure it. A completed thermocouple installation is shown in Fig. A-36. After all the thermocouples have been installed the coil is wrapped in a double layer of 1/2-inch thick Tempmat^{R} high temperature insulation and then in a layer of canvas cloth.

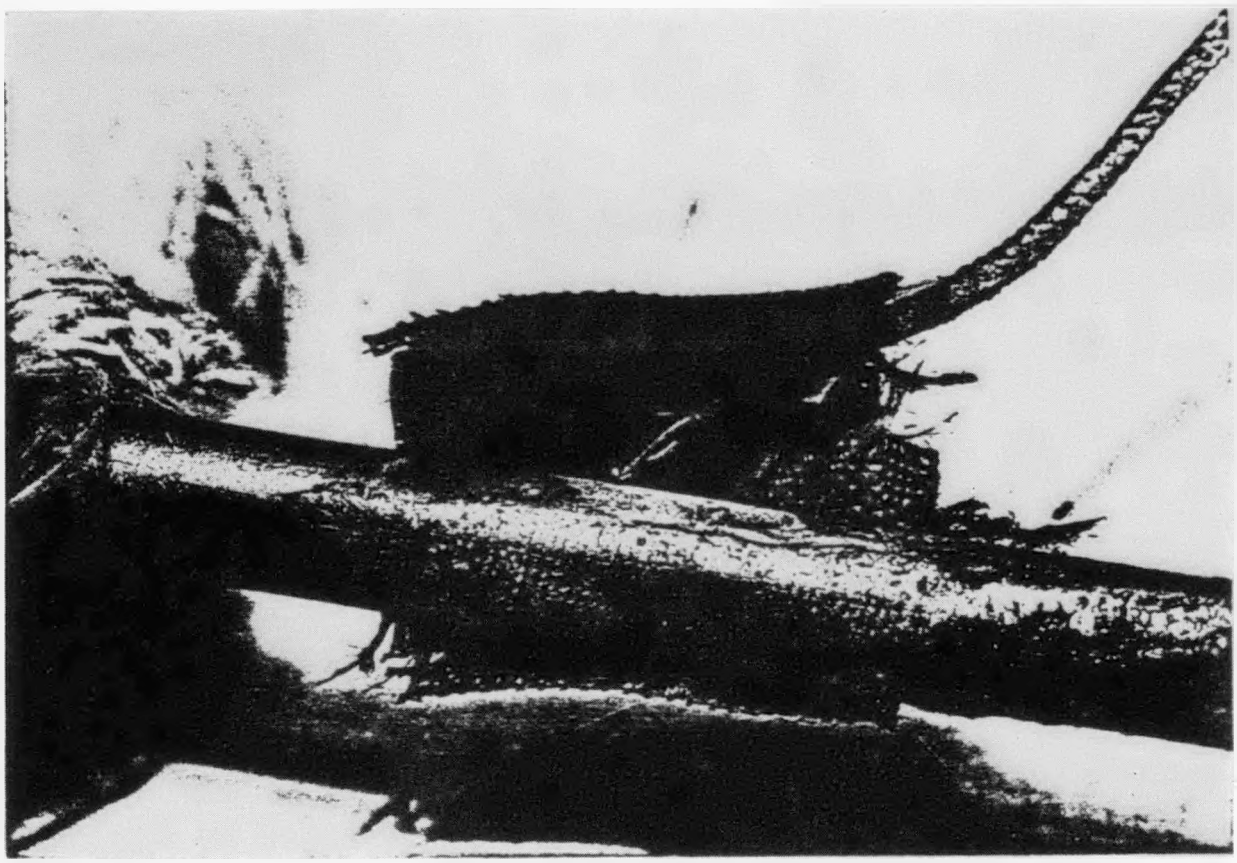

Figure A-35. Thermocouple Resting on Silicate Pad Before Final Installation

Figure A-36. Completed Thermocouple Installation

Thermocouple temperature measurements are made using a Brown Dual Function Potentiometer Pyrometer dial indicator and a Honeywell Elektronik 15 dial recorder for J type thermocouples. Four channels of thermocouple input may be recorded in real time on a Beckman Model SC III Dynagraph recorder using a Precision Electronics amplifier system. The Dynagraph has an additional four channels for monitoring pressures and flowrate.

Pressures were measured in the system at the points indicated in Fig. A-34 either by dial pressure gauges supplied by Foxboro or by a digital pressure sensor located at the inlet and the outlet of the test section. This system is a Thinc Model P-301 digital pressure readout system with Thinc 1207A pressure sensors. The sensors have an operating range of 0-1000 psia and were calibrated using a dead-weight testor.

The power supply for the Texas Tech helical flow loop is a Sorrenson Model DCR 20-1000A, 20 KVA direct current power supply. Two precision meters and a precision shunt were used to measure the electrical power, amperage and voltage supplied to the test section.

A-4.2 Joule Heating Test Data Reduction

The basic data that came out the heat transfer experiments are a set of temperatures measured at a number of points along the test section, the power dissipated in the test section, and pressure measurements at the beginning and end of the test section. The fundamental assumption in all of this work is that we have an equilibrium two-phase flow. In the preliminary experiments to date this assumption

has not been checked. In later experiments the equilibrium assumption will be verified by direct measurement of steam quality and comparing the measured and predicted results.

To convert the power dissipated within the test section into a heat flux, we use the relationship

$$q/L[\text{Btu/hr/ft tube}] = \text{Volts} \times \text{Amps} \times 3.413 \qquad \text{(A-25)}$$

The inside wall temperature at any point is calculated from the measured outside wall temperature by

$$T_i = T_o - \left[\frac{S_e}{4k}\left(R_o^2 - R_i^2\right) + \frac{S_e R_o^2}{2k}\,\ell n\left(\frac{R_o}{R_i}\right)\right] \qquad \text{(A-26)}$$

where T_i = inside wall temperature, °F (calculated)

T_o = outside wall temperature, °F (measured)

S_e = volumetric rate of heat generaion, Btu/ft^3

k = thermal conductivity of tube, $Btu/ft^2hr(°f/ft)$

R_o = outer tube radius, ft

R_i = inner tube radius, ft

The local heat transfer coefficient is given by

$$(h_i)_{\text{experimental}}[Btu/ft^2hr°F] = (q/A)[Btu/ft^2hr]/(T_o - T_i)[°F] \qquad \text{(A-27)}$$

A-4.3 Sample Results For Helical Coil

The preliminary data discussed here were taken using a 0.25 inch OD by 0.028-inch wall, 304 stainless steel tube, 93. inches long.

This tube was coiled to 1 foot diameter, with a pitch equivalent to having twenty tubes coiled in parallel (5-inch separation).

Raw temperature-vs-position data for a sample run are shown in Fig. A-37. The somewhat erratic scatter of the outside wall temperatures are due to the fact that with the present pump arrangement it is difficult to keep a flow rate truly constant. Small fluctuations in flow rate are mirrored as fluctuations in temperature. Also, the temperature resolution on the dial indicators is $\pm$ 3-4°F for the K-type and $\pm$2°F for the J-type. The digital indicators on order will solve this problem. The fluid temperature profile is a calculated profile.

If we smooth the wall temperature data shown in Fig. A-37, we then calculate the heat transfer coefficients shown in Fig. A-38. The most important feature to note in this figure is that the heat transfer coefficient along the outside wall is consistently about 20% higher than on the inside wall. This is a very preliminary indication that the heat transfer along the outer wall is enhanced by the helical flow path. Indeed, heat transfer coefficients both along the inside of the coil and along the outside of the coil are higher than expected for straight tubes.

The digital pressure readout at no time indicated fluctuations greater than $\pm$1 psi, but the irregularity of the flow rate during the test run is evidence of at least a minor pressure fluctuation in the system. Unfortunately, the Dynagraph recorder was not in operation during this run, so any substantive observations about apparent flow stability are not possible.

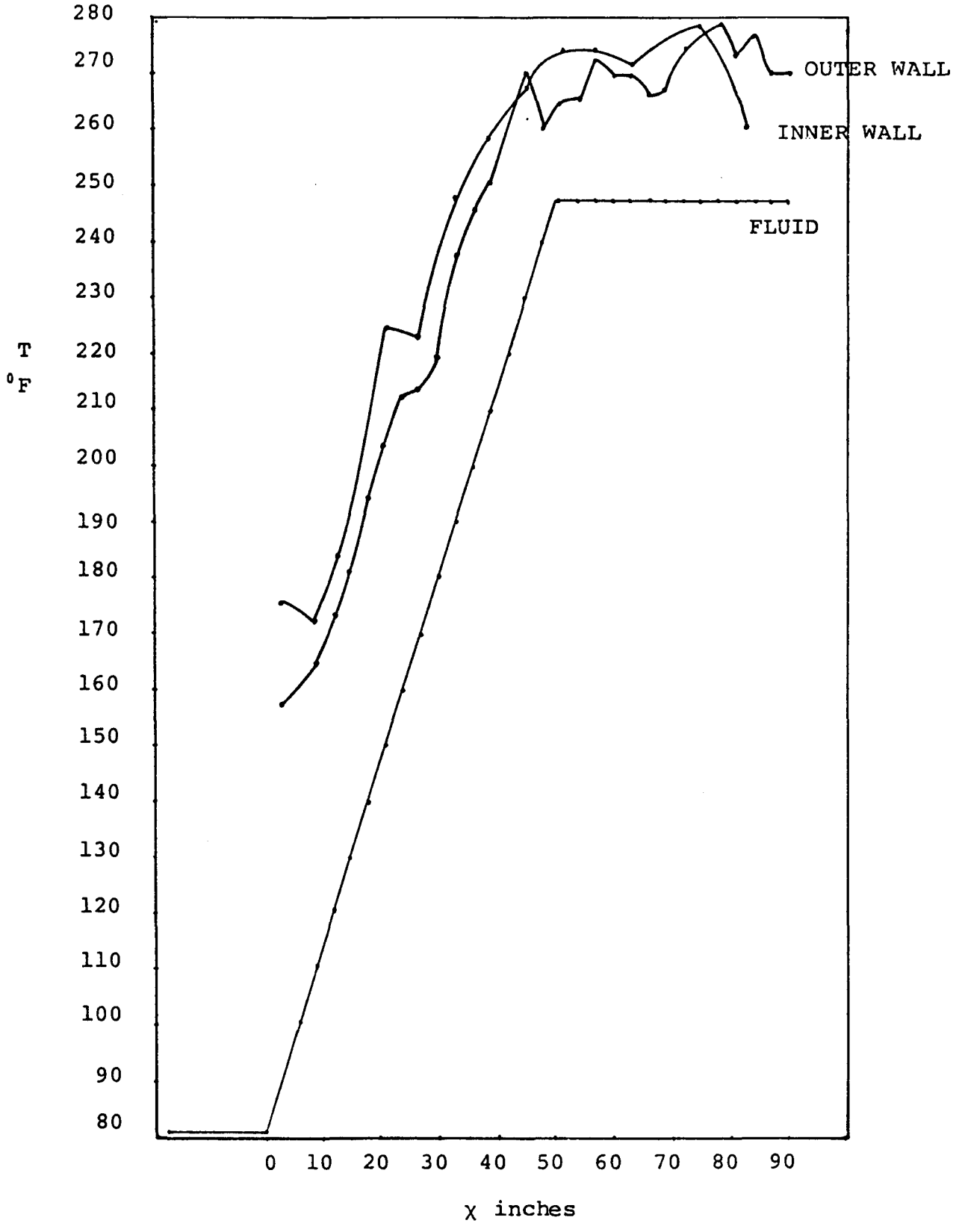

Figure A-37. Tube Outside Wall Temperature During Helical, Developing Two-Phase Flow

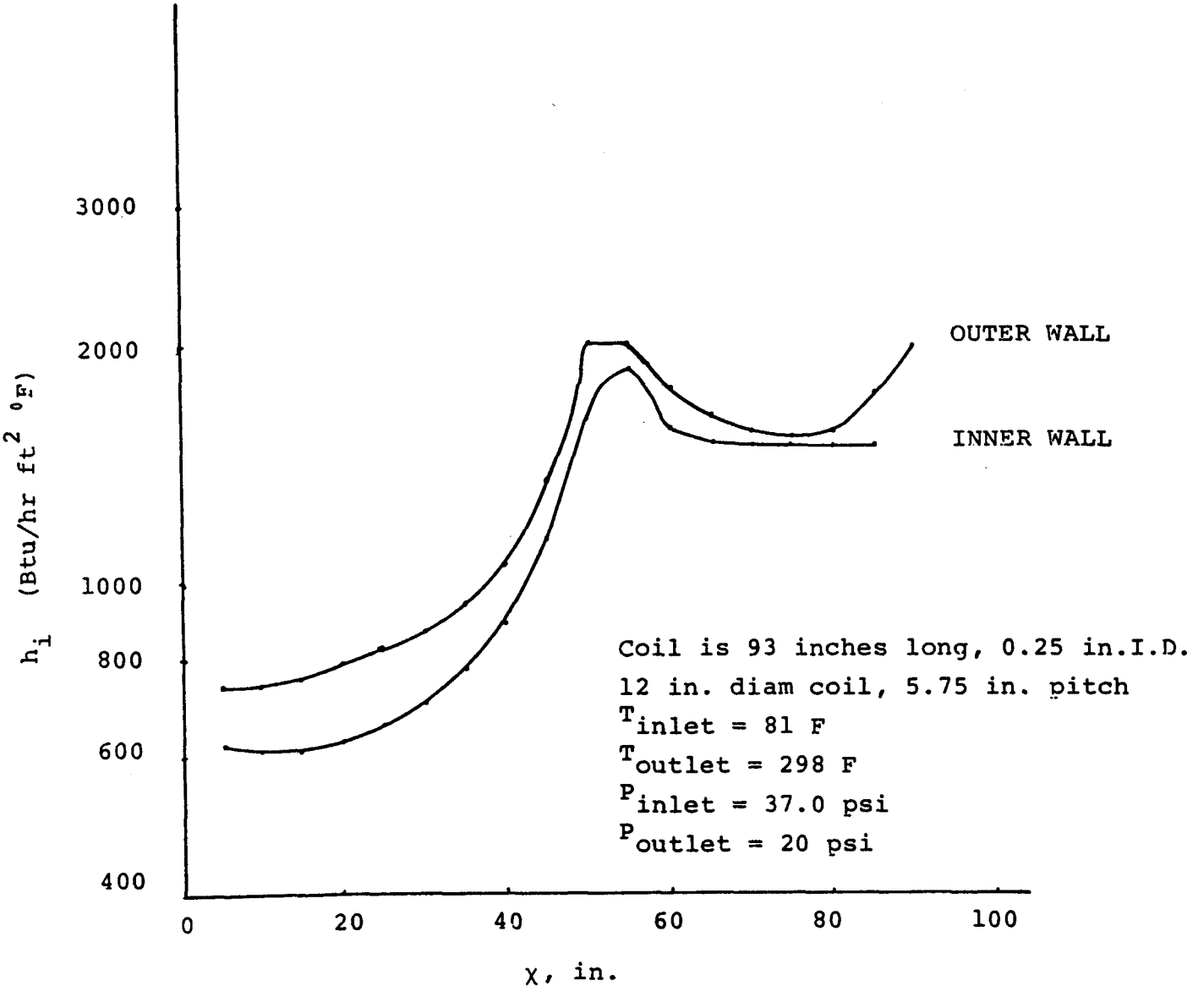

Figure A-38. Internal Heat Transfer Coefficient Behavior for Helical, Developing Two-Phase Flow

A-5 RECEIVER HEAT LOSS TESTS

An additional part of the experimental receiver thermal performance program was to evaluate the convective heat transfer loss coefficients for a helically wrapped coil under conditions of free and forced convective heat flow. The specific purpose was to determine if the non-uniform surface resulting from the exposed 3/8" O.D. tubes caused significant deviations from smooth cylinder convective heat loss predictions. The potential effect would be analogous to surface roughness in internal pipe flow.

A schematic diagram of the test facility is shown in Figure A-39. The test section is a DC joule heated, helically wrapped length of 3/8", 304 SS tubing, close packed, with varying outside coil diameters. Both polished and flat, black-painted surfaces are being tested to evaluate the radiation contribution. Cold surface temperatures range from 300°F to 600°F and the ends are capped and insulated to minimize internal and end convective heat loss.

Measurements include multiple coil outer surface temperatures, electrical power dissipated, free stream temperature, and free stream velocity. Initial tests are being conducted under free convection conditions for both horizontal and 45° inclined positions. These data are being compared to results for smooth cylinders given by McAdams [26]. Subsequent tests will evaluate forced convection heat loss and will also be compared to smooth

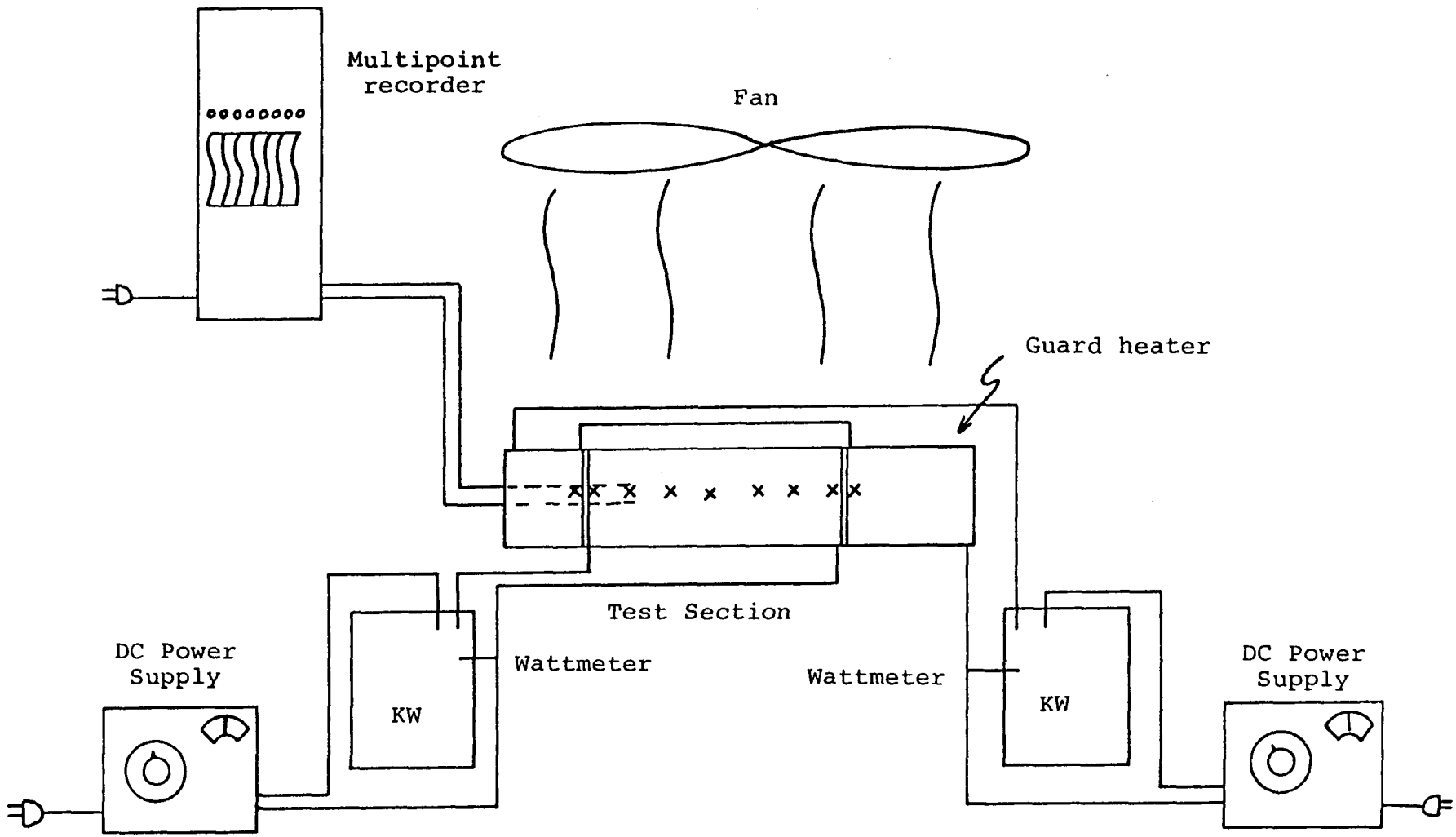

Figure A-39. Receiver Heat Loss Test Schematic

cylinder correlation by Hilpert [27]. Smooth cylinder tests will also be made as a verification of the experimental procedure.

Initial results for experimentally measured free convection heat transfer coefficients are shown in Fig. A-40 plotted relative to calculated smooth cylinder values. The data indicate an increase of from 10 to 20% over predicted smooth cylinder results. However, these data are preliminary and more tests must be performed before these results are accepted.

Additional test data for convective heat losses are included in Appendix L, Wind Tunnel Test Results.

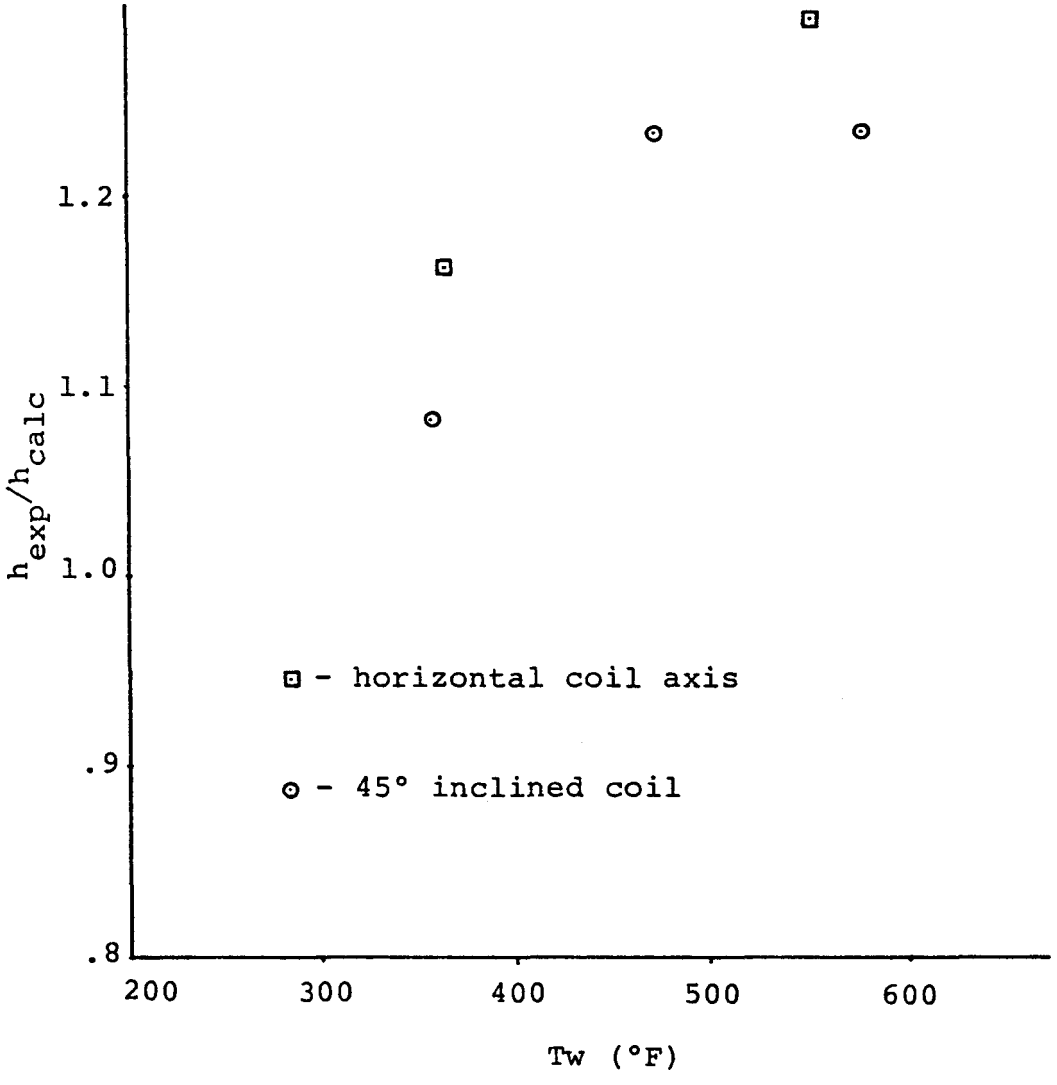

Figure A-40. Ratio of Experimental to Calculated Free Convection Coefficients

A-6 RECEIVER COATING MATERIAL

The recommended candidate for the absorptive coating is Pyromark, a refractory paint manufactured by Tempil Corporation. This is a non-selective, flat black coating which exhibits excellent stability at temperatures as high as 2000°F. Tests were performed on this paint by Langley Research Center, NASA [28] for two substrate materials, as-rolled stainless steel and polished Inconel. Measured values of total emittance varied from 0.78 to 0.90 over a temperature range from 600°F to 2000°F on Inconel and 0.81 to 0.94 for the stainless steel over the same temperature range. In both cases, the measured value of emittance increased with increasing temperature.

Measurements were also conducted at Texas Tech University to determine the absorptivity of Pyromark on an Inconel substrate as a function of angle of incidence. The measurements were carried out using a Model 1A Alphatometer from Devices and Services Company of Dallas, Texas.

Sample absorptivity is measured with the alphatometer by placing the instrument in bright, direct sunlight, measuring first the total incident solar radiation flux density, and then the total reflected flux density from the sample. It is assumed that only diffuse reflection occurs. The absorptivity is obtained by subtracting the reflected from the incident flux density. The technique should be most accurate for materials with high absorptivities.

The alphatometer consists of an omnidirectional thermopile detector with flat response throughout the solar spectrum and a large, flat board for holding the sample, which is mounted on a tripod for aligning it with the sun. The detector is mounted in the center of and about 2.5 cm above the board, and may be rotated directly toward or away from it. In operation, the incident flux is determined by rotating the detector away from the sample, toward the sun, and the reflected flux is determined by rotating the detector 180^0, to directly face the sample. By changing the angle of the sample board relative to the sun, sample absorptivities as a function of angle of incidence were obtained.

Fig. A-41 shows the results for the absorptivity of a thin coating of "Pyromark" paint on a flat Inconel substrate as obtained with the device described above. These data were obtained using a sample sheet of dimensions 8 in. x 8 in. The absorptivity calculated based on the assumption that the absorbing sample is very large in extent, so that all of the reflected flux comes from the sample. The manufacturer has indicated that 8 in. x 8 in. is the minimum sample size acceptable for the use of the instrument supplied.

For low angles of incidence the error introduced by the finite sample size is small, of the order of 1%, but it becomes significant at the larger angles, and probably is responsible for the fall-off in absorptivity at large angles. The effect on sample size is shown in Fig. A-42 where data from a sample only 6 inches on a side are shown. The data shown in Fig. A-42 need to be corrected for this effect, and an effort to do so is currently underway.

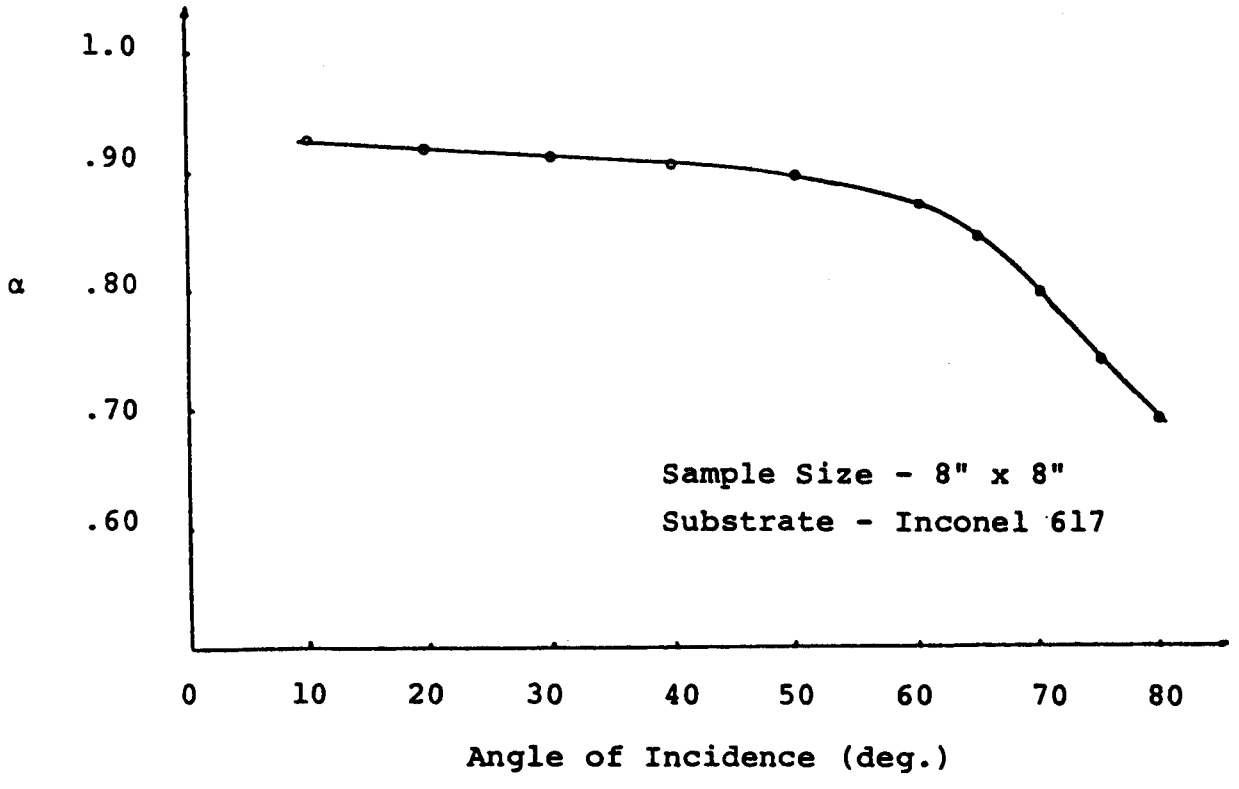

Figure A-41. Solar Absorptance of Pyromark vs. Angle of Incidence

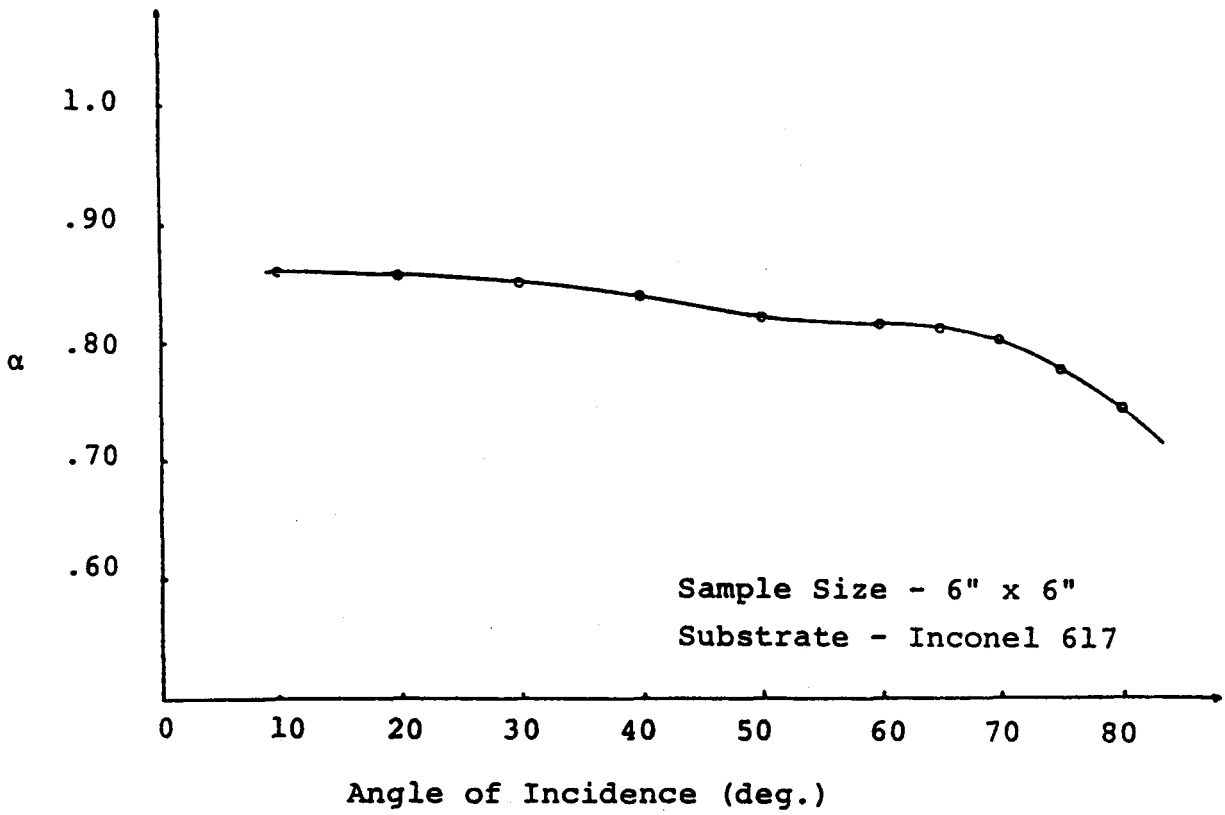

Figure A-42. Solar Absorptance of "Pyromark" vs. Angle of Incidence

A-7 OPTICAL ANALYSIS

An extensive discussion of the various optical calculation strategies developed at Texas Tech and at E-Systems is presented in Vol. II, Appendices C and D of the Interim Report. Subsequent work in the optical area has produced refinements and improved procedures. Methods have been extended to give new capabilities and results. In addition, various optical calculations have been performed in support of the experimental testing and evaluation program. In order to be reasonably brief, only a few optical topics will be mentioned here as an indication of the level of effort.

A-7.1. Perfect Mirror Calculations Treating Errors with the Effective Sun Size Technique

The effective sun size techniques, described in Vol. II, Appendices C and D, have offered a useful guide to the behavior of light from a fininte sun by a mirror with a stochastic error distribution. This is perhaps the simplest useful model which allows for the effect of errors. Continued work of this type will be illustrated with five examples: 1) misaligned receivers, 2) power in multiple bounce radiation, 3) azimuthally averaged power on the receiver, 4) angle of incidence of light on receiver, and 5) mirror region optical value.

1. Extension of Computer Codes to Treat Misaligned Receivers.

A computer code has been developed for evaluating the optical power concentration integral of Vol. II, Appendix C for the case of a spherical segment collector and a conical receiver.

Provision is made for multiple bounce contributions of any order. The code has now been extended to permit computations for misaligned receivers. In addition, the code evaluates the azimuthally averaged concentration in a form useful for thermal performance calculations.

The optical power concentration at a point on the receiver is dependent on many factors, including the position of the sun, the size and orientation of the collector and the alignment of the receiver. Thus, the program requires that several parameters be provided as input. These include:

1) Sun positional parameters. These are solar elevation and azimuth relative to a fixed SOUTH-EAST-VERTICAL coordinate system.

2) Collector orientation parameters. These parameters are also given in terms of the SOUTH-EAST-VERTICAL coordinate system. They include the collector inclination angle (measured between the symmetry axis of the collector and the VERTICAL axis) and the azimuth of the lowest point on the collector rim.

3) Collector size. Normalized coordinates are employed so that the size of the collector is completely determined by the rim angle, i.e. by the angle between the negative symmetry axis and a vector from the center of the collector to the collector rim.

4) Receiver size. This is specified by assigning a value to the cone half angle. Non-conical receivers of any simple shape are treated with the same code by specifying the location and the direction of the receiver surface normal at the point.

5) Receiver orientation. For perfect alignment, the receiver axis should point directly towards the center of the sun. Mis-alignment is then accounted for in terms of the zenith and azimuthal angles between the receiver axis and the vector from the center of the collector to the sun. In order to take into account tracking strategy, a reference line is specified on the receiver in order to determine the position of a fixed receiver coordinate system relative to the collector orientation.

6) Receiver coordinates. Actual concentration values are computed for points on the receiver surface.

Cordinates are given in terms of normalized distance measured along the surface of the cone from the vertex of the cone and an azimuthal angle measured around the axis of the conical receiver. The computer code is sufficiently flexible to allow for a variety of values of these two parameters on any given computer run.

7) Effective sun size. This is given by the sun half angle.

8) Number of bounces. Gives the maximum number of bounce contributions to be considered.

9) Reflection coefficients. The weight of reflection coefficient to the nth power is assigned.

10) Sun Size and Bounce Number. A different sun size can be used for each order of multiple reflection.

Studies of concentration patterns on misalligned receivers are underway, but will not be presented here.

2. Power in Multiple Bounce Radiation as a Function of Angle of Inclination of the Sun

Within the perfect mirror/point sun model, exact analytic expressions have been derived for the amount of light reaching the receiver from any angular band $\Delta\theta$, (range of zenith angle of mirror position measured from the foot of the receiver axis). As a special case, the following example is of interest.

Consider a 60° rim angle, shperical segment mirror with perfectly aligned receiver. Let I be the inclination angle of the sun with respect to the bowl symmetry axis. The single bounce light reaching the receiver from the mirror comes from angles θ between ψ and 60°, where ψ is the angular radius of the receiver cone. The rest of the reflected light is higher bounce radiation. For unit reflectivity (R = 1), the fraction of optical power striking the receiver

in multiple bounce paths is given by:

$$\frac{L_M}{L_T} = \begin{cases} 1 - \frac{1+\cos I}{2\cos I}\left[1 - \frac{2A}{\pi} - \frac{\sin 2A}{\pi}\right] & \text{for } 0 \leq I \leq 60° \\ \frac{1-\cos I}{2\cos I}\left[\frac{2B}{\pi} - 1\right] + \frac{1+\cos I}{2\cos I}\left[\frac{2A}{\pi} + \frac{\sin 2A}{\pi} - \frac{2\tan B}{3\pi}\right] & \text{for } 60° \leq I \leq 9(\end{cases} \qquad \text{(A-28)}$$

where

$$A \equiv \mathrm{Sin}^{-1}\left\{ \frac{\tan\frac{I}{2}}{\sqrt{3}} \right\}$$

$$B \equiv \mathrm{Tan}^{-1}\left\{ \sqrt{3\tan^2\frac{I}{2} - 1} \right.$$

$L_M \equiv$ Power in multiple bounces

$L_T \equiv$ Total input optical power to receiver

$L_S \equiv L_T - L_M \equiv$ Total single bounce power

The quantities L_T, L_S, and L_M are shown as a function of I in Fig. A-43. For convenience L_T is normalized to the value 100 at $I = 0$. Of course, L_T suffers a cos I fall off. Also shown are the two ratios L_M/L_S and L_M/L_T, expressed as percentages. The limit of L_M/L_T at 90° is

$$\left[\frac{2}{\pi}\mathrm{Sin}^{-1}\left\{\frac{1}{\sqrt{3}}\right\} - \frac{2\sqrt{2}}{3\pi}\right](100) = 9.172. \qquad \text{(A-29)}$$

Many similar studies can be easily accomplished with the new analytic approach. Perhaps the most important practical impace of the apporach, however, is mentioned below.

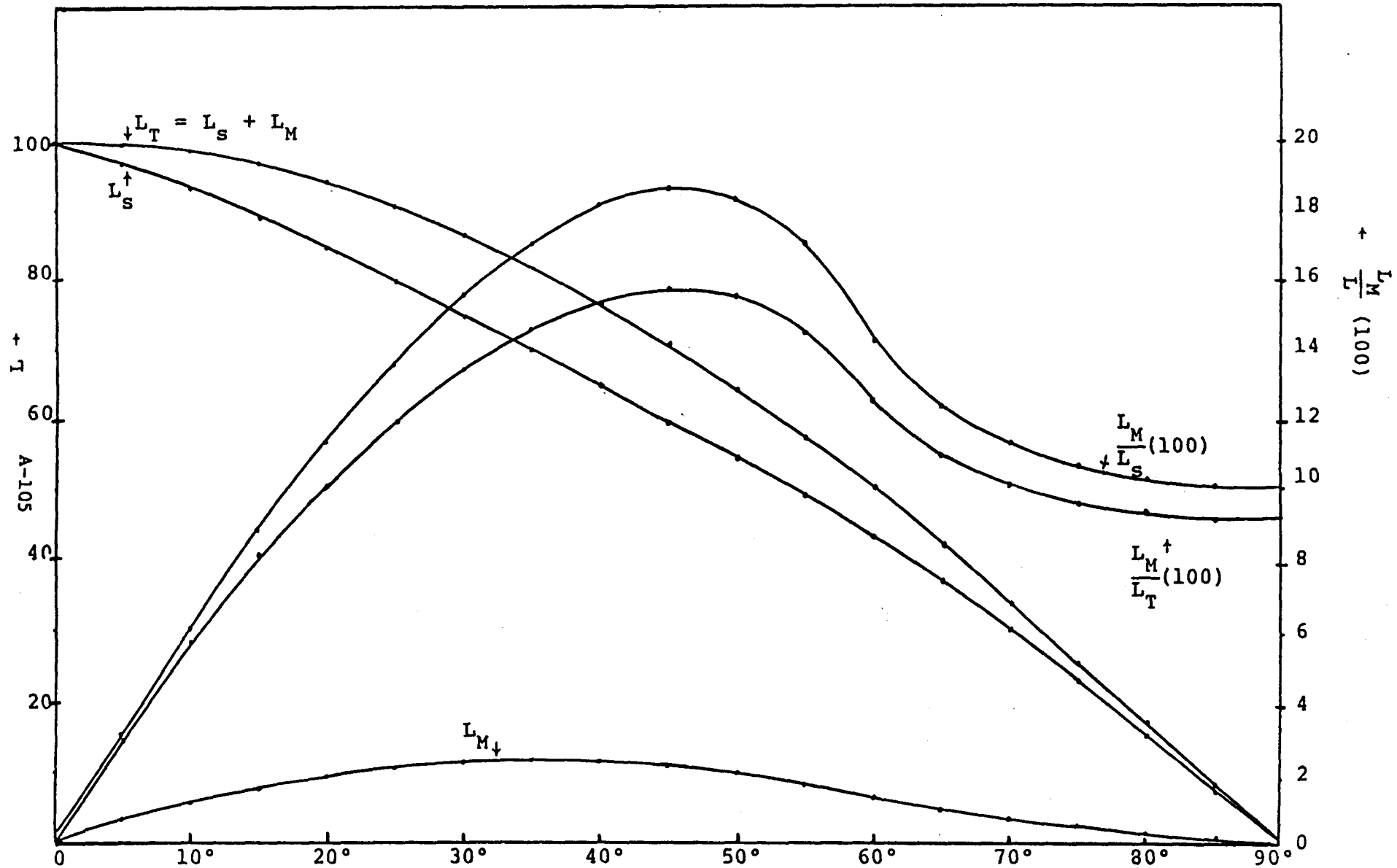

Figure A-43. Single and Multiple Bounce Contributions vs. Sun Inclination

3. Azimuthally Averaged Power on the Receiver

For many thermal performance calculations for the receiver, the desired result is not the concentration, $C(q,\phi)$ at a point on the receiver. Instead, it is more useful to have the concentration averaged in azimuth around the barrel of the receiver:

$$\bar{C}(q) = \frac{1}{2\pi} \int_0^{2\pi} C(q,\phi)\,d\phi \qquad \text{(A-30)}$$

where q in the distance from the receiver location to the center of the spherical segment mirror. Extremely accurate computation of $C(q,\phi)$ is time consuming and expensive. The time and cost are then magnified by the necessity to perform the integration.

The new approach alluded to in the previous subsection offers a way to compute $\bar{C}(q)$ directly without the necessity for evaluating (and then integrating) the more difficult quantity $C(q,\phi)$. Multiple bounce and finite effective suns can be handled with this technique, but the work is slightly more complicated.

Typical curves of $\bar{C}(q)$ obtained by the old approach (compute $C(q,\phi)$ and integrate) are shown in Figs. A-44 to A-48 for inclination angles I = 0°, 15°, 30°, 45°, 60°, 75°. On each figure two curves are shown, corresponding to two effective sun size policies:

a) use $\sigma_{eff} = 2\sigma_a$, where σ_a is the actual angular radius of the sun($\tilde{}$0.25°), for all bounces

b) use $\sigma_{eff} = 2\sigma_a$ for single bounce radiation, but $\sigma_{eff} = 3\sigma_a$ for all multiple bounce radiation.

One notices in the figures that the two policies lead to essentially the same results.

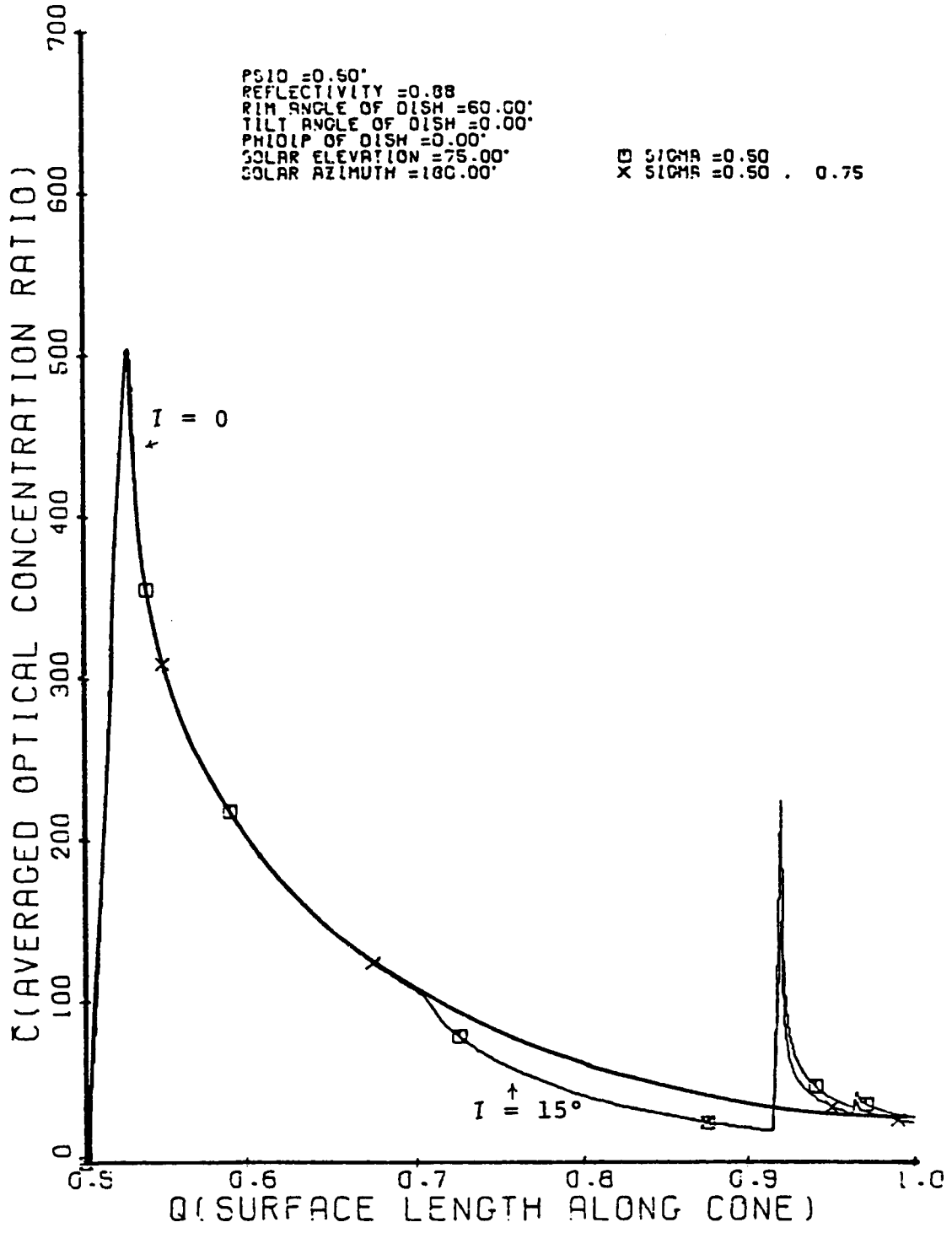

Figure A-44. Azimuthally Averaged Concentration Ratio on Receiver for Sun Inclination $I = 15°$

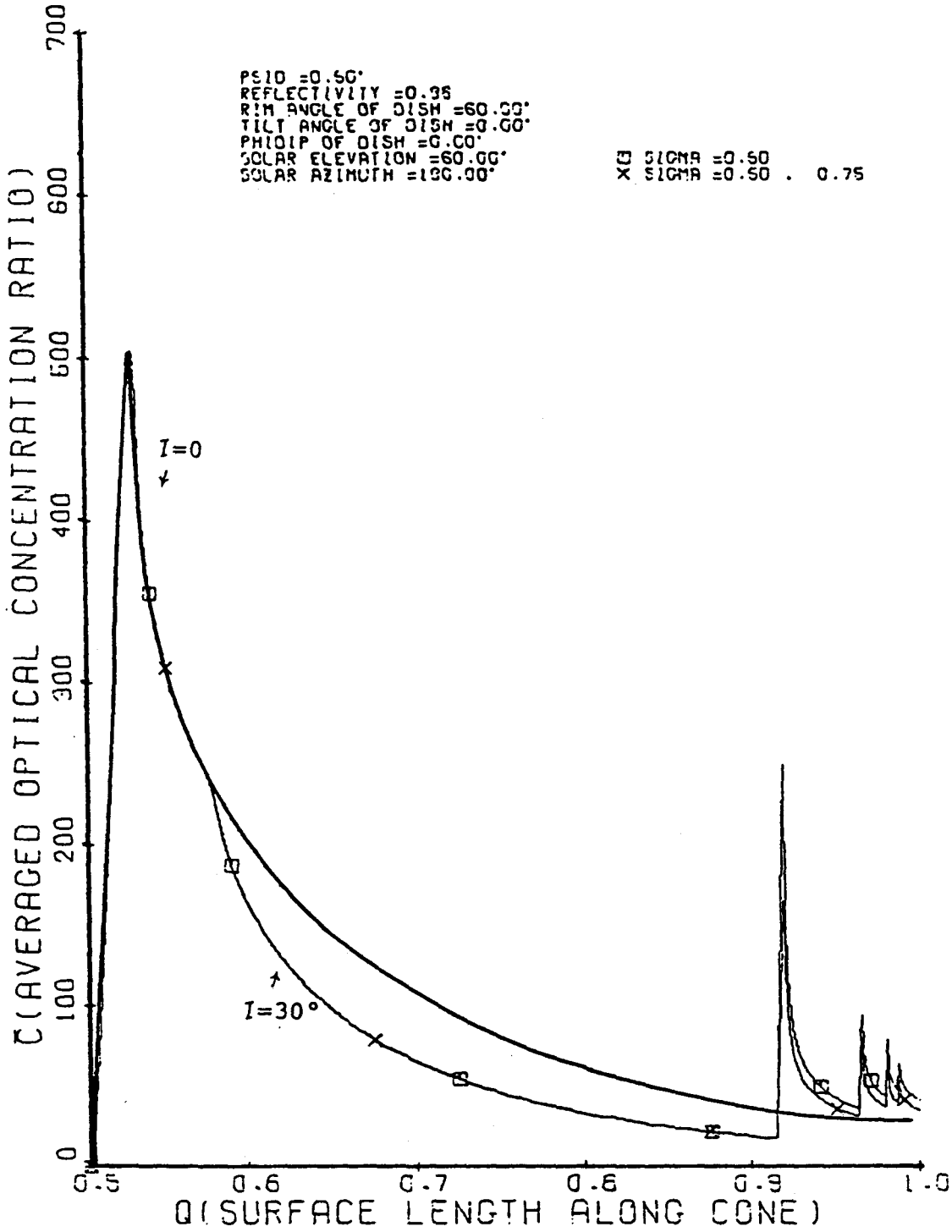

Figure A-45. Azimuthally Averaged Concentration Ratio on Receiver for Sun Inclination I = 30°

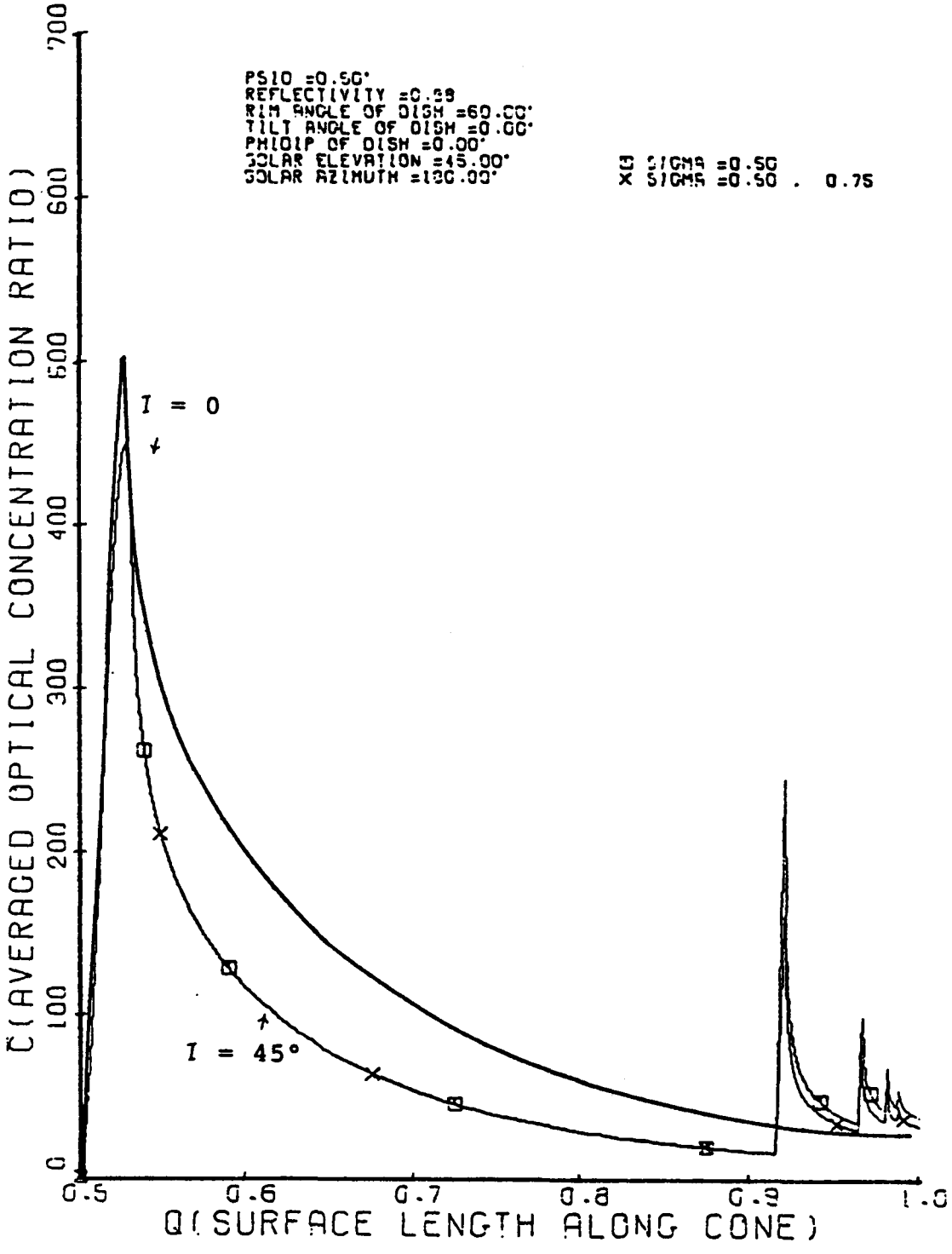

Figure A-46. Azimuthally Averaged Concentration Ratio on Receiver for Sun Inclination I = 45°

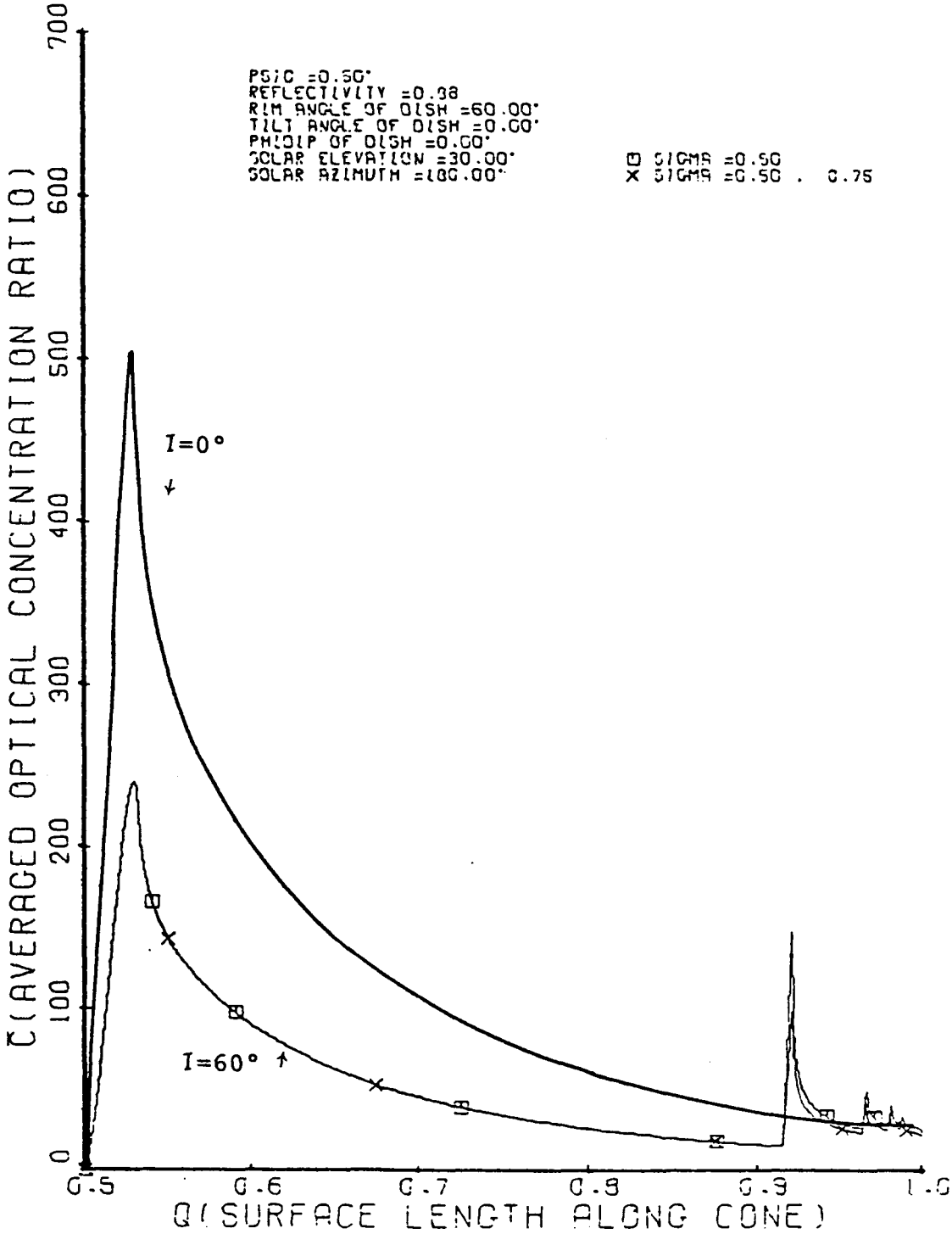

Figure A-47. Azimuthally Averaged Concentration Ratio on Receiver for Sun Inclination I= 60°

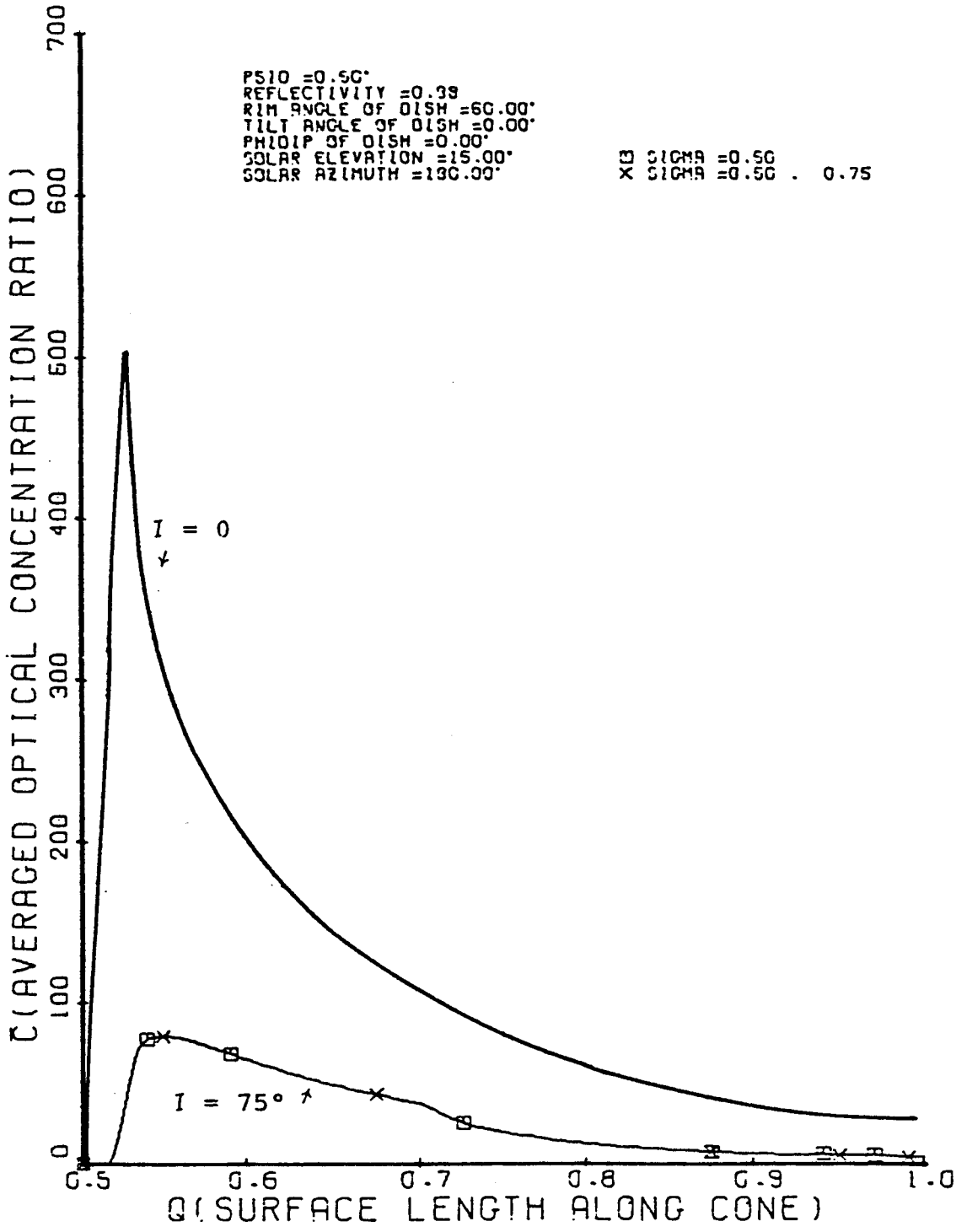

Figure A-48. Azimuthally Averaged Concentration Ratio on Receiver for Sun Inclination $I = 75°$

4. Angle of Incidence of Light on Receiver

In order to support the investigation of energy capture by receiver abosrber coatings with angularly dependent properties, an analytical procedure was developed for computing the distribution density (weighted by power) of the incidence angles, $\tilde{\alpha}$, of the light impinging on the receiver. Between two rings, Q_1 and Q_2, located around the receiver at distances q_1 and q_2 from the receiver cone vertex (center of curvature of spherical segment), an "incidence angle density function" is defined for the light striking the receiver between Q_1 and Q_2. This density $P(\tilde{\alpha})$ is defined such that

$$\int_0^{\pi/2} P(\tilde{\alpha})\, d\tilde{\alpha} = 1 \qquad \text{(A-31)}$$

where the angle of incidence (angle between light input direction and local surface normal) is α and $\tilde{\alpha} \equiv |\alpha|$. The quantity

$$P(\tilde{\alpha})d\tilde{\alpha}$$

may be interpreted as the fraction of the light considered (between Q_1 and Q_2) that lies between α and $\alpha + d\alpha$ or between $-\alpha$ and $-(\alpha+d\alpha)$ for a receiver whose surface is a perfect cone.

For these consideration the angle of incidence α is taken positive or negative depending upon whether or not the light is received from below or from above, whereas $\tilde{\alpha}$ is the same angle, interpreted always as positive. The parameter $\tilde{\alpha}$ is of physical interest because, if the absorptivity is a function of angle of incidence, it

depends only on $\tilde{\alpha}$.

As an example of the expressions derived, consider all of the single bounce light received on the receiver (between q = 0.5 and q = 1.0). The resulting density function is

$$P(\tilde{\alpha}) = \begin{cases} \frac{2}{3-4\sin^2\psi}\,[\cos(\tilde{\alpha}+\psi) + \cos\,(\tilde{\alpha}-\psi)] & \text{for } 0 \leq \alpha \leq \frac{\pi}{6} - \psi \\ \frac{2}{3-4\sin^2\psi}\,[\cos(\tilde{\alpha}-\psi)] & \text{for } \frac{\pi}{6} - \psi \leq \tilde{\alpha} \leq \frac{\pi}{2} - \psi \\ 0 & \text{for } \frac{\pi}{2} - \psi \leq \tilde{\alpha} \leq \frac{\pi}{2} \end{cases} \qquad \text{(A-32)}$$

This result is shown in Fig. A-49 for $\psi = 0°$ and $\psi = 1°$, where ψ is the angular radius of the cone. The discontinuities illustrate that $\alpha < 0$ inputs have been represented (physically) by $\tilde{\alpha}$. There is a sharp lower limit for the negative values of α. For practical purposes, it is sufficient to use the simpler expression resulting from setting $\psi = 0$.

Also shown in Fig. A-49 is another density function $P_c(\tilde{\gamma})$ that has the same meaning, except that the actual outer surface of the receiver is a tightly and compactly (turns essentially touching) circular tube wound on a conical substrate. The expression for $P_c(\tilde{\gamma})$ is:

$$P(\tilde{\gamma}) = \frac{\cos\tilde{\gamma}}{3}\left[\frac{\pi}{6} + \mathrm{Cos}^{-1}\left\{\frac{1-\sin\tilde{\gamma}}{2}\right\} + \mathrm{Cos}^{-1}\left\{\frac{1+\sin\tilde{\gamma}}{2}\right\} + \right.$$

$$\left. + \mathrm{Min}\left\{\frac{\pi}{6},\ \mathrm{Cos}^{-1}\left\{\frac{1+\sin\tilde{\gamma}}{2}\right\}\right\}\right] \qquad \text{(A-33)}$$

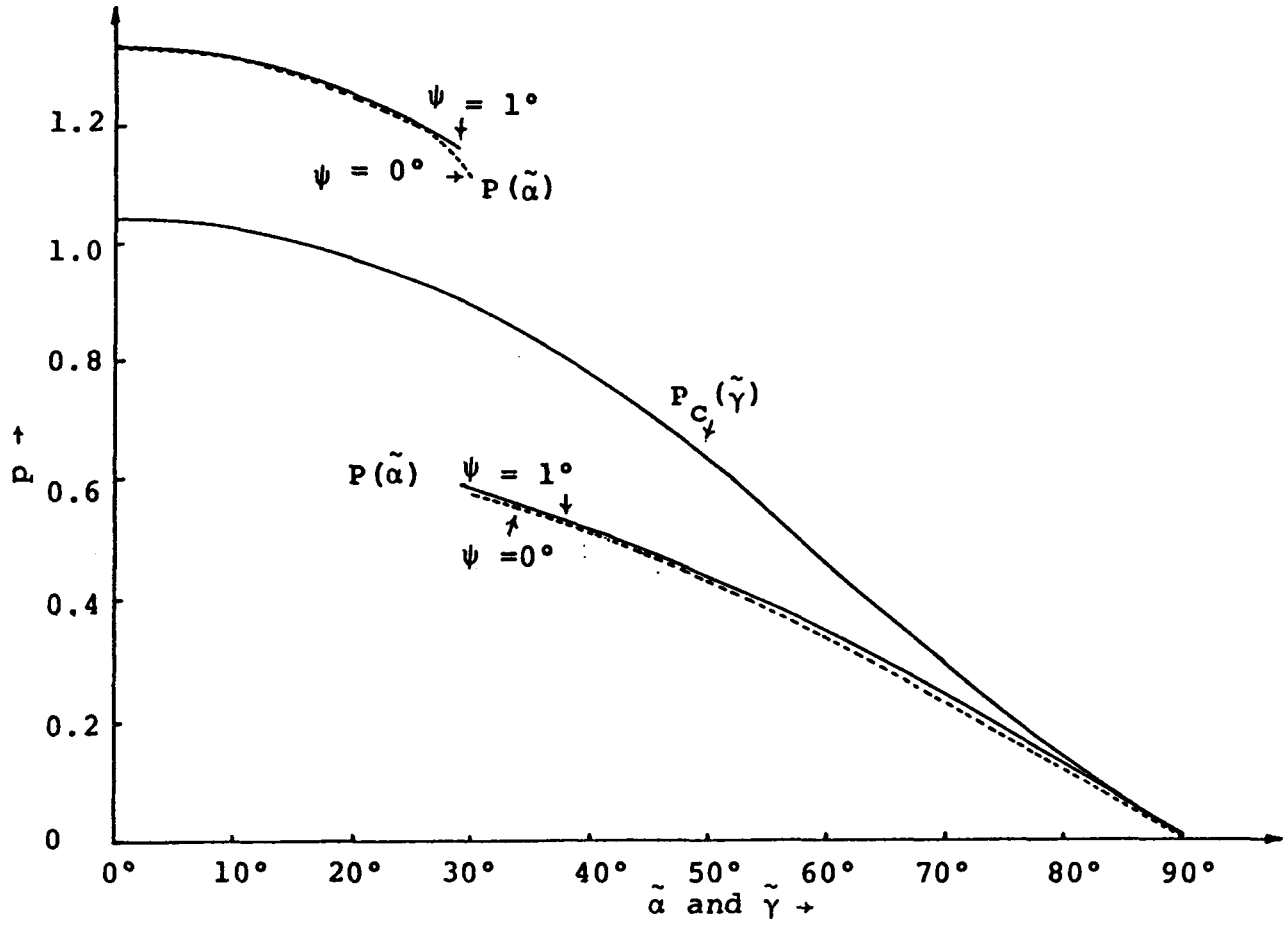

Figure A-49. Incidence Angle Density Functions for Smooth and Tubing-Wrapped Conical Receivers

where $\tilde{\gamma}$ is the magnitude of the angle γ between the light input direction and the actual (coil tube) surface normal (not the substrate cone surface normal). In the Min function, $\pi/6$ is relevant for small values of $\tilde{\gamma}$ and the other selection is the smaller when $\tilde{\gamma}$ is large. Note that the range of $\tilde{\gamma}$ is from 0° to 90°, like that of $\tilde{\alpha}$.

In Fig. A-50, integrals are shown

$$F(\tilde{\alpha}) = \int_0^{\tilde{\alpha}} P(\tilde{\alpha}')d\tilde{\alpha}' \qquad \text{(A-34)}$$

$$F_C(\tilde{\gamma}) = \int_0^{\tilde{\gamma}} P_C(\tilde{\gamma}')d\tilde{\gamma}' \qquad \text{(A-35)}$$

Showing the fraction of the light received at incidence angles less than $\tilde{\alpha}$ and $\tilde{\gamma}$. Note more emphasis on larger angles in the case of the wrapped receiver.

5. Figure of Optical Merit (FOM) for Portions of the Mirror Surface

For purposes of cost/performance trade-off studies, it is of interest to assign a numerical merit to each mirror panel in the collector. One such FOM can be defined as the simple collection efficiency of the point on the mirror, averaged over the year. Since the amount of power directed by a mirror element is proportional to the area that element presents to the sun, the simple collection efficiency is just

$$\hat{e}_s \cdot \hat{n}$$

where $\hat{e}_s$ points to the sun and $\hat{n}$ is the unit normal at the mirror point of interest.

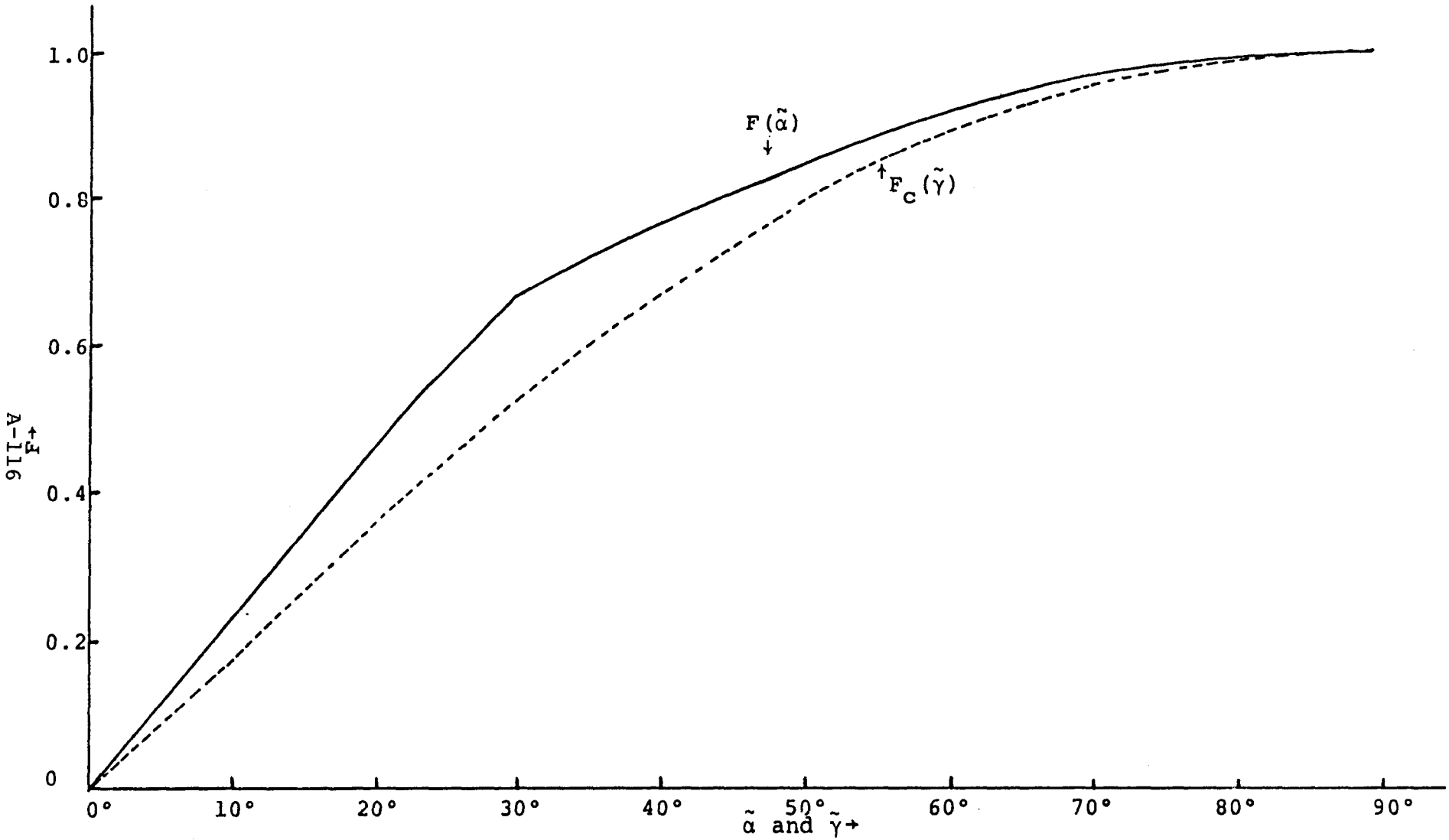

Figure A-50. Light Incident at Angles Less than Specified Incidence Angle for Smooth and Tubing-wrapped Conical Receivers

The FOM is the average:

$$\text{FOM} = \frac{1}{\text{year}} \int_{\text{year}} (\hat{n}\cdot\hat{e}_s)\ U(\hat{n}\cdot\hat{e}_s)dt \qquad \text{(A-36)}$$

The collection efficiency is simply integrated over a full year and normalized to 1 year's time. The function $U(\hat{e}_s\cdot\hat{n})$ is used to cutoff the integrand when the sun is not visible at the point of interest because it is either below the actual horizon at the disk location or because the disk element is shaded by other portions of the dish. The FOM for a point on the mirror is a function of the location of the dish on the earth's surface and the tilt angle between the dish symmetry axis and the local vertical.

A computer code has been constructed to evaluate this FOM as a function of all of its parameters. Example results, relevant to the RPS are shown in Figs. A-51 and A-52. The 60° rim angle mirror segment is located at $\lambda = 33.65°$ (the latitude of Crosbyton, Texas) and tilted 15° south of the vertical. Figure A-51 shows the FOM as a function of azimuth ϕ on the dish rim, measured position to the east from $\phi = 0$ on the south (lowest) point on the rim. Figure A-52 shows the same results, plotted as curves of constant FOM projected onto the aperture plane as if one were looking at such curves on the mirror surface from a distant point on the symmetry axis.

Clearly portions of the dish on the south side ($\phi \approx 0$) are less efficient than those on the north (elevated) side. Requiring all portions of the concentrator to meet or exceed a minimum collector efficiency would demand that portions of the spherical segment dish

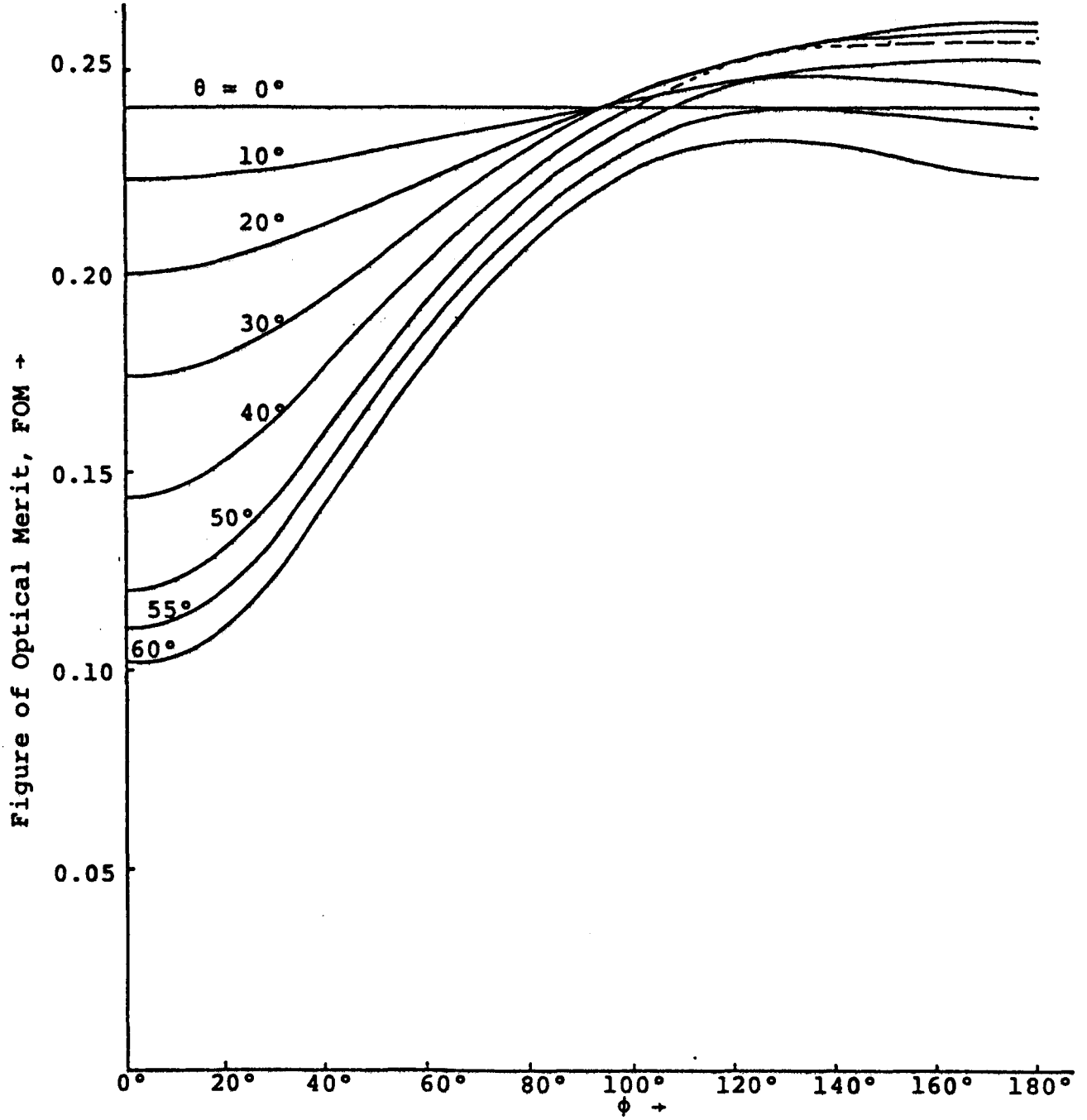

Figure A-51. Mirror Location FOM for RPS at Crosbyton

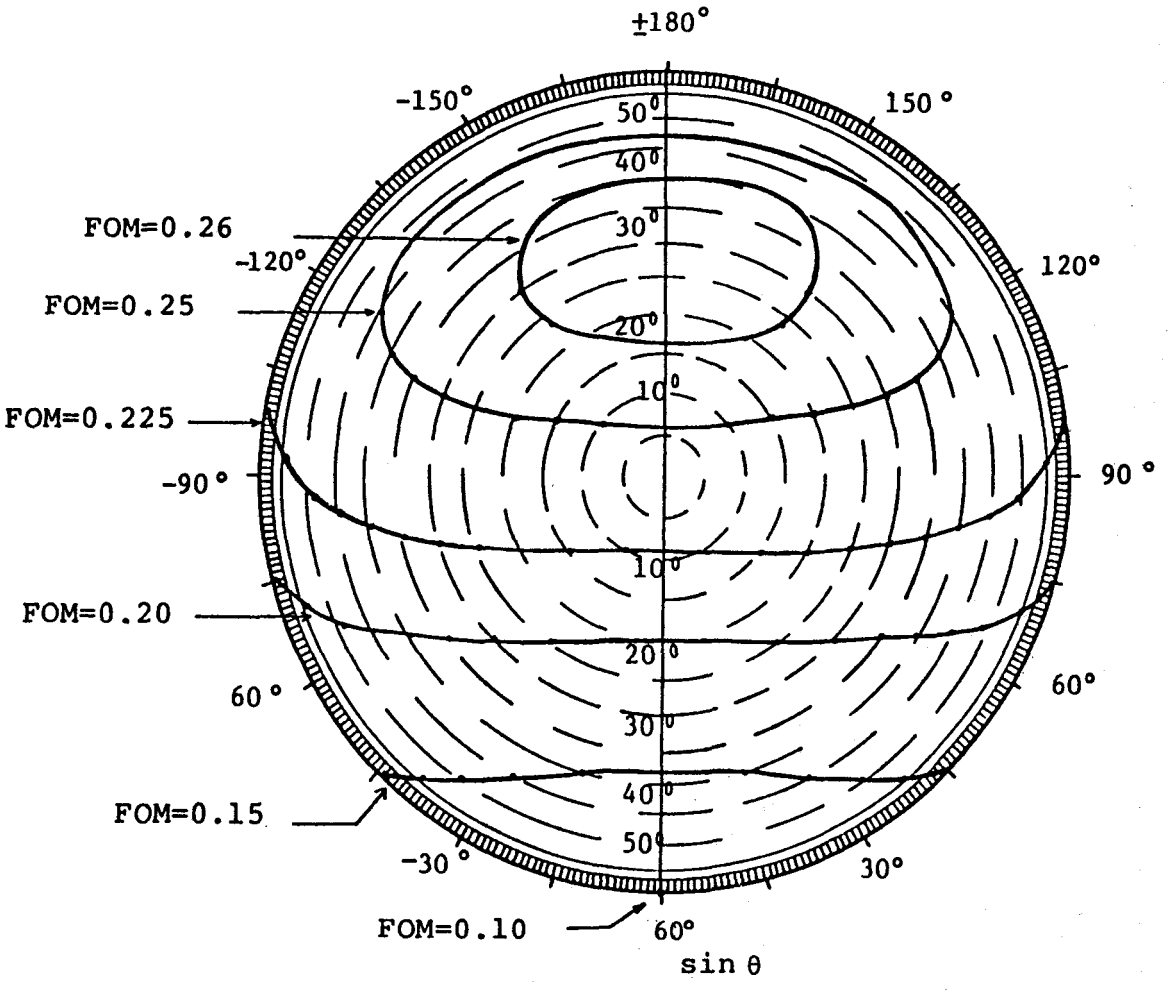

Figure A-52. Curves of Constant Mirror Location FOM Projected Onto Aperture Plane

not be constructed. Note, however, that the least efficient portion of the reflector surface are also the least expensive to construct. The converse is not quite true at Crosbyton. The highest portions of the mirror are not the most efficient according to this FOM.

A-7.2 Statistical Analysis of Light Patterns from Imperfect Mirrors

Although the Effective Sun Size approach might be characterized as the "simplest of all wrong statistical approaches," it offers an effective guide to the role of mirror imperfections. Nevertheless, it is desirable to establish the prediction of the concentration distribution in the presence of stochastic mirror errors upon a firmer statistical base. Starting from the new formulation of the optical concentration calculation:

$$C(\vec{q},\hat{b}) = \frac{1}{\Omega_s} \iint_{\Omega_M} \hat{b}\cdot d\vec{\Omega} \qquad \text{(for } \hat{b}\cdot d\vec{\Omega} > 0 \text{ only)} \qquad \text{(A-37)}$$

and its generalization given in Vol. II, Sect. C-2, it is possible to develop suitable procedures for meaningful statistical calculations. In this equation,

- $\vec{q}$ is the radius vector locating a point on the receiver from the center of curvature of the ideal spherical segment;
- $\hat{b}$ is the unit surface normal to the receiver surface at $\vec{q}$;
- $\Omega_s = 4\pi\sin^2(\sigma_a/2)$ is the solid angle of the sun, where σ_a is the angular radius of the sun;
- Ω_M is the apparent solid angle of the entire sun as viewed in the mirror.

For a concentrating mirror, $\Omega_M > \Omega_s$

Now, at a point on an ideal spherical segment mirror, let $\hat{n}$ be the ideal surface normal directed to the center of curvature. For a non-ideal mirror which can be described by an error $\hat{p}$ in the actual mirror normal $\hat{n}'$ with respect to $\hat{n}$:

$$\hat{n}' = \vec{p} + \hat{n}, \tag{A-38}$$

suppose that the error can be described by a probability density function $P(\vec{p})$ which is independent of position on the mirror and normalized so that

$$\iint_{\frac{1}{\sqrt{2}}(2\pi)} P(\vec{p})\, d\Omega_p = \iint_{(2\pi)} P(\hat{n}' - \hat{n})\, d\hat{\Omega}_{n'} = \iint_{(2\pi)} \tilde{P}(\hat{n}')\, d\Omega_{\hat{n}'}, \tag{A-39}$$

where $\tilde{P}(\hat{n}')$ is the corresponding probability density function for the actual normal. In the absence of a bias, $P(\vec{p})$ should be peaked about $\vec{p} = 0$ and $\tilde{P}(\hat{n}')$ should be peaked about $\hat{n}$.

Mean Concentration Distribution

It can be shown that the "expected concentration" or "mean concentration" at the point $\vec{q}$, $\hat{b}$ is given for single bounce radiation, by:

$$\langle C(\vec{q},\hat{b})\rangle = \frac{1}{2\Omega_s} \iint_{2\pi}' (\hat{b}\cdot d\vec{\Omega}) \iint_{\Omega_s} P\left(\vec{q} + \frac{\hat{e}_s}{\sqrt{2}} + f(\beta)\hat{\varepsilon}\right) d\Omega_s \tag{A-40}$$

where

$$d\vec{\Omega} \equiv \hat{\epsilon} d\Omega$$

$$d\vec{\Omega}_s \equiv \hat{e}_s d\Omega_s$$

$$\vec{q} \cdot \hat{\epsilon} \equiv q\cos\beta$$

$$f(\beta) \equiv \sqrt{1-q^2\sin^2\beta} \quad -q\cos\beta - \frac{1}{\sqrt{2}}$$

and the range of integration for $\overrightarrow{d\Omega}$ is the region of solid angle for which $\hat{b}\cdot\hat{\epsilon}\geq 0$ and for which $\hat{\epsilon}$ points toward a spot on the mirror. This region of integration can be conveniently parametrized by locating $\hat{\epsilon}$ with a zenith angle θ measured from the direction of $\vec{q}$ and an azimuth $\phi\epsilon[-\frac{\pi}{2}, +\frac{\pi}{2}]$. Then one finds the range of integration, for sun inclination $I = 0$:

$$\iint_{2\pi} d\Omega[\ ] = \int_{-\frac{\pi}{2}}^{+\frac{\pi}{2}} d\phi \int_{0}^{\theta_{max}(\phi)} \sin\theta d\theta[\ ] \qquad \text{(A-41)}$$

where, in the shorthand:

$$\gamma_c \equiv \cos\gamma, \quad \gamma_s \equiv \sin\gamma,$$

θ_{MAX}, for a 60° rim angle spherical segment mirror, is determined by:

$$\tan\theta_{MAX} = \frac{\psi_s(\psi_c - \frac{q}{2})\phi_c + (q\psi_c - \frac{1}{2})\sqrt{(\psi_c^2 - \frac{1}{4}) + \psi_s^2\phi_c^2}}{(q\psi_c - \frac{1}{2})^2 - \psi_s^2(1-q^2)\phi_c^2} \qquad \text{(A-42)}$$

The branch of the inverse tangent is determined as follows:

$$\theta_{max} > \frac{\pi}{2} \text{ for all } \phi \in [-\tfrac{\pi}{2}, \tfrac{\pi}{2}] \text{ if } \frac{\psi_c + \sqrt{3}\psi_s}{2} < q$$

$$\theta_{max} < \frac{\pi}{2} \text{ for all } \phi \in [-\tfrac{\pi}{2}, \tfrac{\pi}{2}] \text{ if } q < \frac{\psi_c - \sqrt{3}\psi_s}{2}$$

$$\left.\begin{cases} \theta_{max} < \frac{\pi}{2} \text{ for } (\pm\phi) \in \left[0, \cos^{-1}\left\{\frac{|q\psi_c - \frac{1}{2}|}{\psi_s\sqrt{1-q}}\right\}\right] \\ \theta_{max} > \frac{\pi}{2} \text{ for all other } \phi \in [-\tfrac{\pi}{2}, \tfrac{\pi}{2}] \end{cases}\right\} \text{for all other } q \in [0,1]$$

As an example of the use of Eq. (A-40), consider a "Perfectly Crummy Spherical Segment Mirror" of rim angle 60° and sun directly over the symmetry axis ($I = 0$). A Perfectly Crummy Mirror is a limit case in which the mirror is so bad that the error distribution is flat:

$$\tilde{P}(\hat{n}') \equiv \frac{1}{2\pi}$$

Considering only single bounce radiation (reflectivity is low, perhaps), the resulting expected distribution is given by:

$$\langle C(q) \rangle = G(q) + \frac{1}{4\pi} \int_0^{\frac{\pi}{2}} \left[\text{Tan}^{-1}\{f\} - \frac{f}{1-f^2} \right] \cos\phi \, d\phi \qquad \text{(A-43)}$$

where

$$G(q) = \begin{cases} 0 & \text{for } 0 < q < \frac{\psi_c - \sqrt{3}\psi_s}{2} \\ \frac{1 - \sin\Gamma}{4} & \text{for } \frac{\psi_c - \sqrt{3}\psi_s}{2} < q < \frac{\psi_c + \sqrt{3}\psi_s}{2} \\ \frac{1}{4} & \text{for } \frac{\psi_c + \sqrt{3}\psi_s}{2} < q < 1 \end{cases}$$

$$\Gamma \equiv \cos^{-1}\left\{\frac{|q\psi_c - \frac{1}{2}|}{\psi_s\sqrt{1-q}}\right\}$$

$$\tan^{-1} f \in \left[-\frac{\pi}{2}, \frac{\pi}{2}\right]$$

and

$$f(\phi) = -\tan\theta_{max} \text{ as given in Eq. (A-42).}$$

The integral given in Eq. (A-43) is easily evaluated numerically and the resulting "expected concentration" (using single bounce with unit reflectivity) for the Perfectly Crummy Dish with $\psi = 0.5°$ is shown in Fig. A-53. Note that so much light is lost into multiple bounces that the "expected single bounce concentration" is nearly an order of magnitude less than the zero bounce, non-stochastic, direct solar illumination of the receiver. In Fig. A-53 the receiver cone is not truncated and the full surface from q = 0 to q = 1 is exhibited. The only memory of the usual caustic focus at q = 0.5 is an inflection point with zero slope. For Non-Perfectly Crummy mirrors such as, say:

$$\tilde{P}(\hat{n}') = \begin{cases} \text{Constant for } \hat{n}'\cdot\hat{n}' > \cos\gamma \\ 0 \text{ otherwise} \end{cases}$$

the behavior of $\langle C(q)\rangle$ with γ is easy to imagine. Starting from the $\gamma = \frac{\pi}{2}$ curve of Fig. A-53, as $\gamma \to 0$ the region $q < 0.5$ loses light and the region near $q \approx 0.5$ is expected to receive more and more light, approaching an expected concentration of over 500 suns.

The general result given in Eq. (A-40) seems to be a new and rather elegant representation of the expected concentration dis-

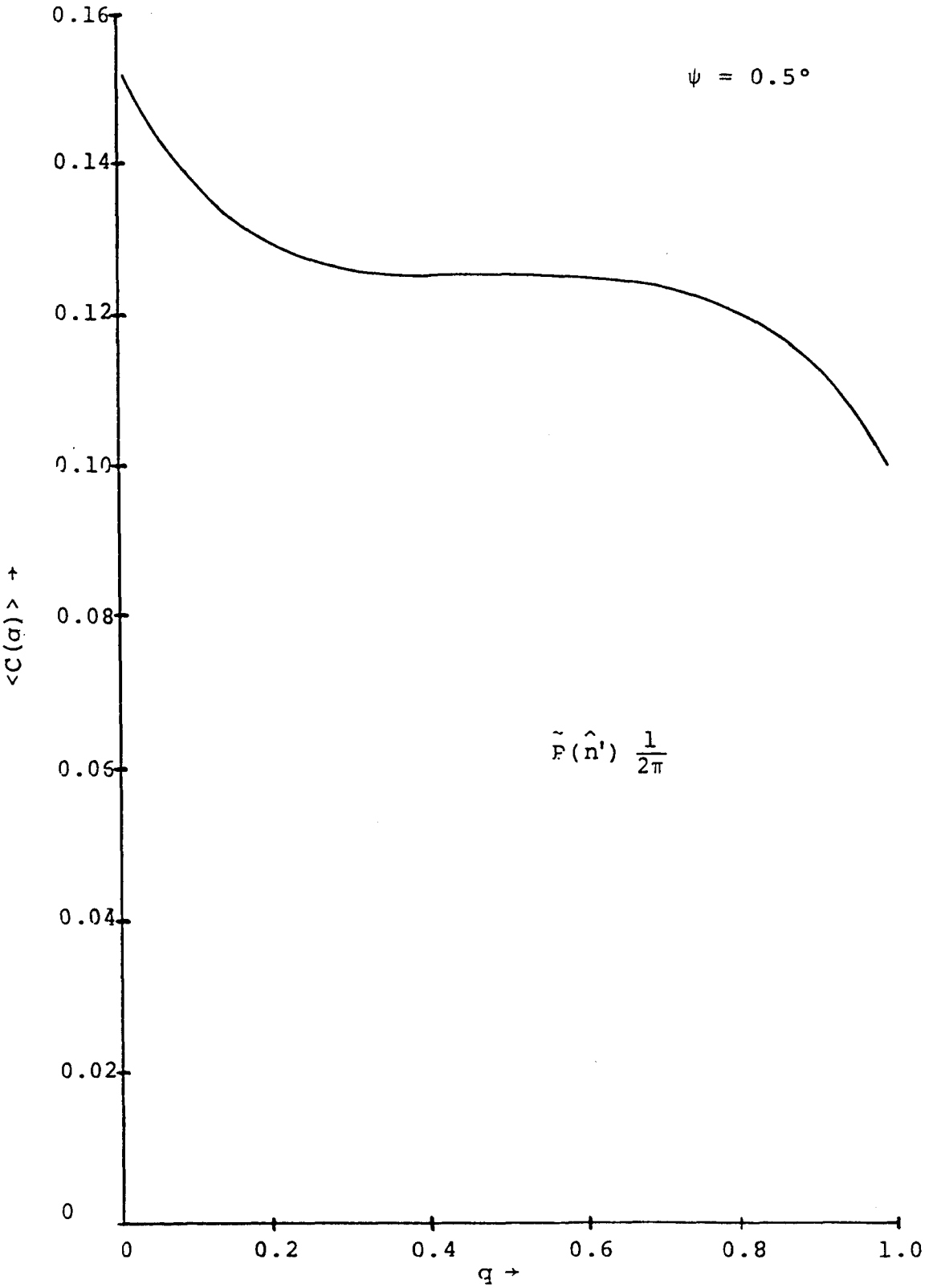

Figure A-53. Single Bounce Expected Concentration for Perfectly Crummy Dish

tribution. Straightforward analytical and numerical techniques can be used to simplify and evaluate the integrals.

Second Moment of the Concentration

As in any "expected value" computation, the question naturally arises: "How likely is the expected value to be observed?" This question is conventionally quantified by evaluating an uncertainty band or standard deviation band employing the second central moment. For concentration distributions, it does not appear that expressions for the error band width have ever before been given. In the course of this study, the following general expression has been derived:

$$\sigma_c^2(\vec{q},\hat{b}) = \langle C^2(\vec{q},\vec{b})\rangle - \langle C(\vec{q},\vec{b})\rangle^2 =$$

$$= \frac{1}{\Omega_s^2}\iint_{2\pi}'(\hat{b}\cdot d\vec{\Omega})\iint_{2\pi}'(\hat{b}\cdot d\vec{\Omega}')\iint_{\Omega_s} Q\left(\vec{q}+\frac{\hat{e}_s}{\sqrt{2}}+f(\beta)\hat{\epsilon}\right)$$

$$S(\hat{e}_s,\hat{\epsilon}',\hat{\epsilon})\,d\Omega_s \qquad (A-44)$$

where

$$Q = P\left(\vec{q}+\frac{\hat{e}_s}{\sqrt{2}}+f(\beta)\hat{\epsilon}\right)\left[1-\frac{1}{\langle P\rangle}P\left(\vec{q}+\frac{\hat{e}_s}{\sqrt{2}}+f(\beta)\hat{\epsilon}\right)\right]$$

$$\langle P\rangle = \iint [P(\vec{p})]^2 d^2\vec{p}$$

$$S = \begin{cases} 1 & \text{if } \dfrac{\hat{e}_s + \sqrt{2}\left[f(\beta)\,\hat{\epsilon} - f(\beta')\,\hat{\epsilon}'\right]}{\left|\hat{e}_s + \sqrt{2}\left[f(\beta)\,\hat{\epsilon} - f(\beta')\,\hat{\epsilon}'\right]\right|} \cdot \hat{e}_{so} \geq \cos\sigma_a \\ 0 & \text{otherwise} \end{cases}$$

and the ranges of integration of $d\vec{\Omega}$ and $d\vec{\Omega}'$ are as in Eq. (A-40). It is possible to simplify the integration limits by parametrizing the solid angles as in the computation of <C>, but such discussion is omitted here.

The integral in Eq. (A-44) required to compute $\sigma_C^2(\vec{q}, \vec{b})$ is troublesome,but straightforward with a computer. The actual concentration observed should lie between the curves

$$\langle C(\vec{q}, \vec{b})\rangle \pm \sigma_C(\vec{q}, \vec{b})$$

with reasonably high probability.

A-7.3 Sizing the Receiver Using Stochastic Mirror Errors

An extremely interesting computation has been performed by E-Systems which allows the receiver to be sized much more precisely than was possible using the "effective sun size" approach. Furthermore, it is indicated that for previously defined error levels, the receiver can be reduced in size (exposed area) by nearly 40% without adversely affecting performance. The multiple bounce radiation was not considered in the calculation, but the savings in thermal losses and other advantages probably more than offset the loss of a portion of the multiple bounce radiation.

The calculational approach used by E-Systems is somewhat similar to that used in Vol. II, Sec. C-7 (for n=1) and will not be presented in detail here. A quantity, $F_{overall}$, the expected value of overall energy interception fraction was defined and evaluated for a gaussian mirror error distribution of standard deviation σ. Results shown in Figs. A-54, 55, and 56 show $F_{overall}$ as a function of the receiver width at various values of x/R, the distance from the center of the spherical segment mirror. The values σ = 2.5, 5.0, and 10.0 arc minutes were used in the three figures, respectively.

Note from the figures that $F_{overall}$ increases with receiver diameter as one would expect, and that larger diameters are required for larger x-values to maintain equivalent $F_{overall}$ - values. These trends are qualitatively the same as those identified with the effective sun size model. However, quantitatively, these trends are substantially different from the previous results. This difference is most clearly shown by replotting the results in a different way;

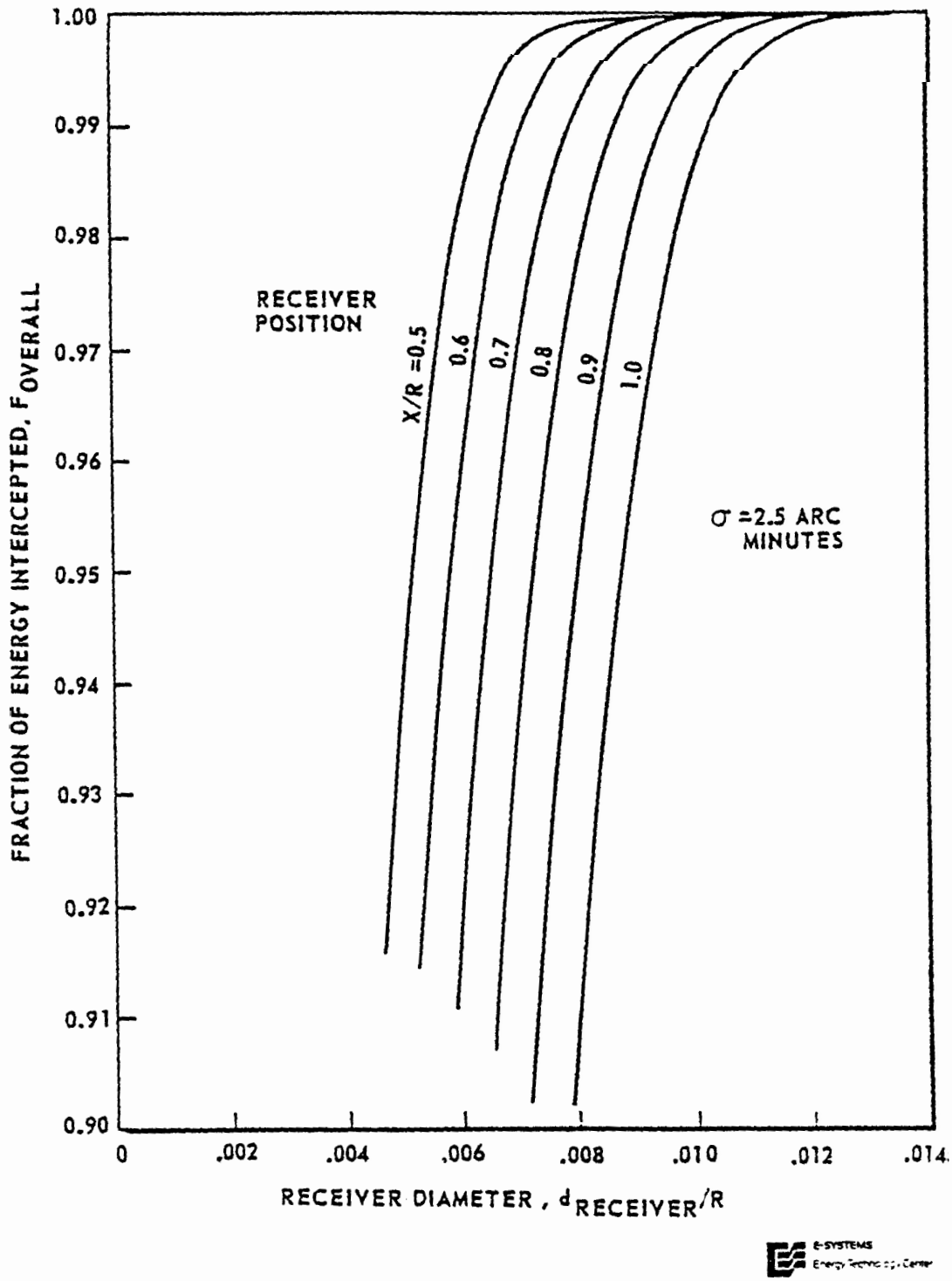

Figure A-54. Fraction of Energy Intercepted vs. FMDF Receiver Diameter

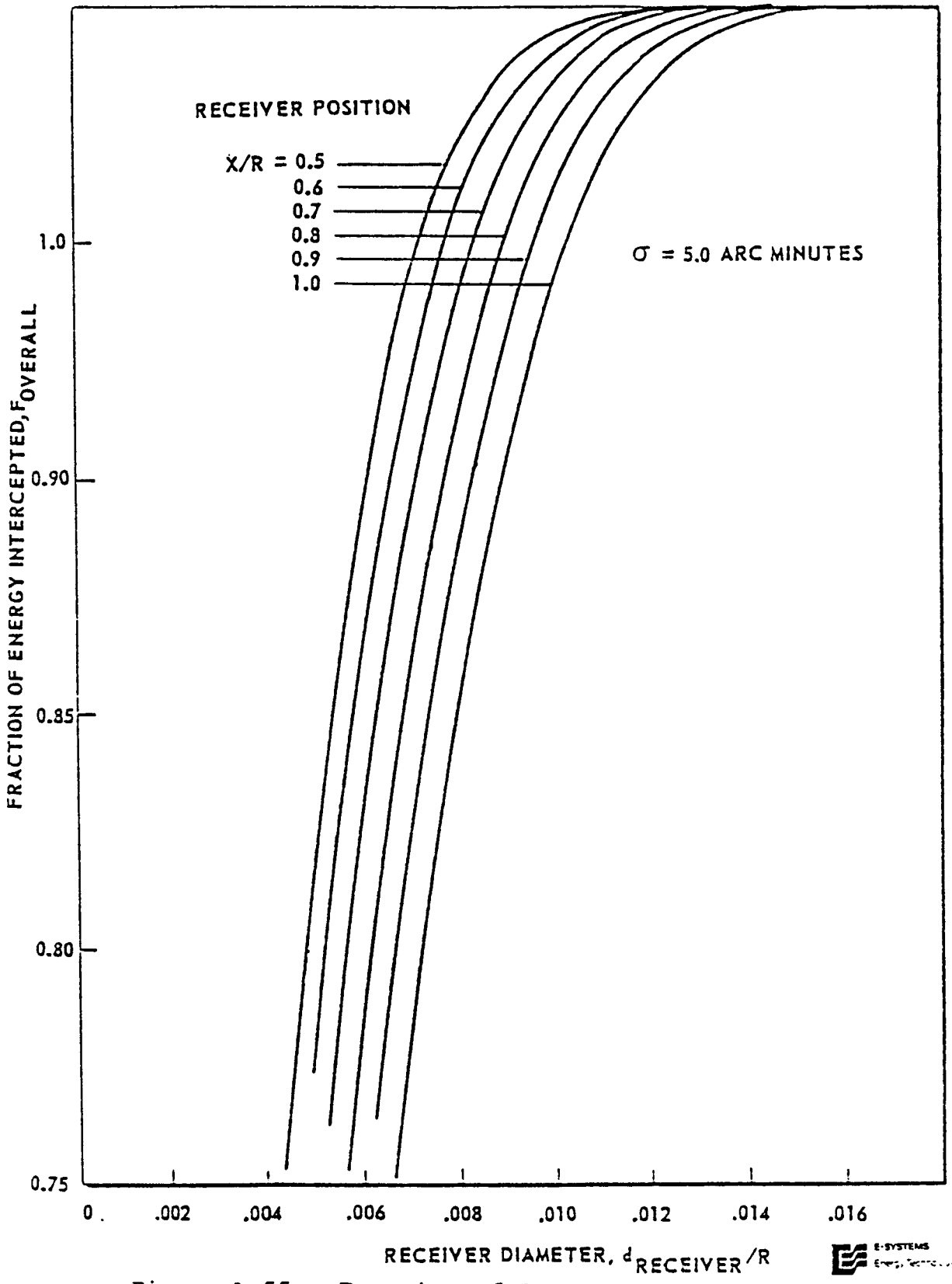

Figure A-55. Fraction of Energy Intercepted vs FMDF Receiver Diameter

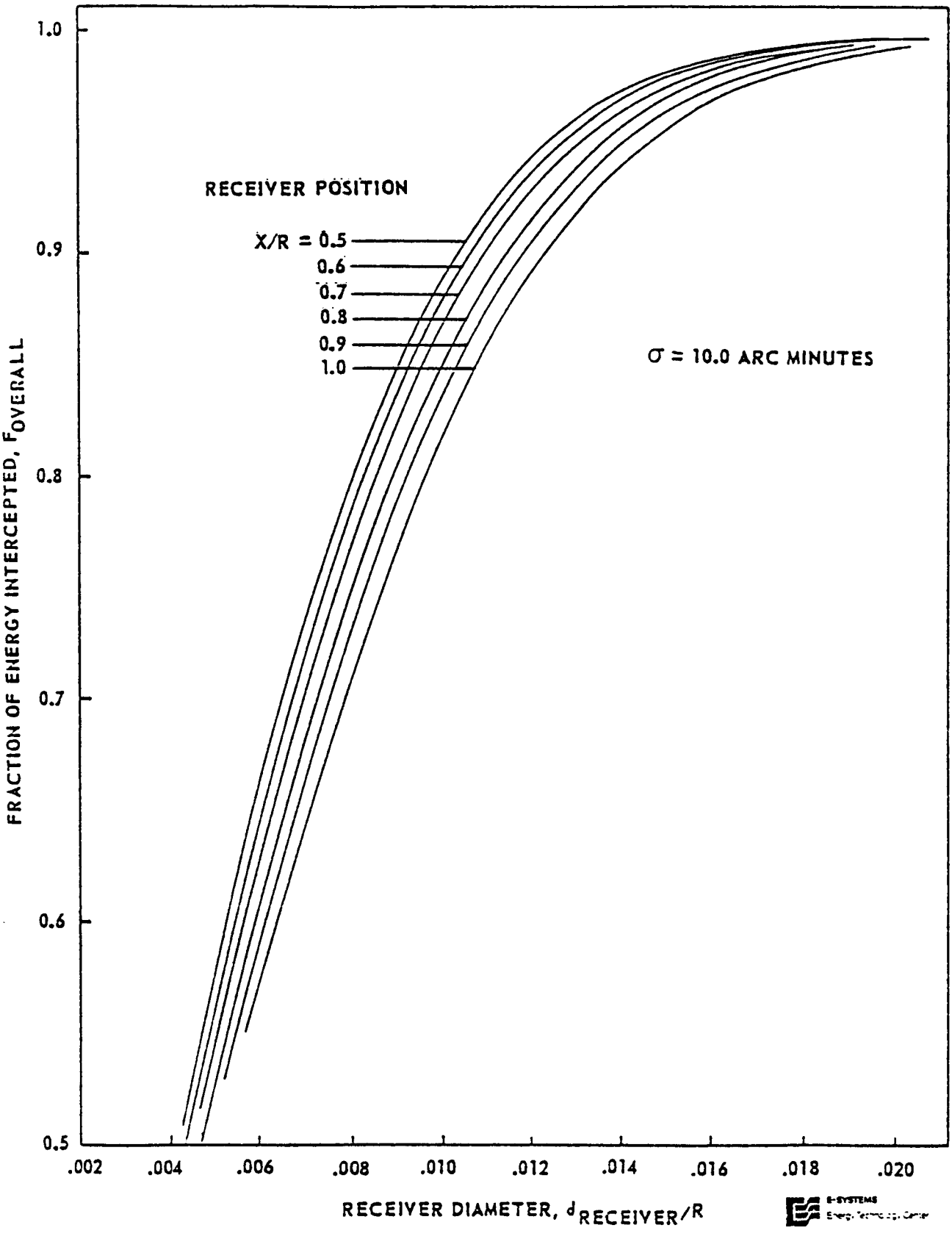

Figure A-56. Fraction of Energy Intercepted vs FMDF Receiver Diameter

Figs. A-57, 58, and 59 present the same data in terms of $d_{receiver}$ as a function of x-location, for different constant values of $F_{overall}$. Thus, these curves can be interpreted as receiver shapes for fixed values of $F_{overall}$. For comparison, the theoretical image is also shown on the figures, i.e., for a perfect reflector, the image would be 100% contained in a truncated cone with its vertex at the center of curvature and an included angle of 32 arc minutes. Also shown in Figs. A-57,58, and 59 is the receiver shape resulting from the previous "effective sun size" analyses for an error corresponding to a σ-value of about 2.5 arc minutes. Note from Fig. A-57 that the current results indicate that the old receiver shape is much larger than required and has a much greater included angle (slope) than required. In fact, the previous receiver shape has 1.6 times as much exposed area as the 99% $F_{overall}$ curve of Fig. A-57.

The possible receiver oversizing which resulted from the previous analyses is due to two effects:

(1) The "effective sun size" approach neglected the smaller effect of errors in the circumferential direction.

(2) The "effective sun size" approach assumed that the reflected energy was uniformly distributed in an oversized image, rather than normally distributed about its ideal position.

Note in Fig. A-58 that for a σ-value twice as large as expected (5 arc minutes), the old receiver (sized for only 2.5 arc minutes with the previous method) is still larger than needed. A receiver shaped according to the 99% $F_{overall}$ -curve of Fig. A-58 would have only 85% as much exposed area as the previous receiver shape.

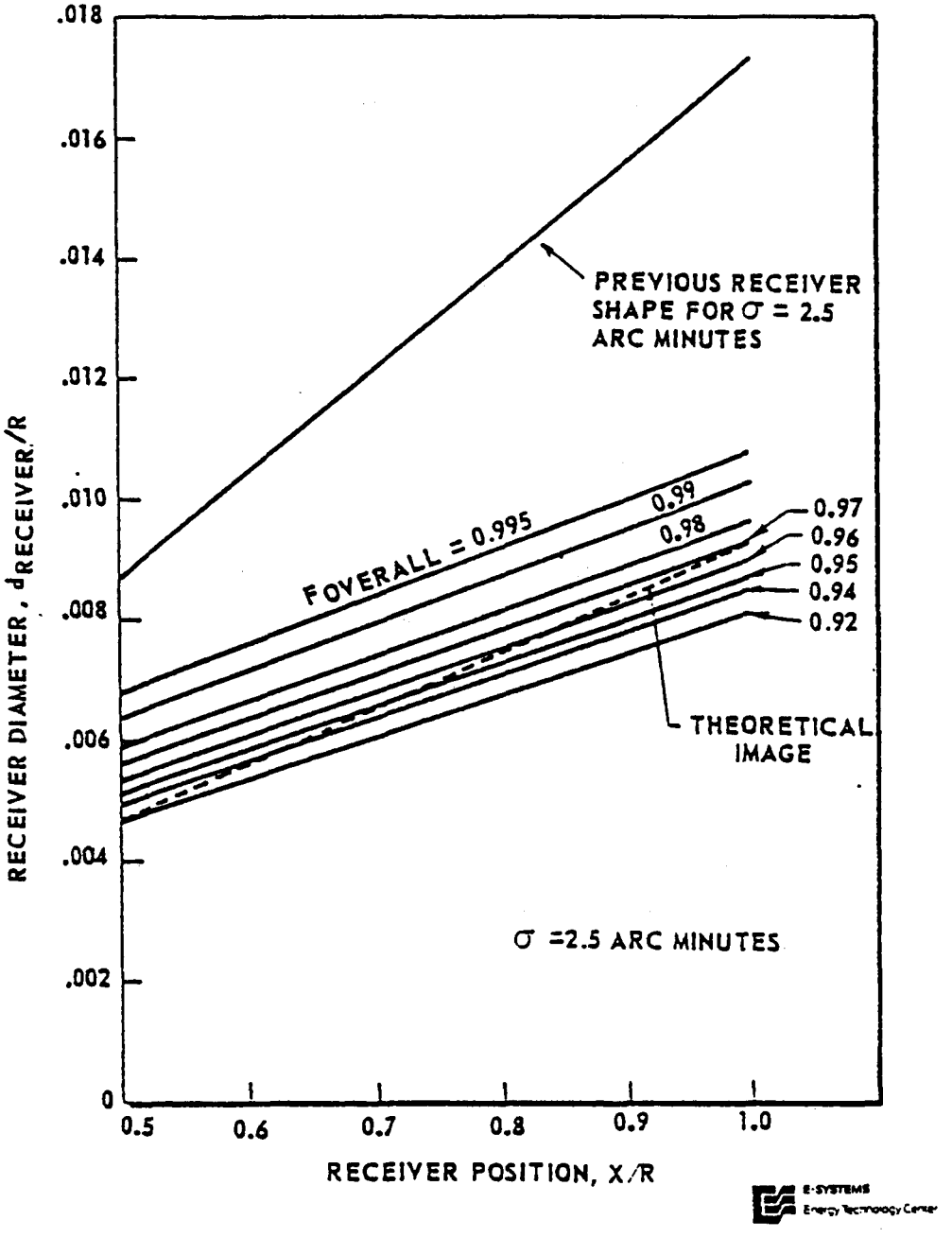

Figure A-57. FMDF Receiver Shape for Constant Energy Intercept Factor

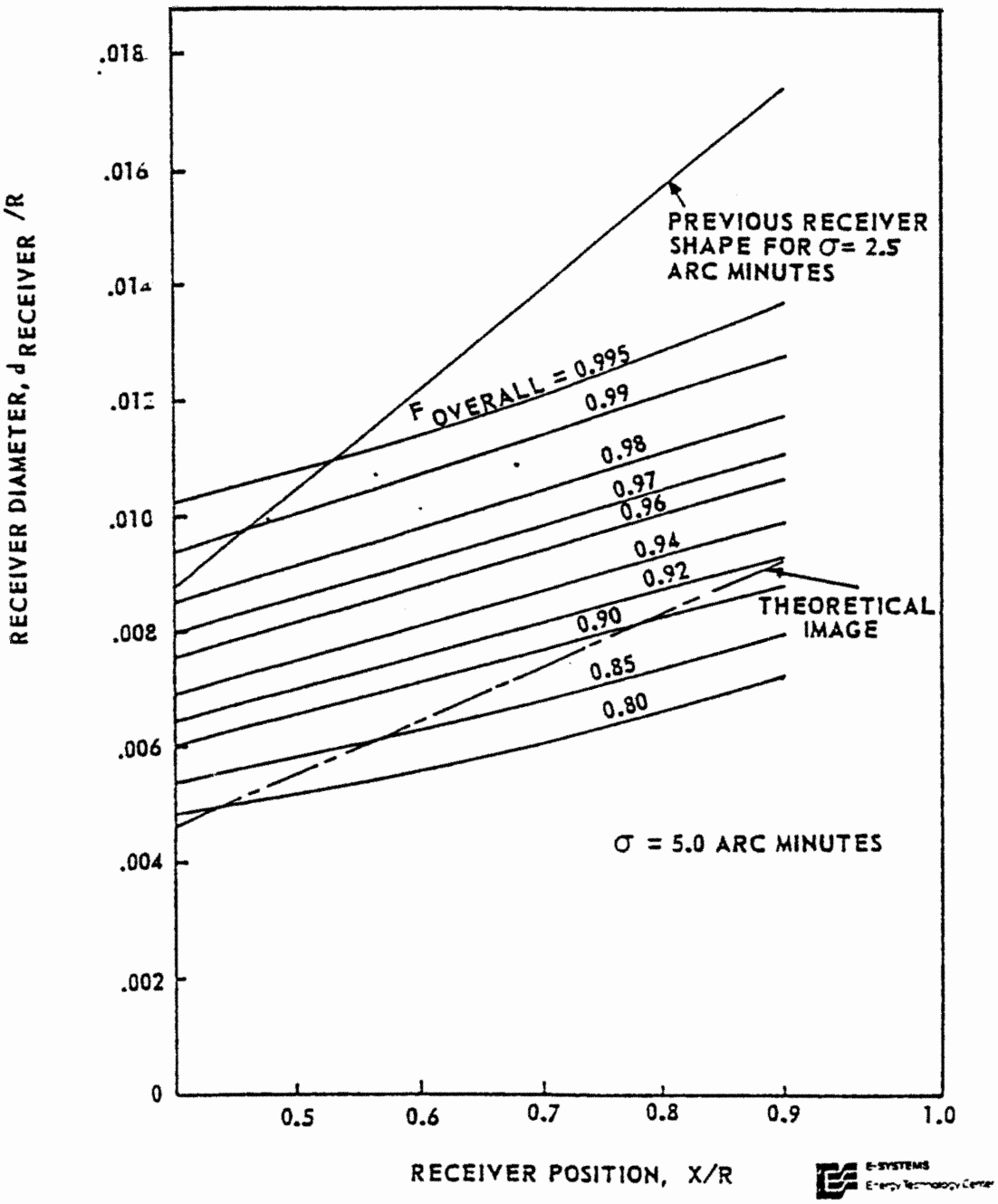

Figure A-58. FMDF Receiver Shape for Constant Energy Intercept Factor

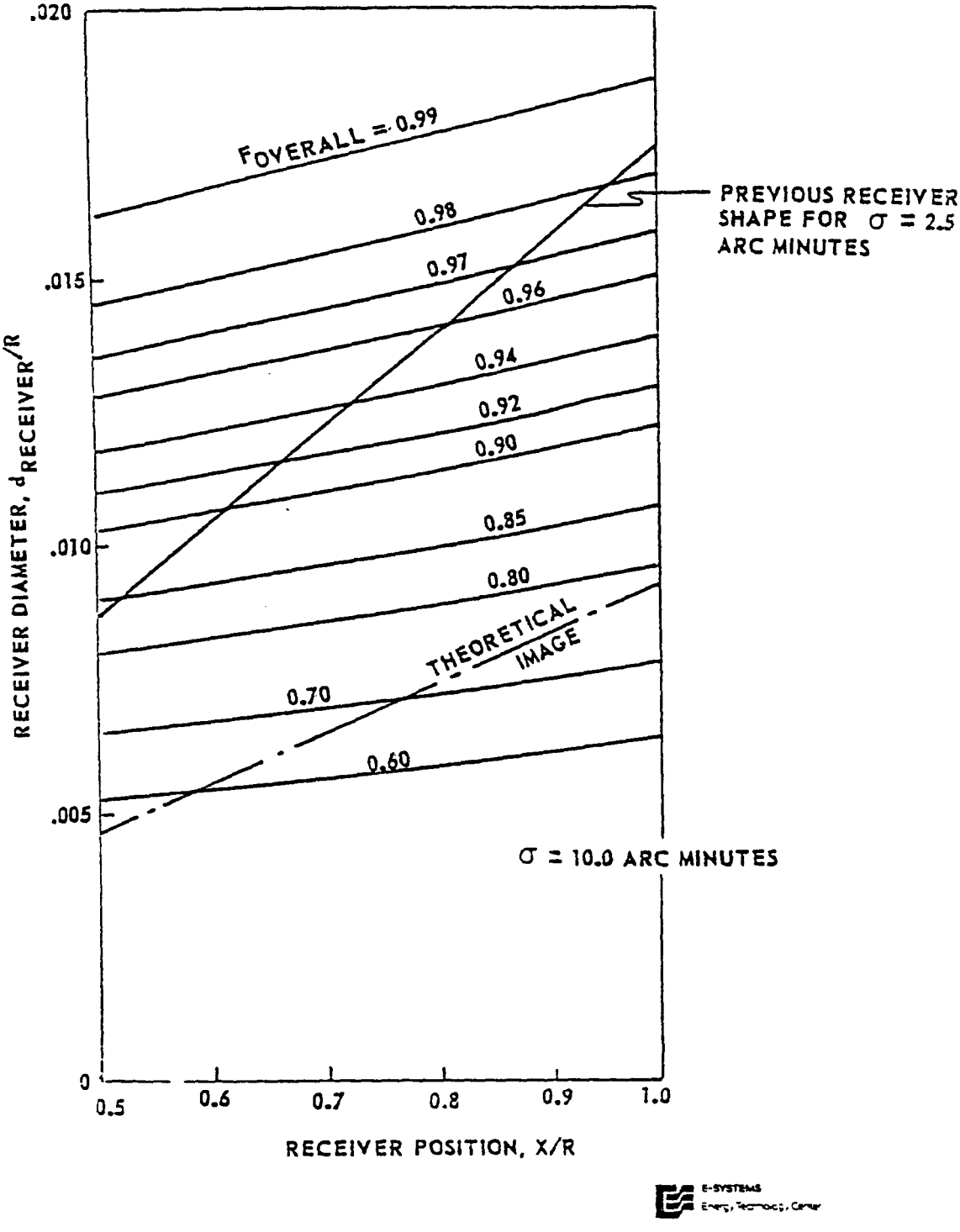

Figure A-59. FMDF Receiver Shape for Constant Intercept Factor

Figure A-59 shows the results for a σ-value four times as big as expected (10 arc minutes). Even so, a receiver shaped according to the 94% $F_{overall}$-curve of Fig. A-59 would have slightly less exposed area than the previous receiver shape.

Further note from Figs. A-57, 58, and 59 that the constant $F_{overall}$-curves are much flatter (lower slope) than either the previous receiver shape or the theoretical image, especially for larger errors. This implies that the receiver can be more nearly cylindrical than previously thought. In fact, a straight cylindrical receiver of roughly the same diameter as the small end of the previous conical shape receiver would have an energy intercept factor ($F_{overall}$) which varies from nearly unity at x/R = 0.5 to about 95% at x/R = 1.0, for a σ-value of 2.5 arc minutes as in Fig. A-57. Since flux levels are higher near x/R = 0.5 than at x/R = 1.0, such a receiver would be adequate with an average $F_{overall}$-value in the high nineties, percentagewise. Such a receiver should be cheaper to fabricate than a conical receiver, since its supporting structure would be of conventional tubular shape. Selection of an optimal receiver shape involves a complex interactive tradeoff analysis involving optical, thermal, structural and economical factors and is beyond the scope of the discussion here.

The axisymmetric (normal incidence) flux profile was calculated for the improved receiver shape, using the closed-form solution that E-Systems has developed for this problem. However, the non-axisymmetric profiles can also be calculated using previously developed computer codes. Figure A-60 presents the axisymmetric

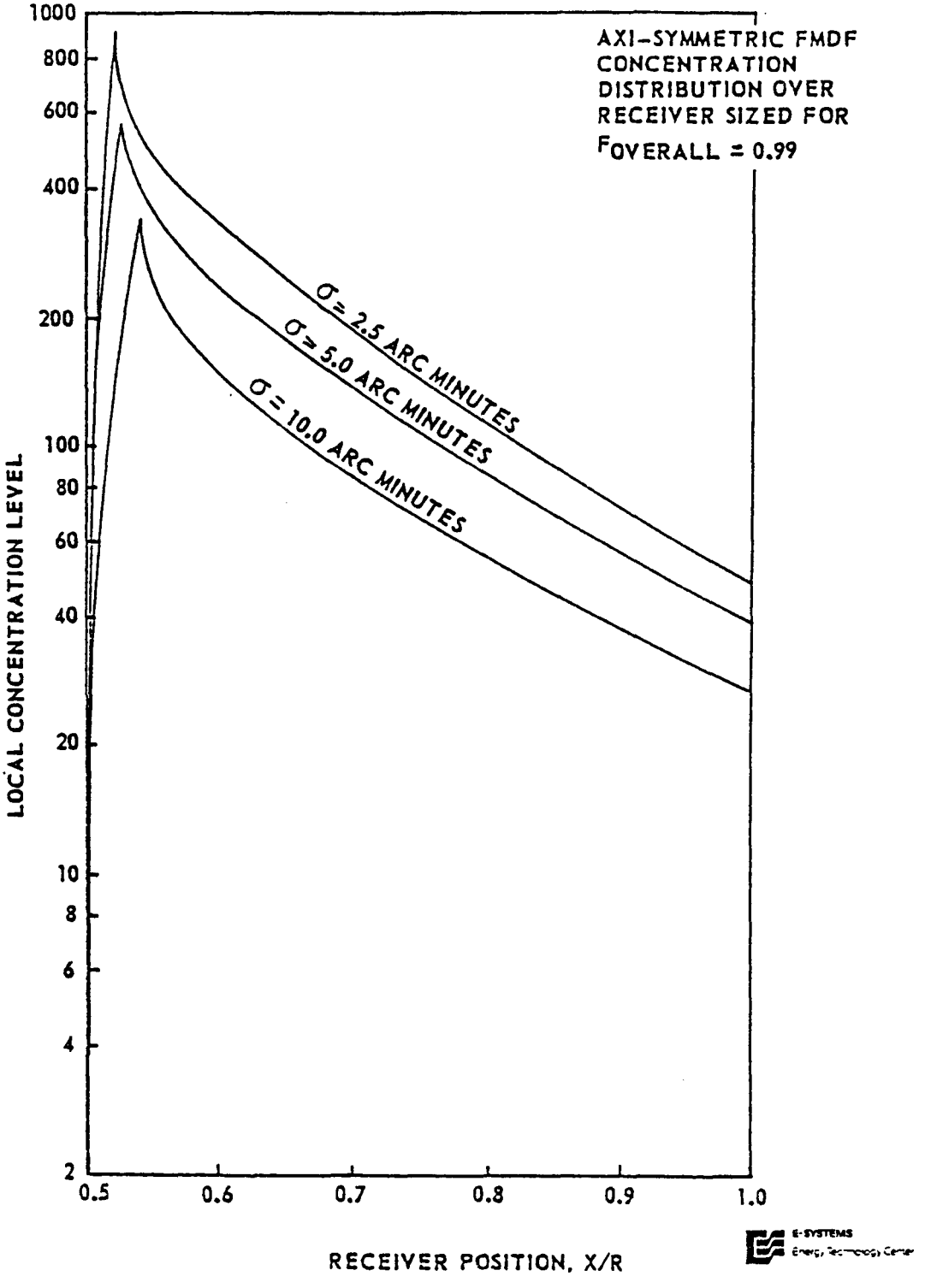

Figure A-60. Axisymmetric FMDF Concentration Distribution Over Receiver Sized for $F_{overall} = 0.99$

flux profile over a receiver shaped according to the $F_{overall}$ = 99% curve of Figs. A-57, 58 and 59 for σ-values of 2.5, 5.0 and 10.0 arc minutes respectively. For the previously specified error level of 2.5 arc minutes, the peak (caustic) flux concentration is over 900, compared to about 660 for the previous receiver shape [29,30]. Similarly, the flux concentration at x/R=1.0 is now 49 compared to the previous 29. For σ = 5.0 arc minutes, the peak flux is nearly as high as previously calculated for σ = 2.5 minutes, while the x/R = 1.0 flux is about 39 compared to 29. Thus, with twice the error, the new profile is higher on average than the previously calculated profile. Thus, the new E-Systems statistical approach to errors indicates that previously calculated optical performance has been overconservative and/or the error budget can be relaxed.

Conclusions drawn from the results above include:

(1) The previously used "effective sun size" approach to FMDF optics is too conservative if slope errors are randomly distributed according to a normal (Gaussian) probability distribution.

(2) Using a statistical approach to the optics, the receiver can be smaller than previously thought and/or the error tolerances for the concentrator can be relaxed.

(3) The receiver shape required to intercept nearly all of the reflected solar energy is not conical with vertex at the center of curvature, but rather a more nearly cylindrical cone with far less than a 2:1 diameter ratio from bottom to top.

(4) All of the effects identified with this statistical optical analysis indicate that collector performance will be better and collector cost lower than previously expected.

REFERENCES - APPENDIX A

(1) Texas Tech University and E-Systems, Inc., "Crosbyton Solar Power Project - Phase I Interim Technical Report," ERDA Contract No. E(29-2) - 3737, Lubbock, Texas, February 1977.

(2) Dittus, F.W., & Boelter, L.M., University of California (Berkeley) Publication. Eng., Vol. 2, 1933, pg 443.

(3) Chen, J.C., "A Correlation for Boiling Heat Transfer to Saturated Fluids in Convective Flow," I & FC Process Development, Vol. 5, No. 3, 1966, pp. 322-329.

(4) Naitoh, M., Nakamura, A. and Ojasaware, H., "Dryout in Helically Coiled Tubes of Sodium Heated Steam Generator," ASME Paper No. 74-WA/HT-48, 1975.

(5) Bishop, A.A., Sandberg, R.O., and Tong, L.S., "Forced Convection Heat Transfer at High Pressure After the Critical Heat Flux," USAEC Report WCAP-2056 Part HC (1964), also ASME Paper No. 65-HT-31 (1965).

(6) Heinemen, J.B., "An Experimental Investigation of Heat Transfer to Superheated Steam in Round and Rectangular Channels," ANL-6213, 1960.

(7) Mendler, O.J., et.al., "Natural Circulation Tests with Water at 800 to 2000 psia Under Non-Boiling, Local Boiling, and Bulk Boiling Conditions," Journal of Heat Transfer, August 1, 1961.

(8) Martinelli, R.C., and Nelson, D.B., "Prediction of Pressure Drop During Forced Convection Circulation of Boiling Water," ASME Paper No. 47-116, 1947.

(9) Ito, H., "Friction Factors for Turbulent Flow in Curved Pipes," Journal of Basic Engineering, June 1959, pp. 123-134.

(10) Thom, J.R.S., "Prediction of Pressure Drop During Forced Circulation Boiling of Water," International Journal of Heat and Mass Transfer, Vol. 7, 1964, pp. 709-724.

(11) Efferding, L.G., DYNAM, "A Critical Computer Program for Study of the Dynamic Stability of Once-Through Boiling Flow with Superheated Steam," GAMD-8656, 1968.

(12) Beckjord, E.S., "Hydrodynamic Stability in Reactors," Nuclear Safety, Vol. 4, 1962, pp. 1-10.

(13) Shotkin, L.M., "The Flow of Boiling Water in Heated Pipe," Nuclear Science and Engineering, Vol. 26, pp. 293-304, 1966.

(14) Shotkin, L.M., "Stability Considerations in Two-Phase Flow," Nuclear Science and Engineering, Vol. 28, 317-324, 1967.

(15) Kjaer-Pedersen, N., "An Integral Analytical Model for the Evaluation of Two-Phase Flow Stability," Nuclear Science and Engineering, Vol. 35, pp. 200-210, 1969.

(16) Yadigarogln, G., and Bergles, A.E., "Fundamental and Higher-Mode Density-Wave Oscillations in Two-Phase Flow, the Importance of the Single Phase Region," ASME paper 71-HT-13, 1972.

(17) Gross, R.J., and See, F.T., "A Contribution to Thermal-Hydraulic Stability Analysis," ASME paper No. 73-WA/HT-23, 1974.

(18) Vexisoglu, T.N., and Lee, S.S., "Instability in Boiling Upward Flows," Concurrent Gas-Liquid Flow, ed. Rhodes, E. and Scott, D.S., Plenum Press N.Y., 1969, pp. 303-344.

(19) Schuster, J.R., and Berenson, P.J., "Flow Stability of a Five-Tube Forced Convection Boiling," ASME Paper No. 67-WA/Ht-20 1967.

(20) Fried, J.R., "Heat Transfer Agents for High-Temperature Systems," Chem. Engr., May 28, 1973, pp. 89-98.

(21) Seifert, W.F., Jackson, L.L., Sech, C.E., "Design and Operational Consideration for High Temperature Organic Heat Transfer Systems," paper presented at 71st National AIChE Meeting, Dallas, TX, 22-24 February 1972.

(22) Central Receiver Solar Thermal Power System Phase 1, First Quarterly Technical Progress Report, SAN 1108-76-1, MDC-G6318, January, 1976.

(23) ibid, Second Quarterly Technical Progress Report, SAN-1108-76-2, MDC-G6382, April, 1976.

(24) ibid, Sixth Quarterly Technical Progress Report, SAN-1108-76-2, MDC G6902, April, 1977.

(25) Alvis, R.L., "ERDA/New Mexico Project-System Design," paper presented at Solar Irrigation Workshop, Albuquerque, New Mexico, 7-8 July, 1977.

(26) McAdams, W.H., "Heat Transmission," 3rd ed., McGraw Hill, New York, 1954.

(27) Hilpert, R., "Wormeabgabe von Greheizen Drahten und Rohren," Forsh. Geb. Ingenieurwes., 4, pg. 20, 1933.

(28) Wade, W.R. and Slemp, W.S., "Measurements of Total Emittance of Several Refractory Oxides, Cements, and Ceramics for Temperatures from 600 °F to 2000 °F, NASA, TND-998, Oct. 1961.

(29) O'Neill, Mark J., "Optical Analysis of the Fixed Mirror/ Distributed Focus (FMDF) Solar Energy Collector," IR&D Technical Report No. 9-19100/TR75-02, E-Systems, Inc., Dallas, Texas, December 1975 (Revised April 1976).

(30) O'Neill, Mark J., "Optical Analysis of the Fixed Mirror/ Distributed Focus (FMDF) Solar Energy Collector," Proceedings of the 1977 Annual Meeting, American Section of the International Solar Energy Society, Volume #1, pp. 35/24-28, June 6-10, 1977.

APPENDIX B. RECEIVER SUBSYSTEM

B-1 INTRODUCTION

The receiver subsystem considered in this appendix consists of two parts: 1) the receiver itself with its helical heat transfer tubes, support cone and attachments, and 2) the structural support system consisting of the tripod supports, receiver boom support, guideways and associated structure. Two types of receiver support systems are discussed: 1) a cantilevered support (recommended), and 2) a simple support (alternate). Results are reported for analyses conducted for the 200 ft. diameter Recommended Power System (RPS) and the 65 ft. diameter Analog Test System (ATS).

The basic solar receiver is a once-through boiler unit consisting of twenty (20) 0.375 inch outside diameter tubes which are spirally wrapped around the outside of a conical support structure. The bottom of the 57 ft. long cone (designated as X/R = 1.0) has a diameter of 2 ft. which tapers to a diameter of 1 ft. at the top of the receiver (X/R = 0.5). The uncoiled straight length of each of the 20 tubes is 431 ft. The relationship between coiled tube length and receiver location (in terms of X/R) is shown on Fig. B-1. The physical and dimensional data for the receiver system analyzed are tabulated in Table B-1. The oil storage receiver is discussed in section B-8.

B-2 RECEIVER TUBE AND CONE MATERIALS

B-2.1 Material Selection

Because of the high creep-rupture and thermal fatigue problems associated with the high temperature and high stress level oper-

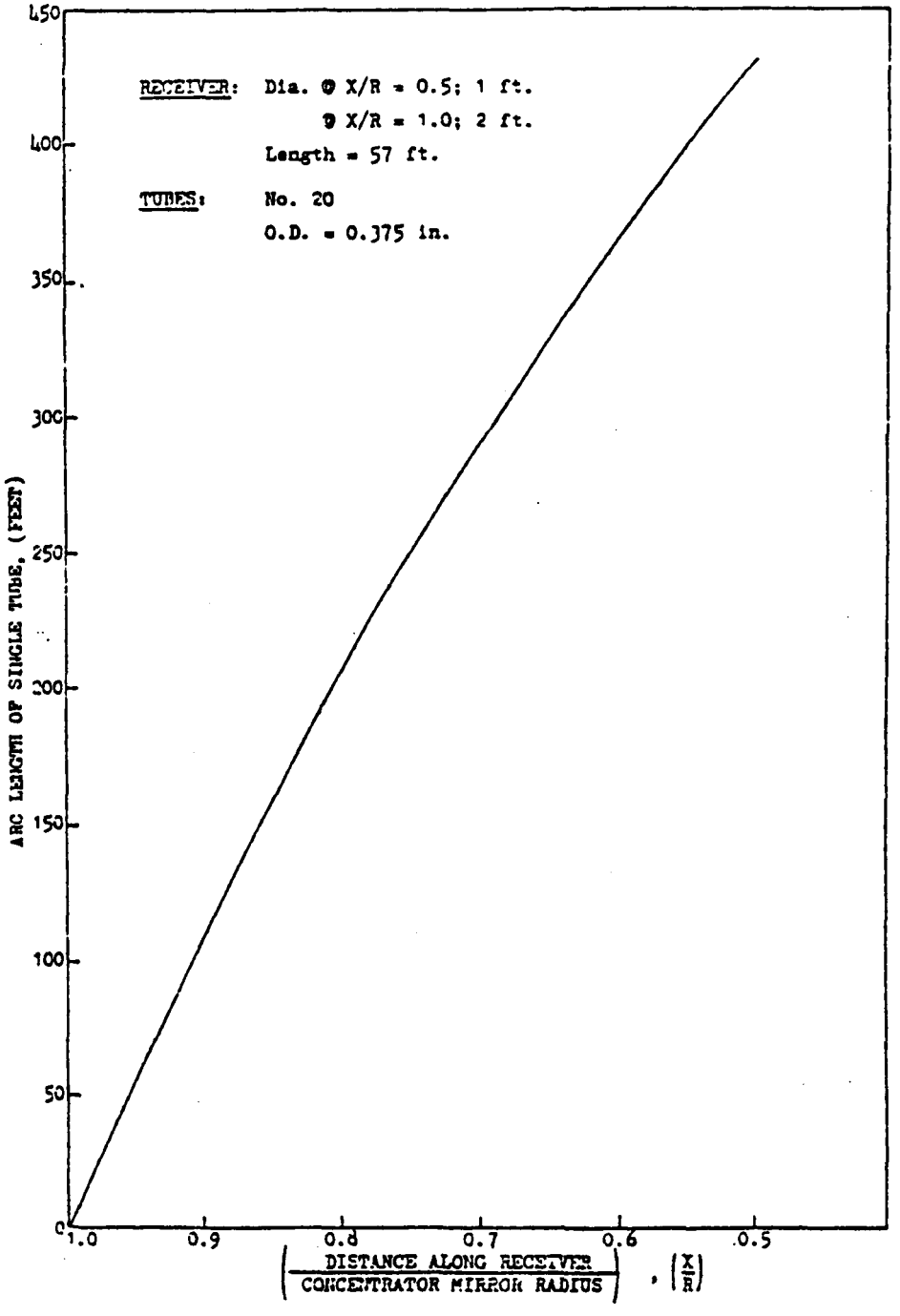

Figure B-1. Tube Length vs X/R

TABLE B-1 RECEIVER PHYSICAL AND DIMENSIONAL DATA

Receiver Support Cone:	
Length	57 ft.
Diameter, Bottom (X/R = 1.0)	2 ft.
Diameter, Top (X/R = 0.5)	1 ft.
Heat Transfer Tubes:	
O. D.	0.375 in.
I. D.	0.250 in.
Length/tube	431 ft.
No. Tubes/unit	20
Tube Material	Inconel 617 or 625
Tube Pattern	Conical Spiral
Flow Conditions:	
Water Inlet Temperature	100°F
Water Outlet Temperature	975°F
Water Inlet Pressure	1000 Psia

ation of the tubes, only four materials were considered as candidate materials. Because of differential expansion problems, to be discussed later, it is believed that the cone could be made of another material, 316 stainless steel, although, this would necessitate that no upper cone material be exposed to the concentrated radiation. Because of this possibility, it is recommended that, for the ATS, a high temperature material be used. This matter is discussed further in Section B-9.

The properties of different candidate materials for the recommended receiver tubes and the support cone are listed in Table B-2. Only two of the materials, Inconel 617 and 625 are suitable for this application. Both materials have suitable strength properties at the normal maximum operating temperatures and stress levels, with Inconel 625 somewhat superior to Inconel 617. At the extremely high temperatures associated with transient emergency operation, however, Inconel 617 is distinctively stronger. Inconel 617 is approximately 40% more expensive than Inconel 625. Until further refinements in the transient emergency analysis are made, or until experimental data is acquired, the material of choice is Inconel 617. Further analysis and testing may, however, indicate a future change to Inconel 625.

B-2.2 Code Classification for Structural Evaluation of Tubes and Cone

At present, it is not clear which of the ASME Boiler and Pressure Vessel Codes is applicable for the solar receiver. Foster

TABLE B-2 HUNTINGTON ALLOYS, INC. MANUFACTURING DATA

YIELD STRENGTH 1000 psi

Temperature	Inconel 625	Inconel 617	Inconel 600	Incoloy 800
100°F	62	45	40	43
1000°F	48	28	32	32
1200°F	48	25	31	29
1400°F	44	29	17	16
1600°F	38	27	9	13
1800°F	18	20	4	8
10,000 hr. Rupture Life Rupture Strength 10,000 psi				
1200°F	40	39	>10	14
1400°F	16	15	6	6
1600°F	5	7	2.5	2.5
1800°F	<1	2.5	< 1	< 1
Fatigue Strength, 1,000 psi for 10^6 Cycles to Failure				
1600°F	37	31	-	-

Wheeler Development Corporation (FWDC) is presently involved in a DOE contract to provide interim recommendations as to Code classifications and standards for solar boilers. The structural evaluation criteria for this receiver must, as a minimum be designed to ASME Boiler and Pressure Vessel Code Section I - Power Boilers. The design philosophy of Section I is to set the wall thickness necessary to maintain the basic hoop stress caused by internal pressure below tabulated allowable stresses. Section I does not require detailed evaluation of the more localized thermal stresses which are known to exist in the FMDF solar receiver. In addition, Section I has no criteria to evaluate creep rupture or fatigue damage. Nor does it contain material properties or allowable stresses for Inconel 617 material. Due to the nature of the cyclic thermal stresses and long-term elevated temperatures associated with the FMDF solar receiver, creep rupture and fatigue are failure modes which must be evaluated. Accordingly, the rules of Section VIII, Division 2 (Pressure Vessels Alternative Rules), as well as some of the applicable sections of Code Case 1592 (Class I Components in Elevated Temperature Service) of the ASME Boiler and Pressure Vessel Code are recommended for structural evaluation. Since concise Code approved rules are not available, the above recommended application of Code rules was used in the analysis of the subject receiver as detailed below. For parts made of Inconel 617, actual material properties were used, along with the general guide lines set forth in the various sections of the ASME Code, to obtain reasonable allowable stresses.

B-3 STRUCTURAL CONSIDERATIONS OF THE CONE/TUBES

B-3.1 Unwinding and Buckling of Helically Coiled Tubes

To evaluate tube unwinding, tube buckling, axial stresses in the tubes, effects of end support conditions, and any requirements for intermediate supports, an ANSYS computer model of ten (10) turns of a helically wound tube (Fig. B-2) was constructed using a three-dimensional curved pipe element (STIF29). Temperature-dependent material properties used for the Inconel 617 tubing were obtained from Huntington Alloy, Inc. (see Table B-3).

Various computer runs, based on this basic model, were made. The first computer analysis model represented a helically wound tube rigidly fixed at one end (node 62) with the rest of the tubing being unsupported. The tubing was subjected to an internal pressure of 1,000 psig. A maximum winding angle of 0.028 degrees was calculated from the computer analysis results by extrapolating the 10 turn model to the full height of the unit. Accordingly, it is judged that there is no significant unwinding effect due to internal pressure.

The second computer analysis model of the helically wound tube was identical to the first model except that the axial thermal gradients corresponding to the bottom 10 turns, and to the top 10 turns of the receiver were applied. These two separate loading cases resulted in a maximum unwinding angle of 0.31 degrees and 0 stress.

In a subsequent computer run both ends of the helically wound tube (nodes 2 and 62) were fixed. The unwinding tendency resulted in a maximum axial stress in the tubing of 133 psi.

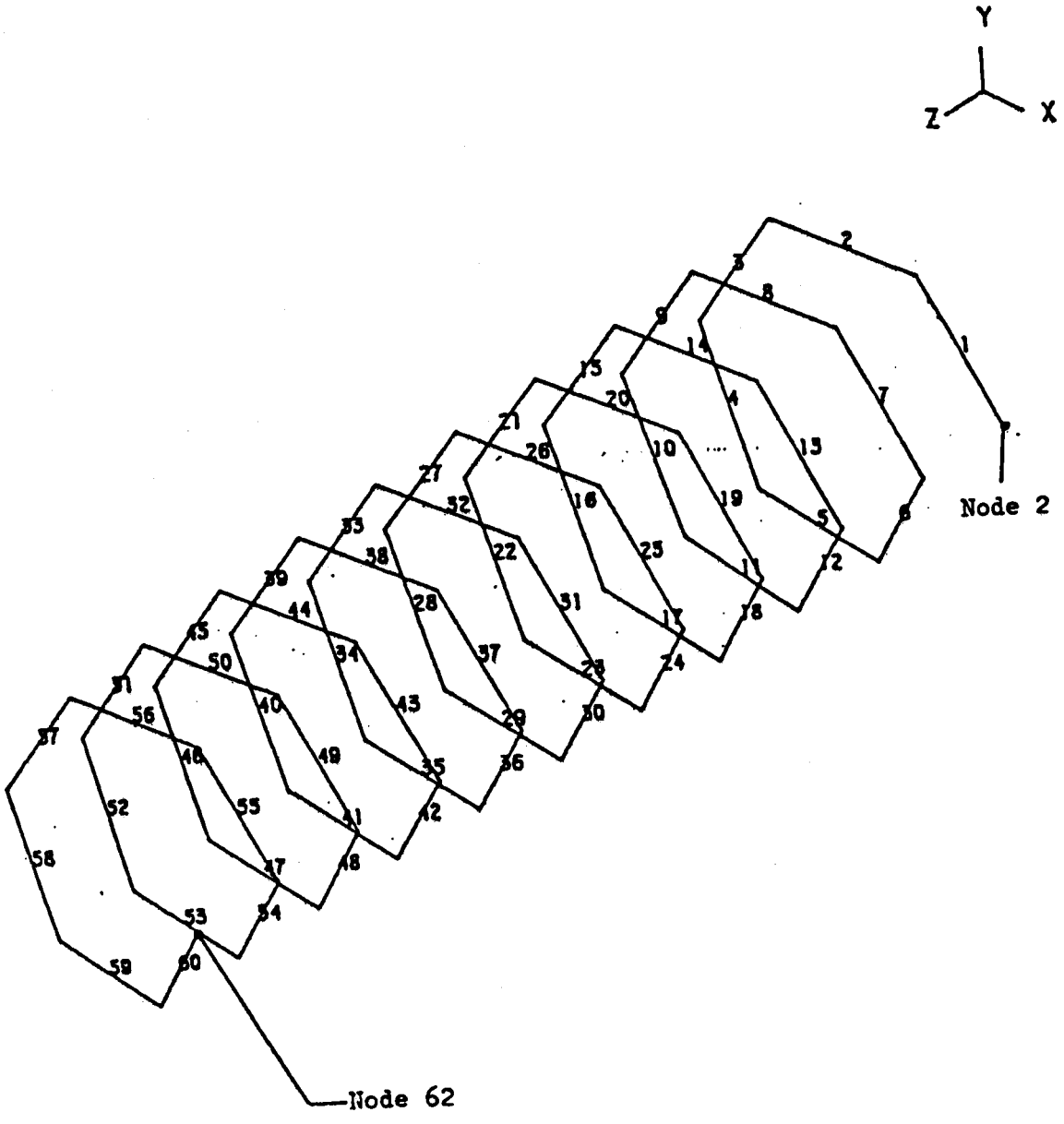

Figure B-2. Helix Coil Finite Element Model

TABLE B-3 MATERIAL PROPERTIES INCONEL 617

Temperature, ^{o}F	Tensile Modulus of Elasticity, 10^6 PSI	Poisson's Ratio
78	30.40	.256
200	29.85	.259
400	28.80	.258
600	27.78	.258
800	26.70	.259
1000	25.58	.258
1200	24.40	.264
1400	23.15	.277
1600	21.77	.296
1800	20.16	.306

Reference Huntington Alloys, Inc. transmittal dated 12-1-77.

Similar analyses were also conducted using material properties of Inconel 625. Similar results were obtained for this material.

These results indicate that there is a negligible tendency for the tubes to unwind due to pressure and thermal loadings. The stresses due to constraining both ends of the tubing are also negligible and no potential exists for buckling due to this mode of loading.

B-3.2 Differential Axial Growth Between Tubing and Supporting Cone

The differential axial thermal growth between the pressurized Inconel 617 tubing and an Inconel 617 supporting cone is 0.557 inch. If it is assumed that the tubing is tightly wound without any space between coils and that the axial displacements at the coil ends are fully restrained (no end flexibility); a hertz contact stress of 183,170 psi is produced between the tubes. This exceeds the allowable bearing stress of 40,500 psi based on the Code criteria of 1.5 times yield stress. In order to reduce this stress, it is essential that either the tube coils have initial axial gaps of 0.0003 in. between each coil, or the tube end connections have the flexibility to accommodate a total displacement of 0.557 in. It is recommended that the latter approach be used.

If the supporting cone is made of 316 stainless steel, the differential axial growth between the tubing and cone is equal to 0.078 in. Accordingly, with a 316SS cone the differential axial growth problem is much less severe.

B-3.3 Differential Radial Growth Between Tubing and Supporting Cone

Problems associated with the differential radial thermal growth between the tubing and the support cone were also studied. In the case of an Inconel 617 cone, the radial growth of the Inconel 617 tubing is larger than that of cone. This radial growth differential is a maximum of 0.0067 in. at the top of the cone (X/R = 0.5) and tapers to a minimum of 0.0007 in. at the bottom. As a result of this differential growth, the tubing column could slide downward. The bottom tube coil would then be subjected to vertical and side load (normal to the cone) components which must react the total deadweight of the tubing. The hertz contact stress due to the vertical component (34,950 psi) is acceptable but the hertz contact stress due to side component (373,200 psi) is excessive. This indicates that a tubing support shelf is required at the bottom of the cone to support the tubing deadweight. Alternately, intermediate tube supports could be used throughout the receiver length.

In the case of a 316 stainless steel cone, the radial growth of the cone is larger than the radial growth of the tubing. If the tubing is tightly wound, this interference can result in unacceptable tube stresses (22,690 psi). This problem can be solved by providing an initial radial gap between the cone and the tubing. A gap of 0.005 in. would be required at the top of the cone, tapering to a value of 0.0002 in. at the bottom. A support shelf at the bottom of the cone is still required for the deadweight support of tubing.

B-3.4 Buckling Analysis of Receiver Cone

The recommended receiver configuration (to be discussed later) consists of the receiver cone cantilevered from the space frame support with the free end of the cone supported by three guy wires (see Fig. B- 7). These wires are pretensioned to support the deadweight of the receiver during operation. This minimizes receiver tip deflection relative to the focus of the fixed mirrors to within acceptable values. The cable tension increases from its initial value of 2,000 lbs. per cable to 7,000 lbs. due to the thermal elongation of the receiver during operation.

A stress analysis was conducted to check the structural adequacy of the receiver cone against buckling. The cone was analyzed as a beam column with combined axial and lateral loads. The axial compressive load considered was due to the total guy wire tension during operation (21,000 lbs.). The lateral load used was the deadweight of the receiver when it is at its maximum declination angle of 57^0 from vertical.

A maximum compressive stress of 15,780 psi was calculated for a receiver cone wall thickness of 0.100 in. This is satisfactory for Inconel 617 material which has an allowable stress of 16,650 psi based on Code criteria.

The Code allowable stress for 316 stainless steel is only 9,600 psi. Thus, a 0.100 in. thick 316 cone cannot be used unless the guy wire tension is reduced or the cone thickness increased. If the guy wire tension is limited to 3,000 lbs. each by using some constant tensioning device, the compressive stress in the cone is 12,760 psi. This still exceeds the Code allowable by 33%. If the cone wall

thickness is increased to 0.150 in., the resultant stress reduces to an acceptable value of 9,480 psi.

In the case where the guy wire tension cannot be limited to a value below 7,000 lbs., the minimum required cone wall thickness for 316 stainless steel material is 0.200 in.

B-3.5 Single Tube Helix Pressure Test

In addition to the computer analysis, a pressure test was conducted on four-turn single tube helix. The purpose of this test was to verify the results of the helically wound tube computer analysis prior to proceeding to more complex computer models.

A single tube helix with four turns was selected as the simplest representative configuration for testing. The test helix was fabricated with constant diameter coils in lieu of the 1^0 cone angle of the actual receiver configuration. The outside diameter of the coils was 12.1 in. and the pitch was 7.5 in. A detailed sketch of the helix, together with dial indicator locations, is shown in Fig. B-3. Computer analysis confirmed that deflections due to temperature could be determined analytically without computer aids by using the coefficient of linear expansion. In other words, configuration of the material was found to have no effect upon the expansion or contraction of the material due to temperature gradients. Therefore, a pressure test was required to verify the pressure deflections determined by the computer analysis. The "ANSYS" computer program utilizing a "curved pipe" element was used in the computer analysis of the receiver tube structure as described in the previous section.

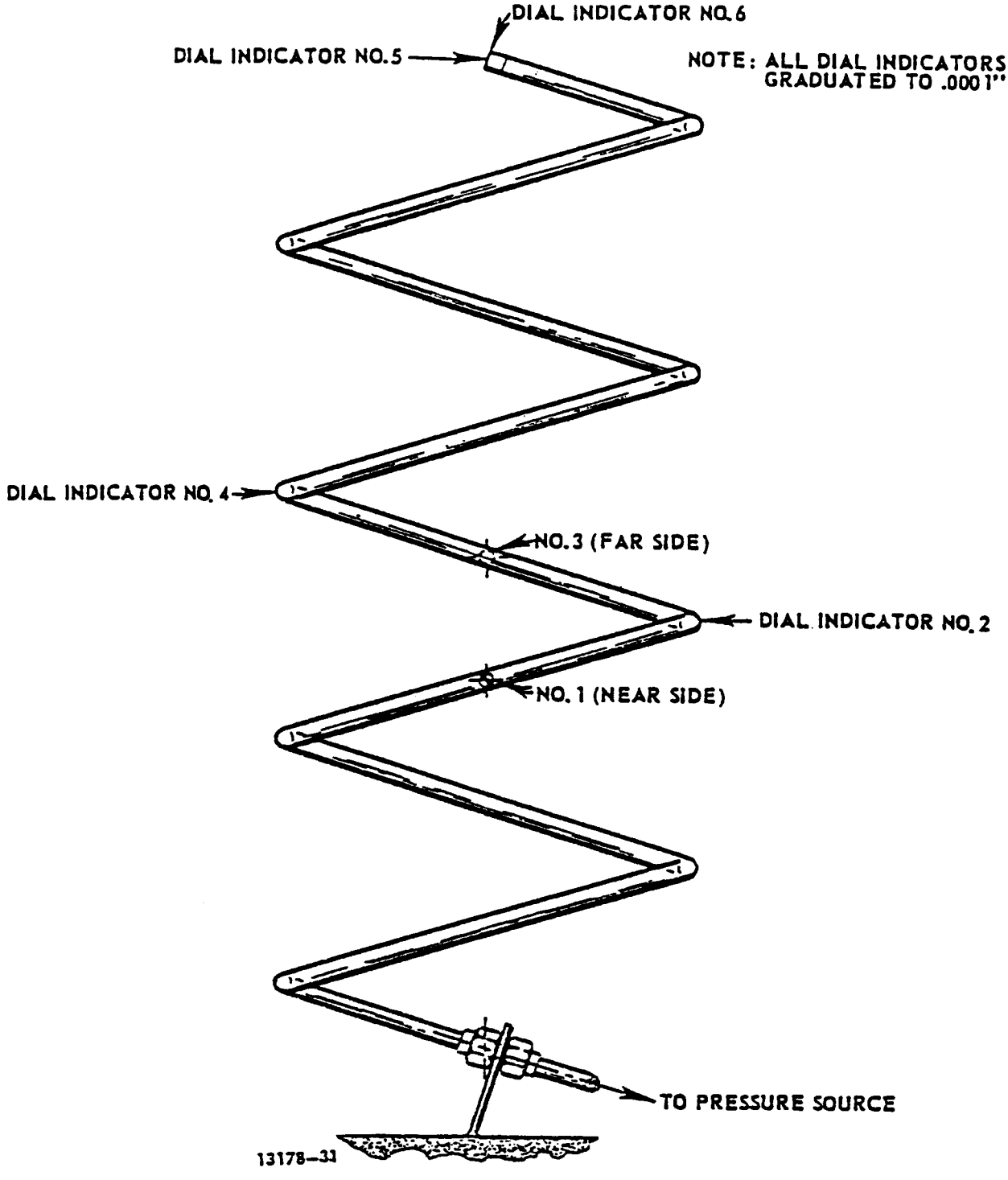

Figure B-3. Dial Indicator Positions For Pressure Tests On Receiver Tube Helix

The test helix was fabricated from 321 CRES seamless tubing in an annealed condition. The 321 CRES material rather than Inconel, was used because it was readily available. A one-inch long specimen of the formed tube was cut from the helix to be measured for flattening effects during forming and to determine the amount of work hardening that occurred during forming.

The helical tube was fixed at the fitting end to a surface table and the remainder of the helix was left freely standing. Six dial indicators were mounted to rigid structure attached to the surface table and extending upward along the helical tube, as shown in Fig. B-3. Although the actual operating pressure of the receiver tube assembly is approximately 900-1000 psi, the helical tube was tested up to 2000 psi to increase the magnitude of the readings.

The flattening of the tube due to forming was measured at 0.8% of the outside diameter (0.003 in.). Since the 12 inch diameter of the helix represents the small end of the receiver, this amount of flattening represents the maximum that would occur during fabrication of the receiver tube assembly.

The results of the pressurization tests indicated that the average measured deflection was negligible, well below 0.001 in., in agreement with computer analyses.

B-4 SINGLE TUBE CROSS-SECTION THERMAL STRESS ANALYSES

Because of the highly asymmetric nature of the incident concentrated radiation, a detailed analysis of the thermal stresses in a single tube cross-section was conducted.

The detailed stress analysis of the tube cross-section was initiated by evaluating the applicability of several different typs of computer programs. Three different finite element programs, "SPACE", "NASTRAN" and "ANSYS", were considered in the analysis of the tube section. When the results from the three computer programs were compared to hand calculations for the case where the load was internal pressure and a thermal gradient was assumed to exist in the tube from inside to outside, the ANSYS program was found to provide the best comparison. ANSYS was therefore chosen for subsequent analyses of the tube section. The computer model that was used to determine the node temperatures was also used in conjunction with the ANSYS model.

Most of the analyses were conducted using Inconel 625 properties. Scaling these results to Inconel 617 by multiplying by the ratio of Inconel 617 strength to Inconel 625 strength will give approximate and conservative results. This is because at operating temperatures Inconel 617 has a somewhat lower coefficient of thermal expansion (97% at 1200^0F) and somewhat higher thermal conductivity (122% at 1200^0F) than Inconel 625, both of which tend to reduce thermal stress levels. These conservatively scaled results are indicated in parenthesis in the discussion below.

In each analysis, the section was treated as having plane stress. Analyses were conducted at an internal pressure of 925 psi and internal temperature of 975^0F. Fig. B-4 shows the node temperatures on the cross-section that was analyzed and the stress intensity is shown in Fig. B-5. The maximum value occurs on the inside surface and is 7202 psi. The temperature that was calculated for

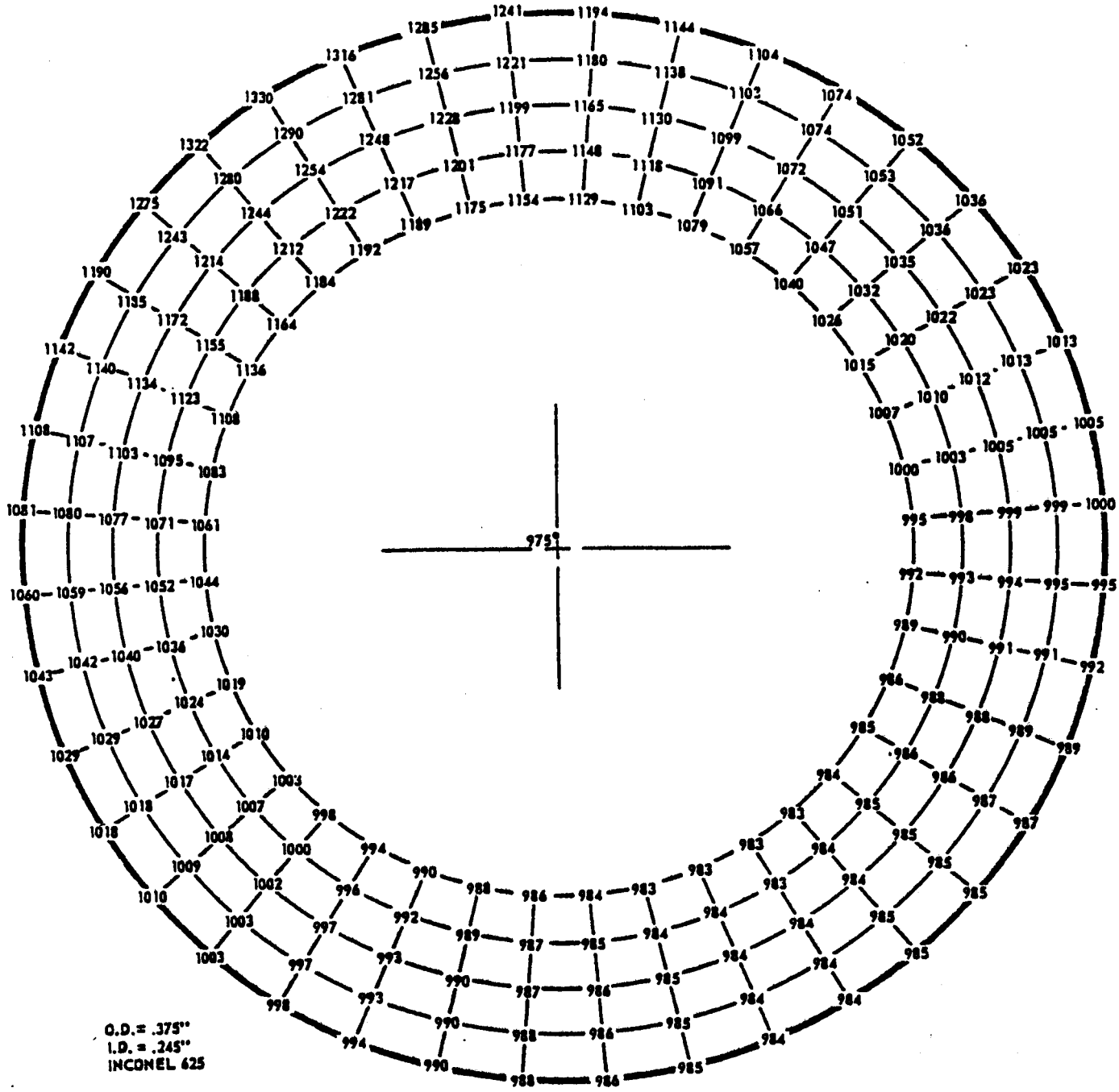

Figure B-4. Typical Node Temperature Distribution on Receiver Tube Cross Section in Worst Case Condition

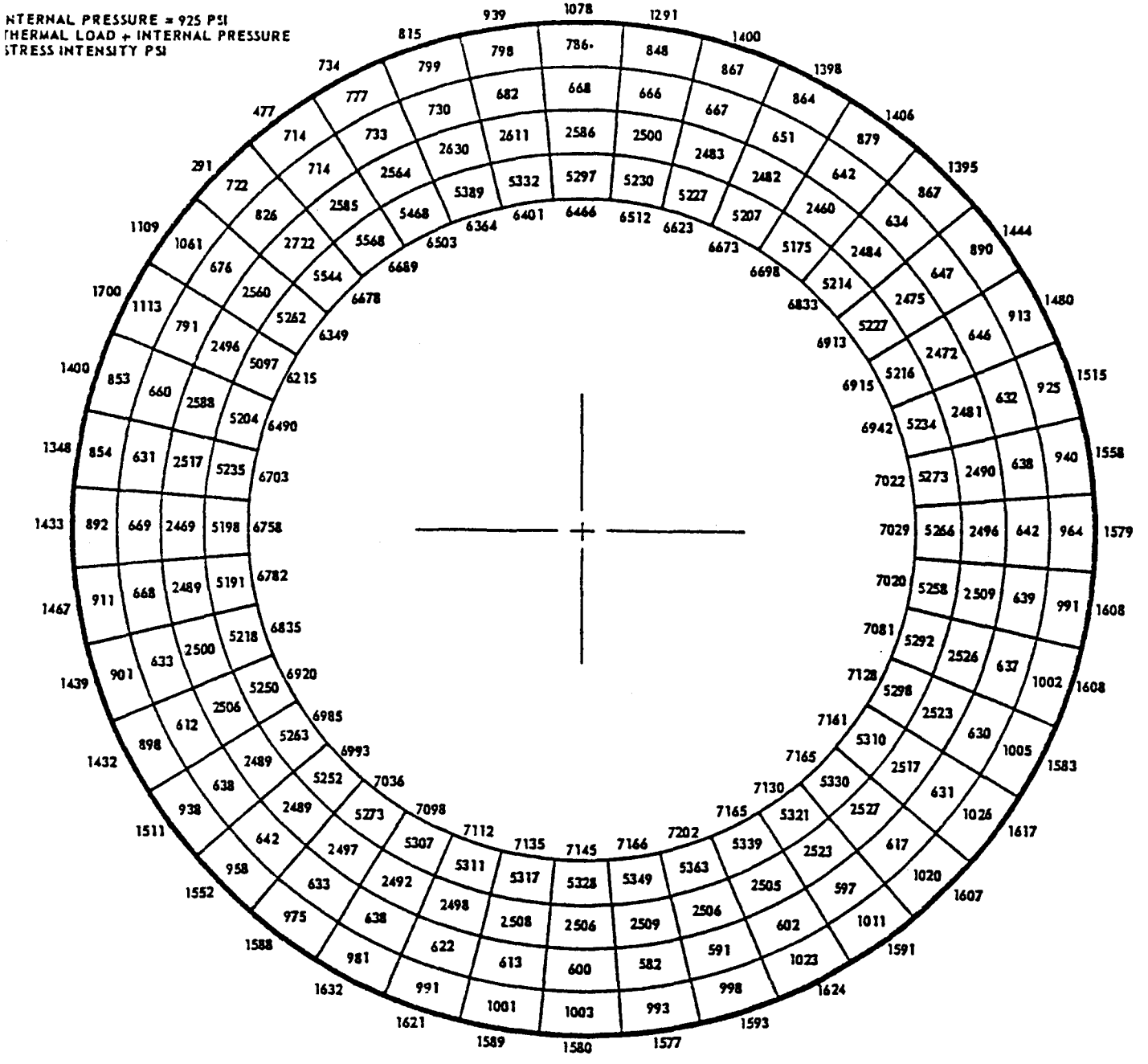

Figure B-5. Stress Intensity Distribution for Receiver Tube at Maximum Operating Internal Temperature and Pressure

for this point is 983°F. The yield strength at this temperature is equal to 48000 psi. The factor of safety based on yield strength is $\frac{48000}{7202}$ = 6.66 (3.89 for Inconel 617).

Looking at the temperature and stresses on the hot side of the tube gives a wall temperature = 1192°F and stress intensity = 6689 psi. At this location the factor of safety is 7.18 (3.73 for Inconel 617).

A conservative estimate of tube creep rupture life would assume a constant stress condition for 9 hours per day for 30 years, or about 98,600 hours. Inconel 625 has a creep rupture strength of 25,000 psi for 100,000 hours at 1300°F. Based on the maximum stress intensity, the factor of safety would be $\frac{25000}{7202}$ = 3.47 (3.19 for Inconel 617).

To estimate the total number of operating cycles that the tube would see over the life of 30 years, it is assumed that there are 10 thermal cycles per day. This would result in approximately 10^6 cycles over the life of the receiver. The fatigue strength of Inconel 625 for 10^6 cycles at 1600°F (which is above the design temperature of this application) is 36000psi. Based on the maximum stress intensity, the factor of safety would be $\frac{36000}{7202}$ = 5.00 (4.30 for Inconel 617).

Based on the above structural data, the Inconel 625 tubing is shown to be satisfactory for the recommended operating conditions and system life. Inconel 617, with somewhat lower factors of safety (more conservatively estimated) is still satisfactory for this application.

B-5 RECEIVER SUPPORT STRUCTURE ANALYSIS

B-5.1 Cantilevered Receiver Support

Description

The cantilevered and polar mounted receiver concept, shown in Fig. B-6, has continued to be considered primarily because of the simplicity of design and a minimum number of moving parts which would reduce installation and operational costs. The cantilevered nomenclature for this concept indicates that the receiver is supported from a central pivot, the center of curvature of the concentrator. The receiver is attached to this pivot point, or load center, by a triangular truss boom structure with counterbalancing. The system shown in more detail in Fig. B-7. The axis of the yoke (shown in more detail in Fig. B-8) which supports this movable boom structure is positioned parallel to the earth's axis of rotation and therefore allows the receiver to be driven at a constant rate about this axis to follow the sun's diurnal motion. Receiver motion about the declination axis, perpendicular to the diurnal or polar axis, is small and requires only slight daily adjustments to compensate for the earth's annual motion about the ecliptic. The annual total angular deviation is $\pm$ 23.5 in declination. The movable structure and drive system are supported on a stationary tripod structure which maintains the intersection of the two axes of rotation at the center of curvature of the concentrator.

The cantilevered receiver support design was examined with regard to the structural integrity required to maintain the alignment of the receiver axis with reference to the sun for various

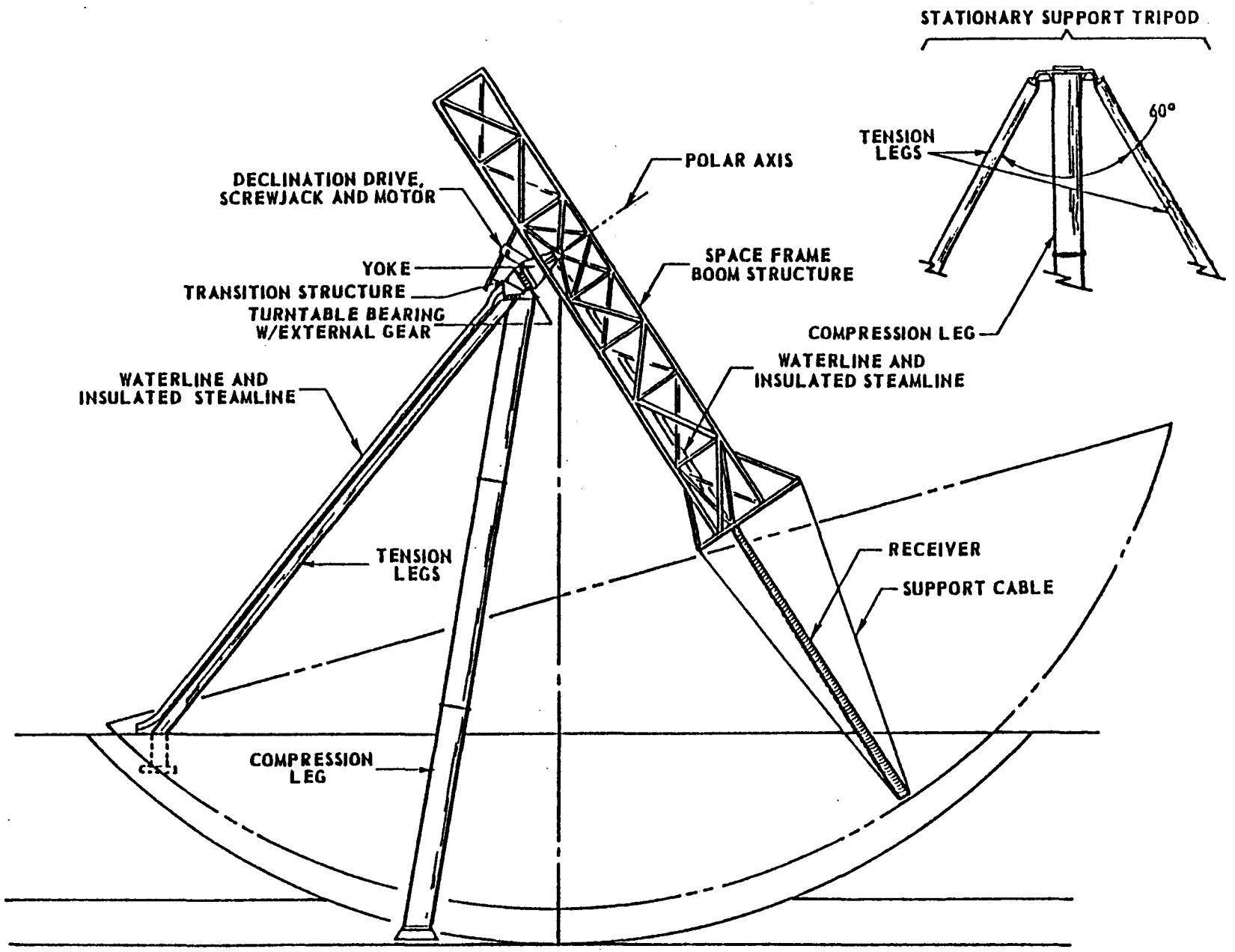

Figure B-6. Cantilevered Receiver Support Structure

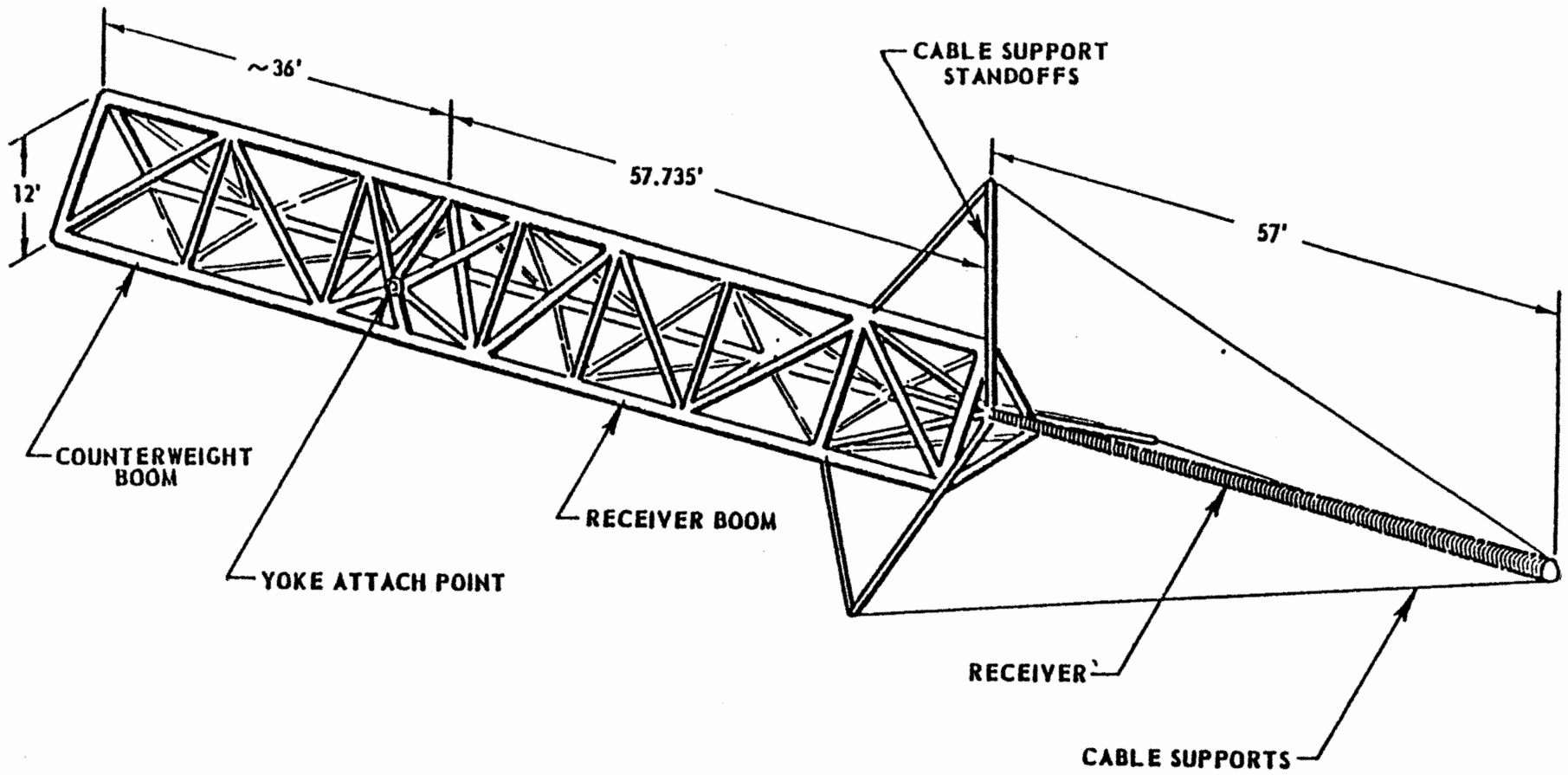

Figure B-7. Cantilevered Triangular Truss Boom and Receiver for 200 ft. Aperture Diameter Collector

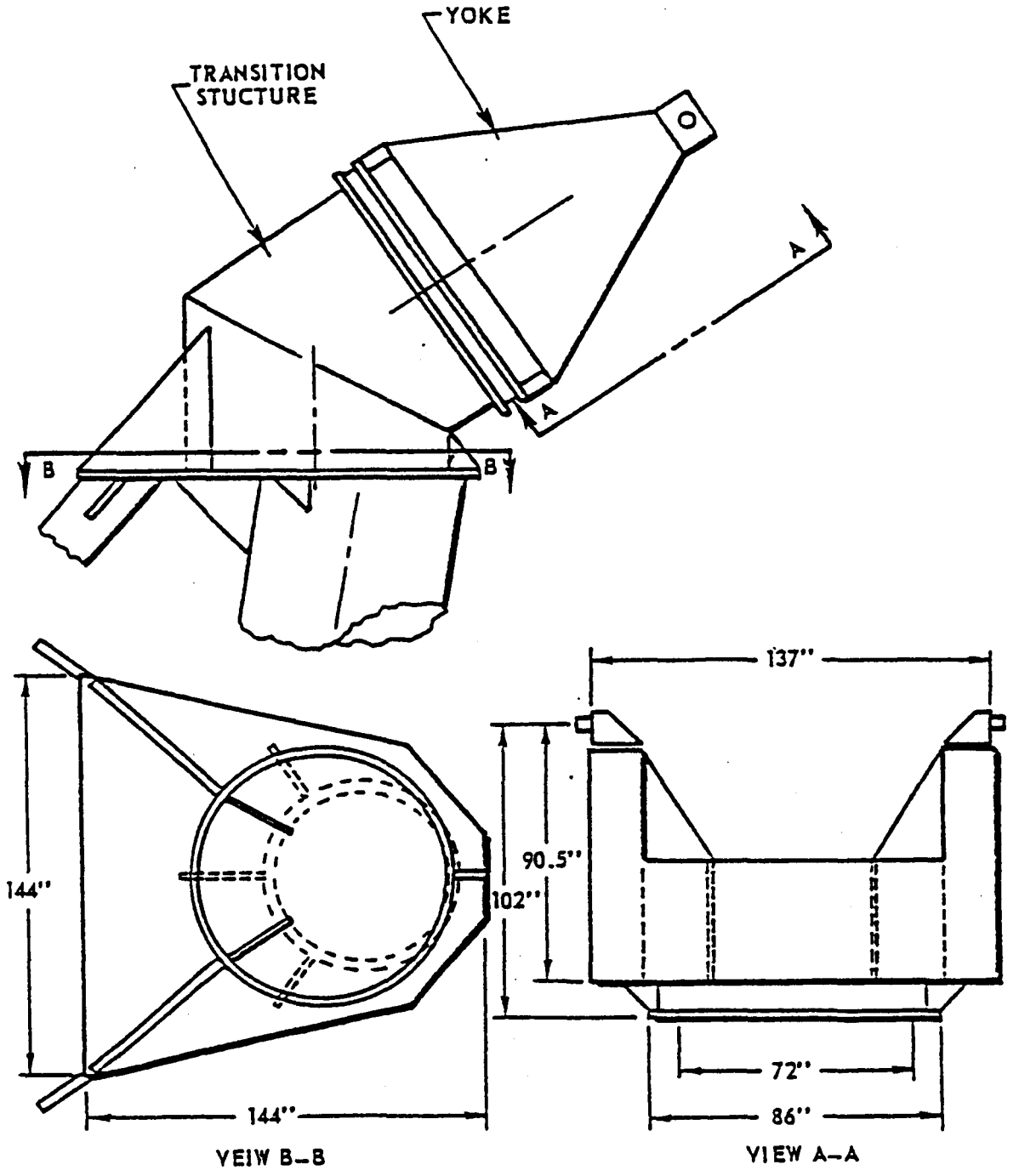

Figure B- 8. Yoke and Transition Structure for 200 ft. Aperture Diameter Collector

loads imposed by the dead weight of the structure, thermal gradient in the structure and winds up to 30 mph during operation. Additional requirement for the receiver support structure is that no permanent structural deformation occurs during a 30 mph survival wind and that the receiver can be driven to a stow position during a 50 mph wind.

Structural Design and Analysis

Previously, initial studies had been carried out to determine nominal dimensions for the cantilevered receiver support based on deflection and survival only. In the current studies the receiver structure also had to conform to dynamic response criteria. The SPACE computer program was used extensively in the structural analysis here to determine loads deflection and stress in constituent members.

The prime load which the cantilevered structure has to support is the weight of a conical receiver tube support cone and the 3/8 in. O.D. receiver tubes helically wound around the support cone. The support cone itself was modeled in detail in the SPACE program and was subdivided axially into 24 members.

The arrangement and size of support members shown in Figs. B-6, B-7, and B-8 were changed a number of times during several design and analysis iterations in order to reduce the structural weight while still meeting the design requirements for stress limits, receiver deflection and dynamic response. The receiver deflection was based on minimizing deflections to the extent that not more than 1% of the energy reflected from the concentrator would miss the receiver due to receiver structure movement.

With a load applied due to dead weight and a 30 mph operational wind deflection of the receiver was determined at dif-

ferent elevation angles. It was found that the fraction of light missing the receiver was a maximum at $\theta = 75^0$ from the vertical. The variation is shown in Fig. B-9.

The member dimensions that resulted from the current analysis are shown in Table B-4 for a 200 ft. aperture diameter collector system. The discussion that follows provides backup information for selection of each of these members.

Five different pipe sizes were used to make up the triangle truss boom as listed in Table B-5 along with the minimum factor of safety over the AISC design allowables. The maximum load on the members occurs either with a wind of 30 mph and the dead weight of the receiver at $\theta = 75^0$ or the receiver dead weight at the vertical stow position $\theta = 0^0$, and a 90 mph wind.

The maximum tension in the receiver support cables was calculated at 11,269 lbs. per cable. The breaking strength for the extra high strength 7-wire galvanized strand is 42,400 lbs. The yield strength is approximately 50% of the breaking strength. The cable factor of safety is $\frac{21200}{11269} = 1.88$.

The buckling criterion for the receiver support cone due to the axial load imposed by the support cables was checked using formulas from "Formulas for Stress and Strain" by R. J. Roark, 3d Ed., page 248. For the cone the allowable buckling load was calculated to be 140,700 lbs. The maximum axial load obtained in the SPACE computer runs was 50,965 lbs. which results in a buckling factor of safety equal to 2.76. Analyzing the receiver cone as a beam column to AISC allowables gives the minimum buckling factor of safety of 1.87.

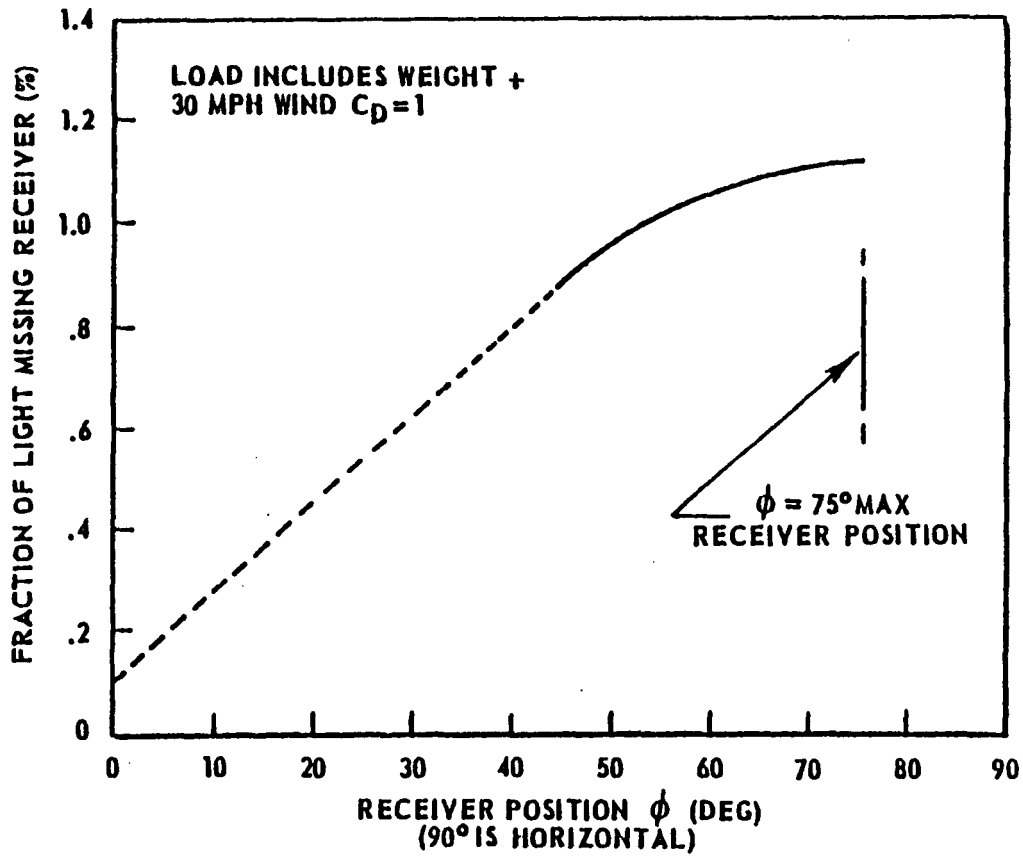

Figure B-9. Change in Optical Loss Due to Receiver Position

TABLE B-4

COMPONENTS OF CANTILEVERED RECEIVER SUPPORT
SYSTEM FOR 200 FT. APERTURE DIAMETER COLLECTOR

DESCRIPTION	MATERIAL	DIMENSIONS	WEIGHT LBS.	FACTOR OF SAFETY	DESIGN CODE	MAINTENANCE REQUIRED
Compression Leg	A36	68" O.D. t = ½"	38,390	4.75	AISC	Paint
Tension Legs (2)	A36	26" O.D. t = ¼"	7,372/ea.	7.41	AISC	Paint
Counterweight Boom	A36	8 3/8", 6 5/8" 4 1/2", 3 1/2"		1.13	AISC	Paint
Receiver Boom	A36	O.D. Pipe Truss Boom		1.08	AISC	Paint
Cable Support Standoffs	A36	6 5/8" O.D. Pipe		1.25	AISC	Paint
Triangular Truss Boom	A36	12' tall Equilateral Triangle	10,768	-	AISC	Paint
Receiver Tubes	Inconel 625	1/4" I.D. 3/8" O.D.		5.10	-	Paint
Support Cone	Inconel 800	1° Cone Length = 684"		1.87	AISC	None
Receiver	-	-	4,653	-	-	-
Support Cables	Galvanized 7-Wire Strand	Two 5/8" O.D. per attachment	307	1.88	-	None
Yoke	A36	-	9,227.6	1.79	AISC	Paint
Transition Structure	A36	-	11,840	-	AISC	Paint
Compression Leg Foundation	Reinforced Concrete	6½' x 6½' x 7'	44,363	1.10	ASCE	None
Tension Legs Foundation (2)	Reinforced Concrete	4½' x 4½' x 6' 7' x 7' x 1'	23,606/ea.	1.15	ASCE	None

TABLE B-5

CONSTITUENT PIPE SIZES FOR TRIANGULAR TRUSS BOOM FOR 200 FT. COLLECTOR

Outside Diameter (in.)	Wall Thickness (in.)	Factor of Safety Over AISC Allowables
8 5/8	.141	1.79
6 5/8	.125	1.25
4 1/2	.125	1.10
4 1/2	.156	1.08
3 1/2	.156	1.43

The yoke (see Figure B-8) supporting the triangular truss boom, counterweight and receiver was analyzed for the most severe loading condition. This will occur when the total load is taken by one arm of the yoke only. The stress was calculated for three different sections down from the center of the attachment shaft. The minimum factor of safety based on AISC allowables was found to occur 48 1/2 in. below the center of the shaft and was calculated to be equal to 1.79.

Figure B-8 also shows the transition structure that was analyzed. The conservative assumption was made that the pipe alone takes the bending and axial load. The section checked was next to the platform. The minimum factor of safety for this system more than exceeded any requirements based on AISC allowables.

The SPACE program was used to determine the loads in the tripod. In the design of the tripod the controling criteria was the spring rate level required for proper system dynamics response. This necessitated a larger compression leg than would be needed just to meet the requirements of buckling. In order to maintain a high spring rate, the included angle between the tension legs was reduced to 60°. The tension legs were sized to be 26 in. outside diameter pipe with a wall thickness of .25 inch. The compression leg was a 68 in. outside diameter pipe with a wall thickness of 0.5 inches. All factor of safeties were based on AISC allowables. The tension

legs' factor of safety for buckling was 7.41, and for tension was 9.3. The compression leg factor of safety for buckling was 4.75.

The tripod foundation support reactions were obtained from the SPACE computer run. The foundation was sized for a survival wind speed of 90 mph. The allowable soil bearing pressure versus depth was taken from the TTU soils report and is shown in Figure B-10. The maximum load on the compression leg foundation occurs with a south wind. The maximum lift load on the tension legs foundation occurs with an ease wind, and the maximum down load occurs with a west wind. All these values are listed in Table B-6.

The size of the foundation for the compression leg was calculated to be 6 1/2 ft. square with a depth of 7 feet. This gave a maximum soil bearing pressure of 4,785 psf. The allowable bearing pressure at this depth is 5,300 psf. The maximum soil vearing pressure due to the moment was calculated to be 4,549 psf. The factor of safety for the soil bearing at this location is 1.1.

The tension leg foundation was sized for uplift as well as compression. To help counteract the uplift on the foundation, a slab with a post was used with the weight of the soil on top of the slab adding to the weight of the concrete. The dimension of the slab is 7 ft. square by 1 ft. high. The post is 4 1/2 ft. square by 6 ft. high. The maximum load resisting the uplift was calculated to be 32,995 lbs. This is a factor of safety for uplift of 1.15. The

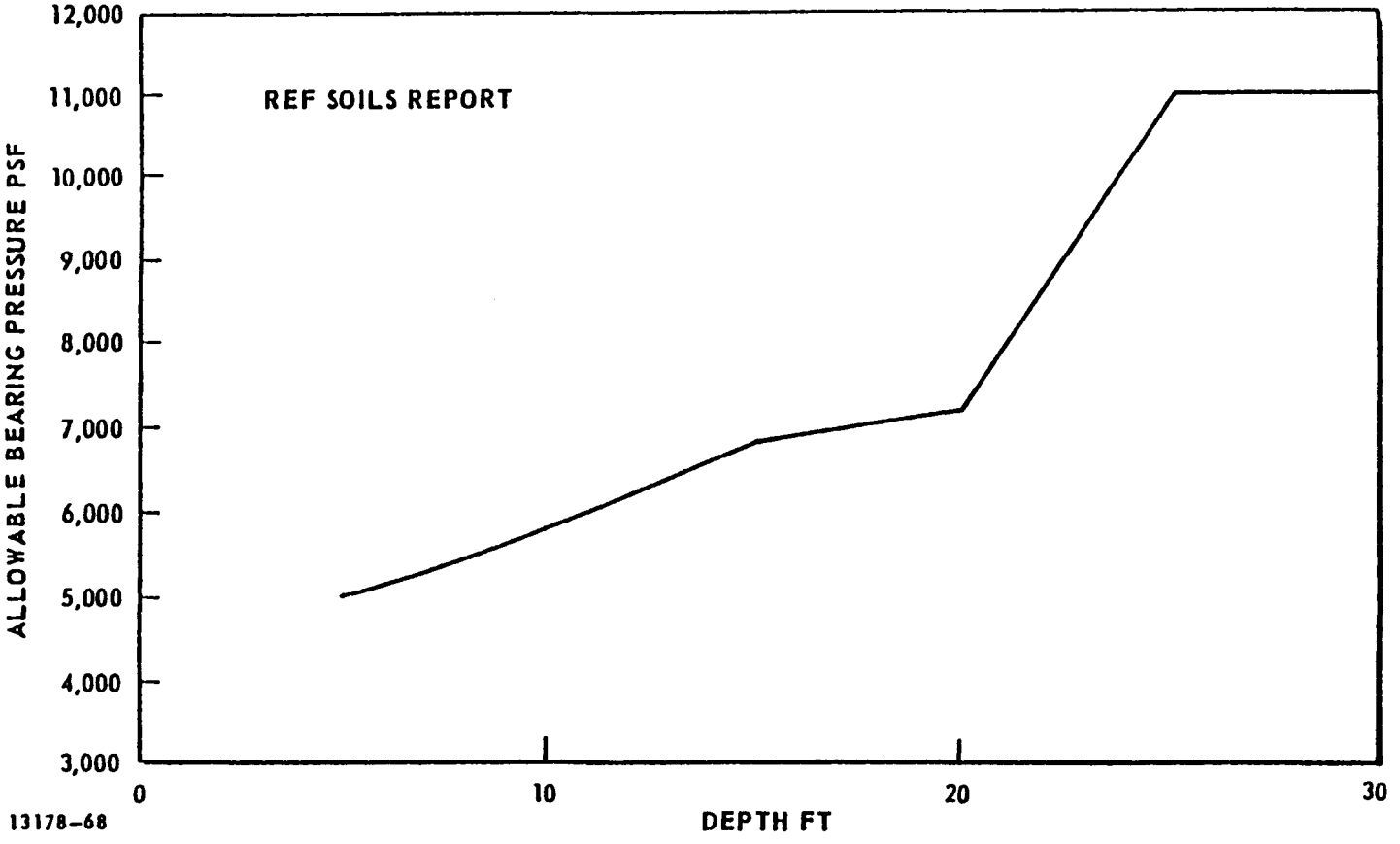

Figure B-10. Soil Bearing at Various Depths at Crosbyton Site

TABLE B-6 TRIPOD FOUNDATION DESIGN LOADS

Member	Cond. Wind (q = 23.9 psf)	Fx lbs.	Fy lbs.	Fz lbs.	Mx 14 lb.	My 14 lb.	Mz 14 lb.
Compression Leg	Weight + wind from south	0	10527.4	157821.5	5795926.7	32.6	44.5
Tension Leg	Weight + wind from east	21610.9	-9759.4	-28667.4	-	-	-
Tension Leg	Weight + wind wind from west	-0505.6	27223.5	15408.95	-	-	-

maximum downward bearing pressure was calculated to be 796 psf, which is a factor of safety of 6.28. The SPACE computer program was run for receivers for three other aperture size collectors. They were 150 ft., 100 ft. and 65 ft. aperture diameter. For each of the sizes the dimensions for the triangular truss boom and the receiver was scaled down from the 200 ft. aperture diameter by the ratio of the diameters. Table B-7 shows the results of the SPACE computer runs on the triangular truss boom and receiver. The resulting values for receiver/boom weight and resonant frequency are plotted in Figure B-11 while the percentage light loss (or receiver structure performance) is plotted in Figure B-12.

Effects of Truncating Receiver Length

A study was made on the effects of truncating the end of the receiver next to the mirror surface. The basis of comparison of course was the receiver length being 100% of R/2, where the maximum energy reception possible from the concentrator could be obtained. The two other lengths checked were 80% of R/2 and 70% of R/2. A brief analysis was also carried out for the receiver length being truncated to 60% of R/2.

The SPACE program analysis included the receiver, support cables, support cable standoffs, receiver boom, counterweight boom, and counterweight. It was assumed the yoke and declination screw jack joint attachments were fixed. The support cable slope to the receiver was maintained at 25°. The factor of safety for each member in the truss was checked for each receiver length and the size was adjusted if required and a final computer run was made for each receiver

TABLE B-7 RESULTS OF SPACE COMPUTER RUNS ON BOOM AND RECEIVER

Receiver Length 100% R/2				
Collector Diameter (ft.)	Resonant Frequency cps	Boom Triangle Height (ft.)	Weight Boom and Receiver (lbs.)	Fraction of Light Missing Receiver %
65	3.60	3.9	998	.37
100	2.41	6.0	3900	.54
150	1.50	9.0	8891	.70
200	1.19	12.0	15728	.94

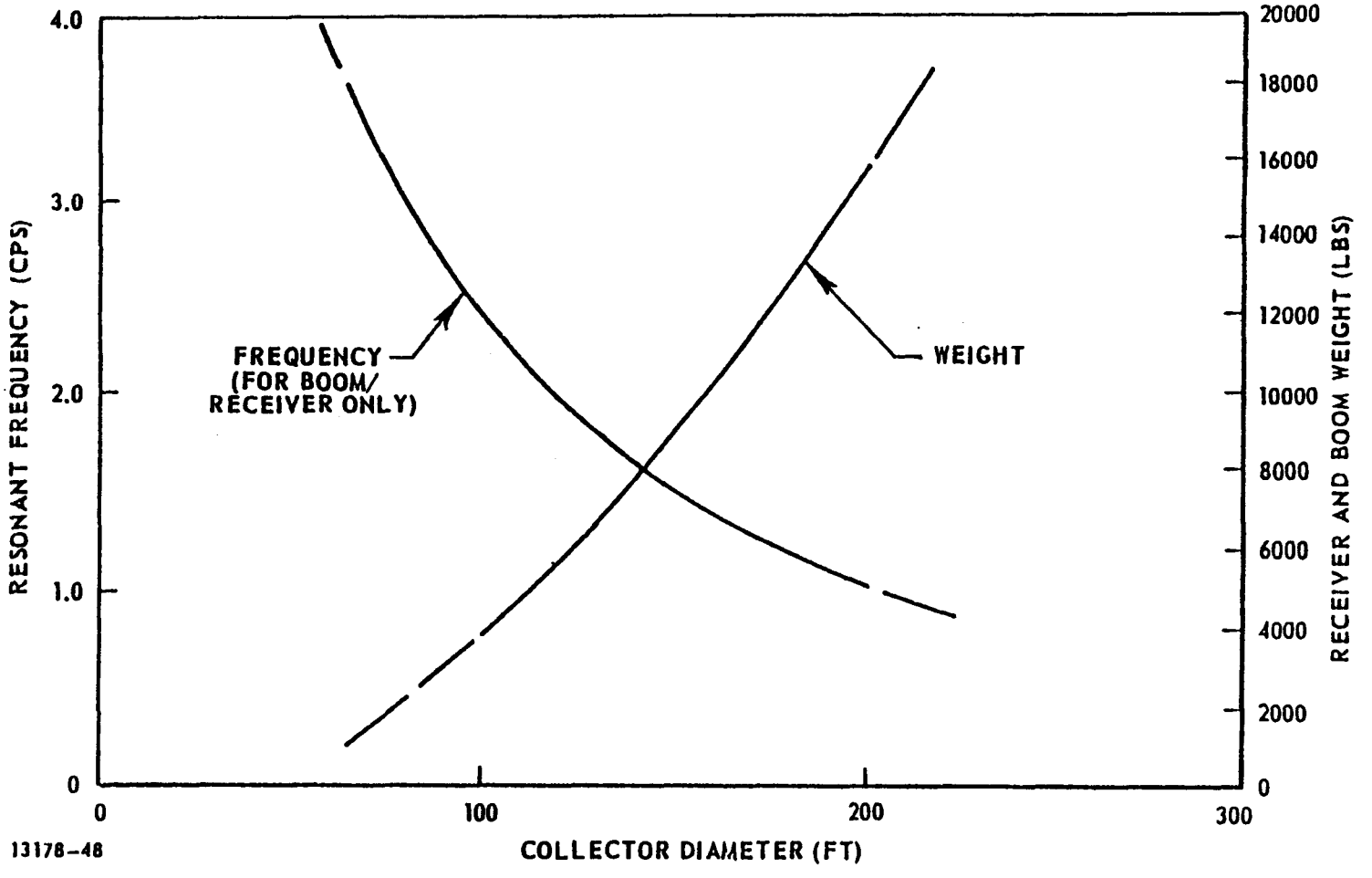

Figure B-11. Cantilevered Receiver Resonant Frequency and Weight for Various Collector Diameters

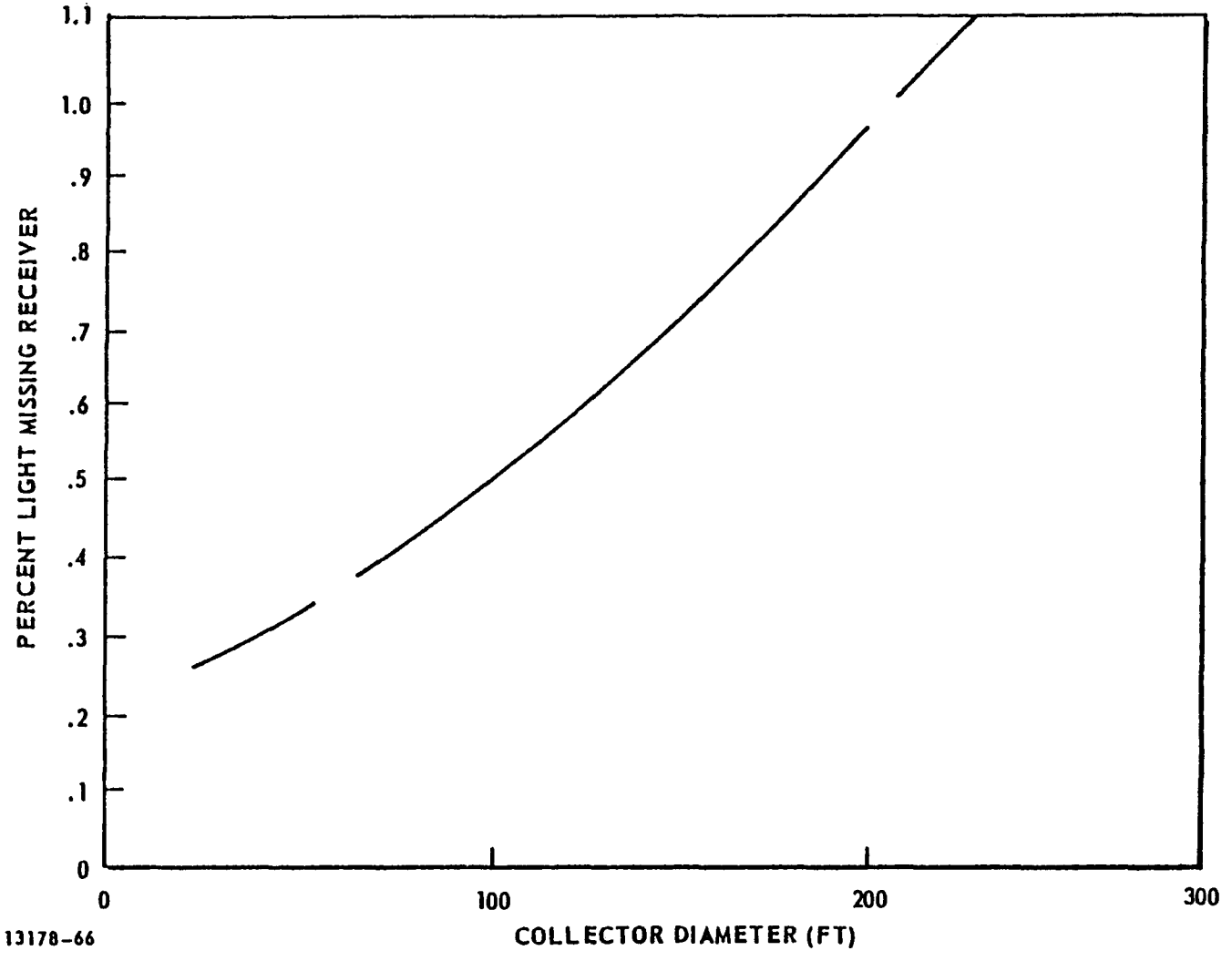

Figure B-12. Light Missing Cantilevered Receiver for Various Collector Diameters

length. With the final configuration for each receiver length, the natural frequency was obtained. It is shown in Figure B-13 that the natural frequency increases readily with a decrease in receiver length while the weight of the receiver/boom decreases appropriately.

For the condition of the receiver being truncated to the length being 70% of R/2, the structural weight decreases by 21%, the natural frequency increases by 29%, and tip deflection of the receiver decreases by 63%, for a loss in annual efficiency of only 2½%.

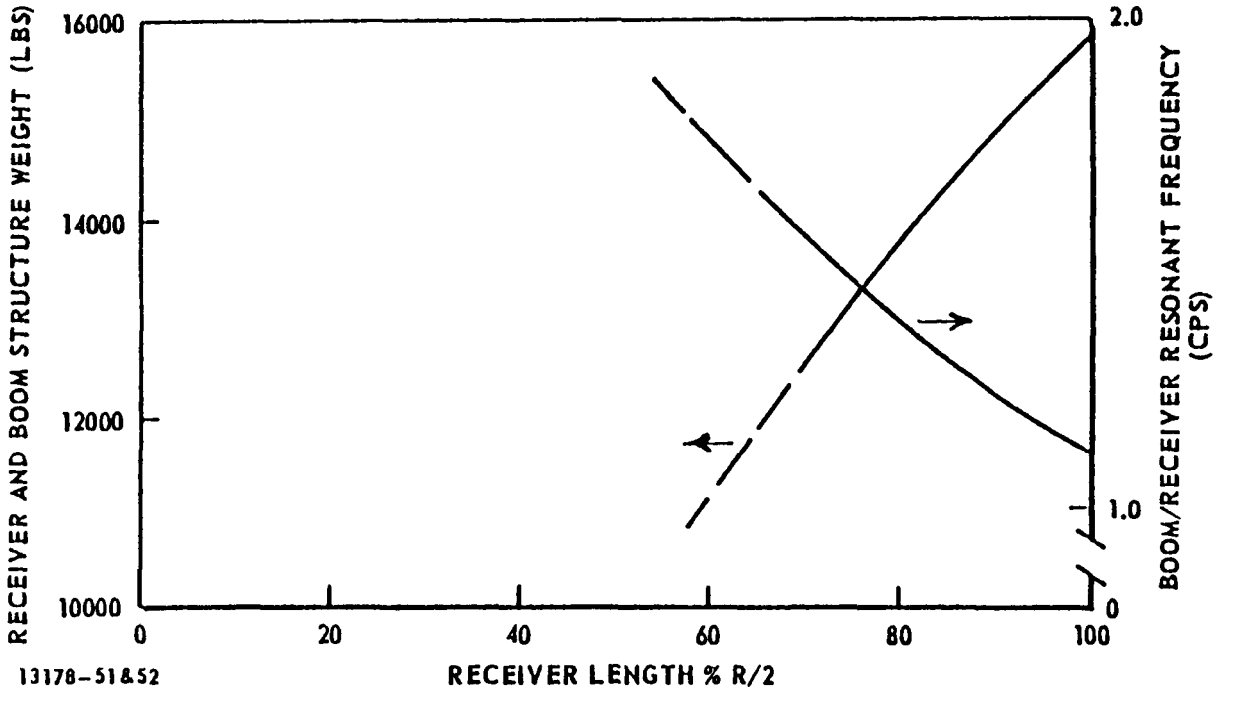

Figure B- 13 Change in Structural Weight and Resonant Frequency Due to Receiver Length

B-5.2 Simply Supported Receiver Structure

Description

The simple support concept (Figure B-14) supports the receiver/boom at the concentrator spherical center and at the receiver/boom end adjacent to the concentrator. The upper end of the receiver/boom is attached to a rotating yoke for two dimensional motion, which, in turn, is mounted to a rigid tripod structure. The lower end of the receiver/boom is attached to a trolly operating within a radial guide track. The radial guide track pivots about a vertical centerline from the spherical radius of the concentrator and sweeps the surface of the concentrator as the receiver/boom travels along the track.

The upper end of the receiver (heat exchanger) is flange mounted to an 18 inch diameter pipe which extends up to the spherical center of the concentrator. At the spherical center, the pipe terminates with two lug ends which attach to the yoke. Four steel, 7-wire galvanized strand wires are circumferentially spaced 90° from each other, and span the length of the receiver/boom to increase the lateral stiffness of the receiver/boom. At the receiver mounting flange is a welded array of four tubular arms perpendicular to the receiver/boom axis which act as stand-offs for the cable assemblies. The cable ends attach to integral fittings at the extremeties of the receiver/boom assembly next to the radial guide track.

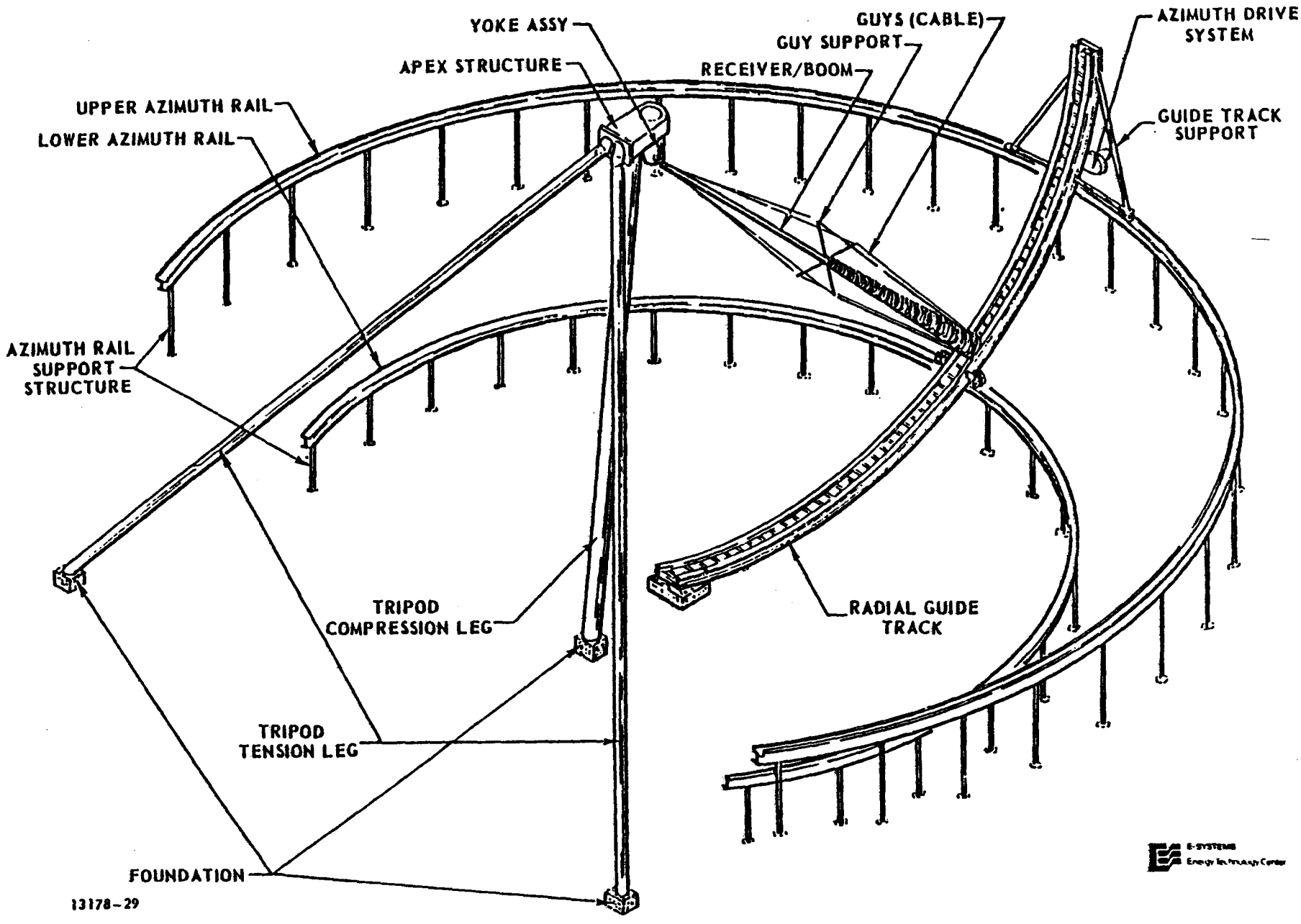

Figure B- 14. Simple Support Concept

The tripod assembly consists of a compression leg and two symmetrical tension legs supporting a yoke cantilevered from the apex. The yoke is at the spherical center of the concentrator and the receiver/boom rotates in elevation inside the yoke. The yoke and receiver/boom rotate in azimuth with respect to the tripod through a bearing in the apex structure. The tripod is arranged to clear the sweep of the radial guide track over the concentrator surface, and the compression leg is also tilted 5° north to assure tension loading of the other two legs. Each tripod leg is fabricated from standard size steel pipe. The intersection-connecting point of the tripod legs to the welded apex structure is offset from the yoke to allow for clearance with the moving receiver/boom structure.

The lower end of the receiver rests on a mobile platform that is guided within the radial guide track. The connection between the platform and the receiver is a "slip-joint" which allows for thermal expansion and contraction of the receiver while transmitting lateral loads. Pins are located between the platform and receiver to transmit torque through the joint to turn the yoke while the radial guide track is rotating across the concentrator.

The radial guide track is a weldment of channels and flat plates extending from a center pivot outwards past the outer rim of the concentrator. A vertical line from the center of the yoke bearing at the tripod apex establishes the pivot axis for the

radial guide track. The radial guide track is further supported by two azimuth rails which also provide the running surface for the azimuth drive system.

The azimuth rails are basically 'I' beam sections curved to the radius desired and are supported by structure grounded to the existing back-up structure of the concentrator. Table B-8 describes the structural elements and physical properties, and factors of safety.

Structural Performance of Receiver Support

The performance of the FMDF receiver is directly affected by deflection of the receiver/boom structure during operation. Maximum deflection was found to occur when the receiver/boom was in a position that is 75° from the vertical, however the computer evaluation was run at 90° from the vertical to simplify the computer modeling.

The first evaluation was for the receiver support cone by itself which was structurally analyzed to determine its required minimum wall thickness. Computer runs of the receiver/boom were made using 0.1875, 0.250 and 0.3125 inch wall thicknesses for the support cone and the deflected shape of each receiver was determined. Based on this data, a thickness of 0.25 (1/4 in.) was selected for the receiver support cone.

The second evaluation was for the boom attached to the receiver. Four different boom designs were modeled and

TABLE B-8 TABULATION OF SPECIFICATIONS FOR SIMPLE SUPPORT RECEIVER FOR 200 FT APERTURE DIP. COLLECTOR

ITEM & DESCRIPTION	MATERIAL	DIMENSIONS	WEIGHT	SAFETY FACTOR	DESIGN CODE	MAINTENANCE REQD.
1 Compression Leg (2)	A-36 STL	42" O.D. x .25 Wall	14,306#	2.61 (Comp) (Bend)	A.I.S.C.	Paint
2 Tension Leg (2)	A-36 STL	42" O.D. x .25 Wall	14,497#	2.29 (Ten) (Bend)	A.I.S.C.	Paint
3 Tension Leg (2)	A-36 STL	42" O.D. x .25 Wall	14,497#	6.79 (Ten) (Bend)	A.I.S.C.	Paint
4 Receiver/Boom	A-36 STL Inconel 800	18" O.D. x .25 Wall (1)	7,374#	1.74 (Comp) (Bend)	A.I.S.C.	Paint
5 Guy Supports	A-36 STL	5.56" O.D. x .38 Wall	1,660#	1.36 (Comp) (Bend)	A.I.S.C.	Paint
6 Guys (Cable	Galvanized Wire	7 Strand	245#	1.28 (Ten)	—	None
7 Radial Guide Track	A-36 STL	Welded Box Section 10" x 18"	12,270#	1.96 (Comp) (Bend)	A.I.S.C.	Paint & Grease
8 Guide Track Support	A-36 STL	3.50" O.D. x .22 Wall	470#	2.73 (Comp)	A.I.S.C.	Paint
9 Upper Azimuth Rail	A-36 STL	W10 x 21 'I' Beam	8,246#	1.11 (Bend)	A.I.S.C.	Paint
10 Lower Azimuth Rail	A-36 STL	W10 x 17 'I' Beam	3,838#	1.16 (Bend)	A.I.S.C.	Paint

(1) Boom Only

(2) Apex Weight Included in Tripod Weight

evaluated by computer analysis; 12, 18, and 24 in. O.D. pipes with 0.25 in. wall and a triangular shaped space frame 8 feet on a side. The deflected shape of each design was determined. The 18 in. diameter boom appeared to be the best choice at this time.

The third evaluation was of the effects of temperature and pretensioning on the four cable guys. At high elevation angles, the lower guys will be at a higher temperature than the upper guys due to the asymmetric flux input from the concentrator. The boom/receiver was analyzed with a temperature difference of 100^0 F between the upper and lower guys. To compensate for this temperature difference the lower guys can be pretensioned at a higher load level than the upper guys, effectively pre-curving the receiver/boom. This procedure is recommended.

A finite element model of the receiver/boom assembly was made, incorporating those features which were previously evaluated as producing the least amount of deflection, and run under the worst case condition of: 30 mph wind and 75^0 to the vertical. Under these conditions, the fraction of light missing the receiver is 1.0%.

Dead weight, operating and survival wind load reactions at the tripod and radial guide track were developed from the receiver/boom design. These loads were then used to design the tripod and the radial guide track.

The tripod assembly was modeled next and the basis for evaluation was a reasonable factor of safety with low weight and deflection. Dead weight and operational and survival wind loads developed from the receiver/boom analysis were used in the tripod design.

The upper and lower stationary azimuth rails were modeled using the dead weight and wind loads developed from the design of the radial guide track. Almost all of the supporting structure for the azimuth tracks can be tied directly to the existing concentrator back-up structure. To allow for flexibility in the ongoing design of the connector support structure, the azimuth rail models were idealized using vertical supports extending to the ground. Thus, the rails themselves could be analyzed and sized. Detailed results of the analyses are summarized in Table B-8.

Resonant Frequency and Dynamic Response

The natural frequency for the simple support concept was analyzed for six different positions of the receiver along the radial guide track in a plane normal to the radial guide track. Two critical positions were found; one at 30^0 to the vertical and another at 75^0 to the vertical. The one at 75^0 to the vertical was more critical with a resonant frequency of less the 0.5 Hertz.

The guide track section was progressively increased in size until the resonant frequency was above 1.0 Hertz. The weight penalty became prohibitive. The radial guide track was then brought back to original size and support members were added which tie the top of the radial guide track indirectly to the azimuth guide track as shown in Fig. B-14. This resulted in a natural frequency slightly below 1.0 Hertz and an insignificant weight penalty. Further increases in natural frequency could be realized by adding a lateral support (in the form of another driving mechanism) between the lower azimuth rail and the radial guide track.

B-5.3 Modeling of Receiver Dynamics

The dynamic analysis of the receiver subsystem was divided into two separate analyses representing the two distinct and separate receiver configurations: the cantilevered support and the simple support concepts. Each of the two was separately evaluated on its own configuration and merit.

Two different approaches, although similar, were utilized to evaluate the dynamic behavior of the two different concepts. The cantilevered system was described as a series of semi-rigid bodies connected by a series of springs. This was a reasonable assumption because of the relatively high stiffnessess of individual components such as tripod, boom, receiver, etc. That is, it was assumed that very little elastic body coupling would be present in the dynamic model of the cantilevered system. This assumption was verified by subsequent analysis of individual components of the model which revealed elastic body resonances well above those of the coupled rigid body mode. Therefore, the assumption that the cantilevered system behaves as a series of coupled rigid bodies was reasonable.

For the two point support system however, this assumption was not a reasonable one. Stiffness requirements on individual components were not as demanding as those for the cantilevered system. This system had pinned joints rather than rigid ones, although its drive system was rigid when compared to the cantilevered system. The flexible body dynamic characteristics of the two point support system were found to be a major contributor to the equations of motion for the coupled system -- in contrast to that found for the

cantilevered system. This factor lead to the use of the finite element program (SPACE 4) in analyzing the two points support system.

The discrete component analysis of the cantilevered system allowed parametric studies to be performed on component parts of the system in order to derive an efficient design.

The cantilevered system was analyzed to determine its fundamental frequency in the declination direction and in the hour angle (diurnal) direction. The declination dynamic model is shown in Fig. B-15 and the corresponding geometric, stiffness and inertia parameters are shown in Table B-9. The fundamental resonant frequency in declination was determined to be 1.20 Hz. The hour angle model is shown in Fig. B-16 and the corresponding geometric, stiffness and inertia parameters are shown in Table B-10. The fundamental resonant frequency in the hour angle direction was determined to be 0.87 Hz.

For the more critical hour angle case the effects of drive stiffness ($K\theta_2$) variation on frequency are shown in Fig. B-17 and the effects of pedestal stiffness on frequency are shown in Fig. B-18.

The two-point (simple) support system was modeled as a series of finite elements. The model included tripod, boom and absorber, and the rail. The rail support was treated as a finite spring and the values were included in the analysis. The model analyzed also includes an added support mechanism used to stabilize the end of the rail. The model was analyzed at various elevation angles and the results are given in Table B-11. The lowest resonance point was further analyzed to give horizontal and vertical resonances of the system at this point which are higher as would be expected.

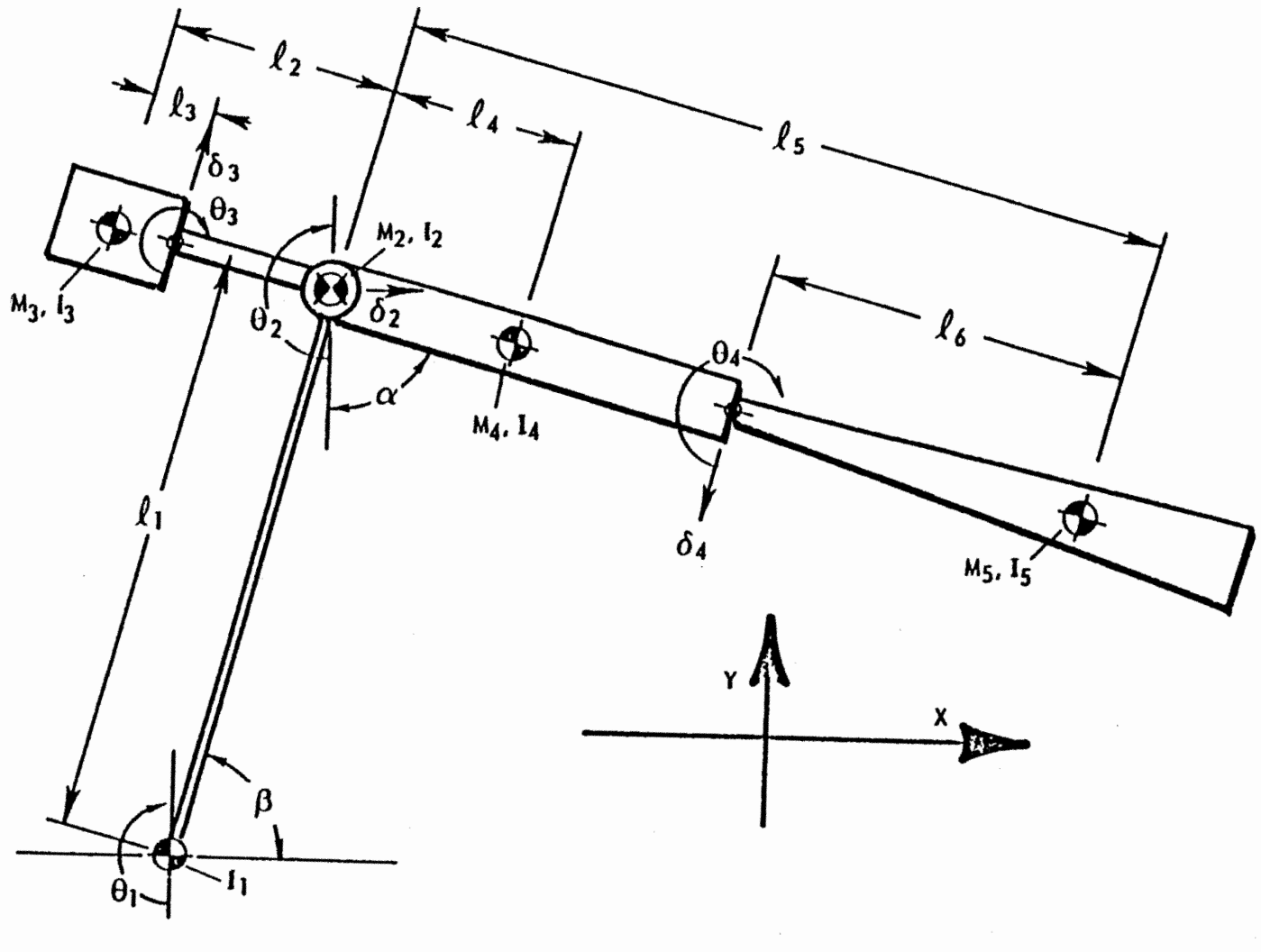

Figure B- 15. Declination Dynamic Model - Cantilevered Support System

TABLE B-9 GEOMETRIC, STIFFNESS AND INERTIA DATA

CANTILEVERED RECEIVER, DECLINATION DIRECTION

Geometry:	Stiffness:		Inertia:	
l_1 = 1386 in.	$K_{\theta_1} = 1.65 \times 10^{10}$	in-lb/rad	$I_1 = 1.13 \times 10^{10}$	lb-in^2
l_2 = 290 in.	$K_{\theta_2} = 4.34 \times 10^{9}$	in-lb/rad	$I_2 = 2.57 \times 10^{9}$	lb-in^2
l_3 = 12 in.	$K_{\theta_2} = 5.74 \times 10^{4}$	lbs/in	$M_2 = 6.30 \times 10^{3}$	lbs
l_4 = 346 in.	$K_{\theta_3} = 1.49 \times 10^{9}$	in-lb/rad	$I_3 = 3.49 \times 10^{7}$	lb-in^2
l_5 = 1072 in.	$K_{\theta_3} = 1.20 \times 10^{4}$	lbs/in	$M_3 = 1.73 \times 10^{4}$	lbs
l_6 = 380 in.	$K_{\theta_4} = 1.17 \times 10^{9}$	in-lb/rad	$I_4 = 4.06 \times 10^{8}$	lb-in^2
	$K_{\theta_4} = 3.12 \times 10^{3}$	lbs/in	$M_4 = 7.00 \times 10^{3}$	lbs
			$I_5 = 2.63 \times 10^{8}$	lb-in^2
			$M_5 = 4.60 \times 10^{3}$	lbs

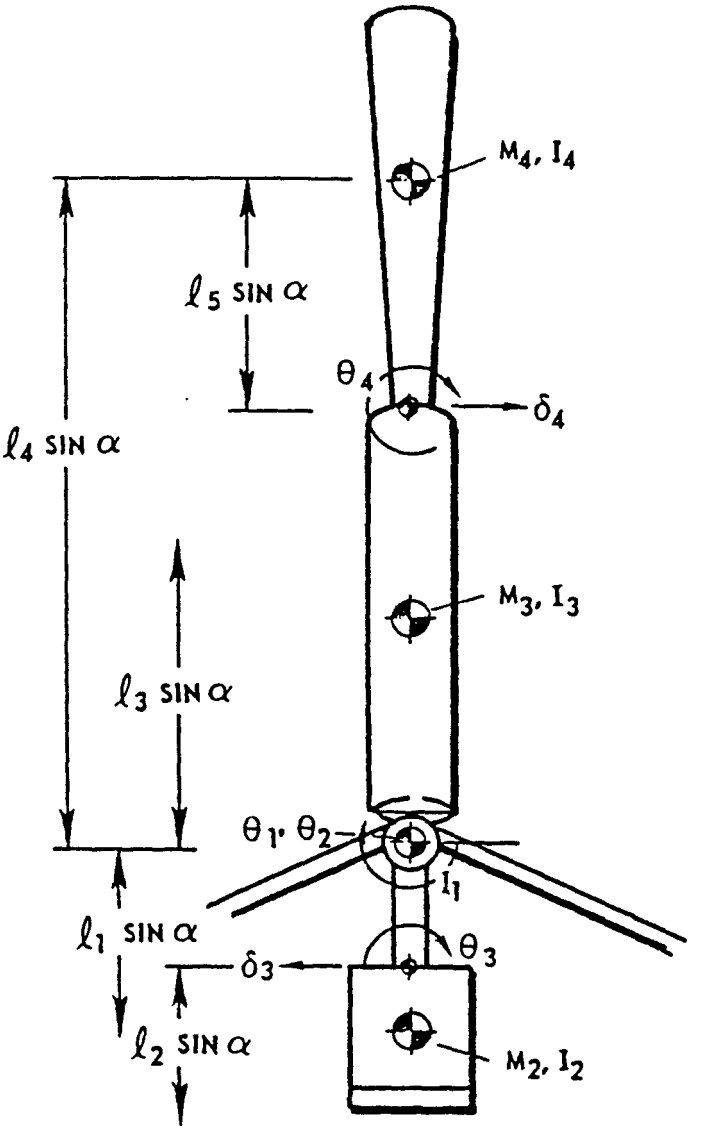

Figure B-16. Hour Angle Dynamic Model - Cantilevered Support System

TABLE B-10 GEOMETRIC STIFFNESS AND INERTIA DATA

CANTILEVERED RECEIVER, HOUR ANGLE DIRECTION

Geometry:	Spring Rate:		Inertia:	
l_1 = 290 in.	$K\theta_1 = 1.05 \times 10^9$	in-lb/rad	$I_1 = 1.41 \times 10^9$	lb-in^2
l_2 = 21 in.	$K\theta_2 = 1.75 \times 10^9$	in-lb/rad	$I_2 = 3.49 \times 10^7$	lb-in^2
l_3 = 346 in.	$K\theta_3 = 6.67 \times 10^8$	in-lb/rad	$M_2 = 1.73 \times 10^4$	lbs
l_4 = 1072 in.	$K\delta_1 = 1.41 \times 10^4$	in-lb	$I_3 = 4.06 \times 10^8$	lb-in^2
I_5 = 380 in.	$K\delta_2 = 6.26 \times 10^8$	in-lb/rad	$M_3 = 7.00 \times 10^3$	lbs
	$K\delta_3 = 3.94 \times 10^3$	in/lb	$I_4 = 2.63 \times 10^8$	lb-in^2
			$M_5 = 4.60 \times 10^3$	lbs

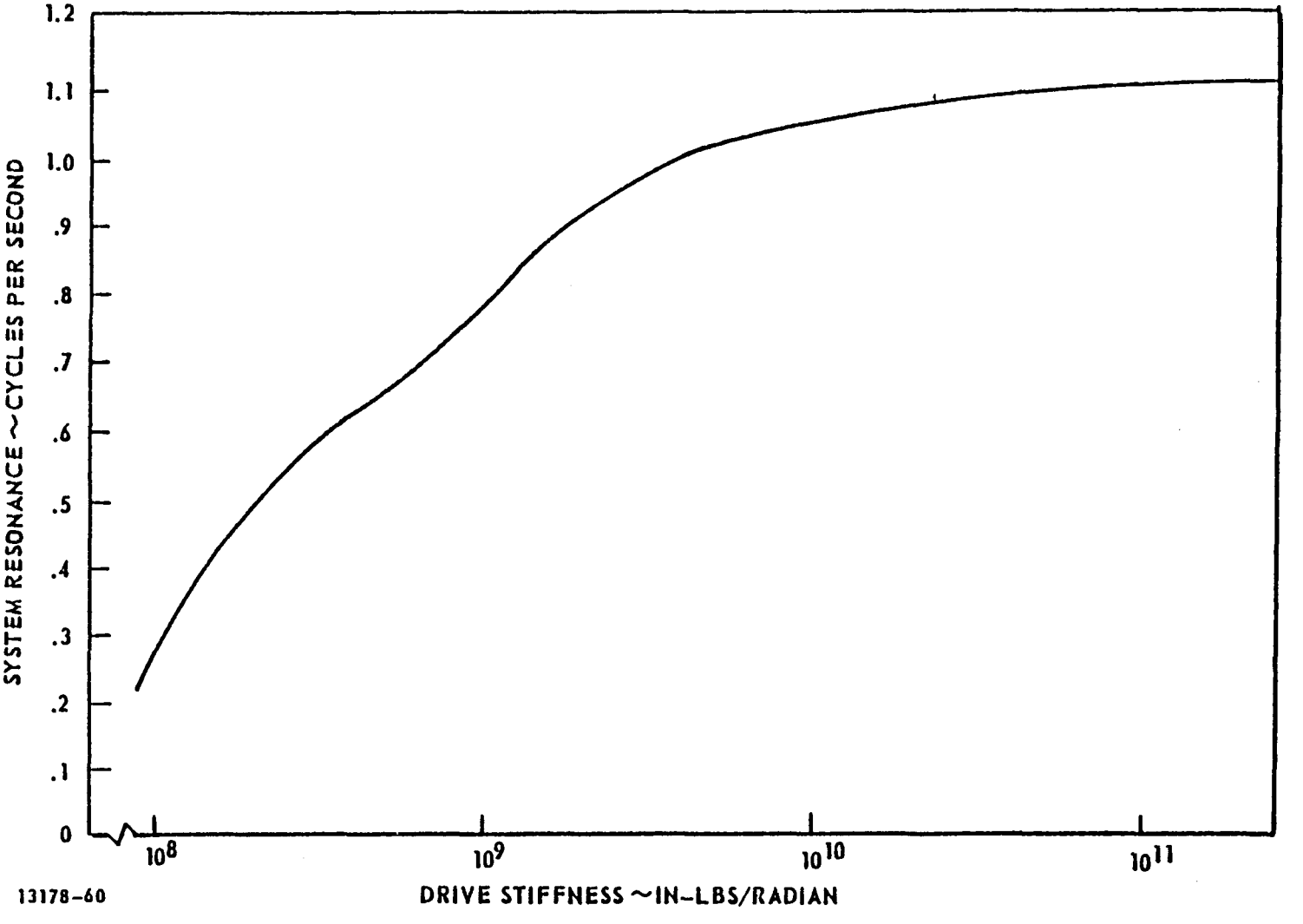

Figure B-17. Cantilevered Support System

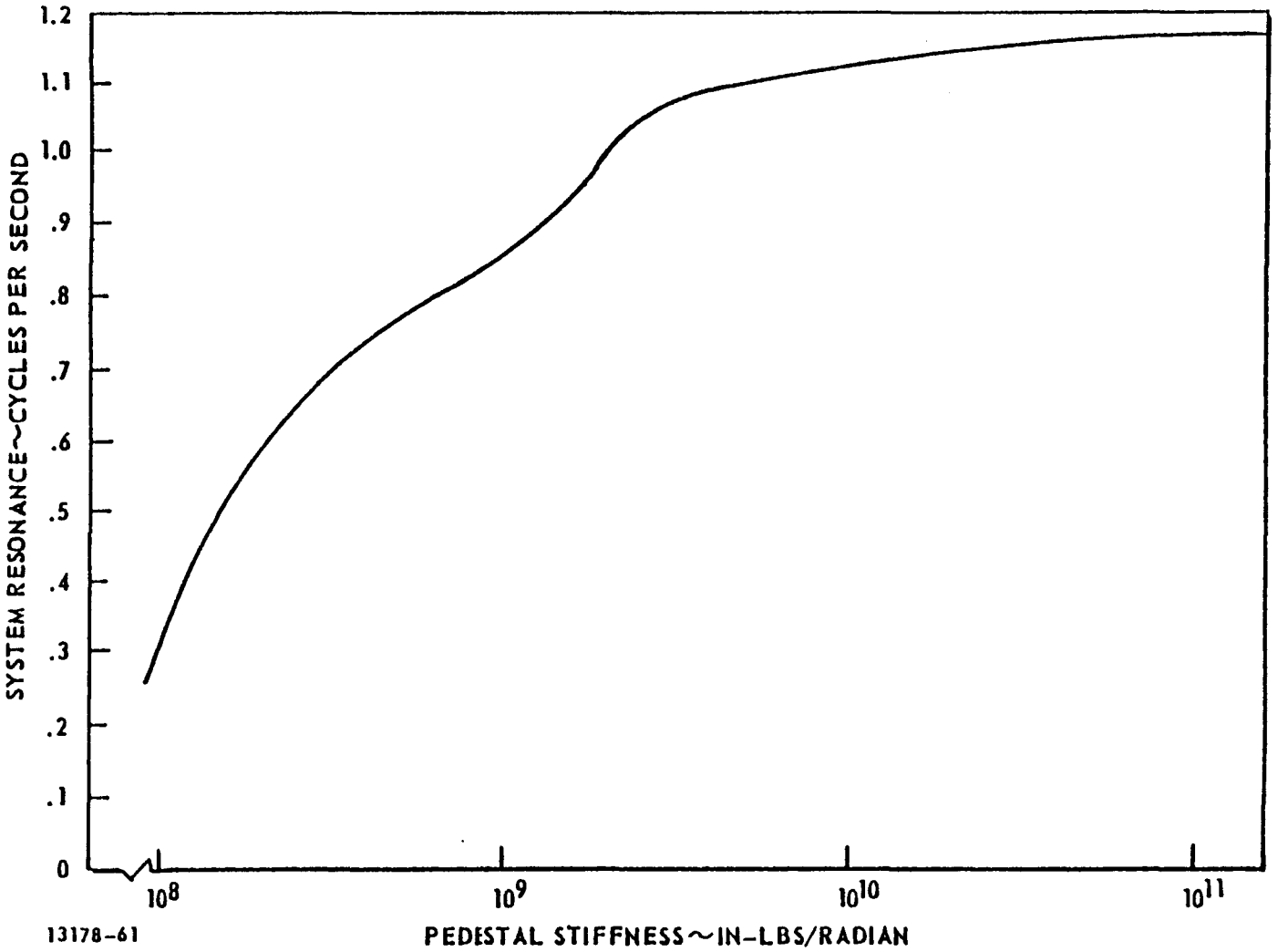

Figure B-18. Resonance vs. Pedestal Stiffness (Cantilevered Support System)

TABLE B-11 RESONANT FREQUENCY VS. ELEVATION ANGLE
TWO SUPPORT SYSTEM

Elevation Angle	Natural Frequency
0^{o}	1.87
15^{o}	1.52
30^{o}	1.87
45^{o}	1.66
60^{o}	1.87
75^{o}	1.65

At Elevation Angle of 15^{o}

f(horizontal) = 1.73 cps

f(vertical) = 1.96 cps

B-6 FLEXIBLE FLUID LOOP CONNECTIONS

The flexible connections provide the components to transport fluid across the rotational interface between the moveable receiver inlet and outlet fluid lines and the stationary lines attached to the tripod support structure. These flexible connections were selected from commercially available components to minimize costs and to provide proven reliability.

Two rotary joints were selected to provide rotation in each axis for the water line connection to the water/steam collector of the RPS, both for the cantilevered support and the simple support receiver. A rotary coupling is provided for each axis of motion (diurnal and declination or azimuth and elevation) as shown in Figures B-19 and B-20. These couplings must be placed in line with the axes of motion to allow non-binding rotation. They are required to withstand only the receiver inlet pressure (not high temperature) so there are many off-the-shelf couplings with commercially proven use and reliability available to meet the pressure requirement.

For the higher temperature application in the steam line and both of the oil lines of the RPS, flexible metal hose was chosen because of its availability and ability to take the higher temperature and pressure simultaneously.

A configuration was developed for the hose flexure to meet the design requirements and vendors specification requirements as shown in Figure B-21 for both axes of the RPS (Figures B-19 and B-20). The hoses are shaped in a loop that lies in a plane perpendicular to the axis of motion so that the hose bend radius changes with the

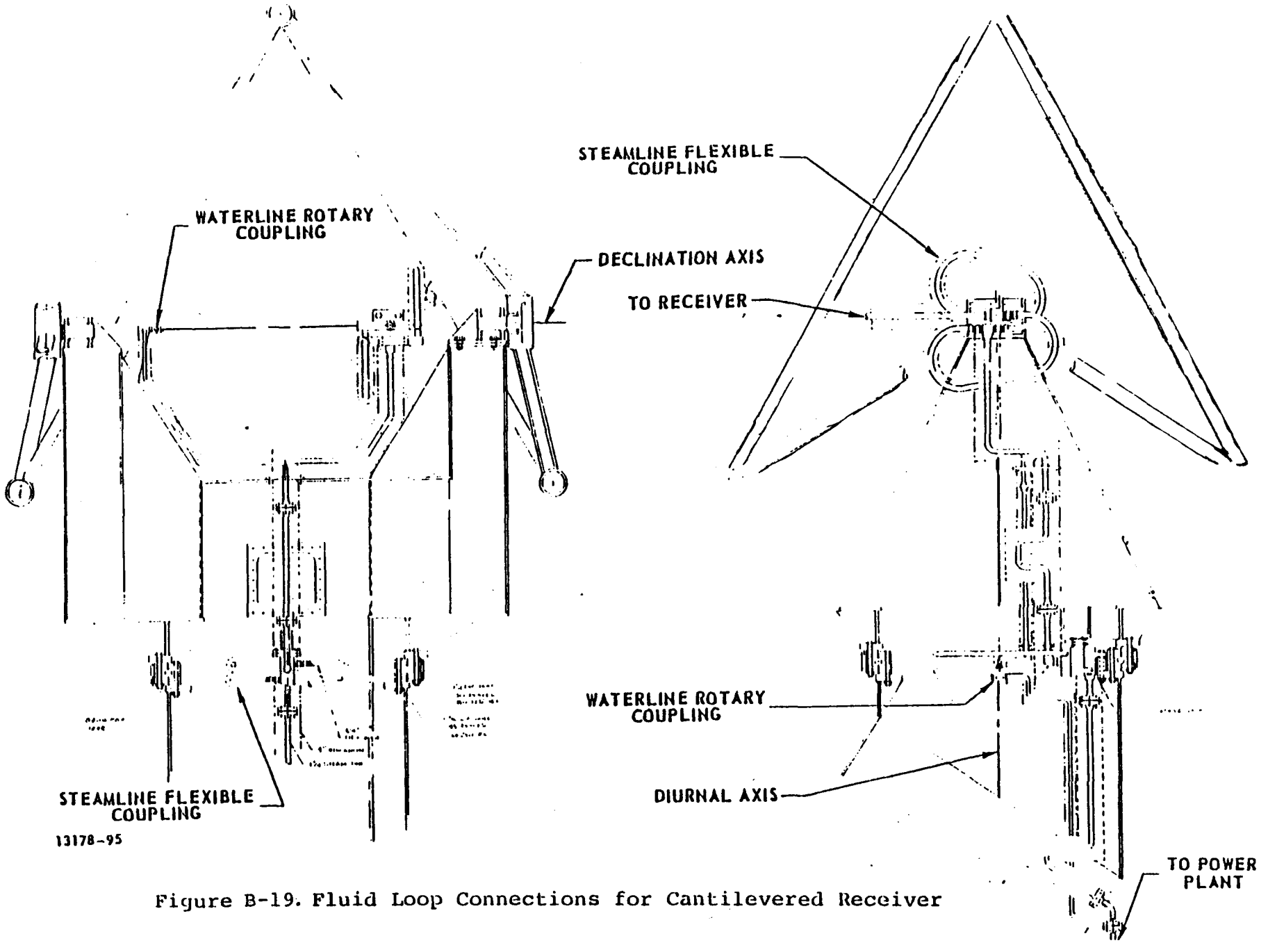

Figure B-19. Fluid Loop Connections for Cantilevered Receiver

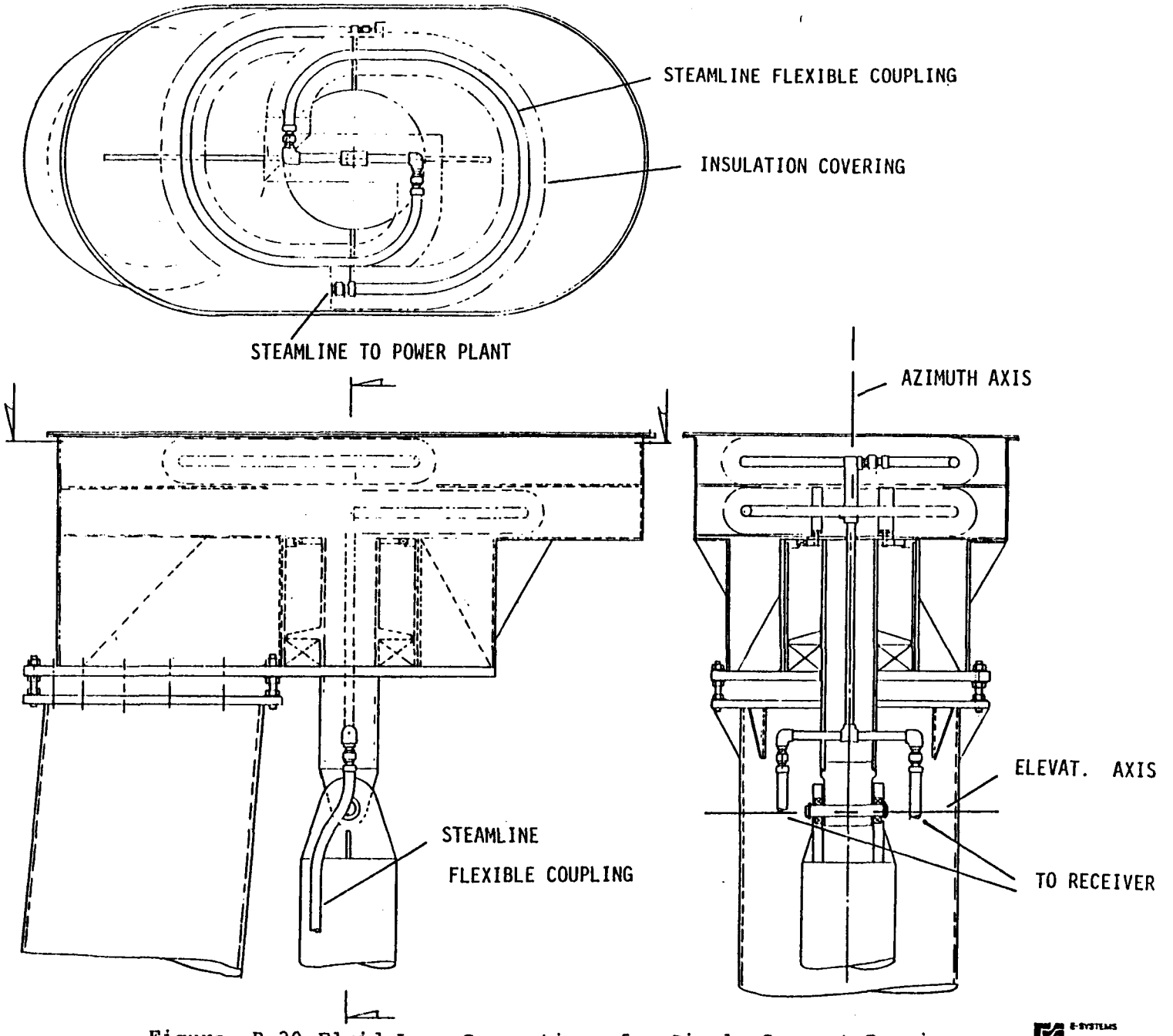

Figure B-20. Fluid Loop Connections for Simple Support Receiver

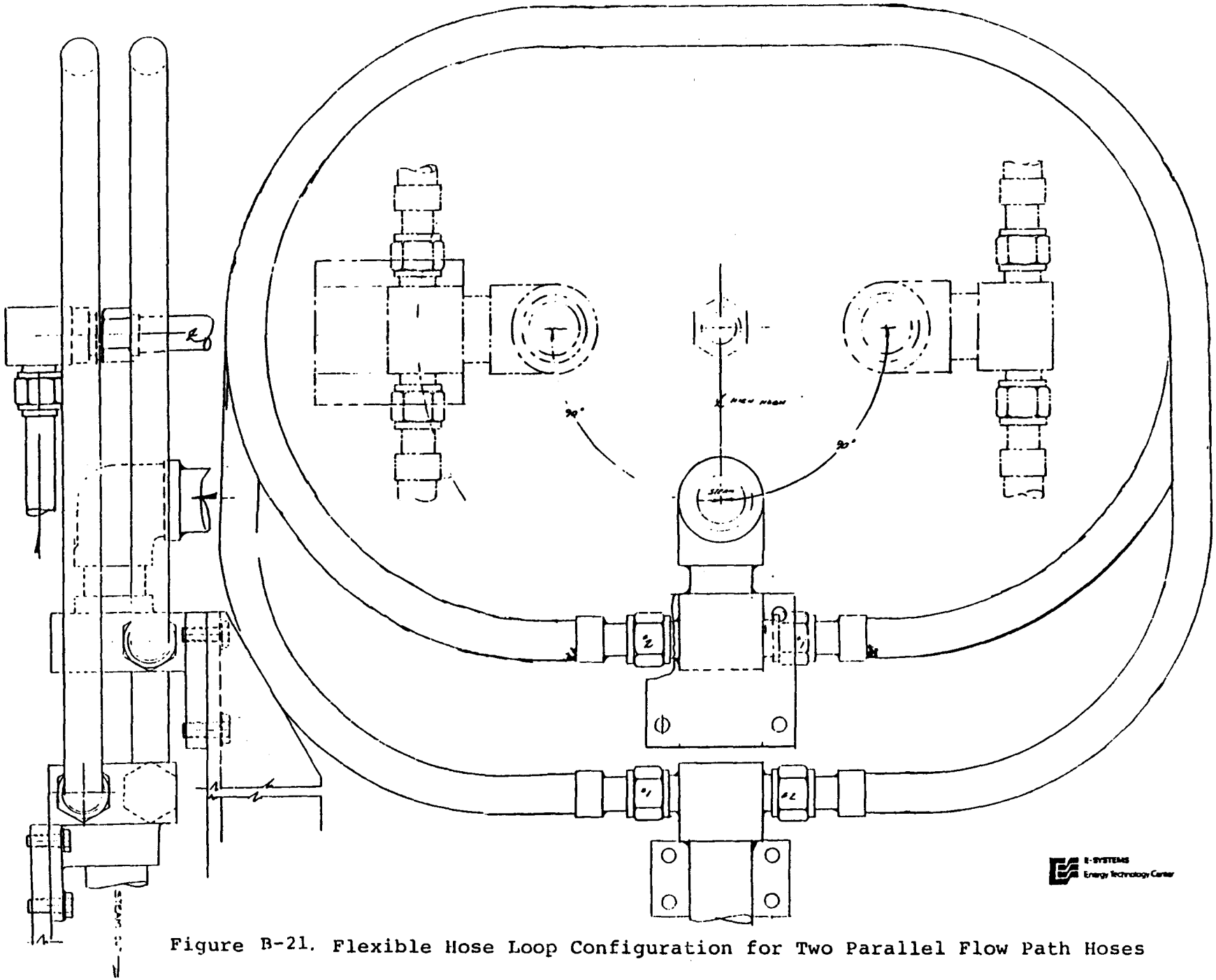

Figure B-21. Flexible Hose Loop Configuration for Two Parallel Flow Path Hoses

angular displacement of the receiver structure about the axis of motion. This provides the necessary flexure under operating conditions while meeting the vendor's requirements described below.

The hose construction is a stainless steel bellows configuration wrapped with a metal braid for added strength. The hose will function properly as long as:

(1) No axial compression or tension is applied externally to the hose. (This can damage or loosen the braid.)

(2) No torsional load is externally applied to the hose during installation or operation. (This can rupture the metal bellows.)

(3) The minimum bend radius is not exceeded during operation.

(4) The catalogue recommended temperature and pressure are not exceeded.

In this application the maximum rotation required is 150^0 in diurnal (hour angle) and 60^0 in declination (or 120^0 in azimuth and 75^0 in elevation). The hose loop is sized so that during operation the tightest loop has a bend radius greater than the minimum bend radius specified. Care must be taken during installation to prevent applying a torsional load to the hose while tightening the fittings and to see that the hose operates smoothly in a single plane of motion. Heat loss from the hose is reduced by a concentric outer flexible metal hose (similar to electrical conduit) packed with glass fiber insulation. Since the metal hose cannot withstand higher pressure and temperatures simultaneously in the larger diameter sizes, it was necessary to parallel smaller diameter sizes for the steam and oil lines in order to meet the operating conditions with an

acceptable pressure drop through the hose. The factor of safety for the steam line (the worst case) is 4.0 at 1,000 F and 990 psi working pressure because the working pressure is specified to be 25% of the nominal design burst pressure.

The flexible hose loop configuration has been installed and is operational on the diurnal and declination axis of the receiver structure for an 11 ft. diameter collector model as shown in Figure B-22. This model has shown the feasibility of this approach with no binding or notable increase in torque required to move the receiver structure with the fluid lines pressurized.

B-7 FABRICATION AND TEST OF A SINGLE-COIL SYSTEM

A single-wrap conical receiver tubing assembly 13.4 ft. in length was constructed and is illustrated in Figure B-23. The receiver is of reduced size and was constructed, among other reasons, to test fabrication and welding techniques. It was constructed of Inconel 600 tubing of 3/8 in. outer diameter and 0.055 in. wall thickness. No serious problems were experienced in wrapping the tubing around a mandrel. Several interesting fabrication experiences were noted and will be incorporated in future fabrication. The tubes were obtained in straight pieces and the pieces were square butt welded together just prior to the wrapping process. After wrapping, the welds were visually inspected and hydrotested at a pressure of 20,000 pounds per square in. with penetrant dye. In addition, other tube samples were welded by the same procedure and sectioned to examine weld penetration and quality. No problems were experienced with the welding and all welds examined were satisfactory.

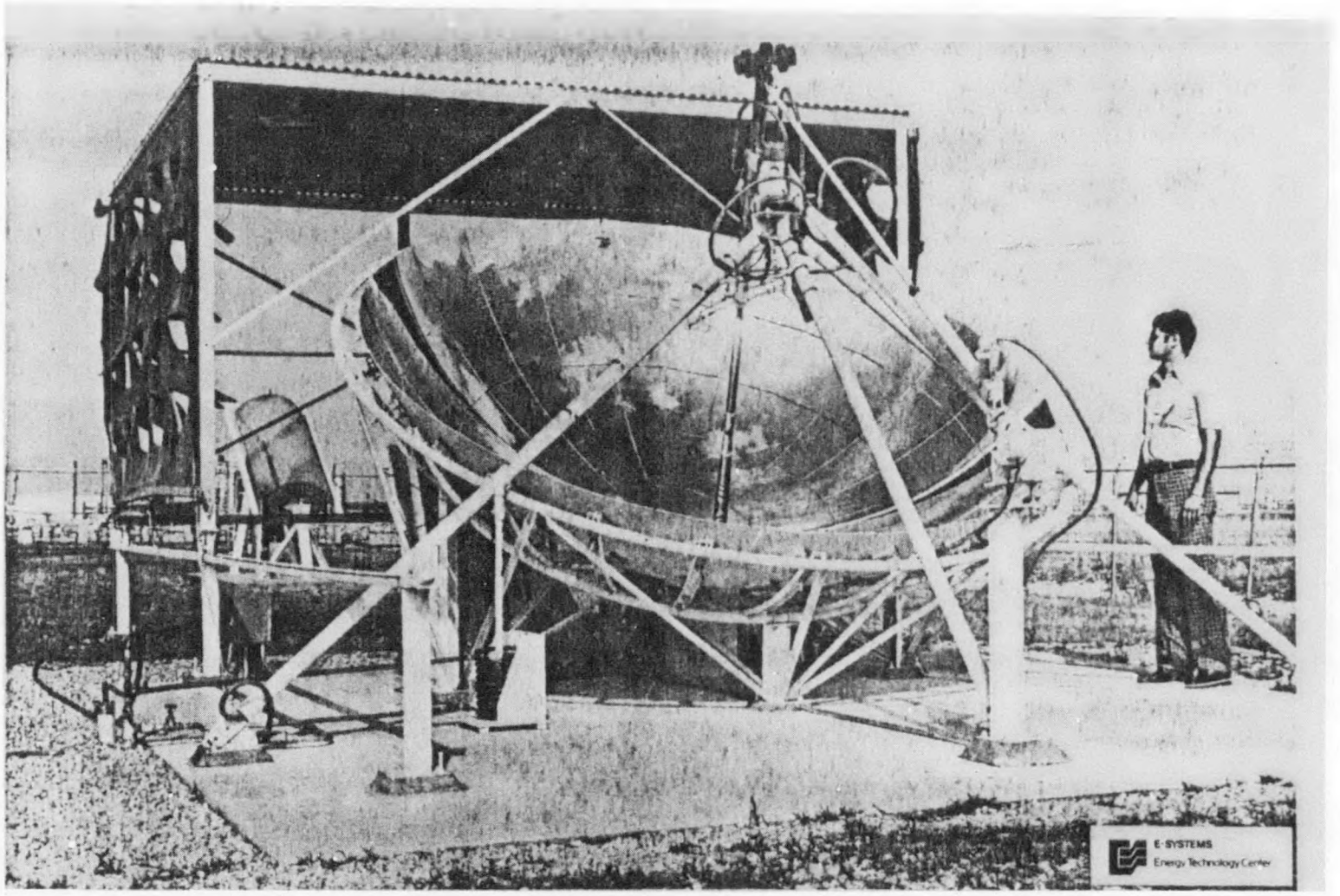

Figure B-22 11 Foot Diameter Collector Showing Receiver Flexible Hose Loop Connections

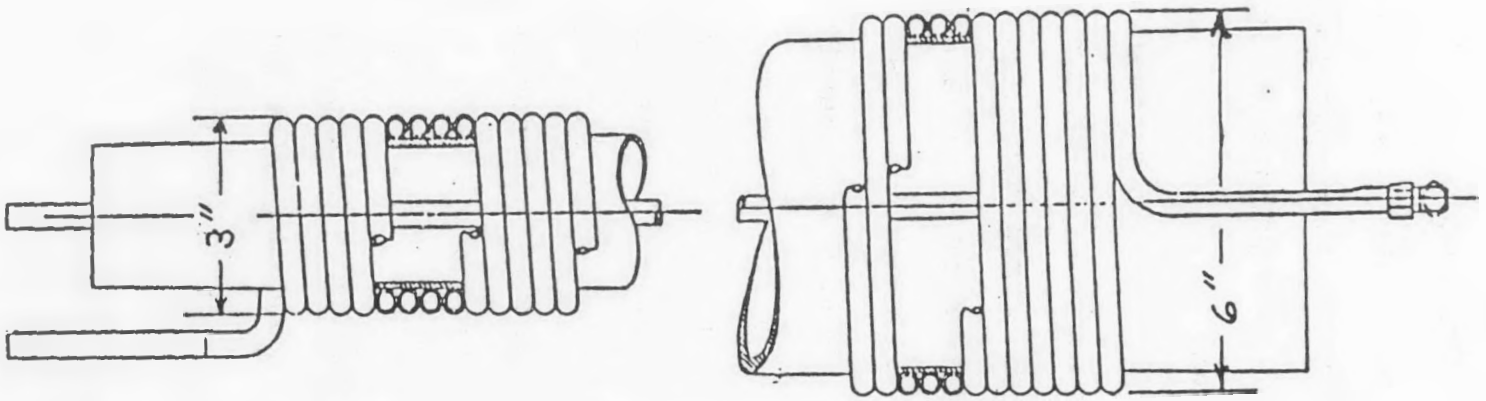

Figure B-23 Single-Wind Downscaled Receiver Tubing

B-8 IMPROVED RECEIVER DESIGN

An improved receiver design was suggested by the Foster Wheeler Energy Corporation which incorporated a mid-span equalization plenum. Two possible plenum arrangements are discussed—a single mid-span plenum and a duel plenum.

A torus shaped plenum is the simplest method for providing an equalization chamber in the mid-span region of the receiver where the tube-side flow is in a saturated condition. This design permits good access to all heat transfer tubing welds during fabrication, as well as during operation of the receiver. In the latter case, this is important for in-service inspection and possible repair. The resulting receiver configuration and flow pattern is shown schematically at the top of Figure B-24. Two 180° returns would be machined to provide a total of 40 tube connections. Twenty holes would be machined below the "horizontal" plane of the torus for the inlet tubes and another twenty provided above this plane for the outlet tubes. Inlet and outlet holes would be off-set to promote mixing and to maximize spacing and clearances between connections. Short, straight tube stubs would be welded to the 180° returns, using backing rings. These rings would be machined out after welding and the welds non-destructively tested. Preformed tube bends would then be orbital welded to each of the straight tube stubs, and the required NDT inspection of these welds would be completed. Two 180° returns would then be welded together, using consumable inserts, to form the torus. The torus would be installed at the required axial location on the receiver, and the heat transfer tubes would be orbital welded to the tube bend ends after wrapping.

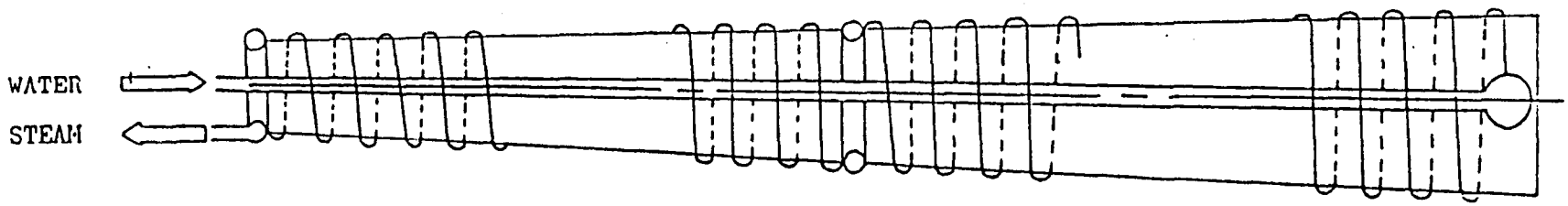

MID-LENGTH EQUALIZATION PLENUM

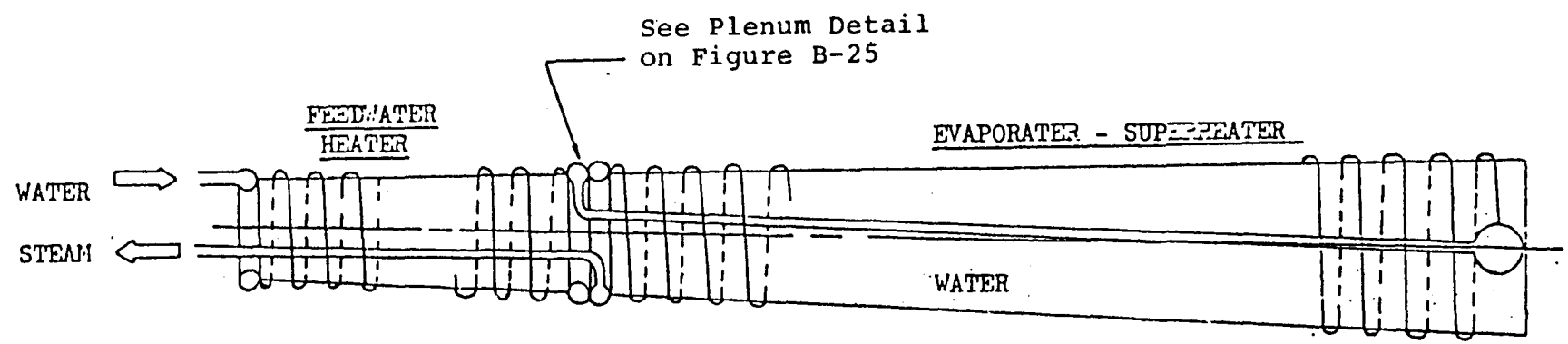

DUAL PLENUM ARRANGEMENT

Figure B-24. Overall Receiver Flow Pattern Arrangements

Another plenum arrangement would consist of two separate flow sections in the receiver; one for pre-heating the inlet water to saturation and a second for boiling and superheating. This suggests the dual plenum flow receiver arrangement shown on the lower half of Figure B-24. The feedwater is fed into a plenum at the top of the receiver (X/R = 0.5) from which it is manifolded into twenty spirally wrapped heat transfer tubes and flows downward. At a plane along the receiver length where the feedwater is at saturation, the tubes are manifolded into a single pipe. The saturated water is piped down to the bottom of the receiver (X/R = 1.0) where it is again manifolded into individual heat transfer tubes. Here it is boiled and superheated. The steam is collected in a fourth plenum and piped out through the center of the receiver.

Although this scheme is relatively complex, it has the distinct advantage of water cooling the tubes in the caustic region of the receiver. This should significantly reduce the maximum tube wall temperature in this section. Additionally, the reflected rays of the sun would be nearly normal to the tube wall in the section of the receiver where boiling would occur. This should substantially reduce the circumferential thermal gradient in the individual tube wall relative to that in the present receiver design. This being the case, less expensive tube material may be usable for the entire receiver, providing a significant cost reduction.

No detailed thermal/hydraulic or structural analysis has been conducted on this proposed system. A possible arrangement of the dual plenums in the center section of the receiver is shown in Fig. B-25. Both the feedwater and exit steam plenums would be torus

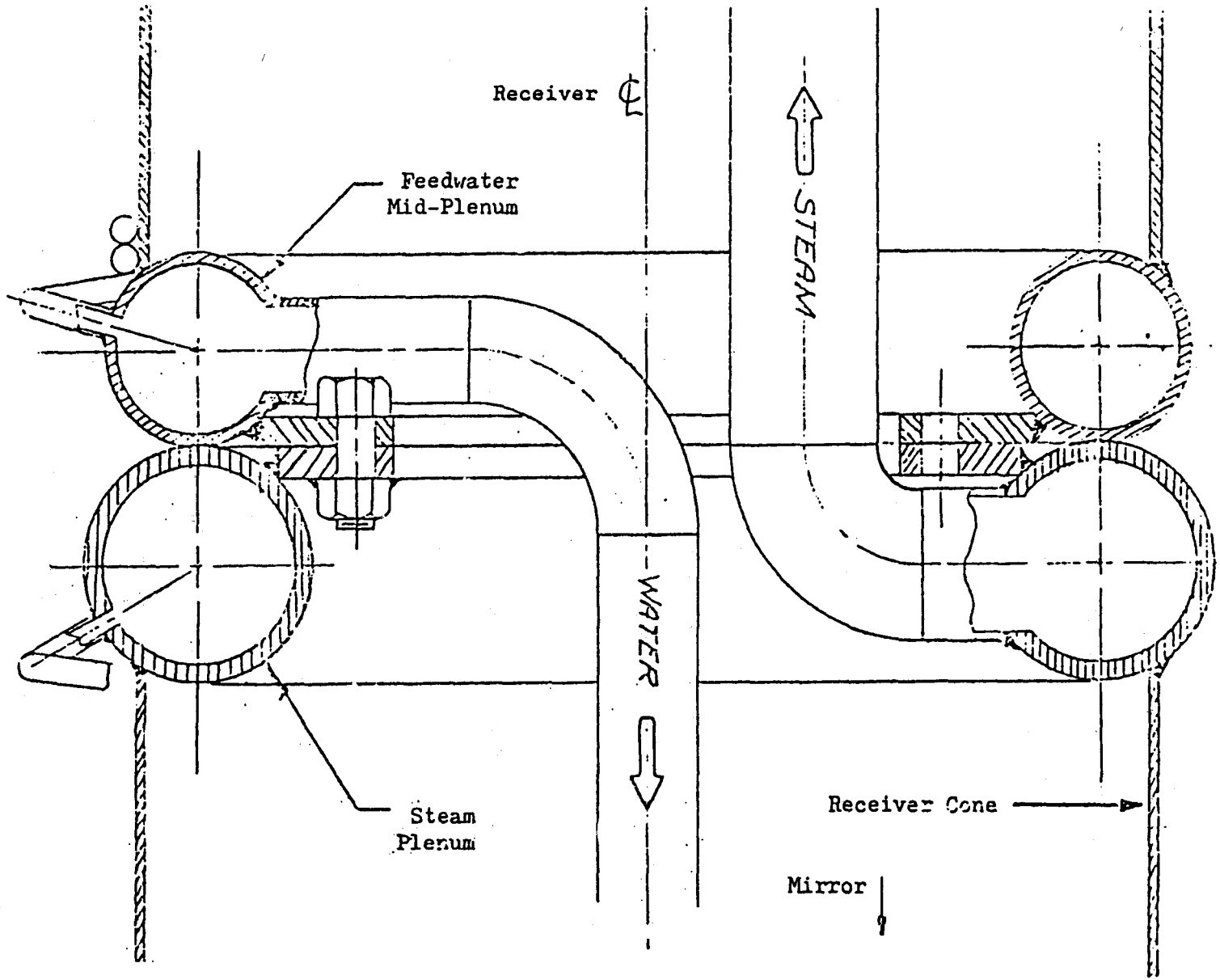

Figure B-25 Dual Plenum Arrangement Concept Design

configurations. A bolted flange arrangement would be used to attach the two plenums (and thus the upper and lower parts of the receiver) as required to permit radial thermal expansion between them. A graphite impregnated asbestos gasket could be used between flanges to reduce thermal conduction between plenums and to promote radial slippage.

B-9 OIL RECEIVERS

The general configuration of the oil receiver is very similar to the water/steam receiver. The tubes will be larger, with an inside diameter of 0.5 inches, an outside diameter of 0.7 inches and a wall thickness of 0.1 inches. In order to avoid decomposition of the oil, maximum internal wall temperatures will be at 600°F with maximum enternal wall temperatures of 725°F. With these lower operating temperatures it will be possible to construct the receiver of less expensive materials such as Inconel 600, Incoloy 800, or stainless steel. Some redesign in support structure will be required since the weight of the oil in residence in the receiver is larger than the weight of the water/steam.

B-10 ATS RECEIVER SUBSYSTEM

In general, all subsystems of the ATS will be similar to those of the RPS so that the ATS can be used to the greatest extent possible to model the behavior of the full scale RPS system. In particular, the ATS receiver will consist of a truncated cone (0.1 inch wall thickness) 18.76 ft. long with diameter varying from 0.33 ft. to 0.66 ft. with two tubes helically wrapped around the conical substrate. For both the water/steam and oil receivers, the tube diameters will be same as for the RPS.

The receiver mateials used will be Inconel 617 or 625 for both the helical heat exchanger coil and conical support substrate for the water/steam receiver. Stainless steel will be used for the helical coil and support substrate for the oil receiver. The coil will be coated with a high temperature flat black paint (brand name "Pyromark") with both absorptivity and emissivity approximately equal to 0.9.

The receiver support structure will include a cantilevered polar mounted receiver with two-axis tracking using diurnal and seasonal drives. The support structure will consist of a steel space frame and pipe construction with a walkway integrated into the fixed part to permit access to the polar tracking mount.

A back-up alternative will be considered. It will consist of a simply supported receiver on a fixed tripod center support and a moving azimuth-elevation track mounted on a fixed rail immediately above the surface of mirror.

APPENDIX C. SYSTEM MANAGEMENT - CONTROL AND TRACKING SUBSYSTEMS

C-1 INTRODUCTION

The Crosbyton Recommended Power System (RPS) incorporates precise control and monitoring systems to ensure optimum conversion of solar energy to electrical power. The management and control system is a refinement of the operational logic and system hardware of the Nominal Power System described in Vol. III of the Interim Technical Report. The description below constitutes the presently recommended control and management subsystem specification.

The operational management and control of the recommended solar thermal electric power installation is provided by the sophisticated system employing microcomputers and electromechanical control devices. The system selected is a distributed processing computer system where data acquisition and control is located at each solar collector in the installation. Figure C-1 illustrates the multiple processor configuration as it would be applied to a system containing ten collectors and a central control site management system.

Primary control is invested in the individual solar collector's controller. The control system overseeing all collectors provides for operator override of control commands and retrieval of system data. The central control system provides timing coordination, receiver pointing command generation (for acquisition), system start-up, system shutdown and other operational direction necessary to carry out safe and efficient conversion of energy.

The systems approach proposed here is the most effective means by which responsive control can be maintained. While otner manual

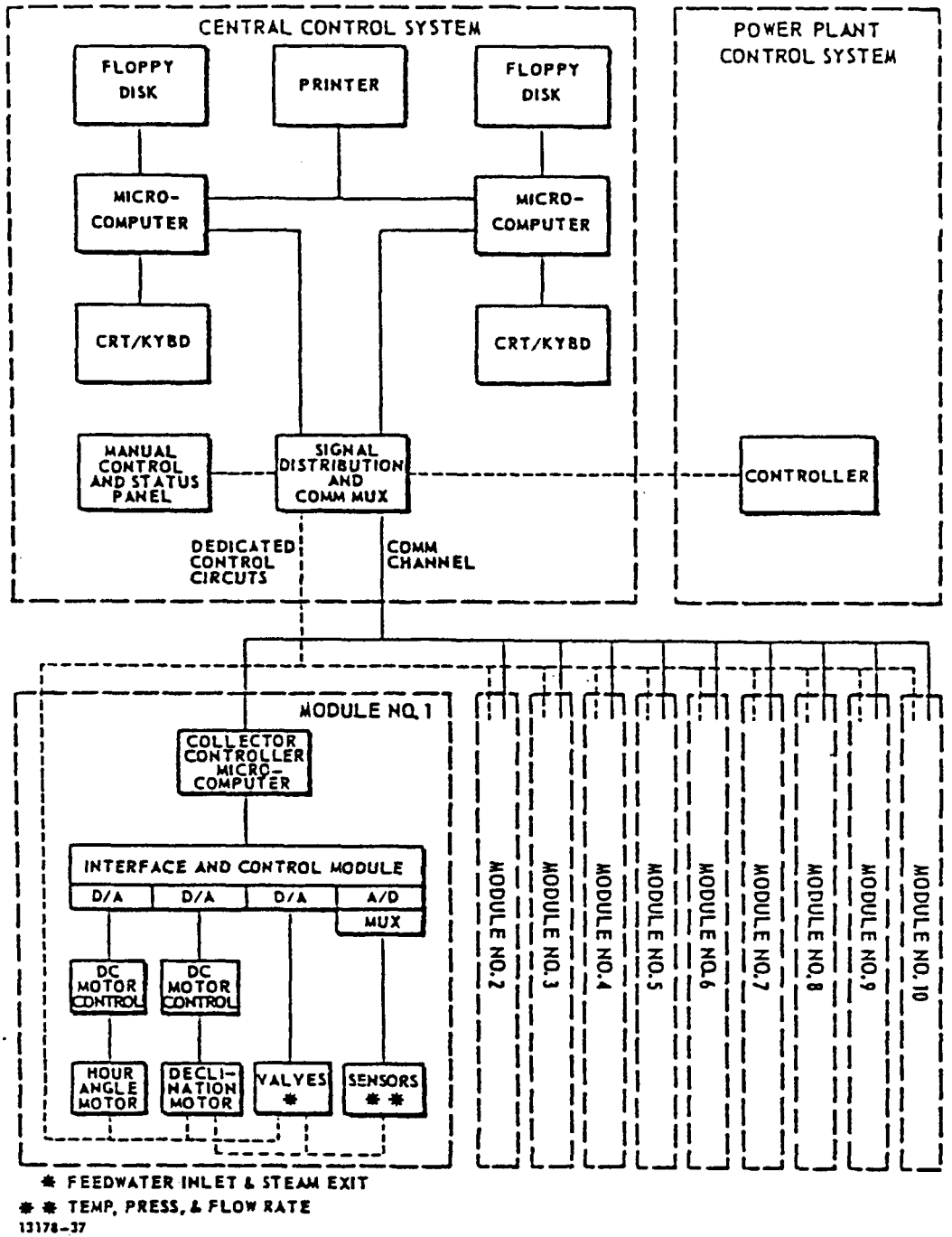

Figure C-1. FMDF STEPS Management and Control Subsystem

and electromechanical methods can be implemented, the microcomputer provides overall management of the project. The purpose of implementing a sophisticated microcomputer control system is to extend the productivity of the system while maintaining safe operating conditions. The application of current computer technology provides for more responsive operation of the solar power system than could be obtained by the use of discrete control devices.

Each individual collector microcomputer will manage the start-up, operate, and shutdown modes of the single collector. Once directed to initiate start-up by the central control system, the collector microcomputer assumes responsibility for repositioning the receiver to the current ephemeris track of the sun and adjusting the feedwater flow to facilitate conversion to superheated steam.

While considerable effort has been made to select reliable equipment and configure the system to maximize on-line operation of each solar collector module, redundancy has not been included at every critical location in the control system. Rather than incur sizable equipment and software costs, a design philosophy of long MTBF (mean time between failures) and short MTTR (mean time to repair) was adopted. This design philosophy ensures that any one of the collectors experiencing a malfunction will be safely taken out of production and brought to ambient temperature and pressure with a minimal disturbance to the balance of the system.

The primary functions performed by the management and control system include:

- o Tracking Control - Calculate and control auto-track motor drive signals and monitor active-track control
- o Process Control - Control and monitor system's feedwater to steam conversion
- o Emergency Control- Protect and control system under potentially dangerous conditions
- o Data Acquisition & Communications - Monitor sensor data and manage data dissemination and communications
- o Site Management - Overall management of Crosbyton solar installation through operator control

These functions are accomplished through a complex series of interrelated software tasks which control the daily operations of the Crosbyton Plant on a real-time basis. Standard software is implemented at the central control system while the collector microcomputer's programs reside in ROM (read only memory). ROM program storage improves the individual collector's reliability. Each of the five functions are also interdependent and interact in the normal course of daily activity. Thus, Crosbyton's Recommended Power System will employ multiple microprocessors in an interdependent system where functional tasks are assigned to the central control processor or the collector microcomputer. The use of individual microcomputers at each collector eliminates the need for a complex central computer processing system and extensive communications capability. The central control system manages the single full duplex communications circuit by polling each microcomputer in sequence.

C-1.1 Tracking Control

Tracking management is performed by a hybrid digital and analog control system. The auto-track mode maintains an ephemeris track in the central controller memory for use in the event the active tracking signal is lost. The stored auto-track coordinates are actual HA/DEC Encoder position data points for the last valid solar tracking day. Precalculated ephemeris position data coordinates are stored in memory to position the receiver for start-up, shutdown, and other system requirements. Figure C-2 illustrates the logic involved in the digital tracking controller.

The active-track mode provides continuous realtime tracking for precise positioning of the receiver whenever sufficient solar insolation is present.

The tracking sensor generates two analog error signals which provide control signals to both hour angle (HA) and declination axes for drive motor speed control.

The sun's position in hour angle (HA) and declination is monitored by an active sensor capable of sensing the sun's movements. Analog control signals are generated by the motor controllers and used to position the receiver in the focal cone position where maximum energy transfer occurs.

C-1.2 Process Control

Process control involves the dynamic control of feedwater flow and steam generation. Each site's steam production is routed to the turbine or storage (if available), depending on the power load demand. Normal turbine generator fluid loop operations will consume

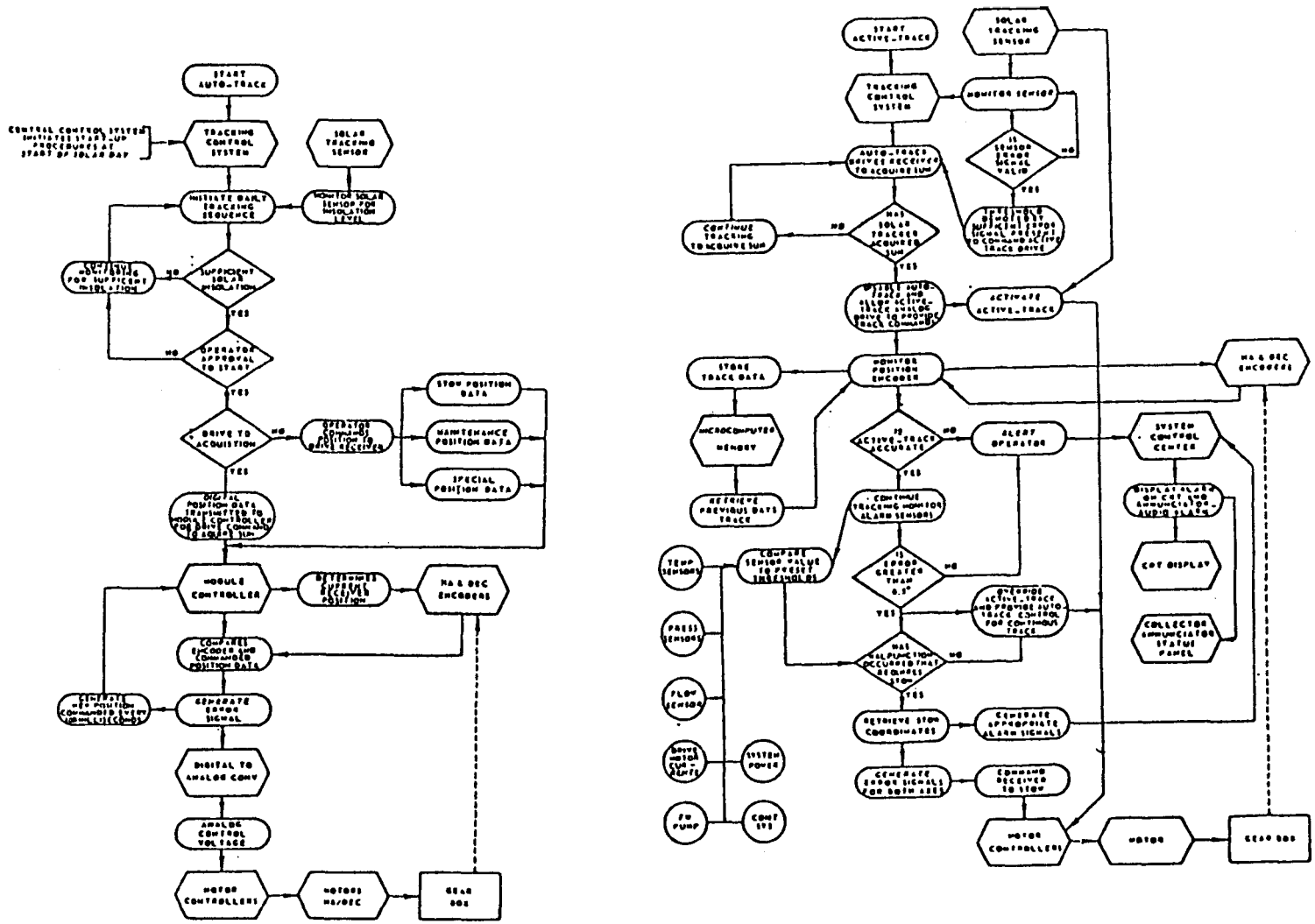

Figure C-2. Track Control Logic

solar generated steam first with the conventional power plant making up the balance of the steam demand. The collector microcomputer provides continuous steam supply status reports to the conventional power system. Process control receives sensor data relating to the status of the collector and determines the valve settings necessary to maintain both the quality and quantity of steam production to meet demand. Data collection necessary to support the daily operational process control is incorporated into the software by the software designers and is not available for modification by the operator. Specific data sampling rate requirements will be evaluated and adjusted during the ATS and RPS operational tests. A final determination of the sampling rate will be selected from results of the RPS prototype. Minor variations will be accommodated by software control.

The process control software samples temperatures, pressure and flow rate at variable intervals. Receiver steam exit temperature and critical surface temperatures may require samples every ten (10) milliseconds. This ensures adequate temperature resolution to meet process control and emergency requirements.

The following paragraphs present a brief discussion of the various operational requirements for process control.

Start-Up

System start-up at the beginning of each solar day will require close supervision to insure that thermal damage does not occur to the receiver. Once sufficient solar insolation is available, the CCM alerts the CCS. If the CCS has operator approval to start, a message alerts process control that the start-up procedure is required. Before the receiver is aligned in the focus (caustic region), feedwater flow will begin. Track control receives a similar start message. Figure C-3 illustrates the sequence of events involved in bringing the solar collector on line.

Process control sets a minimum preselected flowrate by positioning the collector's feedwater control valve to a preselected start-up position. Feedwater heating commences as soon as the receiver moves into the focus position. Feedwater flow control software monitors steam temperature and adjusts the feedwater flow rate to minimize the time required to attain operating temperature.

To prevent damage to the turbine, a bypass valve allows heated feedwater, two phase mixture, or saturated steam to bypass into the condensor during start-up. The conditions (pressure/ temperature) in the steam line at the output of the solar collectors are monitored so that superheated steam can be used to supplement

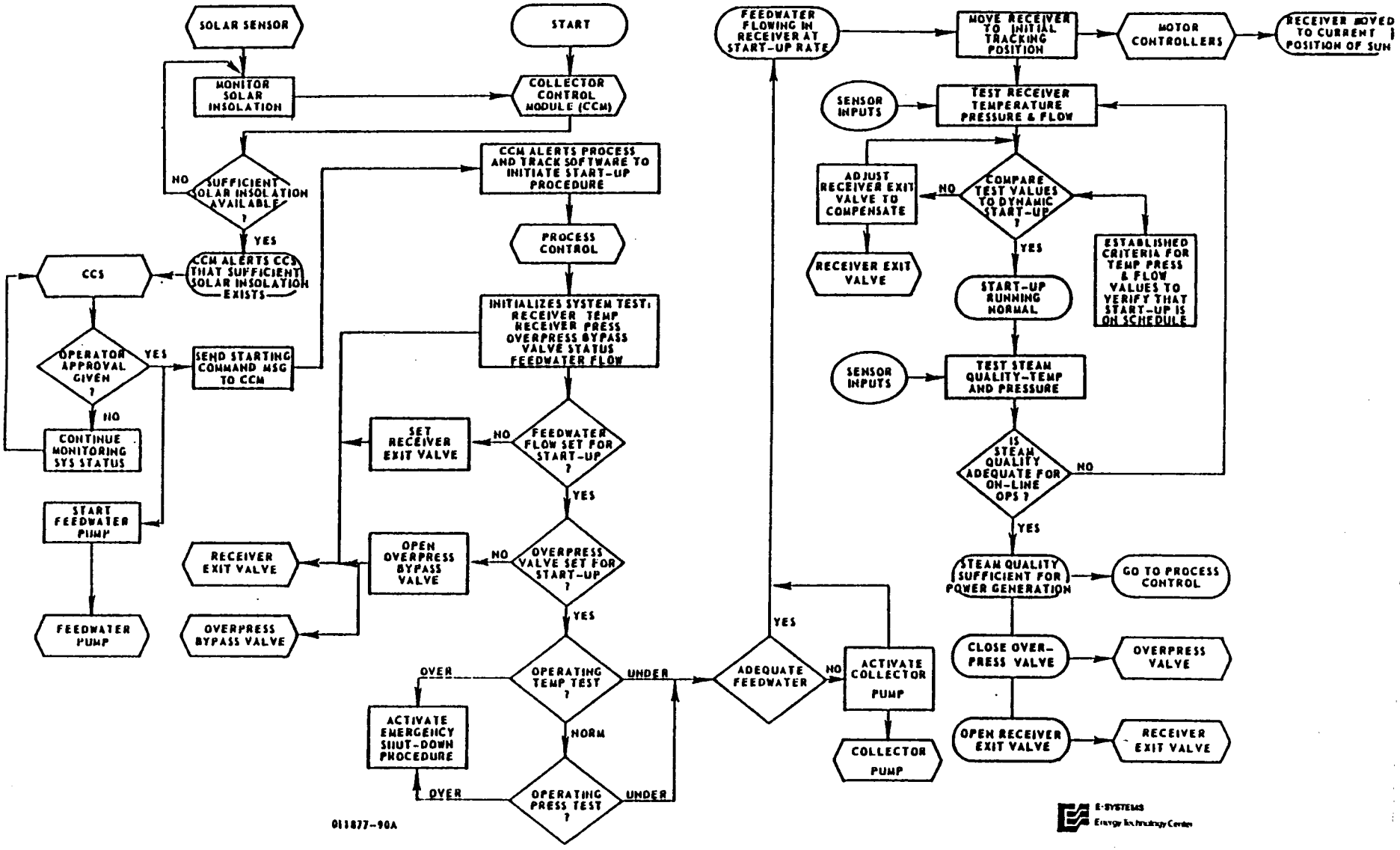

Figure C-3. Startup Process Control

the conventional boiler steam to the turbine as soon as it becomes available from the collector field. The performance and economics of these procedures will be evaluated once ATS operations are underway.

Normal Operation (Constant Insolation)

The standard operating conditions of a solar collector exist when direct insolation is available on a continuous basis. The production of steam, supply of feedwater and consumption of steam is relatively stable. Adjustments to the system are minimized thereby allowing the process control functions to establish a quiescent level of operation. This represents the most stable operational condition. Figure C-4 indicates the sequence of events involved in the normal process control.

Transient Operation (Intermittent Insolation)

Intermittent insolation caused by scattered clouds will require additional control in order to satisfy the dual constraint of maintaining the operating temperature of the receiver within safe levels and to operate at maximum possible collection efficiency where possible.

The primary effect of a cloud overhead is a drop in insolation resulting in a rapid decrease in energy incident to the receiver. Below a specified frequency of intermittency and and above a specified level of insolation, the process control software

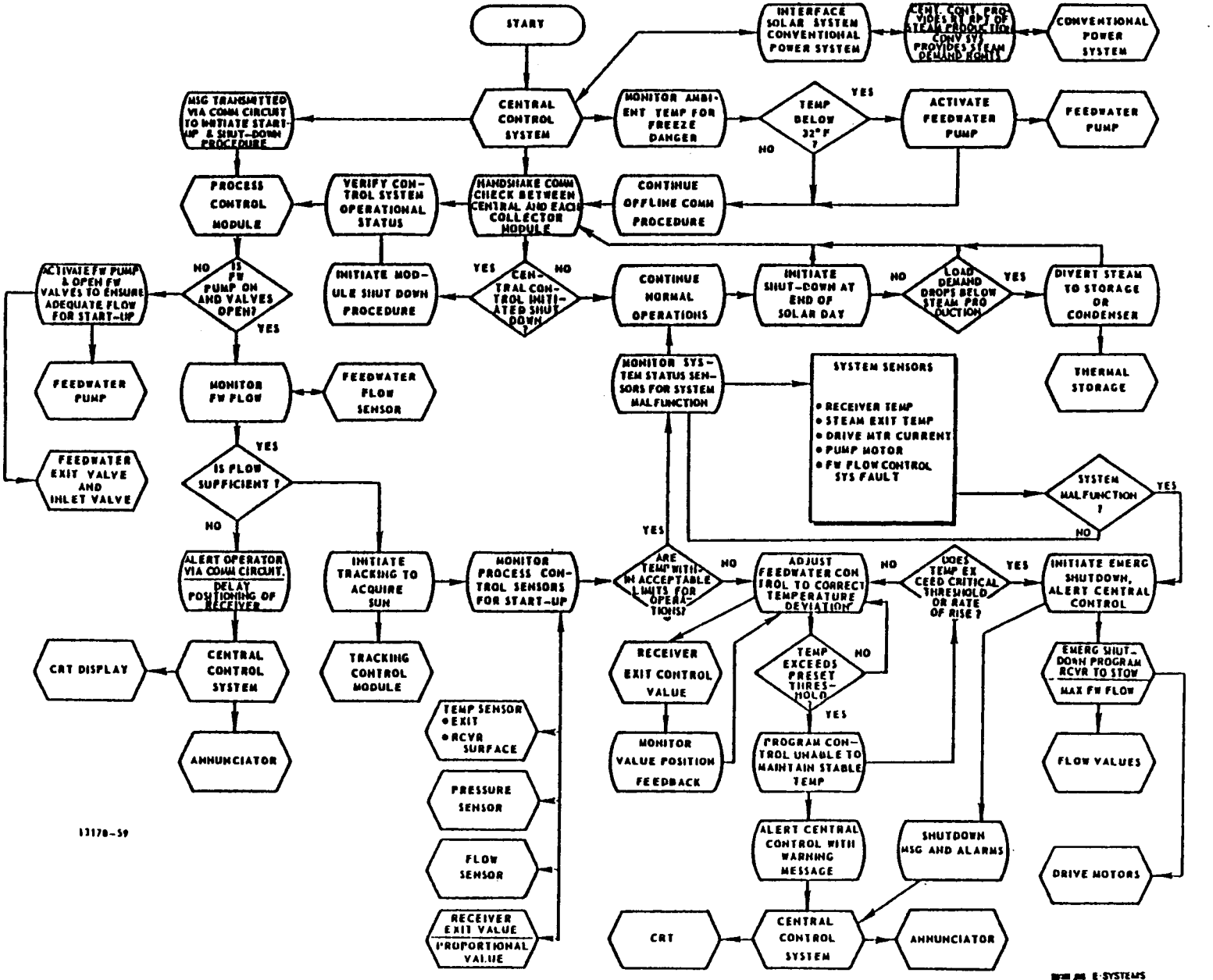

Figure C-4. Process Control Logic

will respond with a comparable reduction in the feedwater flow rate that will allow steam temperature to be maintained, i.e. the flow tracks the transient. The receiver tracks during the intermittent loss of direct insolation.

Above the specified frequency, and below the set level, insolation feedwater flow is maintained to the receiver at a rate sufficient to ensure complete liquid flow on the receiver and thus protect from localized burnout. A bypass valve will reroute this preheated fluid either to the condenser or to feedwater heating for the auxiliary boiler flow loop. When sufficient insolation becomes available, the process control software must activate a similar start-up procedure as described in the previous section.

System Shutdown Sequence

System Shutdown Sequence occurs at the end of a solar day and any time within the period that solar insolation falls below the level necessary to generate steam at the required temperature. The normal shutdown sequence is as follows:

1. Tracking Control recognizes end of solar day or loss of adequate insolation and notifies process control.
2. Receiver is moved at slow speed to the stow position.
3. Feedwater flow is stopped or reduced to a minimum depending on the ambient temperature conditions, by adjustment of feedwater flow control.

4. All systems shut down except CCS and CCM in monitor mode.

C-1.3 Emergency Procedures

A key element in the management of the solar power site is the system's ability to ensure safe operations under all conditions. The control system configuration was designed with safe operations and emergency shutdown as a major requirement. The software that controls the sequence is resident in each collector's CCM. The CCS also monitors the system for emergency shutdown conditions. This insures that in the event of a malfunction of collector's microcomputer, the emergency shutdown sequence can be executed.

The sequence would be initiated if an excessive temperature were monitored within the system or if a component malfunction occurred that would endanger the collector. Activation of the sequence would cause the following:

1. Receiver is moved out of the tracking position at high speed slew of five (5) degrees in ten (10) seconds.
2. Feedwater flow increased to maximum.
3. Mirror washdown system activated for mirror protection.
4. Exit steam valve is closed and the bypass valve opened.
5. Audio and visual alarm activated at central control console.
6. Definitive status message output on console.

Three levels of emergency protection are included as indicated in Figure C-4:

1. Each collector microcomputer will respond to dangerous conditions by initiating an emergency shutdown procedure.
2. The central control system can initiate an emergency shutdown through the collector microcomputer.
3. This protection action occurs only if the collector does not first respond to a potential hazard. In the event all other controls fail to respond, an override circuit applies a D.C. voltage directly across both tracking motors to drive the receiver into stow and the feedwater valves to maximum flow position. The override logic is a "safety valve" similar to the electrical and mechanical limits on the drive axes to prevent system damage.

Control system malfunctions will be cleared within thirty (30) minutes. Other problems involving the structure, fluid flow, valves, motors, etc., when cleared, will allow the controller to restart operations. Malfunctions due to a control system fault at one collector result in a minimal loss of power. Additionally, the system's diagnostics warn of possible problem areas which will be corrected during the off-line time after the end of the solar day.

Controlled initiation of this sequence on the ATS will provide a basis for refinements in these recommendations.

C-1.4 Data Acquisition and Communications

The collection of system data for operational control and status reporting is essential. Key parameters include:

- o Temperature
- o Pressure
- o Flow rate
- o Equipment status
- o Environmental conditions

Temperature, pressure, flow rate, and equipment status are monitored at each collector. All sensor data is used as inputs to the collector control system and to generate status messages for transmittal to the central control system.

Each parameter is sampled at a prescribed rate. Normal sampling occurs at one second intervals while process control requires rates of 100 samples per second. Intervals of 10 milliseconds may be required for proper temperature resolution under worst case transient conditions. The data is used in real time for local control before being formatted into the message structure. Not every data point sampled will be included in the message. The operator selects the rate at which each parameter is included in the message forwarded to the central control system. Decentralized processing allows the collection and temporary storage of data at individual collectors.

The proposed configuration is a store and forward communications network which reduces the need for multiple communication wire line circuits between the central control microcomputer and the collector microcomputers to a single full duplex drop circuit. The communications circuit is polled by the central control microcomputer where each collector has a distinct address.

C-1.5 Production Design

The approach selected in developing the RPS control system is to implement a sophisticated control and data acquisition system for the Analog Test System (ATS) and then develop the RPS system by continually making refinements based on the knowledge gained in the ATS prototype. The microcomputer will allow for significant changes to take place with a minimum of impact on the development program. In fact, the availability of the microcomputer will assist in the development of the final system configuration. Additional system data will be available on which improved solutions can be based.

The proposed approach to designing a final production system is to configure the Analog Test System to emulate the production collector microcomputer system. This configuration will be used in the development of the final production version. Operational tasks that must be added or modified to meet changing

requirements will be identified and included in the system. Once the system hardware and software requirements are finalized, the system software can be optimized. The control system hardware will be production engineered to reduce costs through established value engineering techniques. The proposed microcomputer control system designed is directed to facilitate low-cost, highly reliable mass production in the future.

Specific detail on the control system configuration, hardware, and various algorithms to be utilized in the control and management of both the RPS and ATS is available in other documents.

C-2 OPERATIONAL, SOFTWARE REQUIREMENTS

The E-Systems FMDF design team is responsible for establishing and documenting operational procedures under which the RPS system operates. In order to ensure that the system design includes all required operational capabilities, a detailed evaluation of operational-software requirements was completed. This analysis required determination of the primary control functions as well as the significant number of supporting tasks which must be included in the control system. The software requirements pertaining to the central control system is divided into ten major subsystems:

A. Executive - provides software system management. The function includes task handling, queue management, buffer management, and initialization procedures.

B. Tracking - provides dynamic position control to move the receiver in HA and DEC.

C. Process Control - provides for continuous monitoring and control of the fluid flow system in order to optimize the heat process-transfer.

D. Emergency - provides for automatic shutdown and alarm in order to alert and prevent bodily injury to site personnel and damage to the equipment.

E. Data Acquisition - performs all sensor data collection and conditioning before data is presented to the tracking and process control subsystem for verification.

F. Communications - provides all communication between the central control system (CCS) and the collector controller module (CCM). The communication subsystem will be capable of transmitting and receiving data internal to the system on a demand poll via an asynchronous network.

G. Display - provides for operator interface with the CCS through the use of video display of the system's operational status and allows mutual intervention should a change be desired. Hard copy of data parameters may also be printed.

H. Data Base - provides for the storage and retrieval of CCS data that may be used to provide management with the necessary information to evaluate the CCS and recommend improvements.

I. Diagnostics - provide hardware equipment verification and aid in the isolation of specific malfunctions.

J. Utilities - provides for file manipulation, program edit and debugging aids as well as other general functions such as core memory dumps and the output of mass storage device data to hard copy device.

Figure C-5 includes the six functional software areas and their subtasks which support the control system.

Development of the operational specifications for the control system is the intermediate step between documentation of requirements and definition of the control system configuration. Automation was not necessarily the intent of this effort. However, it became obvious that automation was necessary since the dynamic conditions that exist in the conversion of solar energy to electrical power require rapid and decisive response.

Transient response of heat transfer within the receiver is measured in milliseconds. If the process control and safety functions are to be responsive to dynamic changes occuring in time periods of less than a second, control logic with faster response times must be used. While some individual response times can be met with discrete logic, the complexity resulting

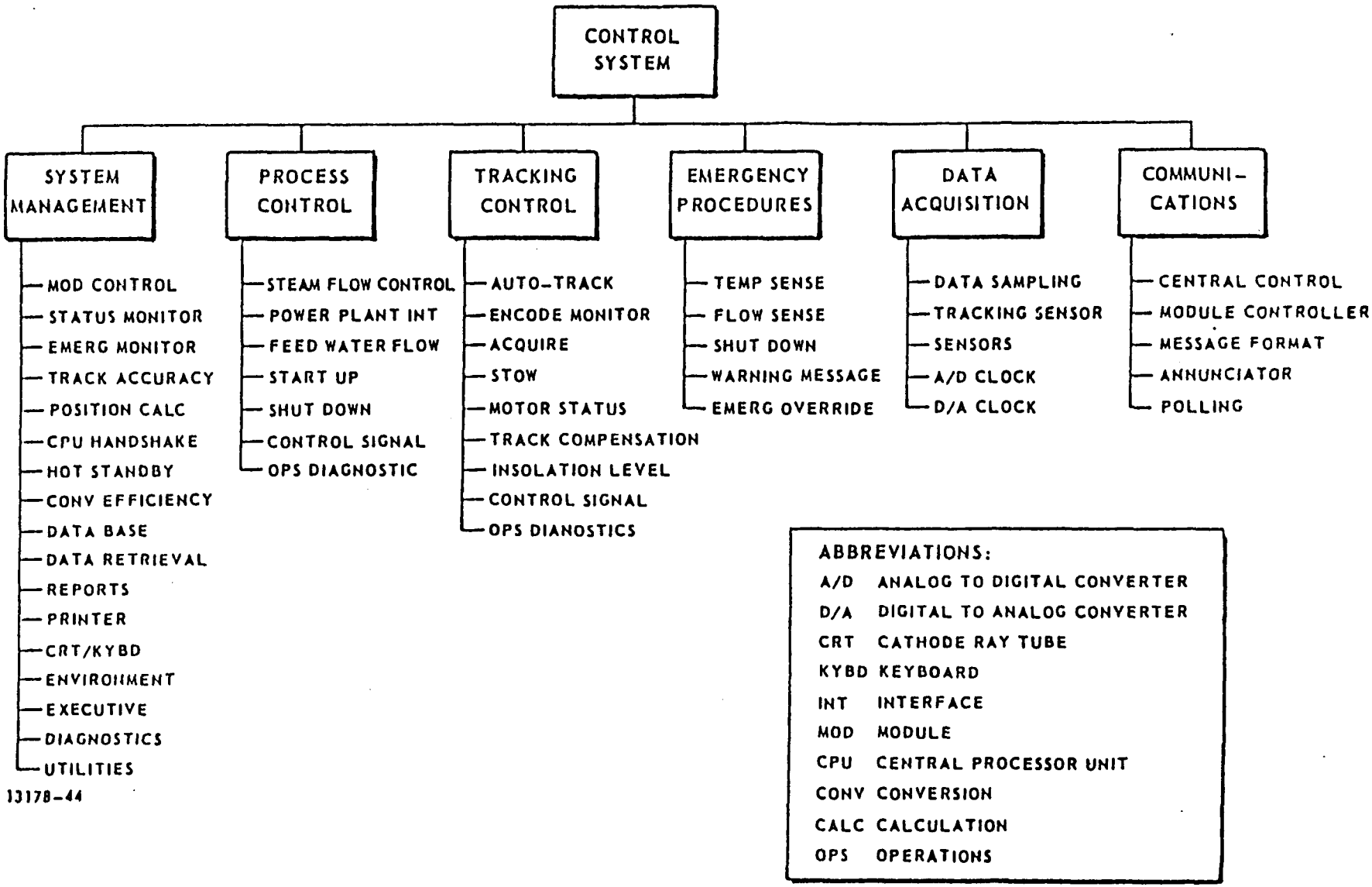

Figure C-5.Major Functions of Control System

from a combination of individual control actions requires a more comprehensive solution. That solution is the implementation of the control system described herein.

C-3 DESIGN REFINEMENTS

Hardware and software design has evolved through several interactions since the initial nominal system definition. Changes to system requirements have been recognized and a better understanding of solutions to the system control problem has resulted throughout the duration of the current FMDF design study.

One area which has experienced change is tracking control. Originally, the auto-track (projected track) and active-tract (sensor track) were to be primarily digital functions. A second microcomputer was located at each collector for digital tracking control and emergency operations. Further investigation has shown the analog tracking approach to be a more cost effective and reliable method of controlling the receiver. The two redundant central control system processors and discrete override logic will provide the necessary control. In effect, those functions which are better performed digitally will remain digital, while those functions which are better performed using analog control circuitry will remain analog.

The design approach selected for RPS implementation is based on matching both software and hardware to the operational requirements as recognized in the operational analysis. Of particular importance are the operational and performance specifications associated with the tracking control system. These are summarized in Table C-1.

TABLE C-1

TRACKING CONTROL SYSTEM SPECIFICATIONS

Tracking Accuracy	0.01°
Servo Resolution	0.01°
Encoder Resolution (Auto-track)	0.09°
Track Velocity	15°/HR (0.25°/MIN)
Operating Wind Speed	30 MPH Wind
Slew Velocity	30°/MIN (0.5°/SEC)
Drive to Stow	90 MPH Wind
Cone of Acquisition	±7.5°
Receiver Tracking Error	
Auto-track	0.2° RMS
Active-track (Wind 30 mph)	0.03°RMS
HA Motor Command Interval	6 sec - 0.025° resolution 4 sec - 0.017° resolution 2 sec - 0.008° resolution
Temperature (outside)	
Storage	-40° - +125°C
Operating	-25° - +70°C
Temperature (inside)	
Storage	0° - 70°C
Operating	0° - 50°C
Humidity	
Outside	0 - 98%
Inside	0 - 90%
Dust and Sand	Electronics sealed or potted to protect against desert environment

Each of these specifications impose an operational function on the control system as well as less obvious support functions that must be performed by software. Software in term determines the hardware requirements.

System hardware and software selection was based on the following criteria:

1. Processor's capability to perform within the constraints
2. Ease of programming
3. Availability of support software
4. Input/output communications requirements
5. Available peripheral support devices
6. Environmental compatibility.

C-4 HARDWARE REQUIREMENTS

C-4.1 Sensors

Several approaches to tracking control were evaluated. Each method surveyed had the capability for positioning the receiver within the required accuracy. Cost and accuracy were the primary considerations in the selection rationale. The active sensor which tracks the sun by comparing differential signals until a null results was selected. The active sensor requires a sensor head with light sensitive solid state devices and analog electronics for signal conditioning. The sensor will be mounted near the caustic region on the receiver in order to accurately position the receiver's caustic region. This

approach has the advantage of compensating for position errors due to gravity (receiver deflection) and wind. The other major contender was a calculated digital system using high resolution encoders at the receiver's rotating yoke. Deflection of the receiver is not included in the positioning loop and must be otherwise compensated. Excessive costs for high resolution encoders (14/15 bit) made the digital approach costly.

Another active tracking sensor which has possibilities is the heat sensitive ring placed in the caustic region. The heat sensor indicates the position providing the highest heat distribution within the caustic region. Use of the heat sensitive ring will provide accurate positioning data while compensating for receiver deflections. This sensor will be evaluated as a secondary tracking device to provide fine positioning control data based on a longer time base. Additional details on the receiver deflection were provided in the previous section.

C-4.2 Microcomputer Selection

Particular attention is given to the selection of the most suitable micro-processor for the Control System application. Of importance is the selection of a micro-processor that is readily available and one that has the potential for good software support.

A total of 26 individual candidate microprocessor units were evaluated for use in system management-control. Data was tabulated for each unit in a total of 29 categories. Weighting factors were then established and assigned to each of the categories and the respective units were rated and the top six ranked.

A trade-off evaluation for these units identified the Mostec Z80 as having a higher rating than the other devices.

The Z80 is the first choice for the ATS where it is housed in a protected environment. For collector controller module (CCM) use in the recommended power system (RPS) and production installations, the militarized version would not need artificial environment controls. Prior to the final design of the RPS CCM, a cost trade-off will be made to determine the most cost-effective approach- mil-spec electronics or environmental controls.

Tables C-2, C-3, and C-4 summarize the hardware requirements for the Analog Test System, Recommended Power System, and Production Power System.

C-5. CONTROL SYSTEM MODELING & ANALYSIS

The control system proposed for the positioning for the solar collector is very similar in concept to the control systems presently used by E-Systems, Inc. in the positioning of large antennas. Extensive programs have been developed for analysis of the antenna applications, and these were adapted to the solar control system analysis. Two primary programs were utilized. The first is a linear analysis program, and the second a non-linear transient analysis program. The non-linear program incorporates random winds, non-linear gear box spring rates, static and running friction models, and backlash simulation.

A complete list of the various constants and parameters necessary to describe each solar system-control system component shown in

TABLE C- 2

ATS CONTROLS HARDWARE

Quantity	Description
2	Microcomputer Z80
2	32K RAM modules
2	Backplane Chassis Assembly
4	Parallel interface
4	Serial interface
2	Video terminal - 1000 character - alphanumeric
2	RS232C Serial Communication Interface
2	Dual floppy disk drive and controller
1	Line printer (300 LPM)
1	Interface and control module w/ - 32 channel multiplexer - A/D converter - 12 bits - (3) D/A converter - 12 bits - Miscellaneous buffers and digital interfaces
2	DC Servo Motor Controllers (5 horsepower)
2	Position Potentiometers
1	Tracking Sensor
1	Manual Control and Status Panel - 16 Channel Annunciator
1	Cabinet and power distribution
1	Signal distribution panel
2	Power supply set
2	Cable set

TABLE C- 3

RECOMMENDED PRODUCTION SYSTEM CONTROLS HARDWARE

Central Control System (CCS)		Collector Control Module (CCM) Components per Collector Ten (10) Assemblies Needed	
Quantity	Description	Quantity	Description
2	Microcomputer Z80	1	Microcomputer Z80
2	RAM Module - 32K bytes	1	E-PROM - 4K bytes
2	Backplane Chassis assembly	1	RAM - 8K bytes
2	Parallel interfaces	1	Serial interface
2	Serial interfaces	1	Parallel interface
2	Video terminals	1	Interface and control module
2	RS232C Serial Comm Interfaces		- 16 channel multiplexer
2	Dual floppy disk and controllers		- A/D converter - 12 bit
1	Line printer (300 LPM)		- (3) D/A converter - 12 bit
1	Manual Control and Status Panel		- Miscellaneous buffers and digital interfaces
	- Graphic display	1	Signal distribution box
	- 64 channel annunciator	1	Enclosure and power distribution
1	Console, equipment	1	Power supply set
1	Power distribution	2	DC Servo Motor Controllers
1	Signal distribution	2	Position Potentiometers
2	Power supply sets	1	Tracking sensor
2	Cable sets	1	Backplane chassis assembly

TABLE C-4

PRODUCTION POWER SYSTEM CONTROLS HARDWARE

Collector Control System		Collector Control Module (CCM) Components per Collector Ten (10) Assemblies Needed	
Quantity	Description	Quantity	Description
2	Microcomputer Z80	1	Microcomputer Z80/Z8
2	RAM Module - 32K bytes		- CPU chip
2	Backplane Chassis assembly		- Counter timer chip
2	Parallel interfaces		- PI/O chip
2	Serial interfaces		- Serial comm chip
2	Video terminals		- RAM chips (8K bytes)
2	RS232C Serial Comm Interfaces		- E-PROM chips (4K bytes
2	Dual floppy disk and controllers		- RS232C chips
1	Line printer (300 LPM)		- Miscellaneous interface/buffer chips
1	Manual Control and Status Panel		- Printed circuit card
	- Graphic display	1	Interface Control Module
	- 64 channel annunciator		- A/D converter (12 bit)
1	Console, equipment		- Multiplexer
1	Power distribution		- (3) D/A Converter (12 bit)
1	Signal distribution		- Sample and hold amplifiers
2	Power supply sets		- Signal conditioning amplifiers
2	Cable sets		- Miscellaneous interface and buffer chips
			- Printed circuit card
		1	Chassis assembly
			- Mother board
			- Connectors
		1	Enclosure and power distribution
		1	Signal distribution box
		1	Power supply set
		2	DC Servo Motor Controll
		2	Position Potentiometers
		1	Tracking Sensor

Fig. C-6 was compiled and used as inputs to a parametric study of both the quasi-steady (linear program) and transient (non-linear program) operating characteristics of the tracking control systems. The analysis presented the predicted response of system variables such as hour angle, declination, azimuth and elevation.

C-5.1 Control System Model

Figure C-6 is the control system block diagram used for the control system transient analysis. Three control loops are used in the system. The inner-most is the current compensation loop with back-emf compensation to linearize the SCR amplifier response. The next loop is the rate loop which uses lead lag compensation to permit the loop to be closed slightly beyond the rigid body natural frequency. The position control loop compensation provides a Type II Servo Loop to minimize steady state positioning errors.

C-5.2 Analog Control System Components

The analog control system block diagram (Fig. C-6) is applicable to both the hour angle and declination control loops. As much commonality of parts as possible is maintained in the two loops. Each system contains a control pre-amplifier for loop compensation, a SCR type motor drive amplifier, a 5 hp permanent magnet D.C. servo motor with tachometer, and position and solar sensors.

In hour angle, the motor drives a rotary turntable through a gearbox, and in declination, the motor drives a "jack-screw" linear actuator. The differences in the two systems are in this actuation drive, in slightly different parameters in the position loop compen-

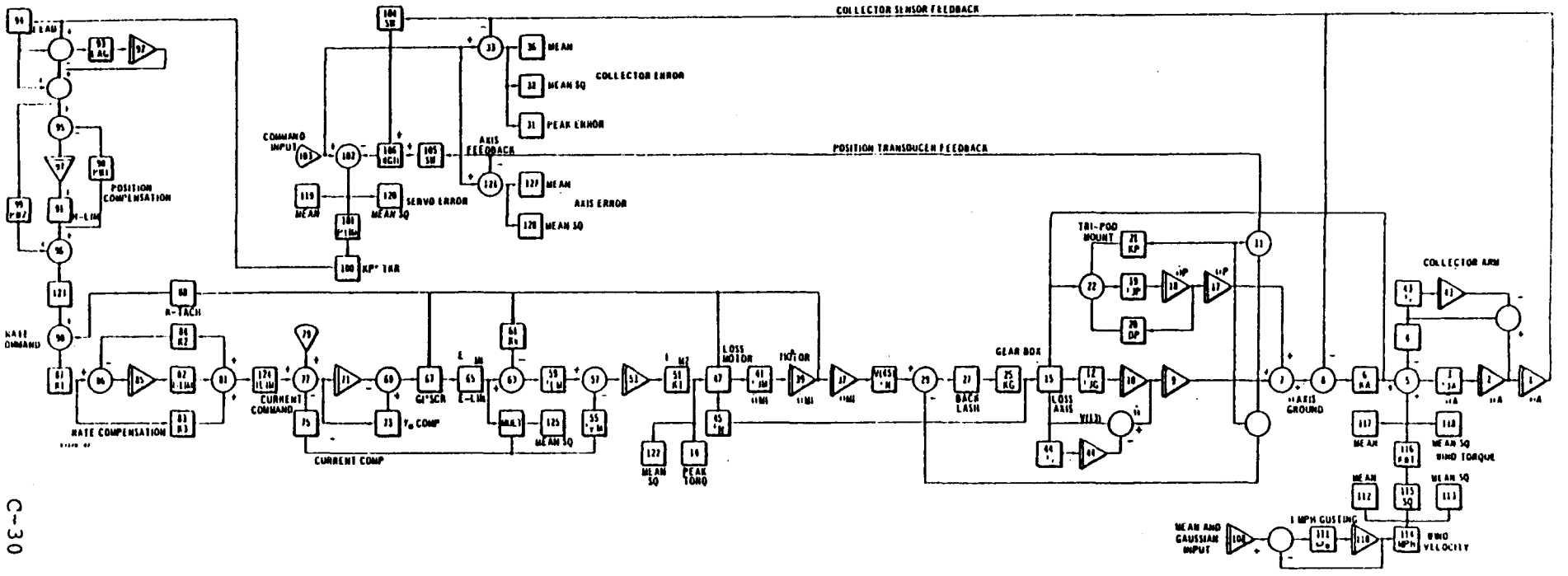

E-SYSTEMS
Energy Technology Center

Figure C-6. Control System Block Diagram

sation. The remaining elements are identical. Each system provides four sensor outputs. These sensor signals represent the motor current, motor rate, drive position, and solar position sensor. Each sensor output is provided to the microcomputer for monitoring and control.

C-5.3 Results of Analysis

Both the cantilevered and the two-point mount systems have been analyzed using the linear and non-linear control subsystem compute mode. In the worst case (hour-angle system with backlash, significant friction levels and gusting winds) the servo errors will be under .02 degrees. Figure C-7 describes the step response for the control system with the complete non-linear model. Figure C-8 illustrates the response of the control system when subjected to a step disturbance of a 30 mph wind applied at time = 0. All of the configured systems have adquate stability margins and provide typical maximum slew rates over 1/sec. Additional test results have been obtained and analyzed.

C-5.4 Operational Modes

Three primary modes of control will be provided. These are an auto-track mode, an active track mode, and an emergency mode.

Auto Track Mode

In the auto-track mode, the microcomputer will provide a desired position command. This will be compared to the shaft position sensor output to provide an error signal to the system. In normal

Figure C-7a. .020 Deg Step Transient Response for Hour Angle

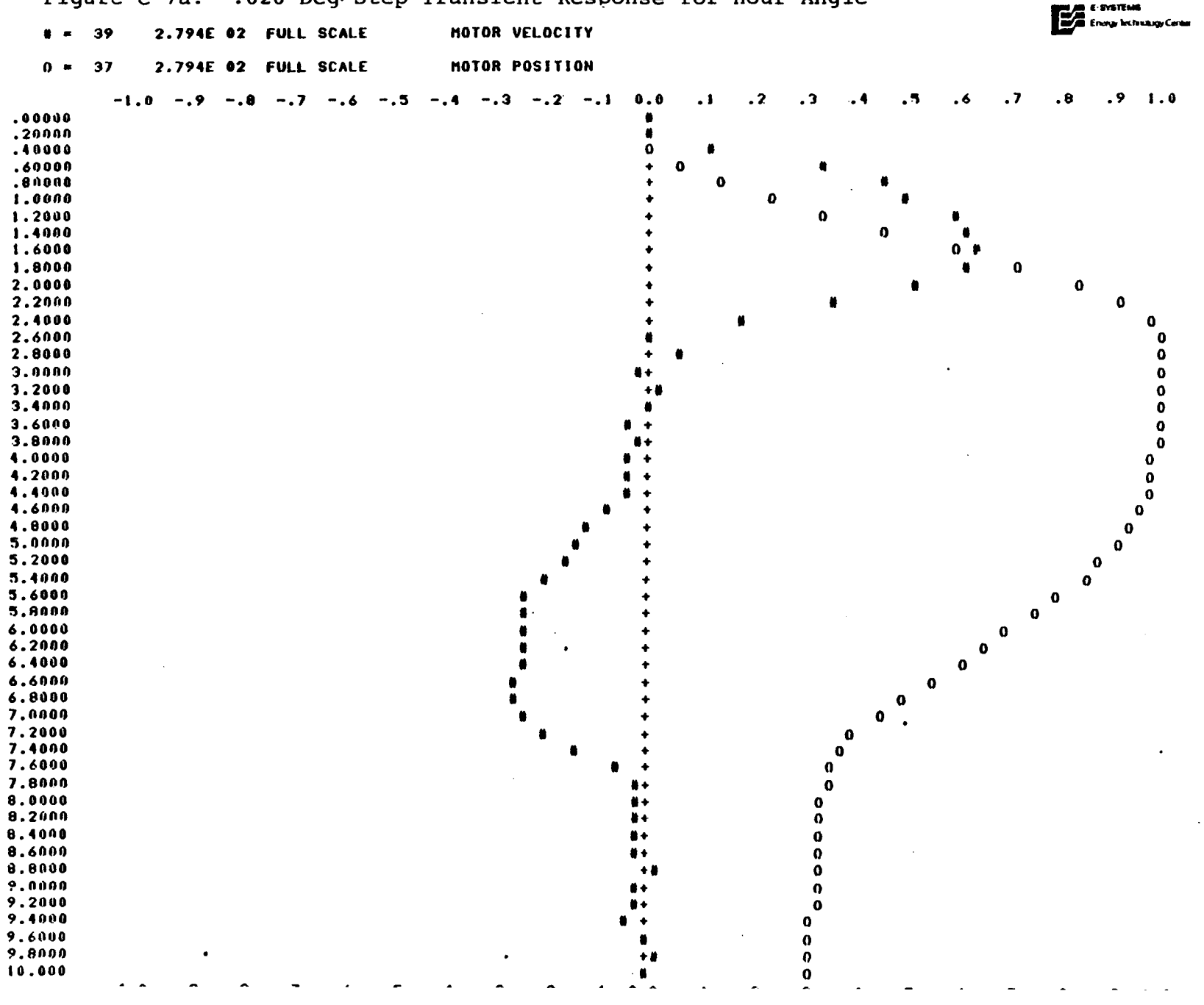

Figure C-7b. .020 Deg. Step Transient Response for Declination

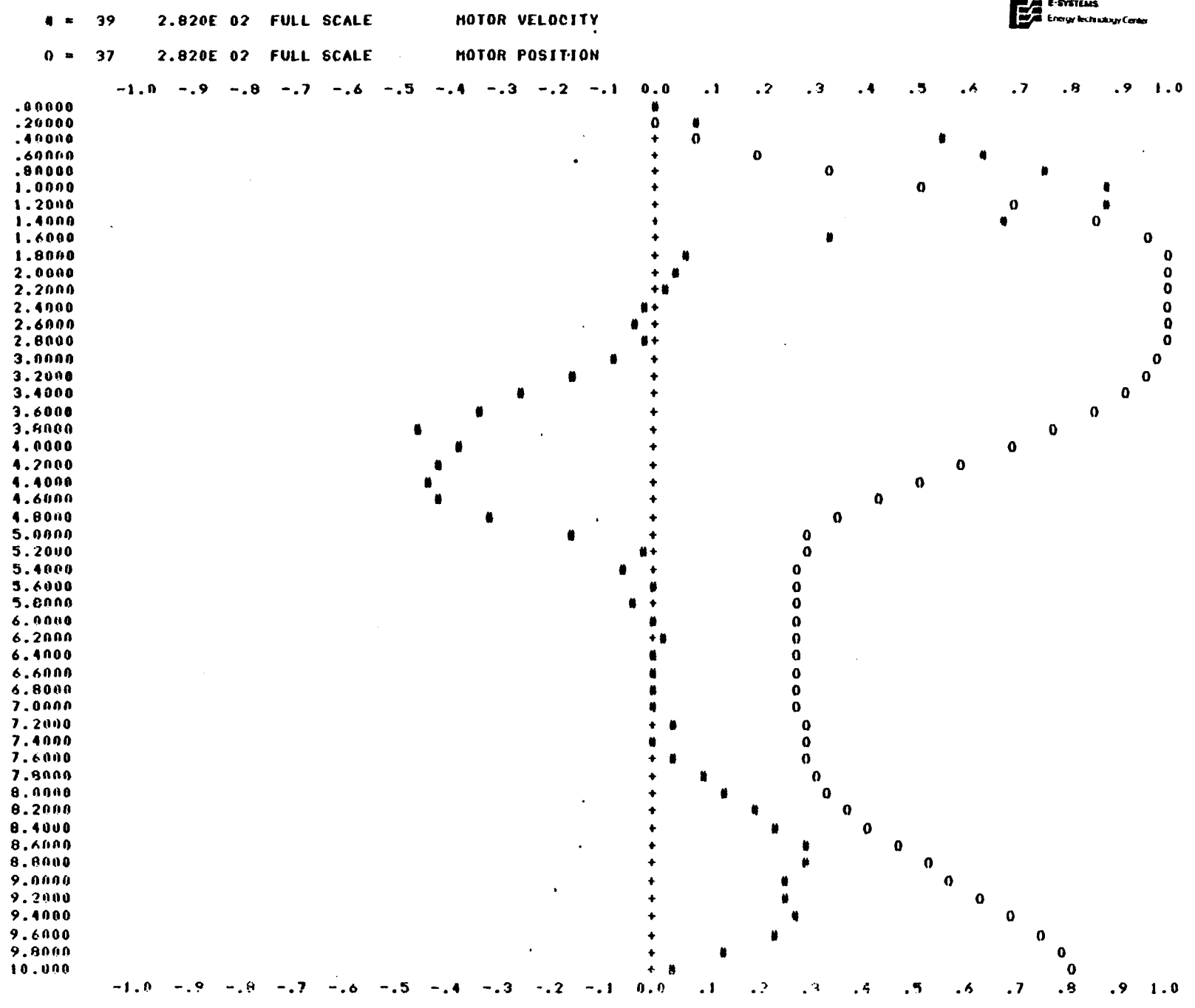

Figure C-7c. .02 Deg. Step Transient Response for Azimuth

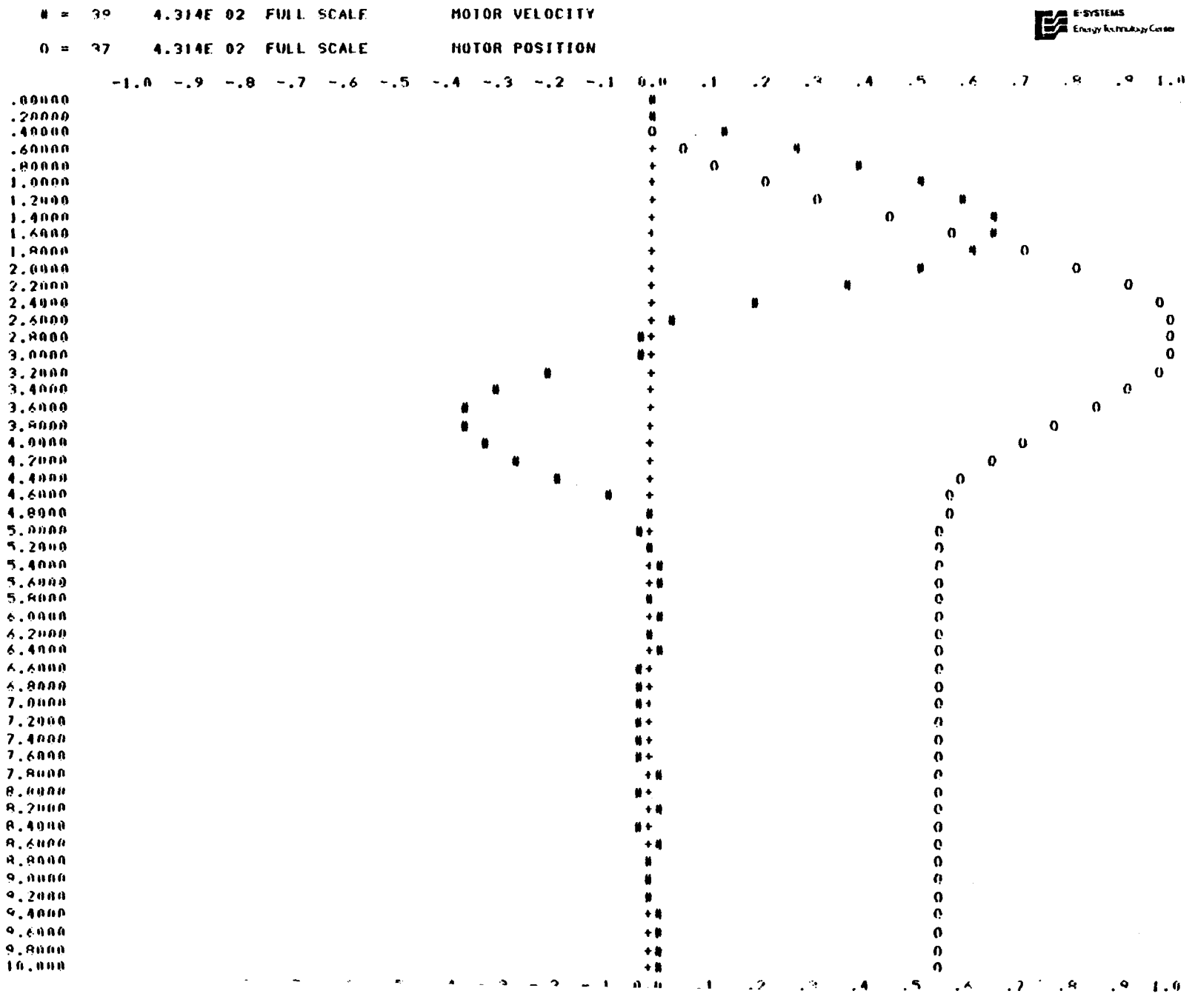

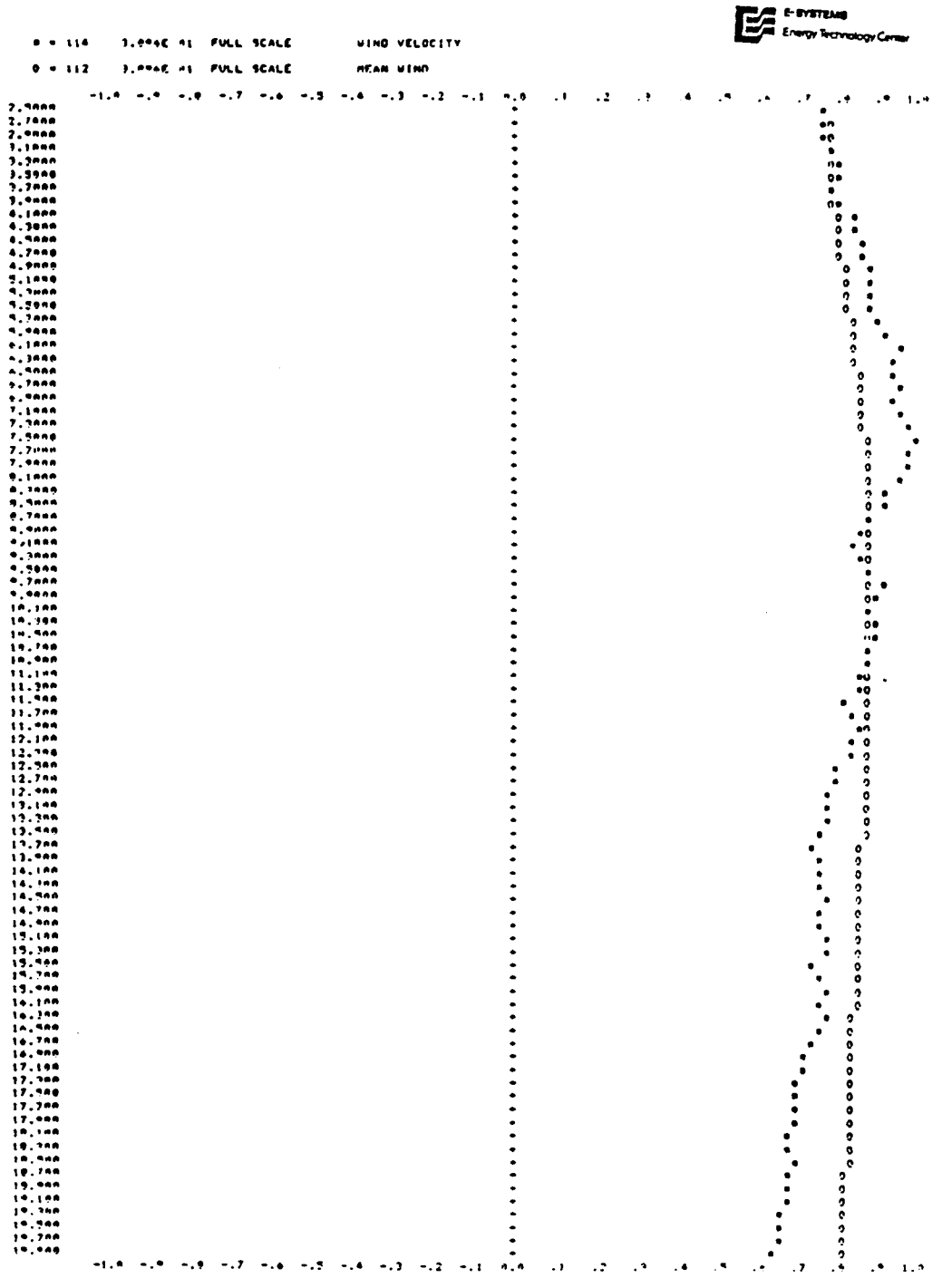

Figure C-8. 30 MPH Random Wind Transient Response For Hour Angle

operation this will primarily be used to position the system to and from the stow position. Once the system is positioned within the collector sensor range, the system will revert to the active track mode. In the event that the active track is lost, due to clouds, etc., the positioning mode will maintain the system at the nominal desired position.

Active Track Mode

In the active track mode, the solar sensor output is fed back directly to the control electronics, and the microcomputer is only used for monitoring. The sensor control will continuously position the receiver in the focal cone position where maximum energy transfer occurs. In the active track mode, the control system will compensate for wind loads, and structural deformations.

Emergency Mode

Emergency shutdown is a vital system function due to the high temperatures and pressures that develop within the system. The potential damage to a valuable installation necessitates a complex and effective system for protection of personnel and the facilities. Emergency shutdown is controlled by a software program designed to protect against all possible malfunctions. Each potential malfunction has an associated action which is designed to facilitate shutdown at a controlled rate.

The program is resident in the collector control module (CCM) in ROM. This will allow the microcomputer to recognize conditions

requiring shutdown and execute the proper actions to bring the solar collector to a safe off-line condition. In the event that the CCM fails to execute the shutdown sequence, the central control system (CCS) overrides the CCM by applying direct control voltages to the drive motor and control values. The CCM is also disabled simultaneously to prevent conflicting control signals.

APPENDIX D. MIRROR SURFACES AND MIRROR PANELS

This section summarizes the results of the development of design, fabrication, and materials recommendations for the concentrator mirrors and mirror panels. The task efforts have included analysis, design and fabrication of candidate full scale reflective mirror panels. Tests of candidate panels were conducted for load supporting characteristics, moisture susceptability, focus distortion, and thermal gradients. Candidate mirror materials were evaluated to determine their reflectance characteristics (new and weathered), weatherability, ease of fabrication, abrasion resistance, impact resistance and thermal properties.

D-1 MIRROR PANELS

The concentrator panels provide a rigid base on which the mirrors can be mounted to the basic concentrator support structure. This panel is a structural member which must withstand wind and dead weight loads while maintaining the desired solar image projected on the receiver. Seven panel designs were identified by E-Systems as having sufficient merit for consideration as candidates for the FMDF concentrator panel. These designs are:

1. Aluminum honeycomb with aluminum or fiberglass faces
2. Paper honeycomb with steel faces
3. Aluminum Z-member panel with aluminum skin
4. Steel Z-member with steel skin

5. Steel cross-corrugated panels
6. Fiberglass reinforced plastics
7. Rigid structural foam with and without reinforcements.

Panels 3 and 6 were eliminated as a result of an initial evaluation based on costs of materials and manufacture, service life, strength and stiffness to weight, physical and mechanical properties and compatibility with the candidate reflective material, mirrored glass. Table D-1 presents manufacturing costs data for the remaining candidate panels. The steel panels followed by the paper honeycomb panel show a definite cost advantage over other candidate panels.

Prototypes of panels a-d were constructed and tested to evaluate fabrication requirements, structural and load bearing characteristics, ability to maintain the desired radius of curvature, impact resistance, and mirror bonding characteristics. Additionally, the Hexcel Corporation made an independent analysis of the panel construction using aluminum honeycomb core material.

As a result of these evaluations (and results discussed in the following paragraphs), the paper honeycomb core panel design has been chosen as the prime panel design for the RPS. Its cost was within 15% of that of the two steel panel designs, the paper honeycomb core design offered a more uniform core support to the reflecting surface with resulting improved resistance to impact and differential thermal expansion problems, and an evaluation of the cost estimates indicated the potential for lower costs than that given in Table D-1.

TABLE D - 1

COSTS TO MANUFACTURE MIRROR PANELS IN LARGE QUANTITIES (300,000 ft.^{2})

Type of Panel	Panel Cost Labor/Materials $/M^2	Mirror Cost $/M^2	Mirror Bond Labor $/M^2	Total $/M^2
a. Steel Z-Member	28.26	6.95*	5.00	40.21
b. Steel Double Corrugated	29.13	6.95	5.00	41.08
c. Structural Urethane Foam	56.40	6.95	5.00	68.35
d. Paper Honeycomb Core	35.20	6.95	5.00	47.15
e. Aluminum Honeycomb Core	68.98	6.95	5.00	80.93

---

* Carolina Mirror Corp. price

D-2 RECOMMENDED PANEL DESIGN

A schematic drawing of the paper honeycomb core recommended panel design is shown in Fig. D-1. The design consists of a composite structure using 3.0 in. thick paper honeycomb core with a 1/8 in. thick second surface mirror and a .036 in. thick steel facing bonded with epoxy resin. Fig. D-2 shows a completed 4 ft. by 6 ft. panel as-assembly.

D-2.1 Structural Analysis

A structural analysis of the candidate panel designs was conducted in the initial phase of the project. At present, a more refined computer model is being formulated, based on load and deflection data from panel tests, which will allow the panel deflections, i.e., optical error, and stresses to be determined analytically.

D-2.2 Fabrication

The purpose during this segment of the project was to determine if production size panels could be produced economically and maintain the contour accuracy required. The tooling required must be built economically and accurately using existing techniques and materials. The panels must use inexpensive, readily available materials that are amenable to high volume production.

One potential problem associated with the paper honeycomb core design was the susceptability of the paper honeycomb to moisture. To solve this problem, the paper honeycomb is resin dipped and cured. This process improved its moisture resistance and strength. Specific

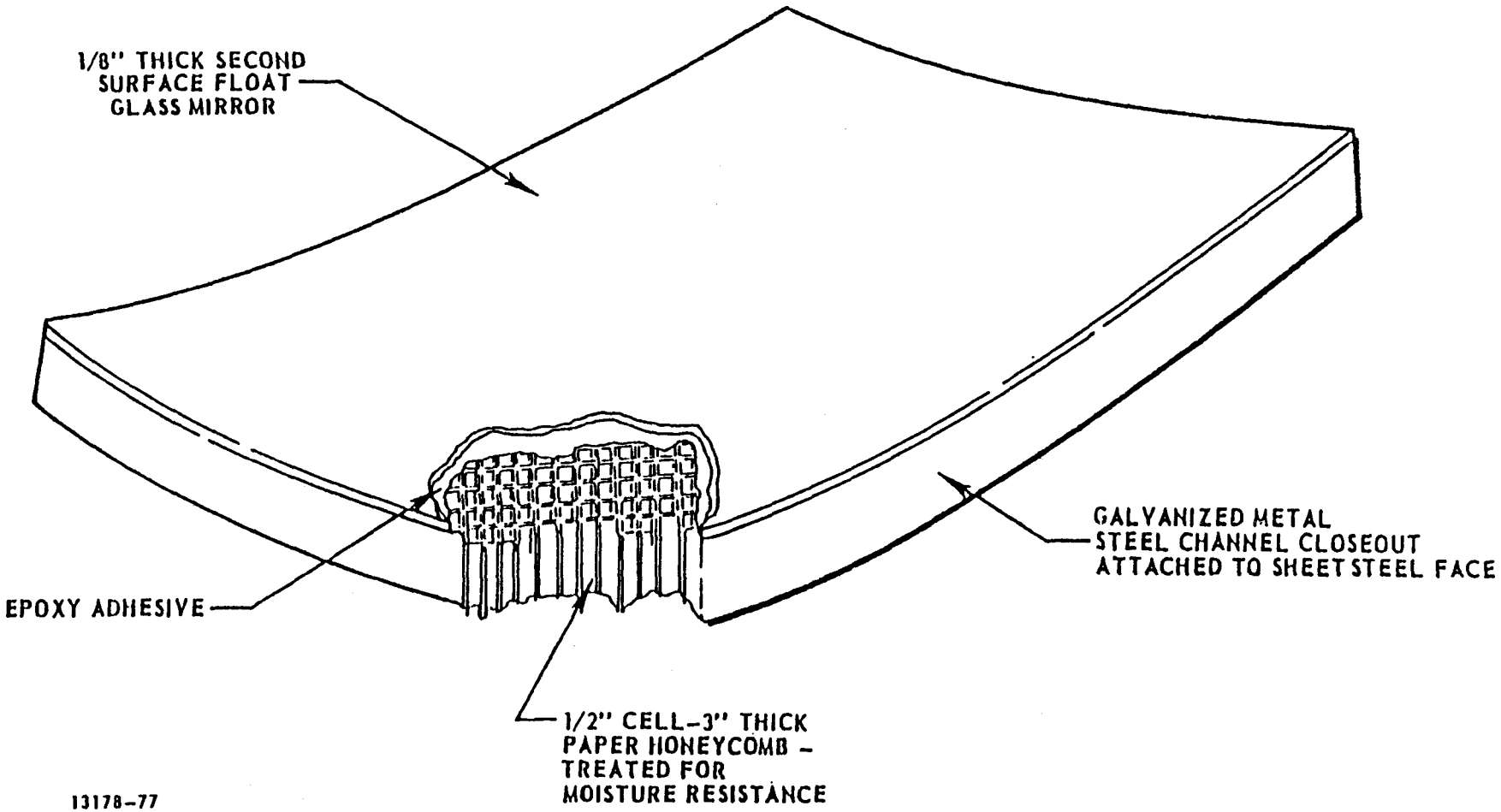

Fig. D-1. Paper Honeycomb Core Panel

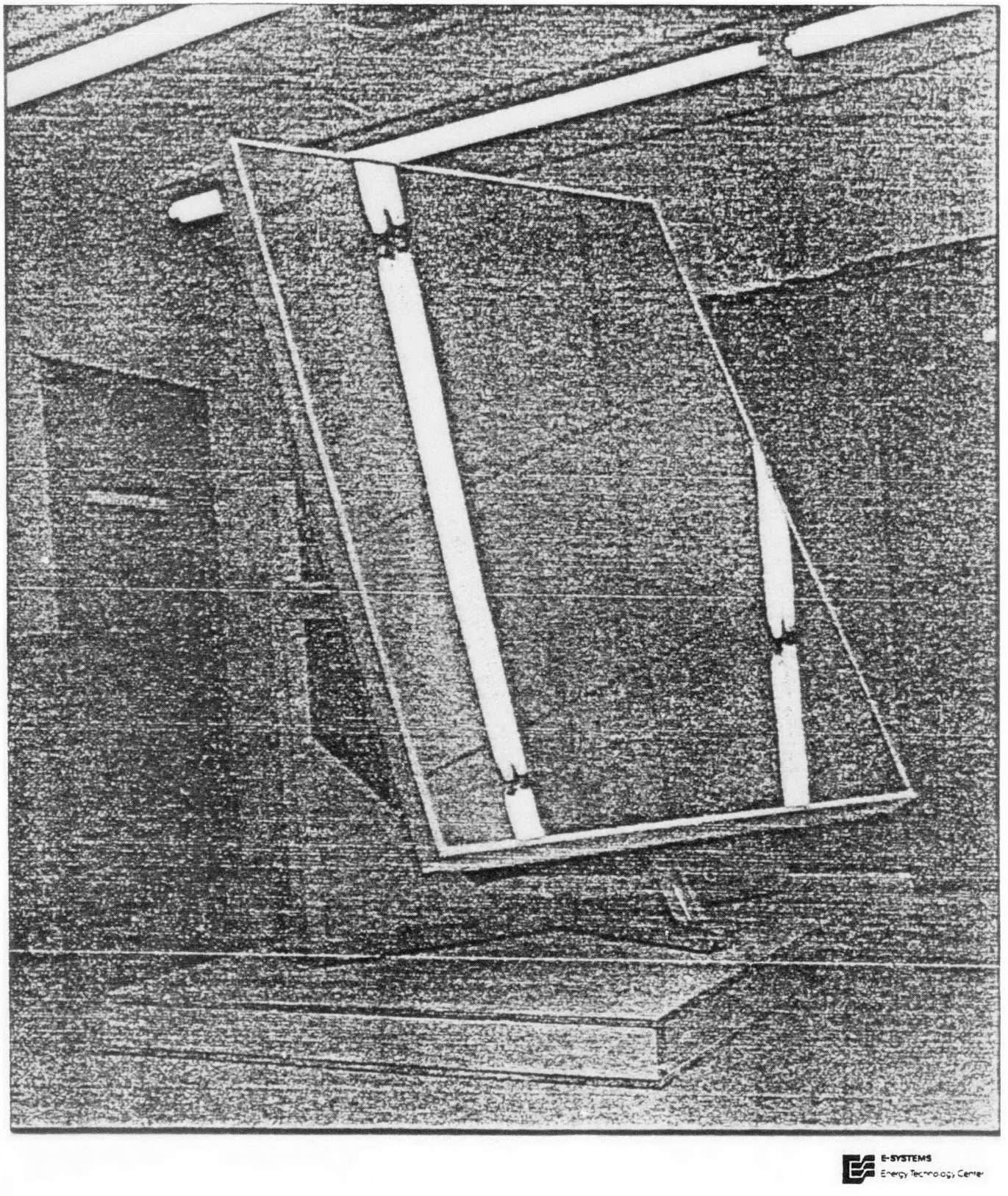

Figure D-2. Completed Panel

tests of a 44" x 44" x 2" panel indicated a weight pickup of the core of only 4.33% with an increase in stiffness by a factor of two. Resin dipped paper honeycomb has been exposed to the environment for approximately six months without any visual deterioration.

A small male mold was fabricated with a 115.47 ft. spherical radius and several 2 ft. by 2 ft. panels were produced initally to check the mold accuracy and fabrication technique. A panel was then checked visually for single and multiple focii and distortion by reflecting the image of the sun on a black surface. The diameter of the image was approximately 10.0 in. with no apparent distortions.

The largest size production panel for a 200 ft. aperture FMDF is approximately 6 ft. by 4 ft. Another mold was fabricated with a 115.47 ft. spherical radius and approximately 110 in. in diameter. Several 3 ft. by 3 ft. panels were produced from this mold to rough check the accuracy.

Image tests were made of these panels and the results indicated a significant variance in images between the panels. This was caused by a non-uniform pressure on the panel during fabrication. This problem was solved by fabricating the panels with a vacuum bag which produces uniform pressure on the panel. Five 4 ft. by 6 ft. panels and two 2 ft. by 2 ft. panels were fabricated on the mold using this technique. These panels were complete with edge closeouts and mounting bolt holes.

D-2.3 Sizes

Table D-2 lists the sizes and quantities of panels required for one 200 ft. aperture FMDF concentrator. The indicated panel dimen-

TABLE D- 2 PANEL SIZES FOR 200 FT. APERTURE DIAMETER CONCENTRATOR

Quantity	Panel No.	Size (including Gap)
41	1	4' - 0.36" X 6' - 0.53"
82	2	4' - 0.36" X 6' - 0.53"
82	3	4' - 0.36" X 6' - 0.44"
82	4	4' - 0.36" X 6' - 0.28"
82	5	4' - 0.36" X 6' - 0.00"
82	6	4' - 0.36" X 5' - 11.65"
82	7	4' - 0.36" X 5' - 11.21"
82	8	4' - 0.36" X 5' - 10.68"
82	9	4' - 0.36" X 5' - 10.07"
82	10	4' - 0.36" X 5' - 9.37"
82	11	4' - 0.36" X 5' - 8.59"
82	12	4' - 0.36" X 5' - 7.73"
82	13	4' - 0.36" X 5' - 6.78"
82	14	4' - 0.36" X 5' - 5.75"
82	15	4' - 0.36" X 5' - 4.64"
66	16	4' - 0.36" X 5' - 3.45"
66	17	4' - 0.36" X 5' - 2.18"
66	18	4' - 0.36" X 5' - 0.84"
66	19	4' - 0.36" X 4' - 11.42"
66	20	4' - 0.36" X 4' - 9.94"
66	21	4' - 0.36" X 4' - 8.38"
66	22	4' - 0.36" X 4' - 6.75"
66	23	4' - 0.36" X 4' - 5.05"
46	24	4' - 0.36" X 4' - 3.30"
46	25	4' - 0.36" X 4' - 1.47"
46	26	4' - 0.36 X 3' - 11.59"
46	27	4' - 0.36" X 3' - 9.65"
46	28	4' - 0.36" X 3' - 7.66"
46	29	4' - 0.36" X 3' - 5.61"
46	30	4' - 0.36" X 3' - 3.51"
46	31	4' - 0.36" X 3' - 1.36"
2085 (Total)		

sions include a nominal 3/16 in. gap around the entire circumference of each panel. The dimensions are mean values relative to the basic 4' x 3', 4' x 4', 4' x 5', and 4' x 6' sizes as the geometry of an individual panel may not be exactly rectangular.

D-2.4 Testing

The testing of the concentrator panels encompasses four areas: structural or load testing, focus, thermal, and impact testing. Load testing is required to prove the structural integrity of the panel under survival conditions and for physical data which will be used to develop computer models. Focus testing is used as a qualitative measurement of tooling accuracy and of fabrication constancy. Focus testing will be used throughout the total production run of panels as a quality control feature. Thermal testing of the panels is required to examine the fidelity of the facing bond to the core and reveal if the temperature gradient within the panel assembly is critical.

Load Tests

A 6 ft. by 4 ft. panel constructed of 3 in. resin dipped paper core honeycomb with 1/8 in. thick glass mirror and 0.036 in. thick steel sheet facings was set on four simple supports at the four corners of the panel. A dial indicator was placed under the center of the panel. Lead shot bags were uniformly distributed over the surface of the panel and the dial indicator readings were recorded. The maximum load on the panel was 650 lbs. and the maximum deflection was .059 in. Figure D-3 shows the results of this test. There was no

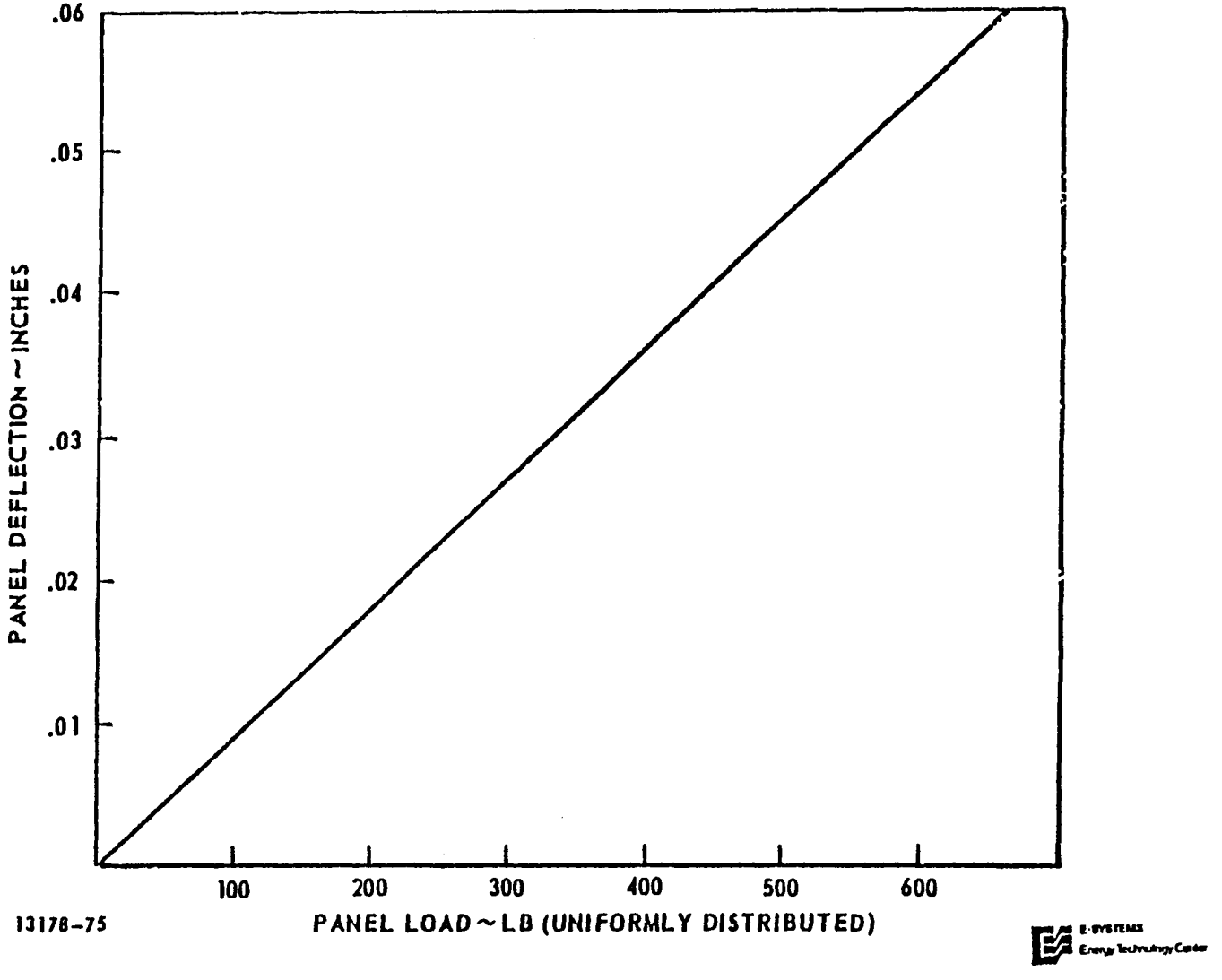

Fig. D-3. Load vs. Deflection for 4' x 6' Panel

permanent damage visually observed as a result of this test. The results of these load-deflection tests were used as input to the mirror panel error analysis to predict the beam deflection errors due to surface deformation.

Focus Tests

At the present time, focus testing is accomplished as shown in Fig. 4. The image tests are made in the morning and in the afternoon when both times are correlated to a 22^0 sun elevation angle. The image focused upon the target is photographed when the sun, mirror and image subtend an angle in a vertical plane so that image aberration is kept to a minimum. The negative of the photographed image is then traversed with a light intensitometer and typical results are shown in Fig. D-5. By integrating the area under the curve, the diameter of the image that represents 95% of the light energy can be established. Comparing this diameter with a theoretically perfect image diameter of 6.44 in. provides a qualitative measurement of the panel manufacturing error. Additional tests are currently in progress in conjunction with the panel thermal tests and will be completed by the end of the contract period.

Thermal Tests

A one foot square panel was fabricated with five thermocouples placed inside the assembly as shown in Figure D-6. The thermal test sequence is described as follows. The instrumented panel along with a 6 ft. by 4 ft., and a 2 ft. by 2 ft. panel is placed in

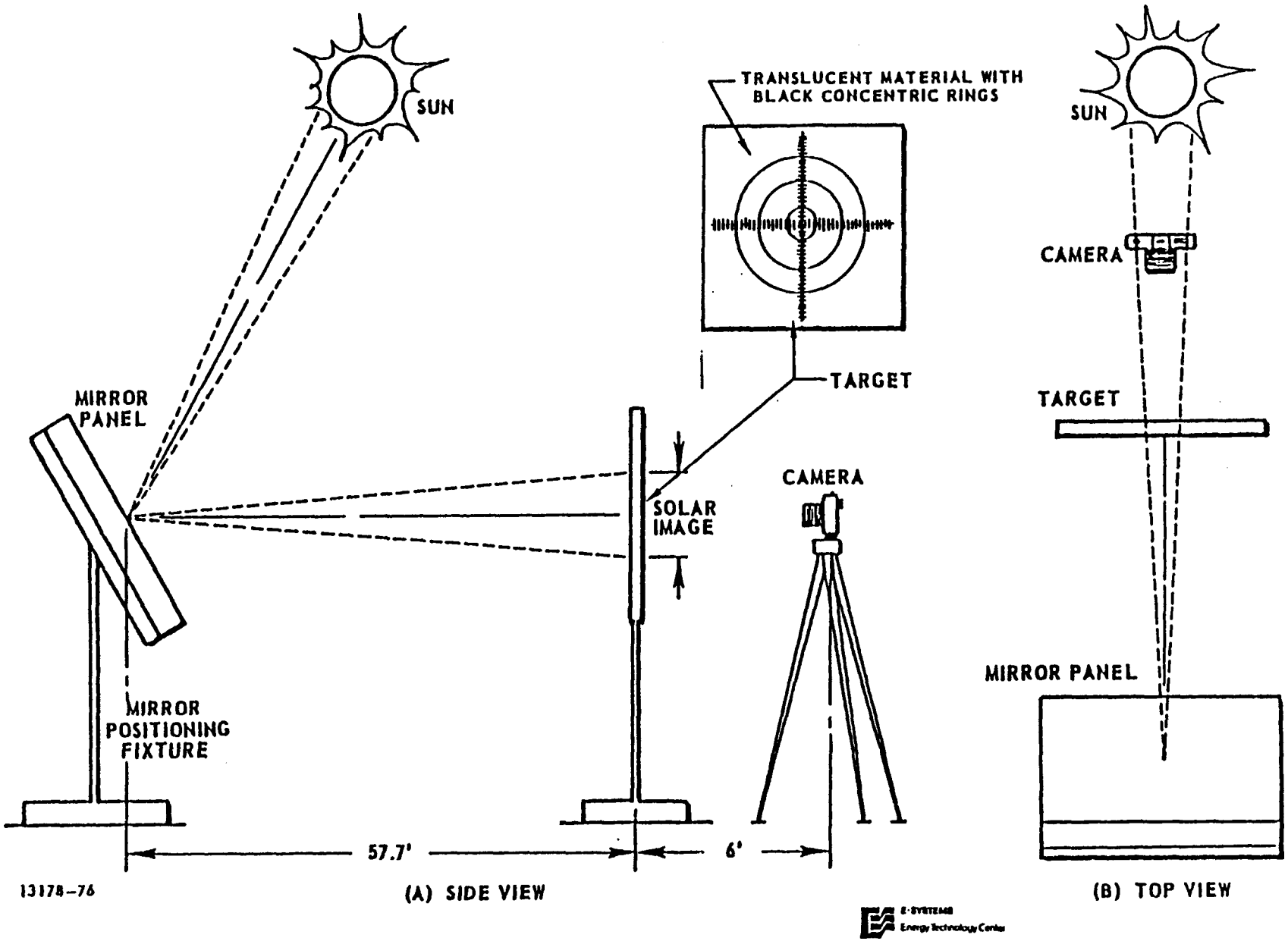

Fig. D-4. Solar Image Test Setup

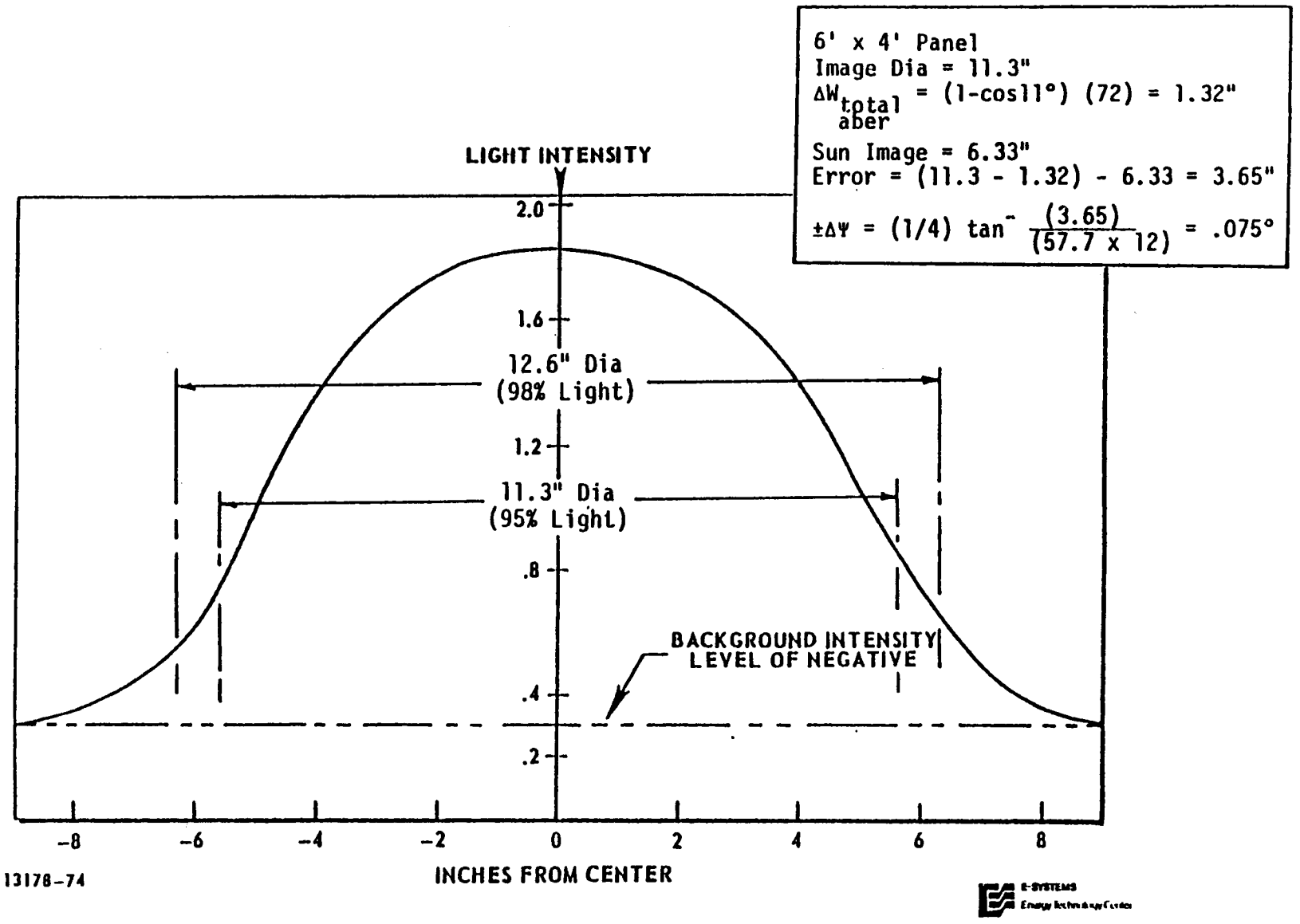

Fig. D-5. Image Light Intensity

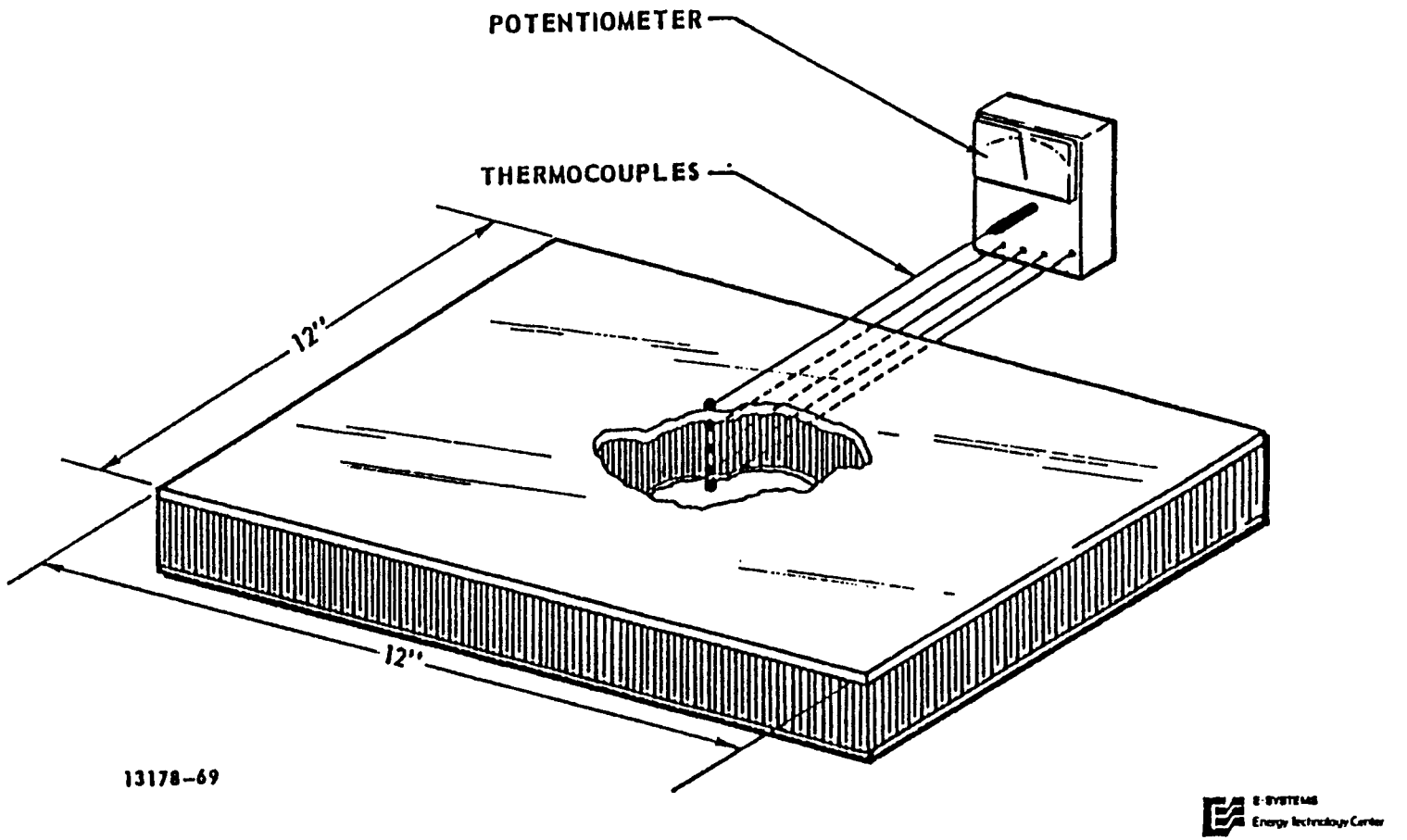

Fig. D-6. Thermal Test Monitor Panel

an environmental test chamber. The panel with the thermocouples is used to monitor the internal temperatures of the panel and compare them to the ambient temperatures. Prior to each thermal test and subsequent to each thermal test, the panels are tested optically by the method outlined in the previous section. Visual inspection of the panels immediately after each test determined if the panel has suffered obvious physical damage. These tests are currently underway and will be completed by the end of the contract period.

The thermal tests to be accomplished are:

1. 120°F soak for 8 hours
2. 0°F soak for 16 hours
3. Cyclic temperature gradient of 60°F to 120°F and 0°F to 75°F for 30 cycles each
4. Thermal shock stabilized panel assembly at 120°F and then sprayed water at 73°F uniformly over panel.

Hail Impact Tests

Hail impact tests on panels configured to the nominal design were conducted by TTU. The prime design performed as expected and resisted hail impact tests without damage to the mirrors. The prime panel design will not be revised at this time. The results of these tests are presented in Appendix F and show a mininimum breakage velocity of 116 mph and an average value of 128 mph for the sample tested.

Projected Improvements

The primary areas to be investigated for improvement are in error definition, mold refinement and improved fabrication. The

focus test discussed in the previous section yields only a broad measure of panel surface accuracy. A laser ray trace test procedure has been identified as having the ability to provide more detailed measurements of surface error. A schematic diagram of the required test facility is shown in Fig. D-7. Using this facility, localized imperfections in the mirror surface can be identified and correlated to the corresponding mold location and corrected if required. It is also felt that an epoxy rather than plaster mold will be used for production panels to achieve improved dimensional stability and durability.

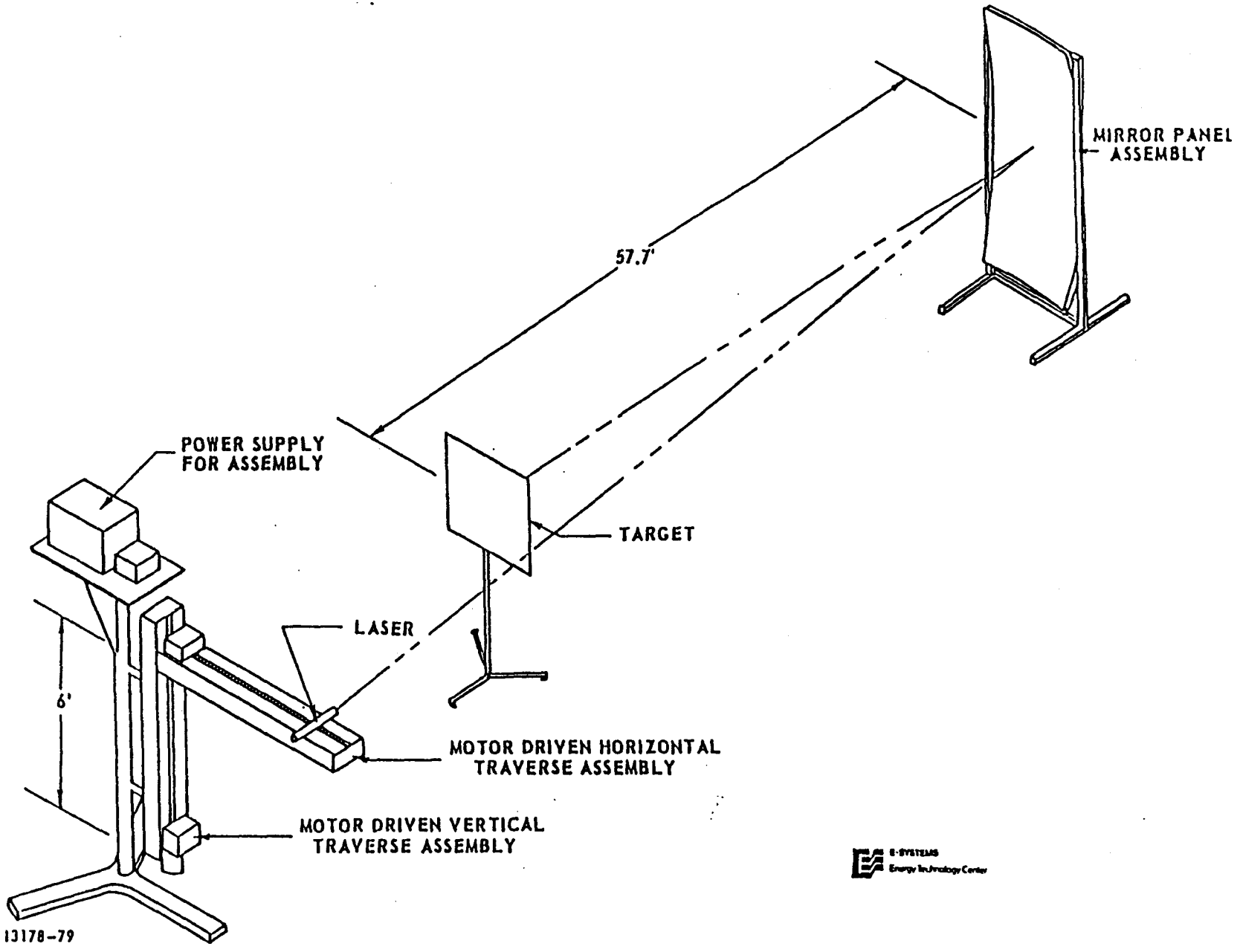

Fig. D-7. Laser Ray Trace Test

D-3 MIRROR SURFACES

A wide range of mirror materials were considered as candidates for the concentrator reflecting surface. These materials fall into five distinct categories: (1) glass mirrors, both first and second surface, (2) thin transparent vacuum metallized polymeric films, (3) vacuum metallized 1/16 in. and 1/8 in. plastic sheets, (4) chemically polished and coated thin sheets of high purity aluminum, and (5) electroplated substrates. Candidate reflective materials within these categories were obtained from known manufacturers. Table D-3 lists the materials considered along with the manufacturer, costs and reported reflectivity. Test samples, 4" x 4", were obtained by E-Systems and sent to Texas Tech University for reflectivity measurements and initiation of environmental/weathering tests. Table D-4 lists the seven candidate reflective materials that were deployed at Crosbyton.

The mirror samples were deployed in the field at Crosbyton for eight months after the reflectivities of all samples had been measured. Eight mirror samples sets were at ground level and three sample sets were at 95 ft. above ground. A set consisted of five mirrors of the same type, each with a different orientation. Four of these mirrors were mounted on the vertical sides of a cubic structure and faced N.W., S.W., S.E., and N.E., respectively. The fifth sample of each set was mounted horizontally on the top face of the cube. Table D-5 shows the deployment scheme used. Additionally, a control sample of each type was kept in the laboratory, out of the weather, for comparison with the exposed samples.

TABLE D-3 CANDIDATE REFLECTIVE MATERIALS

REFLECTIVE MATERIAL	MANUFACTURER	COST -$/Surface^2	Reflectivity, % (Reported by Mfgr. or from Literature)
Scotchcal 5400	3M Company	7.10	85
Aluminized Teflon Solar Mirror-Material	Sheldahl Company	9.25	75 - 87
Second Surface Chemically Deposited Silver Float Glass Mirror Flat (1/8-inch thick)	Carolina Mirror Corp.	6.95	65 - 88
	Gardner Mirror Corp.	7.06	
	Toledo Plate & Window Glass Company	6.68	
Second Surface Chemically Deposited Silver Glass Mirror-Curved (1/8-inch thick)	Donnelly Mirror Co.	17.75	89
Front Surface Glass Mirror	Liberty Mirror Co.	$387 *	97
Aluminized Acrylic 1/8-inch	Rohm and Haas	21.40	80 - 85
Aluminized Acrylic 1/16-inch	Ram Products	19.15	
Kinglux C-4	Kingston Industries	15.20	87
Alzak	Alcoa	20.02	67 - 83
Coilzak	Alcoa	5.26	80

*This mirror is made by vacuum metallizing with silver and protecting with an oxide coating. McDonnell-Douglas Astronautics Company in Reference I-2 reports on a front surface glass mirror having a reflectivity of 90% and a cost of $7.20/M^2; however, samples of this material are not available at this time.

Note: Reflectivity measurement methods are not standardized; as a consequence many of the reported values may be peak values rather than integrated average values. Average values are often 7 - 12% less than peak values.

TABLE D-4 MIRROR TYPES TESTED

TYPE	MANUFACTURER	REFLECTIVITY %	APPROX. COST $/m^2
Scotchal 5400	3M Company	85	7.10
Carolina Second Surface Chemically Deposited Silver Float Glass Mirror Flat (1/8-inch thick)	Carolina Mirror Corp	95	6.95
Donnelly Second Surface Chemically Deposited Silver Glass Mirror Curved (1/8-inch thick)	Donnelly Mirror Corp	89	17.75
Plexiglas Aluminized Acrylic 1/8-inch	Rohm and Haas	83	21.40
Ram Acrylic Aluminized Acrylic 1/16-inch	Ram Products	83	19.15
Kinglux Rolled Aluminum	Kingston Industries	62	15.20
Alzak Rolled Aluminum	Alcoa	61	20.02

TABLE D-5 THE DEPLOYMENT OF MIRROR SAMPLES

Type	Orientation NW	SW	SE	NE	Horizontal
	Ground Level Test				
Scotchcal	#1	2			
Alzak	1	2	3	4	5
Ram Acrylic	1	2	3	4	5
Glass	1	2	3	4	5
Carolina	2	1			
Plexiglass	6	7	8	9	10
Kinglux	1	2	3	4	5
Donelly	1	2			
	Elevated Test				
Glass	#6	7	8	9	10
Plexiglass	1	2	3	4	5
Alzak	6	7			

D-3.1 The Reflectivity Measurements

The mirror reflectivities were measured using an apparatus described in a previous report and shown in Fig. D-8. A nearly parallel beam of light from an incandescent source impinged on the sample and the intensity of the specularly reflected beam was measured using a silicon photocell. This value was compared with the straight through intensity (no mirror) measured with the same detector, and the reflectivity determined from the ratio. The divergence of the incident beam was approximately 2 m rad. and the acceptance angle of the detector was 15 m rad. The incident beam was circular in cross section with a diameter of 0.7 cm. The accuracy of the reflectivities measured with this device is believed to be better than 1% for flat samples.

The Reflectivities of New Samples

The reflectivities of the new, unweathered samples have been reported in considerable detail in a previous report. Typical curves for glass and for plexiglass mirrors are shown in Figs. D-9 and D-10. Because of effects of rolling marks on the reflectivity of some aluminum samples, reflectivities of each sample were measured for two sample orientations differing by a 90^0 rotation about a surface normal. These two values were shown in the figure and for these samples, they represent a measure of the homogeneity of the mirror surface. As a precaution, one sample of each mirror type was retained in order to serve as a standard for guarding against system drifts.

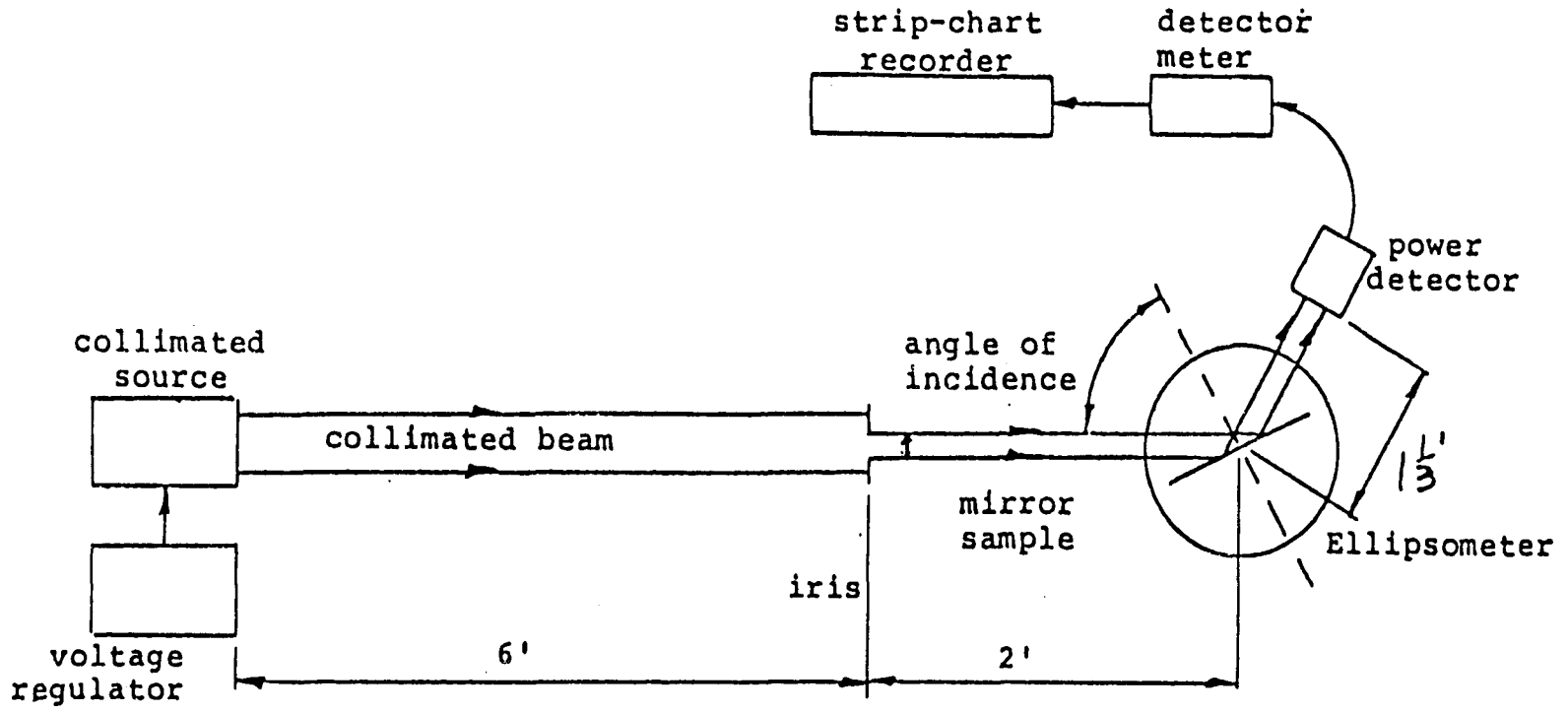

Fig. D-8. Schematic Diagram of the Set-Up to Measure the reflectivity of Mirror

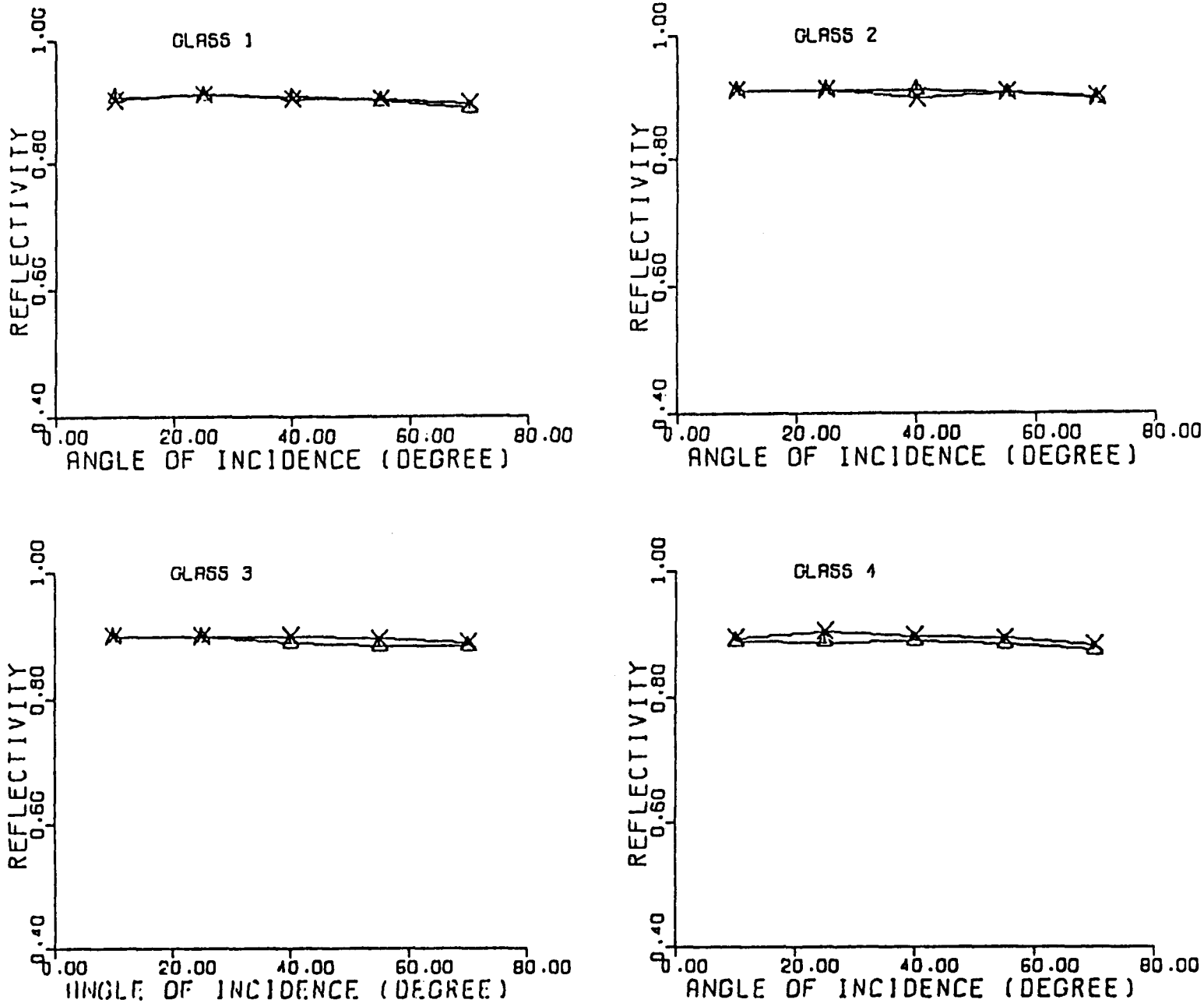

Fig. D-9. Reflectivity for Glass Mirrors

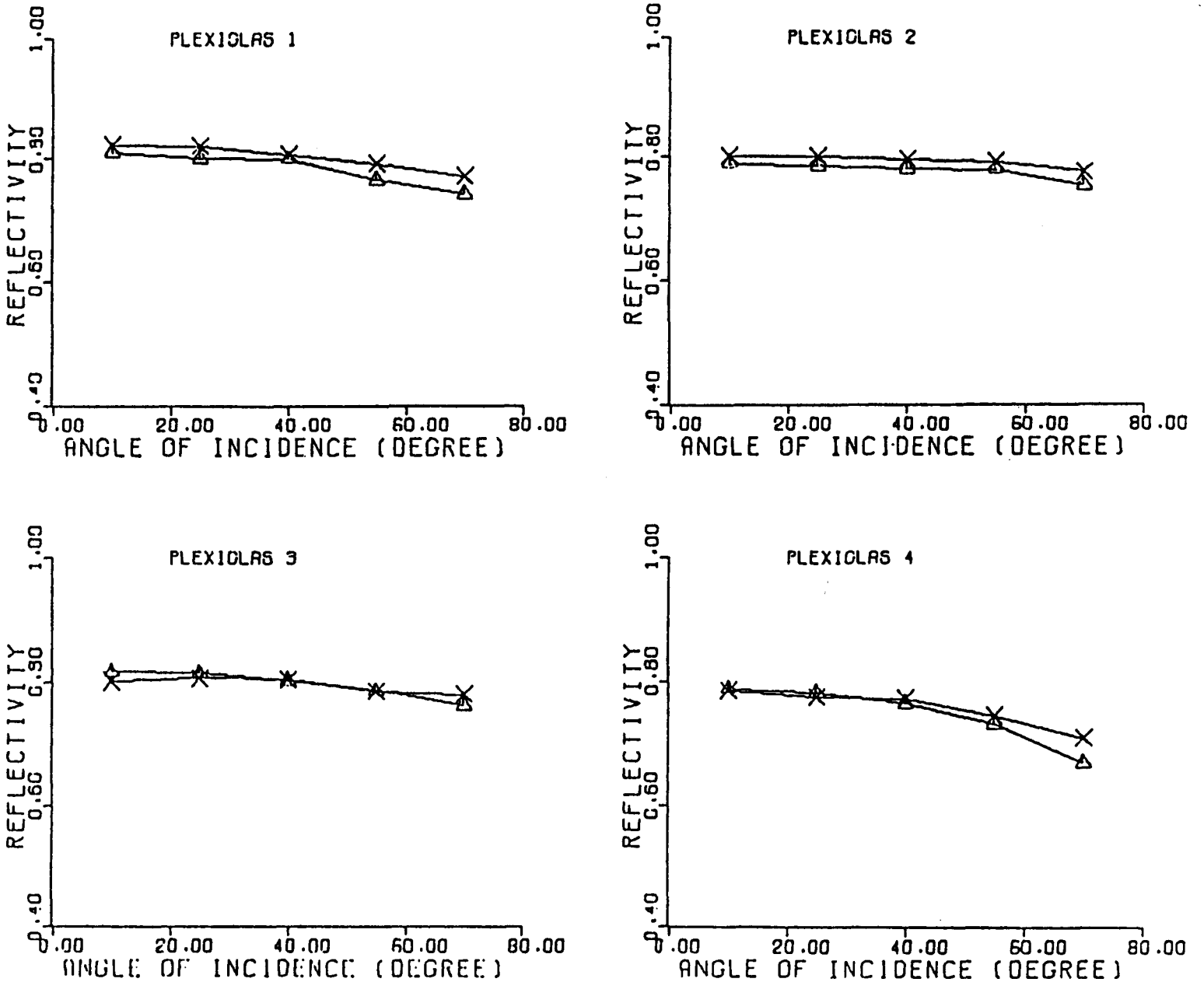

Fig. D-10. Reflectivity for Plexiglass Mirrors

The Reflectivities of Weathered Samples

After the samples had been exposed to the weather at the Crosbyton site for eight months, they were returned to the laboratory for further analysis. After a visual inspection, the reflectivity of each sample was again measured using the same reflectometer as previous employed. In all cases, the samples as received from the Crosbyton site had significantly reduced reflection coefficients. The average reflectivity loss as a function of angle of incidence is shown for each mirror type in Fig. D-11. The error bars represent the standard deviation for these averages. Qualitatively, these results were well correlated with the visual appearance of each sample. Some representative curves for the dirty plexiglass and glass mirrors are shown in Figs. D-12 and D-13.

The Effect of Gentle Rinsing

In order to determine the effectiveness of different cleaning programs, after the reflectivity measurements described above were made the samples were gently rinsed. Some samples were rinsed in flowing tap water, and the rest in a "Sparkleen" detergent solution. After allowing the samples to dry, the reflectivities were again measured. These results are shown for the glass and for the plexiglass samples in Fig. D-14 and 15. Although the statistical noise is large, it appears that the detergent rinse gives somewhat better performance than the water rinse as would be expected since the detergent should dissolve some of the greasy deposits and the wetting agent should reduce spotting from minerals dissolved in the tap water.

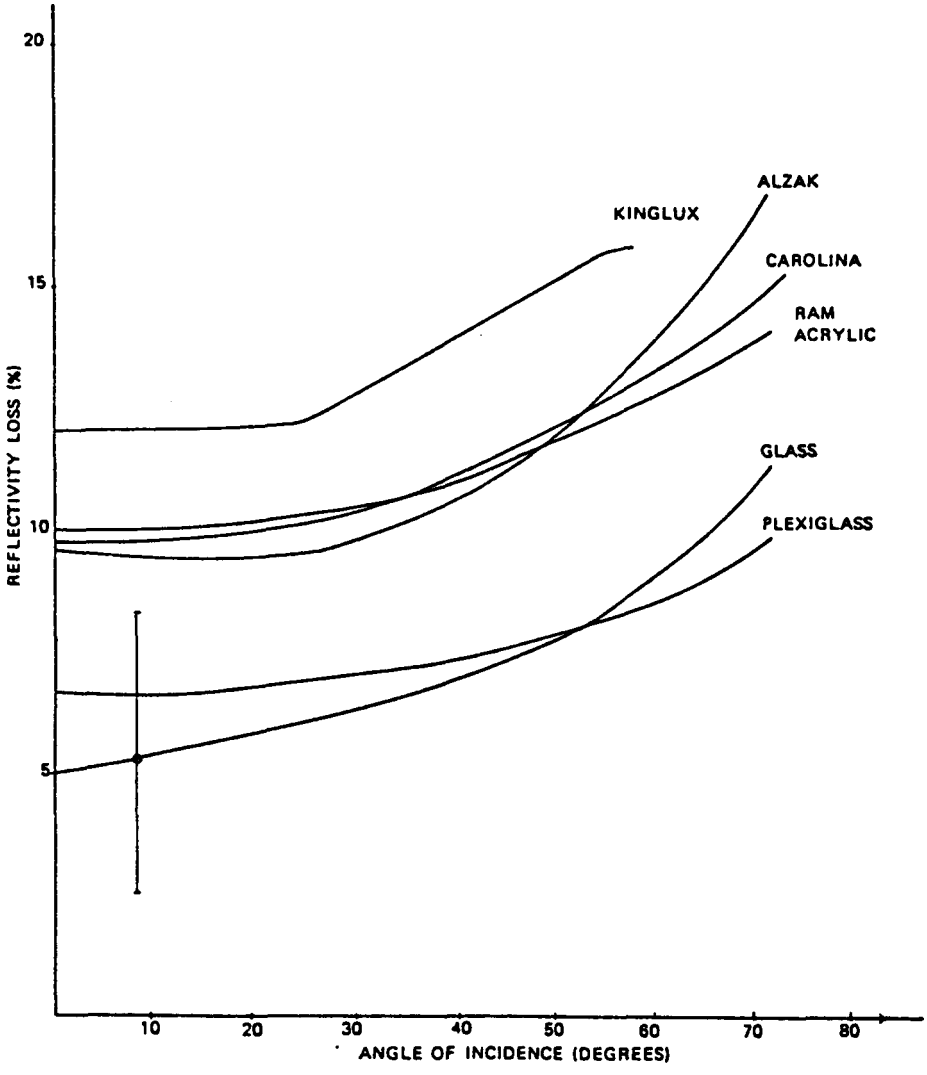

Fig. D-11. AVERAGE REFLECTIVITY LOSS FOR EACH TYPE OF MIRRORS

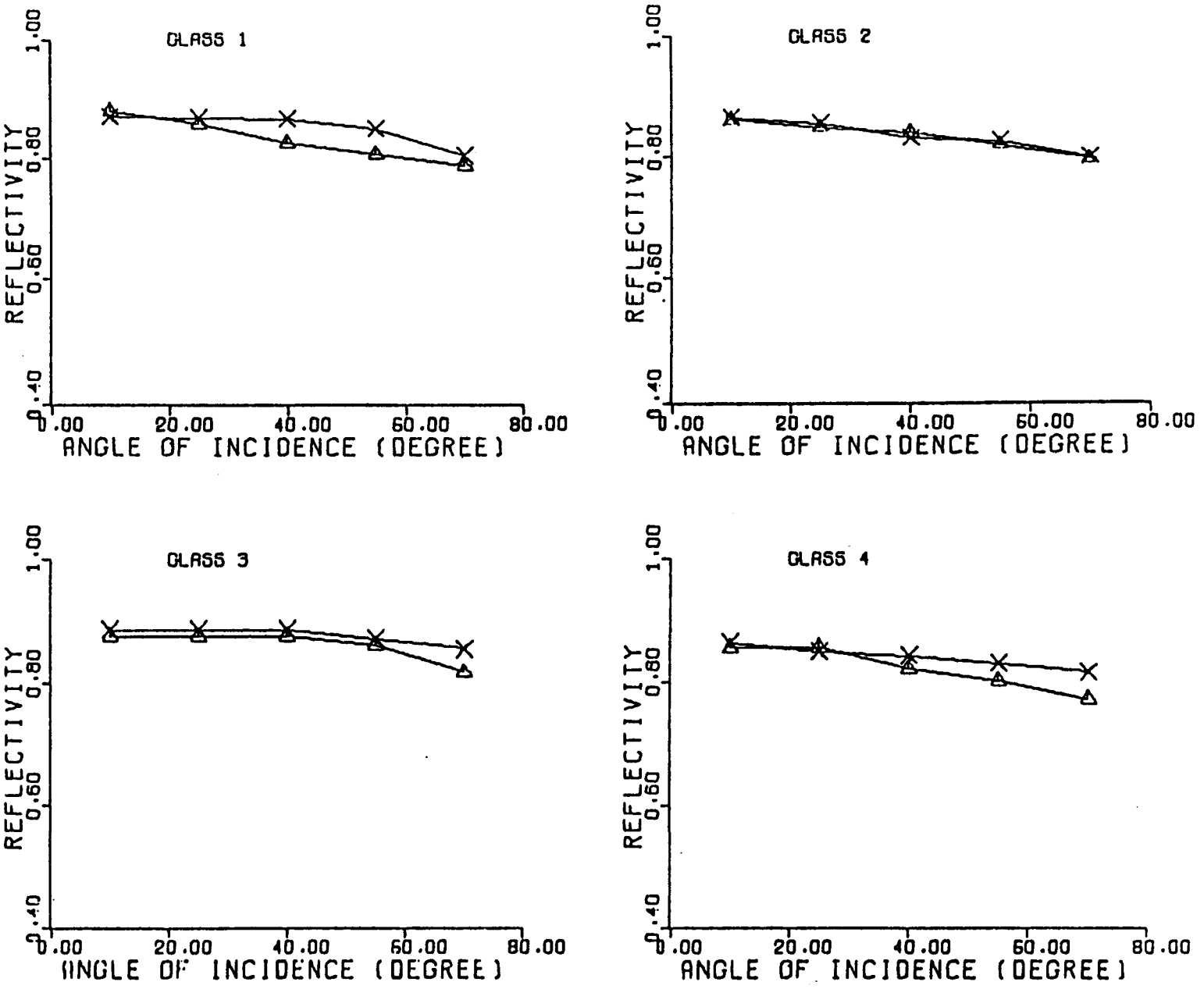

Fig. D-12. Reflectivity for Dirty Glass Mirrors

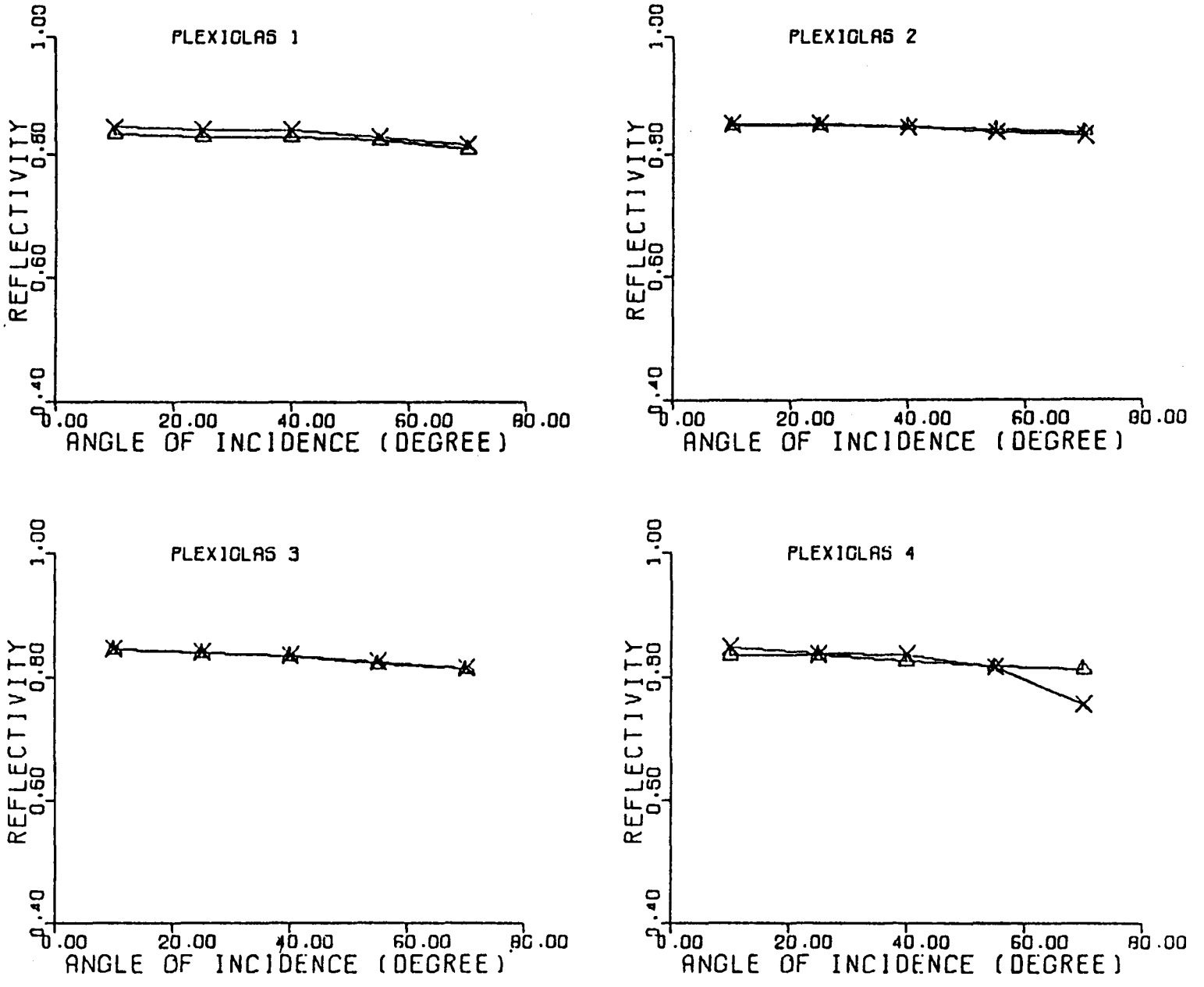

Fig. D-13. Reflectivity for Dirty Plexiglass Mirrors

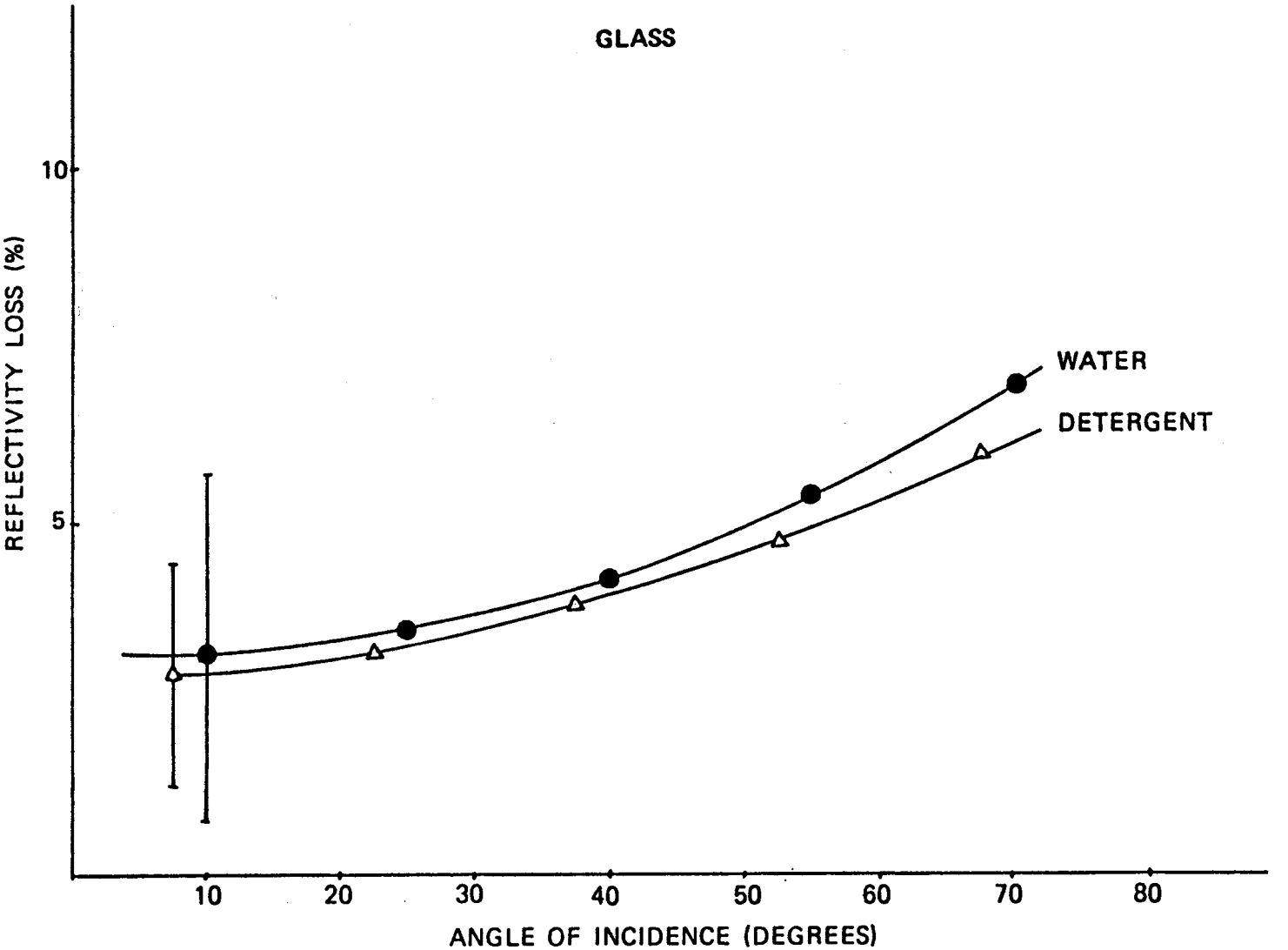

Fig. D-14. REFLECTIVITY LOSS FOR "WATER" AND "DETERGENT" RINSED GLASS MIRROR

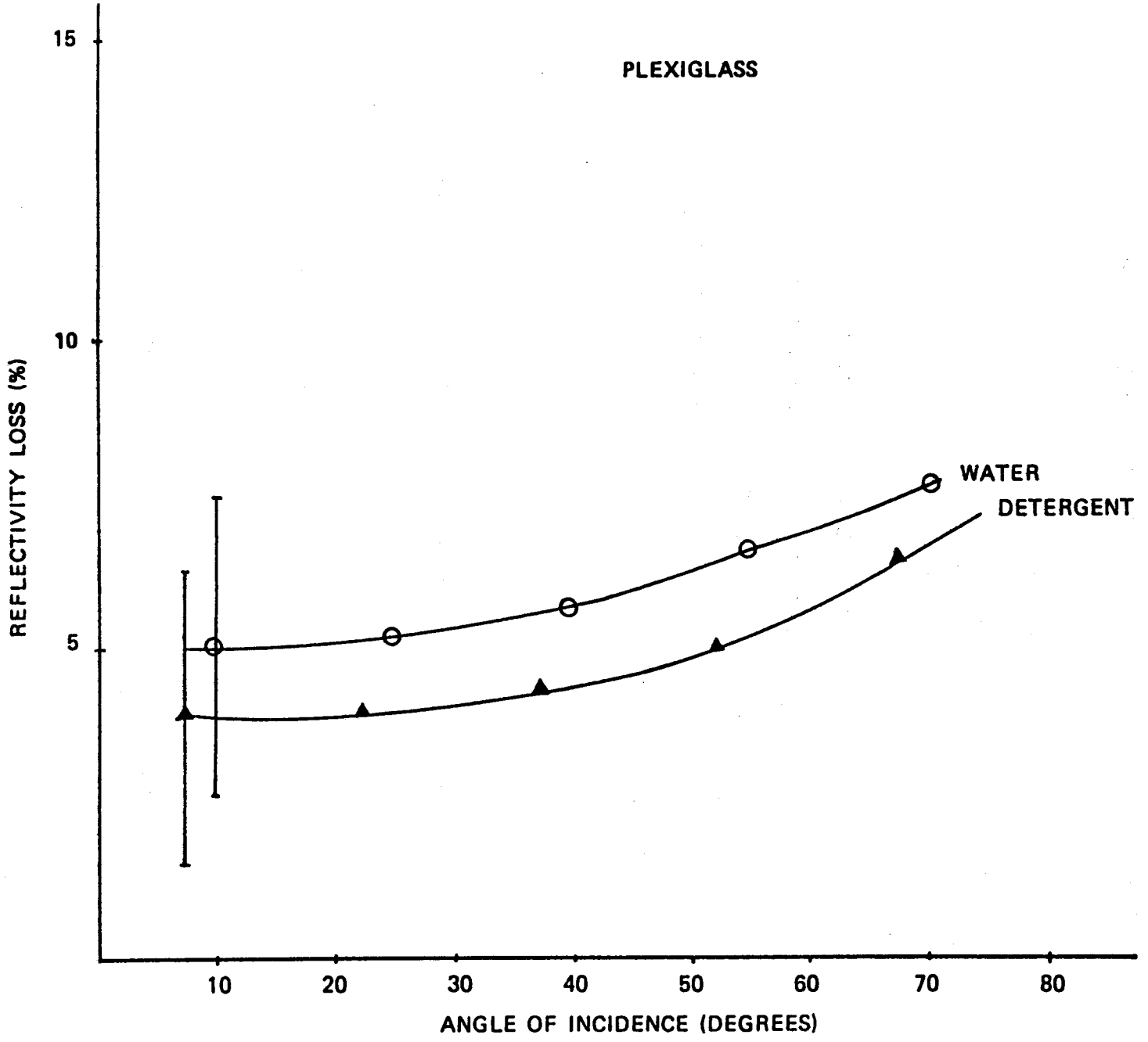

Fig. D-15. REFLECTIVITY LOSS FOR "WATER" AND "DETERGENT" RINSED PLEXIGLASS MIRROR

The Effect of Scrubbing

After these measurements had been made, the samples were gently scrubbed with a wad of soft cotton soaked with the "Sparkleen" solution and then rinsed in tap water and allowed to dry. The reflectivities were then measured again. The results of these measurements are shown in Figs. D-16 and D-17, along with the original, pristine reflectivities. These results indicate that for most mirror types, the residual reflectivity loss of scrubbed mirrors is 1-2%. This value probably reflects the irreversible damage of the mirror by the weathering process. Pitting of all samples was observed and the plastic samples also showed scratches and crazing. More data over longer periods of time needs to be taken in order to determine the cumulative effects on the mirror reflectivity of this damage.

D-3.2 Mirror Flatness

In order to obtain a qualitative measure of the flatness of the mirror samples and of the weathering induced changes, the apparatus shown in Fig. D-18 was used. It has been described in detail in a previous report. Briefly, a collimated beam from the same source used for the reflectivity measurements was reflected from the test mirror at an incident angle of 45^0, and allowed to travel a distance of 22' where it struck a ground glass screen. The resulting image on the screen was photographed using a Polaroid camera with a close-up lens attachment. The size and shape of the image is a direct measure of the mirror flatness. Typical "before and after" pictures are shown in Fig. D-19.

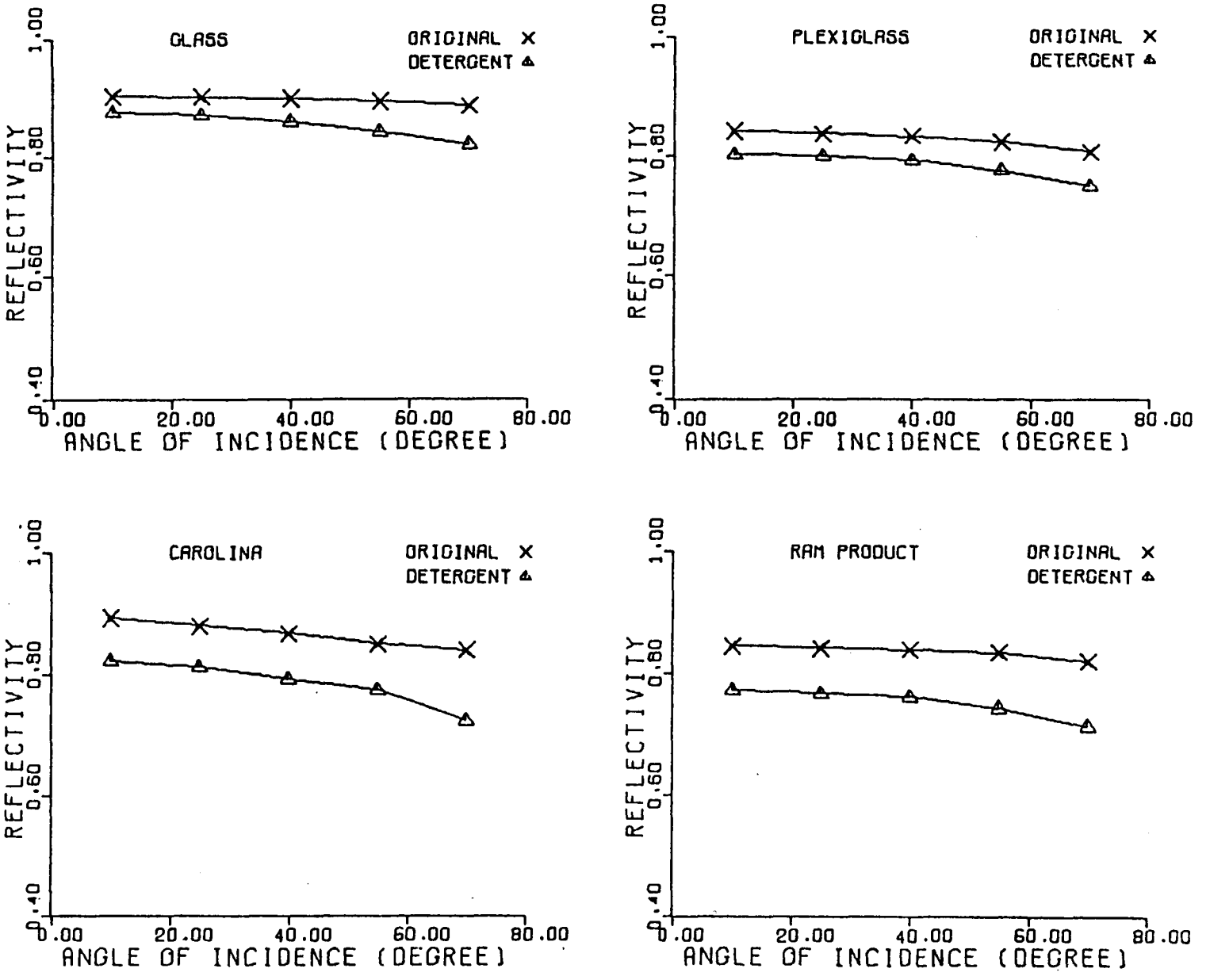

Fig. D-16. Reflectivity for Original and Detergent Rinsed Mirrors

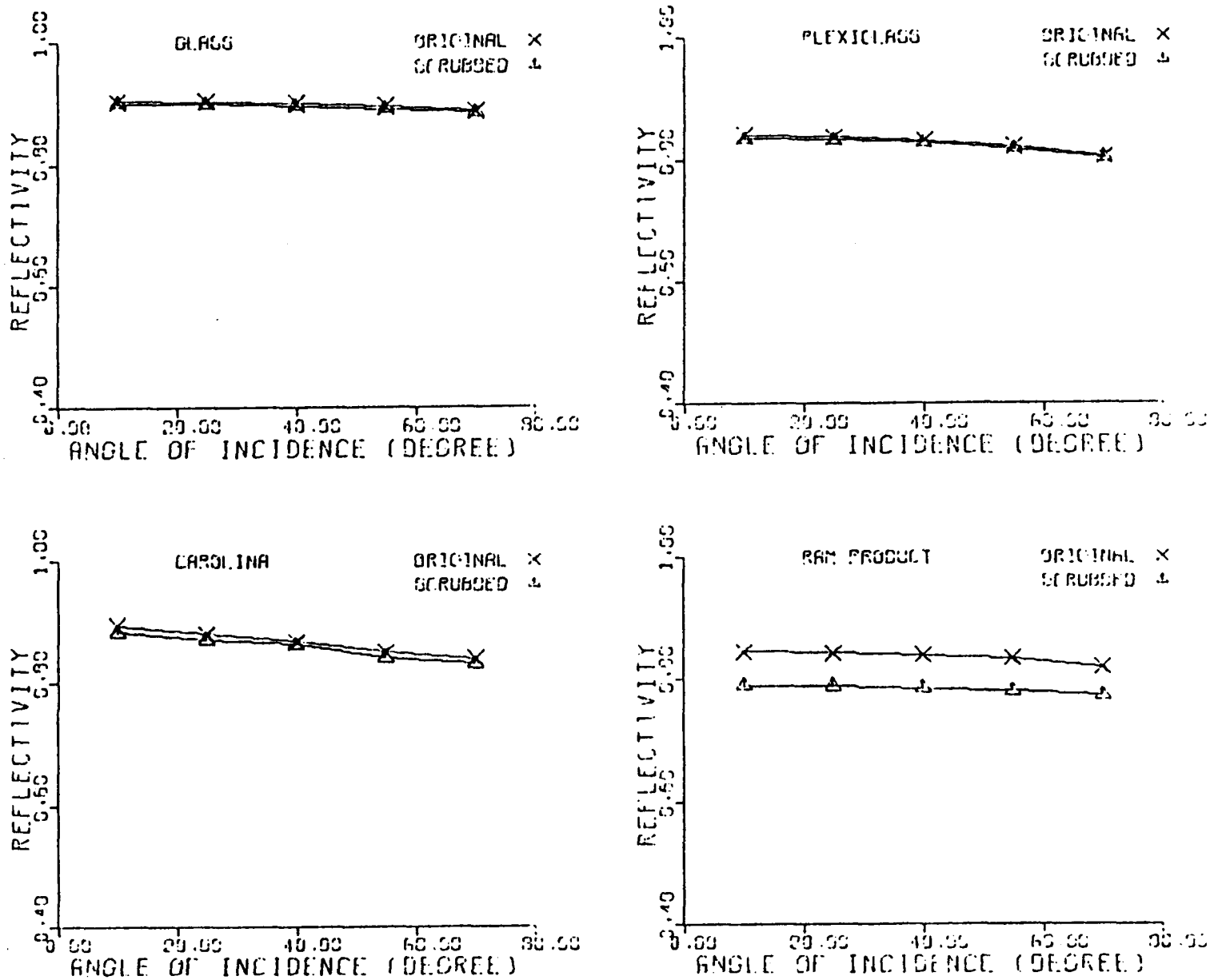

Fig. D-17. Reflectivity for Original and Scrubbed Mirrors

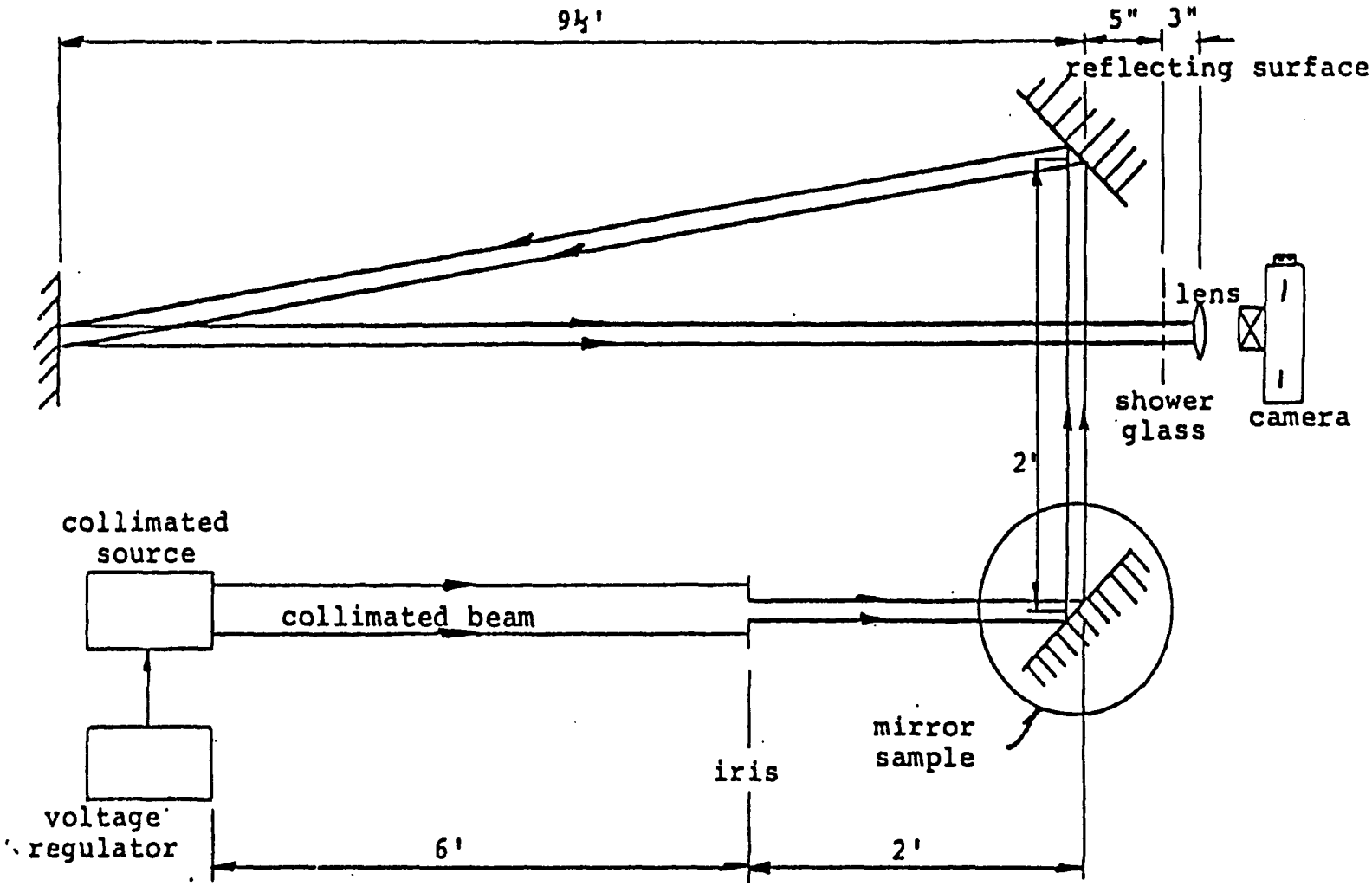

Fig. D-18. Schematic Diagram of the Set-Up to Record the Reflected Pattern

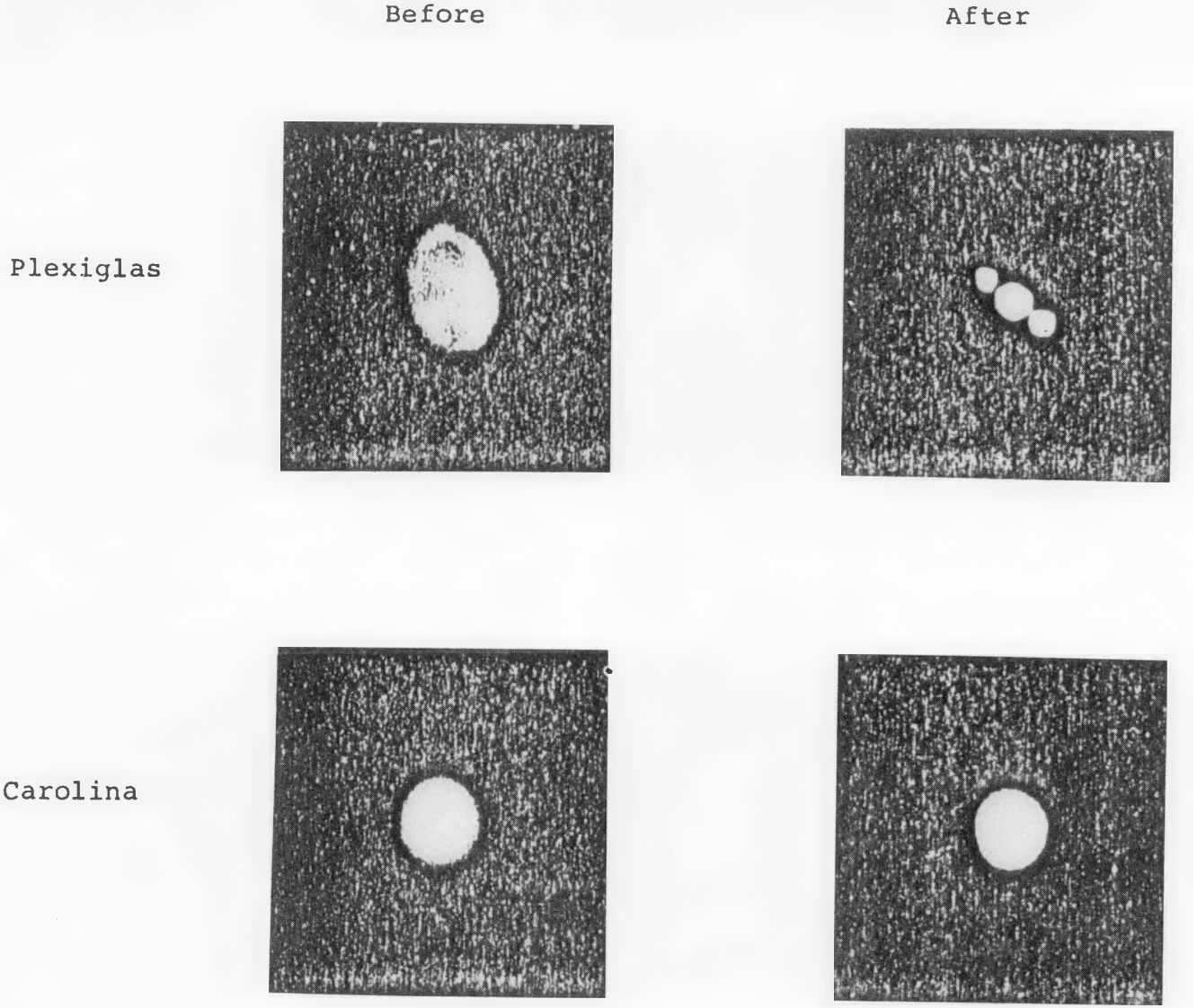

Fig. 19-a. Mirror Flatness Tests

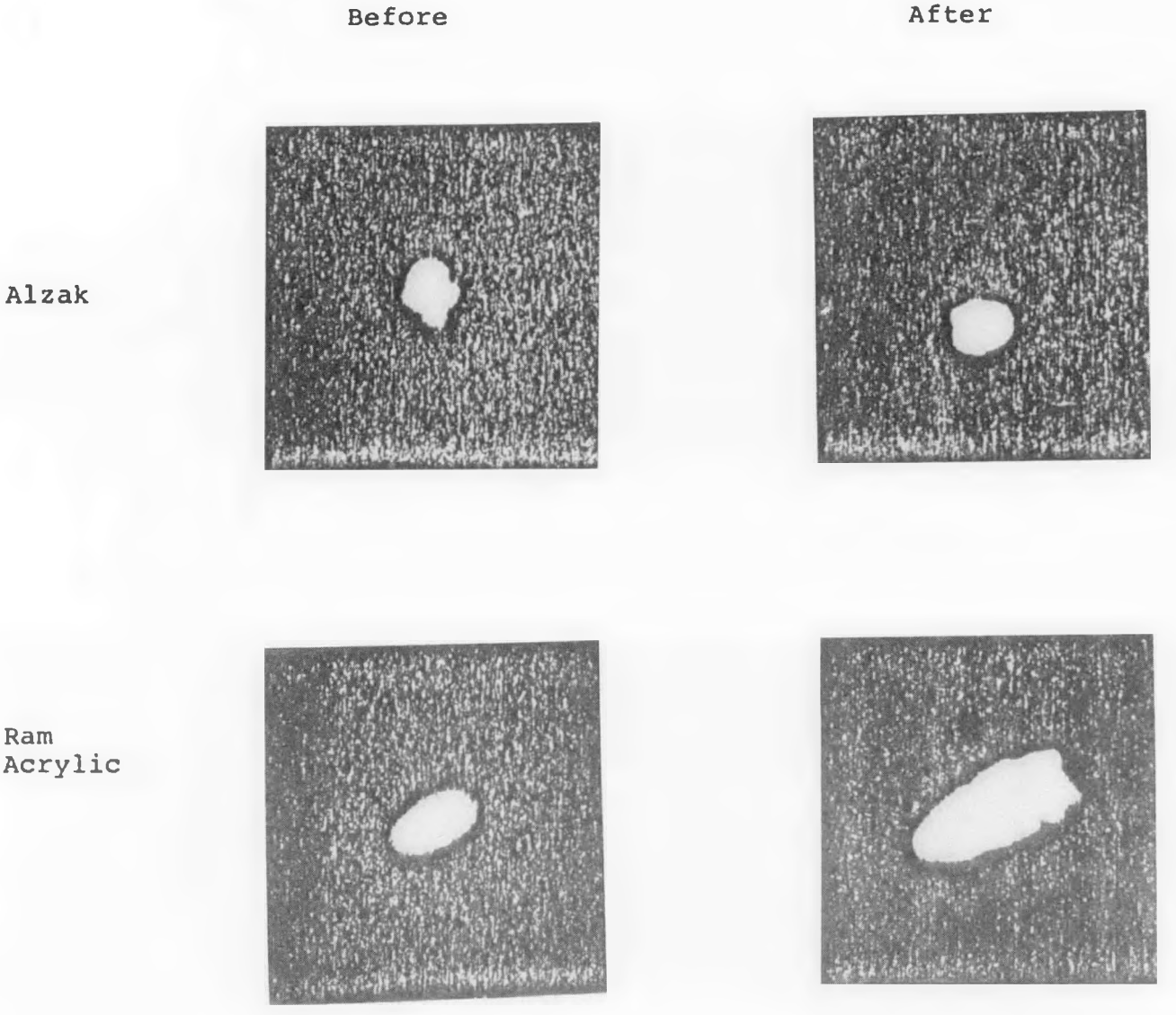

Fig. 19-b. Mirror Flatness Tests

These measurements confirmed what was obvious visually. All of the plastic mirrors suffered considerable warping as a result of the weathering. The mirrors labeled glass, Carolina, Donnelly, Alzak, and Kinglux remained in their as received condition. The Scotchcal samples separated from their adhesive backing and were badly warped.

D-3.3 Conclusions from the Program

As a result of these studes, we have reached the following conclusions:

1. Second surface glass mirrors seem to have the highest initial reflectivity and to weather the best. The normal incidence reflectivity loss after weathering ranged from 6% for the glass mirrors to about 16% for the Alzak mirrors.
2. Gently rinsing the samples with a detergent solution generally restored more than half of the reflectivity loss. Rinsing only with the tap water was not as effective. More work needs to be done in order to determine the optimum cleansing procedure, and the loss in reflectivity to be expected. Also, cumulative effects need to be studied.
3. Gentle scrubbing with a soft cotton wad and a detergent solution restored the reflectivities to nearly the original value. Some residual loss remained, however, and probably represents permanent damage to the mirror surface.

4. Mirror warping is a problem for the plexiglass and Ram acrylic mirrors.

D-4 NOMINAL SELECTION CRITERIA

In addition to reflectivity, other criteria used to more thoroughly evaluate candidate materials were (1) cost, (2) service life, (3) weather-ability, (4) ease of fabrication, (5) abrasion resistance, (6) fragility (includes handling, hail impact resistance and vandalism considerations), (7) weight, (8) thermal factors (includes service/mechanical properties, and (10) availability.

Reflectivity was considered from several different approaches: (1) reflectance as a function of wavelength, (2) reflectance as a function of incidence angle, (3) reflectance as a function of beam spread angle, (4) practical wavelength limits for the solar spectrum, (5) distribution of spectral irradiance at ground level, (6) spectral irradiance vs. air mass, and (7) spectral vs. total reflectivity.

An engineering evaluation of the candidate materials based on the above criteria led to the selection of a 1/8 in. thick, second-surface silvered, float glass mirror as the recommended mirror material. In the future it is planned to use mirrors that have a lower lead content glass for improved reflectivity.

D-5 PANEL ERROR ANALYSIS

The discussion of mirror panel manufacturing, alignment and operational errors is presented in Appendix E-4.2.

APPENDIX E. CONCENTRATOR SUPPORT STRUCTURE

E-1 INTRODUCTION

This section summarizes the results of efforts to date to optimize the concentrator support structure for both performance and construction cost. Factors entering into the investigation include site dependent factors, critical loading, type of structure, materials of construction, and construction techniques.

Results of the study indicate that the structure should be a rigid steel frame supported by a reinforced concrete pier foundation in a spherical excavation. An earth berm is used for protection from storm-water surface run-off.

E-2 CONCENTRATOR STRUCTURE LOADS

E-2.1 Design Environment

The environmental conditions for the concentrator design remain unchanged and are repeated in Table E-1 for convenience.

E-2.2 Load Types

The design loads fall into two categories, those which establish the required strength of the structure and those which need to be checked to determine if they have any effect. In this study a number of different concentrator structural configurations were analyzed to determine the most cost effective design. It was quickly found that the survival wind load and/or snow load established the size of most of the concentrator members. If these requirements were met, the

TABLE E-1 CONCENTRATOR DESIGN ENVIRONMENTAL CONDITIONS

1. Ambient Temperatures

Maximum 110°F
Minimum -10°F
Average 70°F

2. Wind Velocities (100 Year Mean Recurrence Interval)

		Dynamic Wind Pressure
Operational	30 mph	2.25 lbs/sq. ft.
Survival	90 mph	23.9 lbs/sq. ft.

3. Snow Load (No permanent deformation)

Survival 10 lbs. per square foot (non concurrent)

4. Seismic Load (No permanent deformation)

Survival (non concurrent)	
Horizontal Acceleration	± .09 g
Vertical	± .09 g

5. Extreme Frost/Penetration -- 18 inches of depth

6. Rainfall

$$I = \frac{K}{t+b}$$

I = Rainfall Intensity (inches per hour)
K,b = Coefficients
K = 210 for Crosbyton Site
b = 26 (100 year frequency)
t = duration of storm in minutes (2 hour maximum duration

7. Thermal

Maximum temperature differential of 10° across the structure.

structural errors fell well within the original nominal error budgets. The survival wind and snow loads therefore fell into the first category. Other loads such as pure dead weight loads, seismic, operating wind load, fell within the second category. For this reason analysis of these conditions was usually omitted when sizing structural members. In any final detailed design every load condition would have to be checked to make sure they were not the critical ones for some member. The wind loading established both the strength requirements for survival and the magnitude of the operating errors and were consequently studied in detail. The results of these studies are discussed in the following paragraphs.

Wind Loads

Because of the importance of the wind loads in the concentrator design, wind tunnel tests were conducted on a concentrator model to obtain experimental data. A discussion of the tests and the results are presented in Appendix L. Results from these tests were used in the concentrator error analysis in Section E-4.

Snow Loads

Snow loads were applied as a uniform load over the entire inner surface of the concentrator. This is not altogether realistic since not as much snow will stick to the steeper slopes of the concentrator surface as will accumulate in the center area. The American National Standard Building Code Reference E-1 allows a reduction of the snow load at the rate of 2% per degree for the excess over 30 degrees for slopes exceeding 30 degrees. It is probable the remainder would slide into the middle therefore imposing the same total load onto the structure. This middle area is the most lightly load by the wind while the steeper parts along the perimeter are the most heavily loaded by the wind. The variation of snow loads with slope will be calculated in more detail in the immediate future.

It is possible to write a computer program to do this. Once the load coefficients based on depth of snow were generated it would be possible and practical to modify the airloads program to calculate the individual panel and joint loads.

Since for the reasons enumerated the snow loads were not critical, consequently no effort was made to refine the snow load analyses. In any final detailed design this would have to be done. Prior to doing this it would be advisable to obtain data specifically applicable to the Crosbyton site on depth of snow accumulation and accumulated ice thicknesses.

Seismic Loads

The Crosbyton site is an area of low seismic activity, therefore the seismic load factors are low. These factors are taken from the Americal National Standard Building Code (Reference

They are also dependent on the natural frequency of the structure. Since the seismic loads were not critical for most concentrator members and since many concentrator configurations were studied it was not considered necessary to refine these analyses. In some configurations the seismic loads were consequently not analyzed.

In the final detailed design a more comprehensive analysis will be undertaken even though it is not expected to have any significant impact on the structure. It is also a low risk structure since it would probably not endanger human life even in the event of earthquake damage. It is such a highly redundant structure it is unlikely a complete collapse failure could occur. If there were any significant ground displacements the mirrors would have to be realigned in any case.

Summary of Critical Loads for the RPS and ATS Design

In this study the critical design loads for both strength and error occurred when the wind came from the south. A few members were stressed slightly higher with the snow load or seismic loads. The differences were so small and the numbers of subject members so few the former loads were used primarily for setting member sizes in this phase of the study.

It is still being evaluated whether the additional cost required to compact the berm and provide erosion control is justified by these improvement in optical performance. Continued refinement and optimization of the structure will determine the true cost effectiveness of the berm.

E-3 CONCENTRATOR STRUCTURE DESIGN

E-3.1 General Considerations

In this study a number of different types of concentrator structures were conceptually designed, and analyzed in order to establish cost and accuracy relationships versus size, depth of embedment, type of excavation, type of foundation, types of structural shapes, columns and piers. In order to examine as many types of structures as possible, it was necessary to limit the amount of design optimization and refinement. This included using the same geometry and computer model where possible, as few different member sizes as possible, identical foundations, size and types. Particular emphasis was placed on keeping the number of types of members to as few types as possible in order to achieve mass production fabrication economy rather than material economy. The column spacings and member lengths were made large as possible in order to achieve erection and installation economy. Each design was carried to the point that the structure could meet AISC Specifications for the Design and Fabrication and Erection of Structural Steel for Buildings (Reference E-2) with the specific member sizes and weights used in the analyses.

The relative efficiency of the various structures designed to these same requirements were established by comparing their weights and accuracy.

It is obvious under these restrictions a certain amount of judgment had to be exercised in the selection of the various

parameters, such as column spacing, structural type, member types, etc. It is felt, however, that even fairly large changes in column spacing and geometry would not make large differences in the total weight of material used. It is felt the principal effect would be to change quantity and sizes of members.

The surface loads are relatively light when compared to the floor loads of buildings, grandstands, bridges and other structures of comparable size. It was therefore found that the material could not be utilized as efficiently as in these structures. In other words, the stress levels are generally low since member sizes and therefore weights are dictated more by their slenderness ratios, minimum thicknesses of material and elastic stability requirements than by their load carrying capacity. A more efficient use of material could be achieved by designing an electric transmission tower type structure which achieves their material economy by using a large number of small pieces. This would probably help material economy at the expense of erection and foundation economics.

There are two reasons why this approach was not investigated. First, a large amount of time is required to prepare and run these computer models. It was felt it was more meaningful to analyze several simpler structures than just one complex structure. The second one being that at the present time that economy apparently increases (costs decrease) with increase in size. For example, we keep building

bigger buildings, bridges, dams, generators, turbines, trucks, etc. Table E-2 is a tabulation of the various structures analyzed, listing their parameters, and comparing their weights and accuracies. These errors are not absolute but give their order of magnitude. In other words they represent structural accuracies that can be achieved with the given type and weight of structure.

E-3.2 Types of Structures Analyzed

The concentrator structure was divided into two parts, the superstructure and the substructure in order to analyze it using available computers, a CDC 6600 and UNIVAC 1108. There were so many joints and members, the model would have exceeded the computer capacity if run as a single problem.

Superstructure Configuration

The superstructure in turn was divided into 56 subdivisions to reduce the number of computer models and computer runs. Seven representative subdivisions were analyzed for strength and rotation errors. The locations of these subdivisions are shown in Fig. E-1. The same superstructure configurations was used with all substructures in the summaries. Figure E-2 is a computer model of a panel. Mirror panels with dimension 4 ft by 8 ft were used in all superstructure analysis. This was the initial assumption and was retained to provide better weight and accuracy comparisons between different substructure configurations. These mirror panels were supported by east to west panel support trusses

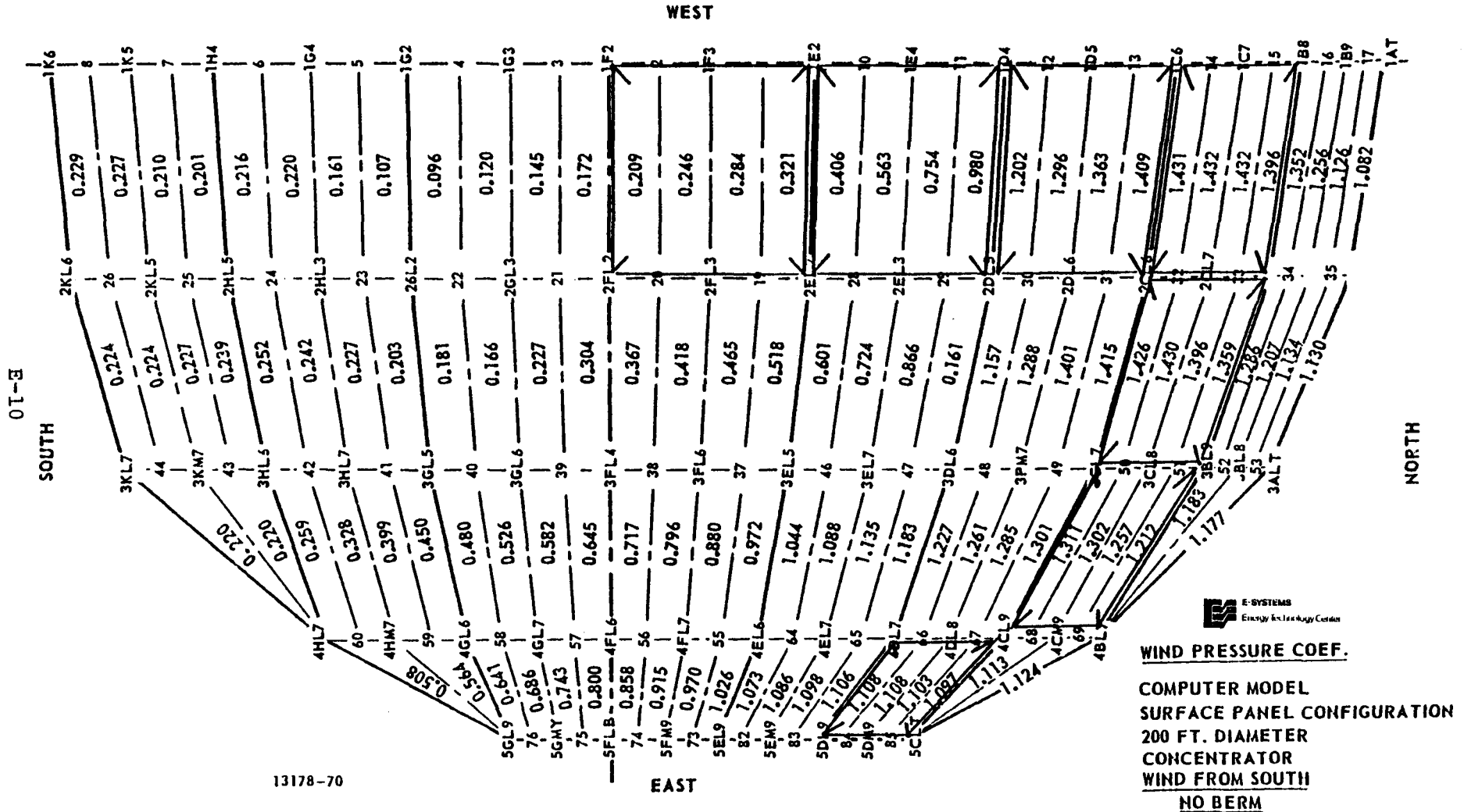

Figure E-1. Presentative Superstructure Subdivisions

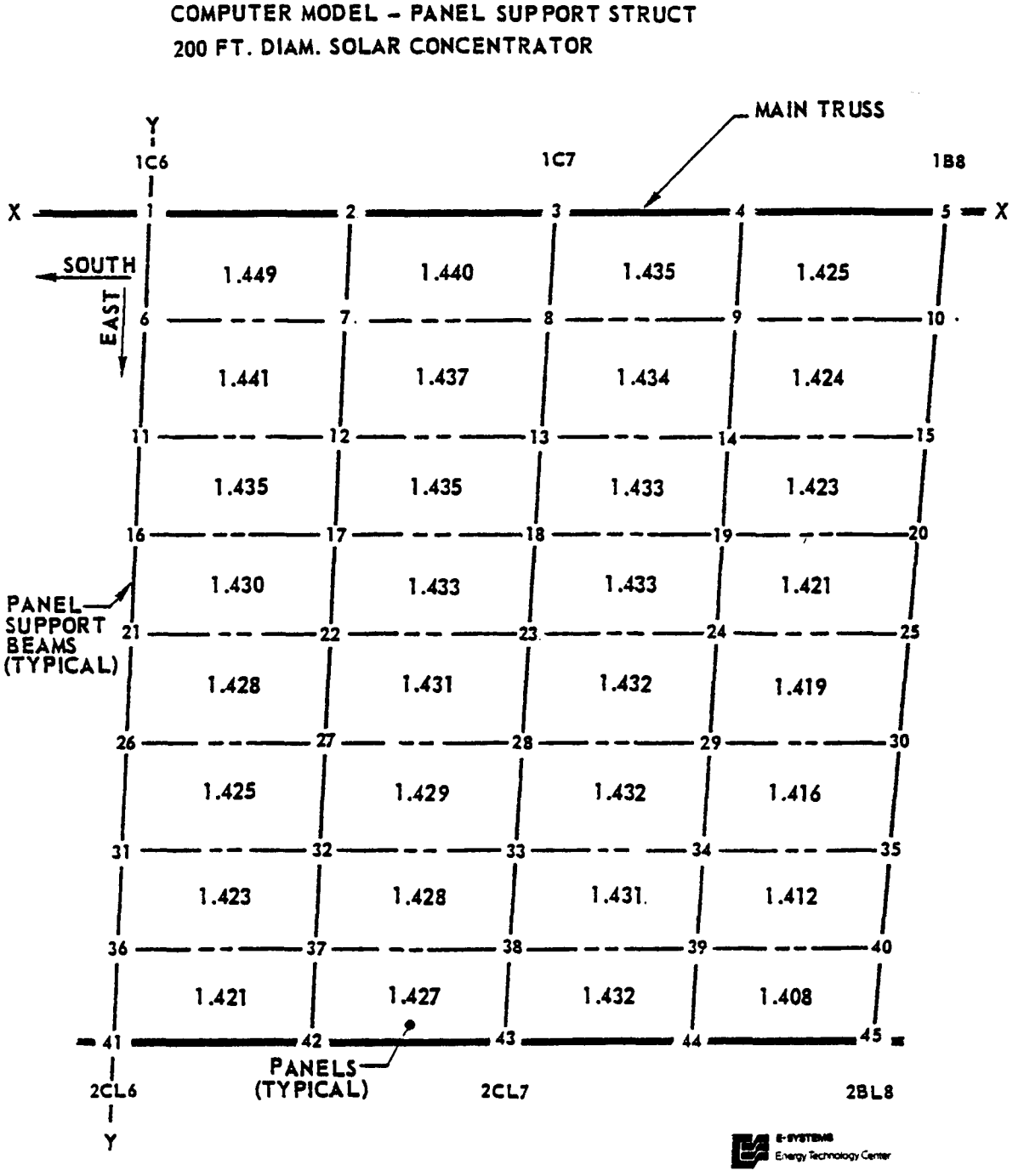

Figure E-2. Computer Model of Typical Superstructure Subdivision Showing Surface Pressure Coefficients

spanning between north to south main trusses.

The main trusses appeared in computer models for both the superstructure and substructure. In the superstructure model they were made rigidly fixed in space at the tops of the columns. In the substructure model they move with the columns. These assumptions while approximate, allow the two structures to be analyzed independently. These assumptions are probably as accurate as any other that could be used (without a massive and expensive computer modeling effort) and are considered to be conservative.

The main trusses therefore are error contributors to both the superstructure and the substructure. In the weight summaries the main trusses weight are added to the superstructure weights since this is more convenient when considering steel superstructures combined with concrete substructures.

One analysis of the superstructures used concrete support beams. These were assumed to be precast beams that were installed similarly to steel beams. The economics of this approach is discussed in the costs and construction tradeoffs sections.

Substructure Configurations

The substructures analyzed were of two basic types, these were trusses and rigid frames. Three types of rigid frames were investigated, these were concrete with lune column configuration, steel with lune column configuration and steel in a rectangular column configuration. These arrangements are illustrated in Figures E-3, Sheets 1-9.

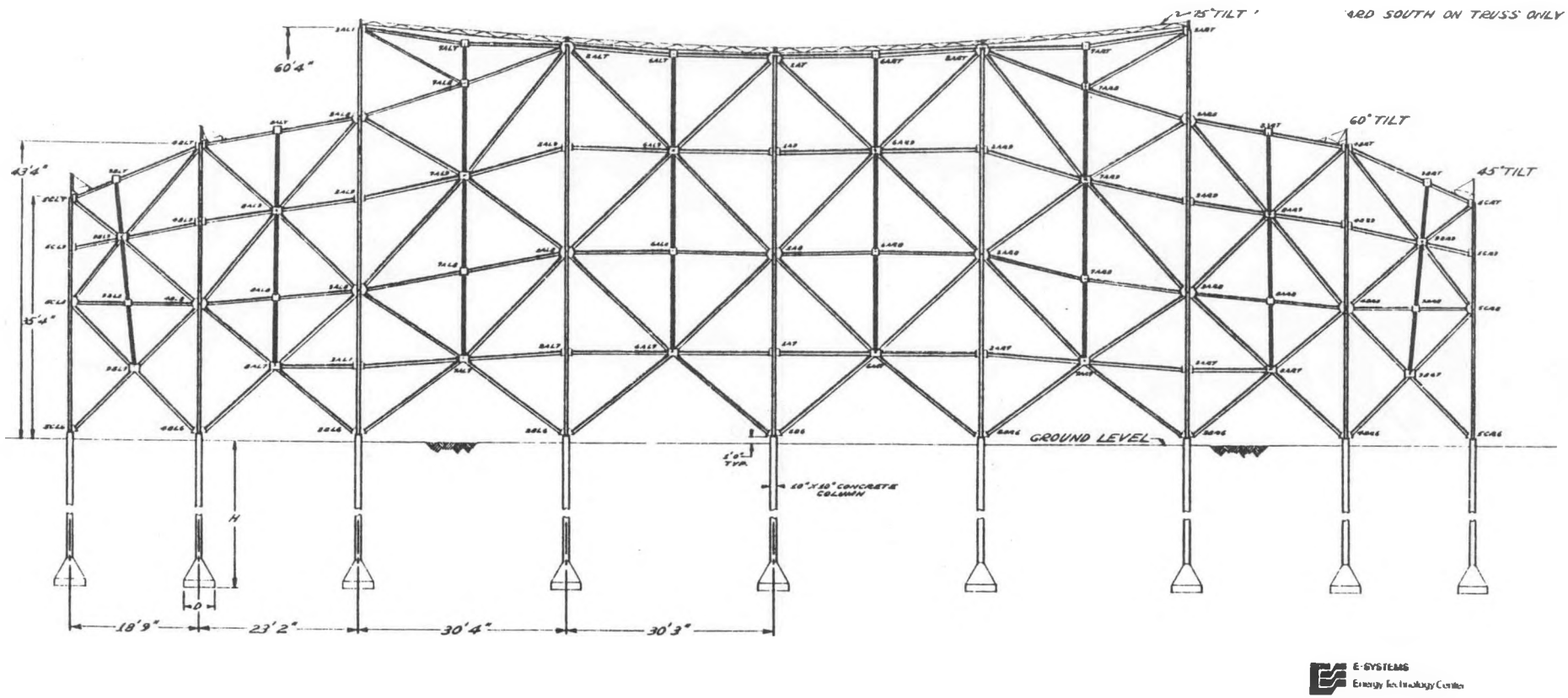

NORTH END LOOKING SOUTH

Figure E-3. Truss Type Concentrator (Steel) North Elevation (Sheet 1 of 9)

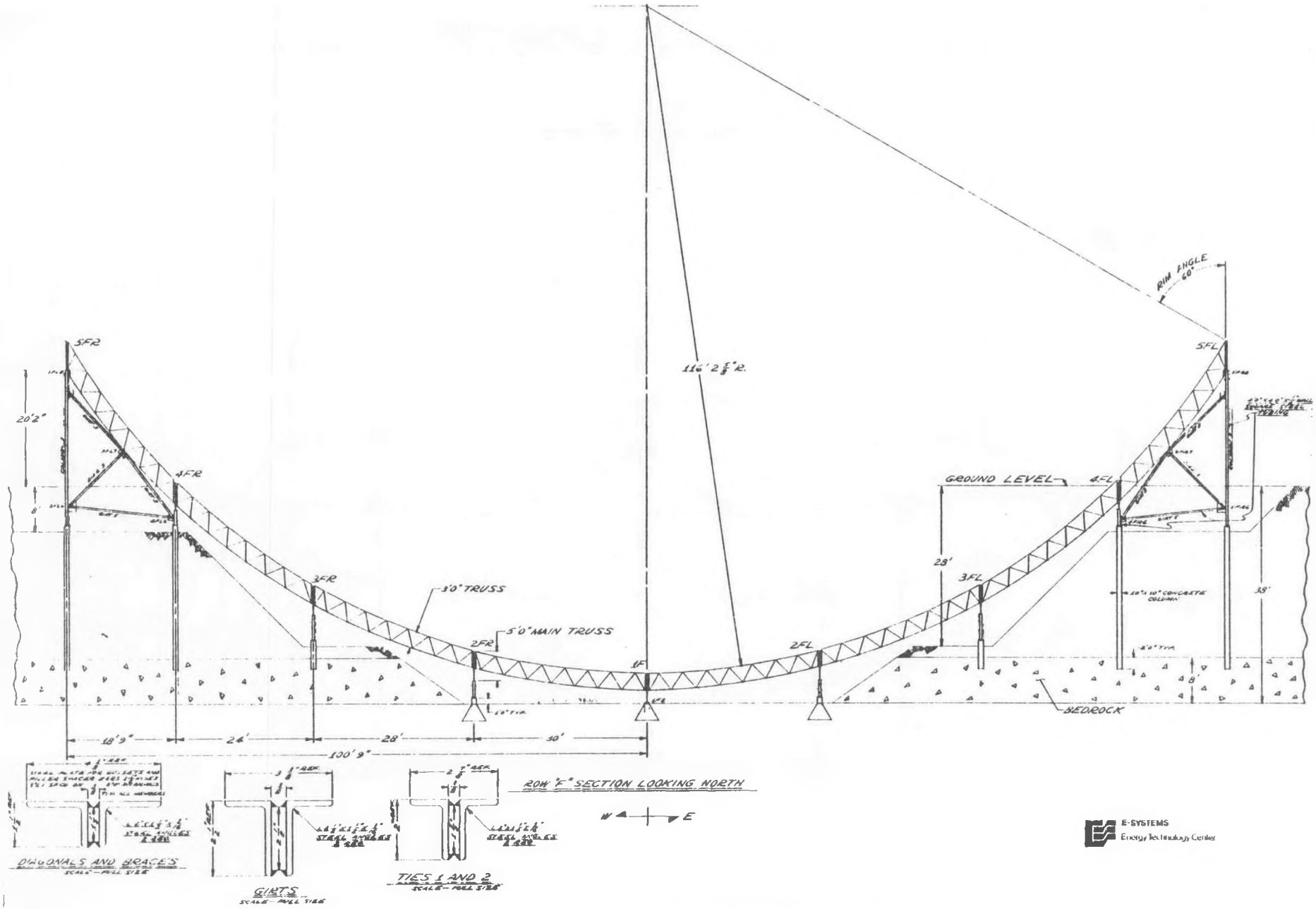

Figure E-3. Truss Type Concentrator (Steel)—East-West Section (Sheet 2 of 9)

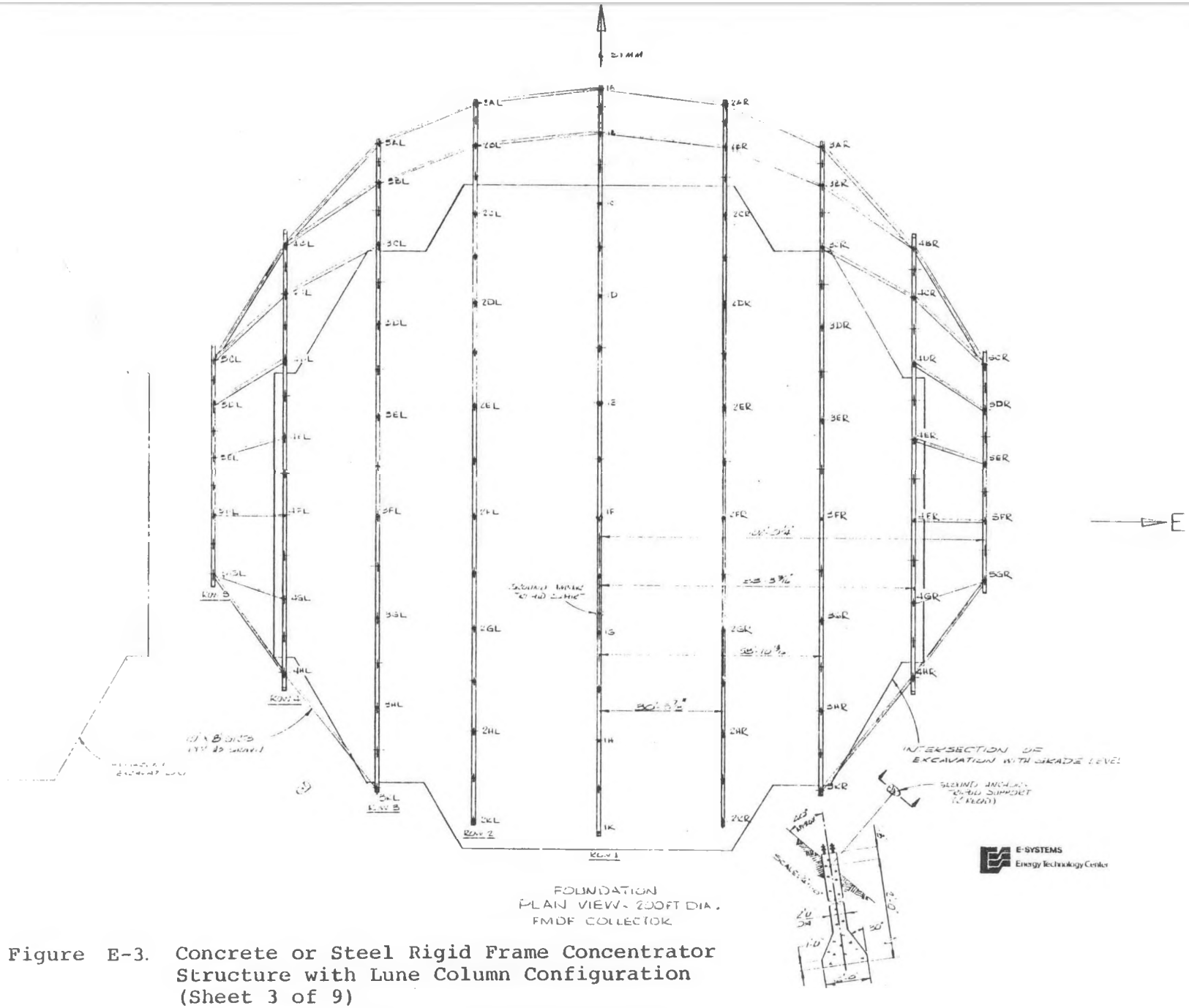

Figure E-3. Concrete or Steel Rigid Frame Concentrator Structure with Lune Column Configuration (Sheet 3 of 9)

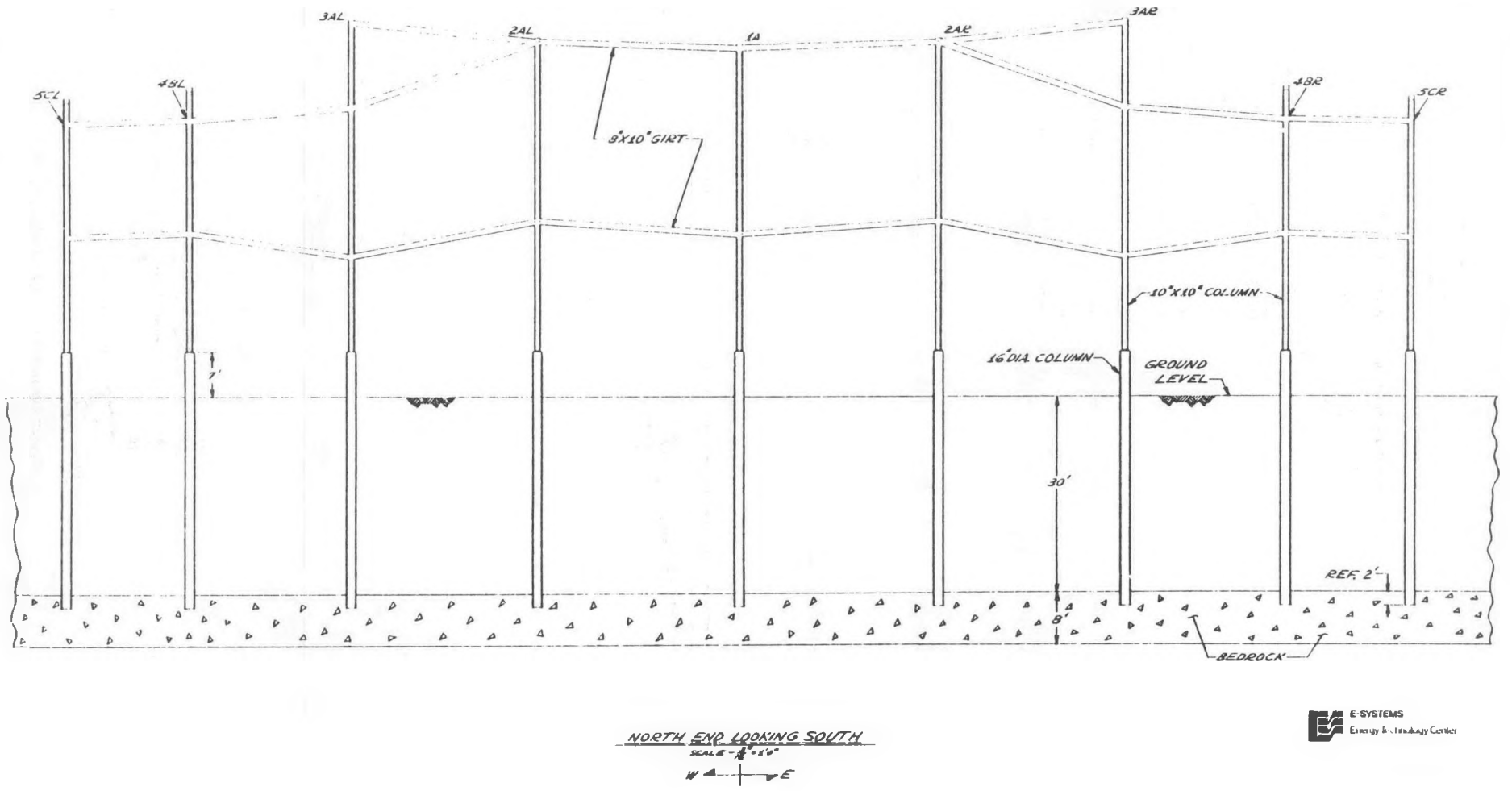

Figure E-3. Concrete or Steel Rigid Frame Concentrator Structure with Lune Column Configuration (Sheet 4 of 9)

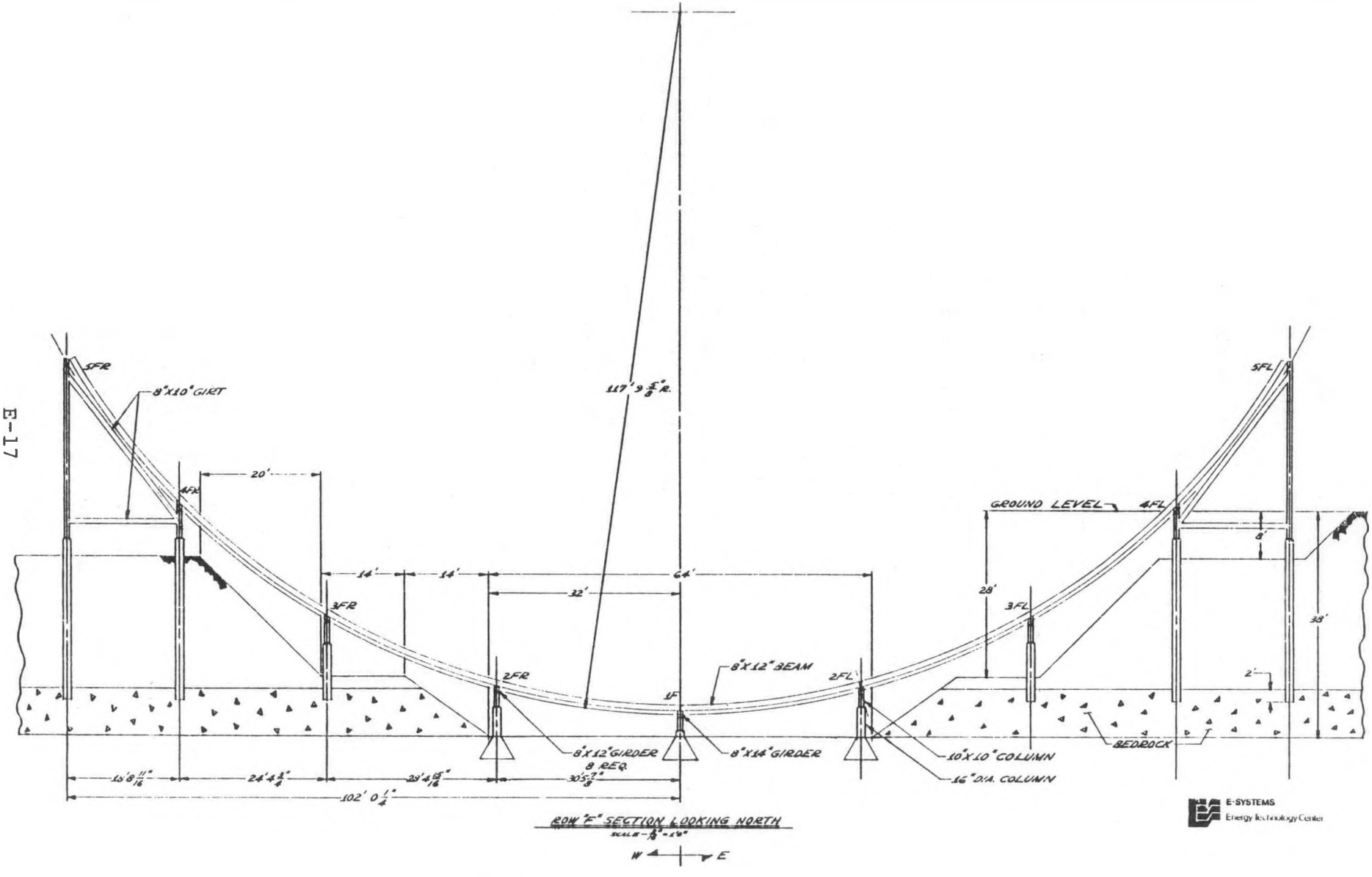

Figure E-3. Concrete or Steel Rigid Frame Concentrator Structure with Lune Column Configuration (Sheet 5 of 9)

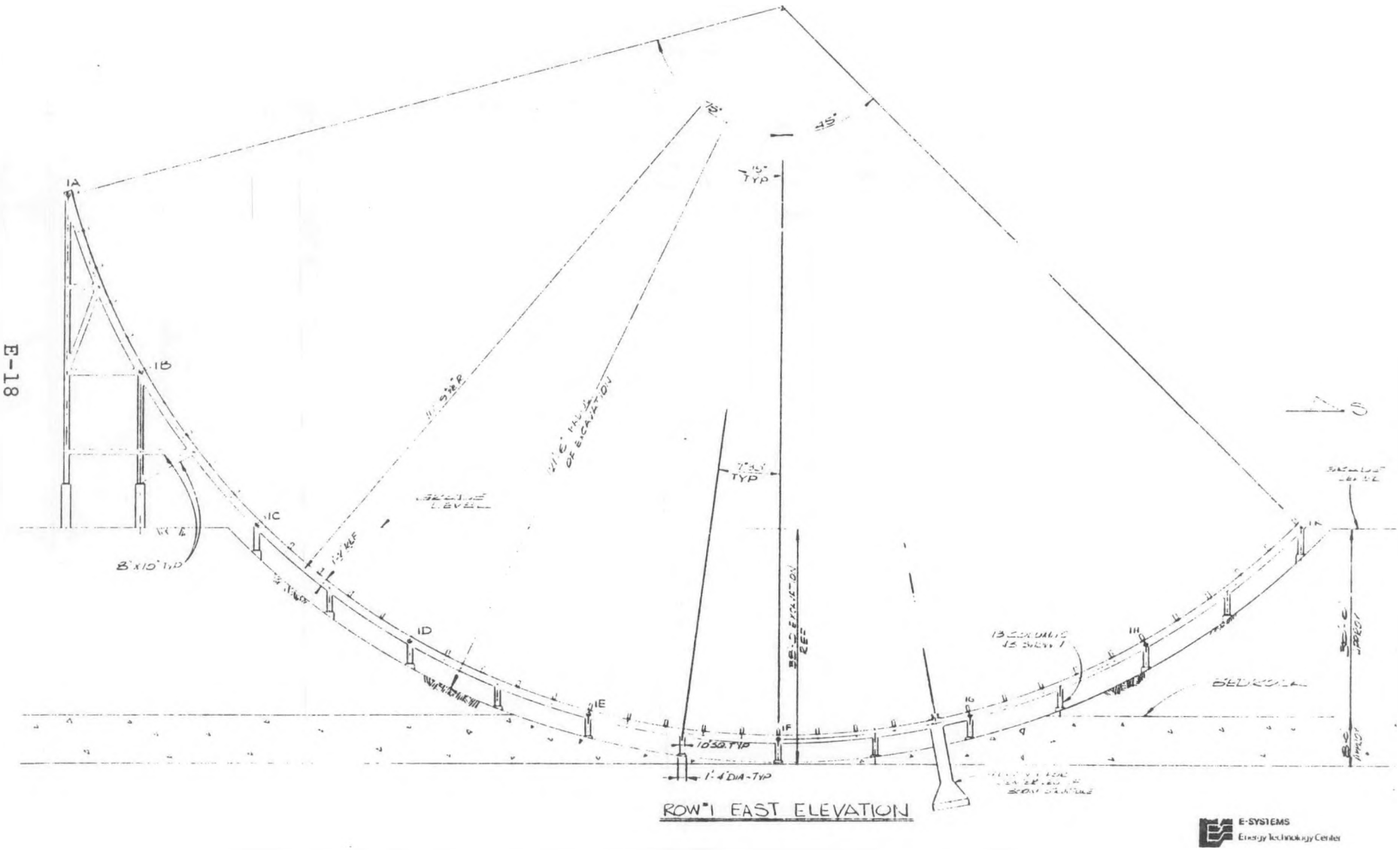

Figure E-3. Concrete or Steel Rigid Frame Concentrator Structure with Lune Column Configuration (Sheet 6 of 9)

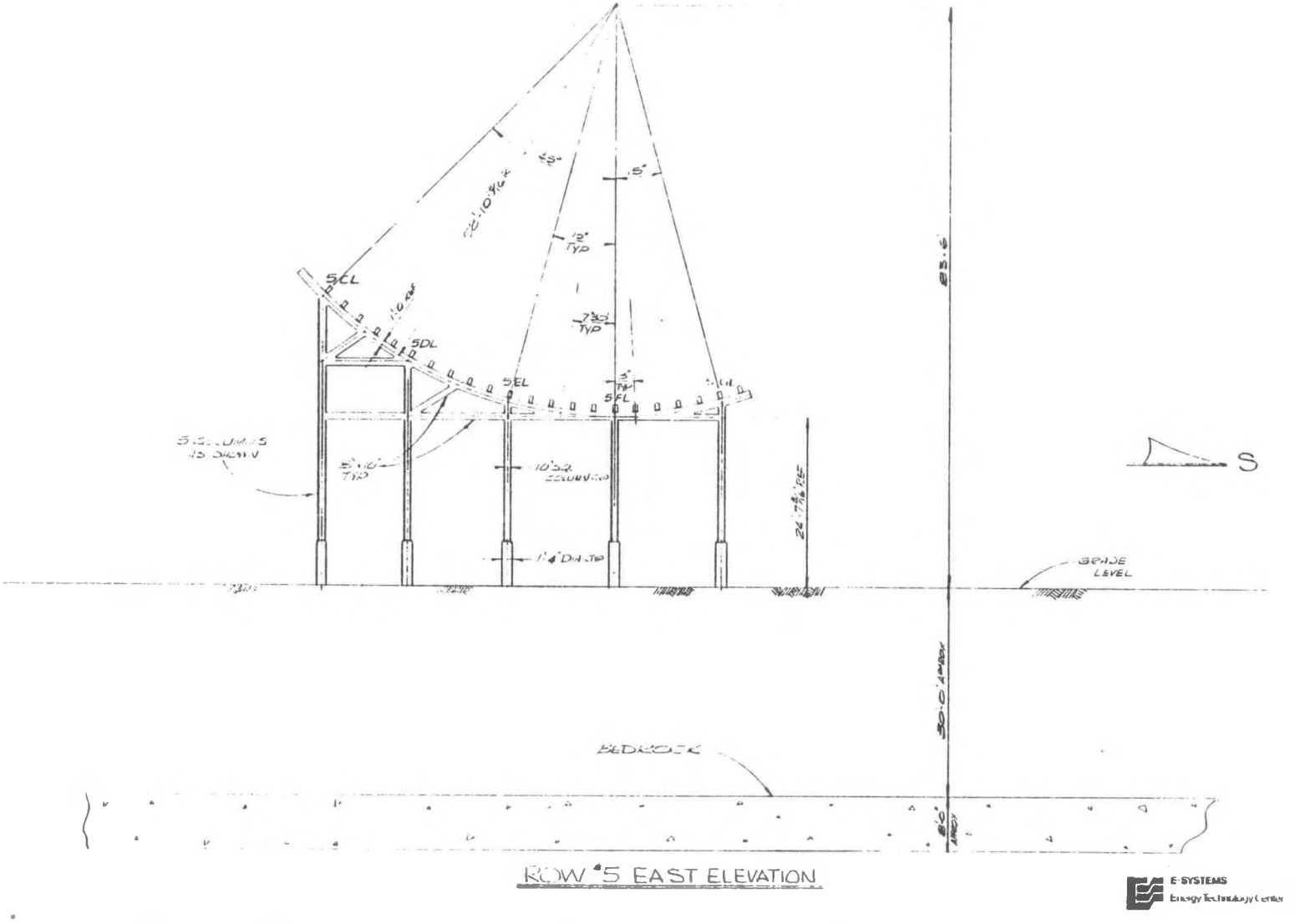

Figure E-3. Concrete or Steel Rigid Frame Concentrator Structure with Lune Column Configuration (Sheet 7 of 9)

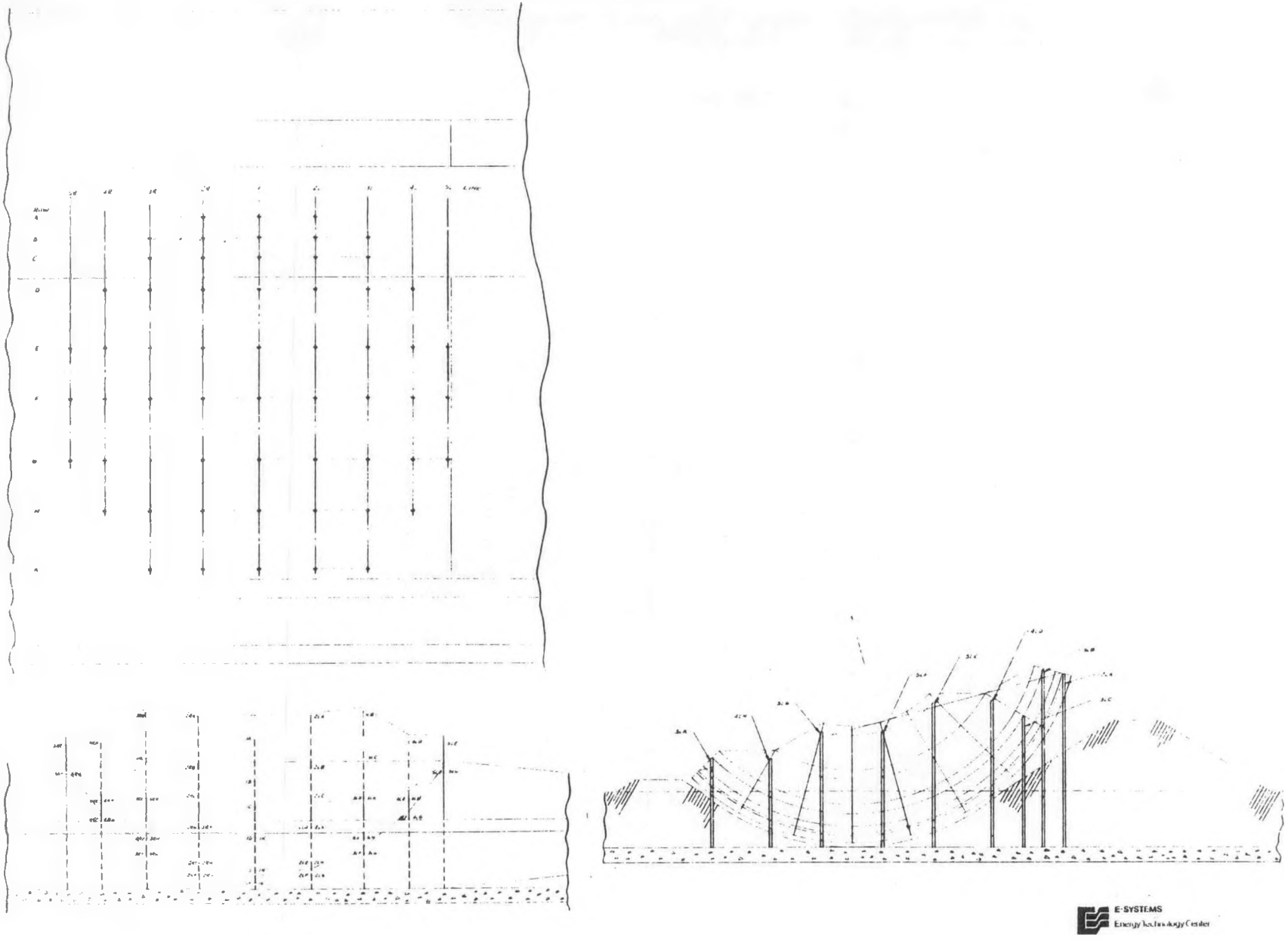

Figure E-3. Diagram of Steel Rigid Frame Concentrator with Rectangular Column Configuration
(Sheet 8 of 9)

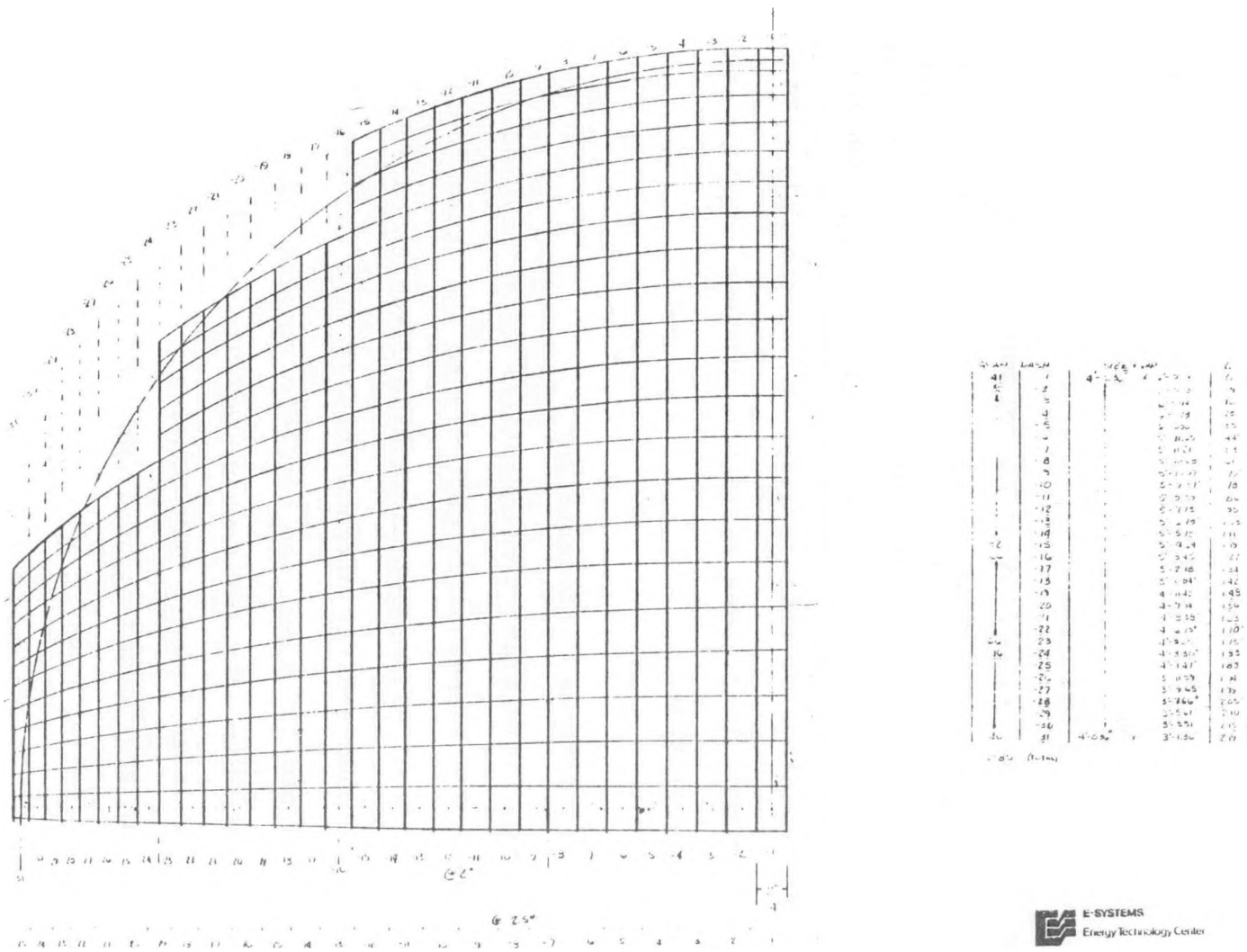

Figure E-3. Surface Panel Pattern - Typical of All Concentrators (Sheet 9 of 9)

Truss Configuration

In the truss concept the main trusses were supported by columns. The columns were all assumed to be pin ended. In addition pin ended diagonal braces and horizontal girts were provided to supply the required shear capability. The columns were also assumed to be pin ended at the column footing interface. In all the truss structures investigated, the columns were aligned in parallel rows in the north to south direction but followed lunes in the east to west direction. The advantage of this arrangement was that all main trusses were identical in span length and therefore provided the best potential for fabrication economics.

Rigid Frame Configurations

Two rigid frame configurations were analyzed. The first configuration was identical in geometry to the truss configuration except the ends of all members were made fixed ended so they could handle shear loads and the diagonal braces were deleted. This structure was analyzed for steel and concrete members. In the concrete version all members were rectangular beams. In the steel versions the main north to south members were trusses.

In the second rigid frame configuration the columns were arranged in parallel rows in both the north-south and east-west direction. The ends of all members were fixed and there were no braces. Only beams, columns and girts were used.

Combined Concrete and Steel Concentrator

An exact analysis was not made for the combined concrete

and steel structure. Since either one will carry the load by itself there is no reason why they could not be combined if it should prove economically desirable. The most practical combination from an erection point of view appears to be a steel superstructure and main trusses, with columns and girts of concrete. Calculated errors would probably be a little higher than for the all steel structure but of the same order of magnitude. Table E-2 is a summary of comparative weights of the different structural configurations.

Excavation Configuration

Most of the analysis were performed for the concentrator recessed into a spherical excavation. This requires the minimum amount of both excavation and steel and/or concrete. In the rigid frame design with the columns arranged in a rectangular (parallel) configuration, an analysis was also performed with the concentrators set in a trench instead of spherical excavation. This is attractive from an ease of excavation point of view and therefore unit cost of excavation. There is a large increase in the quantity of excavation. This may be partially offset by ease of installing the foundation and ease of erection of the structure. Accuracy of the substructure is somewhat lower.

Substructure Foundations

The footing loads were calculated using a computer program which read data from a deflection tape generated during the concentrator structural analyses by the SPACE computer program. It provides the deflection and load for every footing. It was developed during the latter part of this study program so not all

TABLE E-2 SUMMARY OF STRUCTURE WEIGHTS
CRITICAL DESIGN CONDITION - WIND FROM SOUTH (Sheet 1 of 2)

Diameter (Ft.)	100	100	100	300	300	300	65
Depth of Vertex	+3.3	-6.0	-12.0	+10.0	-18.0	-48.0	-10.4
Type of Structure	Truss	Truss	Truss	Truss	Truss	Truss	Truss
Excavation Type	None	Spher	Spher	None	Spher	Spher	Spher
Structural Material	Steel	Steel	Steel	Steel	Steel	Steel	Steel
Column Configuration	Lune	Lune	Lune	Lune	Lune	Lune	Lune
Berm on North	No	No	No	No	No	No	No
Surface Area Used (S.F.)	11,023	11,023	11,023	99,203	99,203	99,203	4,657
Weight Superstructure 1	40,000	40,000	40,000	407,000	407,000	407,000	23,700
Weight Substructure	46,000	30,000	18,000	696,000	421,000	215,000	13,900
Total Weight (Lbs.)	86,000	70,000	58,000	1,103,000	828,000	622,000	37,600

1 Includes Main Trusses

TABLE E-2 SUMMARY OF STRUCTURE WEIGHTS
CRITICAL DESIGN CONDITION - WIND FROM SOUTH (Sheet 2 of 2)

Diameter (Ft.)	200	200	200	200	200	200	200	200
Depth of Vertex	+6.7	-12.0	-32.0	-32.0	-32.0	-32.0	-32.0	-32.0
Type of Structure	Truss	Truss	Truss	Rigid Frame	Rigid Frame	Rigid Frame	Rigid Frame	Rigid Frame
Excavation Type	None	Spher	Spher	Spher	Trench	Spher	Trench	Spher
Structural Material	Steel	Steel	Steel	Steel	Steel	Steel	Steel	Steel
Berm on North End	No	No	No	No	No	No	Yes	Yes
Surface Area Used (S.F.)	44,090	44,090	44,090	44,090	39,861	39,861	39,861	39,861
Weight Superstructure 1	244,000	244,000	244,000	244,000	229,000	229,000	229,000	229,000
Weight Substructure	255,000	152,000	91,000	63,000	113,000*	99,200	48,300*	36,300
Total Weight	499,000	396,000	345,000	330,000	342,000	328,200	277,300	265,300

*Estimated

1 Includes Main Trusses

concentrator configurations were analyzed. For all configurations analyzed the magnitude and load patterns were about the same. The largest loads varied between 40 to 50 kips with the average around 20 kips. Peak elastic deflections were between 0.050 and 0.060 inches. Permanent deflections are estimated at approximately 15% of the peak deflection.

The modulus of elasticity of the soil was estimated from data taken from Reference E-3, D.D. Barkan, "Dynamics of Bases and Foundations." The modulus is related to the soil type, its safe bearing capacity and footing size. For the final design the actual soils modulus of elasticity must be established by tests at the site.

The spring rate of the soil was computed using formulas taken from Reference E-4, EIA Standard RS-411; Electrical and Mechanical Characteristics of Antennas for Satellite Earth Stations. These springs representing the foundation were used in the structural model to simulate the soil reaction to load.

The foundation appears to present no unusual problems. Piers to the rock at the 30 foot level may be the most practical foundation for the steeply sloped sections of the excavation. Neither piers or spread footings appear to be a significant cost item.

The final selection of the foundation type will be dependent on the type of concentrator chosen and the results of additional site tests.

E-4 CONCENTRATOR ERROR SUMMARY

E-4.1 Error Analysis Approach

The basic approach to an error analysis is to identify all possible contributions and to assess the value of their effect on the overall error of the system. Random independent errors are combined statistically with the dependent error to arrive at a statistical error distribution for the system, in particular the 95% error limit is the value of interest and arbitrarily chosen as a measure of merit of the system. The measure of merit will be used to describe a limit on performance expectations based on a given set of operational conditions.

Reflector surface error is the statistical combination of several contributing factors. These factors have been categorized into five discrete contributors which represent panel manufacturing error, panel alignment error, operational environmental loads on individual panels, operational environmental loads on the superstructure panel support structure, and operational environmental loads on the substructure. Each contributor was analyzed on an individual basis and its contribution was combined statistically with the other items to obtain an overall error.

E-4.2 Panel Error

Manufacturing

Manufacturing tolerances are based on the initial full-scale size panels during this segment to represent typical panel fabrication techniques. Measured data from these panels indicate an angular error of .075° which describes the 95% limit of all energy

reflected from the sample panels. There is a high level of confidence that this error limit or better can be achieved over 95% of the panels in a production environment. This factor is based in part on previous experience with panel production/development sequences as well as on the techniques utilized in producing the test panels.

Operational Loads

Environmental conditions, wind, thermal gradients and dead weight, were applied to the individual panels. The airloads were derived from 30 mph winds assumed to be uniform over the surface of the panel. The pressure coefficients are a function of position over the reflector surface. These values were weighed in calculating a 95% performance level for the reflector panels. The thermal loads were based on a calculated 50°F worst case thermal gradient across the reflector panel. The dead weight error due to variations in panel position relative to manufacturing orientation was derived as a function of position on the reflector surface and its contribution evaluated. Details are shown in Fig. E-4.

A finite element structures program was utilized to define the panel structure and correlated with load tests on the full-scale panels. The above mentioned loads were applied to the structure as finite element loads in the computer model. The resulting model displacements were then tabulated and the resulting panel error evaluated.

A typical 4 ft. by 6 ft. panel was modeled for the above mentioned evaluation. When the 95% error limit was calculated for

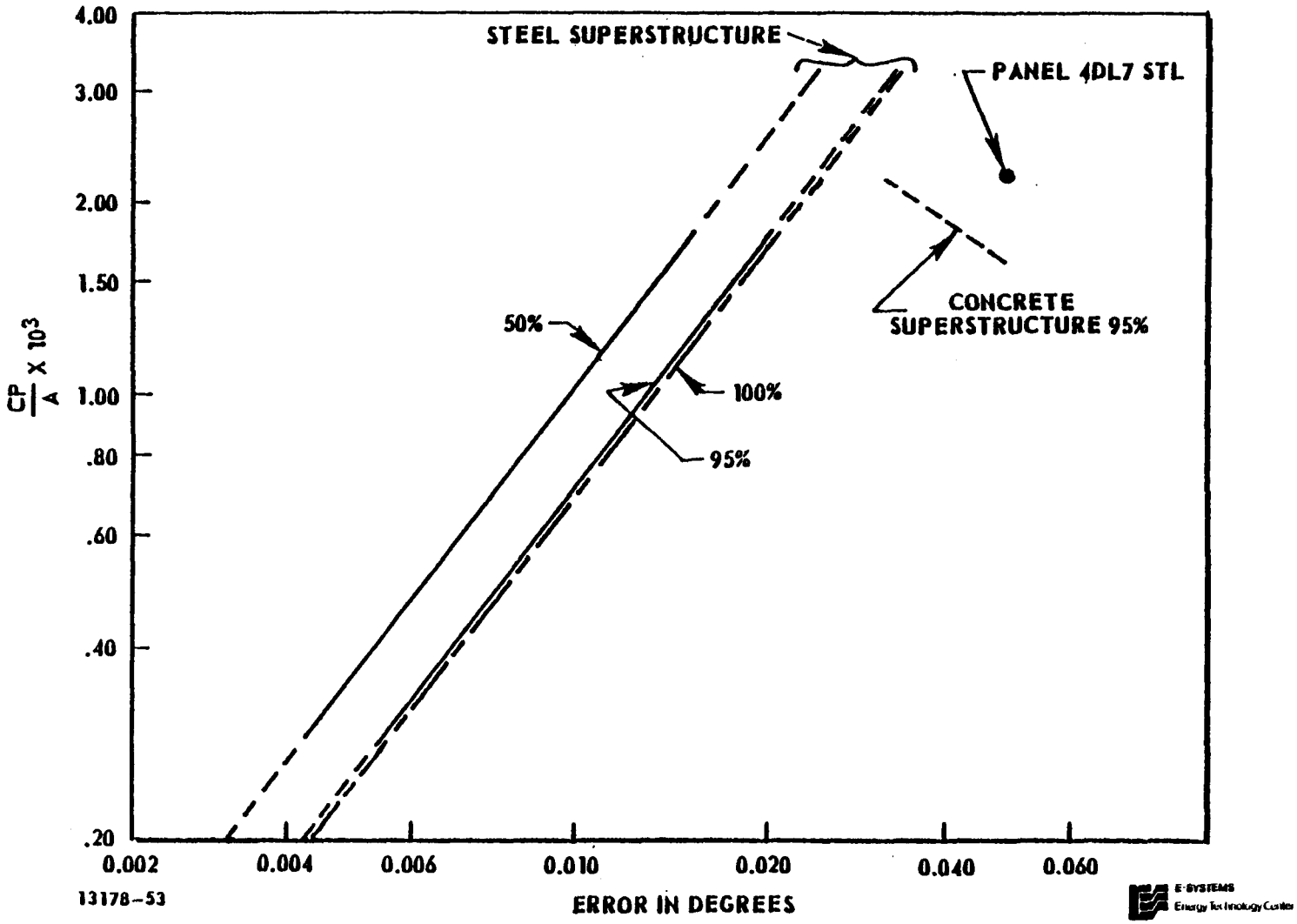

Figure E-4. Plot of Error Versus $\frac{\text{Surface Pressure Coefficient}}{\text{Surface Area (Sq. Ft.)}}$

each condition, the following figures were revealed:

ε_w (wind error) = .0174°

ε_{dw} (dead weight error) = .0580°

ε_t (thermal error) = .0336°

ψ_p (combined panel error) = $\sqrt{\varepsilon_w^2 + \varepsilon_{dw}^2 + \varepsilon_t^2}$

ψ_p = .0693° (95% limit)

The above error values are thought to be representative of the recommended panels.

Alignment Error

Each panel is individually adjustable, therefore any manufacturing error of panel support structure can be neglected because its effect is "biased-out" during the final alignment procedure.

Alignment errors have their origin from two contributing factors which are the ability to align the surface unit normal with the center of curvature of the "as built" sphere and the ability to position the surface of the reflector panel at a specified radius from the center of curvature.

A laser-type alignment system is recommended for final alignment which was used in E-Systems 11 ft. aperture diameter FMDF test system. This laser is placed on a swivel mount located near the center of curvature. Within limits, high precise placement at center of curvature is not necessary due to the fact that once the device is locked in place it then becomes the definition of the center of curvature and the reflector is aligned about this point.

The alignment technique is as follows: the laser beam is reflected from the surface and the return beam displayed on a target whose center is the center of the original beam. The deviation of the returned beam represents the angular panel alignment error. This technique is depicted as follows:

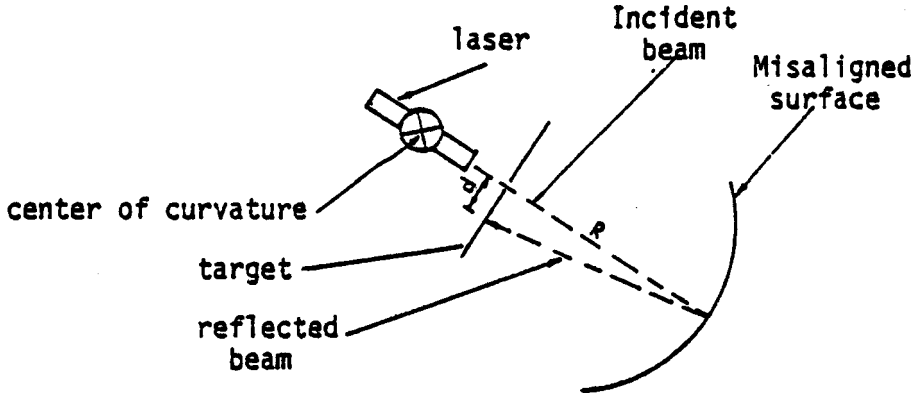

The beam illustrated above travels a distance R and is reflected approximately an equal distance R. The returned beam will deviate a distance 'd' from the original beam. This deviation thus represents an alignment error as follows:

$$\Delta\psi_A \text{ (deg)} = (d/2R)(180/\pi)$$

$\Delta\psi_A$ - Panel tilt alignment error in degrees

d - Return beam deviation in inches

R - Radius of sphere in inches

Preliminary investigation of available lasers and targets indicates that resolutions of 1/8 inch over a distance of 250 ft. is a reasonable value to be expected from the technique outlines above. For a 200 ft. diameter solar collector R is about 1386 inches. Thus:

$$\Delta\psi_A = (.125/2 \times 1386)(180/\pi)$$

$$\Delta\psi_A = .0025°$$

This represents a 95% limit to which the surface tilt can be adjusted.

The radial misalignment of a panel will cause an effective error due to "defocusing" of the concentrated beam, i.e., a loss in concentration will result as though the panel had a tilt error. This equivalent error is given as follows:

$$\Delta\psi_{A_R}(\text{deg}) = \tan^{-1}\left(\frac{2W}{R}\left|\frac{\Delta R}{R}\right|\right)$$

$\Delta\psi_{A_R}$ - Equivalent alignment error due to radial displacement

W - Width of or length of panel in inches

ΔR - Change in sphere radius due to alignment in inches

R - Sphere radius in inches

Techniques exist whereby ΔR can be limited to a few thousandths of an inch; however, these techniques would tend to be time consuming and tedious. A reasonably expedient technique is dictated by the number of individual panels and overall scope of the project. Several techniques were considered that would result in expedient prealignment of panels. Each of these techniques would yield a variation of approximately 3/4 inch panel alignment. It was considered that this alignment could be maintained within this limit at least 95% of the time. Applying this result to the above formula will yield an error as follows for a panel of 8 ft. length.

$$\Delta\psi_{A_R} = \tan^{-1}\left(\frac{2 \times 96}{1386} \times \frac{.75}{1386}\right)$$

$$\Delta\psi_{A_R} = .0045°$$

The above error represents an expected value; however, it could very possibly improve with further investigation of positioning techniques.

Substructure Errors

It was possible to compute all the substructure panel errors directly from deflections computed during the structural analysis of the substructure. These were computed for the identical panels that were used in the superstructure analysis. Figure E-5 shows the panel error and location for a rigid frame substructure.

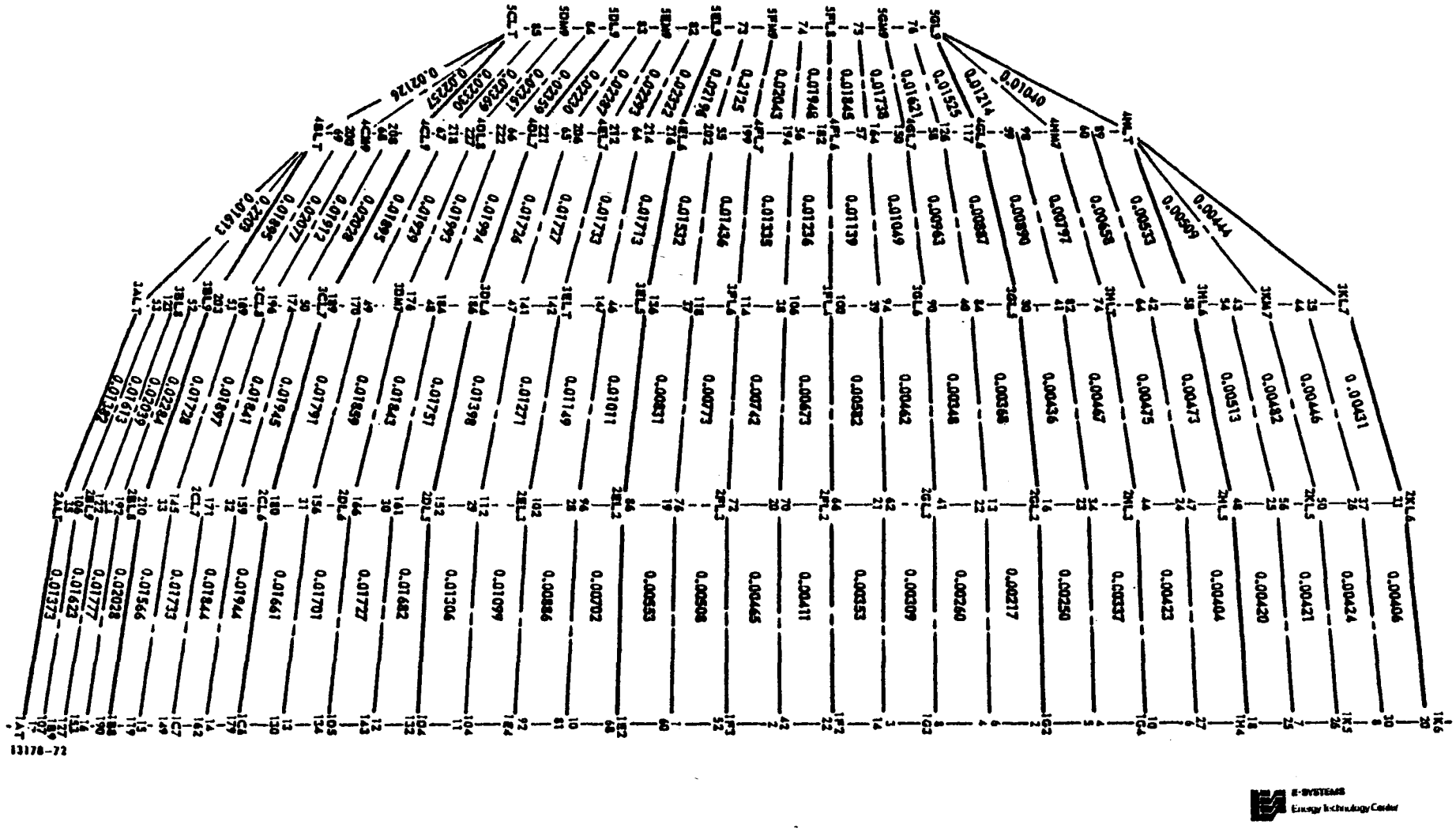

Figure E-5. Super Structure Error Distribution Degrees 200 Ft. Diameter Concentrator (Sheet 1 of 2)

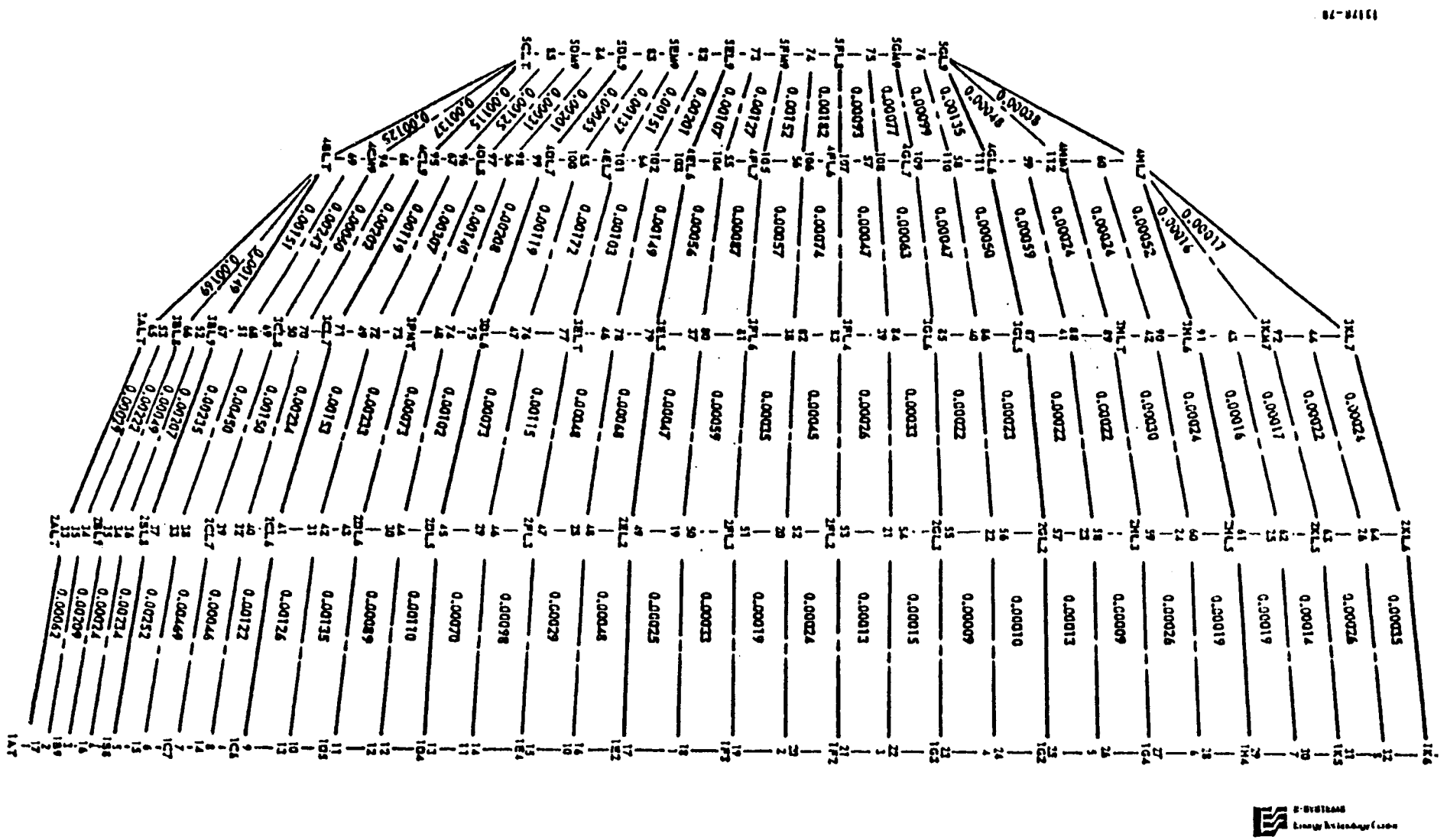

Figure E-5. Substructure Error Distribution Degrees
(Sheet 2 of 2)

with the columns arranged in the lune configuration and the wind from the south. The error here also closely matches the load distribution. Table E-3 is a tabulation of substructure errors for the various concentrator configurations. Differential settlement will contribute also to the substructure errors. At the present these errors can only be estimated since additional soils field testing is required to obtain the modulus of elasticity and the consolidation and settlement properties of the soil. Estimated values are included in the error tabulations.

E-4.3 Error Summary

The errors discussed above are assumed to be independent and random in nature. The individual contributing errors are assumed to possess a mean of "0". Effects of cross correlation are assumed to be second order effects and are considered to be small; therefore the above approach will give a good representation of the concentrator error. Conservative assumptions applied to certain facets of this analysis most certainly outweigh any second order effects due to cross correlation.

The effects of incident and reflected rays must be considered. The angle of incidence is equal to that of reflection; therefore any surface error is in effect doubled, i.e., errors are defined as deviations of the unit normal and the reflected ray has a mirror image of this deviation. Errors are assumed to be uniformly distributed about a mean of zero, thus they are assumed to possess random characteristics of both positive and negative values. The effect of this property is that the range of errors is doubled, thus

TABLE E-3 SUMMARY OF CONCENTRATOR SUBSTRUCTURE WEIGHTS AND ERRORS 30 MPH WIND

DIAMETER	VERTEX DEPTH	STRUCTURAL TYPE	EXCAVATION TYPE	STRUCTURAL MATERIAL	COLUMN CONFIGURATION	FOUNDATION	AIR LOADS TYPE	WIND DIRECTION	SUBSTRUCTURE WEIGHT	ERROR 95%
FT.	FT.								LBS.	DEGREES
100	+ 3.3	Truss	None	Steel	Lune	Spread Ftg.	Parabolic	South	46,000	0.00438
100	- 6.0	Truss	Spher	Steel	Lune	Spread Ftg.	Parabolic	South	30,000	0.00438
100	-12.0	Truss	Spher	Steel	Lune	Spread Ftg.	Parabolic	South	18,000	0.01018
300	+10.0	Truss	None	Steel	Lune	Spread Ftg.	Parabolic	South	696,000	0.02196
300	-18.0	Truss	Spher	Steel	Lune	Spread Ftg.	Parabolic	South	421,000	0.01067
300	-48.0	Truss	Spher	Steel	Lune	Spread Ftg.	Parabolic	South	215,000	0.00883
200	+ 6.7	Truss	None	Steel	Lune	Spread Ftg.	Parabolic	South	255,000	0.00960
200	-12.0	Truss	Spher	Steel	Lune	Spread Ftg.	Parabolic	South	152,000	0.00666
200	-32.0	Truss	Spher	Steel	Lune	Spread Ftg.	Parabolic	South	90,800	0.00824
200	-32.0	Truss	Spher	Steel	Lune	Spread Ftg.	Parabolic	South	90,800	0.00938
200	-32.0	Rigid Frame	Spher	Concrete	Lune	Spread Ftg.	Parabolic	South	40 cy	0.00666
200	-32.0	Rigid Frame	Spher	Concrete	Lune	Spread Ftg.	Spher	South	40 cy	0.00745
200	-32.0	Rigid Frame	Spher	Concrete	Lune	Spread Ftg.	Spher	S.E.	40 cy	0.00558
200	-32.0	Rigid Frame	Spher	Concrete	Lune	Spread Ftg.	Spher	East	40 cy	0.00324
200	-32.0	Rigid Frame	Spher	Concrete	Lune	Spread Ftg.	Spher	N.E.	40 cy	0.00344
200	-32.0	Rigid Frame	Spher	Concrete	Lune	Spread Ftg.	Spher	North	40 cy	0.00458
200	-32.0	Rigid Frame	Spher	Steel	Lune	Spread Ftg.	Spher	South	63,000	0.00235
200	-32.0	Rigid Frame	Spher	Steel	Lune	Spread Ftg.	Spher	South w/Berm		0.00219
200	-32.0	Rigid Frame	Spher	Steel	Lune	Spread Ftg.	Spher	North	63,000	0.00245
200	-32.0	Rigid Frame	Spher	Steel	Lune	Spread Ftg.	Spher	S.E.	63,000	0.00199
200	-32.0	Rigid Frame	Spher	Steel	Lune	Spread Ftg.	Spher	East	63,000	0.00119
200	-32.0	Rigid Frame	Spher	Steel	Lune	Spread Ftg.	Spher	N.E.	63,000	0.00203
200	-32.0	Rigid Frame	Trench	Steel	Rectang.	Spread Ftg.	Spher	South	113,000	0.01217
200	-32.0	Rigid Frame	Trench	Steel	Rectang.	Spread Ftg.	Spher	South w/Berm	99,200	0.00767
200	-32.0	Rigid Frame	Trench	Steel	Rectang.	Spread Ftg.	Spher	North	113,000	0.00546
200	-32.0	Rigid Frame	Trench	Steel	Rectang.	Spread Ftg.	Spher	North w/Berm	99,200	0.00441
200	-32.0	Rigid Frame	Trench	Steel	Rectang.	Spread Ftg.	Spher	S.E.	113,000	0.00200
200	-32.0	Rigid Frame	Trench	Steel	Rectang.	Spread Ftg.	Spher	East	113,000	0.00414
200	-32.0	Rigid Frame	Trench	Steel	Rectang.	Spread Ftg.	Spher	N.E.	113,000	0.00676
200	-32.0	Rigid Frame	Spher	Steel	Rectang.	Spread Ftg.	Spher	South	48,300	0.00521
200	-32.0	Rigid Frame	Spher	Steel	Rectang.	Spread Ftg.	Spher	South w/Berm	36,300	0.00387
200	-32.0	Rigid Frame	Spher	Steel	Rectang.	Spread Ftg.	Spher	North	48,300	0.00244
200	-32.0	Rigid Frame	Spher	Steel	Rectang.	Spread Ftg.	Spher	North w/Berm	36,300	0.00204
200	-32.0	Rigid Frame	Spher	Steel	Rectang.	Spread Ftg.	Spher	S.E.	48,300	0.00430
200	-32.0	Rigid Frame	Spher	Steel	Rectang.	Spread Ftg.	Spher	East	48,300	0.00229
200	-32.0	Rigid Frame	Spher	Steel	Rectang.	Spread Ftg.	Spher	N.E.	48,300	0.00258
65	-10.0	Truss	Spher	Steel	Lune	Spread Ftg.	Spher	South	13,900	0.00329

individual unit normal error is only 1/4 of the total reflected error. The net result is that all errors except radial error $\Delta\psi_R$ must be multiplied by four.

The errors defined above are considered independent as previously stated; therefore, the variance is equal to the sum of the individual variances. Thus the 95% operating error limit may be expressed as follows:

$$4\Delta\psi_T = \sqrt{(4\Delta\psi_A)^2 + (4\Delta\psi_M)^2 + (4\Delta\psi_P)^2 + (4\Delta\psi_S)^2 + (4\Delta\psi_B)^2 + \Delta\psi_R^2}$$

where:

$\Delta\psi_T$ - represents 95% limit on total concentrator error

$\Delta\psi_A$ - 95% limit on alignment error

$\Delta\psi_M$ - 95% limit on manufacturing tolerances

$\Delta\psi_P$ - 95% limit on individual panels due to operational loads

$\Delta\psi_S$ - 95% limit on intermediate panel support structure

$\Delta\psi_B$ - 95% limit on basic support structure

$\Delta\psi_R$ - 95% limit on reflector radial error

For system analyzed:

$$\Delta\psi_A = .0025°$$

$$\Delta\psi_M = .0750°$$

$$\Delta\psi_P = .0693°$$

$$\Delta\psi_S = .0130°$$

$$\Delta\psi_B = .0094°$$

$$\Delta\psi_R = .0045°$$

Thus these values lead to a total concentrator error of:

$$4\Delta\psi_T \text{ (95\% limit)} = .414°$$

Individual contributors to the above total error may be reviewed by referencing the appropriate sections contained within the body of this report.

The 95% error limit $\Delta\varepsilon_T$ was evaluated and found to be 0.103°. This value is slightly over 1/10 degrees and certainly within the limits specified for panels in the overall error budget.

E-5 ANALOG TEST SYSTEM

E-5.1 Purpose

The ATS will confirm or refine computer analysis of the structural system and will provide data on the dynamic characteristics of the soil foundation.

E-5.2 Specification and Preliminary Design Details

The minor support structure will consist of pre-fabricated steel trusset forming a matrix mounted to a rigid frame steel column substructure in an excavation. Intermediate beam trusset will be installed between main beams in a rectangular matrix to form a hemispherical grid with mounting pads for attachment of mirror panels. (See Figures E-6 and E-7)

The concentrator support structure will be placed in an excavation on a pier foundation similar to that planned for the 200-ft. diameter aperture diameter RPS system (See Figures E-6, E-7, and E-8). A berm will be used to determine techniques of integrating the support structure with the foundation and berm. The berm and excavation will be former to provide conditions for simulation of the wind flow patterns in the concentrator similar to a full scale system. A security fence will be provided around the ATS collector and a temporary building for data acquisition.

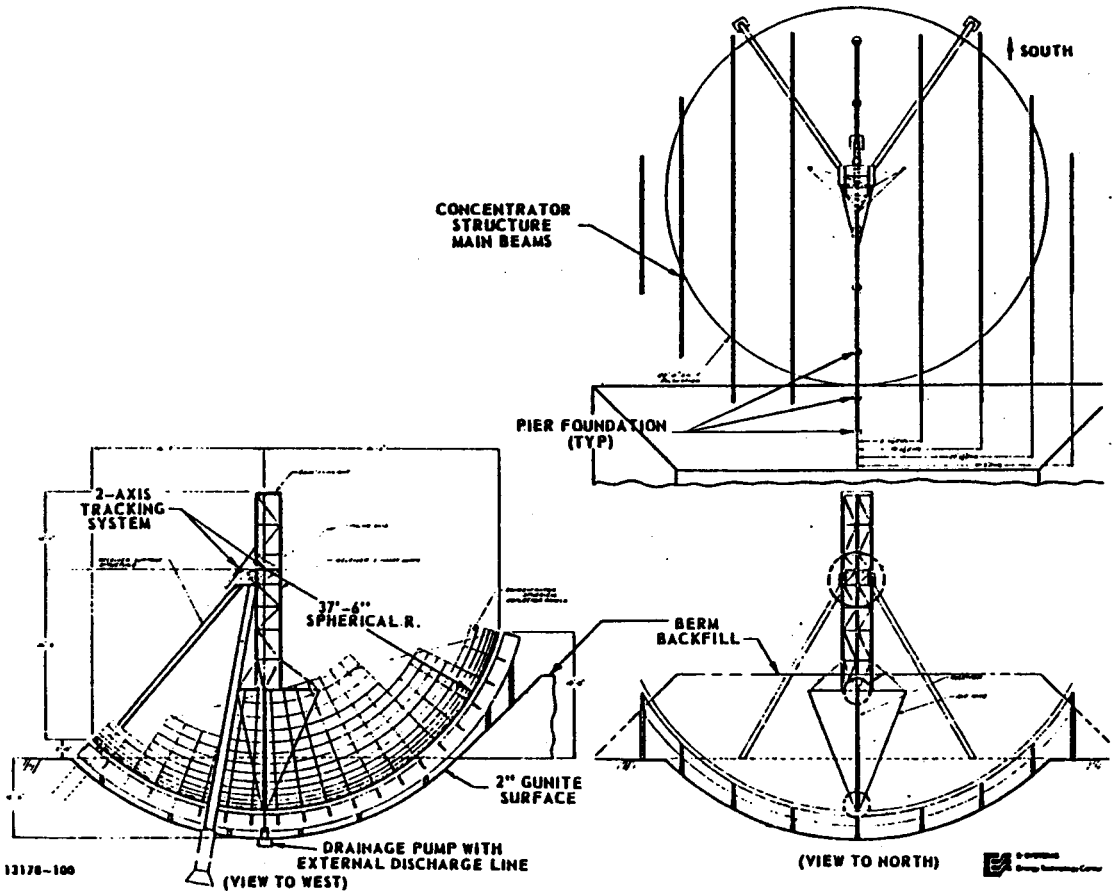

Figure E-6. 65 ft. Aperture Diameter FMDF Analog Test System

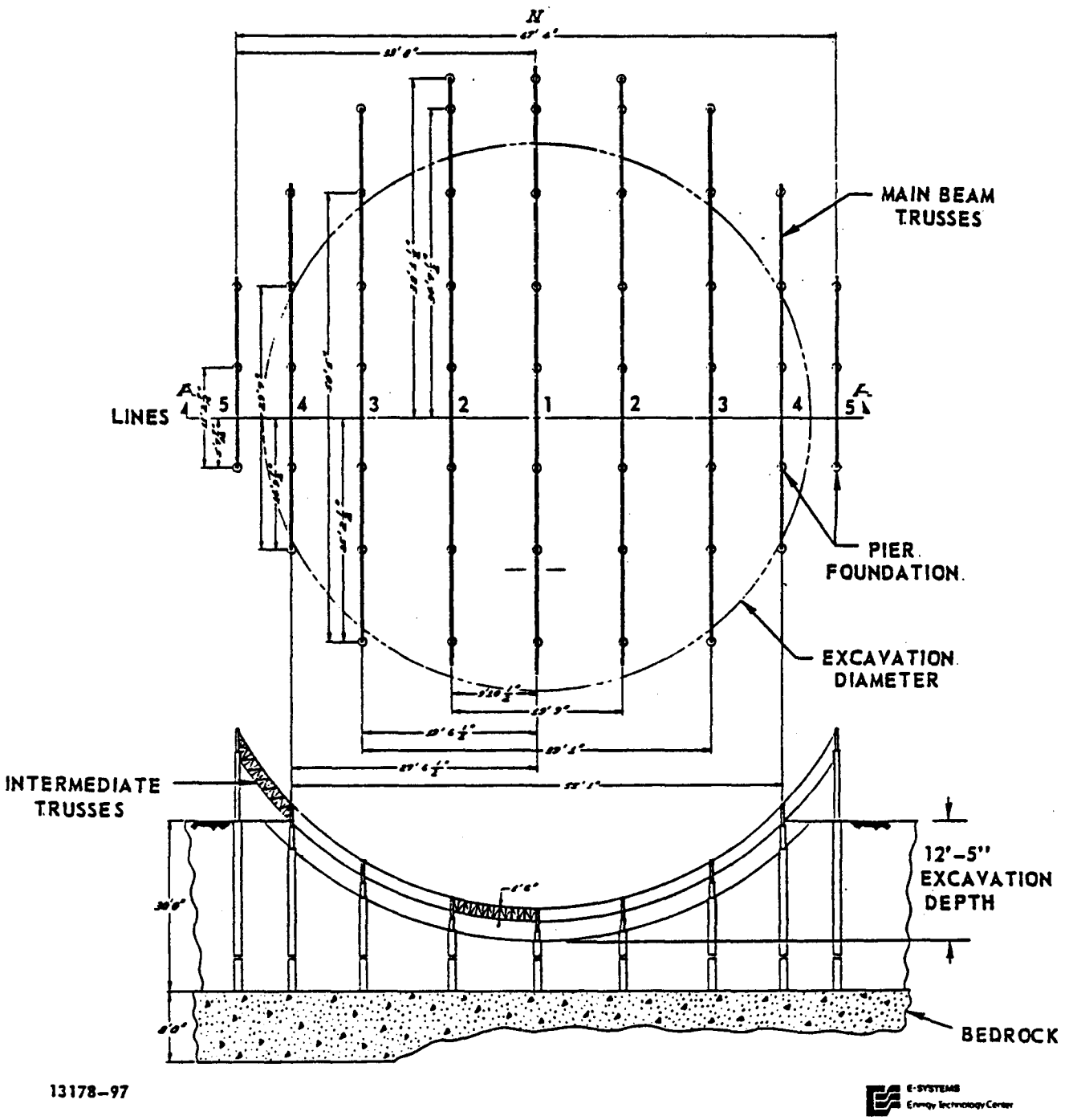

Figure E-7. ATS Concentrator Support Structure and Foundation

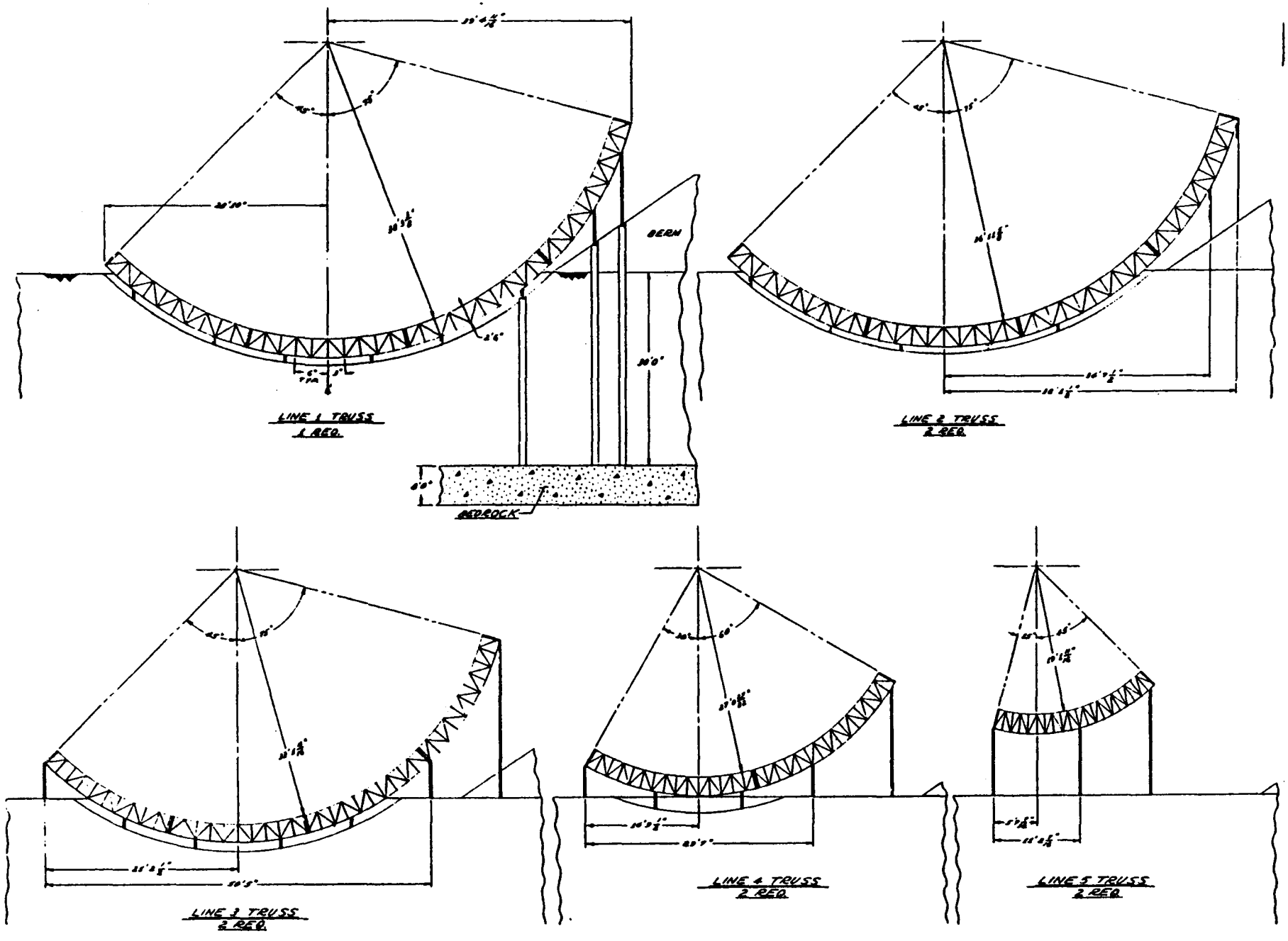

Figure E-8. ATS Sections Showing Main Beam Trusses

E-5.3 Instrumentation of ATS

Weldable and/or general purpose strain gauges will be used on the 65-ft ATS. Strain gauges will be placed on the support beam, tripod, some selected mirrored panels and the main frame. It is estimated that 50 strain gauges will be required. A minimum of 10 accelerometers will be placed on the boom support, receiver, tripod structure and main frame. Fig. E-9 shows proposed location of accelerometers and strain gauges.

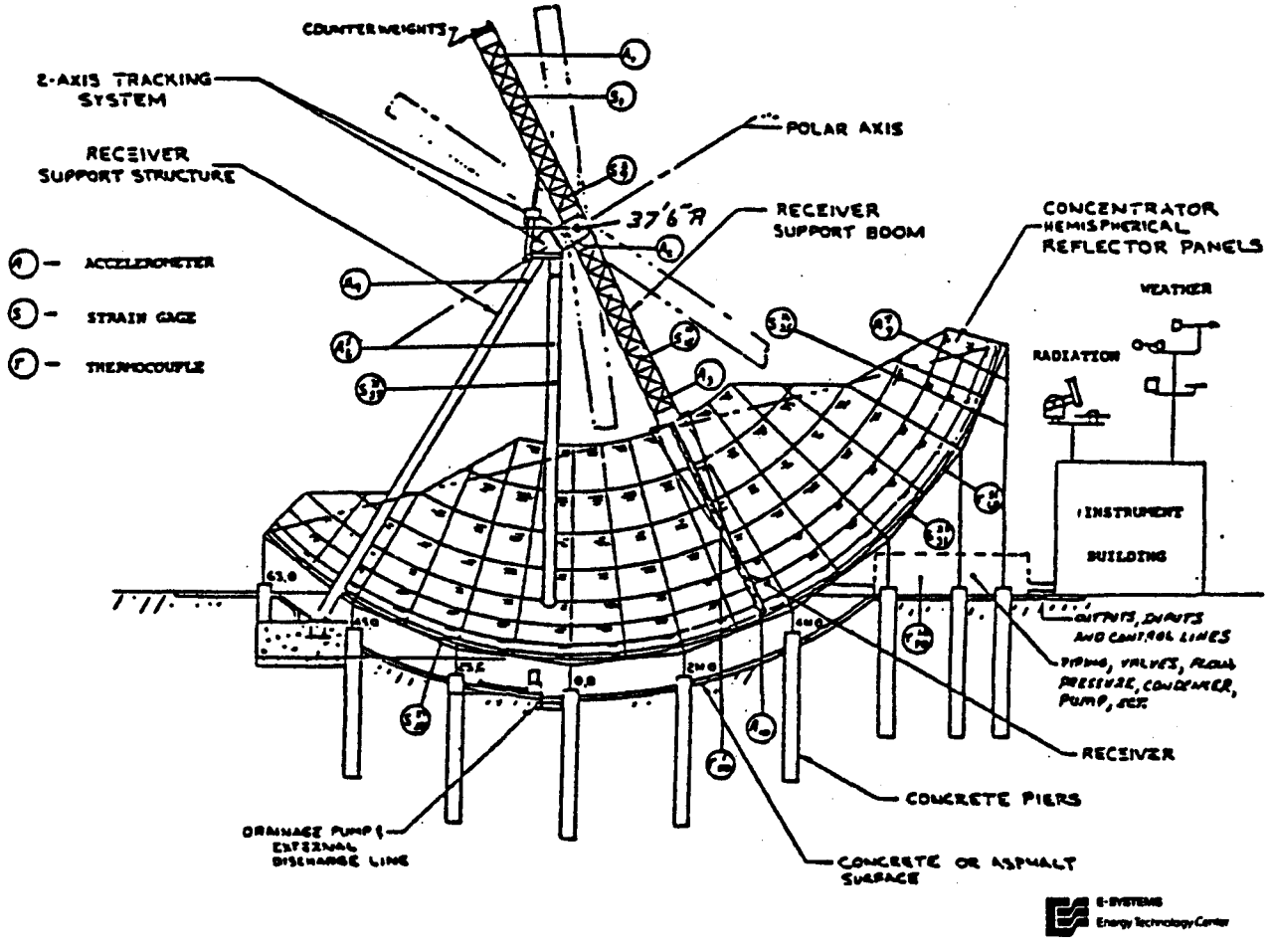

Figure E-9. 65 Ft. Aperture Diameter FMDF Instrumentation

REFERENCES - APPENDIX E

E-1 ANSI A58.1 - 1972 American

National Standard Building Code Requirements for Minimum Design Loads in Buildings and Other Structures American National Standards Institute, 1972

E-2 Manual of Steel Construction American Institutes of Steel Construction, 1970

E-3 DD. B. Barkan, Dynamics of Bases and Foundations McGraw-Hill Book Company, 1962

E-4 EIA Standard RS-411

Electrical and Mechanical Characteristics of Antennas for Satellite Earth Stations Electronic Industries Association, 1973

APPENDIX F. SURVIVABILITY, MAINTENANCE & SAFETY

F-1 MIRROR SURVIVABILITY

The fixed mirror concept by necessity has the mirrors permanently set at specific angles. While this concept may offer advantages in lower cost than that obtainable from other concepts, the fixed mirrors will be exposed to all hazards that occur at ground level. The major hazards are hailstones, wind, wind-blown sand and dust, and solar radiation (infrared to ultraviolet). Survivability of several candidate materials under the above hazards has been examined. These investigations are described in the following sections.

F-1.1 The Hailstone Hazard

The occurrence of hailstorms on the Texas South Plains has been extensively investigated by Mr. Oliver Newton of the Texas Agricultural Experiment Station at Lubbock. Newton has maintained a network of about 40 hailpad instruments over the Texas South Plains area beginning in 1972. These hailpads utilize a foil sheet covering a piece of foam. Hailstone impacts leave the foil with a permanent indentation that can be measured to obtain an estimate of hailstone diameter; also the angle of impact can be determined. The indentation size is approximately one-half of the hailstone's diameter.

Impact angles are determined from the location of the indentation on the foil sheet. The hailpad device and a foil sheet with numerous indentations are shown in Fig. F-1 and F-2.

Measurements of maximum indentation size on each sheet were made for every sheet from every location for the 1972-1976 period. The distribution of maximum recorded hailstone diameter recorded during each hailstorm was used to obtain the distribution in Table F-1; the data in Table F-2 represents a composite for all hailpad locations.

Maximum hailstone diameters for each year for hailpad locations at Crosbyton, Floydada, Abernathy, Idalou, Plainview and Slaton for 1972 through 1977 were used to develop estimates of maximum hailstone sizes expected over various periods of time. These estimates were made using statistical procedures described by Gumble [3] and Suzuki [4]. Similar estimates were made by Gringorten [2] and Gonzales [1] for other locations. Maximum expected hailstone diameters for the Crosbyton-Lubbock area are given in Table F-3; these diameters should be regarded as estimates due to inaccuracies in measuring hailstone impact diameters and the small size of the foil sheets. Nevertheless these estimates are believed to be reasonably accurate.

The angles of impact of hailstones affect mirror surface survivability. If impact angles are measured from vertical, the higher impact angles occur when hailstones are wind blown. Impact angles determined from the foil sheets indicate angles up to 60^{o} may occur for relatively large diameter hailstones. In Table F-4 impact angles are given for hailstones having diameters of 4 cm and greater.

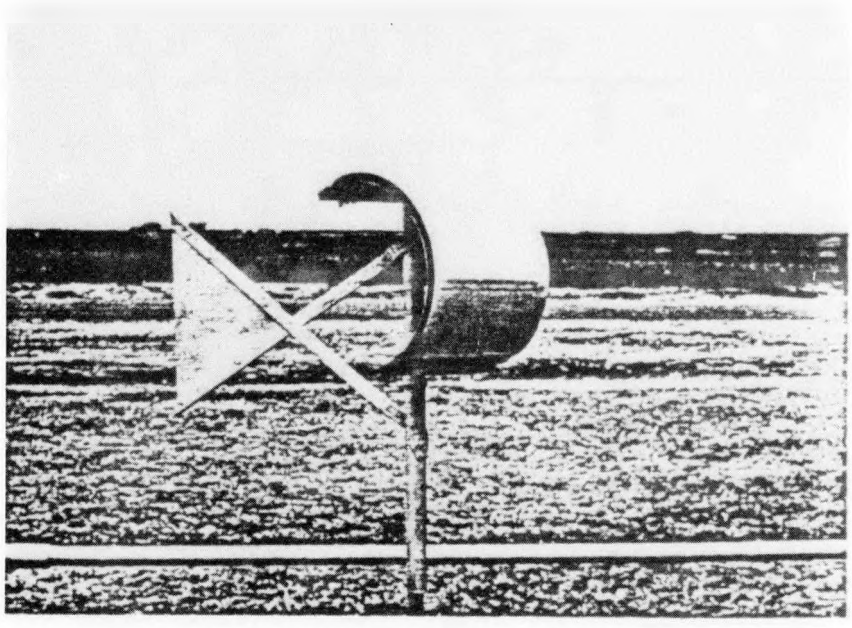

Figure F-1. Hailpad for determining Hailstone size

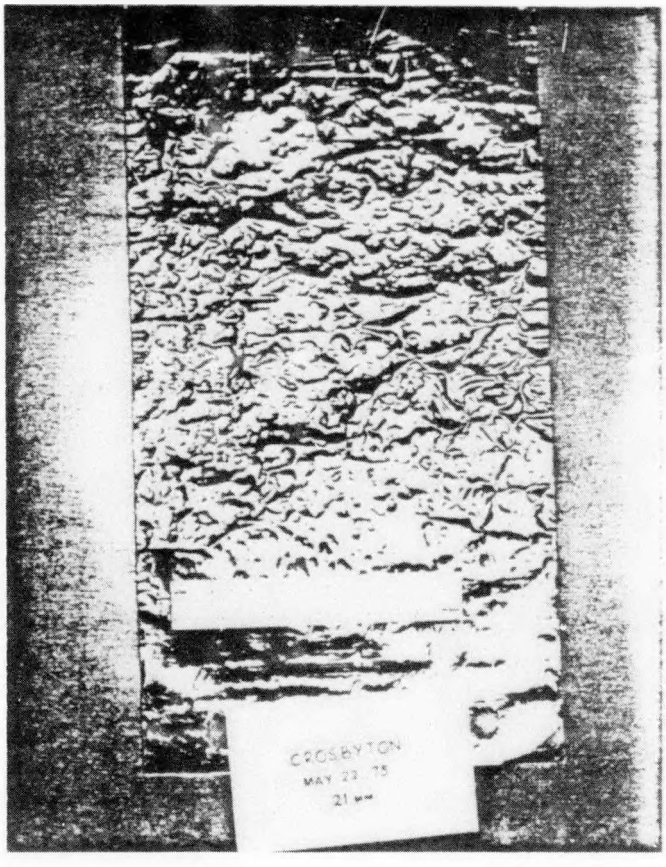

Figure F-2. Foil Sheet from Crosbyton Hailpad

TABLE F-1 DISTRIBUTION OF MAXIMUM HAILSTONE DIAMETERS

MAXIMUM HAILSTONE DIAMETER (cm)	
<2.0	.945
2.0-2.1	.025
2.2-2.3	.008
2.4-2.5	.014
>2.5	.008

TABLE F-2 CROSBYTON HAILPAD DATA

Year	Number of Hailstorms	Maximum Hailstone Diameter (cm)
1972	*	*
1973	2	1.4
1974	3	3.0
1975	2	2.1
1976	0	-
1977	6	1.0

*Data not recorded during the year

TABLE F-3 MAXIMUM HAILSTONE DIAMETERS EXPECTED ON THE TEXAS SOUTH PLAINS

Period (Years)	Maximum Diameter Hailstone Expected	
	(cm)	(in)
5	2.3	.91
10	3.7	1.46
25	4.2	1.65
50	4.6	1.81

TABLE F-4 IMPACT ANGLES OF HAILSTONES WITH DIAMETERS OF 4 cm AND LARGER

Impact Angle (^{0} from vertical)	FRACTION OCCURRENCES
0-15	0.20
16-30	0.06
31-45	0.27
45-60	0.27
>60	0.20

Terminal velocities of hailstones have been characterized by Gokhale as

$$V_T = 15d^{\frac{1}{2}} \qquad \text{(F-1)}$$

where V_T is vertical terminal velocity in m/sec

d is hailstone diameter in cm.

This also can be expressed as:

$$V_T = 53.5d^{\frac{1}{2}} \qquad \text{(F-2)}$$

where V_T is in miles/hour and d is diameter in inches.

The velocity resulting from windblown hailstones is

$$V_R = \frac{V_T}{\cos\theta} \qquad \text{(F-3)}$$

where θ is the angle from vertical of the hailstone impact.

Fig. F-3 gives hailstone velocities (V_R) for a range of hailstone sizes and impact angles.

Hailstone Impact Tests

Facilities were developed at Texas Tech University to permit testing of mirror materials subjected to impacts. The major pieces of equipment are shown in Fig. F-4; the air cannon has interchangeable barrels and can handle missiles with diameters of 2.54 cm (1.0 in.), 3.81 cm (1.5 in.), 5.08 cm (2.0 in.) and 6.35 cm (2.5 in.). A photoelectric timing gate shown in Fig. F-4 is used to start and stop an electronic timer. Hailstones are simulated with iceballs that are cast to obtain a spherical shape.

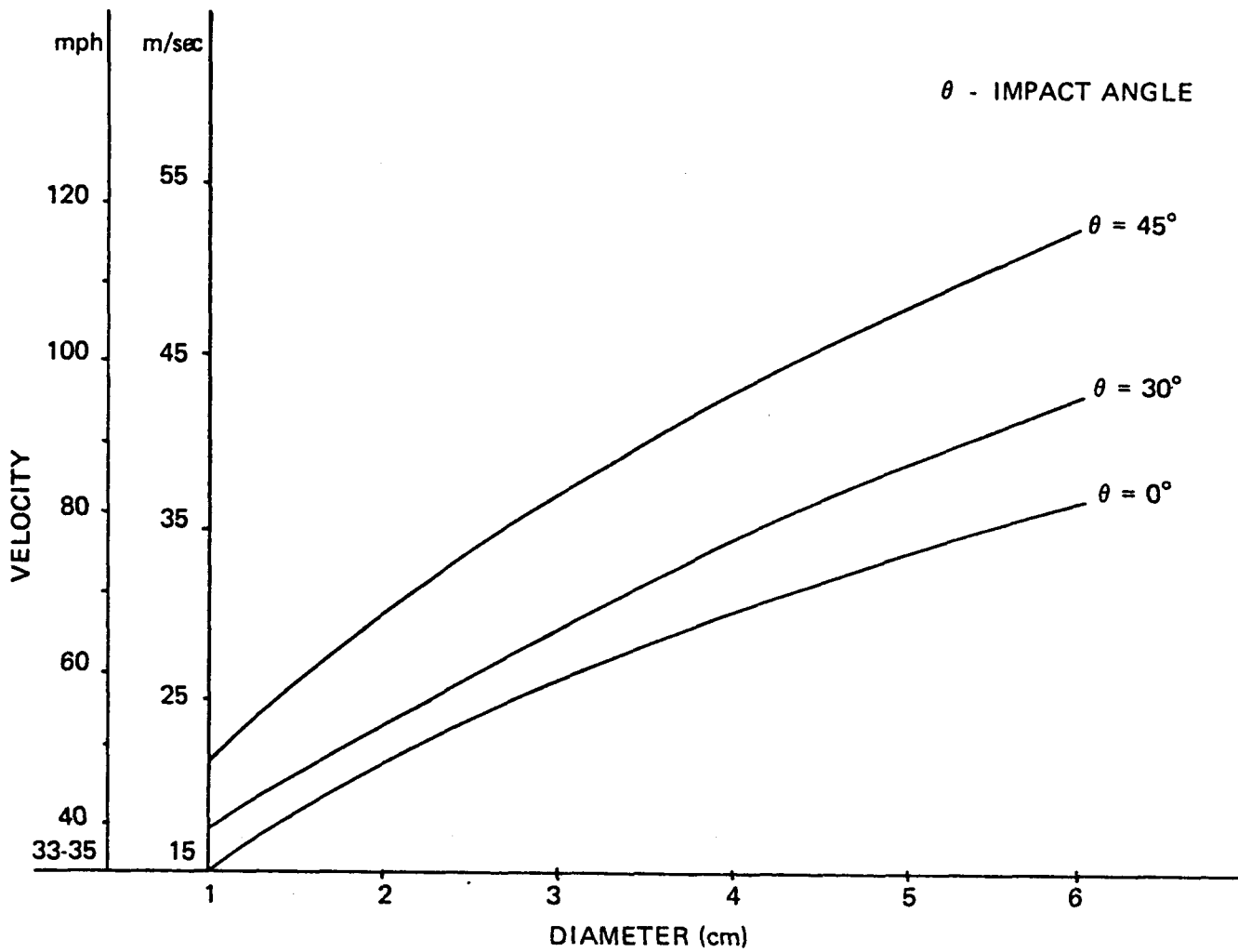

Fig. F-3. THEORETICAL TERMINAL VELOCITIES OF HAILSTONES

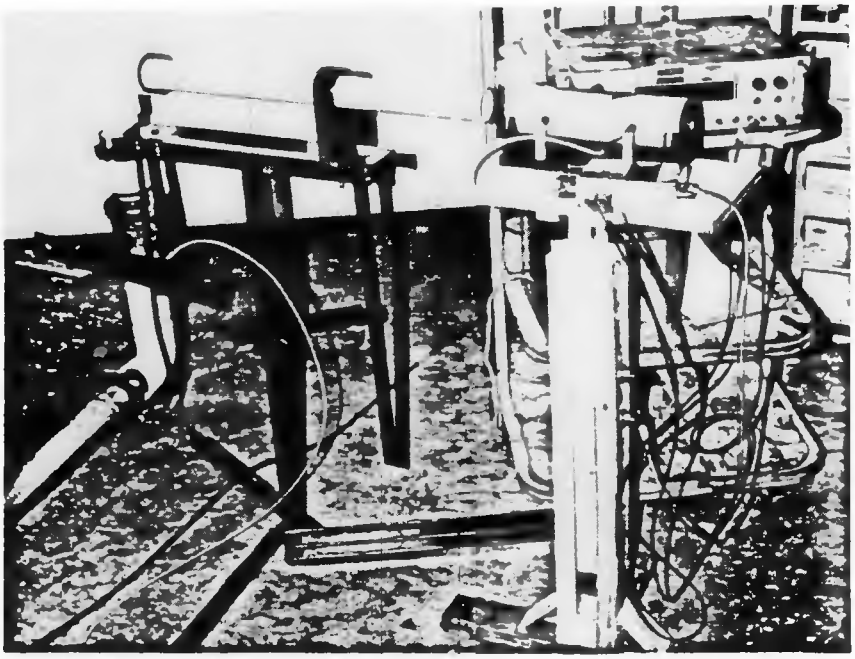

Figure F-4. Hail Impact Test Equipment

The photocell timing apparatus was calibrated by two methods. A radar gun for determining vehicle velocities was able to detect missile velocities up to 76 mph. A linear regression yielded:

$$\text{Photocell mph} = -0.33 + 1.03\ (\text{Radar mph}) \qquad \text{(F-4)}$$

with a correlation coefficient of 0.9996. Gravity drop of a steel ball also was used to verify the photocell timing apparatus. Theoretical velocities were 8% higher than velocities measured by the apparatus. When inaccuracies in manual release of the ball and drag due to air resistance are considered, the measurements from the photocell appear acceptable.

Impact tests were first conducted on float glass mounted in a frame similar to a window. These results are summarized in Table F-5.

Next, tests were made on both flat and concave glass on the honeycomb substrate. Results from these tests are given in Table F-6. Fig. F-4 shows a mirror panel specimen after the completion of impact tests.

The data in Table F-6 provide considerable guidance in selecting materials for the mirror surface. Acrylic has a relatively low breaking velocity and likely will not survive a 1½ in. hailstone. The 0.04 in. and 3/32 in. glass also appears to have low survivability properties. Two types of samples of 1/8 in. glass were available for testing. With a 1½ in. iceball the flat glass had an average breaking velocity of 100.7 miles/hour and a standard deviation of 18.9. Curved glass had an average breaking velocity equal to 127.8 miles/hr. with a 10.7 standard deviation. Both the flat and curved samples broke at 77 miles/hr. with a 2 in. iceball.

TABLE F-5 RESULTS OF IMPACT TESTS ON FLOAT GLASS

Glass Thickness (in)	Iceball Dia (in)	Min Break Vel (mph)	Max Break Vel (mph)	Avg Break Vel (mph)	Std Dev of Break Vel
1/8	1½	31	83	52.6	15.2
3/16	1½	63	135	93.2	26.1
3/16	2	58	89	72.2	9.0
1/4	1½			153.0	

TABLE F-6 HAIL IMPACT TESTS ON SUBSTRATE MOUNTED MATERIAL

Material	Material Thickness (in)	Iceball Diameter (in)	Breaking Velocity (mph) min	max	avg	std dev
Glass (Flat)	0.04	1			41.2	
Glass (Flat)	3/32	1½	52.0	75.8	63.9	16.8
Glass (Flat)	1/8	1½	75.7	119.2	100.1	18.9
Glass (Curved)	1/8	1½	116.0	136.9	127.8	10.7
Glass (Flat)	1/8	2			77.0	
Glass (Curved)	2	2			77.5	
Acrylic (Flat)	1/8	1½	47.0	53.0	50.2	2.9

Table F-6 data indicate 2 in. hailstones likely will break the mirrors. The 77 miles/hour breaking velocity is only slightly above the 75.7 miles/hour terminal velocity of 2 in. hailstones. Only a slight wind will increase the velocity to the observed breaking velocity. Fortunately the 50 year maximum expected diameter hailstone is 1.81 in. Of course, there is a positive probability of damaging hailstones occurring. However, it appears that the proposed 1/8 in. glass mirrors are suitable for the ATS and RPS.

The results of impact tests must be viewed with some caution due to the small number of tests performed. A single piece of 1/8 in. curved glass shown in Fig. F-5 was used for all the curved glass data in Table F-6. However, the average breaking velocity for 1½ in. iceballs was quite high when compared with the theoretical velocities for 1½ in. hailstones. An actual hailstone must be blown by a 96 mile/hour wind in order to achieve a velocity of 116 miles/hour; this was the minimum observed breaking velocity. In order for a 1½ in. hailstone to reach the 127.8 miles/hour average breaking velocity, the hailstone will have to fall in a 110 mile/hour wind. Thus it appears that the 1/8 in. glass mirror can survive 1½ in. hailstones.

There are several factors concerning mirror panel survivability that have not been fully addressed. One of these is the validity of simulating hailstones with iceballs. This practice has been used in several investigations including those at the Jet Propulsion Laboratory, Sandia Laboratory and the National Bureau of Standards. It is possible that iceballs are more uniform and are harder than hailstones; if this is true, the results reported in this section will tend to be conservative in that less damage will be incurred in hailstorms than the test results indicate.

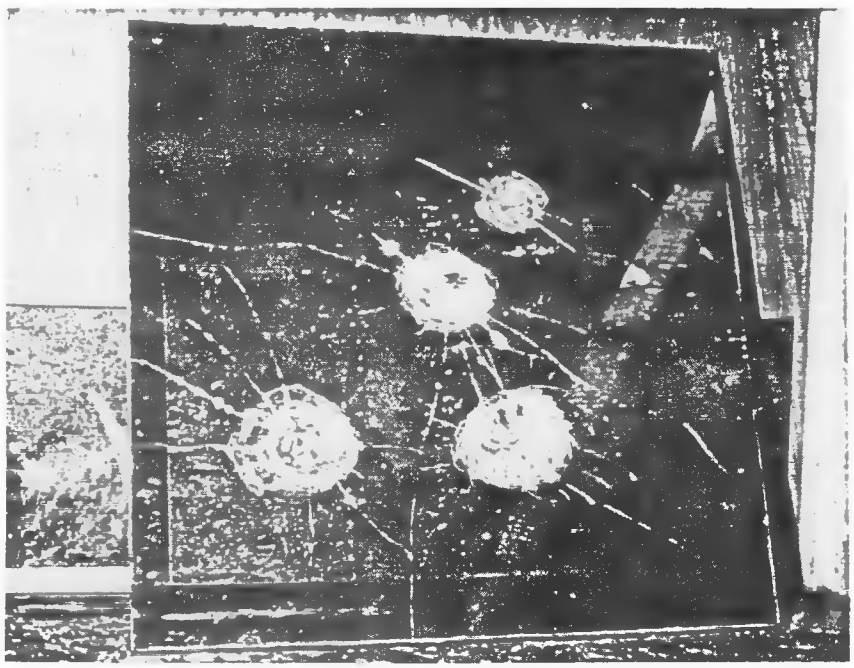

Figure F-5. Curved Glass Mirror After Hail Impact Test

The angle of impact also has not been considered. Regardless of the path of hailstones some will have a normal impact on some panels. However, many other panels will have no impact or else impacts at a very low angle such that no damage results.

The Hailstone Hazard -- Receiver Tubing

A flat plate of Inconel coated with Pyromark 2500 applied in a manner identical to that used in preparing the receiver model was subjected to iceball impact tests. Test results indicated no observable damage from impacts of 2 in. iceballs up to 97 miles/hour. Thus, it appears that the Pyromark coating will not be affected by impacts of hailstones.

F-1.2 Dust and Radiation Effects on Mirrors

The mirror panels are subjected to catastrophic failure from hailstone impact as described in the preceding section. Failure also can occur gradually due to adverse effects of dust and radiation. Investigation of these environmental effects were conducted on samples from several manufacturers. In this section the effects of dust, sand and radiation as they affect mirror life are examined. In Appendix D the environmental effects on reflectivity are considered.

On 18 February 1977 eight mirror sample sets were deployed around the windsock at the Crosbyton airport. The mirror mounting boxes and support poles were designed and fabricated locally. After driving in the support posts, the mirror mounting boxes were aligned NW - SW - SE - NE by use of a transit compass. The top of the mounting

boxes (approx. an 8 in. cube bolted to a flange on the poles) are about 7 ft. above ground. The disposition of the specimens is shown in Table F-7. Pole No. 1 is NW of the windsock. The poles are deployed CCW with No. 8 SSW of the windsock. The poles are 10-12 ft. apart. The support pole/mounting box configuration is shown in Figure F-6.

Additional samples were mounted on boxes identical to those used at the airport site and affixed to the Crosby County sherriff's transmitter tower on 6 June 1977. The mounting brackets are visible in Fig. F-7. Placement of these mirror samples is given in Table F-8.

All observations (except those made on 11 October 1977 after recovery of the samples) were made from the ground using 7 x 50 binoculars. These mounting boxes were also aligned by use of a transit compass.

In order to qualitatively assess the effect of solar radiation and windborne dust on the prospective mirror materials, a relative damage scale has been used. This scale is as follows:

0 no visible change

1 very faint dust film

2 slight dust film

3 significant dust film

4 heavy dust layer

5 very heavy dust accumulation

6 fine scratches

7 dust (any amount) and scratches

8 cracks or crazing

9 failure for any reason

TABLE F-7 PLACEMENT OF MIRROR SAMPLES AT CROSBYTON AIRPORT

Pole No.	Sample	Direction & Mirror Sample Number				
		NW	SW	SE	NE	horizontal
1	Scotchal 5400	1	2			
2	Alzac	1	2	3	4	5
3	RAM Acrylic	1	2	3	4	5
4	Glass	1	2	3	4	5
5	Carolina	2	1			3
6	Plexiglass	6	7	8	9	10
7	Kinglux CH/40	1	2	3	4	5
8	Donnelly	1	2			

TABLE F-8 PLACEMENT OF MIRRORS AT TRANSMITTER TOWER

Elevation	Sample	Direction & Mirror Sample Number				
		NW	SW	SE	NE	horizontal
96.6 ft.	Plexiglass	1	2	3	4	5
97.4 ft.	Glass	6	7	8	9	10
99.0 ft.	Alzak	6	7			

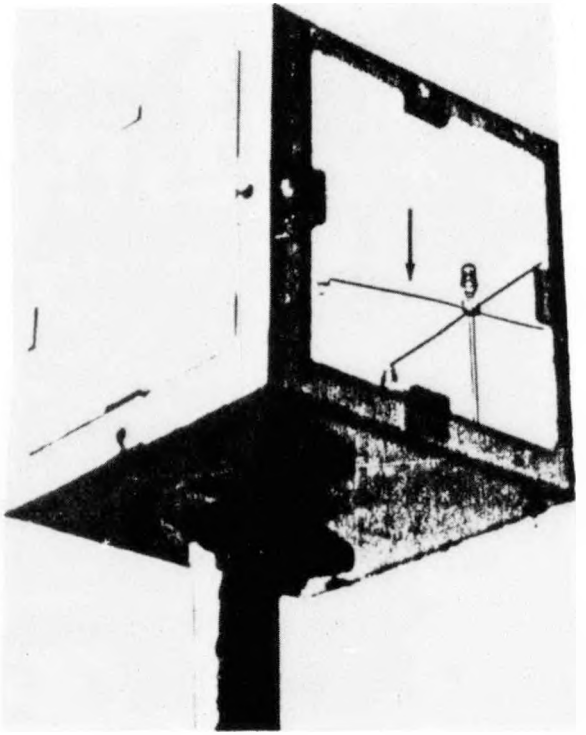

Figure F-6. Mounting Box for Mirror Samples at Crosbyton Airport

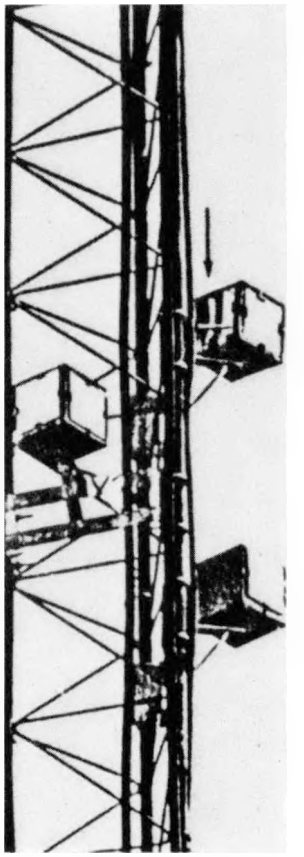

Figure F-7. Mounting Box for Mirror Samples at Transmitter Tower

In this scale we go from a rating of zero indicating no observable change in appearance from that at the time of deployment to nine indicating a wide variety of failures. Ratings 1-5 indicate a a steadily increasing film or deposit of windborne dust on the exterior mirror surfaces. Ratings 6-8 constitute incipient failure due to the presence of fine scratches, scrapes, cracks, or warping. The failure mechanisms are indicated alphamerically as follows:

A. blisters/separations of reflective surface
B. warping
C. regular curvature
D. first surface degradation/disintegration
E. second surface degradation/disintegration
F. broken
G. adhesive bond failure
H. pitting from hailstone strikes

The specimens were observed at approximately one month intervals with additional observations made after duststorms, thunderstorms, or hailstorms. Our assessment of the survivability characteristics of the eight materials tested are presented in graphical form using the characteristics described previously.

The samples of Scotchcal 5400 rapidly developed blistering. The reflective surface separated from the transparent second surface to which it had been attached in as many as 10-15 places, up to 1 cm diameter. The southwest sample (No. 2) failed in this manner after only four days exposure in the field. The northwest sample (No. 1) showed similar failure 5 weeks later. This material is therefore

unsuitable for use in the Crosbyton FMDF system. Characteristics of the performance of Scotchcal 5400 are given in Fig. F-8. The type of failure encountered with this material is shown in Fig. F-9.

Alzak samples showed no physical degradation for the first five (5) months in the field. During that time, all the specimens accumulated dust deposits as shown in Fig. F-10. After six (6) nights of rain between 16-27 June 1977 some cleansing of the specimens was noted. This material did not seem to be affected by the hailstorm at the airport on 23 May 1977. Visual observations on that date confirmed the average diameter of hailstones as 1-1.5 cm. The specimens deployed at the airport exhibited small creases and scratches (No. 2) and warping (No. 3) on 22 July. The degree of warp was very slight as shown in Fig. F-11 and therefore we initially concluded that this material could be marginally acceptable. Additional exposure for $2\frac{1}{2}$ months made it obvious that Alzak is unsuitable for the Crosbyton Solar Energy Project; 5 of the 7 samples showed some amount of warp and the other two, significant scratching.

After 4 months exposure, 4 of the 5 samples of RAM Acrylic (Fig. F-12) had accumulated varying amounts of dust. This dust was probably held on the surface as shown in Fig. F-13 by static electric forces due to triboelectrification. The heavy rains in late June were quite effective in removing the dust accumulations from the vertically mounted specimens (Nos. 1-4). The horizontally mounted specimen (No. 5) became scratched during the first 3 months of exposure. It was not cleaned by the rains in late June. After an additional 2 months of exposure, all 5 specimens showed significant irregular warping or the formation of roughly symmetric curvature as shown in Fig. F-14. It

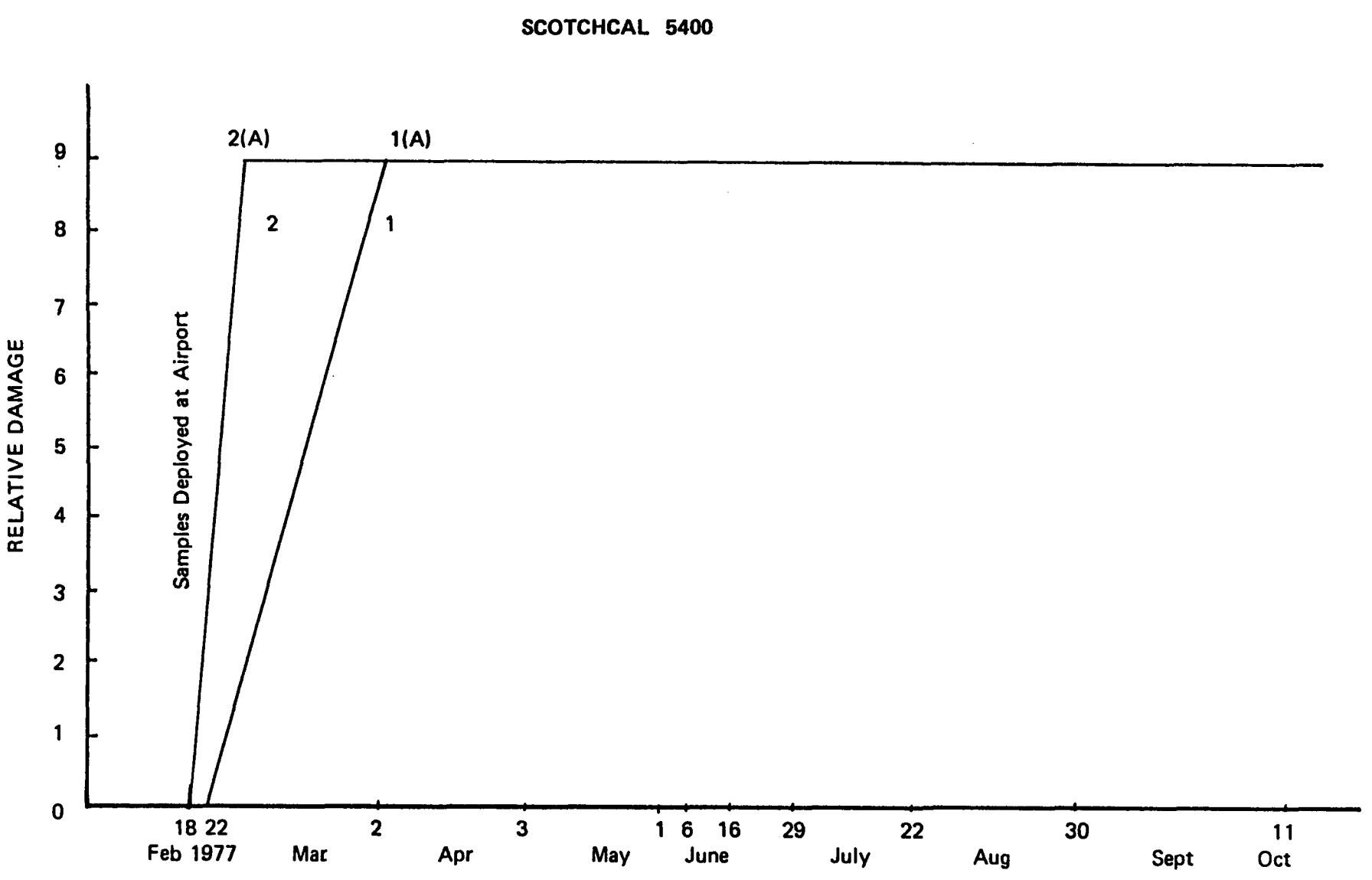

Figure F-8. Scotchcal Performance Characteristics

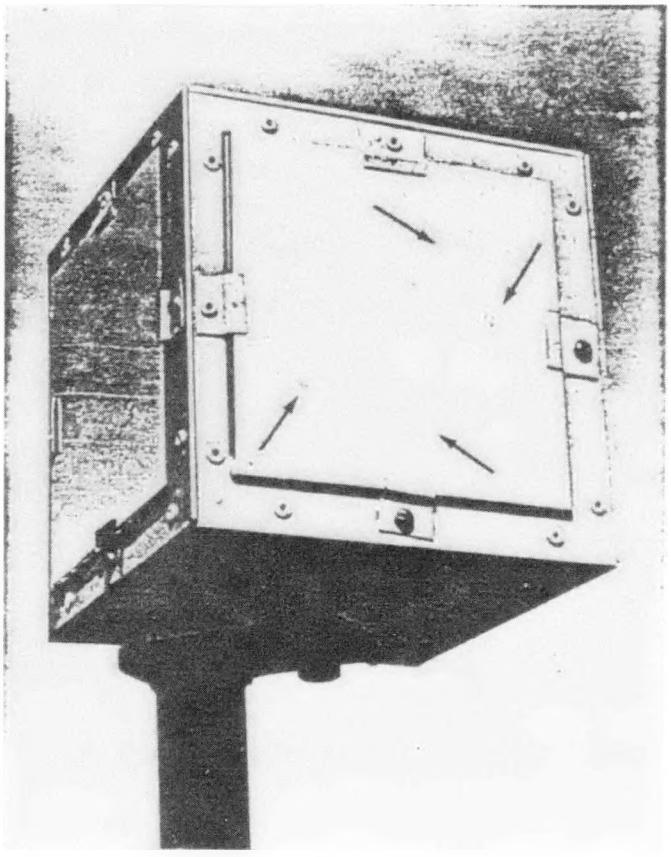

Figure F-9. Scotchcal Mirror Sample

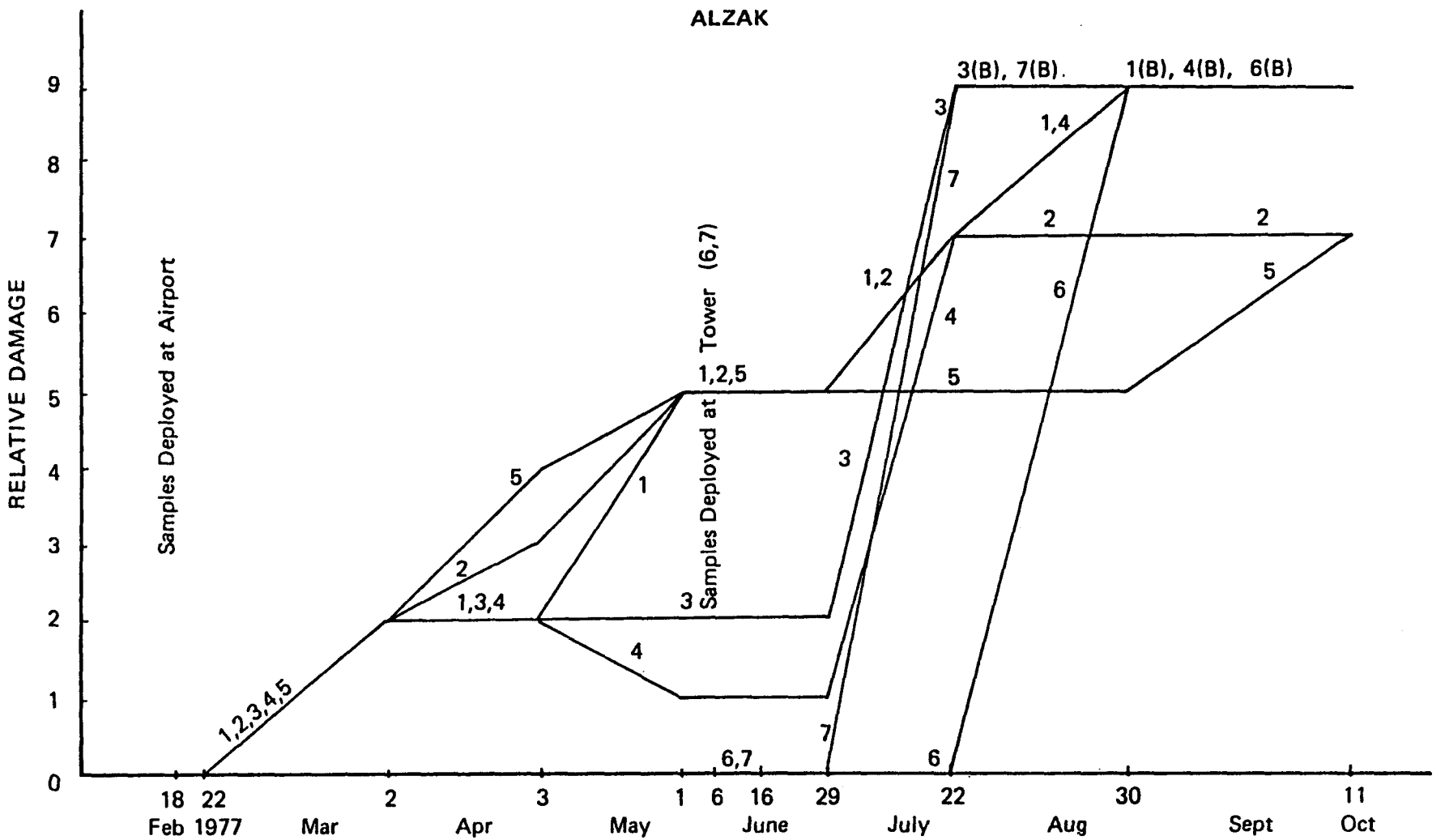

Figure F-10. Alzak Performance Characteristics

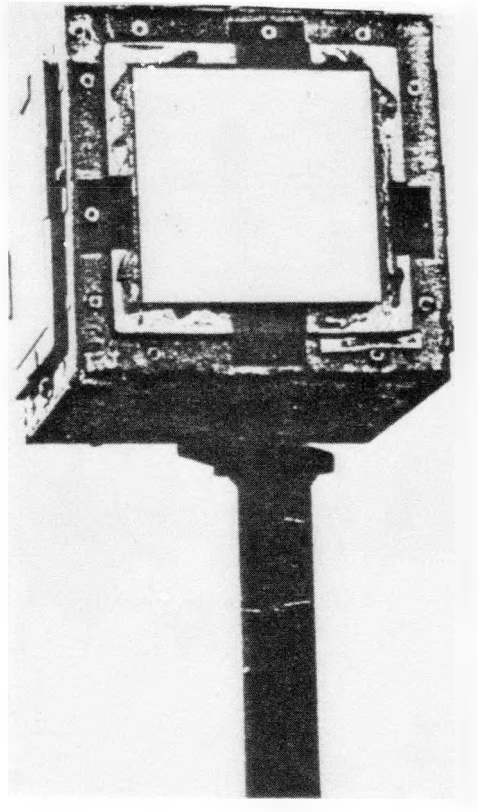

Figure F-11. Alzak Mirror Sample with Warping

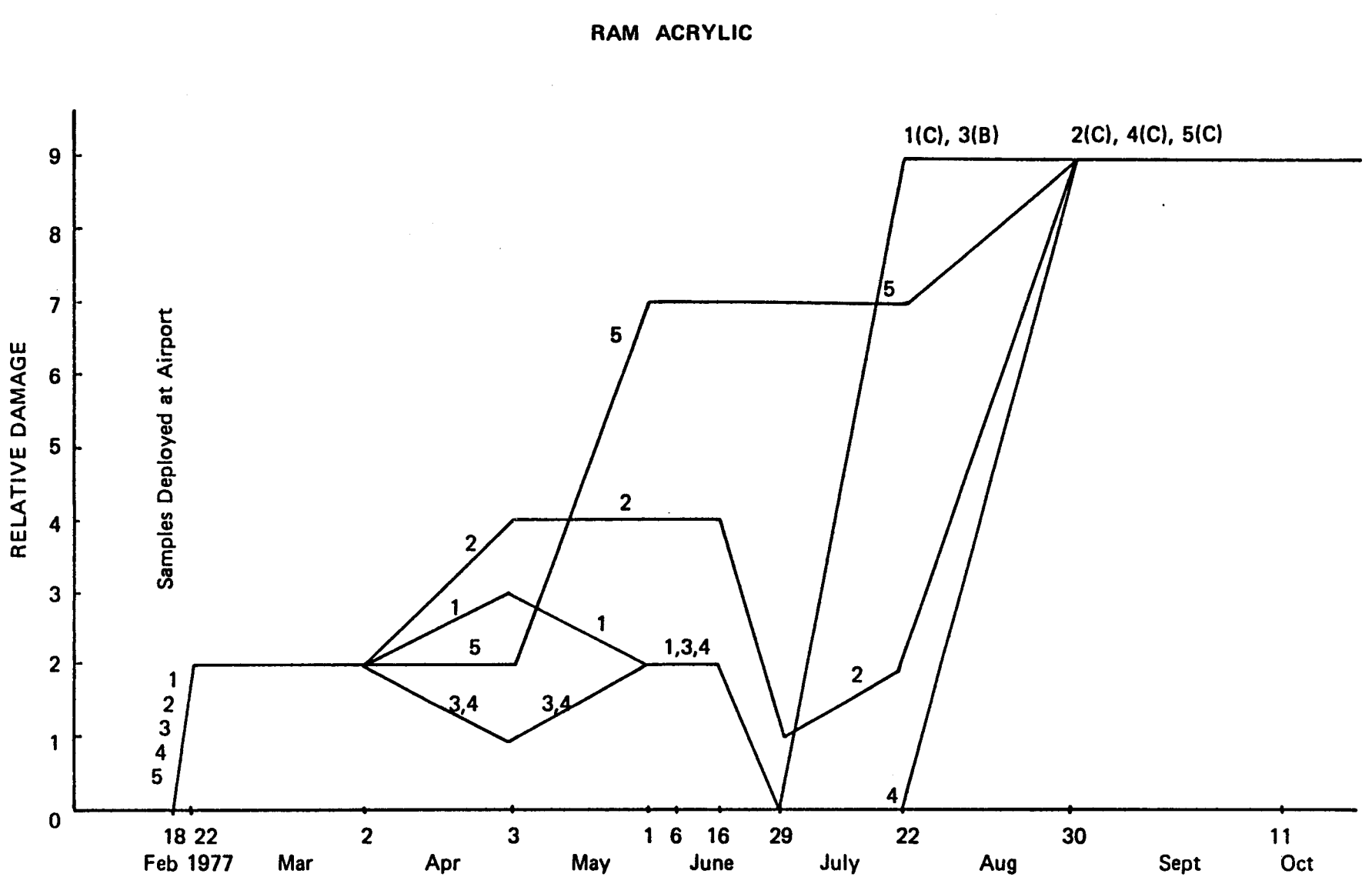

Figure F-12. RAM Acrylic Performance Characteristics

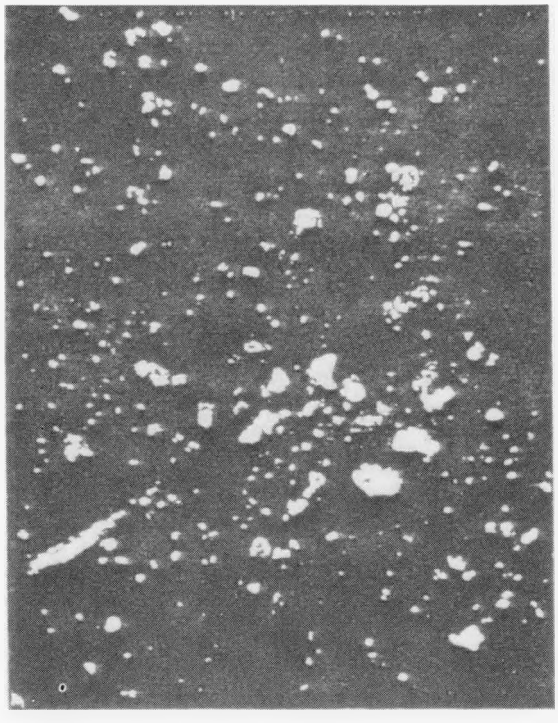

Figure F-13. RAM Acrylic Mirror Sample
at 240X with Dust on Surface

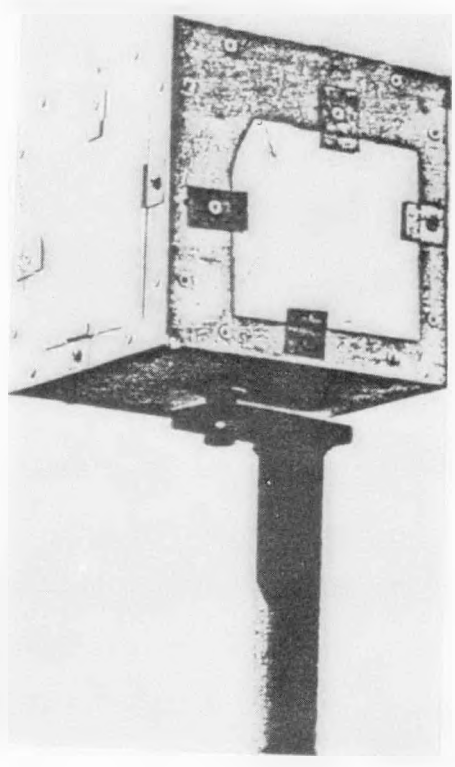

Figure F-14. RAM Acrylic Mirror Sample with Warping

should be noted that the cracks visible on the left side and bottom of the two RAM Acrylic specimens were there when the specimens were received and not due to environmental exposure. RAM Acrylic is unsuitable for use in the Crosbyton Project because of dust accumulation which occurs even during episodes of local blowing dust of low concentration.

Five specimens of glass were initially deployed at the airport (Fig. F-15). The amount of dust accumulation on the vertically mounted specimens appears to be related to exposure direction. During the hailstorm of 23 May, the horizontally deployed specimen (No. 5) was cracked right across the center and one corner was broken off. During the next 4½ months of exposure all but 2 of the remaining 9 specimens developed warping and/or disintegration of the reflective surface. Although glass is apparently easily cleaned by considerable amounts of rainfall, this material is unacceptable because it is mechanically unstable. The type of warping observed was shown previously in Fig. F-6 in the curvature of the image of the left hand arm of the lighting fixture.

After 4 months of exposure, the Carolina samples showed (Fig. F-16) varying degrees of accumulated dust which was only partially removed by the heavy rains of late June. Only one of the specimens showed even faint scratches when exposure was continued for another 4 months. Warping was never observed in any of these specimens. Carolina mirrors possibly should be examined in 5/32 in. thickness for hailstone resistance using the proposed honeycomb support mounting. The horizontal sample (NO. 3) appeared unaffected by the hailstorm on 23 of May. Optical microscopic examination of the surface at 480x showed no pitting or scratching.

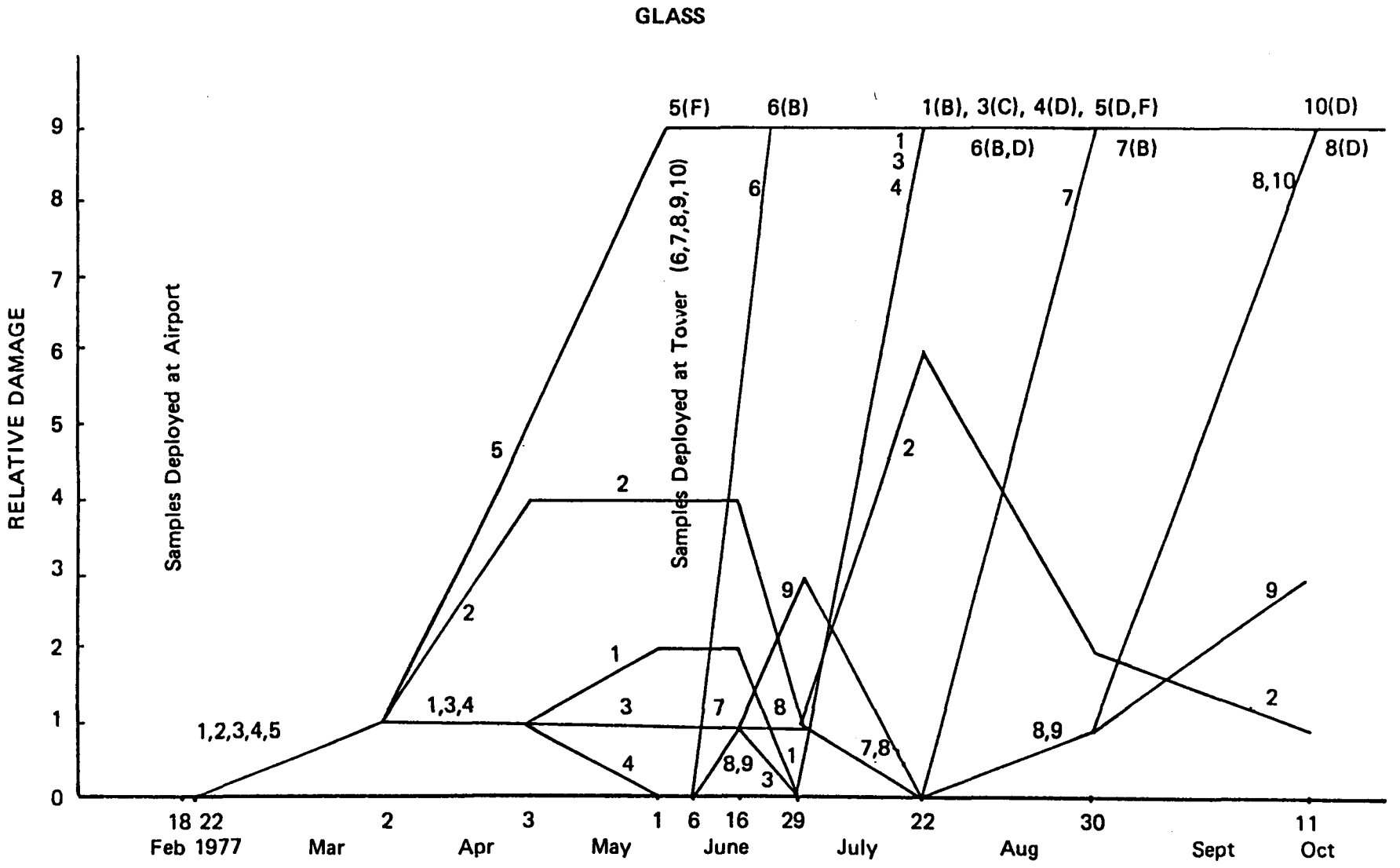

Figure F-15. Glass Mirror Sample Performance Characteristics

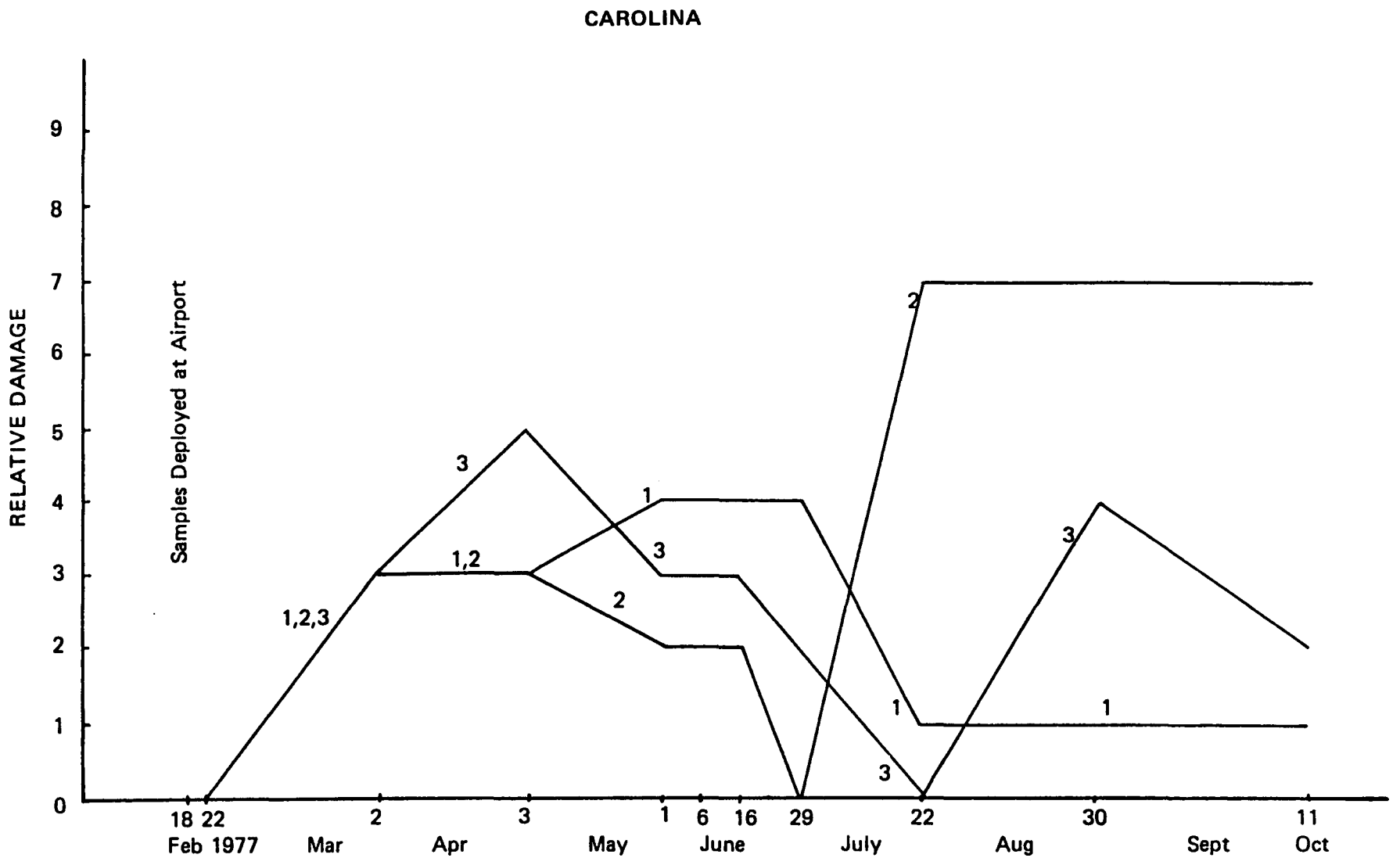

Figure F-16. Carolina Mirror Sample Performance Characteristics

Five samples of Plexiglass (Nos. 6-10) were initially deployed at the airport. Performance characteristics are summarized in Fig. F-17. After 4 months of exposure, no conclusions could be reached regarding the dust adherence to this material. After another month of exposure, 4 of these specimens (Nos. 6-9) showed definite warping as illustrated in Fig. F-7 and F-18. In Fig. F-18, sample No. 8 is visible on the pole in the foreground. The cloud image shows a definite lazy-S warping. In Fig. F-7, the mounting box at the top right was used for Plexiglass samples deployed on 6 June. The left specimen on that box clearly indicates warping by 29 June. The image of the tower frame appears shaped as a left-hand parenthesis. By the time all specimens were recovered on 11 October all Plexiglass samples had either warped or had begun to show reflective surface degradation and are thus double rejected for the Crosbyton solar energy collector. It is interesting to note that after 8 months dust accumulates, clumps, and stays on these specimens along the scratches as shown in Fig. F-19; these dust accumulations likely will eliminate Plexiglass as a suitable material for the mirrors.

Of the five specimens of Kinglux CH/40 deployed at the airport, 2 debonded from the adhesive: one after five weeks, the other after 14 weeks. Performance characteristics are summarized in Fig. F-20. The horizontally mounted specimen (No. 5) clearly shows the effects of the severe hailstorm at the airport on 23 May. The depressions in the specimens as a result of hailstone impacts vary from 4-10 mm. The other two specimens had become significantly warped by 22 July. This material is obviously unsuitable for use in solar collectors for three reasons:

PLEXIGLASS

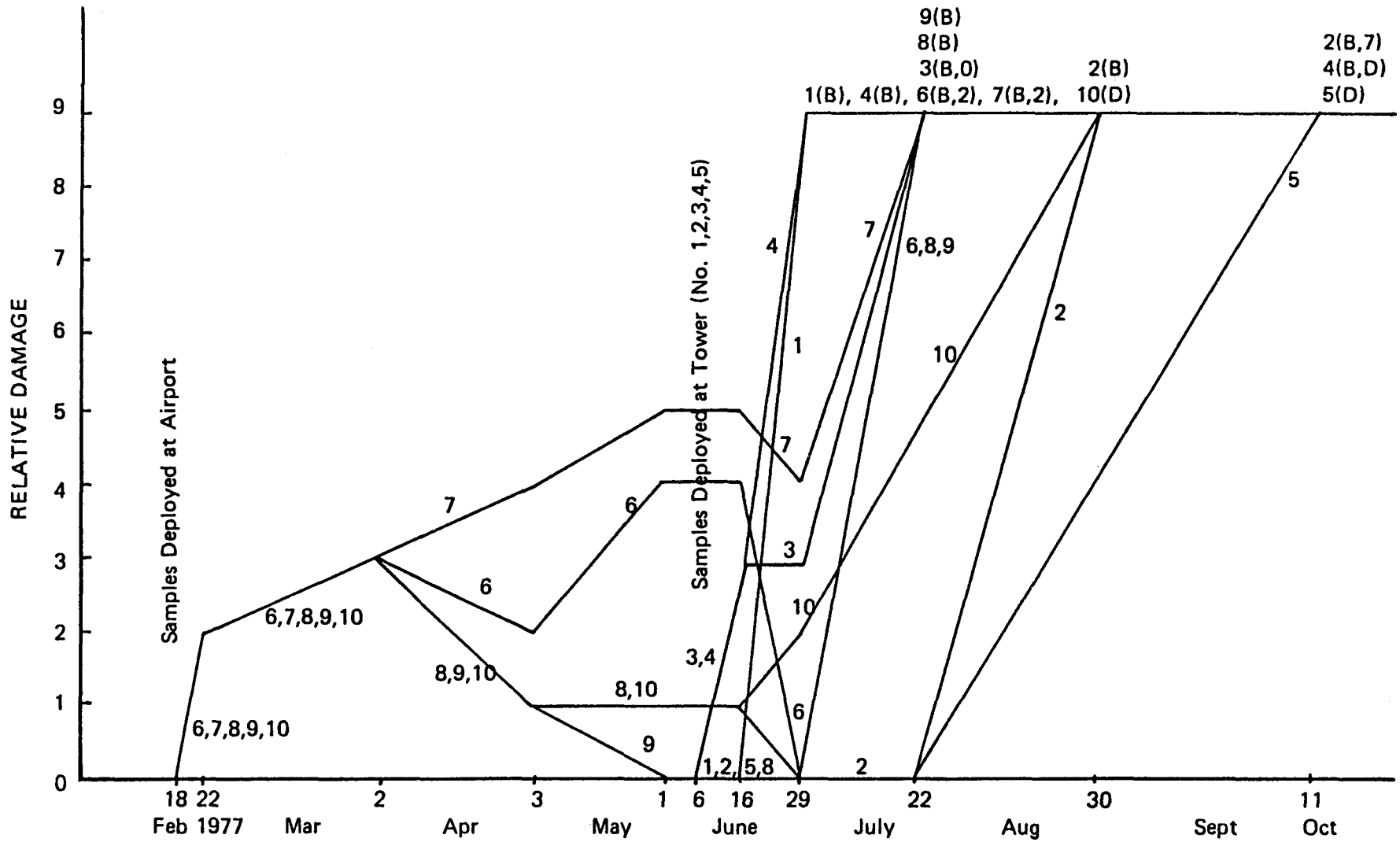

Figure F-17. Plexiglass Mirror Sample Performance Characteristics

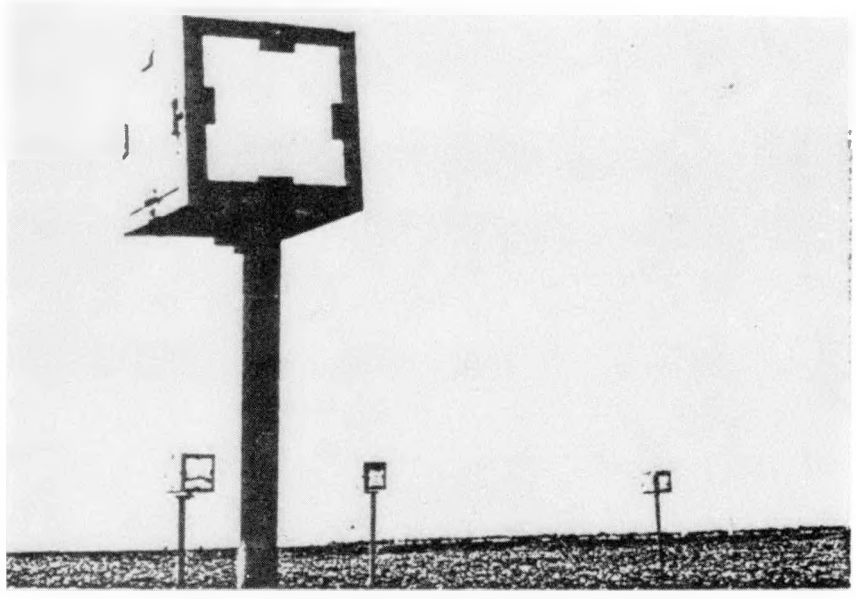

Figure F-18. Plexiglass Mirror Sample with Warping

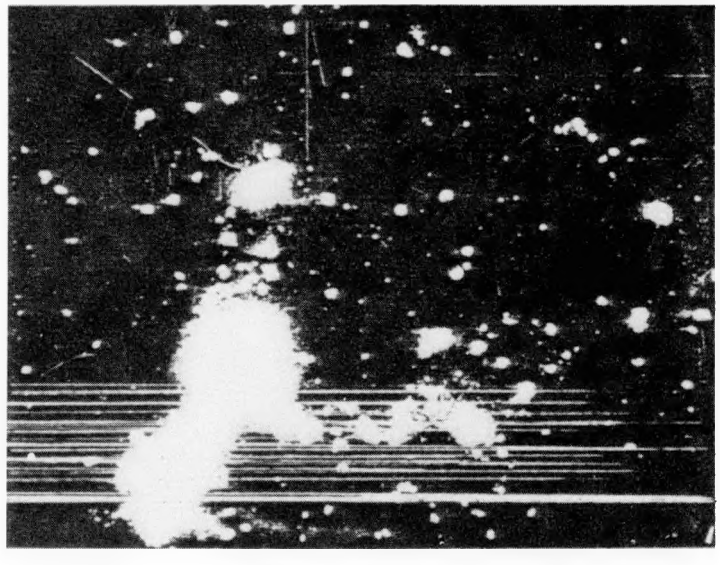

Figure F-19. Plexiglass Mirror Sample at 240X with Dust on Surface

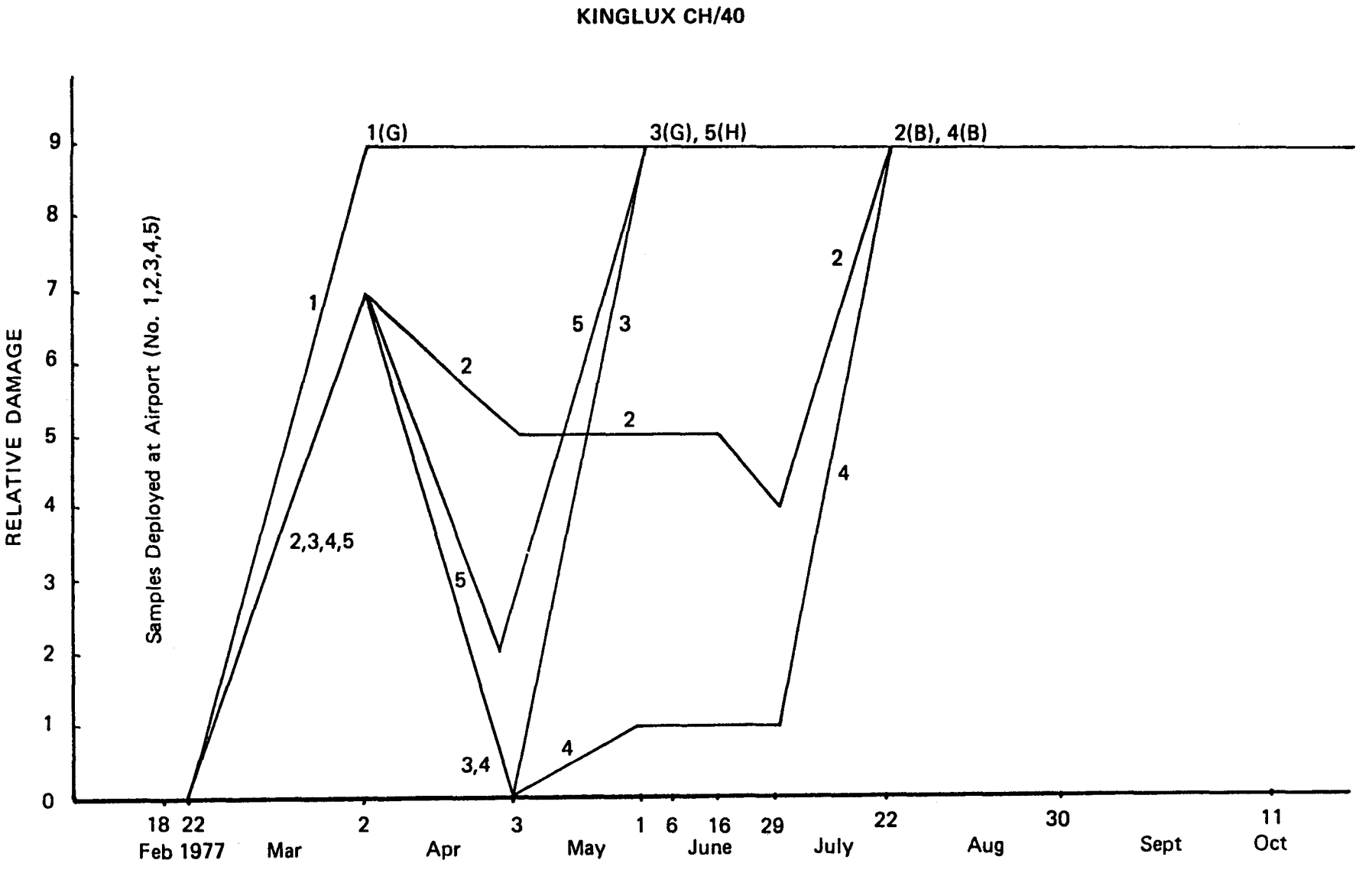

Figure F-20. Kinglux CH/40 Mirror Sample Performance Characteristics

1) mounting adhesive failure,

2) mechanically too soft to resist hail damage, and

3) mechanical instability (warping).

After 2½ months exposure at the airport, both Donnelly specimens showed significant deterioration of their reflective surfaces (Fig. F-21). This is illustrated in Fig. F-22 by the splotched area near the center of the specimen.

Examination of one specimen on 26 July showed that a chemical reaction had occurred between the protective coating, the cement used to affix the sample identification label and the aluminum mounting box. One sample had one 4 mm and about ten ½ mm degradation spots where the reflective surface is now absent. The other sample had 3 areas of reflective surface degradation: one is about 9 mm diameter, the other two are within a 15 mm diameter circle. Both specimens showed a spurtrack grid pattern on their reflective surfaces which must be manufacturing marks. We were later advised that we had been supplied with indoor mirrors and that suitable protective paints are available from the manufacturer. The suitability of any such protective coating must be proven by field exposure tests prior to acceptance.

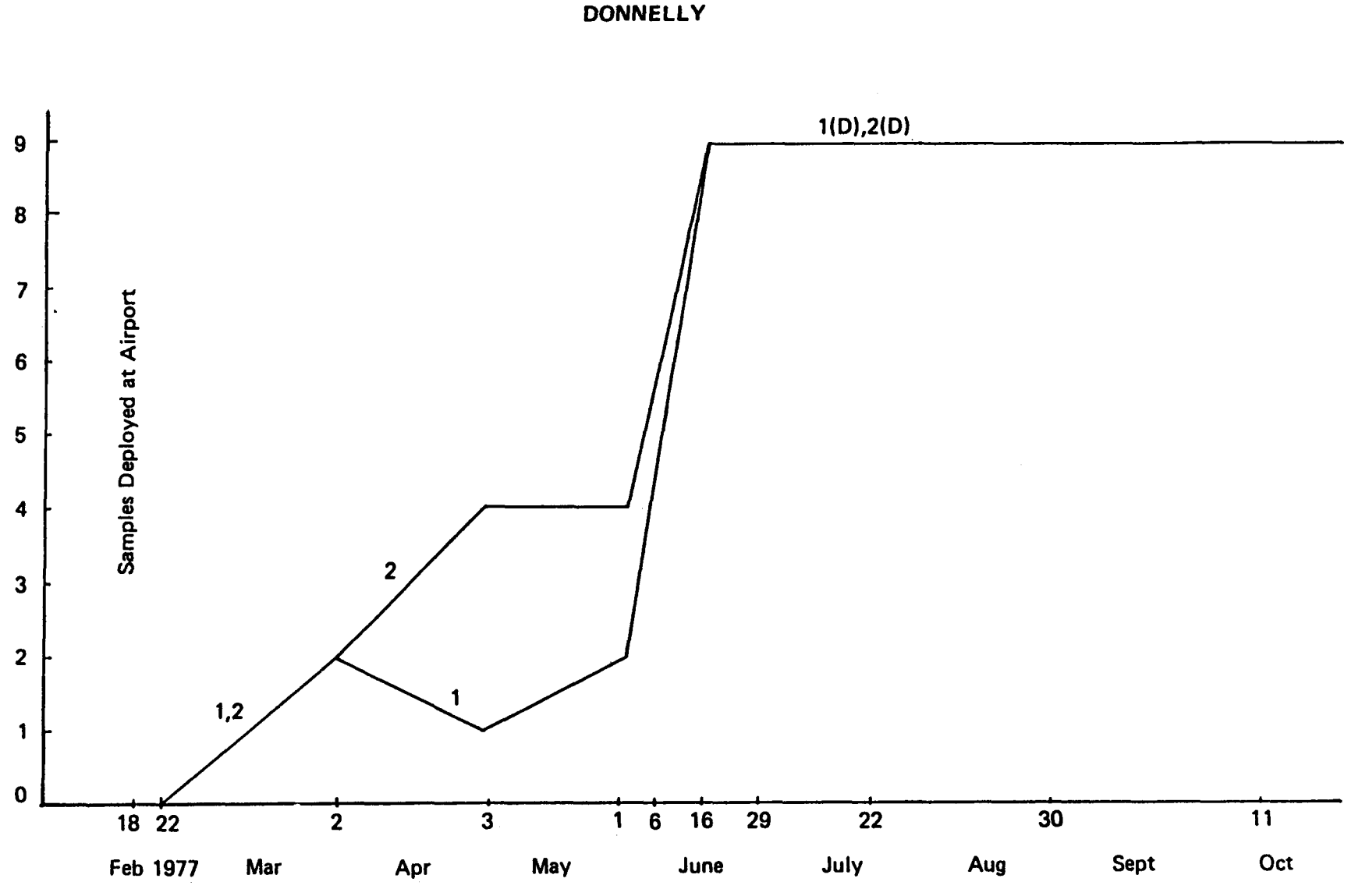

Figure F-21. Donnelly Mirror Sample Performance Characteristics

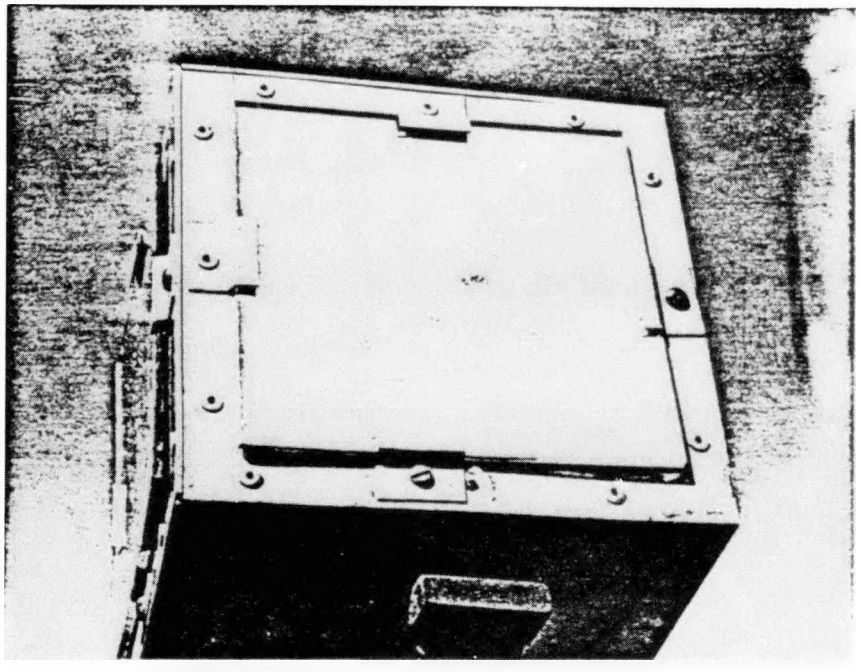

Figure F-22. Donnelly Mirror Sample with Deterioration in Reflective Surface

F-2 MAINTENANCE OF MIRROR SURFACES

The maintenance of mirror panel reflectivity will require two types of cleaning. One type will involve a water spray to remove accumulations of dust on all mirror panels. This will be accomplished by a series of nozzles attached to a boom that will travel around the circumference of the concentrator. The receiver also may be utilized to carry some nozzles to wash panels at the bottom of the concentrator. Water of a suitable content likely will have to be prepared for this cleaning operation. The most likely source of cleaning water will be water from wells; a softening process will be necessary to reduce the amount of deposits left on mirror surfaces as the water evaporates.

Removal of dust and sand accumulations from the bottom of each concentrator will be required following each major dust storm. The depth of dust and sand accumulation cannot be determined at this time; the ATS will be useful in evaluating this. Tests have been made to determine the area of each concentrator that will be covered. A test stand to hold small panels at some angle was utilized in the investigation. The test was conducted to determine the angle at which settling sand and dust would accumulate; this is referred to as the dynamic slide angle. A second test was performed to determine the angle at which sand and dust loaded on a level panel would begin to slide; this is referred to as the static slide angle. Results indicated the dynamic slide angle is 15^0 and the static slide angle is 30^0. In both cases replications of the experiment yielded very similar results. It is believed that the actual angle at which sand and dust will accumulate on the ATS and RPS concentrators will be between 15^0 and 30^0 but will be only slightly above 15^0. The actual areas of the concentrator covered by sand and dust are given in Table F-9.

TABLE F-9 RADIUS AND AREA OF SAND AND DUST ACCUMULATION

System	Radius of Accumulation (ft) Slide Angle		Area of Accumulation (ft^2) Slide Angle	
	15^0	30^0	15^0	30^0
ATS	9.8	19.6	302.6	1211.2
RPS	30.5	61.0	2922.5	11690.0

Removal of the sand and dust likely must be accomplished by some means other than a water spray. The depth may preclude washing the material away. A vacuum system may be the most convenient method for removing the sand and dust. This can be accomplished by having several mirror panels designed to be removed or hinged to provide maintenance personnel access to the mirror surfaces. Two or three such panels should be adequate for the ATS while five removable panels should provide suitable access for the RPS. A vacuum system with a wand than can be extended to 10 or 15 feet would be adequate to reach all accumulations of sand and dust from the 5 access panels in the RPS. All materials of the wand and the attachment to it should be made of materials that are flexible enough to avoid damage to mirror panels if the assembly were dropped by accident on the panels.

F-3 SURVIVABILITY OF OIL USED FOR THERMAL STORAGE

Aspects related to life of oil used as a receiver fluid and as a thermal storage medium are addressed in Appendix A.

F-4 SAFETY OF THE CONCENTRATOR DESIGN

An examination of characteristics of concentrators from the viewpoint of hazards to personnel have revealed inherent hazards associated with tall structures such as the concentrator; however, adequate guard rails and restricted access to the concentrators should reduce the hazard to an acceptable level.

The concentrator-receiver operation may present a slight hazard to birds that fly into the concentrator. However the noise associated with an operating system quite likely will discourage wildlife from entering the concentrator.

F-5 AREAS FOR ADDITIONAL STUDIES

Investigations described in this appendix have resulted in additional questions being raised that may require further study. Continued investigation of impact damage to mirror surfaces should be done including examination of 5/32 in. curved glass mounted on the substrate. The hail impact studies described previously involved a mirror sample with RPS curvature; another test should be performed on a sample with the ATS curvature. Also we should examine effects of ice forming on the receiver and support structure and then falling on the mirror panels; if significant damage can occur, methods for preventing or limiting the damage must be developed. A problem may exist with birds roosting on the receiver support sturcture at night; the design may have to include provisions to make the structure unattractive for this purpose.

Life of glass mirror panels subjected to cold forming stresses should be thoroughly examined. All glass placed under a static load will fail eventually even though the period to failure may be quite long. The ATS will have a radius of curvature of 31.5 ft. while the RPS will have a radius of curvature of 115 ft. If glass thickness is the same for both the ATS and RPS, the stresses in the ATS mirrors will be much higher than those in the RPS. Effects of thermal stress due to uneven heating of panels must be examined also.

An environmental impact study also should be performed for the RPS. The ATS will be very useful in performing this study. The following should be considered:

1. effects of heat loss from the receiver
2. noise
3. effects of failure of pipes carrying steam or hot oil
4. effects of moonlight in the concentrator on birds, and flying insects
5. hazards of tall structures to low flying aircraft
6. effects of venting thermal storage fluid vapors to the atmosphere
7. effects of transmission lines from the plant
8. methods for disposing of wastes such as water for washing the concentrator.

The environmental impact study can begin in the early stages of Phase III but will require observation from the ATS before it can be completed.

REFERENCES-APPENDIX F

1. Gonzales, C. "Low Cost Silicon Solar Cell Array Project: Environmental Hail Model for Assessing Risk to Solar Collectors," Jet Propulsion Laborator Document 5101-45 (1977).

2. Gringorten, I.I., "Hailstone Extremes for Design," Air Force Cambridge Research Laboratories, Air Force Surveys in Geophysics No. 238, AFCRL-72-0081 (1977).

3. Gumble, E. J., Statistics of Extremes, Columbia University Press (1958).

4. Suzuki, E., "A New Procedure of Statistical Inference on Extreme Values," Met. and Geo., vol. R, 1 (1961).

APPENDIX G. ASSESSMENT OF ENERGY STORAGE STRATEGIES AND OPTIONS

G-1 STORAGE STRATEGIES AND OPTIONS

A range of thermal energy storage strategies and options have been considered for the Crosbyton Recommended Power System. Design, performance, and, where available, cost data have been obtained for those candidates considered most promising. These included phase change salts such as "Hitec" and "Thermkeep" with operating temperature limits up to 850°F and various strategies using hot oil sensible heat storage concepts. An assessment of cost, design requirements, and level of current existing technology for individual candidates has resulted in the decision that the thermocline hot oil and rock storage concept represents the one closest to technical feasibility in the time scale of the Analog Test System and possibly even of the Recommended Power System.

A review of the current technology status for this concept was obtained in a trip to the thermocline test facility of Rocketdyne Corp. In addition, tests have been conducted at Texas Tech University to evaluate the static stability-decomposition characteristics of Exxon Caloria HT43 and heat transfer tests are planned for the helical flow receiver geometry. Results of these tests are discussed in Appendix A.

Various options have been considered for the integration of the hot oil thermal storage into the FMDF solar thermal power system. These include the dual loop water-steam, hot oil cycle, a fluorocarbon vapor power cycle integrated with an oil receiver

solar system, and a conventional steam-oil-steam storage system. Each of these is discussed in Appendix H.

The maximum recommended operating temperatures for the heat transfer fluids currently being considered are 600°F bulk oil temperature and 650°F wall temperature.

G-2 ATS STORAGE DESIGN

Preliminary design and sizing has been conducted for the thermal storage system proposed for use in the Analog Test System. Properties used in these calculations were:

$$\rho_{oil} = 54 \text{ lbm/ft}^3 , \quad Cp_{oil} = 0.7 \text{ Btu/lbm } ^\circ\text{F}$$
$$\rho_{rock} = 165 \text{ lbm/ft}^3, \quad Cp_{rock} = 0.2 \text{ Btu/lbm } ^\circ\text{F}$$

With these values and a recommended 25% ratio by volume for oil, the mass fraction of oil in the total system is approximately 0.1. The equivalent system specific heat is 0.25 Btu/lbm °F. The size of the system was based on the capacity necessary to store one entire day's solar collection from a 65 ft. aperture diameter FMDF receiver with a 350°F temperature increase of the oil. This resulted in a calculated volume of approximately 3000 gal. For a recommended L/D = 1, this requires an 8 ft. diameter by 8 ft. height. This storage system would allow an evaluation of the steam-to-oil storage energy transfer performance characteristics, oil stability, and the option to evaluate the performance of an oil receiver design.

APPENDIX H. INVESTIGATION OF POWER CYCLE, ELECTRICAL PRODUCTION, DISTRIBUTION OPTIONS

H-1 CYCLE DEFINITION

H-1.1 Basic Concept

The basic concept for the thermodynamic cycle on which the recommended solar power system will operate is the regenerative Rankine Cycle. A temperature-entropy diagram for an ideal two-stage regenerative Rankine cycle is shown in Fig. H-1. Choice of this cycle resulted from consideration of factors such as cycle thermodynamic efficiency, operational characteristics and requirements of the FMDF solar system, compatability with conventional power generation equipment, and availability of required cycle components. The following sections will discuss details of the recommended cycle configuration, management and operational requirements, performance results and subsystem specifications along with a brief discussion of alternate concepts that were considered and their respective deficiencies.

H-1.2 Cycle Definition, Management and Operational Requirements

System Configuration

Figure H-2 shows a schematic diagram of the fluid flow network and system components for the recommended power system. The thermodynamic cycle for the indicated system is actually a combined simple and regenerative water-steam Rankine cycle. The simple (non-regenerative) portion of the cycle pertains to the fluid energy transfer

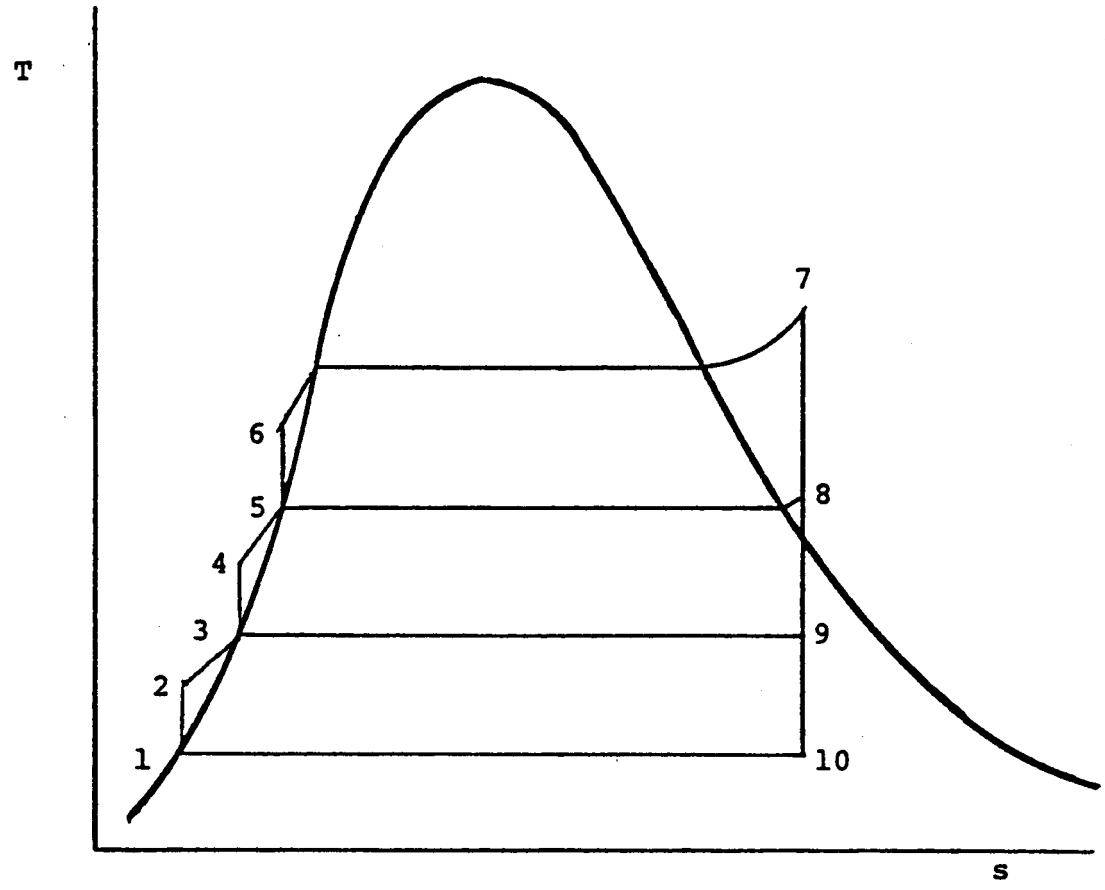

Figure H-1. Regenerative Rankine Cycle T-S Diagram

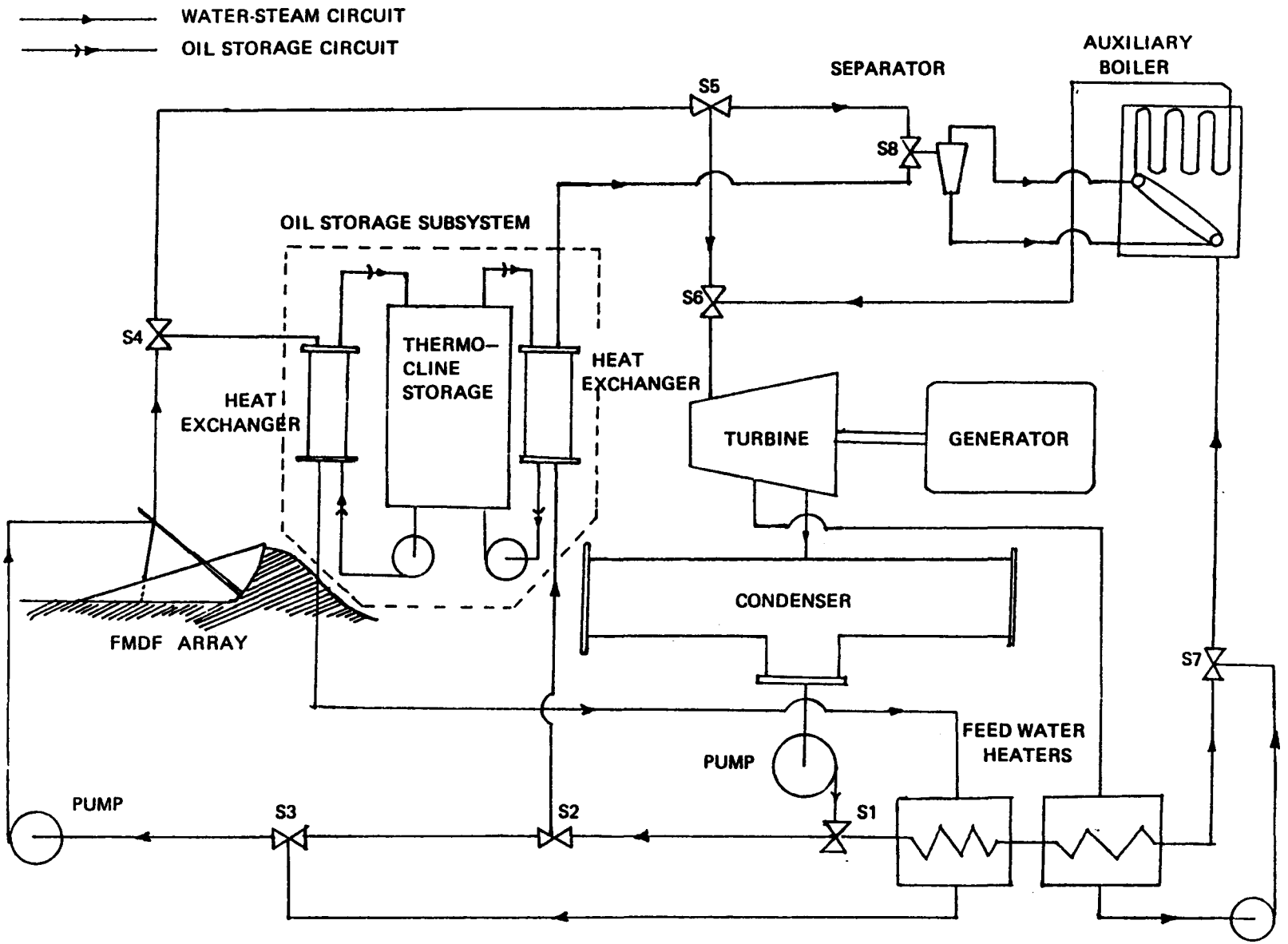

Fig. H-2. SYSTEM POWER CYCLE FLOW SCHEMATIC WITH STORAGE

loop through the FMDF solar array. This selection resulted from the predicted decrease in receiver thermal efficiency with increasing feedwater temperature. Thus it was not advantageous to have regenerative feedwater heating for the portion of the fluid directed to the FMDF array. The regenerative portion of the cycle pertains to the fluid energy transfer loop through the conventional fossil fuel boiler. This selection resulted from cycle efficiency calculations shown in the following section combined with results for predictions of percent load supplied by solar.

As discussed in Vol. I of the Interim Technical Report, current economic and performance analyses indicate that the annualized system cost decreases with decreased storage capacity while the percent load supplied by solar, $1 - Q_{aux}/Q_{total}$, increases with increased storage capacity. However, due to the evolving technology in high temperature thermal storage, the uncertainty of actual solar thermal-storage operating and performance characteristics, and the uncertainty in the appropriate relative weight for these two parameters, the option of the hot oil, thermocline storage has been included in the system concept shown in Fig. H-2. The results expected from the FMDF solar thermal-storage performance evaluation proposed for the Analog Test System will be of prime importance to the final decision as to the system concept proposed for the RPS.

Management and Operational Requirements

The following paragraphs will discuss the management and operational requirements of the recommended system. The three dominant factors in this area were: 1. operational characteristics of the solar

receiver, 2. operational characteristics of the conventional power production system, and 3. operational characteristics and limits of the fluid control subsystem. Thus these results are very closely related to the discussion presented in Appendix C.

Normal Solar Operation (Continuous Insolation)

In this mode, solar thermal energy collection is continuous with the majority of the flow following the solar flow circuit S_1-S_2-S_3-S_4-S_5-S_6-S_1 and the auxiliary fossil fuel boiler circuit operating at minimum turn-down conditions and following the circuit S_1-S_7-S_6-S_1 with extraction feedwater heating used for this portion of the flow. One alternative in this mode of operation would be to use a controlled portion of the flow at S_4 to charge the thermocline storage system with this decision dependent upon the current energy capacity of storage and the grid demand requirements.

Normal Conventional Operation (Zero Insolation)

In this mode, the primary flow circuit is through the conventional boiler with feedwater heating, S_1-S_7-S_6-S_1, with storage, if included, available through circuit S_1-S_2-S_8-S_6-S_1 to provide a portion of the energy requirements for steam generation. This mode would result during either nighttime or continuously heavy overcast conditions.

Transient Solar Operation (Intermittent Insolation)

In this mode, the primary flow circuit would also probably be through the conventional boiler, S_1-S_7-S_6-S_1. However, as useful

energy may be available at the solar receiver, a portion of the flow would be diverted through the solar loop S_1-S_2-S_3-S_4-( ) with the option that at this point the resulting fluid could be directed to the conventional boiler, S_5-S_8-S_6-S_1, if the thermal state were above a specified point or could be directed to feedwater heating, S_4-S_3-S_4. This latter condition would most likely result under conditions where the insolation level was sufficiently low and the frequency of intermittency sufficiently fast that flow stability and control would be difficult and it would be advisable to simply flood the receiver, collect the energy, and use this as feedwater heating for improved conventional cycle efficiency. It is noted that in this mode, the turbine bleed steam, previously used for feedwater heating, could now be decreased resulting in increased output from the turbine.

Additional Operating Modes

The additional operating modes of start-up, normal shutdown, and emergency shutdown are discussed in Appendix C and will not be discussed further in this section.

H-1.3 Performance Calculations

Efficiency calculations were performed both for simple and regenerative Rankine steam power cycles considering manufacturers recommendations for efficiencies of the various subsystem components. The following thermodynamic conditions were used in the calculations: turbine inlet conditions: (a) 620 psi, 760^{0}F, and (b) 850 psi, 900^{0}F; condenser exhaust pressures: 2 and 3 in Hg absolute; and up to three stages of regenerative feedwater heating. Table H-1 summarizes the

TABLE H-1. THERMODYNAMIC & CYCLE EFFICIENCY PREDICTIONS

Cycle No.	Turbine Inlet P(psia)	Turbine Inlet T(^{o}F)	Condenser P(in. hg.)	Turbine Extraction Pressures psia	η_{rc}	η_{c-e}
1	620	760	3	none	24	19.9
2	620	760	3	8	25.3	21
3	620	760	3	8,27	27.6	22.9
4	620	760	3	8,27,96	28.7	23.8
5	620	760	2	none	24.7	20.5
6	620	760	2	30	27.3	22.7
7	850	900	2	none	27.2	22.6
8	850	900	2	30	29.6	24.6
9	850	900	2	30,125	31.1	25.9
10	850	900	2	18,125	31.6	26.3
11	850	900	2	None (Storage feedwater heating)	-	27.5

results of these calculations. The thermal to turbine output Rankine cycle efficiency, η_{rc}, is related to the overall chemical-to-electric cycle efficiency, η_{c-e}, by the relation

$$\eta_{c-e} = \eta_{rc}\eta_g\eta_c$$

where:

η_g = gear-generator efficiency.

η_c = boiler combustion efficiency

Of particular importance are the values η_{rc} = 27.2% for cycle 7 and η_{c-e} = 26.3% for cycle 10. The former value, when multiplied by the generator efficiency to yield 25.8% would be the predicted fluid-to-electrical conversion efficiency for the solar portion of the cycle and the latter value would be the fuel-to-electrical conversion efficiency for the conventional portion of the cycle. It is noted that if energy from storage were used for all feedwater heating, Cycle 11, the fuel-to-electrical conversion efficiency for this cycle would increase to 27.5% as a result of decreased extraction and increased output from the turbines.

It is also noted that turbine manufacturers have indicated that multi-valve, multi-stage equipment is available in designs capable of expansion to 1.5 in. Hg exhaust pressure at sizes down to 2.5 MW at minimal increase in cost. This offers the potential for improved thermodynamic cycle efficiency as well as lower receiver feedwater

inlet temperatures. However, at this point the more conservative 2 in. Hg results have been used in the cycle performance calculations.

H-1.4 Subsystem Specifications

On the basis of the results of the previous section and annual system performance evaluations, the recommended thermodynamic operating conditions of the cycle are 850 psi,900^{0}F at the turbine inlet and 2 in. Hg exhaust pressure in the condenser. Individual component specifications for the RPS are listed as follows:

Turbines: Two 2500 KWe multi-valve, multi-stage, dual extraction turbine generator units; Turbine-generator steam rate, 9.01 lbm/KW-hr; Turbine efficiency = 73.5%; Turbine-generator efficiency = 69.7%.

Surface Condenser: Shell and tube surface condenser rated at 45,042 lbm/hr steam capacity at 2" Hg. Cooling water requirement of 4400 gpm at 95^{0}F inlet temperature.

Cooling Tower: Two-cell, wet cooling tower, capable of delivering 4400 gpm of 95^{0}F cooling water at 98^{0}F dry bulb and 73^{0}F wet bulb ambient temperature.

Auxiliary Boiler: Fossil fuel, fired superheated boiler. Delivery conditions - 45,042 lbm/hr steam flow at 850 psi, 900^{0}F. Dual burners for effective 16:1 turn down ratio. Secondary admission inlet in steam drum to allow for off design input from solar receiver. Combustion efficiency = 87%.

H-1.5 Cycle Improvements for Larger Systems

Principal cycle improvements resultant from the consideration of larger capacity systems occur in the areas of improved operating efficiencies, lower cost per unit capacity, and increased design capability for individual components. For example, relative to a base efficiency value at 2.5 MW, one turbine manufacturer has

estimated the following approximate turbine efficiency increases with increased size: 5 MW - 2%, 7.5 MW - 3%, 10 MW - 4%, and 50 MW - 6%. This would result in a significantly lower steam requirement per unit output for the cycle. In addition to this the cost increase would typically be 2/3 the ratio of the capacity increase for this range. It is also noted that lower exhaust pressure and the capability for additional extraction stages would result with increased size.

While the condenser costs would vary closely with size increase, the improved turbine efficiency and resulting lower steam flow and cooling water requirement would tend to lower relative cost of the condenser, cooling tower, and auxiliary boiler. Thus it is felt that a detailed cost-performance analysis of larger, e.g. 50 MW, systems would result in a significant improvement in the relative economic merit of this solar thermal concept at these capacity levels.

H-2 ALTERNATE SYSTEM CONCEPTS

The following sections present a brief discussion of alternate system concepts that were considered for the power generation cycle and their identified deficiencies.

H-2.1 Organic Fluid Cycle

One alternative cycle proposed for consideration was that of a vapor power cycle using an organic liquid as the working fluid. An analysis was conducted at Texas Tech University with performance information and specifications supplied by Allied Chemical. Figure H-3 shows a conceptual system schematic for the cycle. The main vapor

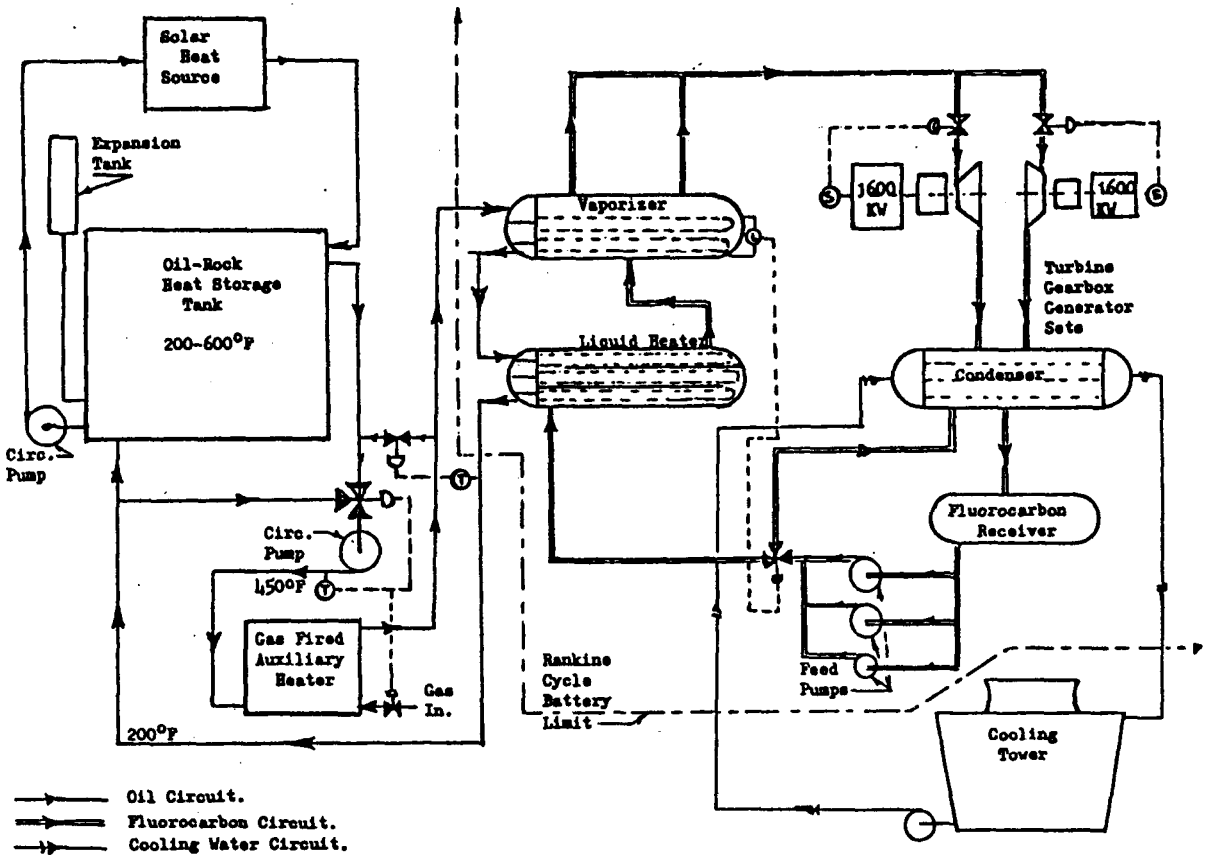

Figure H-3. Conceptual System Schematic of Organic Fluid Rankine Cycle

power circuit for this cycle uses the fluorocarbon G-11 (refrigerant 11) as the working fluid for the low temperature Rankine cycle.

The energy source for the fluorocarbon is solar heated heat transfer oil which operates in the collector-storage-heat exchanger flow circuit shown in Figure H-3. The maximum oil delivery temperature to the fluorocarbon vapor generator is limited to 450° due to the desire to stay with the known long-term (10 year) stability levels of the fluid.

This system concept would have the following advantages relative to the recommended water-steam cycle:

(1) Low Temperature Heat Addition: Lower heat addition temperatures resulting in lower receiver temperatures, less expensive receiver materials, reduced creep rupture conditions, and reduced oxidation corrosion potential. A selective coating could now be considered for the receiver with improved receiver thermal performance.

(2) Reduced System Pressure: With a freon turbine inlet pressure approximately 4 to 5 times less than that for a steam turbine, the maximum system operating pressure would be significantly reduced. Design requirements would be correspondingly reduced for the receiver, articulation devices, and general system piping.

(3) Cycle Temperatures Compatible with State-of-the-Art Thermal Energy Storage: With maximum vapor cycle operating temperatures under 450°F, these values are much more compatible with sensible heat storage in oil at 500 - 600°F resulting in more efficient use of energy storage.

(4) Elimination of Potential Two-Phase Flow Instabilities: In the oil receiver concept, the receiver flow is maintained in the liquid phase and potential two-phase flow stability difficulties would be eliminated.

Disadvantages of the concept are listed as follows:

(1) Low Cycle Efficiency: The most predominant difficulty associated with this cycle is the low freon-to-electric

cycle efficiency. Operating thermal to electric efficiencies of this cycle range from approximately 9 to 15%. A detailed assessment of this factor would require a full scale system performance simulation and economic evaluation.

(2) Environmental Considerations: With recent concern over damage to the ozone layer by flurocarbons, there is likely to be objections to the use of the large quantity of freon which could escape due to a pipe rupture.

(3) Degradation of the Freon and Oil: Unlike water, both the freon and heat transfer oil are subject to decomposition under continual use at elevated temperatures and may have to be replaced at regular intervals.

(4) Estimated Freon System Cost: A preliminary estimate of the freon system cost exclusive of the oil network cooling tower, or solar field was $2,700,000 for a 3200 KW system.

Thus at this point, further consideration has not been given to the use of this concept.

H-2.2 Dual Fluid, Oil Receiver Cycle

The nominal system discussed in Volumes I, II and III of the Interim Technical Report considered the option of a dual fluid cycle using certain receivers with water-steam in a conventional Rankine cycle, and with oil circulating through other receivers dedicated solely to charging storage. Figure H-4 presents a system schematic of this cycle.

The principal technical uncertainties associated with this concept are in the long term decomposition characteristics of the heat transfer oil in continuous use (see Appendix A) at the required operating temperatures and in maintaining the oil receiver operating conditions under the required 600^{0}F bulk temperature and 650^{0}F wall temperature (see Appendix A). A second disadvantage is the significantly

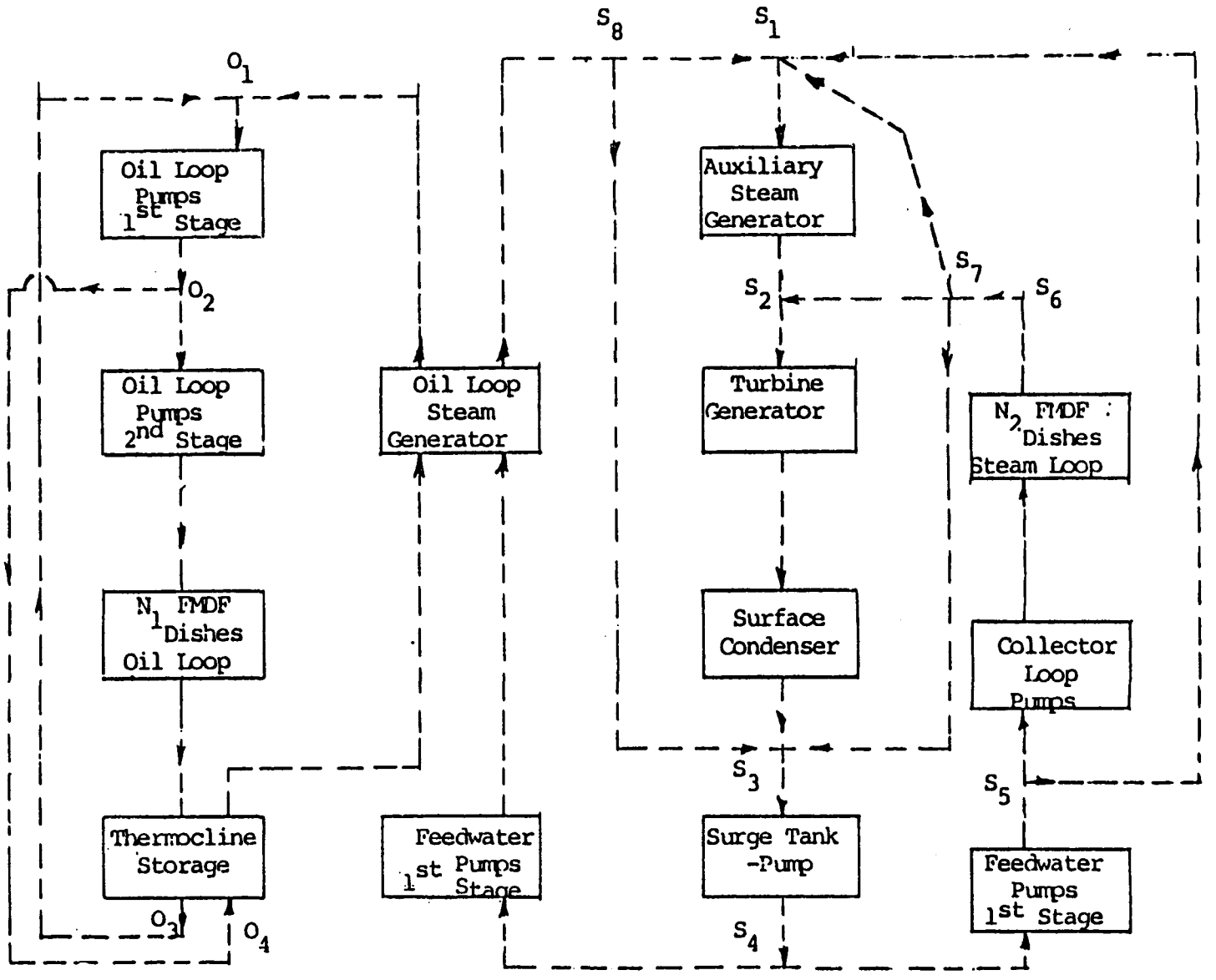

Figure H-4. Dual Fluid System Configuration, Oil & Steam Collector Loops

lower conversion efficiency associated with the lower temperature operation of the oil cycle and its use being largely that of feedwater heating.

For these reasons, the status of this cycle is that of an option with the proposed integration of hot oil storage and possibly an oil receiver in the ATS to be used as a basis for a more quantitative evaluation of these factors.

APPENDIX I. ANALYSIS OF SITE DEPENDENT FACTORS

This appendix indicates the type and extent of site related data being accumulated at Crosbyton, Texas. This data may be grouped under the following topics: general climatological data, solar insolation, suspended particulates and wind components, and soil foundation studies. Most of the instruments for this data collection are located at the site of the Crosby County Sheriff's Department radio transmitter located in the eastern part of the City of Crosbyton. A general view of this equipment is shown in Figure I-1.

I-1 GENERAL CLIMATOGICAL DATA

The temperature, relative humidity and barametric pressure have been recorded on weekly drum charts. Records for these items began in October 1976. Figure I-2 shows a typical week of records for these three variables. Casual observation indicates that a correlation with data recorded by the NOAA office at Lubbock can be made if needed. Monthly weather summaries prepared by NOAA for Lubbock are available but are not included in this report.

I-2 SOLAR INSOLATION

I-2.1 Total Solar

Total solar radiation is recorded in Crosbyton on a continuous drum chart. These data have been recorded since October, 1976. A typical weekly recording is given in Figure I-3. The area under the recorded curve is measured using a planimeter and is converted to total

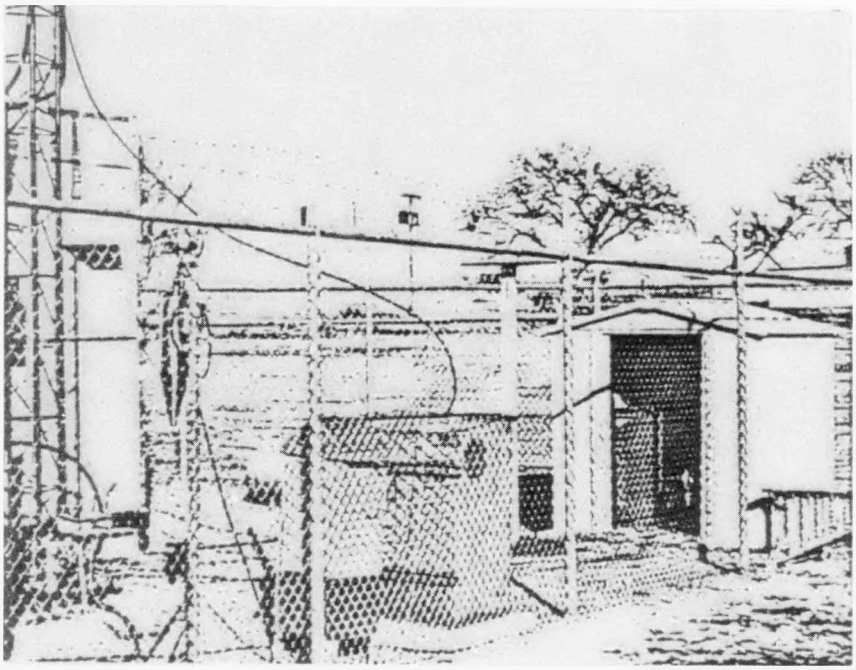

Figure I-1 Instrumentation at Tower Site

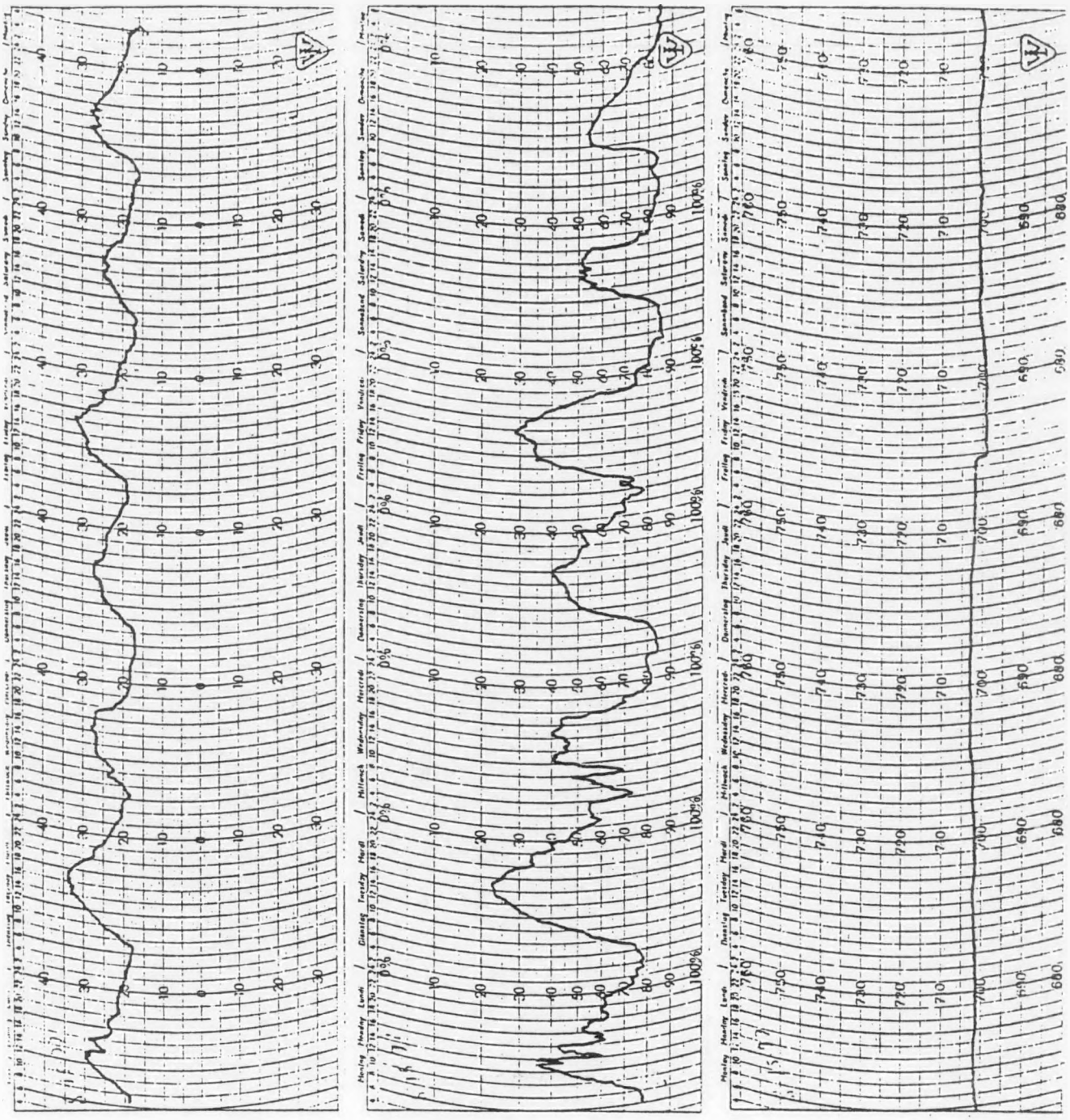

Fig. I-2 Typical Weekly Record of Temperature, Relative Humidity and Barometric Pressure for the Week of August 15, 1977 (Reduced 65%)

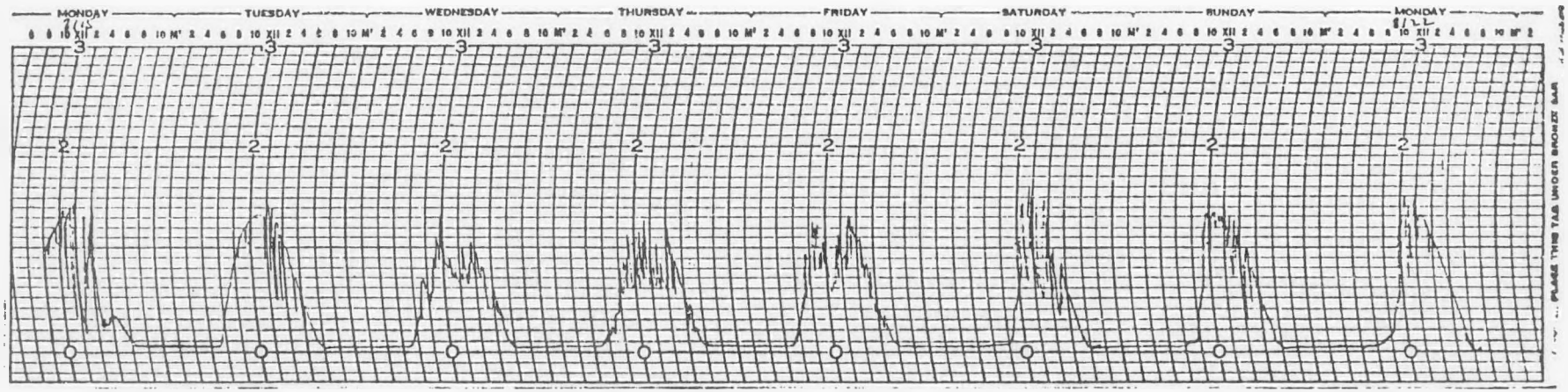

Fig. I-3 Typical Total Solar Radiation Record
for Week of August 15, 1977
(Reduced 65%)
Vertical scale is in Langleys

solar energy received for the day. Table I-1 gives total solar in calories per square centimeters that have been recorded. During the recording interval reported, the maximum value of 836 cal/cm^2 occurred on May 28, 1977. There were 5 days with less than 100 cal/cm^2 received. The mean value over this period was 487.2 cal/cm^2.

I-2.2 Direct Solar

Direct solar radiation has been measured since February 15, 1977, using a Hy-Cal normal incidence pyrheliometer on a tracking mount and a strip chart recorder. Figure I-4 shows this equipment. The strip chart recorder has been operated at a speed of four inches per hour. This speed provides a degree of detail which should be sufficient for most design problems. The equipment is started and aligned each morning and stopped each evening by an observer who also records a general comment on cloud conditions during the day. Gaps in the data are present due to cloud cover and equipment failures. Strip charts are available for about 60% of the days since the equipment was installed.

The strip charts are integrated to compute total direct solar radiation during each hour and the daily totals. The direct solar and total solar energy could be correlated for a site-specific relation if one were needed. An example of the direct solar insolation chart for one day is shown in Figure I-5.

A review of the direct solar recordings indicates that intensity levels and fluctuations may create problems for power generation and control systems. To estimate the magnitude of this problem, the direct solar recordings were divided into three classes. Class 1 was defined as data where the energy level was above 170 BTU/ft^2/hr and only

TABLE I-1 TOTAL INSOLATION AT CROSBYTON, TEXAS

DATE	CAL/CM²	DATE	CAL/CM²	DATE	CAL/CM²	DATE	CAL/CM²
10/5/76	519	12-07	369	2-16	468	3-26	261
10-06	427	1/4/77	126	2-17	468	3-27	432
10-07	151	1-05	134	2-18	459	3-28	---
10-08	511	1-11	276	2-19	480	3-29	522
10-09	527	1-12	268	2-20	480	3-30	676
10-10	561	1-13	260	2-22	360	3-31	432
10-12	494	1-18	318	2-23	489	4-01	550
10-13	435	1-19	---	2-24	498	4-02	700
10-14	427	1-20	310	2-25	162	4-03	630
10-17	460	1-21	310	2-26	480	4-04	---
10-26	276	1-22	134	2-27	489	4-05	720
10-27	42	1-23	234	3-01	387	4-06	666
10-28	25	1-24	318	3-02	432	4-07	666
11-10	352	1-25	354	3-03	432	4-08	720
11-11	126	1-26	362	3-04	489	4-09	702
11-12	318	1-27	343	3-05	234	4-10	576
11-13	184	1-28	327	3-06	585	4-11	---
11-14	402	1-29	234	3-07	477	4-12	162
11-15	276	1-30	201	3-08	540	4-13	190
11-16	402	1-31	443	3-09	432	4-14	208
11-17	326	2-01	402	3-10	414	4-15	550
11-18	393	2-02	108	3-11	414	4-16	306
11-19	402	2-03	396	3-12	522	4-17	388
11-20	435	2-04	432	3-13	630	4-18	---
11-21	435	2-05	441	3-14	450	4-19	460
11-22	435	2-06	423	3-15	657	4-20	514
11-27	142	2-07	54	3-16	342	4-21	496
11-28	276	2-08	396	3-17	414	4-22	778
11-29	270	2-09	441	3-18	558	4-23	676
11-30	432	2-10	180	3-19	639	4-24	702
12-01	306	2-11	216	3-20	657	4-25	---
12-02	387	2-12	468	3-21	630	4-26	666
12-03	387	2-13	468	3-25	414	4-27	756

*ASTERIST INDICATES THAT THERE WAS A LOSS OF A PART OF GRAPH WHEN RECORDING STRIP WAS INTERCHANGED.

TABLE I-1 TOTAL INSOLATION AT CROSBYTON, TEXAS (continued)

DATE	CAL/CM^2	DATE	CAL/CM^2	DATE	CAL/CM^2	DATE	CAL/CM^2
4-28	658	6-01	738	7-05	---	*8-08	567
4-29	622	6-02	766	7-06	729	8-09	585
4-30	658	6-03	748	7-07	747	8-10	387
5-01	765	6-04	784	7-08	315	8-11	450
5-02	---	6-05	756	7-09	720	8-12	486
5-03	468	6-06	810	7-10	801	8-13	549
5-04	522	6-07	676	7-11	---	8-14	495
5-05	261	6-08	694	7-12	792	*8-15	459
5-06	765	6-09	756	7-13	738	8-16	576
5-07	729	6-10	730	7-14	756	8-17	414
5-08	621	6-11	738	7-15	693	8-18	378
5-09	---	6-12	766	7-16	702	8-19	477
5-10	378	6-13	756	7-17	729	8-20	342
5-11	612	6-14	--	7-18	540	8-21	468
5-12	468	6-15	782	7-19	603	8-22	450
5-13	468	6-16	802	7-20	595	8-23	567
5-14	590	6-17	838	7-21	225	8-24	315
5-15	765	6-18	820	7-22	486	8-25	594
5-16	---	6-19	766	7-23	585	8-26	585
5-17	550	6-20	---	7-24	621	8-27	477
5-18	576	6-21	550	7-25	612	8-28	315
5-19	486	6-22	406	7-26	585	8-29	306
5-20	432	6-23	586	7-27	567	8-30	513
5-21	856	6-24	748	7-28	594	8-31	531
5-22	694	6-25	738	7-29	612	9-01	522
5-23	---	6-26	820	7-30	639	9-02	495
5-24	522	6-27	---	7-31	576	9-03	540
5-25	512	6-28	783	*8-01	432	9-04	459
5-26	403	6-29	729	8-02	576	9-05	207
5-27	784	6-30	639	8-03	432	9-06	432
5-28	836	7-01	693	8-04	657	9-07	450
5-29	810	7-02	765	8-05	648	9-08	495
5-30	---	7-03	792	8-06	657	9-09	558
5-31	604	7-04	810	8-07	666	9-10	513

*ASTERISK INDICATES THAT THERE WAS A LOSS OF A PART OF GRAPH WHEN RECORDING STRIP WAS INTERCHANGED.

TABLE I-1 TOTAL INSOLATION AT CROSBYTON, TEXAS (continued)

DATE	CAL/CM^2	DATE	CAL/CM^2	DATE	CAL/CM^2
9-11	513	10-15	468		
9-12	540	10-16	468		
9-13	423	*10-17	432		
9-14	495	10-18	423		
9-15	504	10-19	378		
9-16	477	10-20	423		
9-17	324	10-21	225		
9-18	432	10-22	99		
9-19	432	10-23	-		
9-20	504	10-24	387		
9-21	495	10-25	414		
9-22	468	10-26	72		
9-23	333	10-27	297		
9-24	495	10-28	279		
9-25	504	10-29	252		
*9-26	522	10-30	369		
9-27	477	10-31	-		
9-28	450	11-01	387		
9-29	504				
9-30	495				
10-01	504				
10-02	486				
*10-03	387				
10-04	126				
10-05	189				
10-06	288				
10-07	297				
10-08	468				
10-09	279				
10-10	450				
10-11	468				
10-12	468				
10-13	495				
10-14	459				

*ASTERISK INDICATES THAT THERE WAS A LOSS OF A PART OF GRAPH WHEN RECORDING STRIP WAS INTERCHANGED.

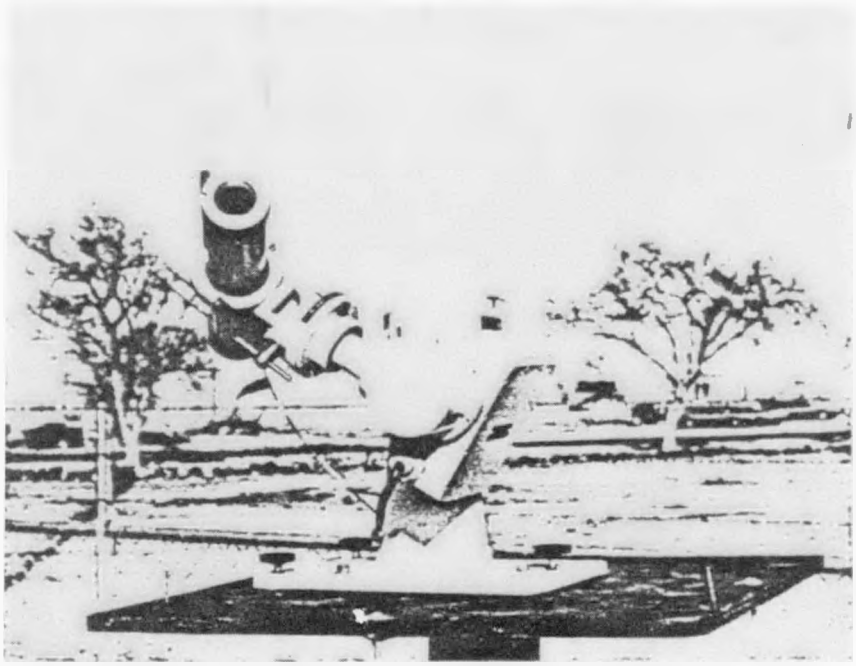

Figure I-4 Normal Incidence Pyrheliometer on Tracking Mount

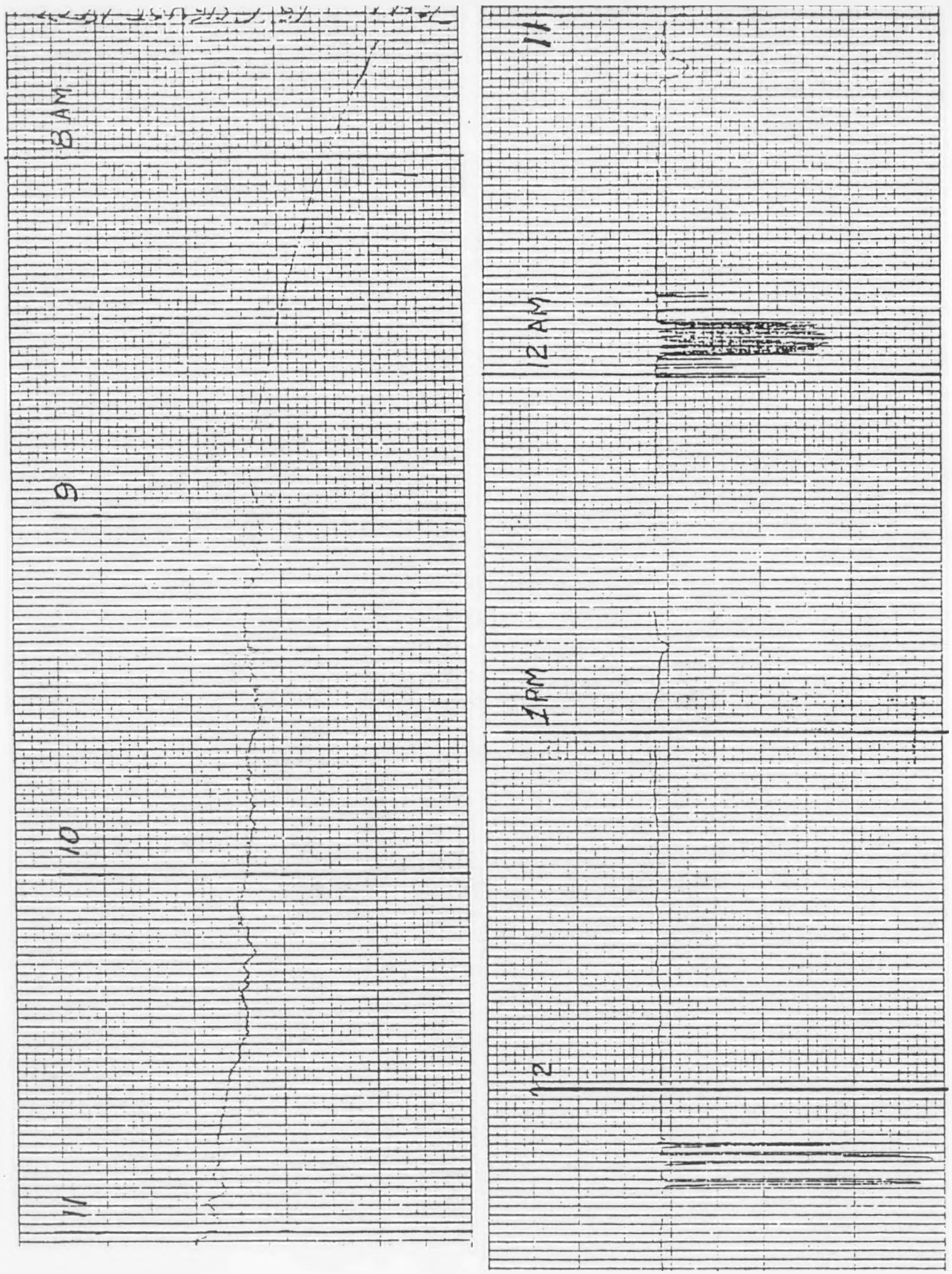

Fig. I-5 Direct Solar Radiation Received August 16, 1977. Full Scale deflection is 10 millivolts or 7.122 BTU/ft^2/min.

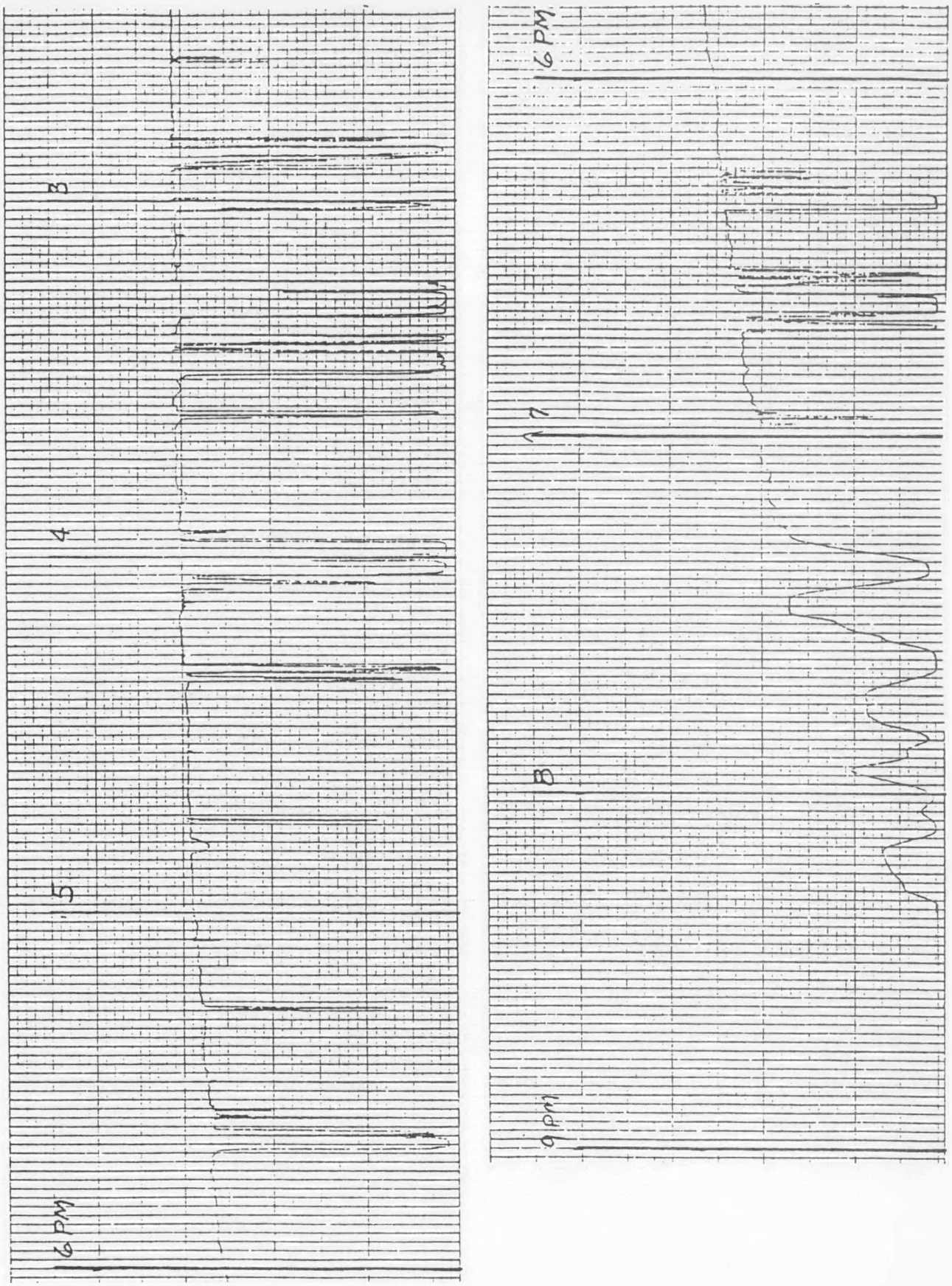

Fig. I-5 Direct Solar Radiation Received (Continued)

small changes with time occur. The reading between hours of 9 AM and 11AM of Figure I-5 would be typical of Class 1 data. Class 1 data would represent input that should cause no problems to the system. Class 3 data has a mean value of less than 85 BTU/ft^2/hr or has large variation of energy levels with lower values near zero. Class 3 data represents inputs that will cause major control or power generation problems. Figure I-5, between the hours of 3PM and 4PM, and also between 7:30PM and 9PM, are typical of Class 3 data. Class 2 data is between Class 1 and 3 and will probably cause some trouble with the control system. The time in each class expressed as a percentage of the monthly recorded time is shown in Figure I-6. Class 1 data occurs on the average about 40% of the time, Class 2 and 3, occuring with equal frequency. The month of May with a Class 1 occuring 22% of the time was a cloudy and wet month.

I-3 SUSPENDED PARTICULATES AND WIND COMPONENTS

Duststorms are a pervasive feature of late winter and spring-time weather on the High Plains. Wind erosion produces short-term, high concentration particulate levels; in addition, dust is present at lower concentrations, but sometimes to at least 15,000 ft. for period of several days. Dust blows into the South Plains from several directions, quite often in a band from Hobbs, New Mexico, to Childress, Texas. Surface, pilot, and satellite data reveal the broad extent of the dust, often including Crosbyton and Lubbock.

I-3.1 Objective

Many studies have been made of near ground dust character-

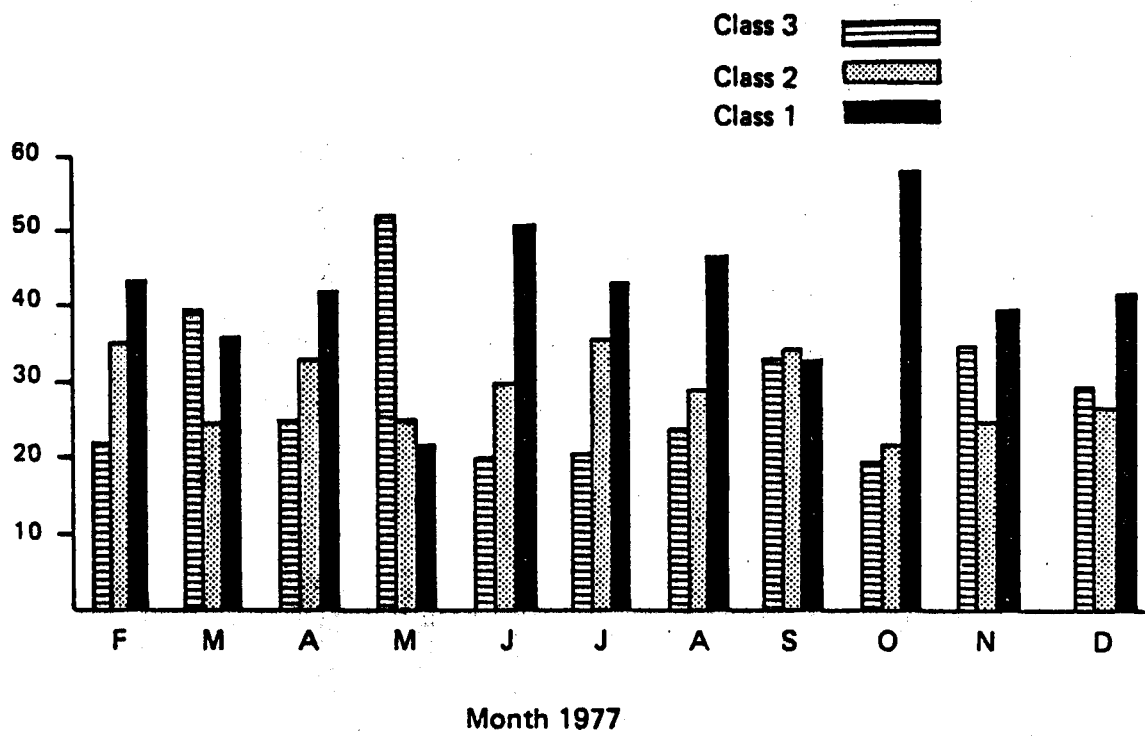

Fig. I-6 Percent of Time in Each Class for Direct Solar Readings Observed

istics based on surface collections. Vertical mass concentrations have been inferred indirectly; differences in particle size sampling cut-off points however, lead to large discrepancies between measuring methods. Little data exists on dust concentrations at various heights measured in situ. For reliable estimates of the effect of particles on solar energy reception, the vertical profile of dust is necessary.

The objective of this work was to collect samples of airborne particulates in the vertical plane and at ground level. These data will be supplemented by simultaneously measured component wind speeds; ambient temperature, pressure and relative humidity; and solar insolation. The samples of total suspended particulates including windborne dust will allow estimates to be made of the extent to which the solar collector must be protected by a water film or by other means to prevent damage by erosion from the sandblasting effect of dust storms. These data will also permit estimates of the decrease in solar intensity due to dust in the atmosphere. Potential decreases in power can then be estimated and if severe, the size of the system increased to provide a constant minimum power level even during dust storms and/or frontal passages which can generate localized blowing dust.

I-3.2 Experimental

High volume samplers for the collection of total suspended particulate samples were deployed in two locations: the Crosbyton airport (40 yds E of hangar under construction) and at the base of the Crosby County Sherrif's radio transmitter tower as shown in Figures I-1 and I-7. Data collection from these samplers began on Oct. 1, 1976, and continued on a daily basis until Jan. 8, 1977 and during dust storms

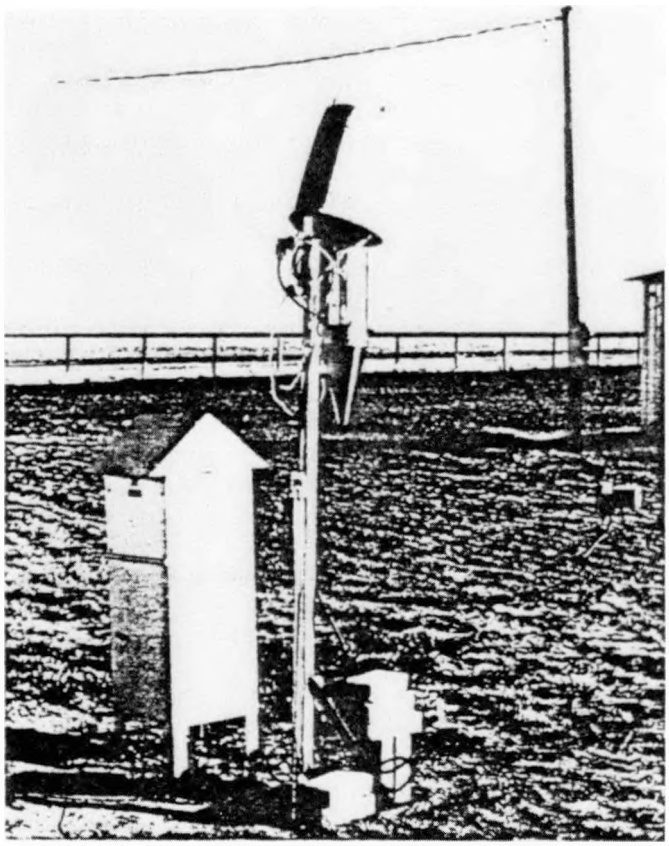

Figure I-7 High Volume Sampler (at left) and Fine Particulates Sampler (on stand) at Crosbyton Airport

since then. Data were not collected on days when any form of precipitation occurred. The dust samples were collected as an advanced science class project by students at Crosbyton High School under guidance of senior project staff members. These data, and the average climatological conditions under which they were obtained are shown in Tables I-2 and I-3. The variability in ground level dust concentrations between the two sampling sites is due to microclimatological and topological differences. The airport data are more representative of undisturbed rural conditions. The tower data reflect the effects of light activity in quasi-rural locales. Seven-day clock drive recorders were installed at the weather station by the Crosbyton power plant and used for the continuous collection of ambient temperature, pressure and relative humidity values. These units were attended regularly by the resident US Weather Bureau observer.

A Gill U-V-W anemometer, Figure I-8, was installed on the transmitter tower at the 90 ft. level on Dec. 27, 1976. The anemometer was calibrated on-site against a drive motor with a known torque output. The individual velocity components were recorded on a multichannel recorder located in a tool shed at the base of the tower next to the transducer signal converter. The orientation of the coordinate axes is U=(12^0 true), V=282^0 (true), and W is in the horizontal plane.

On the same day, a pulley system was installed on the tower. The top pulley is at the 170 ft. level, the bottom one at the 2 ft. level. Motive power for the lift system was provided by a Halliburton logging winch Figure I-9. A cradle designed and fabricated locally to hold a GCA Corp. model RDM 201 portable dust sampler was attached to the end of the lift wire, Figure I-10. This sampler has β-ray

TABLE I-2
TOTAL DUST CONCENTRATIONS AT CROSBYTON TOWER SITE

Date	Average Temperature ^0K	Average Pressure mm Hg	Sampling Time hrs.	Dust Concentration mg/m^3
10/1/76	296.26	675	10.17	0.0754
10/3	296.23	669.5	10.42	0.1037
10/4	288.65	671	11.58	0.3539
10/5	285.02	677	12.08	0.3057
10/8	281.93	681.5	9.25	0.0389
10/9	291.82	686	10.67	0.0660
10/10	295.11	677.6	9.83	0.0948
10/11	293.05	674.8	11.50	0.1068
10/12	292.25	675.4	10.58	0.1012
10/13	290.78	679.6	10.58	0.0755
10/14	291.67	673.9	10.37	0.1390
10/16	280.3	679.2	9.15	0.0641
10/17	282.44	680.7	10.08	0.1458
10/18	283.53	672	10.77	0.1567
10/19	277.38	680.4	9.93	0.1055
11/10	289.70	675.4	9.83	0.1716
11/11	275.50	675.5	9.08	0.1314
11/12	271.22	682.5	9.33	0.0415
12/22	273.17	680	32	0.1270
12/24	277.31	673	21.25	0.2798
12/27	285.25	670.5	19.50	1.0456

TABLE I-2 (CONTINUED)

Date	Average Temperature ^0K	Average Pressure mm Hg	Sampling Time hrs.	Dust Concentration mg/m^3
12/28/76	275.50	672.5	20.50	0.1554
12/29	278.35	669	23	0.2409
12/30	266.50	670	23	0.5195
12/31	263.00	674	2.67	0.9190
1/3/77	280.48	668.5	23	0.0596
1/4	274.50	671.0	23	0.7774
1/5	267.22	676.0	23	0.0660
1/6	278.50	674.5	22.75	2.9410
1/7	276.00	673.0	23	0.3996
1/8	260.00	671.0	21	0.2087
1/19	283.50	673.5	3.98	1.1814
3/2	285.40	695.5	8.5	2.3167
3/10	291.60	690.5	7.75	2.7807
11/1	280.10	696.5	9.83	0.9488
12/4	288.3	692.0	9.42	0.9742
12/5	278.3	697.0	12.3	0.8518
12/16	284.1	691	8.05	9.7308

TABLE I-3
TOTAL DUST CONCENTRATIONS AT CROSBYTON AIRPORT

Date	Average Temperature ^0K	Average Pressure mm Hg	Sampling Time hrs.	Dust Concentration mg/m^3
10/9/76	291.49	685.3	11.92	0.0161
10/10	294.9	677.6	9.5	0.0086
10/11	293	674.8	11.08	0.0093
10/12	291.91	675.4	11.30	0.0218
10/13	290.18	679.6	10.92	0.0623
10/14	291.76	673.8	10.73	0.0141
10/16	280.37	679.2	8.65	0.0557
10/17	282.7	680.7	10.83	0.0147
10/18	283.37	672	11.18	0.0366
10/19	277.18	681	9.75	0.0169
11/3	281.82	682.5	9.38	0.0349
11/4	281.61	681	9.38	0.0142
11/5	288.00	679.5	8.95	0
11/6	288.61	678	14.30	0.0369
11/7	281.50	685.6	9.25	0.0319
11/8	285.00	682	9.10	0.0280
11/10	289.70	675.4	10.28	0.1113
11/12	270.97	682.5	8.15	0.0510
12/22	273.17	680	30.33	0.0377
12/24	277.31	673	21	

TABLE I-3 (CONTINUED)

Date	Average Temperature ^{0}K	Average Pressure mm Hg	Sampling Time hrs.	Dust Concentration mg/m^3
12/27/76	285.25	670.5	19.83	0.2637
12/28	275.50	672.5	20.42	0.0599
12/29	278.35	669	23	0.0477
12/30	266.50	670	23	0.1029
12/31	265.64	674	24	0.0405
1/2/77	270.68	673.5	21.08	0.0594
1/3	280.48	668.5	23	0.0904
1/4	274.50	671.0	23	0.3006
1/5	267.22	676.0	23	0.0776
1/6	276.00	673.0	3	0.6036
3/10	291.60	690.5	7.42	4.492
4/1	295.60	698.5	4.33	1.9545
11/26	290	697	10.83	0.8341
12/16	284.1	691	9.77	4.8111

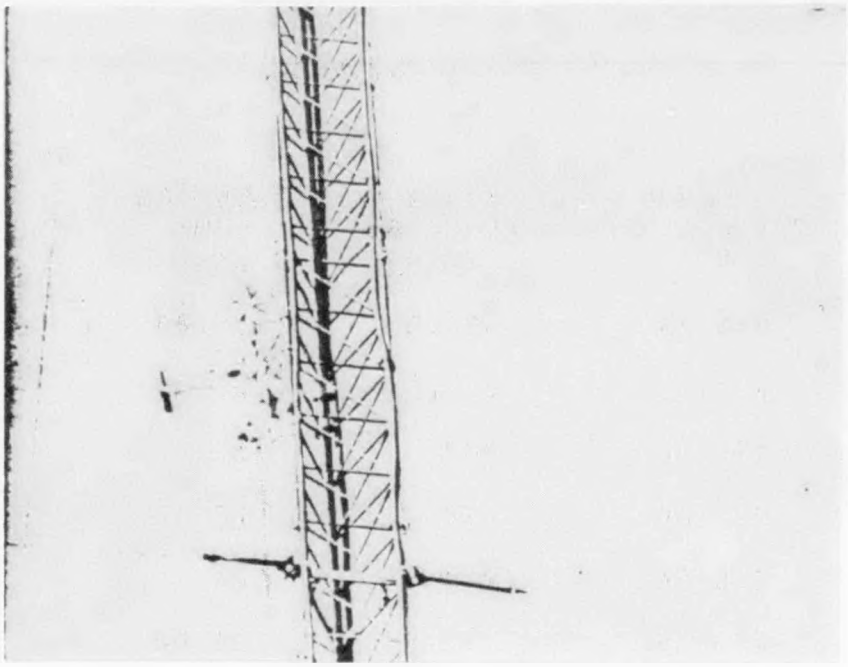

Figure I-8 Gill U-V-W- Anemometer at 90 Foot Level on Radio Transmitter Tower

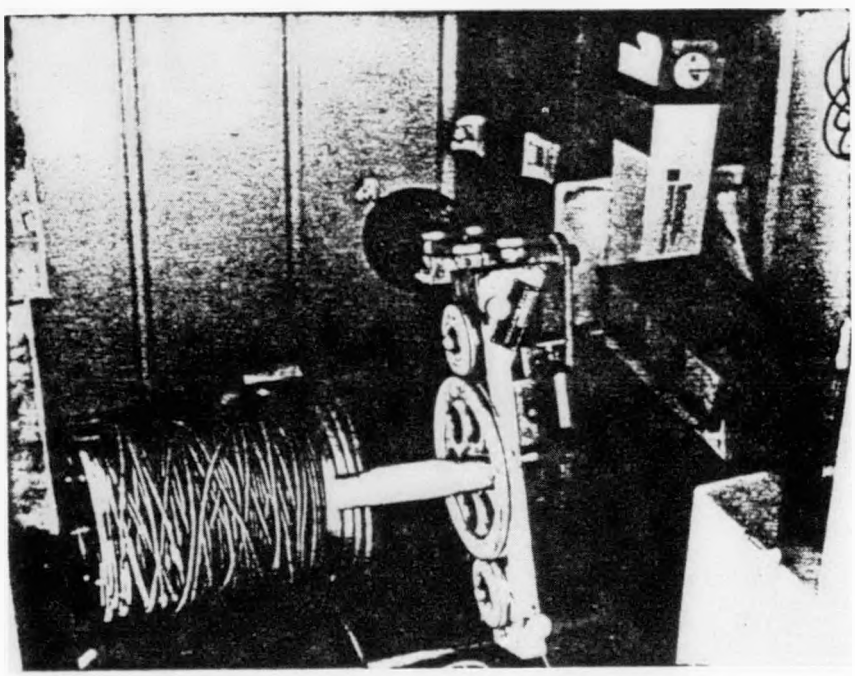

Figure I-9 Logging Winch Used to Raise and Lower Portable Dust Sampler

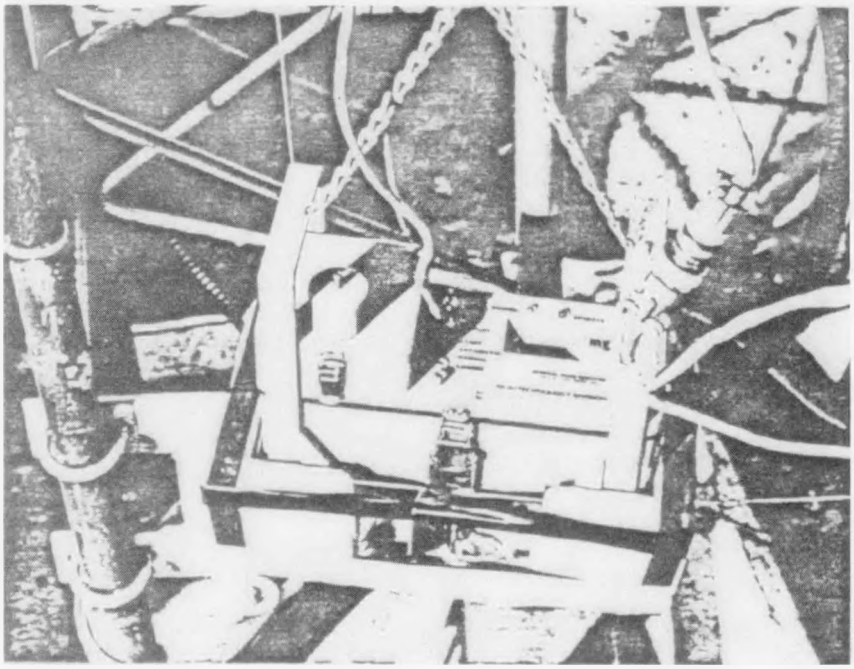

Figure I-10 GCA Corp. Model RDM 201 Portable Dust Sampler as Modified for Remote Operation

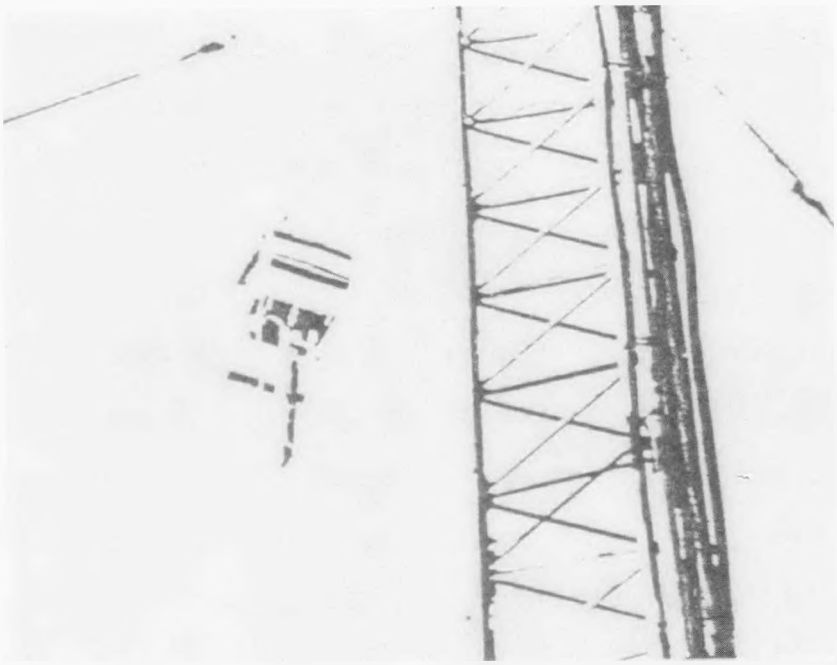

Figure I-11 Portable Dust Samper Ascending During Test Operation

attenuation for direct measurement of the dust collected on a 14.5mm. diameter fiberglass filter. The sampling rate is 2.35 ℓ/min. After an analysis is complete, the microprocessor stores the result for readout when the sampler is brought back to ground level for changing the filter. Depending on the height selected, Figure I-11, samples of total dust can be taken every 5-8 min. with this device.

I-3.3 Results

The ranges of total dust concentrations at ground level obtained during non-dust storm conditions at the tower and airport sites for sampling times of 8-23 hrs. (occasionally 3 up to 32 hrs., depending on weather conditions) were 0.0596 - 2.94 and 0.0086 - 0.6036 mg/m^3, respectively. The mean values (and standard deviations) were 0.350 (0.560) and 0.076 (0.1195) mg/m^3, respectively. These background values can be used to estimate values of dust concentration at one site from those obtained simultaneously at the other site.

The increased dust concentrations on Oct. 4 and 5, 1976 may have been caused by passage of a cold front originating from a low in the vicinity of Gage, OK. The winds in the Crosbyton area that day were 20 mph and higher from the north and northeast. On Dec. 27, 1976, a lee-side trough, oriented from north to south, existed in the Lubbock-Crosbyton area. The front, with WSW winds, passed through Crosbyton during and after the installation of the anemometer and dust sampler lift system. Some blowing dust was observed that day from 9:30AM to after 4PM.

On Dec. 30, 1976, a low between Crosbyton and the Panhandle caused strong SW-N winds, changing to N-NE on Dec. 31 as a result of a

cold air surge from the north. On Jan. 4, 1977, a cold front passed through Crosbyton in the morning with strong, gusty winds initially from the NW, veering to SE. These winds increased in intensity after the dust sampling was complete (3:40PM). During sampling, they were predominantly W-SW. On Jan. 6, 1977, a lee-side low from west to east across the US caused S-SW winds in the Crosbyton area with some surface disturbances as indicated by high volume dust concentrations of 0.6 - 2.94 mg/m^3.

Storm of January 4, 1977

The cold front of Jan. 4, 1977, caused a severe dust storm in Crosbyton. This storm approached from the W-WSW. Using 3 min. samples, the data of Tables I-4 and I-6 were obtained between 1:30 and 3:40PM. The average wind component velocities are shown in Table I-5. From these data, we see an upward velocity component in this storm. The data in Table I-5 are limited in quantity because of the time required to determine the sampling interval necessary to obtain adequate sample masses for dependable determinations of total dust. The storm had visibly abated by 2:50PM, accounting for the relatively low values for respirable dust collected after that time. A sample of the wind component velocities observed during this dust storm is shown in Figure I-12. The wind components, maxima, and ranges are shown in Table I-6 One seeming anomaly in the data needs to be clarified. The ground level high volume sampler at the tower site gave a dust concentration of 0.78 mg/m^3 on Jan. 4. The corresponding visibility was 1.5 miles. This sample started at 11:15AM, before the dust storm reached Crosbyton. Sampling unfortunately continued through 10:15AM on January 5. On

TABLE I-4 WIND COMPONENT VELOCITIES[1] DURING DUST STORM OF 1/4/77

TIME[2]	U, mph			W, mph			V, mph	
	AVG.	MAX.	RANGE	AVG.	MAX.	RANGE	AVG.	MAX.
12:36	2 S	11 S	7 N - 11 S	2 up	8 dn	8 dn - 6 up	24 W	36 W
12:41	3 S	15 S	9 N - 15 S	2 up	9 up	5 dn - 9 up	25 W	33 W
12:46	4 S	15 S	6 N - 15 S	2 up	9 up	5 dn - 9 up	27 W	34 W
12:51	3 N	12 N	12 N - 9 S	2 up	9 dn	9 dn - 8 up	22 W	33 W
12:56	1 S	17 S	10 N - 17 S	2 up	9 up	7 dn - 9 up	25 W	36 W
1:01	1 N	13 N	13 N - 14 S	2 up	6 up	7 dn - 6 up	27 W	36 W
1:06	3 S	19 S	9 N - 19 S	2 up	8 up	6 dn - 8 up	24 W	34 W
1:11	3 S	18 S	5 N - 18 S	2 up	7 dn	7 dn - 6 up	27 W	37 W
1:16	2 S	14 S	7 N - 14 S	2 up	6 up	5 dn - 6 up	25 W	33 W
1:21	2 S	34 S	9 N - 34 S	0	10 up	8 dn -10 up	27 W	37 W
1:26	2 N	10 N	10 N - 6 S	1 up	5 up	5 dn - 6 up	25 W	34 W
1:31	0	7 N	7 N - 15 S	2 up	8 up	6 dn - 8 up	27 W	34 W
1:36	1 S	12 S	8 N - 12 S	1 up	6 up	6 dn - 6 up	25 W	33 W
1:41	1 S	15 S	10 N - 15 S	1 up	8 up	6 dn - 8 up	26 W	33 W
1:46	5 S	20 S	3 N - 20 S	2 up	9 dn	9 dn - 6 up	28 W	37 W
1:51	4 S	18 S	6 N - 18 S	1 up	7 up	6 dn - 7 up	24 W	32 W
1:56	0	18 S	13 N - 18 S	2 up	8 up	6 dn - 8 up	27 W	33 W
2:01	2 N	15 N	15 N - 12 S	2 up	8 up	4 dn - 8 up	24 W	33 W
2:06	3 S	15 S	5 N - 15 S	2 up	7 up	6 dn - 7 up	26 W	31 W
2:11	0	15 S	13 N - 15 S	1 up	7 up	4 dn - 7 up	24 W	28 W
2:16	3 S	15 S	7 N - 15 S	1 up	7 up	2 dn - 7 up	22 W	28 W
2:21	1 S	13 S	10 N - 13 S	2 up	6 up	5 dn - 6 up	21 W	27 W
2:26	3 S	16 S	6 N - 16 S	2 up	9 up	5 dn - 9 up	21 W	29 W
2:31	3 S	17 S	10 N - 17 S	1 up	8 up	5 dn - 8 up	22 W	30 W
2:36	3 S	12 S	6 N - 12 S	2 up	8 up	3 dn - 8 up	22 W	30 W
2:41	2 S	11 S	9 N - 11 S	1 up	5 up	4 dn - 5 up	20 W	28 W
2:46	0	12 N	12 N - 9 S	0	7 up	6 dn - 7 up	19 W	26 W
2:51	3 S	12 S	7 N - 12 S	2 up	7 up	2 dn - 7 up	24 W	29 W
2:56	0	13 S	7 N - 13 S	2 up	7 up	3 dn - 7 up	23 W	29 W
3:01	2 S	12 S	3 N - 12 S	1 up	9 up	4 dn - 9 up	19 W	27 W
3:06	1 S	16 S	12 N - 16 S	1 up	8 up	9 dn - 8 up	21 W	28 W

TABLE I-4 (CONTINUED)

TIME[2]	U, mph			W, mph			V, mph	
	AVG.	MAX.	RANGE	AVG.	MAX.	RANGE	AVG.	MAX.
3:11	3 N	7 N	7 N - 6 S	1 up	6 up	3 dn - 6 up	21 W	28 W
3:16	1 N	8 N	8 N - 7 S	1 up	6 up	5 dn - 6 up	20 W	27 W
3:21	2 N	15 N	15 N - 6 S	1 up	7 up	2 dn - 7 up	18 W	24 W
3:26	2 S	14 S	7 N -14 S	1 up	6 up	3 dn - 6 up	20 W	28 W
3:31	1 S	10 S	10 N -10 S	2 up	9 up	5 dn - 9 up	21 W	27 W
3:36	1 N	10 N	10 N - 5 S	1 up	6 up	3 dn - 6 up	19 W	27 W
3:41	1 N	11 N	11 N -11 S	2 up	6 up	5 dn - 6 up	20 W	26 W
3:46	1 S	11 S	9 N -11 S	2 up	7 up	4 dn - 7 up	19 W	30 W
3:51	2 N	14 N	14 N - 6 S	1 up	6 up	4 dn - 6 up	19 W	25 W
3:56	2 N	10 N	10 N - 5 S	1 up	6 up	3 dn - 6 up	18 W	24 W
4:01	3 N	6 N	6 N - 6 S	1 up	7 up	3 dn - 7 up	18 W	24 W
4:06	3 N	13 N	13 N - 3 S	1 up	7 up	4 dn - 7 up	18 W	22 W

[1] Averages are for 5 minutes starting at indicated time.

[2] Times are central standard.

TABLE I-5
VARIATION OF TOTAL SUSPENDED PARTICULATE CONCENTRATIONS WITH ELEVATION DURING W-WSW DUST STORM ON JAN. 4, 1977.

Time (P.M.)	Elevation ft.	Dust Level mg/m^3	U_{avg} mph	W_{avg} mph	V_{avg} mph
1:30[a]	0	582	2 S	1 up	25 W
1:38	25	783	12 S	1 up	25 W
1:53	50	1052	3 S	2 up	32 W
1:58	75	716	1 N	2 up	34 W
2:09	100	775	2 S	2 up	31 W
2:24	125	768	1 N	2 up	27 W
2:39	150	964	12 S	2 up	29 W

[a]SAMPLING TIMES WITH RDM 201 UNIT WERE 3 MIN.

TABLE I-6 POINT VALUES OF WIND COMPONENT VELOCITIES DURING SAMPLING IN DUST STORM OF 1/4/77

TIME[a]	U, mph			W, mph			V, mph	
	AVG.	MAX.	RANGE	AVG.	MAX.	RANGE	AVG.	MAX.
1:38	2 S	12 S	12 S - 8 N	1 up	6 up	6 up - 5 dn	25 W	32 W
1:53	3 S	12 S	12 S - 6 N	2 up	7 up	7 up - 3 dn	24 W	32 W
1:58	1 N	10 S	10 S - 9 N	2 up	6 up	6 up - 3 dn	27 W	34 W
2:09	2 S	15 S	15 S - 6 N	2 up	7 up	7 up - 6 dn	26 W	31 W
2:24	1 S	11 N	10 S - 11 N	2 up		5 up - 5 dn	20 W	27 W
2:39	4 S	12 S	12 S - 2 N	2 up	6 up	6 up - 3 dn	24 W	29 W
1:30	2 S	15 S	15 S - 10 N	1 up	7 up	7 up - 4 dn	25 W	34 W
2:51	2 S	12 S	12 S - 10 N	2 up	10 up	10 up - 2 dn	22 W	27 W
3:05	3 S	16 S	16 S - 5 N	2 up	5 up	5 up - 3 dn	20 W	28 W
3:18	1 S	10 S	10 S - 7 N	1 up	5 dn	3 up - 5 dn	18 W	25 W

[a]ENTRIES ARE CENTRAL STANDARD TIME. AVERAGE, MAXIMUM, AND RANGE VALUES ARE FOR 3 MINUTES DURATION STARTING AT INDICATED TIME.

0.2 mm/sec chart speed

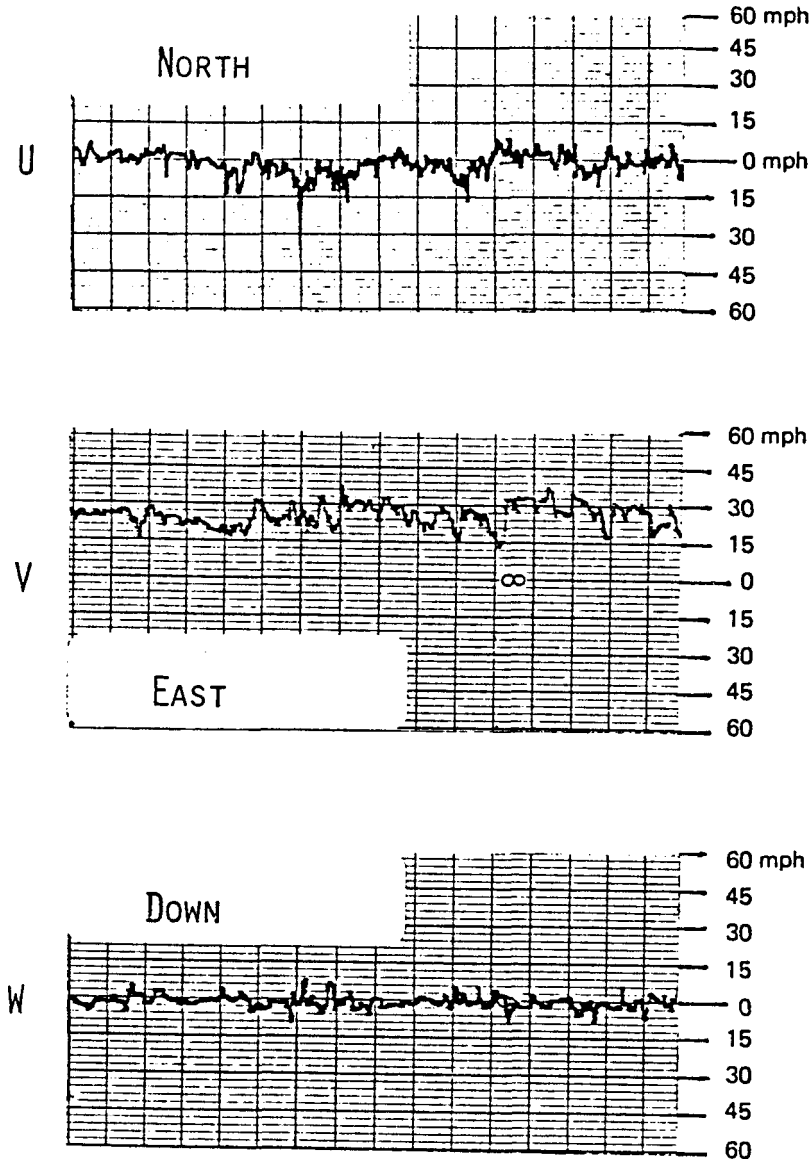

Fig. I-12 Wind Components from Duststorm of January 4, 1977

Jan. 3-5, the average dust level in Crosbyton was about 0.06+ mg/m^3. With a 3-hr. dust storm with steadily rising dust levels followed by a sharp decrease, the seeming disparity of results between the large sampler and the 30 min., essentially point values obtained with the portable sampler is not so great as it would seem.

Table I-7 shows hourly averages and ranges for the wind components at the tower site measured during 12/28/76 - 1/07/77, the dust storm period of 1/04/77 being omitted as at was presented in greater detail in Table I-4. The values in Table I-7 may be considered as representative of the average conditions which can be expected during the winter months.

Storm of January 19, 1977

An unusual front passed through Crosbyton from the N-NE on Jan. 19, 1977. The wind component velocities, maxima, and ranges are shown in Table I-8. It is interested to note that the maximum velocities associated with this front were 4-5 times greater (U) and 2-2.5 times greater (V) than in the storm of Jan. 4. The upward vertical component was about twice that of the storm of Jan. 4. as shown in Figure I-13. Only limited data were obtained during the passage of this front. It approached so rapidly that it was in Lubbock within 20 min. after it was first reported from Plainview. By the time a sampling crew reached the tower site, the dust storm was visibly subsiding. The samples reported in Table I-9 were obtained after the front had passed the tower site and thus probably represent only the slower settling portion of total suspended particulates. This time, the high volume sampler was operated only during the period of visibly

TABLE I-7 NORMAL VARIATIONS IN WIND VELOCITY COMPONENTS

		U, mph			W, mph			V, mph		
DATE	TIME	AVG.	MAX.	RANGE	AVG.	MAX.	RANGE	AVG.	MAX.	RANGE
12-28-76	12:45 P.M.	18 N	26 N	7 N - 26 N	2 up	5 up	2 dn - 5 up	0	8 E	4 W - 8 E
	1:15	16 N	24 N	8 N - 24 N	2 up	5 up	1 dn - 5 up	2 W	8 W	8 W - 4 E
	1:45	13 N	21 N	4 N - 21 N	2 up	4 up	0 - 4 up	3 W	9 W	9 W - 3 E
	2:15	12 N	20 N	4 N - 20 N	2 up	4 up	0 - 4 up	1 W	6 W	6 W - 0
	2:45	10 N	19 N	0 - 19 N	2 up	4 up	0 - 4 up	2 W	5 W	5 W - 1 E
	3:15	9 N	13 N	4 N - 13 N	2 up	4 up	2 dn - 4 up	2 W	9 W	9 W - 0
	4:15	6 N	12 N	1 N - 12 N	1 up	4 up	0 - 4 up	4 W	9 W	1 W - 9 W
	5:15	1 N	6 N	6 N - 3 S	3 up	3 up	0 - 3 up	5 W	9 W	1 W - 9 W
	6:15	1 S	3 S	0 - 3 S	3 up	constant		7 W	9 W	3 W - 9 W
	7:15	3 S	4 S	0 - 4 S	2 up	constant		10 W	13 W	8 W - 13 W
	8:15	4 S	constant		2 up	constant		10 W	13 W	6 W - 13 W
	9:15	3 S	constant		2 up	constant		12 W	15 W	7 W - 15 W
	10:15	7 S	constant		2 up	constant		12 W	15 W	8 W - 15 W
	11:15	7 S	constant		2 up	constant		12 W	15 W	9 W - 15 W
12-29-76	12:15 A.M.	*		8 S - 3 S	1 up	constant		14 W	21 W	9 W - 21 W
	1:15	6 S	12 S	1 S - 12 S	2 up	constant		13 W	15 W	9 W - 15 W
	2:15	7 S	12 S	3 S - 12 S	2 up	constant		13 W	18 W	12 W - 18 W
	3:15	7 S	11 S	2 S - 11 S	2 up	constant		14 W	19 W	9 W - 19 W
	4:15	7 S	10 S	2 S - 10 S	2 up	constant		15 W	20 W	11 W - 20 W
	5:15	7 S	12 S	3 S - 12 S	2 up	constant		15 W	18 E	11 W - 18 W
	6:15	5 S	9 S	2 S - 9 S	1 up	constant		15 W	18 W	12 W - 18 W
	7:15	8 S	12 S	3 S - 12 S	2 up	constant		14 W	18 W	9 W - 18 W

* Gradual decrease from 8 to 3 S

TABLE I-7 (CONTINUED)

DATE	TIME	U, mph			W, mph			V, mph		
		AVG.	MAX.	RANGE	AVG.	MAX.	RANGE	AVG.	MAX.	RANGE
12-29-76	8:15 A.M.	9 S	15 S	3 S - 15 S	2 up	constant		12 W	16 W	6 W - 16 W
	9:15	9 S	16 S	3 S - 16 S	2 up	constant		13 W	18 W	5 W - 18 W
	10:15	10 S	30 S	5 S - 30 S	2 up	4 up	0 - 4 up	12 W	20 W	3 W - 20 W
	11:15	17 S	30 S	3 S - 30 S	2 up	6 up	4 dn - 6 up	13 W	22 W	4 W - 22 W
	11:45	15 S	27 S	4 S - 27 S	1 up	4 up	3 dn - 4 up	12 W	19 W	3 W - 19 W
	12:15 P.M.	12 S	24 S	2 S - 24 S	1 up	3 up	4 dn - 3 up	16 W	22 W	6 W - 22 W
	12:45	14 S	28 S	3 S - 28 S	1 up	3 up	2 dn - 3 up	11 W	18 W	4 W - 18 W
	1:15	20 S	33 S	8 S - 33 S	1 up	6 up	2 dn - 6 up	7 W	13 W	3 W - 13 W
	1:45	24 S	36 S	9 S - 36 S	2 up	4 up	4 up - 4 dn	7 W	15 W	1 W - 15 W
	2:15	27 S	41 S	14 S - 41 S	1 up	3 up	3 up - 2 dn	5 W	12 W	0 - 12 W
	2:45	27 S	40 S	9 S - 40 S	2 up	4 up	4 up - 3 dn	5 W	13 W	0 - 13 W
	3:45	25 S	39 S	10 S - 39 S	0	5 dn	4 up - 5 dn	6 W	14 W	2 W - 14 W
	4:45	17 S	30 S	9 S - 30 S	2 up	4 up	0 - 4 up	5 W	10 W	0 - 10 W
	5:45	5 S	10 S	1 S - 10 S	3 up	5 up	1 up - 5 up	0	3 W	3 W - 1 E
	6:15	7 S	16 S	5 S - 16 S	3 up	5 up	2 up - 5 up	0	2 W	2 W - 2 E
	6:45	15 S	19 S	13 S - 19 S	2 up	2 up	constant	2 W	5 W	2 W - 5 W
	7:15	18 S	21 S	14 S - 21 S	2 up	3 up	2 up - 3 up	6 W	9 W	4 W - 9 W
	7:45	9 S	16 S	6 S - 16 S	2 up	3 up	2 up - 3 up	9 W	15 W	6 W - 15 W
	8:45	8 S	14 S	5 S - 14 S	3 up	4 up	2 up - 4 up	9 W	13 W	6 W - 13 W
	9:45	8 S	15 S	3 S - 15 S	2 up	3 up	2 up - 3 up	12 W	15 W	7 W - 15 W
	10:45	10 S	18 S	6 S - 18 S	3 up	4 up	2 up - 4 up	9 W	15 W	4 W - 15 W
	11:45	10 S	19 S	6 S - 19 S	3 up	4 up	2 up - 4 up	9 W	15 W	5 W - 15 W
12-30-76	12:15 A.M.	13 S	24 S	5 S - 24 S	3 up	4 up	2 up - 4 up	9 W	14 W	1 W - 14 W
	12:45	10 S	19 S	5 S - 19 S	2 up	4 up	1 up - 4 up	12 W	18 W	6 W - 18 W
	1:45	6 S	14 S	3 S - 14 S	2 up	4 up	0 up - 4 up	14 W	21 W	5 W - 21 W

TABLE I-7 (CONTINUED)

DATE	TIME	U, mph			W, mph			V, mph		
		AVG.	MAX.	RANGE	AVG.	MAX.	RANGE	AVG.	MAX.	RANGE
12-30-76	2:45 A.M.	7 S	18 S	3 S - 18 S	3up	4up	2up - 4up	13 W	20 W	8 W - 20 W
	3:45	7 S	13 S	3 S - 13 S	3up	4up	2up - 4up	14 W	22 W	9 W - 22 W
	4:45	7 S	15 S	1 S - 15 S	3up	5up	2up - 5up	14 W	20 W	9 W - 20 W
	5:45	6 S	13 S	0 - 13 S	3up	4up	3up - 4up	13 W	17 W	9 W - 17 W
	6:45	6 S	15 S	0 - 15 S	3up	6up	2up - 6up	15 W	22 W	8 W - 22 W
	7:45	3 S	11 S	11 S - 3 N	3up	4up	2up - 4up	15 W	21 W	8 W - 21 W
	8:15	12 N	42 N	3 S - 42 N	3up	6up	2up - 6up	10 W	14 W	3 E - 14 W
	8:45	10 N	21 N	2 N - 21 N	4up	9up	3up - 9up	7 W	13 W	3 W - 13 W
	9:15	22 N	36 N	11 N - 36 N	4up	5up	0 - 5up	3 W	10 W	6 E - 10 W
	9:45	33 N	46 N	14 N - 46 N	2up	5up	4dn - 5up	5 E	12 E	12 E - 12 W
	10:45	30 N	40 N	10 N - 40 N	2up	10up	0 - 10up	8 E	16 E	1 E - 16 E
	11:45	24 N	36 N	6 N - 36 N	3up	10up	5dn - 10up	10 E	22 E	2 E - 22 E
	12:45 P.M.	29 N	41 N	7 N - 41 N	3up	10up	4dn - 10up	8 E	21 E	0 - 21 E
	1:45	28 N	39 N	7 N - 39 N	3up	12up	5dn - 12up	8 E	17 E	0 - 17 E
	2:45	28 N	39 N	7 N - 39 N	3up	6up	3dn - 6up	8 E	18 E	0 - 18 E
	3:45	26 N	38 N	6 N - 38 N	3up	6up	0 - 6up	9 E	17 E	1 E - 17 E
	4:45	21 N	34 N	6 N - 34 N	4up	6up	3dn - 6up	11 E	18 E	2 E - 18 E
	5:45	18 N	26 N	6 N - 26 N	4up	12up	2dn - 12up	12 E	15 E	5 E - 15 E
	6:45	15 N	27 N	3 N - 27 N	3up	9up	0 - 9up	10 E	13 E	4 E - 13 E
	7:45	13 N	24 N	4 N - 24 N	4up	6up	0 - 6up	8 E	10 E	4 E - 10 E
	8:45	16 N	24 N	4 N - 24 N	4up	6up	2up - 6up	7 E	12 E	4 E - 12 E
	9:45	9 N	16 N	1 N - 16 N	5up	6up	2up - 6up	7 E	10 E	4 E - 10 E
	10:45	10 N	15 N	3 N - 15 N	4up	5up	1up - 5up	5 E	7 E	3 E - 7 E
	11:45	10 N	13 N	6 N - 13 N	4up	4up	3up - 4up	3 E	4 E	2 E - 4 E
12-31-76	12:45 A.M.	8 N	11 N	4 N - 11 N	4up	4up	3up - 4up	3 E	3 E	2 E - 3 E

TABLE I-7 (CONTINUED)

DATE	TIME	U, mph			W, mph			V, mph		
		AVG.	MAX.	RANGE	AVG.	MAX.	RANGE	AVG.	MAX.	RANGE
12-31-76	1:45 A.M.		*	6 N - 0	4up	4up	constant	3 E	3 E	2 E - 3 E
	2:45	1 N	1 N	constant	4up	4up	constant		*	3 E - 0
	3:45	1 N	4 N	4 N - 1 S	4up	4up	constant	1 E	1 E	constant
	4:45	2 S	2 S	constant	4up	4up	constant	1 E	1 E	constant
	5:45		**	2 S - 6 S	4up	4up	constant	0	0	constant
	6:45		**	6 S - 9 S	4up	4up	constant	0	1 E	0 - 1 E
	7:45	9 S	13 S	6 S - 13 S	4up	4up	constant	0	0	constant
	8:45	11 S	16 S	6 S - 13 S	4up	6up	3up - 6up	1 E	2 W	1 E - 2 W
	9:45	13 S	20 S	5 S - 20 S	4up	6up	6up - 3dn	2 E	7 E	0 - 7 E
	10:45	13 S	21 S	5 S - 21 S	4up	7up	0 - 7up	3 E	7 E	0 - 7 E
	11:45	14 S	23 S	3 S - 23 S	4up	6up	0 - 6up	3 E	6 E	0 - 6 E
	12:45 P.M.	14 S	22 S	3 S - 22 S	3up	6up	0 - 6up	4 E	9 E	0 - 9 E
	1:45	13 S	20 S	4 S - 20 S	4up	6up	1up - 6up	5 E	7 E	0 - 7 E
	2:45	12 S	20 S	3 S - 20 S	4up	6up	2up - 6up	5 E	9 E	2 E - 9 E
	3:45	13 S	21 S	3 S - 21 S	4up	6up	1up - 6up	6 E	9 E	3 E - 9 E
	4:45	13 S	20 S	10 S - 20 S	4up	5up	3up - 5up	6 E	9 E	4 E - 9 E
	5:45	8 S	12 S	5 S - 12 S	5up	5up	constant	8 E	11 E	7 E - 11 E
	6:45	6 S	11 S	6 S - 11 S	5up	5up	constant	11 E	12 E	10 E - 12 E
	7:45	6 S	9 S	5 S - 9 S	5up	5up	constant	10 E	10 E	constant
	8:45	6 S	9 S	5 S - 9 S	5up	5up	constant	11 E	13 E	11 E - 13 E
	9:45	5 S	5 S	constant	4up	4up	constant	9 E	11 E	9 E - 11 E
	10:45	3 S	6 S	0 - 6 S	4up	4up	constant	7 E	11 E	6 E - 11 E
	11:45	1 S	3 S	3 N - 3 S	5up	5up	constant	7 E	10 E	5 E - 10 E
1-01-77	12:45 A.M.	1 S	3 S	3 N - 3 S	4up	5up	4up - 5up	7 E	9 E	5 E - 9 E
	1:45	0	3 S	2 N - 3 S	4up	6up	3up - 6up	6 E	9 E	4 E - 9 E

* Gradual decrease from (range)
**Gradual increase from (range)

TABLE I-7 (CONTINUED)

DATE	TIME	U, mph			W, mph			V, mph		
		AVG.	MAX.	RANGE	AVG.	MAX.	RANGE	AVG.	MAX.	RANGE
1-01-77	2:45 A.M.	2 S	4 S	0 - 4 S	4 up	4 up	3up - 4up	6 E	9 E	5 E - 9 E
	3:45	1 S	3 N	3 N - 3 S	4 up	4 up	3up - 4up	6 E	9 E	5 E - 9 E
	4:45	1 S	3 N	3 N - 2 S	4 up	4 up	3up - 4up	6 E	9 E	4 E - 9 E
	5:45	1 S	4 S	3 N - 4 S	4 up	4 up	constant	6 E	9 E	4 E - 9 E
	6:45	1 S	4 N	4 N - 3 S	4 up	4 up	constant	7 E	11 E	5 E - 11 E
	7:45	3 N	7 N	7 N - 3 S	3 up	5 up	2up - 5up	8 E	14 E	6 E - 14 E
	8:45	3 N	9 N	9 N - 2 S	3 up	6 up	0 - 6up	9 E	14 E	5 E - 14 E
	9:45	1 S	9 N	9 N - 5 S	4 up	6 up	0 - 6up	7 E	12 E	5 E - 12 E
	10:45	4 N	10 N	10 N - 3 S	4 up	5 up	1up - 5up	8 E	12 E	4 E - 12 E
	11:45	2 N	11 N	4 S - 11 N	3 up	5 up	5dn - 5up	7 E	11 E	3 E - 11 E
	12:45 P.M.	0	5 N	5 N - 5 S	3 up	6 up	0 - 6up	6 E	12 E	4 E - 12 E
	1:45	1 N	9 N	9 N - 3 S	3 up	4 up	0 - 4up	7 E	11 E	4 E - 11 E
	2:45	2 N	7 N	7 N - 1 S	2 up	3 up	1up - 3up	8 E	10 E	4 E - 10 E
	3:45		*	3 N - 3 S	3 up	4 up	2up - 4up	7 E	9 E	4 E - 10 E
	4:45	2 S	3 S	3 N - 3 S	3 up	4 up	2up - 4up	5 E	8 E	2 E - 8 E
	5:45	2 S	4 S	1 N - 4 S	4 up	6 up	3up - 6up	5 E	8 E	3 E - 8 E
1-03-77	5:30 A.M.	3 S	12 S	3 N - 12 S	1 up	3 up	3dn - 3up	12 W	19 W	8 W - 19 W
	6:30	0	3 S	3 N - 3 S	0	0	constant	10 W	12 W	7 W - 12 W
	7:30	2 S	3 S	1 S - 3 S	1 up	1 up	constant	9 W	12 W	4 W - 12 W
	8:30	5 S	9 S	2 S - 9 S	1 up	1 up	constant	11 W	16 W	8 W - 16 W
	9:30	8 S	16 S	3 S - 16 S	0	1 up	0 - 1up	12 W	15 W	9 W - 15 W
	10:30	7 S	12 S	3 S - 12 S	0	1 up	0 - 1up	13 W	16 W	9 W - 16 W
	11:30	6 S	10 S	3 S - 10 S	1 up	1 up	constant	12 W	14 W	9 W - 14 W
	12:30 P.M.	4 S	9 S	0 - 9 S	0	0	constant	14 W	21 W	9 W - 21 W
	1:30	3 S	9 S	0 - 9 S	1 up	1 up	constant	11 W	15 W	8 W - 15 W
	2:30	7 S	15 S	2 S - 15 S	1 up	3 up	1dn - 3up	9 W	14 W	6 W - 14 W

* Gradual change

TABLE I-7 (CONTINUED)

DATE	TIME	U, mph AVG.	U, mph MAX.	U, mph RANGE	W, mph AVG.	W, mph MAX.	W, mph RANGE	V, mph AVG.	V, mph MAX.	V, mph RANGE
1-03-77	3:30 P.M.	15 S	22 S	3 S - 22 S	1 up	3 up	3 dn - 3 up	8 W	12 W	2 W - 12 W
	4:30	15 S	31 S	3 S - 31 S	0	6 dn	6 dn - 2 up	11 W	19 W	4 W - 19 W
	5:30	19 S	37 S	6 S - 37 S	2 dn	6 dn	0 - 6 dn	13 W	25 W	4 W - 25 W
	6:30	17 S	33 S	4 S - 33 S	1 dn	3 dn	3 dn - 2 up	10 W	22 W	4 W - 22 W
	7:30	17 S	30 S	5 S - 30 S	1 dn	6 dn	3 up - 6 dn	4 W	12 W	3 W - 12 W
	8:30	15 S	30 S	6 S - 30 S	1 dn	2 dn	0 - 2 dn	6 W	9 W	3 W - 9 W
	9:30	17 S	21 S	9 S - 21 S	0	0	constant	4 W	7 W	1 W - 7 W
	10:30	15 S	23 S	12 S - 23 S	0		1 dn - 1 up	6 W	9 W	3 W - 6 W
	11:30	14 S	25 S	13 S - 25 S	1 up	1 up	constant	10 W	16 W	4 W - 6 W
1-04-77	12:30 A.M.	9 S	20 S	6 S - 20 S	2 up	3 up	0 - 3 up	16 W	22 W	5 W - 16 W
	1:30	10 S	21 S	3 S - 21 S	1 up	4 up	0 - 4 up	14 W	22 W	8 W - 22 W
	2:30	11 S	19 S	2 S - 19 S	1 up	3 up	0 - 3 up	14 W	21 W	7 W - 21 W
	3:00	4 S	20 S	3 N - 20 S	2 up	3 up	1 dn - 3 up	13 W	18 W	7 W - 18 W
	3:30	3 S	12 S	3 N - 12 S	2 up	3 up	0 - 3 up	16 W	24 W	10 W - 24 W
	4:30	2 S	8 S	6 N - 8 S	1 up	3 up	0 - 3 up	17 W	21 W	9 W - 21 W
	5:30	3 S	10 S	3 N - 10 S	1 up	3 up	2 dn - 3 up	16 W	21 W	11 W - 21 W
	6:30	3 S	10 S	3 N - 10 S	1 up	4 up	4 dn - 4 up	18 W	24 W	12 W - 24 W
	7:30	3 S	9 S	5 N - 9 S	2 up	4 up	3 dn - 4 up	18 W	25 W	10 W - 25 W
	8:30	3 S	15 S	7 N - 15 S	2 up	8 up	5 dn - 8 up	21 W	30 W	11 W - 30 W
	9:30	4 S	21 S	12 N - 21 S	0	12 dn	12 dn - 6 up	29 W	42 W	15 W - 42 W
	10:30	1 N	18 S	18 N - 18 S	0	12 up	10 dn - 12 up	31 W	42 W	11 W - 42 W
	11:30	1 S	18 S	14 N - 18 S	1 up	13 up	10 dn - 13 up	30 W	42 W	12 W - 42 W
1-04-77	Duststorm									
	4:30 P.M.	4 N	12 N	12 N - 7 S	1 up	10 up	6 dn - 10 up	17 W	26 W	8 W - 26 W
	5:30	1 S	6 N	6 N - 6 S	2 up	4 up	2 dn - 4 up	9 W	21 W	4 W - 21 W

TABLE I-7 (CONTINUED)

DATE	TIME	U, mph			W, mph			V, mph		
		AVG.	MAX.	RANGE	AVG.	MAX.	RANGE	AVG.	MAX.	RANGE
1-04-77	6:30 P.M.	2 S	6 S	2 N - 6 S	2 up	3 up	1up - 3 up	9 W	13 W	6 W - 13 W
	7:30	0	4 S	3 N - 4 S	2 up	2 up	1up - 2 up	10 W	14 W	6 W - 14 W
	8:30									
		Possible time lag -- Chart appears to have stopped and then restarted								
	9:30	14 N	27 N	5 N - 27 N	2 up	3 up	3up - 3 dn	6 E	12 E	3 E - 12 E
	10:30	15 N	27 N	4 N - 27 N	2 up	3 up	3up - 2 dn	6 E	11 E	2 E - 11 E
	11:30	14 N	26 N	4 N - 26 N	2 up	3 up	0 - 3 up	4 E	8 E	0 - 8 E
1-05-77	12:30 A.M.	20 N	26 N	10 N - 26 N	2 up	2 up	1up - 2 up	1 E	3 E	3 E - 2 W
	1:30	14 N	25 N	3 N - 25 N	2 up	3 up	1up - 3 up	3 E	8 E	0 - 8 E
	2:30	19 N	34 N	9 N - 34 N	2 up	2 up	0 - 2 up	3 E	6 E	0 - 6 E
	3:30	17 N	31 N	6 N - 31 N	1 up	3 up	0 - 3 up	3 E	6 E	0 - 6 E
	4:30	13 N	18 N	4 N - 18 N	1 up	3 up	0 - 3 up	3 E	7 E	2 E - 7 E
	5:30	15 N	23 N	6 N - 23 N	1 up	1 up	0 - 1 up	2 E	4 E	0 - 4 E
	6:30	14 N	20 N	7 N - 20 N	1 up	3 up	0 - 3 up	2 E	4 E	1 E - 4 E
	7:30	15 N	26 N	5 N - 26 N	2 up	3 up	0 - 3 up	3 E	9 E	0 - 9 E
	8:30	13 N	22 N	3 N - 22 N	2 up	4 up	0 - 4 up	4 E	8 E	1 E - 8 E
	9:30	11 N	20 N	3 N - 20 N	2 up	4 up	0 - 4 up	5 E	9 E	2 E - 9 E
	10:30	12 N	21 N	2 N - 21 N	2 up	5 up	5up - 2 dn	5 E	9 E	2 E - 9 E
	11:30	11 N	21 N	3 N - 21 N	3 up	6 up	0 - 6 up	7 E	11 E	3 E - 11 E
	12:30 P.M.	13 N	20 N	3 N - 20 N	3 up	5 up	0 - 5 up	7 E	12 E	3 E - 12 E
	1:30	11 N	19 N	4 N - 19 N	3 up	5 up	0 - 5 up	7 E	10 E	3 E - 10 E
	2:30	7 N	14 N	14 N - 1 S	1 up	3 up	3up - 2 dn	6 E	9 E	1 E - 9 E
	3:30	6 N	11 N	2 N - 11 N	3 up	3 up	constant	3 E	7 E	1 E - 7 E
	4:30	6 N	12 N	12 N - 0	3 up	3 up	constant	3 E	4 E	1 E - 4 E
	5:30	4 N	9 N	9 N - 0	2 up	3 up	0 - 3 up	4 E	6 E	0 - 6 E

TABLE I-7 (CONTINUED)

DATE	TIME	U, mph			W, mph			V, mph		
		AVG.	MAX.	RANGE	AVG.	MAX.	RANGE	AVG.	MAX.	RANGE
1-05-77	6:30 P.M.	1 N	4 N	4 N - 0	3 up	4 up	2 up - 4 up	2 E	3 E	3 E - 3 E
	7:30	6 N	10 N	10 N - 0	3 up	5 up	1 - 5 up	4 up	6 W	0 W - 6 W
	8:30	1 N	10 N	10 N - 5 S	3 up	3 up	constant	3 E	5 E	0 - 5 E
	9:30	4 S	10 S	1 S - 10 S	3 up	3 up	constant	2 E	5 E	5 E - 5 W
	10:30	2 S	6 S	0 - 6 S	3 up	3 up	constant	3 W	6 W	1 W - 6 W
	11:30	3 S	7 S	3 S - 7 S	3 up	3 up	constant	3 W	3 W	1 W - 3 W
1-06-77	12:30 A.M.	6 S	10 S	5 S - 10 S	3 up	3 up	constant	6 W	7 W	4 W - 7 W
	1:30	8 S	13 S	4 S - 13 S	3 up	3 up	constant	7 W	9 W	4 W - 9 W
	2:30	11 S	15 S	8 S - 15 S	3 up	3 up	constant	5 W	6 W	4 W - 6 W
	3:30	11 S	17 S	7 S - 17 S	3 up	3 up	constant	8 W	11 W	6 W - 11 W
	4:30	10 S	18 S	2 S - 18 S	3 up	5 up	1 - 5 up	12 W	19 W	6 W - 19 W
	5:30	8 S	18 S	1 S - 18 S	3 up	8 up	0 - 8 up	14 W	19 W	7 W - 19 W
	6:30	3 S	15 S	12 N - 15 S	4 up	6 up	0 - 6 up	14 W	24 W	6 W - 24 W
	7:30	4 N	18 N	18 N - 9 S	5 up	7 up	0 - 7 up	15 W	24 W	6 W - 24 W
	8:30	8 N	27 N	27 N - 6 S	4 up	7 up	0 - 7 up	12 W	19 W	6 W - 19 W
	9:30	9 N	21 N	0 - 21 N	5 up	7 up	1 up - 7 up	10 W	15 W	1 W - 15 W
	10:30	11 N	21 N	0 - 21 N	5 up	7 up	2 up - 7 up	5 W	13 W	13 W - 1 E
	11:30	13 N	23 N	0 - 23 N	5 up	7 up	2 up - 7 up	4 W	10 W	10 W - 3 E
	12:30 P.M.	15 N	22 N	5 N - 22 N	5 up	9 up	3 up - 9 up	1 W	6 W	6 W - 3 E
	1:30	13 N	18 N	4 N - 18 N	5 up	6 up	4 up - 6 up	1 E	3 E	3 W - 3 E
	2:30	11 N	15 N	4 N - 15 N	6 up	6 up	constant	1 E	1 E	0 E - 1 E
	3:30	13 N	15 N	7 N - 15 N	6 up	6 up	4 up - 6 up	2 E	3 E	1 E - 3 E
	4:30	13 N	15 N	7 N - 15 N	5 up	6 up	5 up - 6 up	2 E	3 E	1 E - 3 E
	5:30	13 N	14 N	6 N - 14 N	5 up	6 up	5 up - 6 up	3 E	4 E	2 E - 4 E
	6:30	7 N	13 N	0 - 13 N	5 up	6 up	5 up - 6 up	3 E	4 E	2 E - 4 E

TABLE I-7 (CONTINUED)

DATE	TIME[a]	U, mph			W, mph			V, mph		
		AVG.	MAX.	RANGE	AVG.	MAX.	RANGE	AVG.	MAX.	RANGE
1-06-77	7:30 P.M.	0	3 S	3 S - 2 N	5 up	6 up	4up - 6up	4 E	6 E	3 E - 6 E
	8:30	2 S	6 S	0 - 6 S	5 up	6 up	5up - 6up	3 E	5 E	3 E - 5 E
	9:30	13 S	21 S	6 S - 21 S	4 up	6 up	4up - 6up	2 W	4 E	3 W - 4 E
	10:30	14 S	18 S	11 S - 18 S	4 up	5 up	4up - 5up	5 W	8 W	3 W - 8 W
	11:30	11 S	12 S	9 S - 12 S	5 up	5 up	constant	7 W	8 W	6 W - 8 W
1-07-77	12:30 A.M.	10 S	13 S	6 S - 13 S	5 up	5 up	constant	7 W	9 W	6 W - 9 W
	1:30	7 S	13 S	3 S - 13 S	5 up	6 up	5up - 6up	8 W	10 W	6 W - 10 W
	2:30	5 S	7 S	3 S - 7 S	6 up	6 up	constant	7 W	10 W	4 W - 10 W
	3:30	8 S	15 S	6 S - 15 S	6 up	6 up	constant	5 W	6 W	3 W - 6 W
	4:30	17 S	25 S	12 S - 25 S	4 up	6 up	3up - 6up	3 W	8 W	8 W - 0
	5:30	18 S	30 S	9 S - 30 S	4 up	6 up	3up - 6up	2 W	6 W	6 W - 0
	6:30	22 S	35 S	12 S - 35 S	4 up	6 up	0 - 6up	2 W	9 W	9 W - 0
	7:30	27 S	36 S	11 S - 36 S	4 up	6 up	3dn - 6up	3 W	10 W	10 W - 1 E
	8:30	24 S	37 S	11 S - 37 S	4 up	6 up	0 - 6up	3 W	12 W	12 W - 0
	9:30	24 S	39 S	11 S - 39 S	4 up	8 up	0 - 8up	3 W	10 W	10 W - 1 E
	10:30	28 S	31 S	14 S - 31 S	5 up	8 up	1up - 8up	2 W	8 W	8 W - 8 E

[a] Values for any time represent the average, maximum, and range of values until the next time entry, unless a break of more than 1 hour occurs. In that case the last entry before a break represents a 1 hour period.

TABLE I-8 WIND COMPONENT VELOCITIES[1] DURING DUST STORM AND NORTHEASTERLY FRONTAL PASSAGE ON 1/19/77

TIME[2]	U, mph		W, mph			V, mph	
	AVG.	MAX.	AVG.	MAX.	RANGE	AVG.	MAX.
12:15	41 N	57 N	4 up	14 dn	14 dn - 9 up	6 E	16 E
12:20	43 N	53 N	4 up	10 up	4 dn - 10 up	8 E	14 E
12:25	36 N	57 N	4 up	11 dn	11 dn - 9 up	9 E	20 E
12:30	39 N	58 N	4 up	10 up	3 dn - 10 up	10 E	15 E
12:35	37 N	47 N	4 up	10 up	9 dn - 10 up	10 E	17 E
12:40	37 N	52 N	4 up	11 up	4 dn - 11 up	10 E	16 E
12:45	39 N	56 N	5 up	10 up	6 dn - 10 up	9 E	15 E
12:50	36 N,	52 N	5 up	12 up	3 dn - 12 up	11 E	18 E
12:55	36 N	51 N	4 up	10 up	6 dn - 10 up	9 E	15 E
1:00	34 N	50 N	4 up	9 up	3 dn - 9 up	10 E	12 E
1:05	34 N	48 N	4 up	10 up	5 dn - 10 up	10 E	15 E
1:10	38 N	51 N	5 up	12 up	6 dn - 12 up	11 E	15 E
1:15	35 N	45 N	5 up	9 up	4 dn - 9 up	10 E	17 E
1:20	36 N	52 N	5 up	11 up	6 dn - 11 up	11 E	17 E
1:25	34 N	57 N	5 up	10 up	4 dn - 10 up	13 E	18 E
1:30	36 N	45 N	5 up	9 up	3 dn - 9 up	14 E	18 E
1:35	32 N	37 N	5 up	9 up	3 dn - 9 up	12 E	15 E
1:40	35 N	45 N	5 up	10 up	3 dn - 10 up	13 E	18 E
1:45	36 N	45 N	5 up	11 up	3 dn - 11 up	14 E	21 E
1:50	36 N	45 N	5 up	10 up	2 dn - 10 up	13 E	18 E
1:55	35 N	47 N	5 up	9 up	4 dn - 9 up	12 E	16 E
2:00	32 N	42 N	5 up	12 up	2 dn - 12 up	12 E	18 E
2:05	34 N	44 N	5 up	9 up	3 dn - 9 up	11 E	16 E
2:10	28 N	39 N	5 up	8 up	3 dn - 8 up	11 E	16 E
2:15	30 N	44 N	5 up	10 up	6 dn - 10 up	11 E	15 E
2:20	27 N	40 N	5 up	10 up	3 dn - 10 up		
2:25	28 N	38 N	5 up	11 up			
2:30	27 N	38 N	5 up	11 up	4 dn - 11 up		
2:35	29 N	39 N	5 up	9 up	3 dn - 9 up		
2:40	29 N	38 N	5 up	9 up	2 dn - 9 up		
2:45	28 N	40 N	5 up	10 up	2 dn - 10 up		

TABLE I-8 (CONTINUED)

TIME[2]	U, mph		W, mph			V, mph	
	AVG.	MAX.	AVG.	MAX.	RANGE	AVG.	MAX.
2:50	28 N	40 N	5 up	9 up			
2:55	31 N	39 N	5 up	9 up		11 E	15 E
3:00	29 N	43 N	5 up	11 up	3dn - 11up	8 E	14 E
3:05	28 N	38 N	5 up	9 up		8 E	10 E
3:10	34 N	41 N	5 up	8 up	2dn - 8up	8 E	12 E
3:15	33 N	42 N	5 up	6 up		8 E	12 E
3:20	30 N	39 N	5 up	8 up		7 E	12 E
3:25	31 N	43 N	5 up	6 up		8 E	12 E
3:30	29 N	42 N	5 up	6 up		8 E	13 E
3:35	30 N	38 N	5 up	8 up		7 E	9 E
3:40	29 N	38 N	5 up	8 up		7 E	11 E
3:45	30 N	39 N	5 up	6 up		7 E	9 E
3:50	29 N	42 N	5 up	6 up		7 E	10 E
3:55	28 N	38 N	5 up	6 up		7 E	12 E

[1] Averages are for 5 minutes starting at indicated time.

[2] Times are central standard, starting at 12:15 p.m.

0.2 mm/sec chart speed

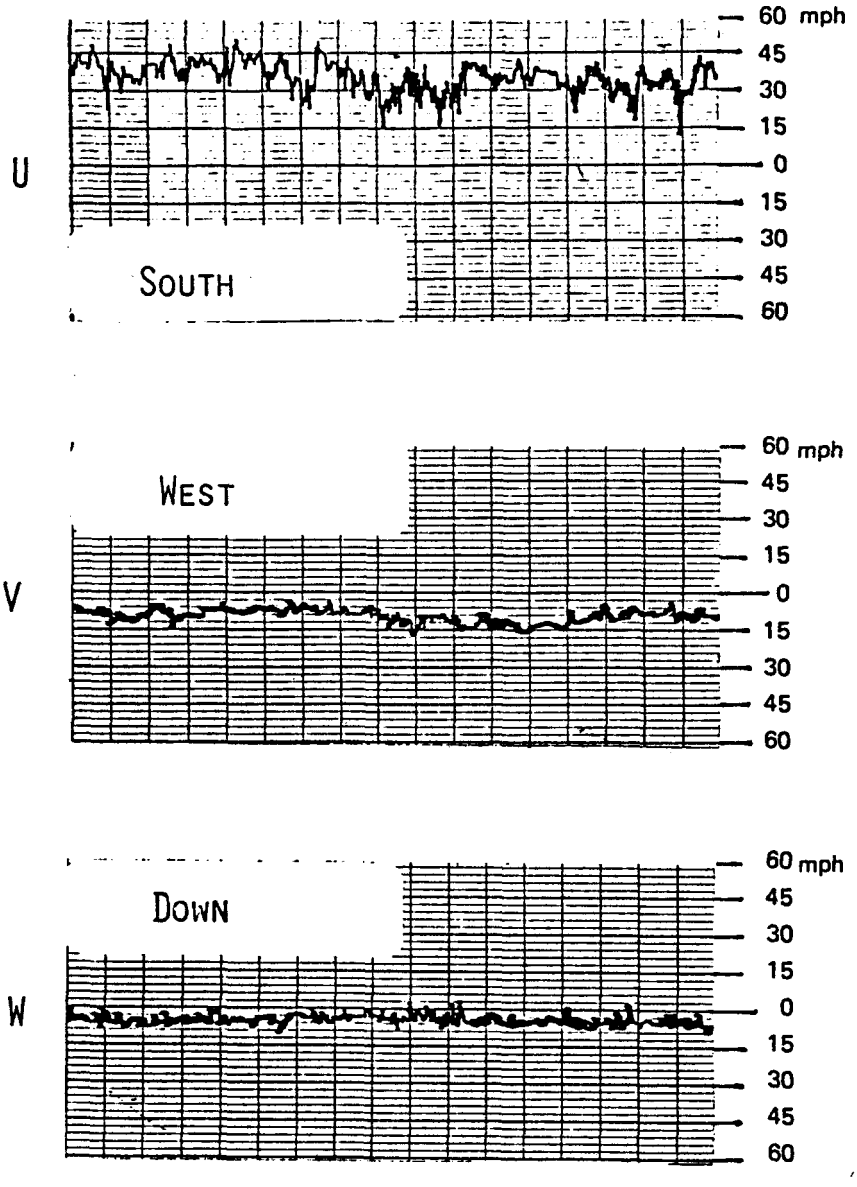

Fig. I-13 Wind Components from Duststorm of January 19, 1977

TABLE I-9 DUST CONCENTRATIONS AFTER NORTHERLY FRONTAL PASSAGE ON 1/19/77

Sampling Start p.m.	Duration min.	Elevation ft.	Dust Level mg/m^3	U avg mph	W avg mph	V avg mph
2:24	2	0	0	23 N	4 up	NA[b]
2:27	3	0	6.37	27 N	5 up	NA
2:38	4	0	5.80	27 N	4 up	NA
2:50	4	25	0	29 N	4 up	NA
2:58	5	25	0	30 N	5 up	10 E
3:10	10	50	0	35 N	4 up	8 E
3:25	10	50	0	31 N	5 up	7 E

[a]Sampling time with RDM 201 unit

[b]NA - not available because of recorder channel malfunction.

blowing dust. The total dust concentration so obtained at ground level was 1.18 mg/m^3, which is still more than 10-fold higher than the national ambient air quality standard set by EPA. The effect of the upward wind component on dust concentrations above ground was quite marked. The visibility during this storm decreased to 3/4-mile.

Storm of February 22, 1977

On Feb. 22-23, 1977, one of the biggest dust storms in several years occurred. A deepening upper level trough in the western United States was accompanied by a surface storm system which intensified on the High Plains of Texas. A lee-side trough on Feb. 21 gave way to a deep surface low in eastern Colorado on Feb. 22. By Feb. 23, the still deeper surface low had moved into south-central Nebraska. The associated cold front sped from eastern Arizona to East Texas during the same 24-hr period. Surface winds above 50 knots over a broad region of the southern High Plains persisted in the wake of the storm. The dust removed from topsoil mixed to great heights and over the next three days spread across the southeastern US and into the Atlantic Ocean. The wind components observed during this storm are shown in Figure I-14.

No dust samples were obtained during this storm as the entire project team was in Lubbock for the Phase I project review. The visibility in Lubbock at times was as low as 1/2-mi. From the color of the storm and its long persistence, we infer that most of the dust was in the fine particulate range, probably below 25 micrometers aerodynamic diameter.

0.2 mm/sec chart speed

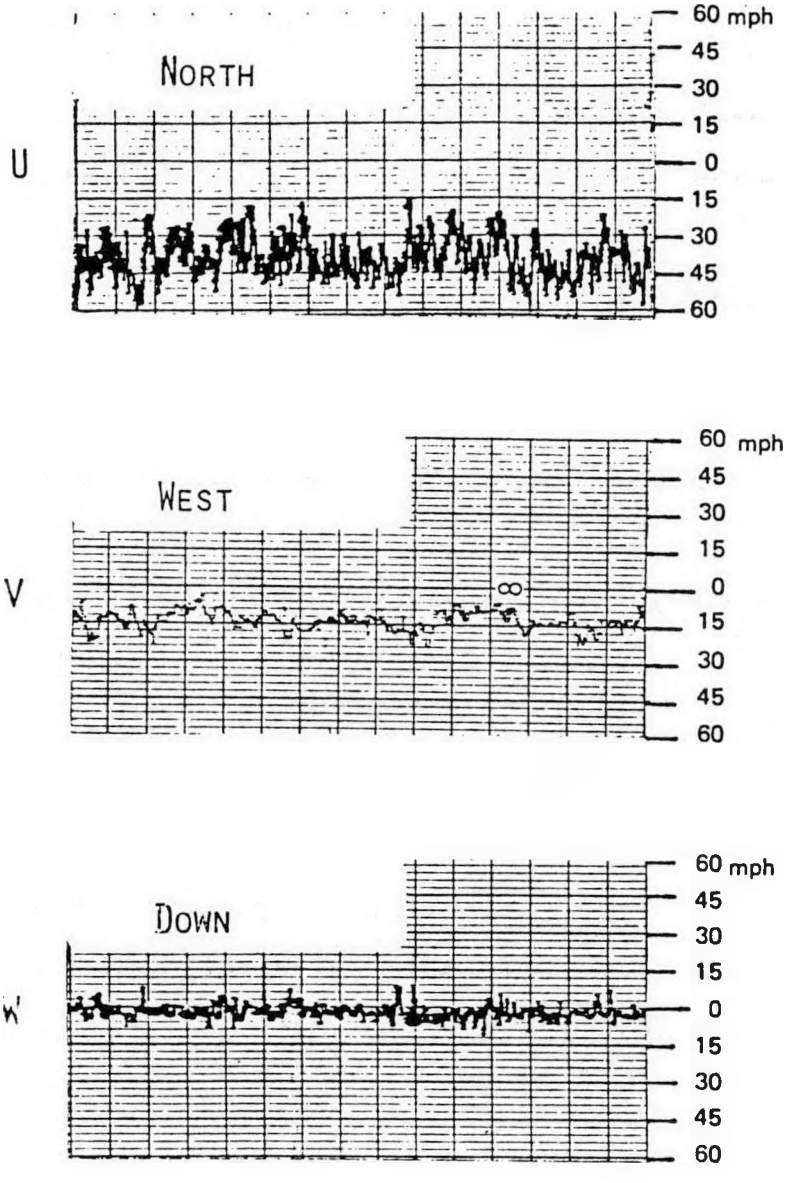

I-14 Wind Components from Duststorm of February 22, 1977

The blowing dust on Mar. 2, 1977, was associated with a surface low located in southeastern Colorado which intensified because of the eastward movement of an upper level trough from the northwestern United States into the Southern Rockies. Dust occurred with the deepening cyclogenesis and passage of the associated rapidly moving cold front. The average dust concentration measured at the tower site was 2.32 mg/m^3. Based on the average background concentration ratio of 4.6 of tower to airport total dust, we estimate the blowing dust at the airport to be about 0.5 mg/m^3 which is consistent with values observed at the airport during other similar frontal passages. During the height of this storm, the visibility was reduced to 2-1/2 miles. A similar situation occurred on Mar. 10, 1977, with the surface low located in eastern Colorado and movement of an upper level trough from the western US into the Central Rockies. During this storm, the total dust concentrations ranged from 2.78-4.49 mg/m^3. Visibility decreased to 3/4-mile.

On April 1, 1977, the blowing dust was associated with a weakly organized surface low in Colorado with southerly winds over the South Plains. The winds were generated by surface heating and a downward transport of momentum from a strong jet stream extending SW to NE over West Texas. The dust concentration at the airport due to this storm was 1.95 mg/m^3.

Strong northerly surface winds on November 1, 1977, caused fairly wide-spread dust extending east-west and pushing southward beyond Midland. The dust concentration at the tower site was 0.95 mg/m^3. Visibility was 4 miles.

On November 26, 1977, southwesterly winds caused by surface heating and a down-mixing of a strong high-speed upper flow generated

blowing dust beginning in the morning with clearing after dark. Blowing dust extended from Roswell, NM to east of Lubbock including Clovis and Plainview with pilot reports of dust tops at 11,000 feet. From the 2 mile visibility, we estimate that the dust concentration at about 1.5 mg/m^3.

The presence of a very strong WNW upper flow developing a lee-side trough across the South Plains and the passage of a short upper wave on Dec. 3, 1977, led to cyclogenesis in the NE Panhandle of Texas. Increasing WNW surface winds over the South Plains (up to 35 knots) led to dust reports from the vicinity of Roswell, NM to east of Sweetwater, TX on Dec. 4, 1977. Pilot reports indicated dust up to 7,000 feet. Dust concentration for this storm measured at the tower site was 0.97 mg/m^3. The dust observed on Dec. 5, 1977, was probably a continuation of the recently developed weather conditions or rapid surface heating. The concentration of dust at the tower was 0.85 mg/m^3.

Storm of December 16, 1977

On Dec. 16, 1977, Crosbyton experienced a major dust storm. The dust activity began on Dec. 15 with many stations in the Great Basin reporting strong surface winds and blowing dust due to a short upper wave moving eastward from the West Coast. Dust suspended from atmospheric activity in the West produced a yellowish sunrise in Lubbock on Dec. 16. At approximately 9:30AM, the surface winds picked up rapidly due to the short upper wave just to the west of the South Plains and the surface cold front (from surface low in western Kansas) moving rapidly to the East. Official visibility was less than 1/8 mile (down to 1/2 block on the campus of Texas Tech University). Significant variations in dust color (and size distribution or possibly source)

were observed during this storm. Figs. I-15 and I-16 illustrate the visibility from the twelfth floor of our Business Administration Building. Fig. I-16 which is a view of the sun shows the gradation in density of the dust storm. The dark burnt orange observed is caused by large particles and corresponds to blowing sand and dirt. The bluish gray seen at other time during the storm is characteristic of fine size particle distributions. Dust concentrations were 4.81 to 9.73 mg/m^3 in Crosbyton. Pilot reports indicated dust up to 12,500 feet and wind gusts peaking at 55 mph. The next day the dust led to greatly reduced visibilities across the eastern two-thirds of Texas and as far as Jackson, MS.

A westerly upper flow produced a lee-side trough on Dec. 22, 1977, thus generating strong SW winds on the South Plains. On Dec. 23, a cold front developed in the trough due to a short upper wave when upon passing the South Plains shifted the winds to NW.

On Dec. 29, a surface low was located in the Oklahoma Panhandle and there was a westerly upper flow with short waves. On Dec. 30, the localized blowing dust occurred with the passage of the upper trough and the exit of the surface low from the region.

I-3.4 Conclusions

Based on the data available to date, the supporting structure for the solar collector must be able to withstand wind velocities of at least 58 mph in the horizontal plane, upward components of 12 mph, and downward components of 14 mph.

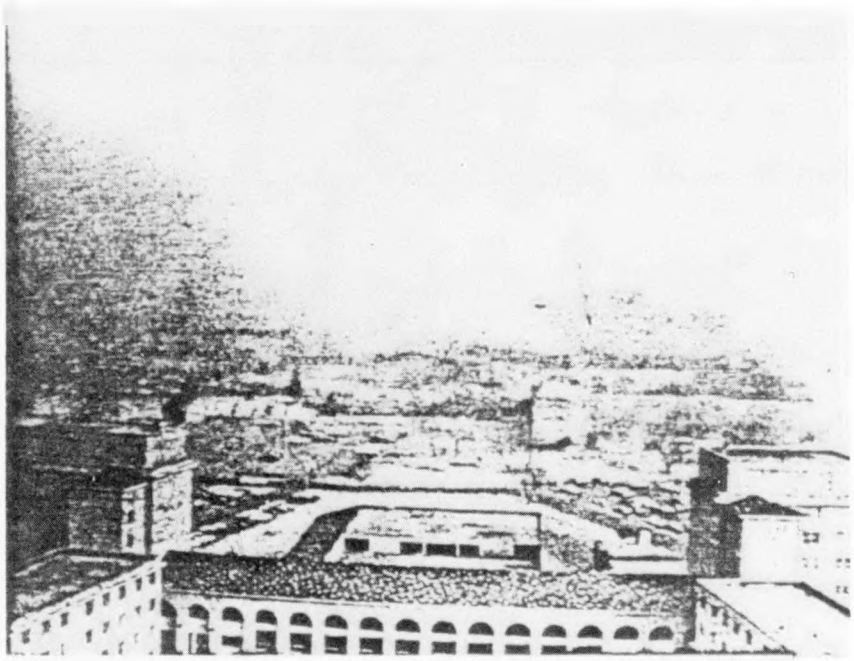

Figure I-15 Visibility at 11:30 CST, Dec. 16, 1977
12th Floor - Business Administration Building

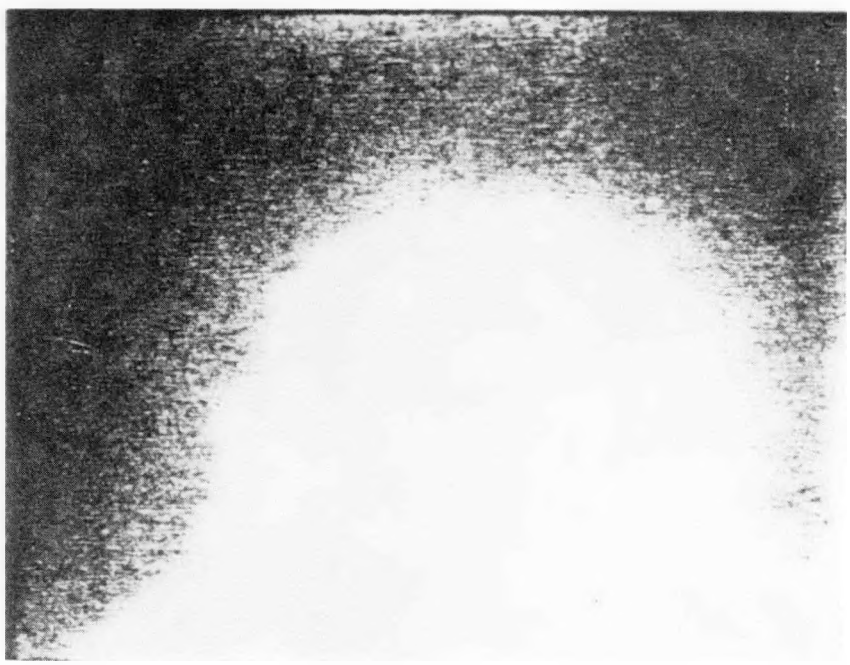

Figure I-16 View of Sun at 11:30 CST, Dec. 16, 1977
12th Floor - Business Administration Building

I- 4 SOIL - FOUNDATION

Soil exploration plan and boring logs were provided on page II-11 to 21 and Appendix B of CSP-Interim Technical Report. The results reported are sufficient for design of ATS structure. Further detailed tests could possible be required depending on final structural design of ATS. Further laboratory tests are not anticipated at this time.

APPENDIX J. SYSTEM AND ECONOMIC MODELING AND SIMULATION

This appendix includes discussions on two separate but related areas; the economics of the FMDF system, and considerations of system modeling. The economics discussion presented in the first section below is an updated and extended version of the previous work reported in the first Interim Technical Report, and includes a parametric analysis of levelized busbar costs as a function of various cost factors and operating conditions. The remaining sections of the appendix address various aspects of system modeling.

Concerning the topic of system modeling and simulation, the Recommended Power System description includes the use of oil receivers to heat oil for thermal storage. Additional computer analyses involving the circulation of a heat transfer oil through a receiver have been conducted and are discussed in a later section of this appendix.

The main thrust in the area of system modeling during the early work done on this project was to conduct analyses of various subsystems during steady-state operation. A complete system modeling and simulation to determine annual performance assuming steady conditions was conducted and reported in the first Interim Technical Report. Since that time, effort has been expended in developing a mathematical model of the dynamical behavior of the system. Part of this effort has included an analysis of the thermal behavior of the receiver under transient insolation conditions, and consideration of possible modes of system operation under reduced insolation conditions. Both of these

topics are also discussed below.

The major objective for developing a dynamic model, or simulation, of the system is to establish the control management system which will maximize the useful energy production. The process of developing such a model is an iterative one involving the ATS. The main area of mathematical uncertainty is the fluid-thermal characteristics of the receiver. Not only is this a most critical area for the overall performance of the system, but it is also the least understood aspect of the system from the standpoint of its dynamical performance. A suitable model is going to require the use of experimental data from both the ATS and component tests. These data, when incorporated into the model, will allow the investigation of various management schemes without the danger of failure of the hardware.

The results of the initial model have indicated that the receiver may quickly fail (less than 15 sec.) if the cooling is inadequate. This result has led to a very conservative management scheme for intermittent insolation using the ATS during its early operation. If the insolation is reduced by cloud cover, the control system will initiate a shutdown sequence. After the insolation has been sensed to have reestablished itself for a significant period of time, a normal startup procedure will start. This control management scheme will safeguard the receiver at the expense of energy production during periods of intermittent insolation. However, it will also provide the very important information regarding the transient behavior of the system during shutdown and startup. Once these data have been successfully incorporated into the mathematical model, the model may be used to explore other responses to loss of insolation. This will result

in a slightly less conservative management scheme which, when implemented, will result in experimental data being incorporated into the mathematical model to further expand its applicability.

This iterative process of improving the management scheme, using the resulting transient data to improve the mathematical model, using the model to improve the management scheme, etc., may be one of the most important aspects of the ATS. The results of this process will be a model, with experimental verification, which may be used to design a management and control system for the RPS which will maximize the energy generated from available insolation without hardware failure. In addition, the model may also be used to investigate the use of the solar energy system for tasks other than the generation of steam for turbine-generator power production.

J-1 ECONOMIC ANALYSIS OF FMDF STEPS

In the initial economic analysis of the FMDF system for Crosbyton, Texas, previously reported in the Interim Report, load factors and operating levels were tailored specifically for the situation existing at the Crosbyton site. In this follow-on analysis, done at E-Systems, conditions were opened up to allow a parametric analysis of levelized busbar costs as a function of various cost factors and operating conditions. Four levels of solar collector cost, three fuel escalation levels, system concepts ranging from all solar to all fossil fuel under varying plant capacity factors and different insolation levels were analyzed. In addition, two business categories were considered: (1) municipal utility with the ability to issue tax free bonds for capital formation and break-even operation; and (2) a private

utility with capital formation consisting of 40% from common stock, 10% from preferred stock and 50% from debt, having an overall cost of capital of 9.6% and a 40% tax rate.

J-1.1 Economic Model Methodology

The methodology employed is that recommended by DOE/EPRI as discussed in JPL Report Number JPL 5040-29 for comparison between various investment alternatives. It is essentially a discounted cash flow, present value analysis of the entire investment of building and operating a plant over a nominal life of 30 years. The capital investment required is divided into 15 different accounts, each of which can be escalated at its own rate. A base year and the first year of commercial operation, is established. The capital accounts are escalated over a design and construction period, and interest during construction is calculated based on the time of cash requirement for each capital account. In this way the capital investment at first year of commercial operation is calculated.

Operating costs are escalated from the base year and operating yearly cash flow are discounted to the first year of commercial operation. The assumption is made that this annuity must be paid out in equal increments each year for the life of the plant and is, therefore, the yearly revenue required. The annuity payment consists of two parts: capital recovery and interest payments on the initial capital investment, and a charge for operating costs each year with anticipated cost increases and escalations for the entire 30 years. The sum of these two payments is the so called levelized busbar cost which, if charged each year, would cover all costs plus escalations and increases

and recover the capital investment made in the first year of commercial operation.

Although the product costs thus determined are highly artificial, comparisons made in this way between various alternatives are meaningful. Of the available alternatives, the one with the lowest levelized cost is the most attractive over the full life of the plant. However, no statement can be made about the actual price to be charged on a year by year basis or the relative costs of the two alternatives in any one year.

Before calculating levelized busbar cost, the present value of the investment to build and operate the plant was converted to a 1978 present value by the appropriate deflation factor.

In actual practice a public utility would attempt to adjust its product cost on a year by year basis to reach some desired rate of return on capital assets. Regulatory bodies evaluate and approve price increases based on maintaining the approved rate of return.

The DOE economic methodology, which stops with the determination of levelized cost as described above, has been extended in this analysis to give a more realistic cost to be charged for the product. For a municipal plant, the assumption is made that the required rate of return on assets is zero. That is, the utility would adjust its product charge each year to cover operating costs, pay interest on the capital investment and recover, by a depreciation charge to operation, a portion of the capital investment. The capital recovered would be used to pay off bond holders or be reinvested at a comparable interest rate. In either case, the net effect would be to decrease the interest charge to operations by the amount of capital recovery from year to year.

J-1.2 Operational System Concepts

Pure Solar Plant With No Storage

In the no storage configuration, the solar field was sized to give name plate capacity under peak conditions. Peak insolation for the 65% clear day geographical location was defined as 290 $Btu/ft^2/hr$. Overall peak efficiency for the system was defined as 17%, made up of 65% thermal collection efficiency and 26% cycle efficiency for energy conversion. Under these conditions one KW of capacity requires 69.2 ft^2 of FMDF solar collector aperture.

Plant capacity factor for the pure solar no storage case is a function of the total insolation at the site of the plant. For the case of Fort Worth, for which E-Systems has a year of actual insolation data, the yearly average turns out to be 741,000 Btu/ft^2. Combining this with the average collection efficiency fo the system gives a plant capacity fo 15.4%.

Since the above configuration represents a minimum capital investment, the economics were investigated both as a stand alone solar plant and as a hybrid plant under the assumption that all solar generated energy would be used, and the extension to off hours would be accomplished by fossil fuel. A cost of $\$10/ft^2$ for the solar collector was assumed in all the cases considered.

Fig. J-1 shows levelized busbar costs as a function of plant capacity for various levels of fuel escalation for the hybrid portion of the plant based upon the economic factors summarized in Table J-1. The plot shows a rather interesting result in that an all solar plant operating at 15% plant capacity factor, Fort Worth insolation level, is economically attractive when compared to a

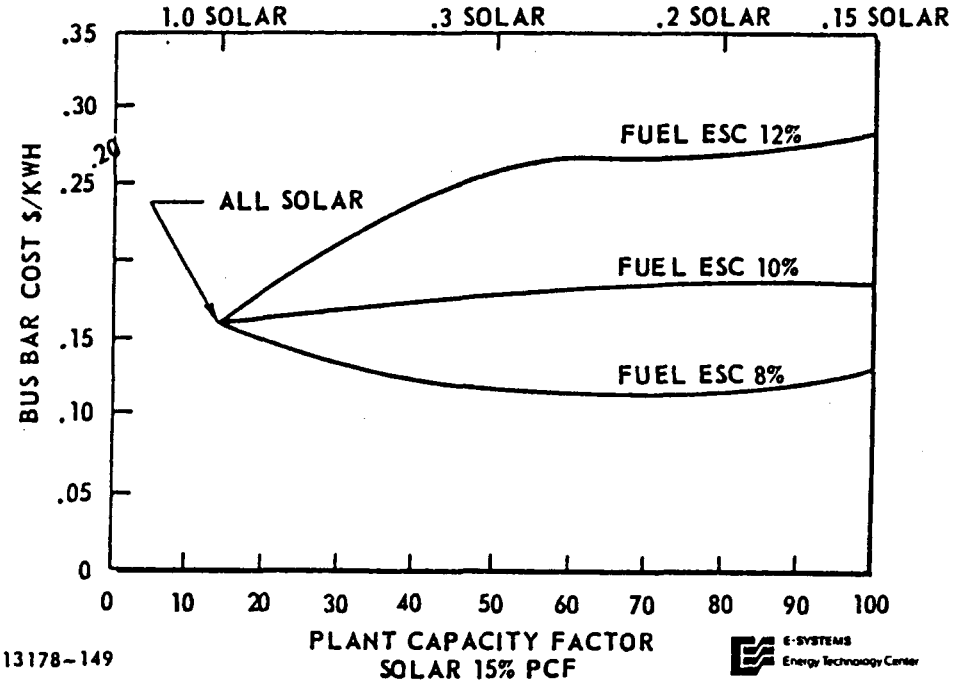

Figure J-1. Levelized Energy Cost vs. PCF (No Storage) Municipal Utility

TABLE J-1

ECONOMIC FACTORS FOR MUNICIPALLY AND PRIVATELY OWNED UTILITIES

	Public Utility	Private Utility
N (Plant Life)	30	30
CRF (Capital Recovery Factor)	.0726	.1025
g (General Inflation Rate)	.05	.05
Base Year for Constant Dollars	1978	1978
Price Year for Cost Information	1978	1978
First Year of Commercial Operation	1985	1985
Capital Formation Source		
Fraction Common Stock	-	.40
Fraction Preferred Stock	-	.10
Fraction Debt	1.00	.50
Interest Rate	.06	.08
Common Stock Rate	-	.12
Preferred Stock Rate	-	.08
Fixed Charge Rate FCR	.0951	.1712
Payments in lieu of tax rate	.02	-
Operating and Maintenance Costs	$ 30/KW	$ 30/KW
Electric Power Plant Capital	$ 991/KW	$ 991/KW

hybrid plant or pure fossil fuel plant operating with fuel escalation rates above 10%, at any plant capacity factor. At 8% escalation a hybrid plant is more attractive than either alternate of pure solar without storage or pure fossil.

Levelized busbar costs were also determined for a privately owned utility under the economic constraints imposed on a privately owned utility. The difference between private as opposed to public utilities in the case of solar energy, is that life cycle costs must be much more heavily oriented toward capital recovery than to operating costs. This is in rather sharp contrast to the case of fossil fueled plants. This is because capital recovery is taxed as a profit and must be larger by the tax fraction than in the case of a public utility while fuel costs are not similarly taxed.

Fig. J-2 shows the same relationship as Fig. J-1 for a private utility. The heavy penalty of higher cost of capital and the tax structure makes pure solar and hybrid operation economically unattractive until fuel escalation rates of substantially higher than 12% are encountered.

Pure Solar Plant With Storage

Although the preceding section shows that fuel escalation rates of 10% make a pure solar plant operating without storage attractive for a municipal utility, it is worth examining situations with storage considered. In many ways, storage can be used as a trade-off with fossil fuel hybrid operation since both extend the plant capacity factor and amortize the initial capital investment over more power production. The trade-off is that the amortized life cycle cost

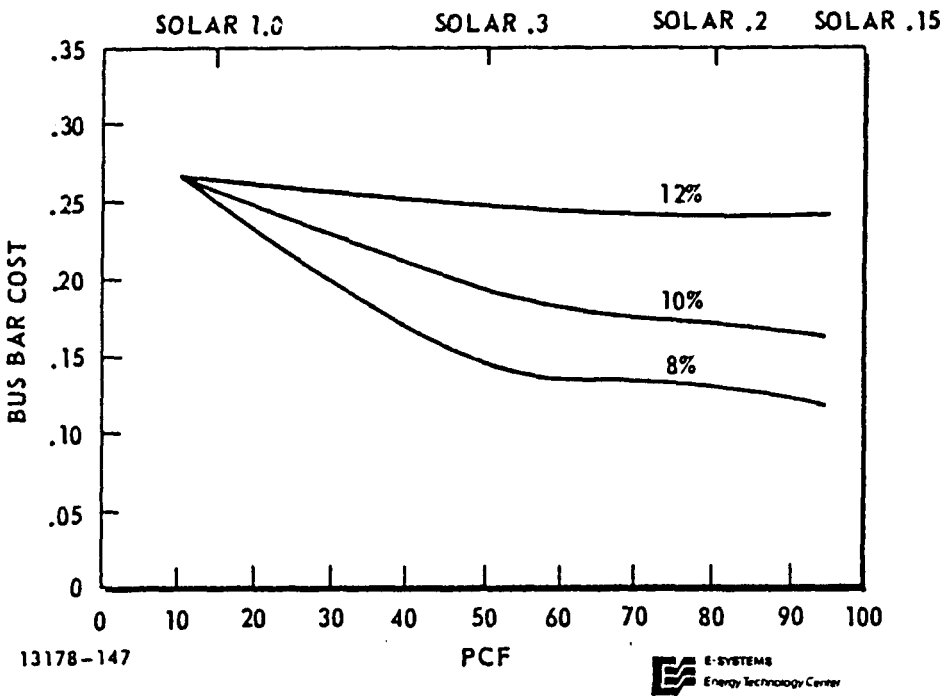

Figure J-2. Levelized Energy Cost vs. PCF
(No Storage) Private Utility

of storage must not exceed the escalated and discounted cost of fossil fuel over the life of the plant.

For this economic analysis a conceptual storage medium having a heat capacity of 0.25 Btu/lb/^{0}F between 700^{0}F and 900^{0}F was chosen. Calculations show that each one million pounds of storage increases the PCF of a solar plant 3 percent above the no storage 15%. For each storage level the solar field was resized to provide the additional energy required to charge storage at 50% efficiency and the capital investment increased proportionately.

Three levels of storage cost were investigated, and busbar energy costs were calculated. The results, plotted in Fig. J-3, show that at $1.50/lb cost of storage, or $.03/Btu, the amortized cost of storage and increased solar field size is exactly equivalent to the amortized cost of the no storage solar plant and no reduction in busbar cost is shown as a function of storage and increased plant capacity factor. This is equivalent to an escalation rate of fuel of approximately 8-9% over the life of the plant. At storage costs below $1.50/lb. reductions in busbar cost result from extending the plant capacity factor with storage.

Having now extended the flexibility of the solar plant with storage, the options of varying levels of hybrid operation at varying solar fractions can be investigated. Fig. J-4 plots solar fraction, obtained by varying the size of the solar field and the amount of storage, versus levelized busbar costs for a base load plant operating at 0.8 plant capacity factor. Storage costs were $1.00/lb or $.02/Btu of storage. For fuel cost escalation rates of greater than 8%, a pure solar plant having 22 x 10^6 lbs of storage and a solar field

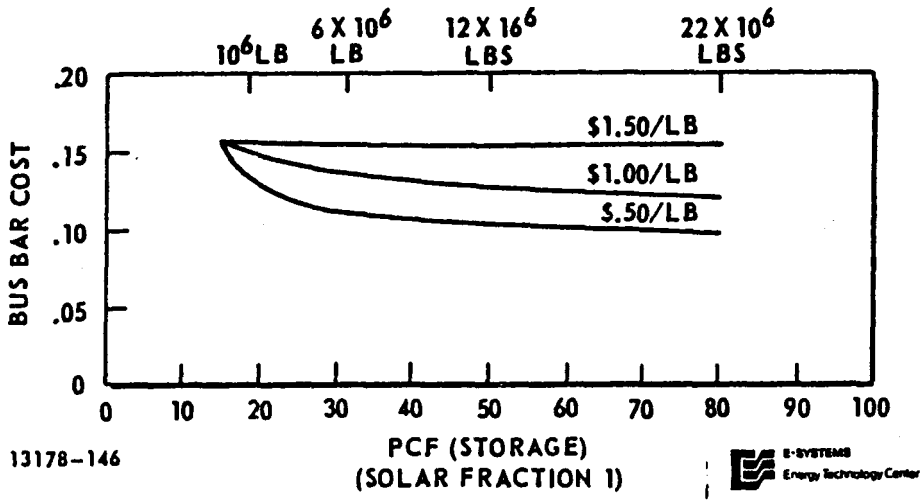

Figure J-3. Levelized Energy Cost $/KW vs. PCF (Storage)

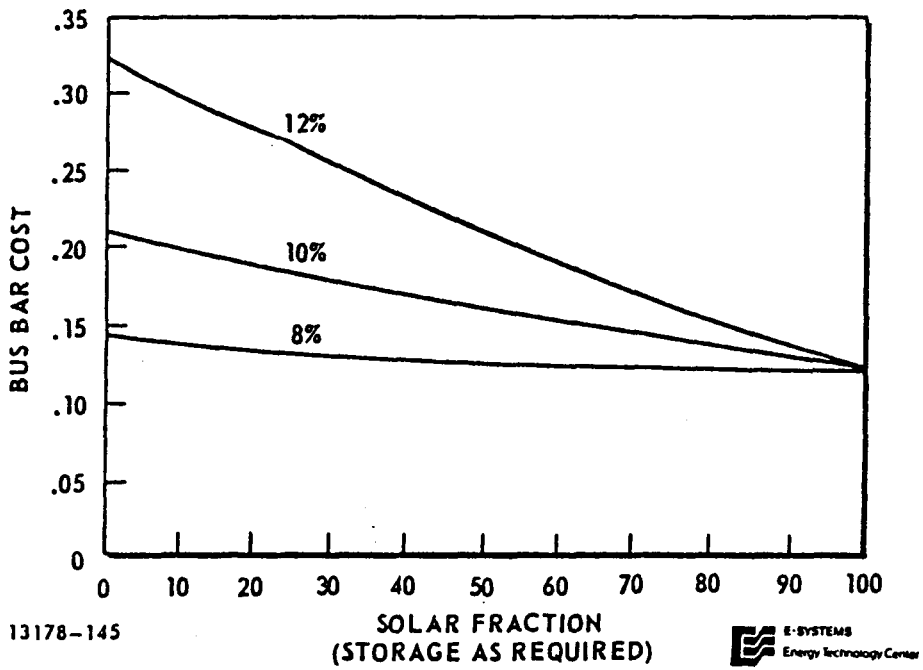

Figure J-4. Levelized Energy Cost $/KW vs Solar Fraction
Municipal Utility, PCF = .8

of 373 ft^2/KW of capacity is economically more attractive than any combination of all fuel or hybrid operation, if operated under the financial structure of a municipally owned plant.

J-1.3 Conclusions

The level of fuel escalation to be experienced over the next 30-50 years is crucial in the economic decisions of utilizing solar energy. At sufficiently high fuel escalation rates any cost of solar energy can be made to look attractive. The converse of this statement is that under conditions of a fuel cost escalation rate at or below the general economic inflation rate, solar energy is economically unattractive for collector costs greater than $\$2/ft^2$. In the particular case of FMDF STEPS, economic attractiveness begins with fuel cost escalation rates of 7%, 2% above the currently assumed general inflation rate and becomes increasingly more attractive as those rates are increased. A seven percent fuel cost escalation is well within the range forecasted for the rest of this century and therefore suggests the FMDF STEPS concept is promising enough to continue its development and construction.

Actual Anticipated Cost of Energy for FMDF STEPS

As stated in the introduction to this section, levelized busbar costs are a highly artificial technique of comparing various economic options. They do not allow determination of the actual costs of energy on a year by year basis. In order to be aware of what actual year by year costs of energy from a public or private utility would be, some other approaches to amortizing the life cycle costs of the

FMDF STEPS will be considered.

Levelized costs assume that the present value of an annuity is amortized in equal payments over the life of the annuity in exactly the same manner that a mortgage on a private dwelling is paid off. Interest payments start as a large fraction of the fixed payment over the life of the annuity and debt amortization starts small and increases. There are many other amortization schedules that could apply to the calculated present value of building and operating a plant for 30 years. One approach is to assume that the busbar energy costs to customers would escalate at the same rate as general inflation.

Fig. J-5 shows this assumption applied to a pure solar plant operating at 0.8 PCF with storage. The levelized cost for this case is $0.124/KWH. Escalating busbar costs with the general inflation, the rate would start at $.08 KWH in 1985 which in 1978 dollars is $.057/KWH and go to $0.35 in 2015 dollars.

Extensions of Investigation

The economic analyses reported here have been performed at an optimistic cost of $10/sq. ft. for the solar collector. Fig. J-6 shows how levelized busbar costs vary with cost of collectors under various operating conditions. Using the line of reasoning presented above, a higher collector cost raises the fossil fuel escalation rate at which solar becomes economically attractive. Although optimistic collector costs have been used in this analysis, the level of insolation chosen was not optimum, but chosen for the site for which the best data were available. The analysis will be extended to sites with greater insolation levels and to systems larger than 5 MWe, where energy

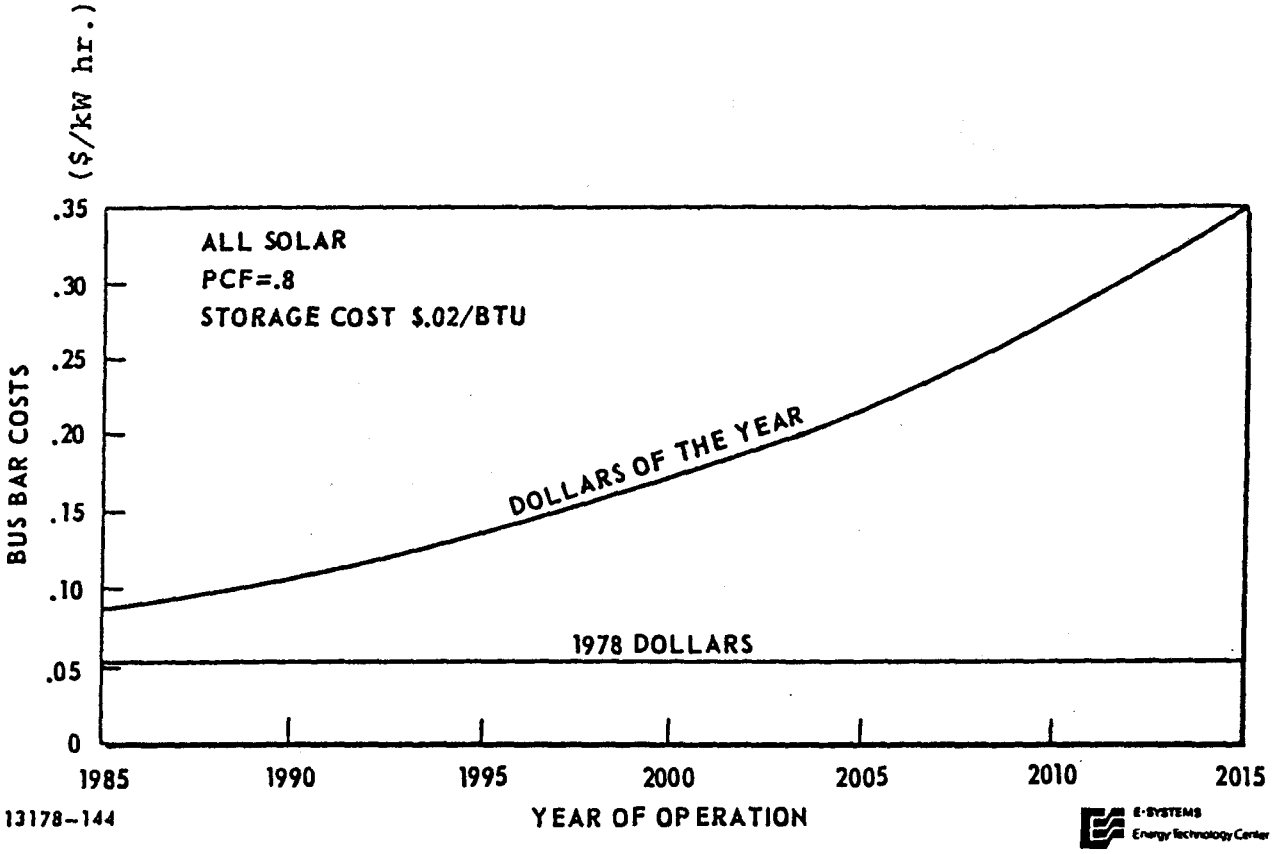

Figure J-5. Energy Cost $/KW hr if Busbar Cost Inflate at 5%/year

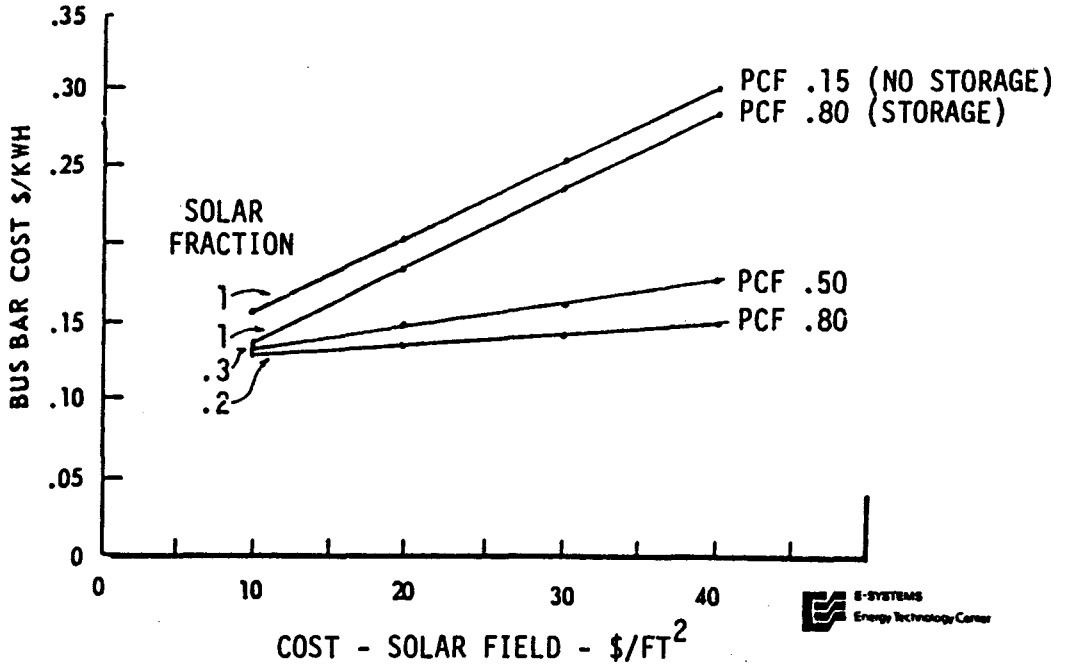

Figure J-6. Levelized Energy Cost vs. Solar Field Cost (Esc.=8%)

conversion efficiencies on the order of 30-35% would be feasible. Both of these factors will offset higher collector costs with higher pure solar plant capacity factors and greater efficiency of solar energy conversion.

J-2 TRANSIENT THERMAL ANALYSIS OF THE FMDF RECEIVER

The objective of the transient thermal analysis of the FMDF receiver is to describe the thermal response of the receiver to variations in insolation level, mass flow rate, external wind speed, etc., and to define the transient operational behavior of the collector system. To accomplish this task it is necessary to develop a generalized mathematical model which can predict the time varying temperature distribution and thermodynamic state of the heat transport fluid along the entire length of the receiver. Results from the analysis will be used to provide design guidelines for the control system during start-up, shut-down, intermittent cloudy periods, and failure modes.

The mathematical model used to predict the time-dependent thermal response of the receiver is sufficiently general such that the combined effects of single phase, two phase and phase transition are treated. Under normal operating conditions three separate flow regimes occur. They are: heating of the liquid from inlet conditions to the boiling point; constant temperature boiling of the liquid to saturated vapor conditions; and superheating the vapor to the final outlet conditions.

Typical results from the transient analysis are shown in Fig. J-7. To initialize the calculation, the receiver is assumed to be operating in a steady-state mode with a fluid outlet temperature of 896^0F and a pressure of 900 psi. The result shown is the transient

Conditions: Fluid: water/steam, P = 900 psi, T_{inlet} = 100°F,
$\dot{m}$ = 190 lbm/hr-tube, $T_{ambient}$ = 70°F, V_{wind} = 10 mph,
h_{ext} = 4 Btu/hr-ft^2 -°F, h_{int} = 1000 Btu/hr - ft^2 - °F,
$\alpha = \varepsilon$ =0.90, ρ = 0.88, $\Delta\psi$ = 1.0°, ϕ_{max} = 60°
γ_o = 0.01563 ft., γ_i = 0.01042 ft., δ = 0.625 ft.

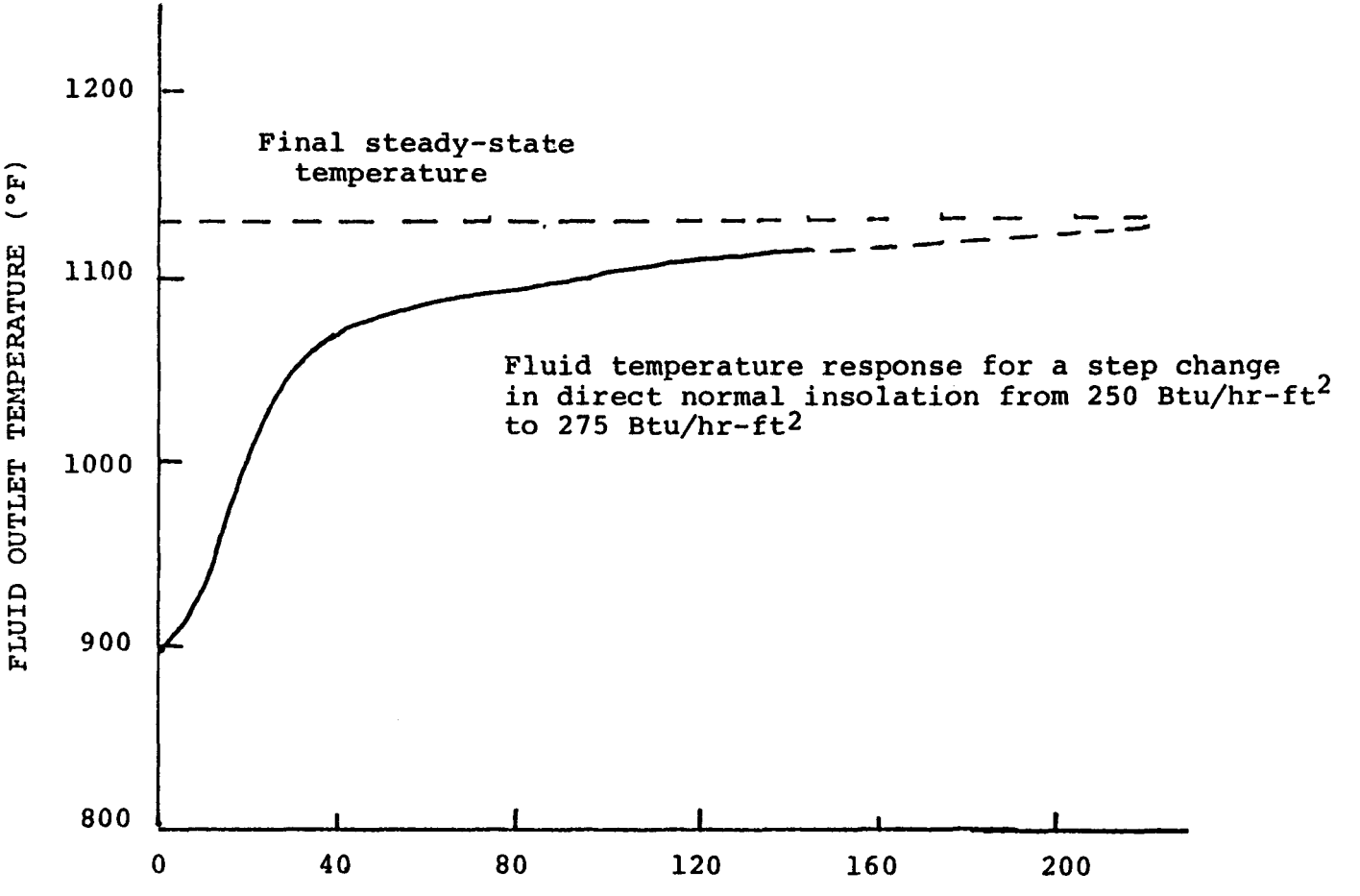

Figure J-7. Transient Effect on Fluid Outlet Temperature for a Step Change in Direct Normal Insolation

fluid response when the direct normal insolation is changed instantaneously from the steady-state value of 250 Btu/hr-ft^2 to 275 Btu/hr-ft^2. As shown in the figure, approximately 80% of the total change in fluid temperature occurs in the initial 60 seconds.

J-3 USE OF HEAT TRANSFER OILS IN FMDF RECEIVERS

In the previous Interim Report we indicated the possibility of using a heat transfer oil such as Caloria HT-43 directly in the receiver of an FMDF system. This was a means of charging a thermocline heat storage system. In this phase our efforts have been divided into three segments:

1. Computations for a nominal FMDF system to find the best trade-off between mass flow rate and peak inside wall temperature.
2. Computational experiments to determine the effects of changing flow path within the receiver.
3. Some static experiments to confirm data on heat transfer oil stabilities when exposed to extremes of temperature (Discussed in Appendix A-1.4).

Computations using the Texas Tech heat transfer simulation program have been done to seek the optimum trade-off between mass flow rate of the heat transfer oil and the peak inside wall temperature. The inside wall temperature at the caustic region has to be kept at or below approximately 600-650^{0}F as a means of minimizing the amount of thermal degradation of the heat transfer oil.

Results of several computations are shown in Fig. J-8. In this figure we see that overall heat losses to the environment tend to decrease in a smooth manner with increasing mass flow rate in the receiver. These decreasing heat losses however, are more than balanced by an increasing pump load as a result of an increasing pressure drop

Figure J-8. Thermal Energy Losses and Pump Work Requirements as a Function of Mass Flow Rate for the RPS Hot Oil Receiver

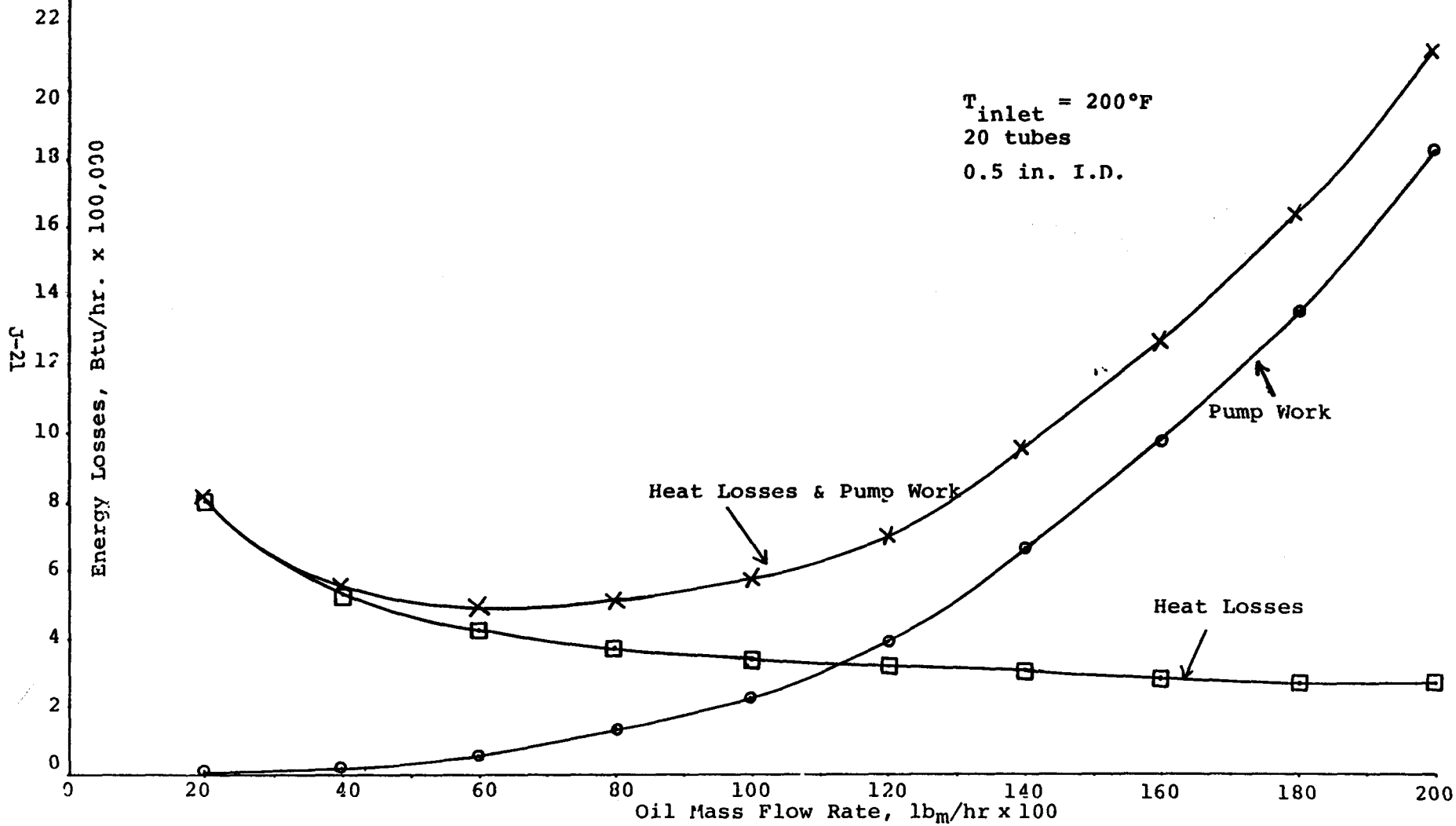

for the higher mass flow rates.

The overall trade-off between heat loss and pump load is better seen in Fig. J-9, where the composite energy losses due to pumping and to heat losses to the environment are shown as a function of receiver mass flow rate. Here we see a definite minimum occurring in the range of 40,000-80,000 lbs. per hr. This suggests that there is an cptimal range in which we can operate our oil receiver. In addition, as we see in Fig. J-10, the inside wall temperature at the caustic region decreases in a smooth fashion with increasing flow rate, as does the overall temperature rise of the fluid through the receiver. It is also important to note that at a mass flow rate of 80,000 lbs. per hr. the caustic inside wall temperature is approximately 600^{0}F. This is certainly within acceptable limits for fluid stability purposes. It is also important to note in Fig. J-10 that for flow rates below approximately 60,000 lbs. per hr. the inside wall temperature in the caustic region is in excess of 650^{0}F, suggesting that any turn-down of fluid flow rate inside the receiver would not be advisable.

It is possible that by rerouting the heat transfer oils in a manner other than flowing from the bottom upward as in the figures cited above that we can avoid the excessive inside wall temperatures and still have a lower total mass flow rate through the FMDF receiver. This would have the positive effect of increasing the overall temperature rise of the fluid as it passes through the receiver and make possible either a once-through, or, at most, a twice-through operation to raise the fluid from an inlet 200^{0}F to an outlet 600^{0}F. However, we find in looking at Table J-2 that a variety of schemes

Figure J-9. Effect of Mass Flow Rate on Total Energy Losses in the RPS Hot Oil Receiver

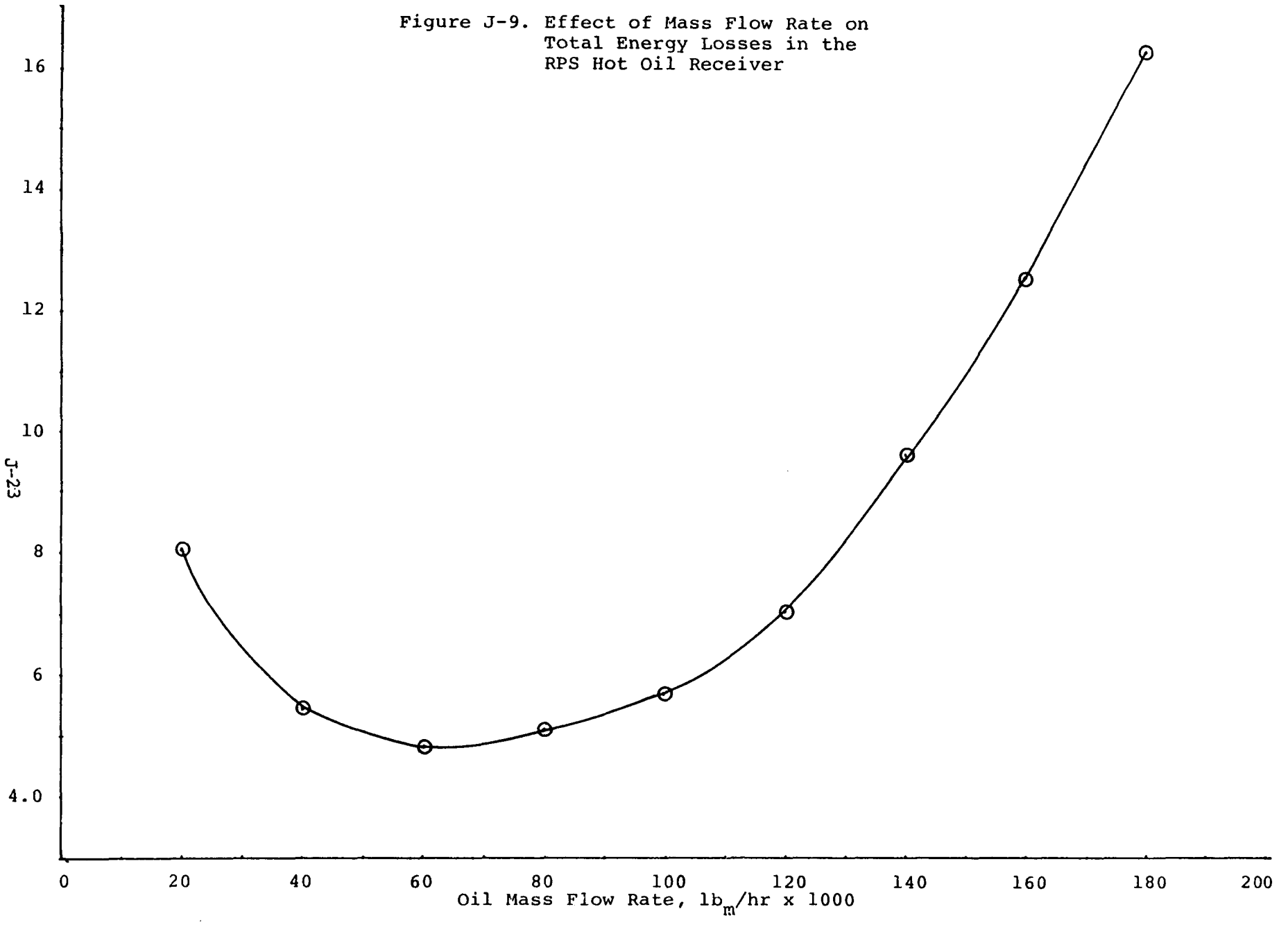

Figure J-10. Dependence of Critical Temperature Variables on Mass Flow Rate For the RPS Hot Oil Receiver

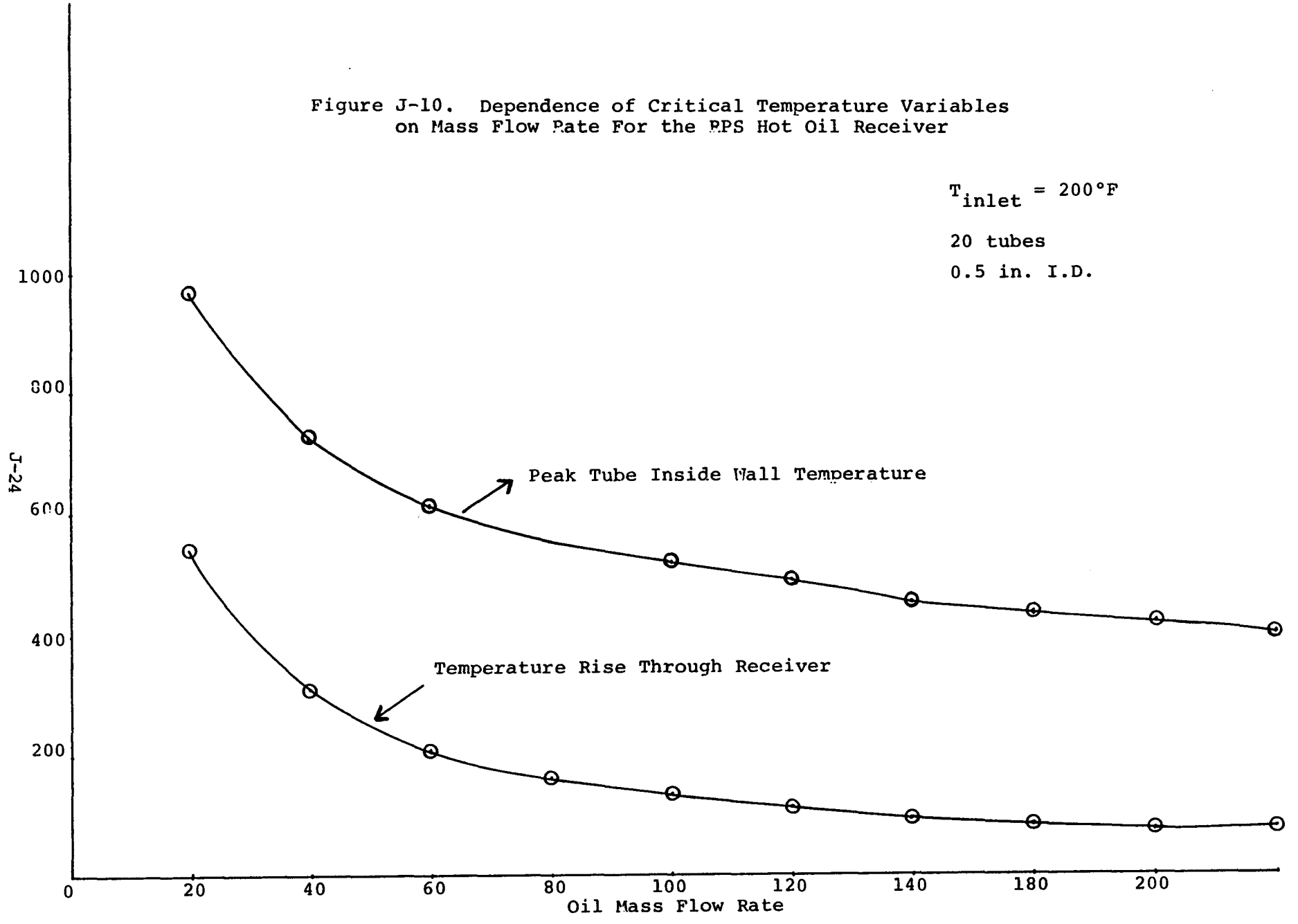

TABLE J-2. EFFECT OF CHANGING FLUID FLOW PATH ON PEAK INSIDE WALL TEMPERATURE, OVERALL HEAT LOSSES, AND FLUID PRESSURE DROP

Receiver flow: 80,000 lb_m/hr Inlet Temperature: 200°F

Flow	$(T_i)_{max}$,°F	Q_{loss} BTU/hr	ΔP,psi	$\Delta T_{overall}$,°F
Bottom-up	604	378,000	244	166
Top-down	634	509,000	215	164
Bottom-up to X/R=.6, then top down	601	378,000	244	166
Bottom-up to X/R=.75, then top down	609	400,000	241	166
Bottom-up to X/R=.67, then top down	602	384,000	243	166

* 200 foot aperture diameter receiver is made of 20, 0.5 in. ID coiled tubes.

for rerouting the fluid flow really makes very minimal effect both in terms of the peak inside wall temperature or in terms of the overall temperature rise as the fluid goes through the receiver. All of the data shown in the table are for a receiver mass flow rate of 80,000 lbs. per hr. with an entry temperature of 200^{0}F.

Perhaps one of the most interesting features of these results is that if we flow from the top down, having the coldest fluid next to the tube wall in the caustic region, we actually have a somewhat higher inside wall temperature than for the other schemes. This is because the cooler fluid has a lower heat transfer coefficient than a warmer fluid. In addition, we see that the overall heat losses for the top down operation are approximately 35% higher than in the case of bottom up flow. The reason for this much higher heat loss is the fact that there is a higher overall average receiver temperature. This is important when we consider the fact that the extremely large area of the lower part of the receiver is going to be at a higher net temperature than for any of the other schemes shown.

It is also interesting as we look at Table J-2 to note that for any of the more complex schemes, such as routing from the bottom up to $\frac{x}{R}$ = 0.6 and then running from the top down, that there is no real improvement in terms of inside wall temperature or in terms of overall heat losses. In fact, this type of an operation would be more difficult because of the extra plumbing and inconvenience required in fabricating the actual receiver to do this work.

The results given in Table J-3 are for an inlet temperature of 200^{0}F and an outlet temperature of approximately 370^{0}F. Since thermal storage needs to be charged to 600^{0}F to gain the most from it,

TABLE J-3. EFFECTS OF FLOW RATE ON PEAK INSIDE WALL TEMPERATURE AND OUTLET TEMPERATURE

Top-down Flow — Inlet Temperature: 400°F

Receiver Mass Flow Rate, lb_m/hr	Peak Inside Wall Temperature °F	Outlet Temperature °F
40,000	777	649
80,000	625	535
120,000	565	492
160,000	532	470

it is obvious that a single pass through a hot oil receiver is insufficient to charge storage. It is interesting that the results in Table J-3 show that if the heated (400^{0}F) oil is flowed from the top down through another receiver of the same dimensions, that for a flow rate of approximately 80,000 lb_m/hr there results a final fluid temperature of 535^{0}F with a peak inside wall temperature of 625^{0}F. These results indicate that a hot oil system made up of pairs of collector dishes similar to that shown in Fig. J-11 could provide a reasonable way to include a storage made in an RPS. Flow from the bottom-up, while minimizing heat losses, will result in excessive inside tube wall temperatures.

J-4 OPERATION OF A ONCE-THROUGH FMDF RECEIVER DURING PERIODS OF REDUCED INSOLATION

A vital question in system management for the RPS is to determine the point at which the system can no longer provide steam at design temperature and pressure conditions and reverts to some other operational mode.

Some candidate backup modes include:

1) Provide hot water for boiler preheat

2) Operate so as to maintain an acceptable tube temperature in the caustic region and accept produced steam at less than design conditions

3) Shut down

Before choosing a backup operational mode, it is useful to answer the leading question: If we match flow rate with insolation, how far can be back off before

a) we can no longer maintain 100% steam in the outlet?

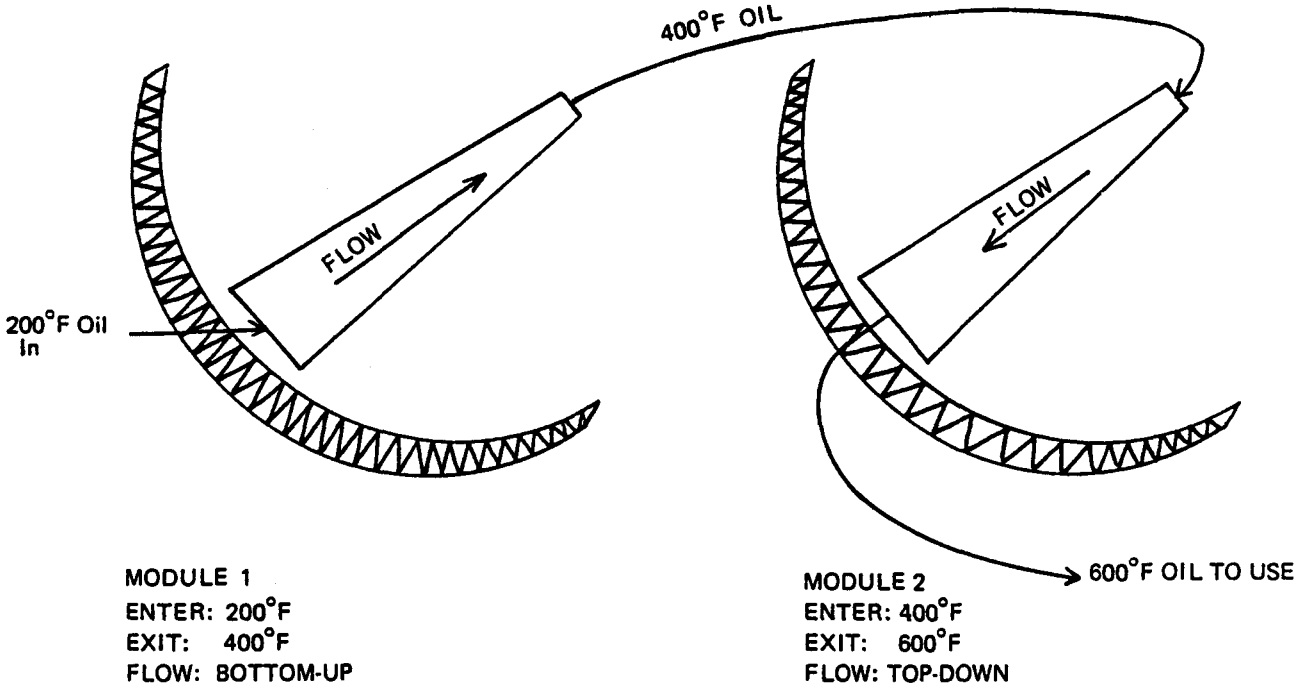

*IN RPS FLOW RATE IS ABOUT 80,000 lb_m/hr FOR A PAIR-WISE MODULE

Figure J-11. PAIR-WISE SCHEME FOR OPERATING FMDF RECEIVERS WITH HOT OILS AND STORAGE

b) we can no longer ensure heat transfer integrity at the caustic region?

In an attempt to address this set of questions a scenario using the RPS was posed. According to the TTU receiver thermal simulator computer program, the RPS can produce 6000 lb_m/hr of steam at 750 psi, 850 F at full solar insolation (300 Btu/ft^2hr, reflectivity = 0.88, absorptivity = 1.0). Then as shown in Table J-4 the mass flow rate and the percent of total solar insolation were reduced proportionately.

It is evident from the table that heat transfer integrity as measured by peak tube inside wall temperature is never really a problem. However, at an insolation level of approximately forty percent of peak, the temperature of available steam falls dramatically. By the time the insolation falls to twenty percent of peak it is impossible to maintain saturated steam effluent from the receiver without even more sharply reducing mass flow rate.

Table J-4 suggests that somewhere around thirty to forty percent of peak insolation it may be advisable to produce hot water, instead of stem. It must be emphasized that these calculations are for axisymmetric (solar noon) heat input. In the case of non-axisymmetric heat input, the situation becomes much more complicated. While further analytical study of this problem certainly is warranted, the real "optimal" policy can best be determined using the ATS.

TABLE J-4. EFFECT OF REDUCED INSOLATION AND WATER MASS FLOW RATE ON OUTLET STEAM TEMPERATURE AND QUALITY FOR THE RPS

(Assume insolation max. = 300 Btu/ft^{2}hr, reflectivity = 0.88, and absorptivity = 1.0)

Water Mess Flow Rate, lb_m/hr	Percent of Peak Insolation	Peak Inside Wall Temp., F	Steam Outlet Temp., F	Steam Quality
6,000	100%	815	850	1.0
4,800	80	744	765	1.0
3,600	60	728	760	1.0
2,400	40	670	605	1.0
1,200	20	654	510	0.8

APPENDIX K. INSTRUMENTATION AND DATA PROCESSING FOR THE ANALOG TEST SYSTEM

The fundamental purpose of the ATS is to serve as a device to produce, under appropriately realistic conditions, data relevant to the performance, cost survivability, and maintenance of the RPS. The instrumentation for gathering those data is described in the first subsection. The data acquisition system is considered next. Then the relationship of the data to various RPS subsystems is indicated and, finally, the nature of the knowledge to be gained is surveyed by R and D area.

K-1 INSTRUMENTATION CATEGORIES

The ATS instrumentation is divided into eleven categories (counting the general "dress rehearsal" information):

A.	Site Data	soil, insolation (total and direct normal), wind direction and speed, clouds, rain, dust, snow, and hail conditions, ambient temperature, humidity, barometric pressure
B.	Photometry	optical concentrations (receiver, mirrors, support structures), reflectivities, absorptivities
C.	Thermometry	receiver skin, mirrors and panels, support structures, fluid transfer loop, test load (expander/condenser), storage
D.	Odometry	strains, displacements of receiver, mirror surface, support structures
E.	Accelerometry	dynamic motions of receiver, receiver support, concentrator support
F.	Barometry	fluid pressures at receiver inlet, receiver outlet, stations in the transfer loop

G.	Flow Metering	flow rates in the fluid loops
H.	Wind Convection Measurement	nature of air flows at various points in the vicinity of receiver and support structures
I.	Receiver Positioning	receiver location/alignment and rate of movement
J.	Electrical Metering	pump and drive motor power, sensor signals, control signals, sensor and controller behavior
K.	Dress Rehearsal Experience	general information about system construction, performance, and operation

The nature of the hardware is described below by category:

Instrumentation Hardware Requirements by Category

A.	Site Data	Soil structure previously analyzed from extensive core samples obtained during first six months of Segment I. Additional information will be obtained from ATS excavation and construction. Pyrheliometer and pyranometer for direct and total insolation measurement (already deployed and in use at Crosbyton) Weather station type hardware for measurement of: wind, barometric pressure, relative humidity, dust, and ambient temperature (already deployed and in use at Crosbyton). Rain, snow, hail, and cloud data will not be gathered electronically
B.	Photometry	Radiant flux sensors for measurement of optical concentrations Reflectometer for periodic measurement of receiver and mirror surface reflectivities

C.	Thermometry	Thermocouples deployed on: receiver (at least 50 stations), selected mirror panels (at least 20 stations), frame, boom, tripod structure, and at various stations in the fluid loops
D.	Odometry	Weldable and/or general purpose strain gauges attached to support boom, tripod structure, main frame, and selected mirror panels (approximately 50 locations)
E.	Accelerometry	Accelerometers for measurement of motions of boom support, receiver, tripod structure and main frame (approximately 10 locations)
F.	Barometry	Pressure gauges (approximately 10) and pressure transducers (approximately 8) for fluid pressure measurement at receiver inlet and outlet, across flexible couplings, and at other locations in the heat transfer loop
G.	Flow Metering	Turbine meters (3) and rotameters (3) for measurement of fluid flow rate in process and condenser water loops
H.	Wind Convection Measurement	Probe-type anemometer for measurement of air flow patterns inside and around dish
I.	Receiver Positioning	Data on receiver position and rate of motion will be available from the tracking control sensors. In addition, an optical television camera and a grid network on the mirror surface will be used to monitor movement in the boom and receiver. Results will be recorded on video tape
J.	Electrical Metering	Wattmeters for measurement of power required for all motor-driven equipment Sensor and control signals will also be recorded by data acquisition subsystem

Indication of some of the sensor locations is given in Fig. K-1.

Specific instruments have been designated to acquire the required data. A survey of available instrumentation will be continued to obtain the sensors best suited for our application. The complete system will be capable of expansion as needed to fulfill the requirements of the test program.

K-2 DATA ACQUISITION SYSTEM

The data acquisition subsystem and the system control and management subsystems will be housed in an instrumentation trailer providing the necessary air conditioning, lighting, and environmental protection for equipment and personnel. Another trailer will be used for storage of equipment and supplies.

The system control and management subsystem will monitor the overall system performance in real time. It will include the displays and instrument readouts required to give the observer/operator all necessary information on system operation. Instantaneous solar insolation, fluid state and flow rates, temperatures, and other data will be monitored.

The data acquisition system, on the other hand, is concerned with data for subsequent analysis off-site; e.g., at the Texas Tech University Computer Center or at E-System, Inc. Energy Technology Center. The system will be programmed to scan the various sensors at various rates appropriate to the nature of the data requirements. The system will digitize and convert the raw data to more applicable formats and record the data as required for off-site analysis. This system will provide a permanent record of the pertinent parameters

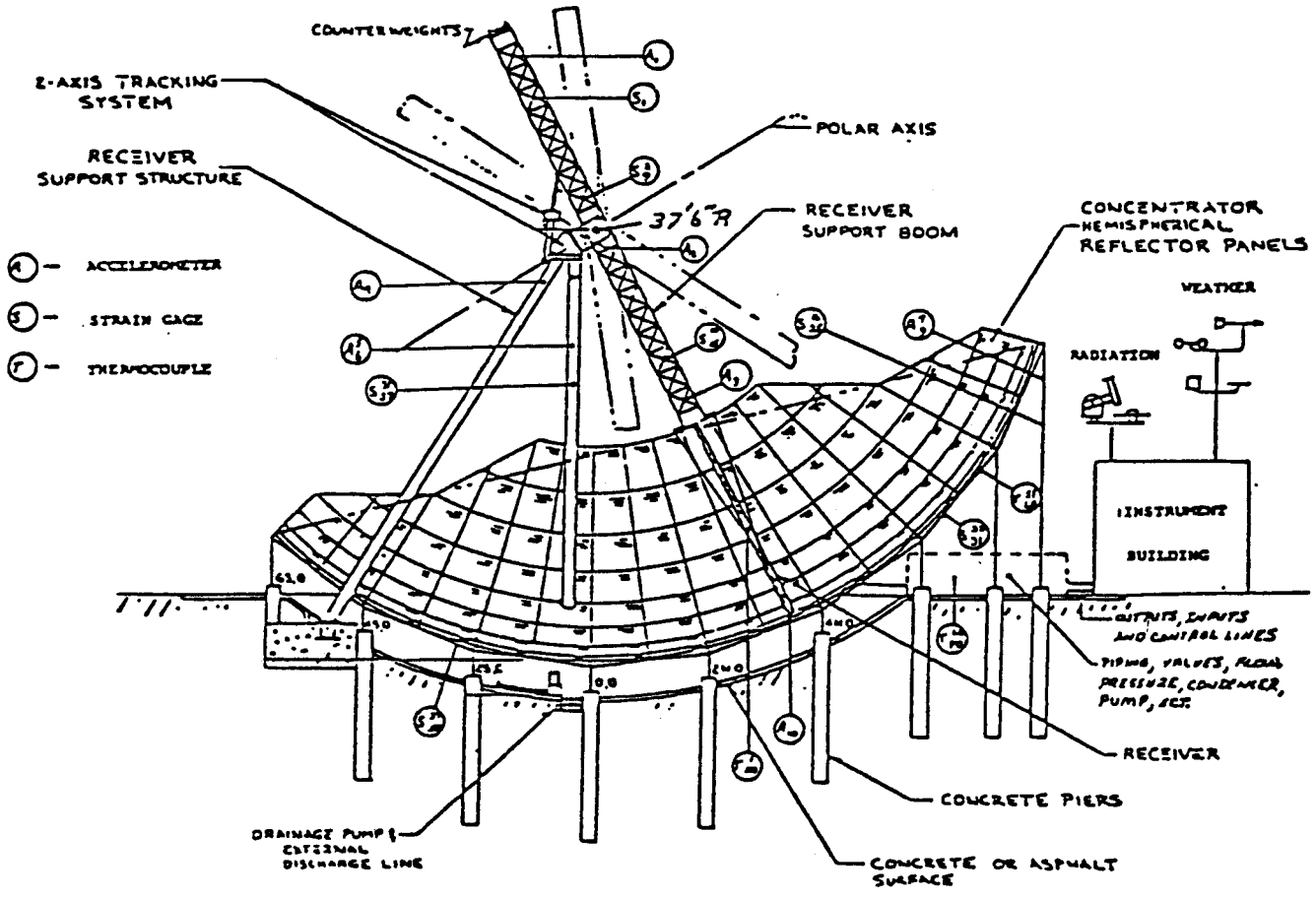

Fig. K-1. 65 Ft. Aperture Diameter FMDF Instrumentation

during each test phase, independent of the system controller. This allows an independent analysis of problems associated with any and all aspects of the ATS operation.

The components of the data acquisition system will include signal conditioning interfaces with the sensors, scanners to time multiplex the sensor data for the digital conversion equipment, a magnetic tape system to record the data, a graphical display for monitoring of data during test setup and operation, and a programmable controller to manage the overall operation of the data acquisition subsystem.

K-3 RELATIONSHIP OF THE DATA TO THE R AND D PROGRAM

As documented above, a great amount of data of many types will be obtained from the ATS. These data are required so that the performance, cost, survivability, and maintenance can be estimated for the RPS. The R and D Program for the ATS can be conveniently divided into twenty-one R and D Areas. The following chart surveys the applicability of the eleven instrumentation categories described above to the twenty-one R and D Areas to be considered in the next subsection. The code number 1, 2, 3 used in the chart indicate the importance of the data to the R and D Area requiring that information.

RELATIONSHIP BETWEEN INSTRUMENTATION CATEGORIES & R and D AREAS

1: 1st order requirement
2: 2nd order requirement
3: 3rd order requirement

	1. Site Characteristics	2. Civil Works	3. Concentrator Support and Configuration	4. Reflector Surface & Panels	5. Optical Concentrations	6. Receiver Support	7. Tracking & Tracking Mount	8. Receiver Configuration and Materials	9. Receiver Thermal-Fluid Behavior	10. Heat Transfer Loop	11. Storage	12. Auxiliary Energy Source	13. Turbine - Generator	14. Load, Demand	15. Process Control	16. System Management Policies	17. Safety, Survivability, Maintenance	18. Instrumentation and Data Acquisition	19. System Costs	20. Construction Sequencing, Preassembly	21. Economic Strategy, Impact
A. Site Data																					
soil	1	1	1								2						2		1	1	1
insolation (total and direct normal)	1		2		1		2	2	1		1	1	2	1	1	1	2		2		1
wind direction and speed	1	1	1	1	2	1	1	2	1	2	3	3		2	2	2	1		2	3	2
clouds, rain, dust, snow, hail	1			1	1				1			1			1	1	1	2			
ambient temperature, humidity, pressure	1		1					1	1	1		2		1		2	2				
B. Photometry																					
optical concentrations (receiver, mirror, support structures)			1	1	1		2	1	1		1				1	1	1		1		
reflectivities and absorptivities				1	1			1	1		3	3			1	1	1		1		
C. Thermometry																					
receiver skin					1		3	1	1						1	1	1		1		
mirrors and panels			2	1	1											1			2		2
support structures		2	1	1	1	1	3		3							3	1				
fluid transfer loop					2				1	1	1	1	1		1	1	2				
test load (expander/ condenser)									1	1	1	1	1	1	1	1					1
storage									1	1	1	1	1	1	1	1	1		1		1
D. Odometry																					
receiver								1	2							1	1		1		
mirror surface		1	1	1	1				2							2	1		1		
support structures						1	2	2	3							2	1		1		
E. Accelerometry																					
receiver					2	1	1	1	2						2	1	1		1		
receiver support		1			3	1	1	2	2							2	1		1		
concentrator support		1	1	1	1				1						2	1	1		1		
F. Barometry																					
receiver input/output								1	1	1	1	1	1	2	1	1	3				2
transfer loop stations									1	1	1	1	1	2	1	1	2				
G. Flow Metering																					
fluid loops									1	1	1	1	1	1	1	1					
H. Anemometry																					
wind flow patterns	1	1	1	1			1		1						2	2	1		2		
I. Receiver Positioning																					
location/alignment					1	1	1	2	1						1	1	2				
rate of movement						1	1	2	2						2	1	1				
J. Electrical Metering																					
pump and drive motor power							1		1	1	1	1	1	2	1	1	1		1		
sensor signals					1		1		1	1	1	1	1	1	1	1		1			
control signals					1		1		1	1	1	1	1	1	1	1					
sensor/controller behavior							2		2	2	2	3			1	1	1	1			2
K. Dress Rehearsal Experience	2	1	1	1	1	1	1	1	1	1	1	3		3	1	1	2	1	1	1	3

K-4 R AND D AREAS REQUIRING ATS DATA

As introduced in the chart above, the data from the ATS is required for twenty-one R and D Areas. Some of the issues to be studied in these twenty-one areas are surveyed in this subsection. In the table below, the left column lists the R and D Areas and some of the issued pertinent to each area. The use of the ATS data is presented in the middle column which indicates some of the topics to be studied. The third column points out the relevance of the 65 ft. ATS study to the 200 ft. RPS. It is this utility that justifies the ATS.

R AND D AREAS	STUDY WITH 65 FT. DISH (ATS)	RELATION TO 200 FT. DISH (RPS)
Site Characteristics		
Insolation, wind, temperature, humidity, pressure, cloud cover, rain, dust, snow, hail, soil	Baseline of data continued	Completely appropriate baseline
Civil Works		
Excavation technique	(Not necessarily the same as for RPS)	Techniques well known
Berm on north for support	Soil stabilization requirements; relationship of berm to cost and concentrator stability	Some stabilization techniques to obtain required stability; cost model
Windbreak on southwest	Effects of size and shape on wind flow patterns	Can be extrapolated.
Concentrator Support and Configuration		
Static and dynamic stresses and strains	Effects of static and dynamic loads	Confirmation of computer codes at ATS scale to increase reliability of their RPS predictions
Environmental effects	Effects of thermal gradients and transients; diurnal cycling	Direct application of results
Materials	Adequacy of the selected materials	Direct application of results
Reflector Surface and Panels		
Attachment	Adequacy of attachment method to achieve desired accuracy in presence of static and dynamic structural strains	Direct application of observations

R AND D AREAS	STUDY WITH 65 FT. DISH (ATS)	RELATION TO 200 FT. DISH (RPS)
Reflector Surface and Panels (Contd.)		
Stability of alignment	Reliability of optical concentration in presence of static and dynamic loads	Direct application of results
Reflectivity	Average reflectivity of segments; changes in reflectivity due to environmental effects and cleaning	Direct application of results
Performance degradation	Effects of hail, moisture, temperature	Direct application of results
Lifetime	Various aging mechanisms for panels, bonding agents, and reflector surface	Direct application of results
Production characteristics	Variation of properties from segment to segment	Direct application of observations
Optical Concentrations		
Mirror imperfections	Effects of actual surface deviations on concentration patterns	Direct extrapolation of results
Alignment errors	Effects on concentration pattern; evaluate effective sun size model	Direct application of results
Cloud cover and dust	Effects of unsymmetrical reflection	Direct application of results
Transients	Effects of wind and other dynamic loads and various system responses	Direct extrapolation of results
Tracking errors	Implications for energy capture	Direct application of results
Receiver deformations	Thermal and mechanical distortions	Direct extrapolation of results
Signals to tracking control	Various methods for determining misalignment of receiver	Direct application of results

R AND D AREAS	STUDY WITH 65 FT DISH (ATS)	RELATION TO 200 FT. DISH (RPS)
Receiver Support		
Static and dynamic stresses and strains	Effects of static and dynamic loads	Confirmation of computer codes at ATS scale to insure reliability of their RPS predictions
Environmental and concentrator effects	Effects of thermal gradients and transients; diurnal cycling	Direct application of results
Materials	Adequacy of the selected materials	Direct application of results
Tracking and Tracking Mount		
Static and dynamic loads	Ability of the tracking system to detect receiver misalignments and respond effectively; survivability of components	Direct extrapolation of results
Optical concentration variations	Response of tracking systems to clouds and other perturbations on the nominal optical distributions	Direct application of results
Receiver support	Sensitivity of tracking control to receiver support strains	Direct extrapolation of results
Drive motors	Power and torque requirements	Direct extrapolation of results
Tracking control	Applicability and reliability of the control system	Direct application of results
Receiver Configuration and Materials		
Receiver flow channels	Effects of the thermal and mechanical loads on the local stresses and strains; relationship of attachment methods to channel deformations; various failure events that may occur; observations of channel dynamical motions	Direct extrapolation of results and direct application of observations

R AND D AREAS	STUDY WITH 65 FT. DISH (ATS)	RELATION TO 200 FT. DISH (RPS)
Receiver Configuration (Contd.)		
Receiver conical substrate	Observations of possible deformations and dynamical motions	Direct application of observations
Articulation	Behavior of flexible couplings	Direct application of results
Coil and substrate material	Behavior in presence of high temperatures and thermal cycling when subjected to the actual static and dynamic loads	Direct application and extrapolation of results
Absorber surface coating	Properties and behavior of Pyromark paint and other possible coatings	Direct application of results
Receiver Thermal-Fluid Behavior		
Steady heat transfer and fluid mechanics	Effects of two-phase internal heat transfer coefficients and friction factors by direct measurement of local channel wall temperature and inlet and outlet fluid temperature	Direct application of results Note: The ATS is modeled to give the same L/D, D and cone angle as the RPS. The number of tubes and total mass flow of the ATS is adjusted to give the same channel mass flow as the RPS. Under these conditions, the channel Reynolds number, average velocity, average heat transfer coefficient and total pressure drop will be the same for both designs. The radial accelerations are unavoidably different but the effect is considered secondary.
Heat transfer and fluid mechanics during transient insolation conditions	Effects of interactions between process control strategies and receiver integrity	Direct application of results
Channel flow instabilities	Effects and nature of instabilities in flow channels caused or aggravated by * two-phase flow * manifolding * process control strategy * time varying heat addition	Extrapolation of results Note: Due to the complex nature of two-phase flow instabilities, the relation between the ATS and RPS is not totally predictable at this time. However, if instabilities

R AND D AREAS	STUDY WITH 65 FT. DISH (ATS)	RELATION TO 200 FT. DISH (RPS)
Receiver Configuration (Contd.)		
Channel flow instabilities (contd.)		are found to occur in the ATS. techniques that are developed to alleviate the undesirable effects can be applied to the RPS design. Considerable information is to be gained from currently running experimental studies on the ATS channel configuration.
Degradation of interior heat transfer surface	Effects of scale and coking deposits on heat transfer and pressure drop; effects of corrosion and erosion	Direct application of results
Water chemistry	Effects of water treatment on rate of scale buildup in receiver	Direct application of results
Oil degradation	Effects of prolonged exposure to elevated temperatures on degradation of oil	Direct application of results
Heat Transfer Loop		
Flexible couplings	Effects of repeated thermal and mechanical cycling on survivability	Direct application of results
Conventional hardware	Effectiveness of standard components (valves, pumps, heat exchangers, insulation, etc.)	Direct application of results
Storage		
Thermocline	Effects of inlet design and flow rate on ability to maintain adequate thermocline	Direct extrapolation of results

R AND D AREAS	STUDY WITH 65 FT. DISH (ATS)	RELATION TO 200 FT. DISH (RPS)
Storage (Contd.)		
Storage/system interface	Integration of available storage strategies with system management policies	Direct extrapolation of results
Auxiliary Energy Source	Requirements for auxiliary fuel and energy sources (No auxiliary energy source included in ATS)	Direct extrapolation of results Note: Studies conducted under other R & D areas, e.g. 9, 14, and 16, provide results leading to design specs for the RPS auxiliary energy source.
Turbine-Generator	Requirements for turbine-generator, particularly off-design performance requirements (Load simulated in ATS by use of expander/condenser and by removal of heat from storage)	Direct extrapolation of results
Load, Demand	Compatibility of various load characteristics with system output	Direct extrapolation of results
Process Control	Adequacy of process control hardware and software to maintain desired receiver fluid temperature, pressure, and flow rate under various operating conditions including start-up, normal insolation, intermittent insolation, normal system shut-down, and emergency shut-down	Direct extrapolation of results
System Management Policies	Ability of management system to manage tracking orientation and process control effectively, optimizing energy capture while providing personnel safety and protection of equipment from catastrophic failure	Direct application of results

R AND D AREAS	STUDY WITH 65 FT. DISH (ATS)	RELATION TO 200 FT. DISH (RPS)
Safety, Survivability, Maintenance		
Safety	Nature of potential thermal, mechanical, and optical hazards; operational procedures to alleviate hazards	Direct application of results
Survivability	Effects of hail, wind, rain, and temperature on concentrator panels	Direct application of results
	Integrity of receiver coating; effects of internal corrosion of receiver; structural integrity of receiver after mechanical and thermal cycling	Direct application of results
Maintenance	Techniques of mirror cleaning and required time intervals; possible receiver coating and general receiver maintenance; requirements for maintaining soil stabilization; general system maintenance	Direct application of results
Instrumentation and Data Acquisition		
Instrumentation	Adequacy of optical sensors to provide desired tracking control accuracy	Direct application of results
	Adequacy of flow meters and pressure and temperature sensors to provide desired process control	Direct application of results

R AND D AREAS	STUDY WITH 65 FT. DISH (ATS)	RELATION TO 200 FT. DISH (RPS)
Instrumentation and Data Acquisition (Contd.)		
Instrumentation (contd.)	Adequacy of accelerometers and strain gauges to provide required information on receiver and concentrator support structure motions	Direct application of results
	Adequacy of instrumentation in heat transfer loop, storage tank, expander/condenser, and associated heat exchangers to provide required information for various system management policies	Direct application of results
Data acquisition	Adequacy of data acquisition system, procedures, and data handling techniques	Direct application of results
System Costs	Comparision between actual and predicted ATS costs	Direct extrapolation of results
Construction Sequencing, Preassembly	Feasibility of proposed RPS construction sequencing and preassembly concepts	Direct application of results
Economic Strategy, Impact	Total integration of system performance, possible system management policies, and present and future load characteristics to obtain maximum economic benefit	Direct application and extrapolation of results

APPENDIX L. FMDF CONCENTRATOR/RECEIVER WIND TUNNEL TEST RESULTS

L-1 INTRODUCTION

L-1.1 Purpose

The purpose of this appendix is to discuss the analysis of wind tunnel test data obtained during the testing of a 1/75 scale model of a 200 ft. diameter solar concentrator. These tests were conducted in the Vought Corporation Low Speed Wind Tunnel, at Grant Prairie, Texas, and were part of an overall program to obtain detailed thermal and structural design information concerning wind effects on the Fixed Mirror Distributed Focus (FMDF) Solar Collector. The tests were conducted according to the plan provided in Ref. L-1, while additional test details were described in Ref. L-2.

L-1.2 Scope

Wind Load Tests

The load tests measured the concentrator surface pressures and wind forces for different wind velocities, wind direction, tilt angles of the concentrator, depth of embedment of the concentrator below the ground surface, the effect of a berm on the north side of the concentrator, the boundary layer velocity profiles, and the surface airflow patterns. Only a single concentrator model without a receiver structure was used in the test. Figure L-1 is a photograph of the concentrator model in the wind tunnel with (a) and without (b)

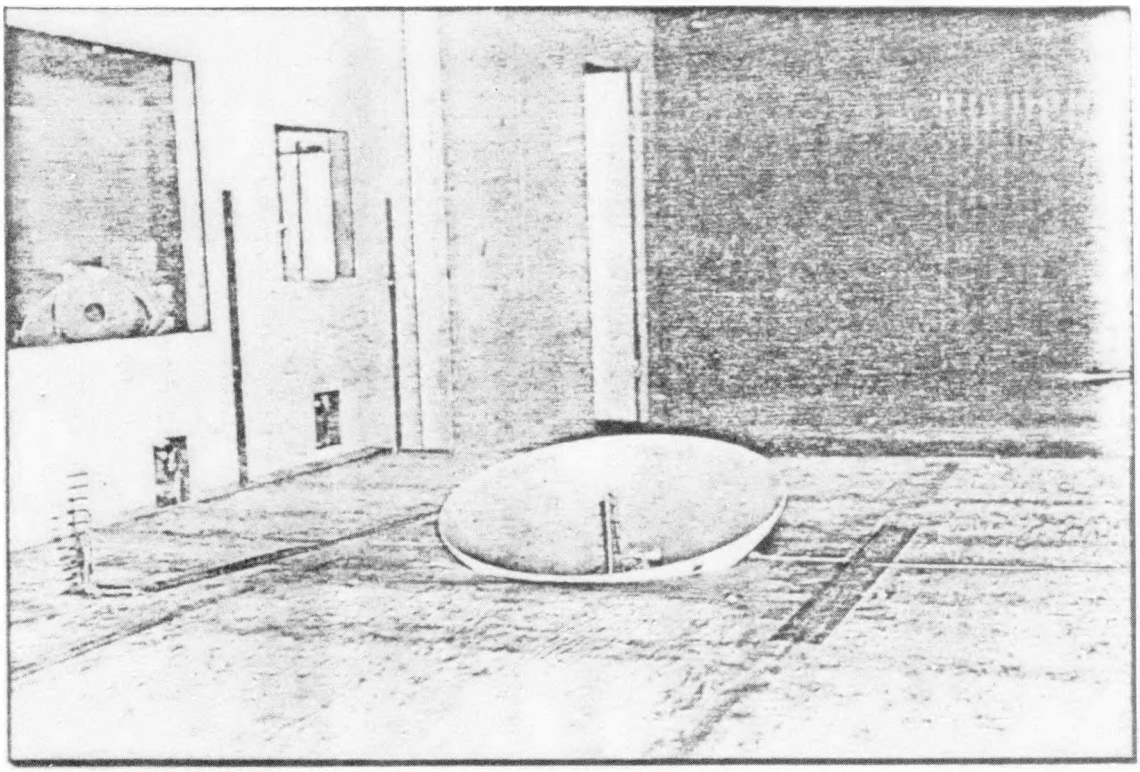

(a)

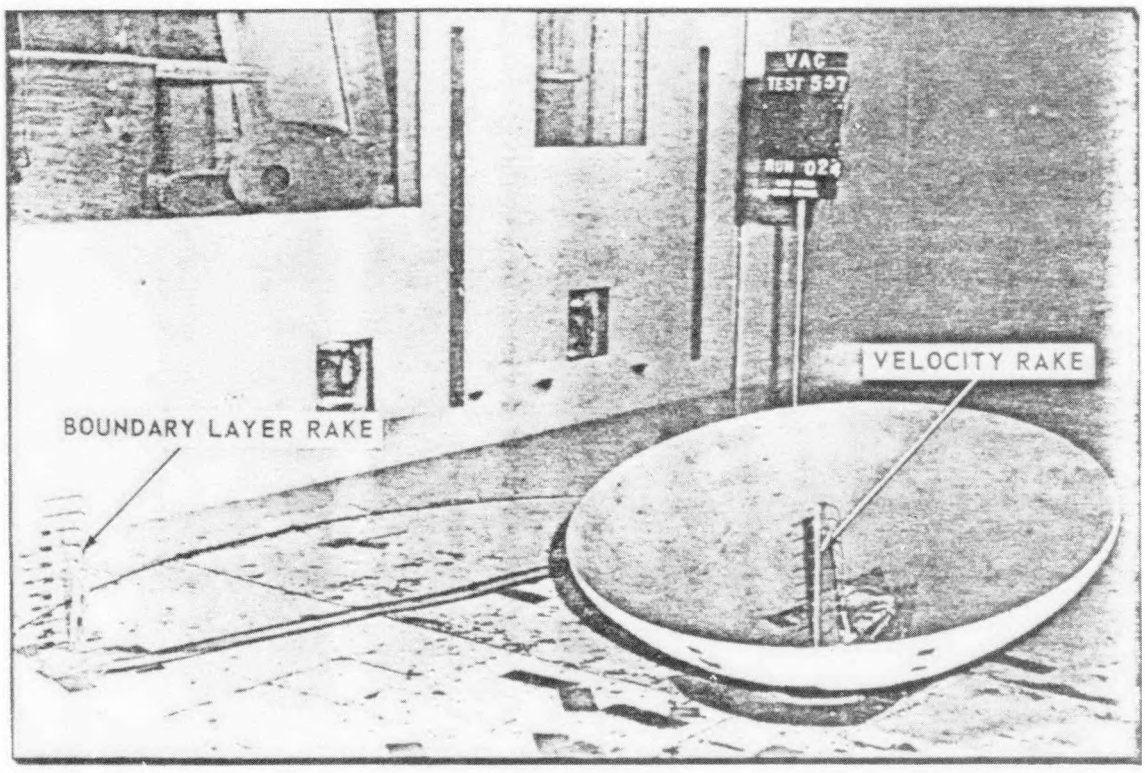

(b)

E-SYSTEMS
Energy Technology Center

Figure L-1 (a) Top - Model with Ground Plane
(b) Bottom - Model without Ground Plane

the ground plane and tilted at 15 degrees. Figure L-2 is a photograph viewing the model from the north (a) and south (b) with the ground plane and berm in place. The ground plane was used to simulate the partial embedment of the concentrator below the ground surface.

Receiver Thermal Loss Test

The first tests preformed were for air flow normal to the receiver model for comparison to literature values. The thermal loss tests were then conducted on the model receiver positioned in the model concentrator and data obtained for different wind directions and velocities with nearly constant receiver surface temperature. Details of the thermal tests will be presented in a section following the discussion and results of the load tests.

L-1.3 Data Reduction

A computer program was written to read and analyze the wind load data directly from the computer data tapes generated during the wind tunnel tests. It used the surface pressure coefficients to calculate drag, lift and side force coefficients and the pitch, roll and yaw moment coefficients and compare them with the measured values.

L-1.4 Accuracy and Applicability of Data

After reviewing the raw wind tunnel data and the results of the analyses it was concluded that the measured surface pressure coefficient data could indeed be used to develop the wind loads applied to the concentrator structure.

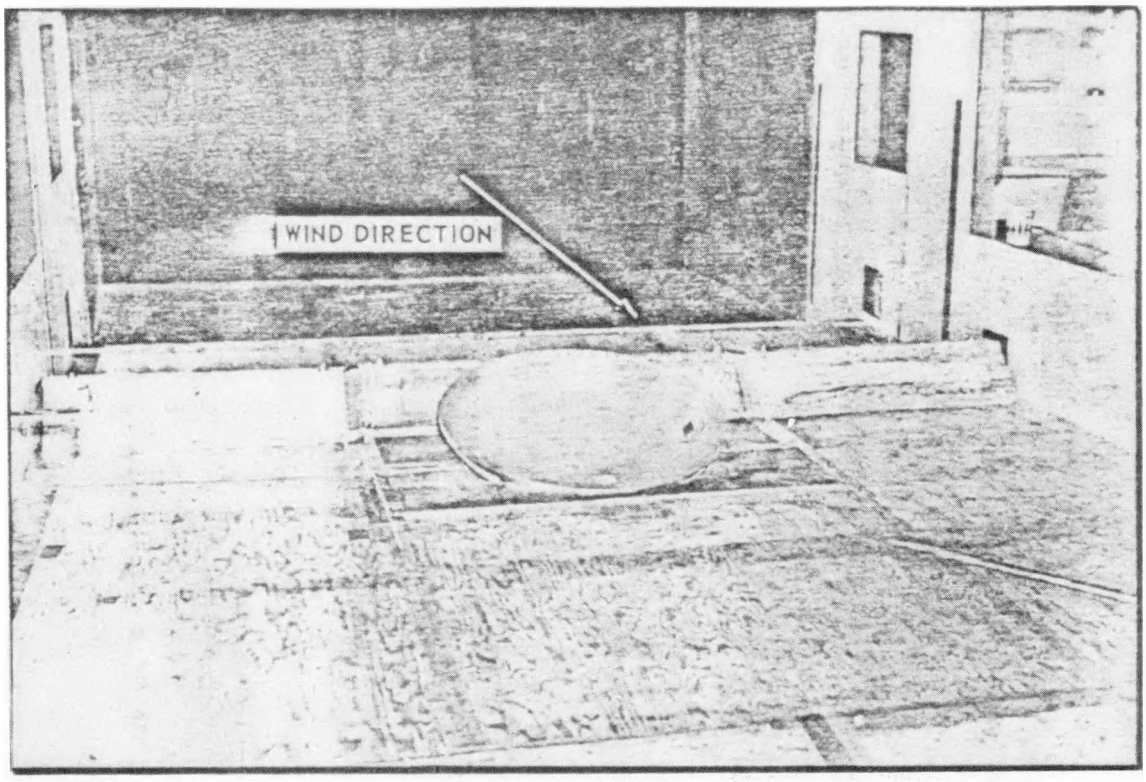

(a)

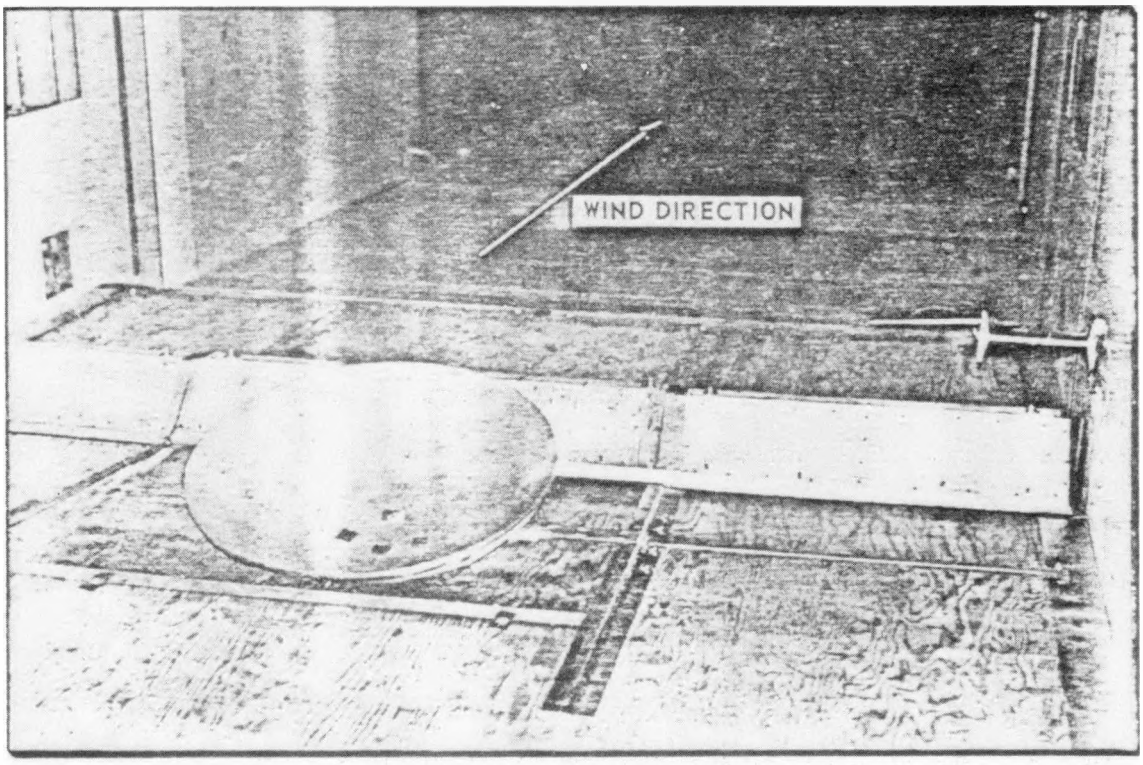

(b)

E-SYSTEMS
Energy Technology Center

Figure L-2 Model with Ground Plane and Berm
(a) wind from north (b) from south

Comparison with Parabola

The calculated wind forces for the embedded concentrator showed close correlation with those calculated using surface pressure data obtained from tests of a parabolic antenna model (Ref. L-3). This parabolic data had been used previously to calculate the concentrator design loads prior to obtaining the shperical surface wind load data.

L-2 DISCUSSION

L-2.1 Description of Test

The test was run in the Vought Corporation Low-Speed Wind Tunnel at their Grand Prairie, Texas, facility on 9 through 10 May, 1977. It is thoroughly described in Vought Report No. LSWT 537 dated June, 1977 (Ref. L-2). Some of the description is repeated here to clarify the discussion of the analysis of the test results.

Model Description

The model is a spherical segment with a total included angle of 120°. The inside radius of curvature is 18.5 inches with the aperture diameter being 32 inches as shown in Fig. L-3. The spherical segment is fabricated from 0.216-inch thick steel. As shown in Fig. L-3, the spherical segment has a bracket for mounting directly to the wind tunnel balance. The spherical segment has 41 pressure taps on the inside surface and an equal number on the back surface. The taps were located along radial lines at 45 degree increments, starting with the north line, around the model. Each tap has a unique identification number.

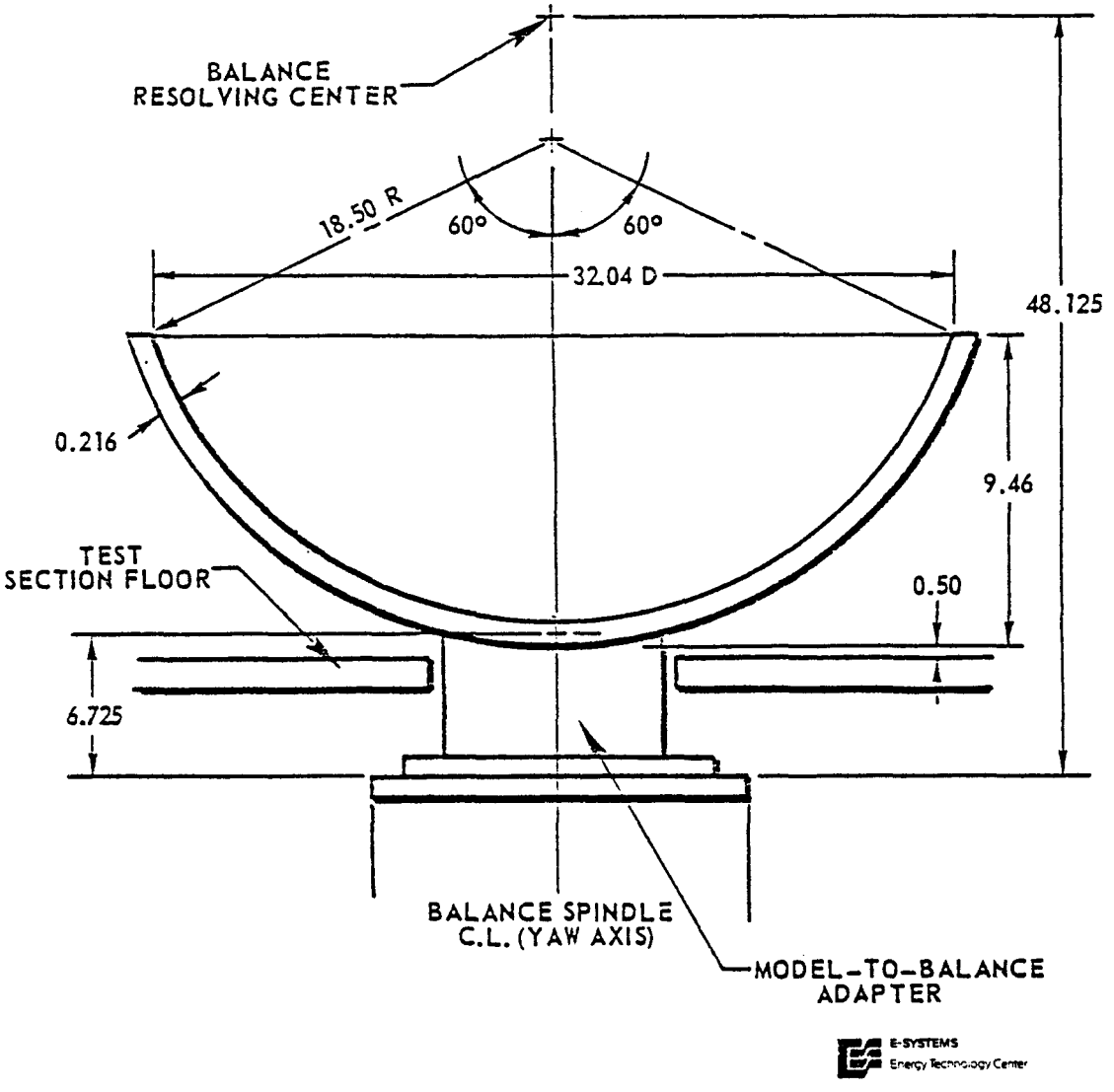

Figure L-3 Test Model Geometry

Test Procedures

The model was mounted in the test section to the external balance with an adapter designed to place the model 0.50 inches above the test section floor. The balance was offset to +90.0 degrees with respect to the test section centerline; this arrangement permitted the model to be yawed from 0.0 to -180.0 degrees.

The pressure tubing from the model was routed down through the external balance spindle (yaw axis) to the room balance and the pressure scanner unit.

Provisions were made in the model so that the tilt angle could be fixed at either 0.0, 15.0 or 30.0 degrees.

A pitot-static probe was installed in the test section forward of and above the model. The test section dynamic pressure at the model for the model alone was determined in the classical manner from the clear test section calibration. The relationship between dynamic pressure at the model and that indicated from the pitot-static probe was noted.

A ground plane was installed for a portion of the test in a manner to simulate the collector dish being placed in an excavation in the ground. The ground plane extended the full length and width of the test section and measured 5.90 inches from the test section floor to the top of the ground plane.

An earthen berm was also simulated downwind of the model and then again upwind of the model. The berm simulation extended the full width of the test section. Photographs of the model instal-

lation are presented as Figs. L-1 and L-2.

The tests were run for three different tilt angles: 0°, 15°, and 30°. For the latter tilt angles, the yaw angle was varied in 45° increments from 0 to 180°. The dynamic pressures were 10, 50 and 100 psf.

Nomenclature and Symbols

The nomenclature and symbols used for the force, moments and direction vectors followed normal aircraft practice. They are shown in Fig. L-4 and Table L-1 to help in the interpretation of the test results.

It should be noted while the force vectors follow the normal right hand rule the moment vectors do not. These same symbols are used in the test data tabulations.

L-2.2 Analyses of Wind Tunnels Test Data

The analyses of the test results proceeded along conventional lines. As previsouly noted, the objective was to determine the accuracy, the reliability, and the applicability of the data to the design of the concentrator.

Effect of Wind Velocity

The first step in the analysis study was to plot part of the surface pressure coefficients against the dynamic pressures

VI. NOMENCLATURE AND SYMBOLS (continued)

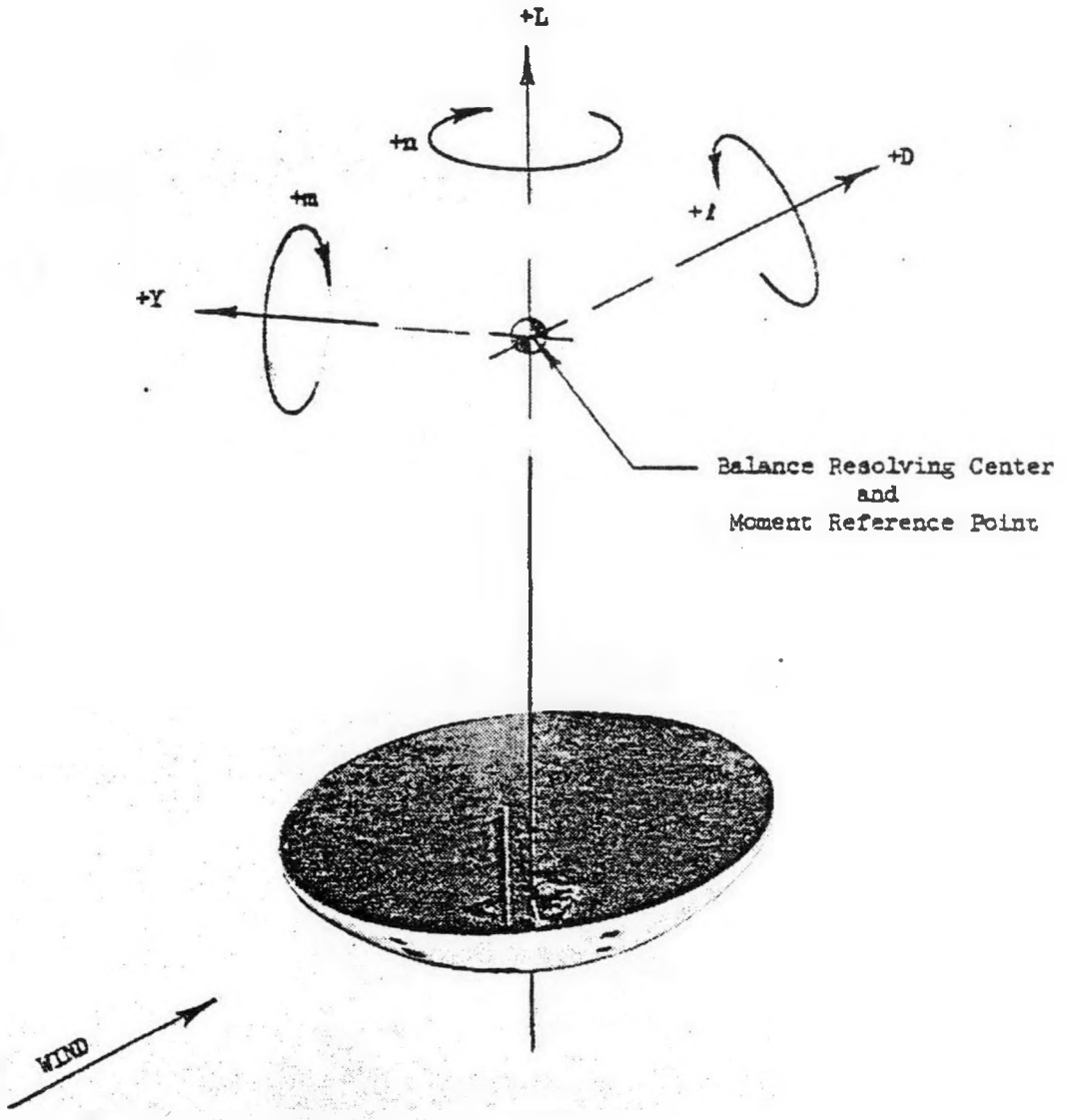

Figure L-4 Force and Moment Directions

VI. NOMENCLATURE AND SYMBOLS

Symbol	Definition
C_D	Wind axis drag coefficient
C_L	Wind axis lift coefficient
C_m	Wind axis pitching moment coefficient about the balance resolving center
C_n	Wind axis yawing moment coefficient about the balance resolving center
C_p	Pressure coefficient
C_{p_F}	Model inside pressure coefficient
C_{p_R}	Model outside pressure coefficient
ΔP	Measured pressure relative to atmospheric pressure
C_l	Wind axis rolling moment coefficient about balance resolving center
C_Y	Wind axis side force coefficient
D	Drag, pounds
L	Lift, pounds
m	Pitching moment, foot-pounds
n	Yawing moment, foot-pounds
l	Rolling moment, foot-pounds
Y	Side force, pounds
Ψ	Model angle of yaw, degrees
Θ_T	Tilt angle, degrees
q	Test section dynamic pressure corrected for solid and wake blockage and compressibility
q_{set}	Piezometer differential pressure used to monitor q, inches of water

VI. NOMENCLATURE AND SYMBOLS (continued)

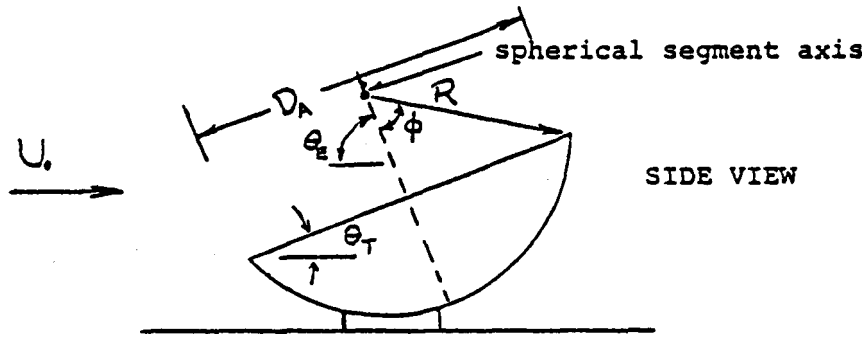

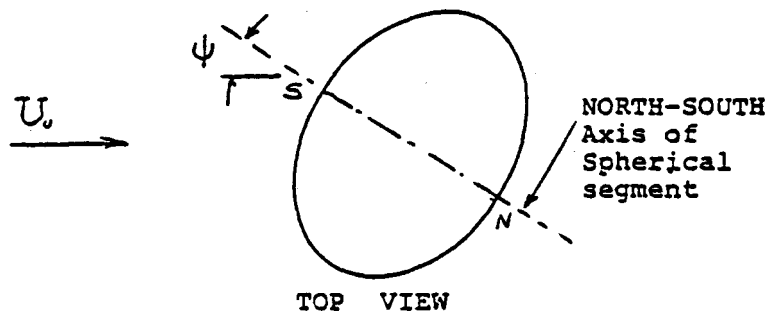

TOP VIEW

D_A = Aperture Diameter of segment

R = Radius of inside curvature

U_∞ = Main Stream Velocity

U = Local Velocity

θ_E = Elevation angle

θ_T = Tilt angle (Angle of Attack)

ψ = Azimuth or yaw angle

ϕ = Rim angle (Max Value = 60°, Included rim angle = 2ϕ = 120°)

of 10, 50, and 100 pound per square foot. Next the Coefficients of Drag, Lift and Side Force were plotted against the wind direction for the same pressures. These plots showed that the data were consistent and that there was a slight, constant increase in the coefficient values with an increase in wind speed (Reynolds Number effect). For the present purposes this effect was considered to be negligible for several reasons. First, the Reynolds Number for the actual structure was much higher than could be achieved in the wind tunnel, but it was felt there would be only a negligible increase in the values above those recorded for the 100 pound per square foot wind pressures. The surface pressure coefficients associated with the 100 psf pressure were therefore selected for use in calculating the concentrator wind loads. Second, the use of the higher surface pressure coefficient values for the lower full-scale wind velocities would be conservative in calculating the optical errors due to structural deflections of the full-scale concentrator.

Comparison of Different Test Configurations

Comparisons of the Drag, Lift and Side Force coefficients for the various concentrator test configurations were made by plotting these coefficients against wind direction. These are shown in Fig L-5. These configurations were: the above-ground concentrator with no tilt, with 15 degree tilt; a concentrator with a ground plane (simulating a partially embedded concentrator); and a concentrator with a ground plane and berm. The wind force coefficients for a

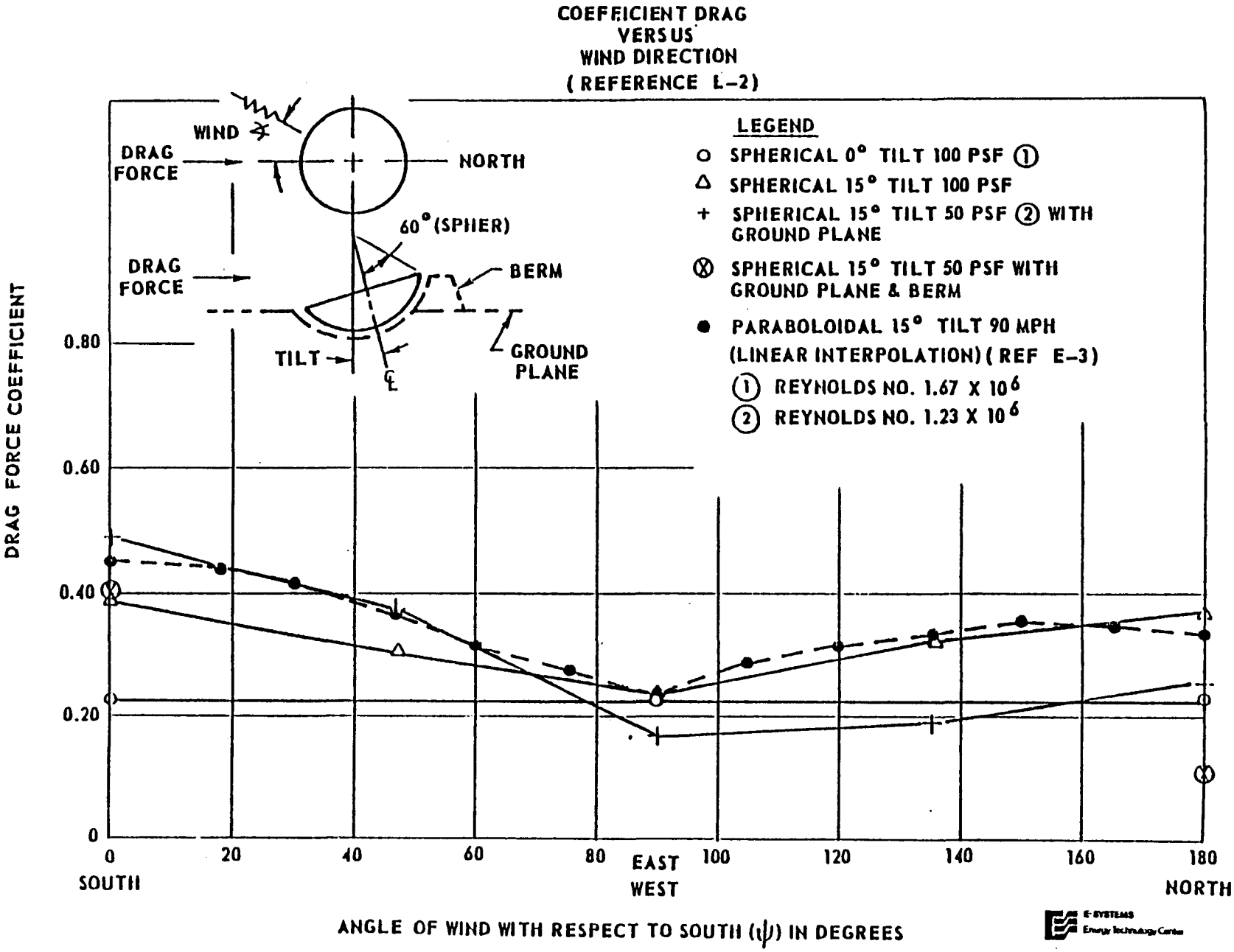

Figure L-5 Comparison of Test Configurations 1 of 2

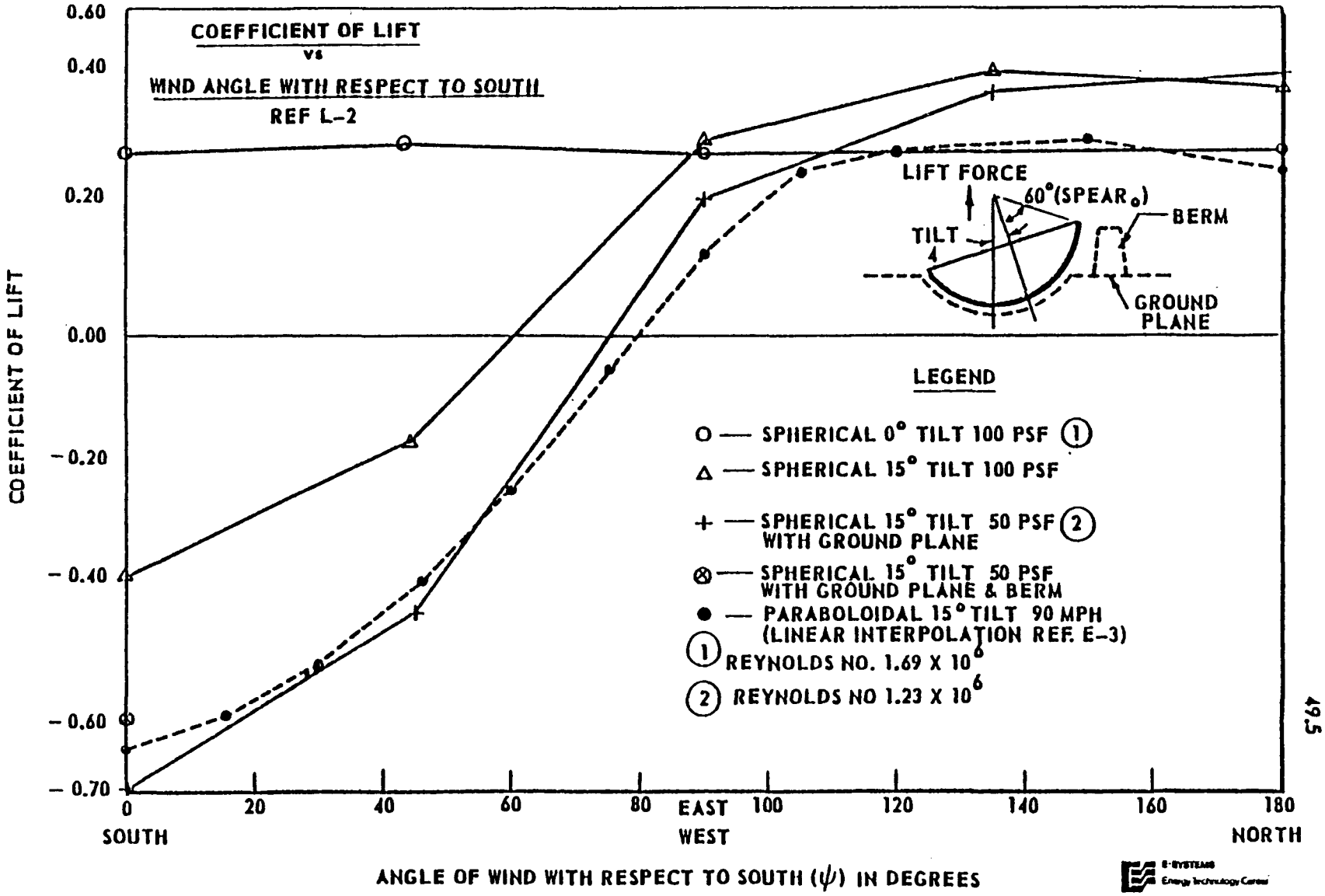

Figure L-5. Comparison of Test Configurations 2 of 2

similarly proportioned parabolic antenna (Ref. L-3) were also plotted on the same chart.

The results were not exactly what might have been anticipated. The concentrator with the ground plane and 15 degree tilt generally had higher wind force coefficients than the fully exposed model with the 15 degree tilt. It appears that the fully exposed concentrator represents a more streamlined shape since air flows completely around it. The concentrator that is only partially exposed develops some abrupt changes in air flow paths at the intersection of the ground plane and concentrator shell. Also the leading edge of the ground plane and concentrator used in the test probe appears to create a slightly different streamline flow than thought with the clean test section.

The parabolic antenna data were very close to that obtained for the partially exposed concentrator. It was expected that the curves would be similar but with a greater difference in values. Since the parabolic data were used in the initial design, it was fortunate they were so close since it minimized the amount of structural redesign required.

Effect of Berm

The effect of the berm could be tested only for wind from the south and from the north. It reduced the drag force when the wind was from the north but only slightly when the wind was from the south. It had very little effect on lift or crosswind forces (see Fig. L-5).

Review of Test Data

It is difficult to establish just how accurately the wind tunnel test duplicates the actual structure. However, it is thought that the full-scale concentrator surface pressure coefficients would be equal to or less than those measured on the model.

The model boundary layer velocity profile parallels and is slightly higher than that given in Ref. L-4 for heights up to approximately 30 feet above the ground, and averages a little lower between 30 feet and top of concentrator. Since there is more concentrator structure located below the 30 feet elevation than above, these difference should come close to cancelling one another. For the above reasons it is felt that the model wind pressure distribution approximately duplicates those applied to the full-scale structure.

Surface Pressure Patterns

Surface pressure data was examined by making contour plots of the surface pressure coefficients. The surface pressure data was first processed by a computer using a computer program which used curve fitting techniques to generate the contour data. The data were transferred to the magnetic plot tapes for use by the Calcomp plotter.

A typical plot is shown in Fig. L-6. Due to the expense, only the most useful sets of data were plotted. To check the Calcomp plots, contours of surface pressure coefficients

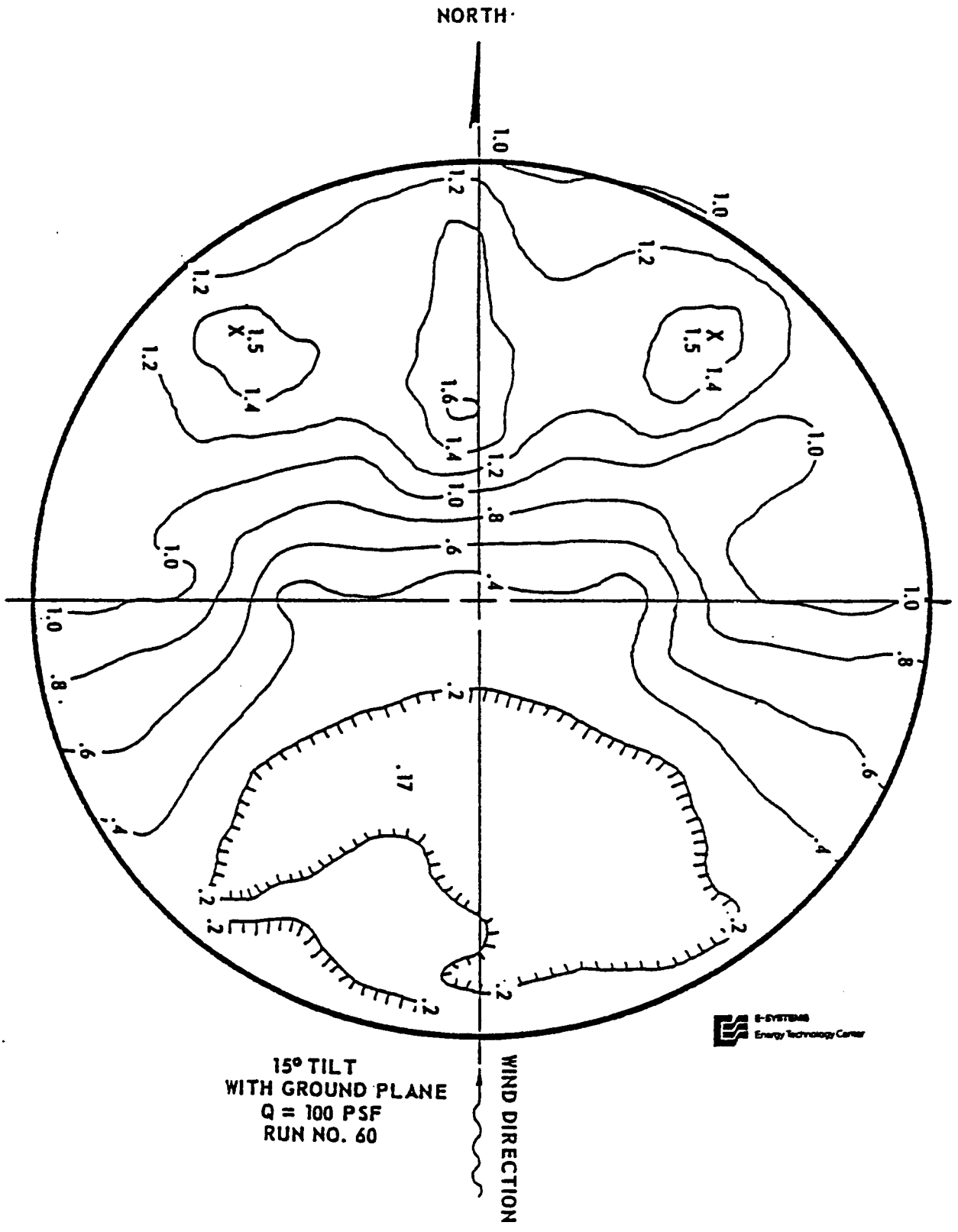

Figure L-6. Contour Plots - Surface Pressure Coefficient

obtained during test run No. 60 were drawn manually and are shown on Fig. L-7. This compares favorably with Fig. L-6 which is the same data drawn by the plotter.

Surface Pressure Charts

An existing antenna airloads program was modified to print the surface pressure coefficients in an array similar to the pressure tap configuration. This gave a better idea of the pressure distribution over the concentrator face. These plots are included in Ref. L-5.

There were apparently a few anomalies in the test data. One was in the test run with the berm, test run No. 43. This point was adjusted and the model airloads rerun. Certain other pressure tap readings were suspect but it was thought that the errors were random and would tend to average out; therefore the data was left unchanged.

Calculation of Wind Forces

The same airloads program used to plot the surface pressure coefficient charts was used to compute the concentrator wind forces using only surface pressure coefficient data.

In the computer model the concentrator wind tunnel model surface was divided into 48 panels. The outer 40 are approximately equal in surface area and were each centered on a pressure tap. The inner 8 are triangularly shaped and each contains approximately 1/7

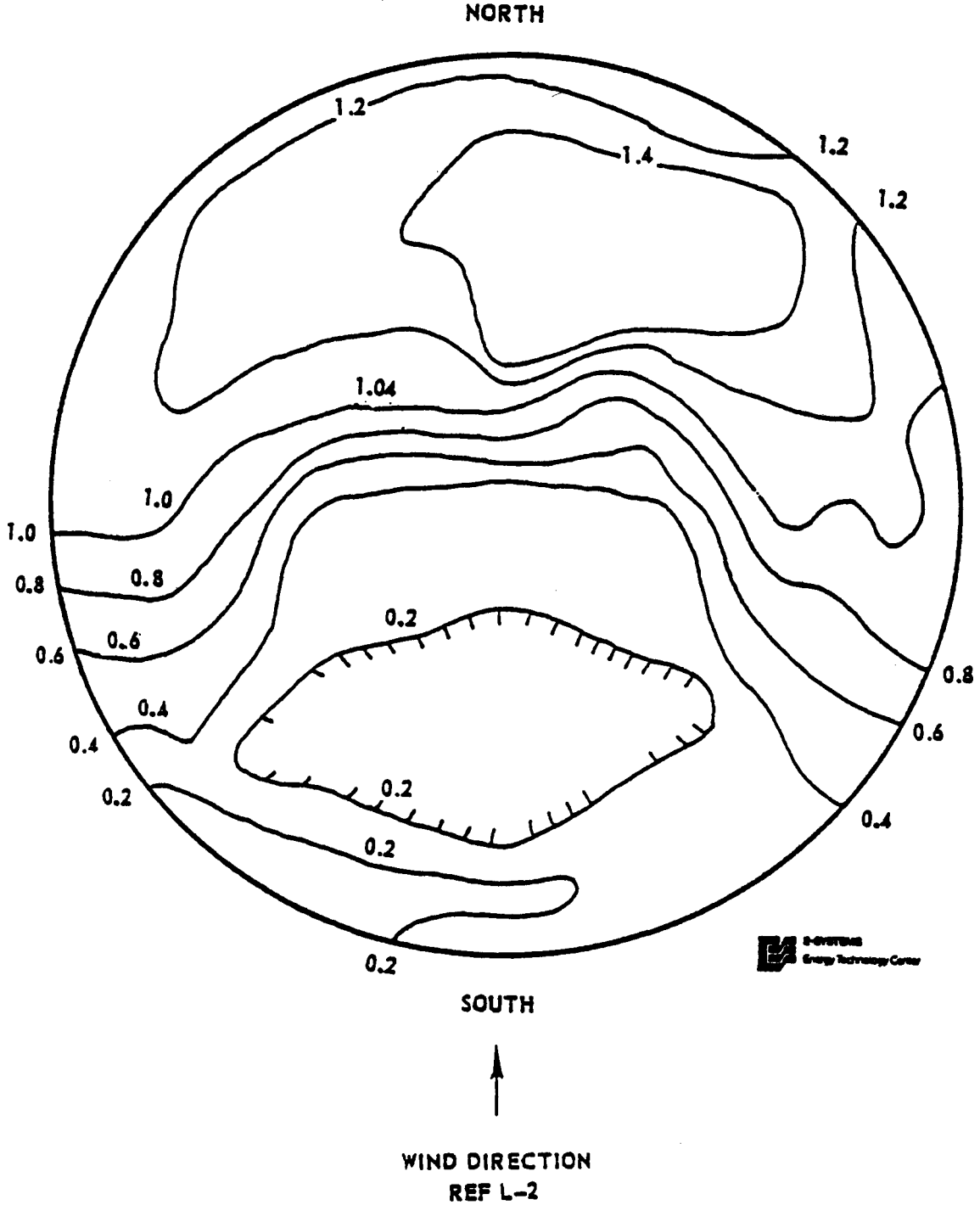

Figure L-7. Manual Contour Plot

the area of the outer ones, and were symmetrically located with respect to, but not centered on, a pressure tap.

The pressure coefficient data used in the airloads program were modified slightly by using the average value of symmetrically located pressure taps. That is taps that were mirror image with respect to both structure and wind direction were averaged. Only the data for wind from the south or north could be treated in this fashion. Data for all other wind azimuth angles were used unchanged.

Computer Program Description

The computer program read in the joint coordinates, and panel identification data from cards, and the surface pressure and wind force data directly from the tapes generated by the wind tunnel computer during the test. It then computed the panel areas and their centers of gravity, then interpolated the surface pressure data to derive the surface pressure coefficients at the center of gravity of the panels. It multiplied the pressure coefficient by the surface area of the panel to establish the panel normal wind load. This load was distributed equally to the four corners and resolved into x, y, and z force components. These components were summed and then resolved into the wind axis forces of drag, lift and side force. The wind moments about the wind tunnel balance center were also computed. These computed forces and moments were listed along with the measured ones. These results are available as a listing of the surface pressure coefficients.

Airloads Program Accuracy

Next a check was made to determine the accuracy of the computer program used to calculate the airloads for the structural analysis. This was done by using the surface pressure coefficients calculated by it, for each panel, to plot the surface pressure coefficient contours. These are shown on Fig. L-8. These contours compare favorably with those of Fig. L-6. It was therefore thought that the wind load program satisfactorily computed the wind loads.

Comparison of Calculated and Measured Wind Forces

The calculated and measured wind force coefficients were plotted to obtain a direct comparison. A typical plot for the lift is shown in Fig. L-9. Only the data for the exposed and recessed configuration with the 15 degree tilts were comapred as they were the only ones of interest in this study.

When reviewing the plots, it was found that generally the computed drag was lower than the measured, the computed lift was higher than the measured, the side force approximately the same as the measured for both the model with and without the ground planes.

The large hub used to support the test model and the sizable bundle of tubes used to transfer the surface pressures to the test transducers created higher measured drag forces, particularly for the all above-grade structure. The low calculated drag forces can be therefore explained since the skin friction drag and drag of

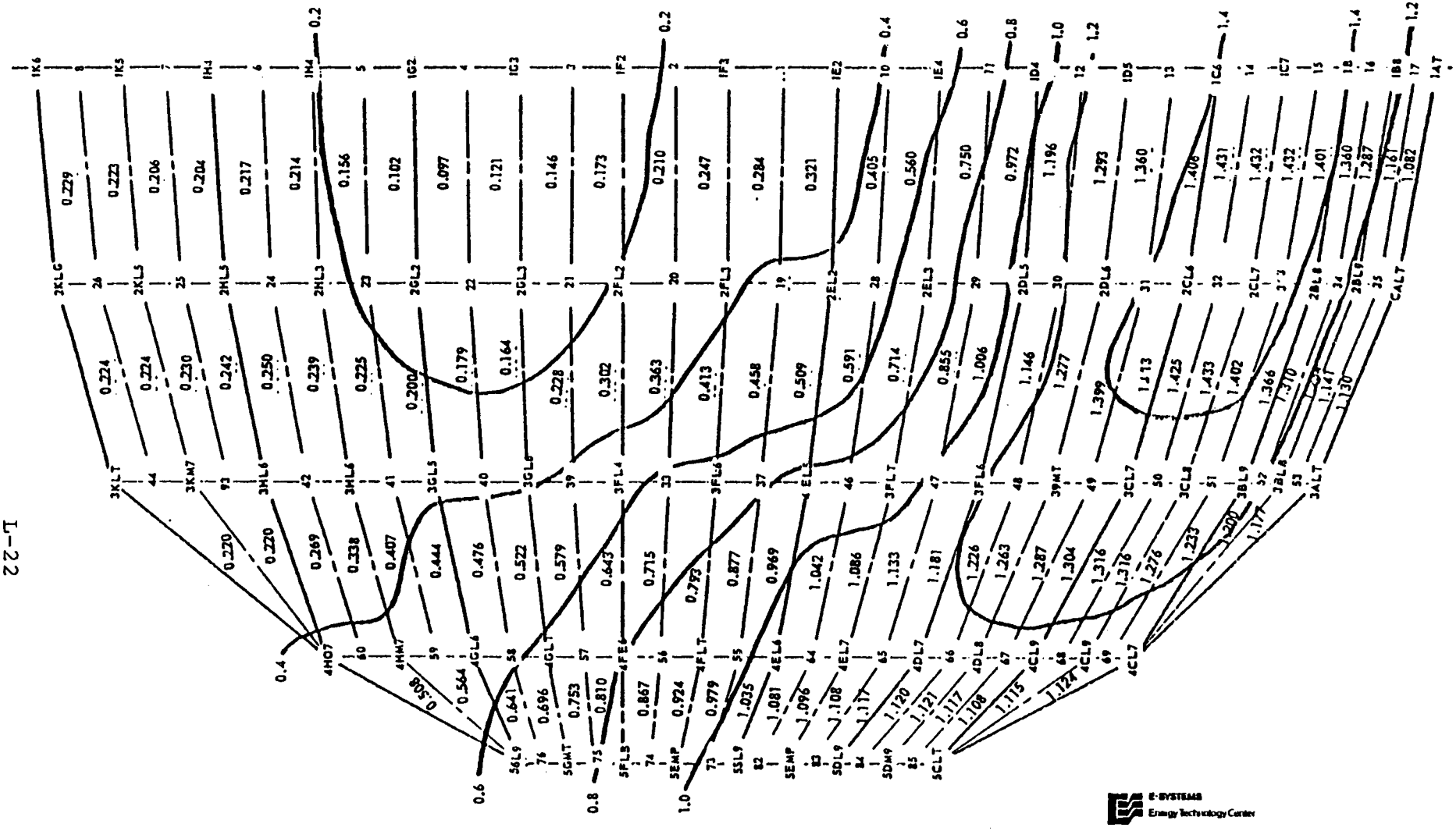

Figure L-8. Surface Pressure Contour

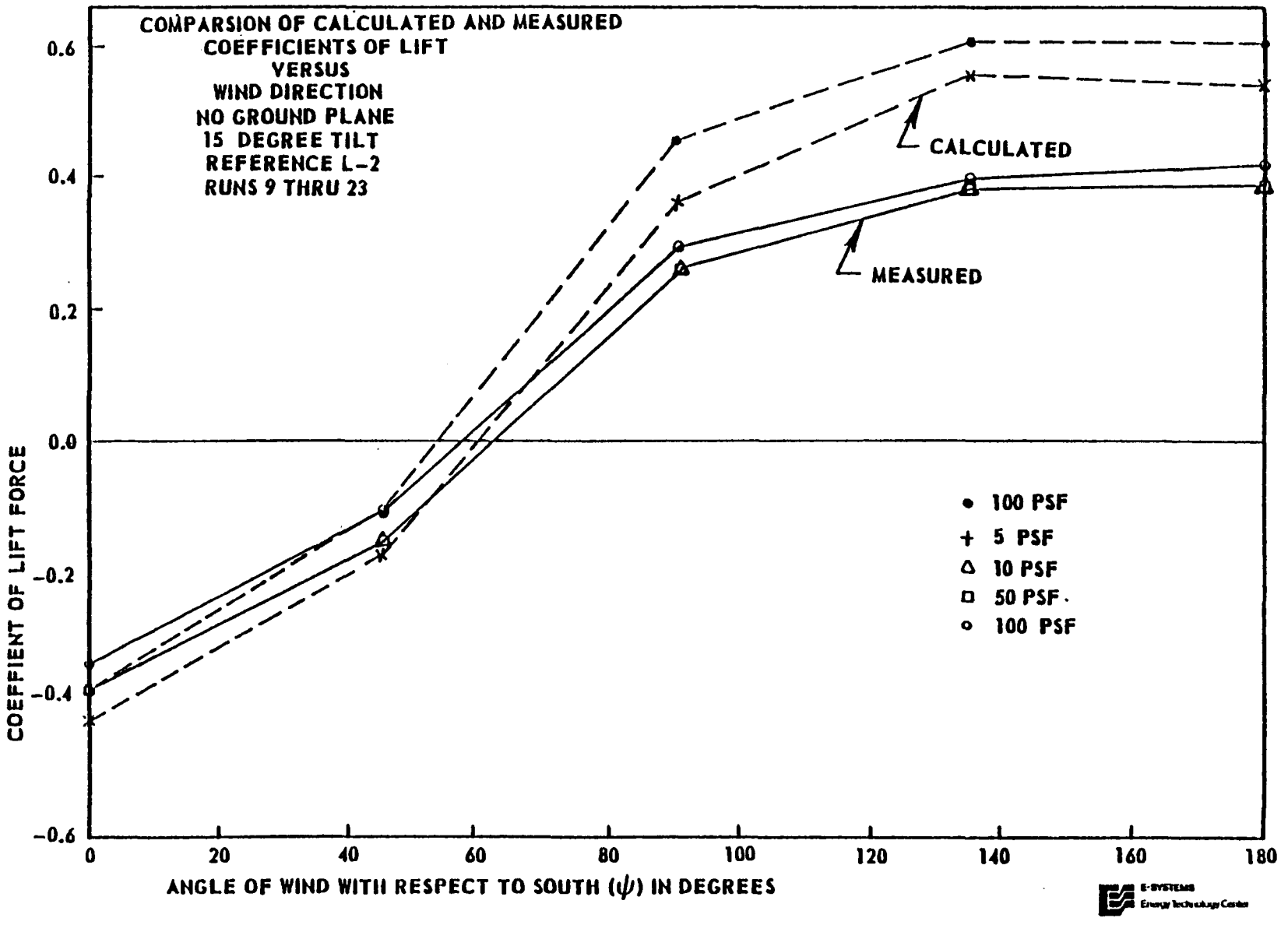

Figure L-9. Wind Force Coefficients

the concentrator model support hub are not a function of the surface pressures measured at the concentrator surface. Therefore, their effect would not be included in the calculated values since the computer program used only the concentrator surface pressures in calculating the wind forces and moments acting on the concentrator.

The results of the calculated and measured wind forces were also compared. It was found that they deviated less from one another than the drag and lift components since it is a sum of balancing forces on the model.

L-3 APPLICABILITY OF TEST RESULTS TO ACTUAL STRUCTURES

After reviewing the raw wind tunnel data and the results of the analyses, it was concluded that the measured surface pressure coefficient data could be used to develop realistic wind loads for the concentrator structure. The rationale for this conclusion follows.

L-3.1 Surface Pressure Effects

The surface pressure data was fairly accurate and provides the actual loads applied to the panels and panel support structure. Since analyses of the concentrator structure shows that the deflection of this portion of the concentrator structure generates the largest surface deviation, using the data gives the most realistic surface deviation error values.

L-3.2 Wind Forces

While the measured drag forces are higher than the calculated, it is felt that the wind forces produced by the actual members supporting the full-size concentrator would be lower than those measured on the model with the hub since their cross sections are proportionately much smaller than the support hub of the model. Many of the actual support members are in the wind shadow of the surface panels, therefore would have a minimal effect. There is very little data available on the effect of shielding on a structure as complex as the concentrator; however, based on experience with similar structures it is expected the drag of support members would be less than 5% of total drag.

The fact that the calculated resultant wind forces for the embedded concentrator are equal or higher than the measured is an indication that the total design load applied to the concentrator structure will equal or exceed the actual wind loads.

The effect of higher calculated lift values is to apply greater loads to the concentrator panel support beams and equal or higher loads to the columns. Bracing loads are lower due to the lower calculated drag loads. However, the analyses of the concentrator structures shows that the beams and columns are the critically stressed members, while the stress levels in the braces are low. This is due to the fact the sizes of the bracing members are usually dictated by elastic stability requirements rather than stress levels. Also the loads tend to redistribute themselves throughout the structure.

There should not be any significant differences between the calculated and actual member stress levels.

For the reasons previously enumerated it is felt that the use of the test surface wind pressure coefficients obtained in the wind tests to calculate the design wind loads will yield wind loads that are of the right order of magnitude and on the conservative side.

L-4 DESIGN SURFACE PRESSURES

On the basis of data in American National Standard, ANSI A58.1-1972, Ref. L-6, it was decided that a 90 mph survival wind at -10°F was adequate. This gave a basic dynamic wind pressure of 23.9 pounds per square foot. No gust factor was used since data from Ref. L-4 indicated that the gust velocities would be only approximately 10% higher than the steady wind velocity at midheight of the 200 ft. concentrator.

The design pressures given in American National Standard ANSI A58.1-1972 Building Code Requirements for Minimum Design Loads in Buildings and Other Structures (Ref. L-6) was compared to the dynamic wind pressure loading on the concentrator. It was noted that for flat, open terrain they are higher than those used in the analyses. They contain gust factors which bring the actual wind speed up to 109 mph. This is very conservative when compared to the data from Ref. L-4.

The gust length must be greater than eight times the length of the structure before the structure can feel the full effect of the gust. For the 200 ft. concentrator this would correspond to

a 99 mph gust lasting approximately 11 seconds. There is only a 10% probability of such a gust under the most extreme climatic conditions according to Ref. L-4. It was felt that this could be disregarded during the preliminary design stage.

L-5 RECEIVER THERMAL LOSS TEST

L-5.1 Description of Test

A thermal loss test of a scale model receiver was performed to provide a firm empirical base for receiver heat loss calculations. This test was performed in the LTV los speed wind tunnel (wind velocities less than 240 mph) at Grand Prairie, Texas. Wind velocity and direction relative to the concentrator/receiver model, air temperature and pressure, and power input to and temperature of receiver model were measured and recorded during the experiment. Data was first obtained with air flow normal to the model receiver so that the results could be compared with literature values. These tests varied receiver surface temperature and air velocity. Good comparison with literature values was obtained, providing confidence in the experimental technique and equipment. The model receiver was next positioned in the concentrator model and data obtained for different wind directions and velocities was nearly constant receiver surface temperature.

Model Description

The model used for the receiver thermal loss test was a 1/75th scale conical receiver model designed to the same scale as the

concentrator assembly model. The model is 9.25 inches long with a diameter of .28 inches at the base and narrows to .12 inches at the tip. The receiver conical shape was machined from carbon steel. The receiver was then wrapped with 30 AWG insulated wire to provide the necessary heating element. The model receiver was finally instrumented with thermocouples and covered with a low emittance thin aluminum adhesive-backed film. Three thermocouples were positioned directly under the aluminum film but exterior the wrapped wire, spaced along the receiver length and radially around it. These thermocouples were used to determine the receiver surface temperature. An additional thermocouple was imbedded within the wire wrap next to the metal cone to measure the receiver core temperature. Monitoring of the core temperature helped prevent the use of excessive energy fluxes that could overheat and damage the wire insulation. The ends of the receiver were insulated with molded high temperature epoxy to reduce end heatloss from the heated receiver model.

Test Procedures

Parameters varied were wind direction relative to concentrator, wind speed, receiver temperature, and receiver location within concentrator. Test were also run with flow normal to the receiver in order to establish the reliability of the measureing technique and to provide a basis of comparison for the heat loss for a receiver installed in a concentrator

Data Reduction

Data analysis involved determination of the experimental Reynolds and Nusselt numbers, correlating these dimensionless parameters, and calculating the experimental uncertainty in the results. The Reynolds number, Re, and Nusselt number, Nu, were calculated from:

$$Re = \frac{V_\infty D_o}{v_f}$$

and $$Nu = \frac{h_o D_o}{k_f}$$, respectively,

where V_∞ = free stream air velocity, ft/sec.

D_o = mean receiver diameter, ft

v_f = kinematic viscosity of air at mean film temperature ft^2/sec

h_o = convective heat transfer coefficient, $Btu/hr\text{-}ft^2\text{-}F°$

k_f = thermal conductivity of air at mean film temperature, $Btu/hr\text{-}ft\text{-}°F$

The mean receiver diameter was used for all data correlation and was determined from the measured receiver length and exposed surface area (area of aluminum foil covering). This method of diameter determination was used since the surface thermocouples provided surface protrusions of about 10% of the mean diameter, thus causing direct diameter measurement impractical.

The free stream air velocity was calculated from wind tunnel data measurements of free stream air temperature, absolute pressure, and effective wind stagnation pressure (pitot tube measure-

ment). The convective heat transfer coefficient was determined from solution of the equation of heat transfer between the receiver model surface and air stream. Since energy exchange rate (power input) and surface temperature were known, calculation of the convective heat transfer coefficient was straight forward. However, the measured power input was corrected for radiation heatloss and heatloss of the lead-in wires while the surface temperature was adjusted for the effects of the aluminum covering adhesive thickness.

L-6 TEST RESULTS

L-6.1 Receiver Normal to Air Flow

Close agreement with reported literature results of Hilpert for flow normal to a cylinder was obtained. Error analysis indicated an experimental uncertainty interval of only four to five percent of the measured Nusselt number. Results are presented in Fig. L-10 where Nusselt number is plotted as a function of Reynolds number. At a fixed Reynolds number corresponding to the receiver positioned in the concentrator the Nusselt number is always less than the resulting Nusselt number for flow normal to the receiver. Thus, for a given wind velocity, the receiver thermal loss is always less when the receiver is positioned in the concentrator compared to flow directly normal to the receiver.

L-6.2 Concentrator/Receiver Results

The results of the wind tunnel heatloss calculations are listed in Table L-2. All data was obtained for wind velocities of about

Figure L-10. Nusselt Number vs. Reynolds Number

Data Based on Mean Diameter of Conical Receiver and Mean Film Temperature

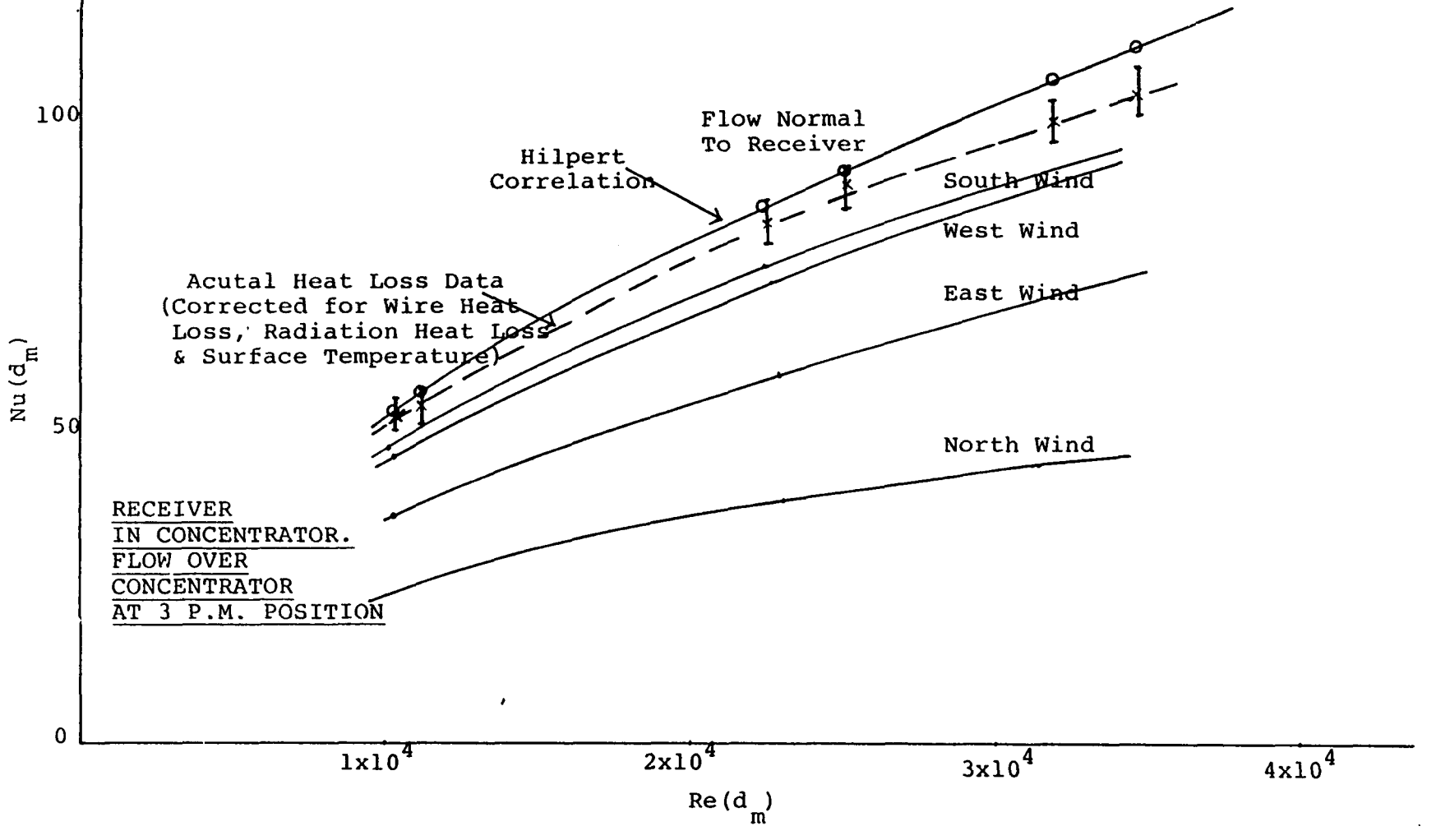

90 - 300 fps resulting in Reynolds numbers of 10,000 to 33,000. All calculated Nusselt numbers had a resulting experimental uncertainty error of 3.9 to 5.3 percent, being lower at the igher Nusselt numbers. This error band is represented in Fig. L-10 for the case of air flow normal to the receiver. However, this band exists for all the experimental data points.

Heat transfer theory indicates a correlation between Nusselt, Prandtl and Reynolds numbers in the form:

$$Nu = k_1 \, re^{k_2} \, Pr^{k_3}$$

where Pr represents Prandtl number. Experimental verification of this relationship with Prandtl number was not possible since Prandtl number varied less than 0.5% (even though surface temperature was varied by as much at 60°F). However, the Prandtl number exponent based on theory is about 0.4 so this value was used for k_3. Further analytical investigation revealed that the Reynolds number exponent, k_2, was constant and independent of wind direction. This was true for all receiver positions as well as for air flow normal to the receiver. The Reynolds number exponent was determined to be 0.586. The constant, k_1, necessary to satisfy the above equation is shown in Fig. L-11 as a function of wind direction for a 3pm receiver position. The corresponding Nusselt numbers for Reynolds numbers of 10,000 and 30,000 are also shown. The maximum Nusselt number (and corresponding constant k_1) occurs with a southwest wind with about a two fold increase from its minimum to maximum value. Table L-3 presents the value of con-

FIGURE L- 11

NUSSELT NUMBER VS. WIND

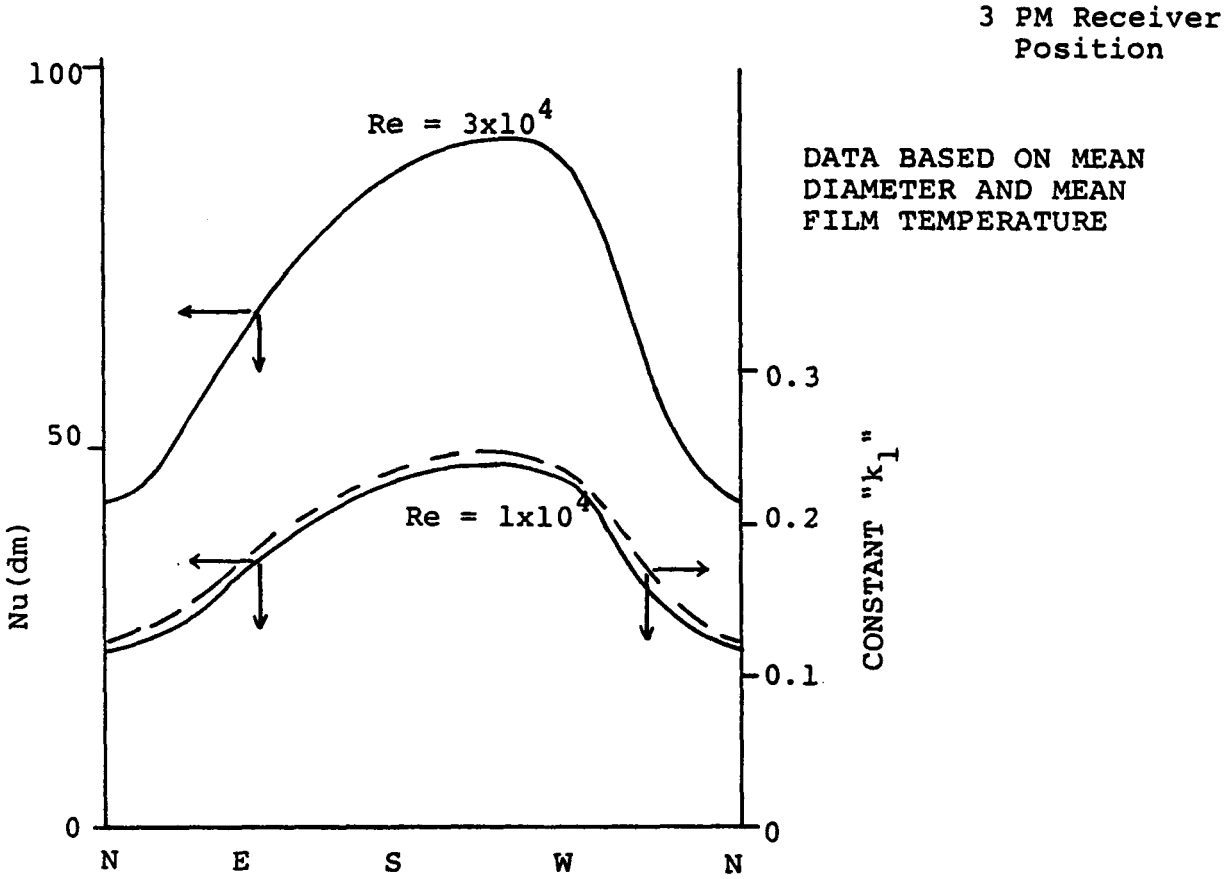

$$Nu = k_1 (Re)^{0.586} (Pr)^{0.4}$$

#	°F T_Δ	fps V_∞	°F T_{AVE}	°F T_∞	Watts * P_M	Watts * P_W	°F ΔT_{skin}	°F T_S	Watts P_R	°F T_f	$\frac{ft^2}{sec \times 10^4}$ ν_f	$\frac{Btu}{hr\text{-}ft^2\text{-}°F}$ k_f	Re/ft	$\bar{Nu}$
S1	351	94.69	250	85	94	5.38	7.1	242.9	.87	164	2.18	.0170	1.01	46
S2	417	212.71	261	90	152	8.20	11.5	249.5	.90	170	2.21	.0171	2.24	75
S3	459	301.64	267	93	184	9.60	14.0	253.0	.92	173	2.23	.0172	3.14	90
W1	302	94.69	236	85	83	5.02	6.2	229.8	.77	157	2.13	.0168	1.03	45
W2	372	212.71	251	90	138	7.77	10.4	240.6	.83	165	2.18	.0170	2.27	76
W3	388	300.32	246	90	162	8.98	12.2	233.8	.78	162	2.16	.0169	3.24	65
N1	276	94.69	245	85	47	2.93	3.5	241.5	.86	163	2.17	.0170	1.01	23
N2	302	212.32	238	88	71	4.31	5.3	232.7	.78	160	2.15	.0169	2.30	33
N3	339	300.82	264	90	94	5.48	7.1	256.9	.96	173	2.23	.0172	3.14	43
E1	317	24.0	240	77	72	4.24	5.4	234.6	.83	156	2.13	.0168	1.03	38
E2	370	210.38	247	78	117	6.52	8.8	238.2	.86	158	2.14	.0169	2.29	53
E3	400	292.76	251	82.5	114	7.67	10.7	240.3	.86	161	2.15	.0169	3.23	77

D_o = .279"

t = .0015"

*Resistance Radio Method

TABLE L-2 MODEL RECEIVER WINDTUNNEL HEATLOSS DATA AND RESULTS

stant k_1 for the experimental correlation between the mean Nusselt and Reynolds numbers based on the wind tunnel heatloss data. Thus, $Nu = k_1 \, Re^{0.586} \, Pr^{0.4}$ provides correlation within the experimental uncertainty error of the Nusselt number for the Reynolds number range 10,000 to 35,000 where only k_1 is a function of receiver position and wind direction.

TABLE L-3

WIND TUNNEL DATA CORRELATION

$$Nu = k_1 (Re)^{0.586} (Pr)^{0.4}$$

$$k_1 = f(\text{Wind Direction})$$

k_1	DIRECTION
0.120	N
0.186	E
0.233	W
0.243	S
0.263	Normal

Agreement at all points in Re Range ($1x10^4 \rightarrow 3.5x10^4$) within experimental error.

REFERENCES - APPENDIX L

L-1. Walters, R. R., "Test Plan for Wind Tunnel Tests of a Fixed Mirror Distributed Focus Solar Collector Model," E-Systems, Energy Technology Center, April 1977.

L-2. Holbrook, J. W., "Low Speed Wind Tunnel Test of 1/75 Scale Fixed Mirror Distributed Focus Solar Collector," Report LSWT 537 Vought Corporation, Dallas, TX, May 1977.

L-3. "Air Loads and Pressure Distribution on a Parabolic Antenna Model," M.I.T. Lincoln Lab Report 71C-5 November, 1962.

L-4. Climatic Extremes for Military Equipment, MIL-STD-210B.

L-5. Sheard, W. B., "Tabulations of Pressure Distributions on Spherical Fixed Mirrored Distributed Focus Solar Collector," E-Systems, Energy Technology Center, July 1977.

L-6. Building Code Requirements for Minimum Design Loads in Buildings and Other Structures, ANSI A58.1-1972, American National Standards Institute, pp. 21-22.

☆U.S. GOVERNMENT PRINTING OFFICE: 1984- 746-081/2316 REGION NO. 4